# NUMERICAL SIMULATION OF THE FLOW IN MODEL SKELETAL MUSCLE VENTRICLES

by

Francesca Iudicello

A dissertation submitted to
City University
in fulfilment of the requirement
for the degree of
Doctor of Philosophy

November 1995

Department of Mechanical Engineering & Aeronautics
City University
London

TO MY HUSBAND

# TABLE OF CONTENTS

Page

Page

## LIST OF TABLES

## LIST OF FIGURES

Figure 4.2 Streamlines. (a) Contracting pipe ($\alpha = -1$). (b) Expanding pipe ($\alpha = 1$). From Uchida and Aoki (1977).

Figure 4.3 Distributions of axial velocity ((a) and (b)), and radial velocity ((c) and (d)). (a) and (c) Contracting pipes. (b) and (d) expanding pipes. From Uchida and Aoki (1977).

Figure 4.4 Grid used to model the semi-infinite pipe.

Figure 4.5 Comparisons of the distributions of (a) axial and (b) radial velocities. Expansion at $Re = 0.1$. Single-block version.

Figure 4.6 Comparisons of the distributions of(a) axial and (b) radial velocities. Contraction at $Re = 10$. Single-block version.

Figure 4.7 Comparisons of the distributions of(a) axial and (b) radial velocities. Expansion at $Re = 1.67$. Single-block version.

Figure 4.8(a) Comparisons of the distributions of (a) axial and (b) radial velocities. Expansion at $Re = 1.67$. DT = 5 ms. Single-block version.

Figure 4.8(b) Comparisons of the distributions of (a) axial and (b) radial velocities. Expansion at $Re = 1.67$. Simulation time 2 s. Single-block version.

Figure 4.8(c) Comparisons of the distributions of (a) axial and (b) radial velocities. Expansion at $Re = 1.67$. Simulation time 3 s. Single-block version.

Figure 4.8(d) Comparisons of the distributions of (a) axial and (b) radial velocities. Expansion at $Re = 1.67$. Simulation time 3 s. DT= 5 ms. Single-block version.

Figure 4.9(a) Comparisons of the distributions of (a) axial and (b) radial velocities. Expansion at $Re = 0.1$. Multi-block version.

Figure 4.9(b) Comparisons of the distributions of (a) axial and (b) radial velocities. Contraction at $Re = 10$. Multi-block version.

Figure 4.10 Comparisons of the distributions of (a) axial and (b) radial velocities. Expansion at $Re = 1.67$. Multi-block version.

Figure 4.11 Comparisons of the distributions of (a) axial and (b) radial velocities. Expansion at $Re = 1.67$. Simulation time 2 s. Multi-block version.

Figure 4.12 Comparisons of the distributions of (a) axial and (b) radial velocities. Expansion at $Re = 1.67$. Simulation time 3 s. Multi-block version.

Figure 4.13 Comparisons of the distributions of (a) axial and (b) radial velocities. Expansion at $Re = 1.67$. Simulation time 3 s. DT= 5 ms. Multi-block version.

Figure 5.1 *In vitro* model SMV

Figure 5.2 Simple rigid/compliant model ($L_{ventricle} = 3 \times R_{inlet}$)

Figure 5.3 Flow structure predicted at the maximum volume for the simple rigid/compliant model ($L_{ventricle} = 3 \times R_{inlet}$)

Figure 5.4 Simple rigid/compliant model ($L_{ventricle} = 6 \times R_{inlet}$)

## ACKNOWLEDGEMENTS

I wish to express my sincere gratitude to the British Heart Foundation for funding this project.

I wish also to thank my supervisor Prof. M.W. Collins for the guidance and advice he generously provided throughout this project.

My sincere thanks go to Dr. F.S. Henry for his valuable consistent help and advice, particularly on the numerical techniques.

I would like to thank Drs. A. Shortland, R. Black, J. Jarvis and, in particular, Prof. S. Salmons for their many helpful suggestions and discussions in the course of the project. Special thanks to Dr. A. Shortland for his help in the use of the experimental data, and to Dr. J. Jarvis for his advice on various medical aspects.

I would also like to thank Dr. M. Ciofalo, University of Palermo, for some useful suggestions on numerical aspects.

Finally, I would like to thank my family for the encouregement and support they provided throughout the hard times of the project.

## DECLARATION

I grant powers of discretion to the University Librarian to allow the thesis to be copied in whole or in part without further reference to the author. This permission covers only single copies made for study purposes, subject to normal conditions of acknowledgement.

# ABSTRACT

Until recently, the only realistic form of treatment available to patients in end stage heart failure was transplantation. In the last few years, the possibility of diverting skeletal muscle from its normal function to perform a cardiac assist role has emerged as a potential alternative to transplant surgery. The introduction of an Skeletal Muscle Ventricle (SMV) to the circulation is a potential long-term hazard, as the patient's blood comes into contact with the non-endothelialised surfaces of the wall of the new ventricle and the connecting conduits. This may trigger a cascade of events leading to deposition of thrombus, whose formation is dependent on the nature of the blood flow. The potential problem of haemostasis may arise in the apex of the artificial ventricle, where little mixing and large residence times may occur. There is therefore a strong need for carrying out flow analysis studies to address in detail the questions of haemostasis and thrombogenesis and in this context to evaluate possible candidate SMV configurations.

Research on the dynamics of the flow inside model SMVs has been carried out on physical and numerical models with the objective of analysing the effect of the size and shape of the ventricle and inlet/outlet orientation of the duct. Due to the physiological limit on the power available to pump the blood out of the ventricle, the efficiency of these potential assistance devices has to be maximized. It is also necessary to minimize the risks of haemolysis and thrombogenesis, which are both related, in different ways, to the level of shear stress on the wall and within the flow. A common feature of these flows is the formation of vortex rings. Vortices enhance mixing, and this is a useful process to encourage in an SMV, as it could assist in the mixing of the blood components and in the reduction of apical residence time. Being able to predict accurately the dynamics of the vortices is therefore important, as this will affect the prediction of residence times and shear stresses at the wall and within the flow. It is also very important to know whether numerical codes can predict vortex ring dynamics from both qualitative and quantitative points of view.

In order to study the dynamics of the formation of these vortices, first, mathematical models were studied. The general purpose CFDS-FLOW3D code was used in all numerical simulations. Initial investigations of this research project concerned a progressive validation of the numerical solution predicted by the code when the domain where the flow is calculated had moving boundaries. Firstly, comparisons were made with the analytical solution for expanding/contracting pipes. An adapted compliant SMV model was then generated with a truncated apex using sinusoidally prescribed motion of the wall. With this model, two vortex rings could be predicted as in the experiments. The spherical-end model also gave good agreement with experimental flow patterns (Iudicello et al., 1994). Frequency-dependent studies were carried out over the range of cardiac values using single- and multi-block versions of the code.

A further validation exercise involved the use of sigmoidal filling curves in the *in vitro* models (Shortland et al., 1994). Experimental data provided by such studies were used to drive the wall motion in the numerical simulations, and parametric studies of several simulation parameters were carried out. Flow field features and trajectories of the vortex paths were compared with the experiments for different filling curves, with reasonable agreement. However, because shear stress discontinuities occurred in the predictions a strict volume-defined analytical model was constructed for wall movement with smooth spatial and temporal behaviour reproducing experimental filling curves. Numerical predictions showed not only an improvement in the qualitative features of the flow compared with the experiments, but also a quantitative improvement in the prediction of the vortex core paths. Also the shear stress discontinuities were no longer evident. In order to be able to estimate residence times, instantaneous streamlines and particle tracks were produced. Analysis of shear stresses in the fluid and generation of particle pathlines for residence calculation in 3-D geometries will be carried out in the next feature for model candidates for the final SMV design. Some of the material published during the course of the project is included in APPENDIX I.

In this thesis, attention is paid to the SMV fluid dynamics. However, SMV behaviour is a coupled fluid-solid problem. Future work will be carried out in the muscle modelling. To this end, a careful review has been carried out, and is included in the thesis. Implications for future work are also discussed.

## NOMENCLATURE

| | |
|---|---|
| **B** | body force |
| Cr | Courant number |
| E | energy or Young's modulus |
| F | force |
| $g_{ij}$ | metric tensor |
| $I_1$, $I_2$, $I_3$ | strain invariants |
| p | static pressure |
| P | muscle force or power |
| Pe | Peclet number |
| Q | volume flow rate |
| Re | Reynolds number |
| $S_{ij}$ | strain rate tensor or Kirchoff's stress tensor |
| t | time |
| T | cardiac period |
| $\Delta$T, DT | time step |
| **u** | velocity vector |
| u,v,w | velocity components |
| $v$ | muscle contraction velocity |
| W | work or strain energy function |
| $x_i$ | reference state coordinates |
| $y_i$ | deformed state coordinates |
| x,y,z | spatial coordinates in rectangular space systems |

### Greek Symbols

| | |
|---|---|
| $\dot{\gamma}$ | strain rate |
| $\Gamma$ | diffusion coefficient |
| $\delta_{ij}$ | Kronecker delta |
| $\zeta$ | vorticity function |
| $\lambda$ | thermal conductivity |
| $\mu$ | coefficient of dynamic viscosity |
| $\nu$ | coefficient of kinematic viscosity |
| $\xi$, $\eta$, $\zeta$ | curvilinear coordinates |
| $\rho$ | fluid density |
| $\sigma_{ij}$ | stress tensor |
| $\tau$ | shear stress |
| $\psi$ | stream function |

# CHAPTER 1

# INTRODUCTION

Heart desease is a major cause of mortality and morbidity in the Western World. For some years the surgical treatment of end-stage cardiac failure has been restricted to cardiac transplantation and the temporary use of mechanical assist devices as a bridge to transplant. The shortage of donors, problems of rejection, and high cost of the transplant programme severely limit the number of patients who can benefit from this treatment. In the United States, for example, only 10% of the estimated need for heart donors are available (Evans et al., 1986). Mechanical assistance, in the form of total artificial heart or ventricular assist devices has shown a degree of promise; however, because of the high incidence of infection and thromboembolic complications, these devices are currently limited to temporary support as a bridge to transplantation (Hill, 1988). There is therefore a strong case for seeking alternative therapeutic approaches that could be extended to a broader category of seriously affected patients. Research into the harnessing of skeletal muscle for cardiac assistance has an important part to play in the search for a practical surgical alternative for the large number of patients suffering cardiac failure.

In the area of cardiac assist device development, the overall significant challenge is to provide devices that have the requisite physical size, biocompability, reliability, efficiency, operating life, and cost characteristics. Engineering methodology and techniques have been important tools in the study of the interaction between mechanical heart assist devices and the cardiovascular system. They have permitted the evolution of quantitative criteria and the formulation of practical procedures for optimization of assistance. These techniques have served as an important adjunct to animal experiments and to clinical trials.

The latest computational dynamics techniques and the new generation of supercomputers provide a powerful tool for the investigation of the fluid dynamics involved in cardiac assist devices and in potential model Skeletal Muscle Ventricles (SMVs). This would help in research related to the final design of candidate models to harness as skeletal muscle ventricles, with the benefit of limiting the need for *in vivo* experiments. Moreover, computational fluid dynamics may well give a comprehensive analysis of all fluid- and hemo-dynamics parameters involved, such as shear stress at the wall or in the fluid, residence times and particle pathlines. This would be more 'complete' than available experimental techniques (shear stresses are not obtainable *in vivo*), and involve much less effort. However, numerical techniques have to be validated against experimental evidence, and thus a close collaboration between experimental researchers and computational fluid dynamics specialists has to be established.

This dissertation concerns the numerical analysis of the flow inside model SMVs. The research work involved in such analysis is part of a comprehensive research pro-

gramme on model SMV's promoted by the Skeletal Muscle Assist Research Group and directed by Prof. Salmons, comprising *in vivo*, *in vitro* (carried out by our collaborators at the University of Liverpool), and numerical studies. Due to the important role of fluid dynamics in the hemodynamics involved in the SMVs, the numerical studies focus on gaining and analysing detailed information on flow field, shear stresses at the wall and in the fluid, estimation of residence times and particle pathlines, by means of computational fluid dynamics techniques. Most of the work presented has as a main objective the validation of the numerical calculations. Numerical predictions of the flows inside model SMVs are validated against an available analytical solution for a simple problem and *in vitro* experimental measurements. Some numerical designs for the final model SMV are also proposed and discussed.

## 1.1 MEDICAL PROBLEM

The idea of using skeletal muscle to repair, enlarge, augment or even replace the function of a damaged heart has been around for more than 50 years. Early investigators failed to take adequate account of the important physiological differences between the two types of muscle, and were defeated ultimately by the inability of skeletal muscle to sustain continuous work without fatigue. The discovery that long-term electrical stimulation of fast -twitch mammalian skeletal muscle induces an *adaptive transformation* (Salmons and Vrbova, 1969) which includes a marked increase in its resistance to fatigue, has generated a remarkable resurgence of interest in this area. Advantages of the use of cardiac assist devices powered by skeletal muscles include no requirement for an external power supply, no generation of unwanted heat, and no problems of donor shortage or rejection, which remain the major drawbacks of the otherwise successful heart transplant programme (Salmons, 1990a).

Chronic stimulation at low-frequency induces profound changes in the mechanochemistry of contraction, the kinetics of calcium transport and storage, and the metabolic pathways responsible for the generation of ATP. These changes enable the muscle to support sustained work without fatigue by decreasing the energy needed for contraction while increasing the capacity for generating that energy through aerobic routes. Although fully transformed muscles can develop a considerable proportion of cardiac power, they have slower contractile characteristics (Salmons,1990a). One current objective of the research on the optimisation of the stimulation parameters is therefore to identify the patterns that can produce muscles that are faster and resistant to fatigue.

Skeletal muscle-powered cardiac assist devices have been under investigation in several laboratories worldwide. Many different approaches toward harnessing the energy of contracting skeletal muscle have been studied. These approaches will be discussed in detail in the next chapter together with the most commonly used cardiac assist devices. The most conservative approach to skeletal muscle assistance is to wrap the muscle around

an existing structure, such as the heart (cardiomyoplasty) or aorta (aortomyoplasty), to provide an uninterrupted endothelial interface with the blood (Salmons and Jarvis, 1992). The power available for assisting the heart can be harnessed most efficiently by configuring the skeletal muscle as a separate auxiliary ventricle connected to the patients circulation and used either in a counter-pulsatory mode or in parallel with the heart. In the former case, the SMV acts in a similar fashion to an intra-aortic balloon pump, augmenting aortic pressure during diastole and reducing left-ventricular pressure during systole.

Pumping chambers have been fashioned from the *preconditioned* muscle following the procedure illustrated in Fig. 1.1, and it has been demonstrated that the power output generated by these auxiliary ventricles is sufficient to replace the work done by the right ventricle or provide partial replacement or assistance of left ventricular function. These muscle pumps have been built from different skeletal muscles. The latissimus dorsi (see Fig. 1.1) has been most commonly used owing to its ease of harnessing and its minimal donor disability. The power that is potentially available from a skeletal muscle was discussed in relation to the power required for sustained cardiac assistance by Salmons and Jarvis (1992). In terms of the energy available, a skeletal muscle ventricle could be designed to provide a continuous partial assist of 1-2 l/min, with flows of up to 8 l/min sustainable for limited periods. Surgical manipulation of the muscle will affect the volume and length of the formed ventricle (Oda et al., 1993), while the stimulation patterns adopted to train the muscle to develop fatigue resistance, may govern its ejection fraction.

Progress to date has ranged from acute animal work to clinical applications of cardiomyoplasty. In experiments in dogs, ventricles of this type have pumped in circulation for periods up to 2 years (Mocek et al., 1992). However, many questions remain to be answered concerning the optimization of functional parameters such as the power available from skeletal muscle in the long term, the conditioning and activation patterns, and the configuration parameters. Answering these questions requires collaborative research between biological, surgical, and bioengineering research groups.

### Haemodynamics Aspects

A detailed understanding of the haemodynamics of the SMV can help to avoid the possibility of failure of surgical procedures which would then necessitate repeated design iterations. Despite its attractions, the SMV approach poses a significant problem in requiring an additional, potentially thrombogenic, surface to be placed in the circulation. In skeletal muscle wraps a blood/surface interface should be avoided as a raw muscle is potentially thrombogenic.

It is known that artificial hearts and cardiac assist devices are prone to failure due to haemolysis, thrombus formation, and sac calcification of the artificial pump. Substantial evidence indicates that abnormal flow phenomena, such as elevated shear stress, high turbulence levels, prolonged stasis, cavitation and rapid changes in shear, form substantial obstacles to routinely successful application of many cardiovascular devices and

treatments. Prolonged exposure of blood constituents to non-endothelialized surface entails a risk of thrombus formation. In spite of improvements in biomaterials, events at the blood-surface interface still limit the duration of assistance that can usefully be obtained with mechanical assist devices. If the SMV approach is not subject to the same limitations, it will be necessary to avoid artificial materials in the lining of the skeletal muscle ventricles. The current option to prevent thromboembolism within the artificial ventricle is the utilization of available biological materials.

Thrombus formation, propagation, composition and disintegration may be substantially flow-induced (Goldsmith and Turrito, 1986). Therefore improved flow dynamics in the device may result in reduced damage to blood components and reduced thrombus formation with its associated effects, such as infection. For these reasons, it is extremely important to address a preliminary analysis of the fluid-dynamics involved inside model SMVs.

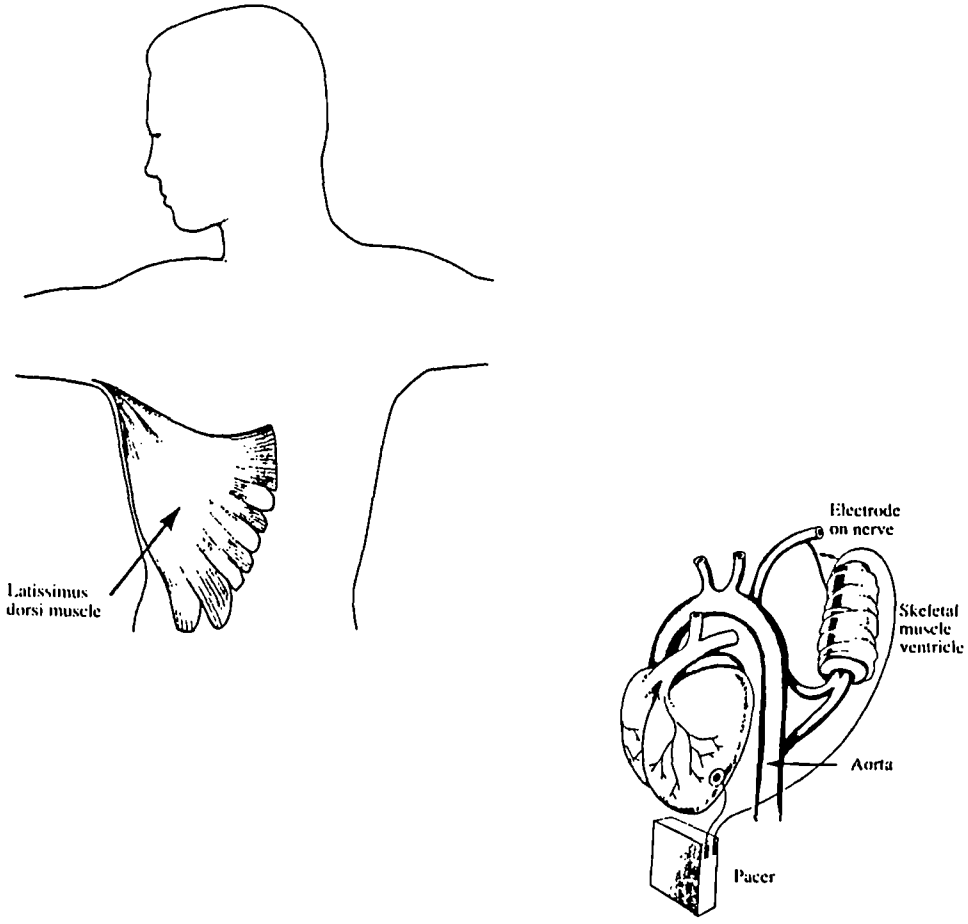


Figure 1.1 The skeletal muscle ventricle procedure. The latissimus dorsi is taken from the back of the patient, electrically transformed and wound round to act as an auxiliary ventricle controlled by a pacemaker.

## 1.2 GENERAL FEATURES OF THE FLOW IN MODEL SKELETAL MUSCLE VENTRICLES

Research on the dynamics of the flow inside model SMVs has been carried out on physical and numerical models with the objective of analysing the effect of the size and shape of the ventricle and inlet/outlet orientation of the duct. Due to the physiological limit on the power available to pump the blood out of the ventricle, the efficiency of these potential assistance devices has to be maximized. It is also necessary to minimize the risks of haemolysis and thrombogenesis, which are both related, in different ways, to the level of shear stress on the wall and within the flow.

The fluid dynamics of model SMVs are particularly complex because of (i) the rheological properties of blood, (ii) the three-dimensionality and pulsatility of the flow, (iii) the time-dependent three-dimensional geometry, and (iv) the mechanical properties of the compliant ventricular wall. The flow is likely to be highly disturbed and a wide range of shear stresses is possible; flow recirculation and areas of stagnation could all be present simultaneously. Flow pattern characteristics are dictated largely by the size and orientation of the connections to the ventricle, the stroke volume, rates of contraction and shape of the chamber.

Model SMVs may be operated in a variety of modes. For example, continuous cyclic filling and pumping has been experimentally and numerically simulated. Also, quiescent periods have been interposed between cycles in some of the *in vitro* models (Shortland et al., 1993). A common feature of these flows is the formation of vortex rings. Similar structures of the flow have been shown to exist, both experimentally (Sobey, 1985) and numerically (Tutty, 1992), in pulsatile flows in channels with rigid constrictions.

To date, the *experimental studies* have been carried out to visualise flows in one simple two-dimensional configuration for an SMV. The conduit connecting the SMV to the aorta is considered not to affect the ventricular flow patterns. Clinical devices are likely to be geometrically more complex, with separate inlet and outlet conduits connecting the ventricle to the aorta and with possible valved configurations. The two-dimensional flow visualization technique used for the *in vitro* experiments would be inadequate to describe the three dimensional flow patterns produced in the three-dimensional configuration currently under investigation. In order to understand and quantify the mixing properties of the vortical structures within the model ventricles, studies of residence times and dye visualisation experiments need to be conducted. These should identify regions of stagnation in the fluid where the risk of thrombus formation might be greatest clinically. Laser Doppler velocimetry will allow measurements of stresses in models.

*In vitro* data have been used to prescribe a series of computational grids varying in time on which a CFD simulation has been performed. The results of this simulation have been compared to flow patterns observed in vitro in order to assess the ability of the CFD code to model physiological flows. To examine the haemorheological implications of cardiac assistance from SMVs more fully, more realistic models of SMVs should be

investigated to include the influence of inlet/outlet geometry and simulated aortic flow.

Although substantial progress has been made through *in vitro* model studies by using laser Doppler anemometry or flow visualization techniques, these usually involve some degree of simplification, such as idealized geometry, steady or simple oscillating flow, rigid wall and Newtonian fluid, which may well be questionable in the modelling of the fluid dynamics of the blood. In addition, investigation techniques for *in vivo* flows are lacking in the provision of accurate and detailed analysis. Similar limitations have also applied to most previous numerical simulations. However, the current generation of CFD codes offers all the modelling capabilities required to perform a comprehensive low cost detailed analysis of the flow and therefore represents a very powerful tool in the design of a human SMV candidate.

## 1.3 NUMERICAL MODELLING

Computational Fluid Dynamics (CFD) has been used for numerical prediction of fluid flow and heat transfer since the 1960s. With the development of computer hardware, computational techniques have been vigorously proposed, tested and refined to the point that these are recognized as a cost-effective and convenient means of design in modern engineering practice. Traditionally, *experimental* and *theoretical* methods have been used to develop designs. With the advent of computers, a third method, the *numerical* approach has become available.

The fundamental equations of fluid dynamics are represented by the continuity equation, the momentum equations, and the energy equation. These are complex non-linear partial-differential equations, which can be solved using numerical approaches. Historically, the preferred numerical method to discretize the Navier-Stokes equations has been the finite difference method; however, more recently finite element methods have been used particularly in the field of blood flow, see for example (Perktold et al. 1994; Perktold and Rappitson, 1994).

Computational Fluid Dynamics represents a new method of research into blood flow in the cardiovascular system. Numerical simulation of blood flow through arterial systems, in particular through prosthetic valves, bends, arterial bifurcations, stenoses, grafts, natural and artificial ventricles has been of special interest in recent years because of the speed and low cost, and detailed information of local flow patterns it can provide. These have been extensively studied in the context of the work on blood flow modelling developed in the Biomechanical Research Group at City University over the last decade. The complex characteristics of blood flow throughout the cardiovascular system make mathematical analysis a challenging problem. Recent developments in computer hardware and advances in numerical methods have led to the point where complex three-dimensional unsteady flows bounded by moving walls can be simulated. This is an essential feature in the modelling of physiological flows, since they are mostly driven by the periodical wall motion.

Analysis of blood flow in artificial hearts and assist devices is an area of active interest. Numerical analysis represents an important tool in the design of more efficient devices. It is also very useful in investigating areas of low and high shear stresses, and regions of stasis. Few researchers have included the consideration of the motion of boundaries in the simulation of flows in the cardiovascular system.

The application of CFD to the simulation of model SMVs is demanding because it involves wall-driven unsteady flows and time dependent gridding. Modelling of the flow mechanics requires either transient or adaptive gridding in the CFD programs, and comprehensive modelling of the stress-strain behaviour of the wall. The numerical models should therefore make provision for

(i) arbitrary three-dimensional geometry
(ii) moving grid/boundary capability
(iii) (laminar) flow pulsatility
(iv) non-Newtonian blood flow characteristics
(v) wall compliance/muscle behaviour

The rheological properties of blood and its constituents play an important role in the physiology of the circulation of the blood. Blood is generally non-Newtonian, its viscosity varying with shear rate. In large vessels, blood can reasonably be considered a homogeneous incompressible fluid. It is universally agreed that at very high shear rate ($>$ 1000 $s^{-1}$) blood can be assumed as Newtonian. In the numerical simulations performed in model SMVs, non-Newtonian behaviour of blood was not taken into consideration for simplicity. Further, since the *in vitro* experiments on model SMVs were carried out using Newtonian fluids, the validation of the numerical predictions had to be performed modelling the fluid as Newtonian.

Many powerful CFD programs are available based on different numerical methods with varying degrees of modelling capabilities. Modern CFD codes solve the equations governing unsteady, three-dimensional flows in complex, moving geometries. Among these programs CFDS-FLOW3D has the advantage of providing all the capabilities required in the modelling of the flow in model SMVs.

CFDS-FLOW3D is a general purpose code for the numerical solution of compressible and incompressible, laminar and turbulent flows with heat transfer in three-dimensional geometries. The code uses a finite volume method to solve the governing equations on a general, three dimensional, non-orthogonal, body fitted grid with moving boundaries. Moving wall/grid facilities are provided by both the single-block (Release 2.4) and multi-block versions (Release 3.2.1, Release 3.3.), validation of which for flows in a semi-infinite expanding/contracting closed-end pipe is presented in Chapter 4. The multi-block grid capability allows the simulation of flows in solution domains with significantly more complex non- axisymmetric geometries. This allows the consideration of flows in SMVs with curved inlet tubes. Also the hemispherical ends of the ventricle can be modelled more accurately.

Extensive applications and tests on FLOW3D have been performed at City Uni-

versity since 1986 on a wide range of problems. A number of numerical studies are now in progress there, which are supported by the predictions of CFDS-FLOW3D. Nowadays, much of the interest in blood flow modelling is focused on the fluid-structure interactions occurring at the interface between blood and vessel wall. The research at City University is currently engaged in two projects aimed at developing codes capable of solving the coupled problem. The first is based on the finite volume code CFDS-FLOW3D, modified to allow the modelling of the solid wall. The second project is based on the use of a FEM code called FEAT, developed by Nuclear Electric's Engineering Analysis Group.

Numerical simulations of fluid-solid coupling in blood vessels or ventricles is a 'fore-front' topic of the current research in computational methods applied to biomechanical problems. The first comprehensive time-dependent 3-D model of flow through the left side of the heart was developed by Peskin and McQueen (1993), who used the Immersed Boundary Method developed by Peskin (1977). The complete computational solution of such flow problems is complicated by the requirement to solve the complex relationship that exists between the wall mechanics and the fluid-dynamics. Such a solution requires that the solid- and fluid-mechanical codes are coupled to a transient computational grid.

In the initial study in this thesis, the wall motion has been prescribed; however, the ultimate goal of the research will be to predict SMV wall position by solving, in a coupled manner, the equations for both the fluid and solid. A review of ventricle modelling with special attention paid to muscle modelling is presented in the next chapter. Muscles are not passive tissues, and therefore, in a coupled approach, not only are the fluid and solid mechanics equations coupled, but so also are the muscle mechanics equations. In order to have realistic ventricular models, solid mechanics equations have to allow for large deformation, and non-linear elastic and visco-elastic material with orthotropic properties. In modelling muscle mechanics passive and active states have to be considered separately. In the passive state, anisotropy cannot be neglected. In the active state, body forces have to be included in the equilibrium equations. When the muscle is operating actively, the constitutive equations are represented by force-length, and force-velocity relations available from experimental data.

Historically, the development of fluid and solid mechanics codes has developed separately, and in parallel. CFD codes commonly use a finite volume approach, while solid mechanics codes use the finite element method. In order properly to address the compliance and muscle effects of the physiological tissue, the most comprehensive solid mechanics available today is required (non-linear, anisotropic, visco-elastic, large deformation, large strain). Application of Finite Element Analysis (FEA) to structural problems has proved to be successful in many cases, and biomechanics applications have also been performed (Reuderink, 1991; Perktold and Rappisch, 1993).

## 1.4 OBJECTIVES OF THE RESEARCH AND STRATEGIES EMPLOYED

The objective of the research presented in this thesis is to study the dynamics of the flow inside these ventricles using an established 3-dimensional computational fluid dynamics code with accommodation of wall behaviour. The reliability of the predictions will be established by critical validation against *in vitro* data. Validations of the qualitative and quantitative flow patterns have been carried out. Clinically relevant parameters such as residence times and shear stresses will be calculated in the near feature from the raw velocity data produced by the numerical code. This will allow the evaluation of design specifications of SMVs for use in patients.

Validation Exercise

In order to be able to rely on the numerically predicted flow patterns, numerical results have to be validated against experimental data available from the *in vitro* and *in vivo* studies. In addition, analytical solutions of simplified problems may be used to test the numerical solutions. The sources of errors which may arise in the numerical predictions obtained using CFD may be attributed to: (i) the mathematical model, (ii) the discretisation method, and (iii) the numerical algorithm. The magnitude of the discretisation error is dependent upon both the discretisation approach and the mesh density. This error can be reduced by either using a higher-order discretisation formula designed to reduce the truncation error, or refining the grid. The latter is problem dependent. The errors associated with the numerical algorithm are dominated by the convergency criteria.

No CFD codes give guaranteed reasonable and accurate results to any kind of problem, even within the code's capability. Their successful use often requires experienced staff, and even then, the degree to which the codes can be routinely used as 'black boxes' may be quite limited. It is highly desirable, therefore, to perform external validations for particular problems. In general, code validation exercises may involve one or all of the following comparisons:

(a) comparison with the analytical solution if one exists,

(b) comparison with laboratory data set up specifically for validation purposes,

(c) code to code comparison,

(d) comparison with a wide range of experimental data.

Although accurate results (grid-independent and/or time-independent) are the first requirement for reliable numerical predictions, large-scale engineering applications of computational fluid dynamics typically involve such wide ranges of length and time scale that the use of cells and time steps sufficiently small is prohibitive.

As stated in section 1.2, a striking feature of the flows inside the model SMVs is the formation of vortices. Vortices enhance mixing, and this is a useful process to encourage in an SMV, as it could assist in the mixing of the blood components and in the

reduction of the apical residence time. Being able to predict accurately the dynamics of the vortices is therefore important, as this will affect the prediction of residence times and shear stresses at the wall and within the flow. It is also very important to know whether numerical codes can predict vortex ring dynamics from both qualitative and quantitative points of view.

In order to study the dynamics of the formation of these vortices, numerical ventricle models have been studied . Initial investigations have concerned a progressive validation of the numerical solutions predicted by the code for moving boundary flow domains. Firstly, comparisons were made with the analytical solution for expanding/contracting pipes of Uchida and Aoki (1977), and results are presented in Chapter 4.

An adapted compliant SMV model was then generated (rigid/compliant pipe) with a truncated (flat-end) apex using a sinusoidally prescribed motion of the wall. A spherical-end rigid/compliant model was subsequently constructed. The flows are driven by prescribed sinusoidal motion of the wall in both radial and axial directions. The predicted flow structures show that the number of vortex rings formed at the time of maximum ventricular volume is a function of the frequency of the wall motion. Predicted flow patterns of these two models were qualitatively compared with experimental flow patterns and discussed in Chapter 5. Subsequently, numerical analysis of the flow inside a model SMV with wall motion prescribed experimentally was performed. The predicted results are qualitatively compared with the corresponding *in vitro* data in Chapter 6.

In order to obtain a qualitative and quantitative validation of the numerical predictions, the dynamics of the formation of the vortices were studied in models where sigmoidal filling curves were used to define the wall motion driving the volume change. *In vitro* data provided by such studies were used to define the wall motion in the numerical simulations. Flow field features and trajectories of the vortex paths were compared with the experiments for different filling curves. However, because shear stress discontinuities occurred in the predictions a strict volume-defined analytical model was constructed for wall movement. This discussion is presented in Chapter 7.

Designing SMVs

Blood pump design involves much more than hydraulic design and pumping capability. A large number of investigators have worked in the field of determination of the optimal haemodynamic conditions in which assist devices should operate, and although considerable progress has been made, few have achieved the actual goal. Among the key fluid dynamic criteria for the design of a cardiovascular pump are the reduction of high shear rates, local accelerations, and high residence times of blood cells in contact with the biomaterial surfaces. It has been hypothesized that spiral three-dimensional vortices leading to a 'wash-out' of the pump chamber is advantageous in reducing thrombus formation and possibly blood sac calcification, and also in inducing remarkably low haemolysis, thereby avoiding any high stress condition in blood and stagnation areas (Umezu, 1994).

The introduction of a SMV to the circulation is a potential long-term hazard,

as the patient's blood comes into contact with the non-endothelialised surfaces of the wall of the new ventricle and the connecting conduits. This may trigger a cascade of events leading to deposition of thrombus, whose formation is dependent on the nature of the blood flow. The potential problem of haemostasis may be particularly involved at the apex of the artificial ventricle, where little mixing and large residence times may occur. Flow analysis studies are therefore required to address in detail the questions of haemostasis and thrombogenesis and in this context to evaluate possible candidate SMV configurations.

The role of the fluid dynamicist is to design an SMV to encourage blood flow patterns which inhibit mural thrombus formation, by increasing local mixing and decreasing peak residence times while maintaining moderate shear stresses throughout the fluid. Designers of mechanical left ventricular assist devices have concentrated on the inlet/outlet configuration and inlet valve orientation to produce a single large recirculation during filling (Jin and Clarke, 1993). In this way, a new blood volume introduced during filling will wash the wall of the device before being ejected (Tarbell, 1986).

Few numerical studies have been reported in the literature concerning the utilization of CFD methods to improve design features of cardiac assist device models. This lack of numerical simulation studies may be due to difficulties encountered in the treatment of realistic cardiac assist devices models. Generally, flows inside cardiac assist devices are three-dimensional, time-dependent, and often turbulent. An essential feature is the capability to accommodate the geometries of moving boundaries. This has been introduced very recently in the computational fluid dynamic packages and still has not been sufficiently tested against experimental data. Another important feature is the three-dimensionality of the problem, which requires very powerful grid capabilities, with special attention on the refinements necessary where boundaries are in motion. Furthermore, the grid has to undergo changes for each time step, which in turn has to allow for the 'accurate' solution to be established without overloading the calculation too much. The new generation of supercomputer hardware combined with new computational fluid dynamics algorithms has increased remarkably both the computer power and the ability of modelling. However, a lot of work still needs to be done to validate the newly available facilities against experimental evidence, and thus a close collaboration between experimental researchers and haemodynamic specialists has to be established.

For the purpose of helping in the SMV design, three-dimensional model SMVs are being investigated. Numerical simulations of flows in cardiac assist devices can be used to study the effect on the flow of the shape and size of the device, and of the orientation of inlet and outlet ducts. A three dimensional analysis of the flow inside SMVs is very important in order to have a reliable estimate of the variables of medical relevance, and consequently to be able to contribute to the design of model SMVs. However, computing time limits 3-D investigations very strongly. It is very likely that in the final design the duct that feeds the SMV is not a straight tube. This implies that in the numerical modelling two dimensional cylindrical models cannot be used. When the duct is a curved

cylinder or is a T-junction a truly 3-D model has to be considered.

Preliminary numerical studies on some 3-D models are presented in Chapter 8. It is shown how changes in shape and inlet/outlet configuration may affect the resulting flow fields for design considerations. One significant finding with respect to inlet geometry is that a curved inlet appears to produce in the SMV a purging type of flow, similar to that seen in the normal left ventricle. This would promote mixing of the blood components and reduce significantly the residence times of particles.

Calculations of flow shear stress and particle pathlines, to be performed in the near feature, will give a more accurate evaluation of the optimal configuration on the basis of the haemodynamic conditions which are formed inside the ventricle. The ultimate aim of the research is to establish the relationship between the geometrical configuration of an SMV and its hydraulic performance, to analyse critically the effects of shape, size and inlet/outlet configuration on the fluid dynamics, and use the information to prepare well-founded guidelines for the surgical construction and use of SMVs in patients.

Calculations presented in this thesis were carried out on the Convex C3860 supercomputer at ULCC, and on the SUN Sparcstation 5 at City University. Post-processing was performed on a Sun Sparcstation 2 at City University.

# CHAPTER 2
# LITERATURE SURVEY

## 2.1 INTRODUCTION

In this chapter, engineering and medical aspects concerning the harnessing procedure and numerical modelling of the skeletal muscle ventricle are reviewed. First a general review of all cardiac assist devices will be reported in section 2.2, followed by a detailed review of muscle-powered assist devices in section 2.3. Section 2.4, dedicated to general muscle structure and mechanics, is followed by a discussion of further literature on the engineering and biochemical aspects of harnessing the skeletal muscle power for cardiac assistance. In order to obtain a comprehensive solid and fluid-dynamic model of the skeletal muscle ventricle it is necessary to couple fluid-dynamics equations with solid mechanics equations (for the wall) and the muscle mechanics equations. Blood flow modelling is presented in section 2.6, together with a review of the numerical modelling of cardiac assist devices reported in the literature to date. This is followed by a section dedicated to the modelling of the natural heart (section 2.7).

The overall literature review will be concluded with a review of the solid mechanics equations in section 2.8, and a further review of the coupled solid-fluid models in section 2.9. However, a separate chapter will be dedicated to surveying the numerical methods for solving the equations of the fluid-dynamics, as they are the main tool used in the numerical modelling of skeletal muscle ventricles so far. It should be stressed that because the final goal of the project (which extends beyond the Ph.D. itself) is the coupling of solid/fluid behaviour in model SMVs, a correspondingly extensive literature survey has been conducted on solid mechanics methods and muscle mechanics to be coupled with the fluid-dynamics equations.

## 2.2 CARDIAC ASSIST DEVICES

The technological challenge to develop temporary and permanent circulatory assist devices and artificial hearts arises from statistical evidence concerning the incidence of cardiovascular mortality and morbidity in industrialized society. Currently, the patient with end-stage heart failure has few therapeutic options. These include cardiac transplantation, mechanical assist devices, and medical therapy. Despite recent advances in all types of treatment, *ideal* therapy for the patient with a failing heart has yet to be offered. Such an option should provide independence from external mechanical attachments, minimize rejection problems and effects associated with blood-surface interaction (Unger, 1979). Cardiac assist devices powered by skeletal muscle have the potential to meet these requirements. Due to the limited availability of donor organs for cardiac

transplantation, many candidates succumb before a suitable donor organ becomes available. A number of these severely ill patients have survived until (and following) their transplants with the aid of a mechanical support device (Joyce et al., 1986). Numerous techniques of mechanical cardiac assistance have been studied during the past quarter of a century, but only two have as yet become recognized as standard clinical procedures: artificial oxygenation and circulation of the blood by means of a pump-oxygenator, and the intra-aortic balloon pump. However, a number of promising techniques have been, and are being, extensively investigated.

The heart is a pump so it is logical to consider replacing it with a mechanical pump. Gibbon was the first (Gibbon, 1954) to demonstrate a successful apparatus to bypass the heart and the lungs in animals and one human patient during cardiac surgery, through the use of heart-lung machines. The advent of pumps and prosthetic devices buttressed the idea that a small man-made pump might be designed for implantation in the thorax as a substitute for the damaged human heart. The effort towards this goal may be subdivided into four groups of devices: (i) emergency assist devices; (ii) temporary assist devices; (iii) permanent assist devices; and (iv) artificial hearts.

In the following section first a historical review will be presented. Then, some principles of cardiac assistance will be discussed. Some of the more commonly used assist devices will be reviewed. In-series cardiac assist devices will be treated in more detail. This is also preliminary to the understanding of section 2.6.2.6, where numerical models of cardiac assist devices will be reviewed.

### 2.2.1 Historical Background

Historically, research on mechanical assistance for the heart started in 1812 with LeGallois (1813) who first addressed the complexity of replacing the heart. The feasibility of the design of a *roller pump* by De Bakey in 1934 (De Bakey, 1934) provided the basic principles for operating a heart-lung replacement device and for left ventricular assistance. To overcome the limiting factors of the roller pump (low output and haemolysis), left ventricular assist devices were developed on the basis of the membrane pump design. The design of this pump is based on the early constructions of Akutsu and Kolff (Akutsu and Kolff, 1958) which employ a U-turn geometry for the blood flow. In 1966 Kantrowitz and his group (1968) implanted U-shaped avalvular auxiliary ventricles for permanent cardiac assistance in two patients. Also in 1966 De Bakey (De Bakey, 1971) successfully used a left ventricle (LV) bypass pump for temporary circulatory assistance. In 1967 Bernhard (Bernhard et al., 1968) designed an axi-symmetrical pump, in which the blood crosses the pump unidirectionally.

At the same time, other modalities of circulatory assistance were attempted by different groups. LV assist systems were developed for both in series and parallel supports. To avoid roller pumps the concept of propeller pumps was developed by Bernstein (Bern-

stein, 1970), while bypass ventricles in series and in parallel to the heart were developed by Kantrowitz et al. (1965) and Thoma (1973), respectively. Many different possibilities of cannulating the heart have been tried. In 1961 Dennis (Dennis et al., 1962) demonstrated the left heart bypass by inserting an inflow cannula into the left atrium through the atrial septum and returning blood through the femoral artery. This principle was varied: Peters made cannulations to unload the left ventricle via apex (Peters et al., 1977), Zwart through the aortic valves (Zwart, 1966), and Litwak through the left atrium (Litwak, 1974). In addition, cardiac assistance can be performed with *counterpulsation*. In 1961 Moulopoulos et al. (1962) developed their *intra – aortic balloon pump* (IABP), which after the first clinical applications by Kantrowitz in 1967, became a well-established tool offering great benefits in cases with well defined indications.

Heart replacement by an artificial heart is based on the early experiments over 30 years ago by Akutsu and Kolff (1958). Although in the beginning it was very difficult to achieve long-term survival in animals, the artificial heart seems now to be coming of age and can be discussed as a temporary replacement in combination with consecutive transplanation. Hardy and Chavez (Hardy and Chavez, 1968) attempted to transplant a chimpanzee heart into a man in 1964. The first successful allotransplantation of a human heart was performed by Barnard in 1968 (Barnard, 1968). The development of a total artificial heart (TAH) or a permanent left ventricular assist device (LVAD) that becomes a routine clinical application is a great challenge that can be met only by a broad interdisciplinary collaboration of surgeons, cardiologists, engineers, chemists, physicists, and veterinarians. All these initial anecdotal experiences stimulated intensive research and development which has blossomed today into the clinical stage of applications.

### 2.2.2 Principles of Mechanical Assistance

Many methods of mechanical assistance to aid the failing heart have been, and are being, extensively investigated. The haemodynamic goals of the different methods being studied vary depending upon the problems of the patient. However, they all fit into three general categories:

- decreasing the work of the failing myocardium by reducing the load on the left ventricle;
- increasing blood flow through the coronary circulation, and consequently increasing the oxygen supply to the hypoxic tissue; and
- increasing cardiac output, and thus increasing the blood supply to the peripheral organs.

Increase of coronary blood flow should be mainly achieved by increasing coronary perfusion pressure, since flow through severely diseased vessels is pressure-dependent. Mechanical cardiac assistance is the only currently available intervention that will fulfil these requirements, as pharmacologic agents lead to undesired secondary effects.

Mechanical assistance can be effected by following two principles (Moulopoulos, 1989):

1. An external or internally implanted energy source may provide the circulatory system with the missing power to achieve adequate flow to the peripheral organs;

2. A mechanical device can be used to affect haemodynamic parameters within the two phases of each cardiac circulatory cycle, in order to increase peripheral flow to normal values.

It should be noted however, that if the heart is contracting, even if the output is reduced, the application of an additional energy source will have to be positioned within one or both phases of the cycle. As a consequence, the use of an auxiliary energy source will necessarily involve not only the first but the second principle too. Therefore, analysis of the assistance techniques used should proceed according to the phase (systolic or diastolic) during which they are applied.

Blood Pump Design

Blood pump design involves much more than hydraulic design and pumping capability. It is an overall challenge of high significance to provide devices that have the requisite physical size, biocompatility, reliability, efficiency, operating life, and cost characteristics. Design methods have recently been reported by Rosenberg (1994).

One of the most serious technical problems confronting designers of circulatory support devices is the development of a material that is compatible with the blood. Materials tend to damage blood constituents, promote clotting and generate abnormal plasma proteins. Many problems arise in the area of biomaterials: these must be biologically sufficiently compatible and withstand the rather excessive loads of a long-term period of implantation. Also valves must not create high shear stresses or turbulence which would lead to thrombus formation. The driving system must also be minimized to allow the patients mobility and guarantee an acceptable quality of life.

Power requirements to drive any type of fluid-mechanical device for cardiac assistance exceed that of the artificial pacemaker by several orders of magnitude. The work done by the left ventricle, W, may be approximated for one heart beat by

$$W = \int_T p(t)Q(t)dt \tag{2.1}$$

where p, Q are pressure and volume flow rate respectively. For an average value of aortic pressure of 100 mmHg and replacing $\int_T Q(t)dt$ by a stroke volume of 75 $cm^3$, it follows that

$$W = 10 \times 13.6 \times 10^3 \times 75 \simeq 10^7 erg$$

Assuming that T = 1.0 s, the power $P \simeq 10^7 erg/s = 1W$ for the left ventricle only. An upper bound for the output of the heart may be obtained by multiplying by four (four chambers), and by five (for exercise levels of output), resulting in 20 W. Allowing for

the efficiency, power requirements for circulatory assist devices and artificial hearts have been set in the range of 30-100 W. Power sources under study include electrical energy systems, radioisotope (Pu-238) powered thermonuclear engines, and biological fuel cells (such as muscles).

Assisted circulation can be categorized into six often interrelated and overlapping activities (Ghosh, 1989):

| | |
|---|---|
| 1.In-series mechanical ventricular assistance: | counterpulsation with for example IABP |
| 2.Parallel mechanical ventricular assistance: | Ventricular Assist Devices (VADs) |
| 3.Mechanical Replacement: | Total Artificial Heart (TAH) |
| 4.Bridges: | VADs or TAH as bridges to transplantation |
| 5.Biological Replacement/Assist: | Heart and heart-lung transplantation |
| 6.Biomechanical Assistance: | Cardiomyoplasty, Aortomyoplasty, Skeletal Muscle Ventricles (SMVs), Skeletal Muscle Tube Ventricles (SMTVs). |

Major emphasis in this discussion will be laid on the cardiac assist devices which work in series with the heart because the SMV can be harnessed as one of such.

### 2.2.3 In-series Mechanical Ventricular Assistance

In-series cardiac assistance, also known as *counterpulsation* or *diastolic augmentation*, was originally intended for those patients who suffered from secondary effects to acute myocardial infarction. Its use has now been extended to include applications in patients who can benefit from effects of temporary cardiac support.

In-series cardiac assistance by mechanical means attempts to achieve three major goals: 1) a reduction in myocardial oxygen demand through the assumption of a portion of the work of the left ventricle and a reduction of the workload of the heart; 2) an increase in oxygen supply to the ischemic myocardium obtained by enhancement of blood flow to the coronary circulation; and 3) an increase in blood supply to the peripheral system. These objectives can be accomplished by creating a pressure or flow perturbation in the central aorta which is repeated with each cardiac cycle. This is achieved through the use of a device which is synchronized to the cardiac cycle and phased in such a way as to reduce aortic pressure during systole and augment it during diastole (Fig.2.1). The high augmented diastole produces a significant high flow in the coronary arteries. In systole the heart faces a reduced ejection resistance, so the heart work is reduced (25% by an intra-aortic balloon pumping) (Unger, 1979).

Kantrowitz and Kantrowitz (1953) reported, in 1953, the earliest attempt to perform diastolic augmentation on an experimental animal. Wide clinical application of temporary cardiac support by counterpulsation became possible with the introduction

of a new intraarterial device, the intra-aortic balloon pump (Moulopoulos et al. 1962). Details on the modalities of work of this device will be reported below. In the past, several devices have been proposed and evaluated; however, most of those did not work sufficiently.

The systems available fall into the following two methods:

(a) Non-invasive Methods:

1. Body Accelerating Synchronous Heartbeat technique (BASH);
2. External Compression (ECP);

(b) Invasive Methods:

1. Intra-aortic Balloon Pump (IABP)(Fig.2.2);
2. Aortic Ring;
3. Aortic WindKessel ventricle (AWK);
4. Inter-aortic Ventricle (IAV);
5. External Ventricle (EV);
6. Pulsatile Assist Device (PAD);
7. Intraventricular balloon;
8. Compression Cups;
9. Auxiliary Ventricle;
10. Dynamic aortic patch (DAP);
11. U-shaped mechanical auxiliary ventricle (MAV);
12. Percutaneous Access Device (PAD).

Comprehensive literature on these methods is readily available in (Unger, 1979; Unger, 1984; Unger, 1989). Here only the most commonly used will be treated in detail.

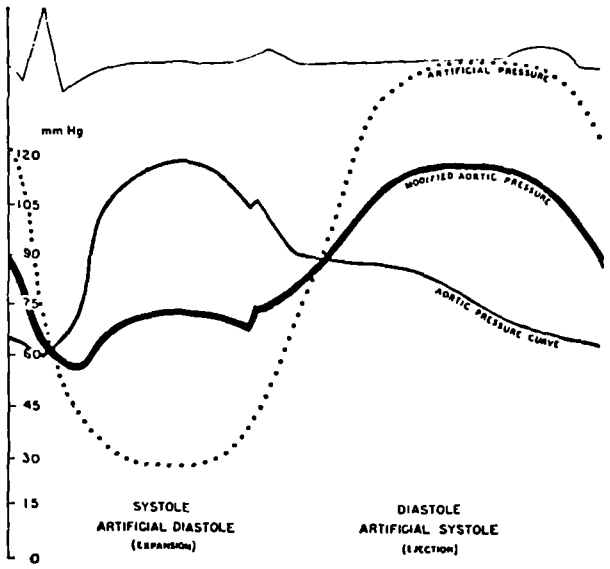


Figure 2.1 Relationship of the pump to the circulation during counterpulsation and intended effects on the arterial pressure curve. From Moulopoulos (1989).

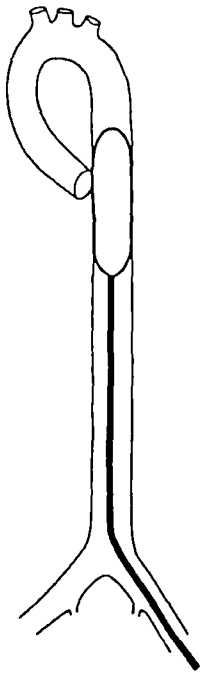

Figure 2.2 Intra-aortic balloon pump. From Unger (1979).

#### 2.2.3.1 Intra-Aortic Balloon Pump

The main clinically established method for intra-aortic counterpulsation is the Intra-Aortic Balloon Pump (Fig.2.2). Since its evaluation by Moulopoulos (Moulopoulos et al., 1962) and its first clinical implantation in 1967 by Kantrowitz, the IABP has become the most widely used of the methods available for circulatory support, because of its relative ease of use. In relation to patients undergoing cardiac surgical procedures, the IABP has been advocated preoperatively, intraoperatively, or postoperatively, for patients with low cardiac output (Creswell et al., 1992).

An elongated polyurethane balloon, mounted over one end of a catheter, is introduced into the aorta. Pressurized helium is admitted to the balloon catheter through a solenoid valve. A comprehensive discussion of the early research on IABP is reported in Weber and Janicki's review (Weber and Janicki, 1974). Recent investigations on the IABP concern its clinical use as long-term circulatory support (Kantrowitz et al., 1989; Creswell et al., 1992).

### 2.2.4 Parallel Mechanical Ventricular Assistance

Ventricular assistance can be simply defined as unloading of one or both ventricles by taking over and shifting the blood volume. Ventricular Assistance Devices, VADs, work in parallel with the ventricle in situ, unloading the left ventricle by taking up the blood volume from the left atrium or the left ventricle and returning it to the great

vessels (aorta or pulmonary artery). In the venoarterial bypass the total blood volume bypasses the heart, unloading also the left heart chamber completely. Ventricular assist pumping can support both systemic and pulmonary circulation or either individually. At the same time it unloads the failing ventricle, decreases myocardial oxygen demand and consumption, and allows metabolic recovery of the myocardium. The main requirement is a working right ventricle. If the right ventricle fails an additional device on the right (a Right Ventricular Assist Device, RVAD) side is necessary. Furthemore, biventricular assistance (Biventricular Assist Devices, BVADs) provides a functional heart replacement.

The first clinical use of a left heart assist device was reported in 1963 by Liotta et al. (1963). All VADs basically consist of (a) conduits (or cannulae - inflow and outflow) and (b) pump. Unger (Unger, 1979) discussed all the inflow and outflow cannulation sites in his lucidly illustrated review. In the case of LVADs, there are two methods of implantation, with access via the left atrium or via the left ventricle. A left atrio-aortic method is sufficient only for partial support of the heart. For a permanent implantation or for bridging to transplantation, a transapical left ventricular access can be used. The arterial return with both methods is to the ascending or descending aorta or the abdominal aorta.

The search for an ideal pump for ventricular assistance has been going on for more than a century. We may differentiate between *pulsatile* devices with artificial heart chambers, which are driven pneumatically or electrically, and *non-pulsatile* blood pumps. Devices currently used are artificial ventricles (driven pneumatically or electromechanically), roller pumps, and centrifugal pumps. The optimal volume of flow through the parallel circuit of the VAD required for ideal circulatory assistance is not known. Flow capacity of different designs of assist pumps varies from 3.5 l/min (Utah pump of Peters) to 14 l/min (Thoratec Model VIC).

### 2.2.5 Mechanical Replacement: Total Artificial Heart

The demand for the development of the artificial heart has arisen due to the complications in heart transplanation, and the problem in the selection of donors and their availability. The old dream of replacing a failing heart by an artificial heart was first realized in 1957 by Kollf's group (Kollf et al., 1959). The first artificial heart consisted of a pair of sac-type ventricles. The main progress has been achieved by Kollf's group with hemispherical ventricles driven pneumatically with a diaphragm-type membrane. Numerous complications, such as hemorrhage and thromboembolism, plague clinical implantation of pneumatic TAHs. The main limiting design factors are represented by the biomaterials, the artificial valves, and the driving systems. The required biomaterials have to withstand loads with defined physical and chemical properties lasting up to 5 years.

The ultimate goal in designing artificial hearts has been a totally implantable device

consisting of ventricles and integrated energy and control systems with electrical driving systems. The transmission of energy through the skin could be realistic within the next few years. The use of an electrostimulated skeletal muscle as an internal source of energy has also been proposed (Frey et al., 1986; Ugolini, 1986).

### 2.2.6 Bridges to Transplantation

The idea of using an artificial heart as a bridge to a consecutive transplantation dates back to the 1969 operation performed by Cooley. In the eighties several centres started adopting the bridge concept to sustain patients awaiting transplantation, as an alternative to impeding death from terminal heart disease (De Vries et al., 1984). The possible options for the bridges are: (a) IABP, (b) LVAD, (c) BVAD, (d) TAH, (e) biological bridge, (f) partial cardiac replacement. To date more than a hundred artificial hearts have been implanted and about a hundred pulsatile ventricular assist devices. The indication for bridging is given for a highly selected group of patients. The Jarvik TAH has been successful as a bridge in 55% of cases.

The prospects are promising that in the next years we will see the demonstration of a biologically activated energy converter capable of assuming the full pressure and volume work of both ventricles. The next section will be devoted to a review of such devices.

## 2.3 SKELETAL MUSCLE-POWERED ASSIST DEVICES

The concept of biomechanical assistance dates back more than 50 years. A functional autologous powered skeletal muscle is utilized as a source of energy to replace or assist a failing or insufficient heart. Such a device would be completely implantable and need no transcutaneous transfer of energy, conduits or immunological intervention.

The idea of using a skeletal muscle for active assistance of the heart was introduced by Leriche and Fontaine (1933) in 1933. The first experiments were performed on dogs applying pectoralis major muscle grafts. The same muscle was first applied in humans by De Jesus (De Jesus, 1931) [1] and then by Beck (1935) with promising results. In 1958 Kantrowitz and McKinnen (1958) reported their method of wrapping diaphragm around the heart and the aorta to compress them rhythmically, with synchronous stimulation of the phrenic nerve in each systole. Shepherd (1969) first studied inlay and onlay grafts of the heart as enlargement procedures using diaphragm muscle. Petrovsky used skeletal muscle (diaphragm) on a large number of patients to reinforce the left ventricular wall (Petrovsky, 1966). Termet and co-workers (1966) were the first group to use pedicled latissimus dorsi (LD) muscle flaps and to indicate its advantages. In the next decade,

[1] Although, chronologically, De Jesus was the first to use skeletal muscle for cardiac assistance, the first attempt is often attributed to Leriche and Fontaine, because De Jesus's work was unknown for sometime, presumably because it was reported in a South American journal

Kusaba et al. (1973), Spotnitz et al. (1974), von Recum et al. (1977), and their colleagues experimented with diaphragm or rectus abdominis as pouches or onlay grafts. Each group recognized the potential of these skeletal muscles for cardiac assistance from the physiological point of view, but also their many limitations. All these investigators found insuperable hindrances in muscle fatigue on repetitive stimulation at rates sufficiently high to provide meaningful circulatory assistance.

Around the same time some major basic physiological concepts emerged which influenced the whole approach of biomechanical assistance. Salmons and co-workers (Salmons and Sreter, 1967; Salmons and Vrbova, 1969; Salmons and Henriksson, 1981) reported on the nature of skeletal muscle plasticity and adaptive changes. In 1982 the concept of electrical induction of fatigue resistance in skeletal muscles for use in cardiac reconstruction was advanced by Macoviak's group (Macoviak et al., 1982). Since then, the research groups in Montreal (Dr. Chiu), Philadelphia (headed by Dr. Stephenson and Dr. Andersen), Stanford, and Seattle have successfully conditioned the skeletal muscles to become fatigue resistant at low frequencies without adverse effects. They documented the partial histochemical conversion of fast-twitch fatiguable type II fibres to aerobic slow-twitch fatigue-resistant type I fibres, rich in mitochondria, and more durable when stressed with tetanic stimuli. However, a number of other problems, including graft fibrosis, denervation atrophy, growth of the graft, blood/muscle interface, and thromboembolism, also exist. These problems need to be addressed before skeletal muscle biomechanical assistance can be evolved into a widely practised clinical procedure.

Depending on the type of surface seen by the blood, there are two main methods of utilization of skeletal muscle for biomechanical assistance (Salmons and Jarvis, 1992):

1. preserving the natural endothelium lining of the patient's cardiovascular system: cardiomyoplasty or aortomyoplasty
2. adding an additional surface (artificial material or autogenous biological lining) of an independent structure that is connected to the patient's circulation: pouches, SMV, SMT, energiser for TAHs or LVADs.

In general, those approaches fall into three main approaches to the use of skeletal muscle:

1. Wrapping a layer of muscle around the heart, *cardiomyoplasty*, to produce intermittent compression of the patient's left or right ventricle (see Fig.2.3 (A)) (Chagas et al., 1989; Hagege et al. 1990); or wrapping a layer of muscle around the aorta, *aortomyoplasty*, to produce compression of ascending or descending aorta directly (Fig.2.3 (B)) (Pattison et al., 1991), or indirectly arranging to inflate a cuff placed around the vessel for contraction of the muscle (Fig.2.3 (C)) (Kochamba et al., 1988).
2. Configuring a layer of muscle as a separate, auxiliary ventricle, to operate either in parallel with the right or left ventricle or in counterpulsation with the left ventricle.

These include for example auxiliary pouch-shaped or tube-shape ventricles, as a *skeletal muscle ventricle* (SMV) (see Fig.2.3 (D)) or a skeletal muscle tube ventricle (SMT) (Fig.2.3 (E)), that can be connected to the circulation as a synchronous or counterpulsatory assist (Acker et al., 1986; Anderson et al., 1991).

3. Using a skeletal muscle as the power source for mechanical assist devices, such as mechanical artificial hearts or ventricular assist devices, via mechanical (Fig.2.3 (F)), hydraulic (Fig.2.3 (G)), or electrical (Fig.2.3 (H)) actuation (Frey et al., 1986; Ugolini, 1986).

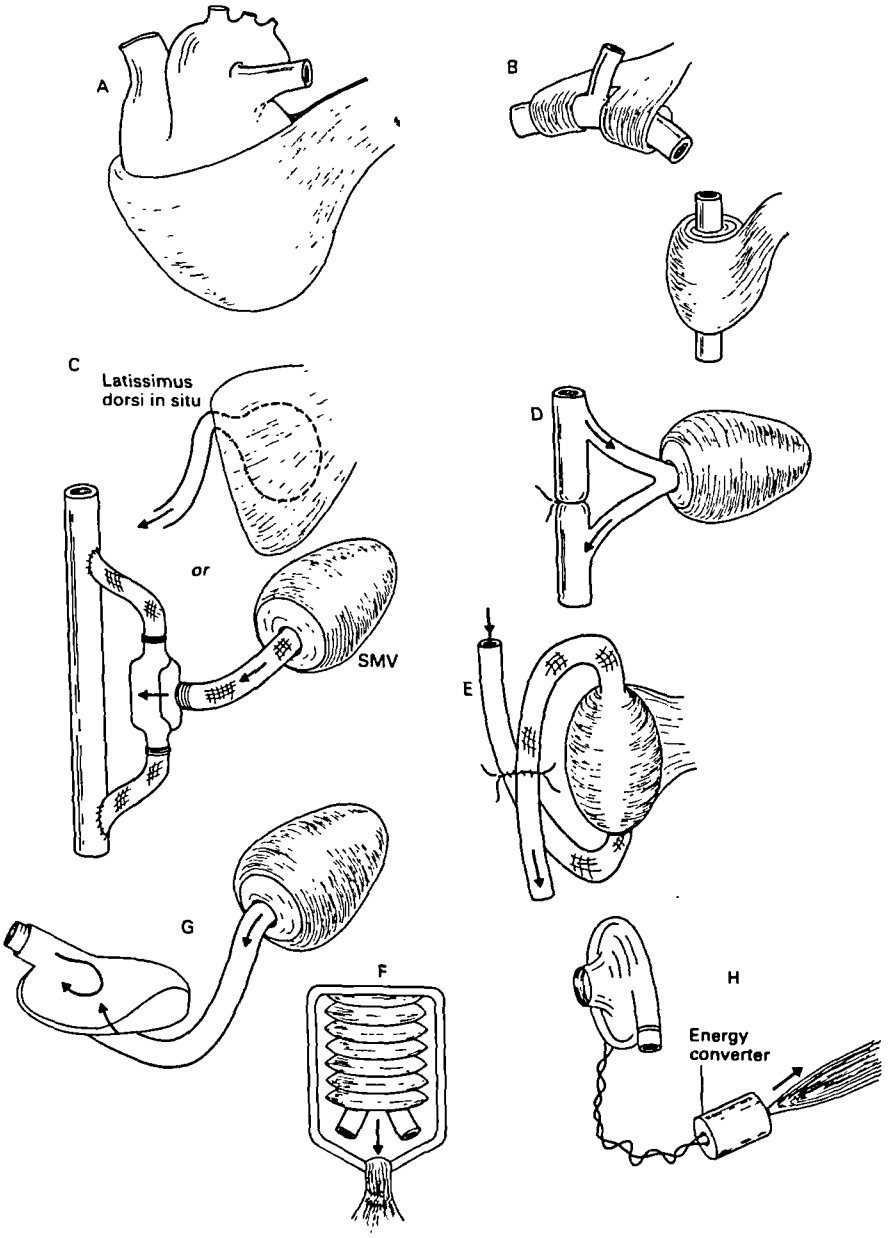


Figure 2.3 Schematic examples of the approaches for skeletal muscle-powered assist devices: (A) cardiomyoplasty, (B) aortomyoplasty, (C) compression of aorta by a cuff, (D) skeletal muscle ventricle, (E) skeletal muscle tube ventricle, (F) LVAD energised mechanically, (G) LVAD energised hydraulically, (H) LVAD energised electrically. From Salmons and Jarvis (1992)

All three approaches involve substantial bioengineering contributions in the development of specialized implantable pacemaker and electrodes, valves, and non thrombogenic linings, and in the formulation of engineering science models for the evaluation of pressure, flow, and shear stresses. 'The first approach represents the most conservative option, since the presence of an uninterrupted endothelium minimises the risk of thromboembolic complications' (Salmons and Jarvis, 1992). However, cardiomyoplasty has been shown not to produce sufficient developed pressure compared with the SMV (Anderson et al., 1988a). This is due to the geometric configuration. In fact, LDPGs represent only one layer of muscle applied to the surface of the heart, while SMVs are contructed with multiple layers wrapped in a spiral fashion to form a cone or a tube. Because in the latter case the radius is smaller the pressure developed will be greater according to Laplace's law. The first attempt to power biologically a mechanical blood pump was made by Kusserow and Clapp (1964) in 1964. Twenty years later, the same concept was applied by Ugolini and associates (Ugolini, 1986).

In the next subsections the approaches of biomechanical assistance will be discussed in detail. A more specific review on muscle characteristics will be presented in the next sections, where cardiac muscle features (chemical, physiological, anatomical) will be compared with the features of 'normal' and 'conditioned' skeletal muscle.

### 2.3.1 Cardiomyoplasty and Aortomyoplasty

Carpantier and Chachques introduced the term 'dynamic cardiomyoplasty' for cardiac reconstruction with skeletal muscle grafts applied directly to the beating heart or the aorta preserving the natural endothelial lining. There are three basic techniques for cardiomyoplasty:

(a) Ventricular reinforcement, consisting of an electrostimulated LD wrapped around the ventricles (Fig.2.4(a)).
(b) Ventricular substitution by means of a new biological cardiac wall composed of a patch of autologous pericardium as neoendocardium and the electrostimulated LD as myocardium (Fig.2.4(b)).
(c) Ventricular substitution and reinforcement of the remaining ventricular wall (combination of procedures 1 and 2) (Fig.2.4(c)).

When substitution of the ventricular wall procedures are applied, in order to avoid thrombogenic surfaces, the autologous pericardium has been used as the blood/biomaterial interface. An alternative is to leave behind native endocardium.

Numerous investigators have grafted skeletal muscle to the heart. While skeletal muscle ventricles have shown to generate adequate force for months (Acker et al., 1986) the performance of a muscle wrap in cardiomyoplasty is less clear. Ironically, cardiomyoplasty has been the only clinical application of skeletal muscle augmentation to

date. The technique was first applied to a human patient in 1985 in Paris by Carpentier and Chachques's group (Carpantier and Chachques, 1985) using a pedicled LD muscle graft stimulated synchronously with a significant increase of the wall motion and ejection fraction.

It is possible to apply LDPGs to the heart in several different configurations. It was found that graft orientation affects the cardiac output, and that the best performance is obtained when fibre orientation of the two types of muscles coincides. This type of assist suffers from a major limitation: the geometry of the pump is dictated by the size and shape of the existing organs. In consequence, a grossly hypertropied heart may be too large to be wrapped effectively by the patient's latissimus dorsi, and the small lumen of the aorta restricts the stroke volume which can be achieved by compressing it. The fixed geometry imposes loading conditions on the muscle wrap which are far from the peak of its power curve (Salmons and Jarvis, 1992).

Nowadays over 24 institutions in Europe, Latin America, Canada, and the United States are assessing the technique for the treatment of patients with severe heart failure. The current procedure uses the pedicled latissimus dorsi muscle (usually that of the left side) secured around the cardiac ventricle. The muscle flap is then stimulated to contract synchronously with the heart by means of a programmable, implantable muscle stimulator triggered by R wave of the electrocardiogram. For the initial two weeks, blood supply recovers and an adhesion of the flap to the heart is allowed, with the stimulator off. A programme of graded stimulation is then initiated to transform the muscle. Clinical results following cardiomyoplasty have been encouraging, with improvements in the majority of patients (Hagege et al., 1990).

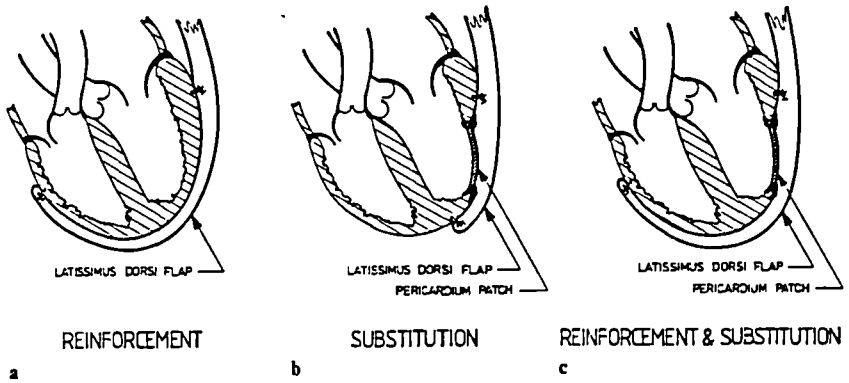


Figure 2.4a-c Different approaches of dynamic cardiomyoplasty. From Chachques et al. (1989)

The first attempt in aortomyoplasty was by Kantrowitz 1958, who mobilized the muscular part of the left hemidiaphragm and wrapped it around the distal descending thoracic aorta. This augmentation was short-lived, owing to rapid muscle fatigue, but laid the foundation for the development of the intra-aortic balloon pump.

The major advantage of using aortomyoplasty is that it circumvents the problem of blood-surface interaction. The effect of aortomyoplasty treatment is reminiscent of the volume displacement produced by an intra-aortic balloon. Therefore, the benefits of counterpulsation, with skeletal muscle contracting in diastole, ensue for both the heart and the muscle itself. Successful counterpulsation has been achieved over several weeks (Pattison et al., 1991). The muscle is stimulated 2 days after the operation to achieve muscular contraction and conditioning at the same time (Cumming et al., 1991).

Effects of cardiomyoplasty combined with aortomyoplasty on dogs were reported in a recent work of Takahashi and his colleagues (Takahashi et al., 1993). LD was used around the heart, while the major pectoralis muscle wrapped around the ascending aorta. Their work was carried out in Japan where for social reasons heart transplantation is not practiced, and hence, use of skeletal muscles for assisting patients with heart disease represents almost the only option for such patients. Results were compared with the two treatments performed separately. They confirmed the findings of Carpentier's group (Chachques et al., 1988; Chachques et al., 1989) that using cardiomyoplasty, hemodynamic parameters such as the systolic aortic pressure, dp/dt and the left ventricular pressure increase significantly, while diastolic pressure remains unchanged. When cardiomyoplasty was combined with aortomyoplasty all parameters improved. The reason for this is thought to be the fact that aortomyoplasty acts as a new ventricle and decreases left ventricular afterload.

### 2.3.2 Skeletal Muscle Ventricles

An alternative approach to the use of skeletal muscle for circulatory support is to configure it as an auxiliary pumping chamber. The great advantage of this approach is that the geometry of the ventricle can be optimized to provide the most favourable loading conditions for the muscular wall, so that the pumping capabilities of the muscle are used maximally. The only limitations of this approach, therefore, are the size, shape and fibre orientation. A blood/muscle interface should be avoided as raw muscle is potentially thrombogenic. In this case an additional surface is placed between the muscle and blood, which may be a polymeric material (smooth segmentedpolyurethane) or an autogenous biological lining. Consequently, there is the need to ensure that the introduction of such a device into the patient's circulation does not cause thrombus formation, with the attendant risks of obstruction of flow through the device and embolism to vital organs.

#### 2.3.2.1 Construction of Skeletal Muscle Ventricles

Skeletal Muscle Ventricles can now be constructed and made to pump in vivo either against mock circulation devices or in the circulation for weeks (Acker et al., 1986; Acker

et al., 1987a; Acker et al., 1987b). Because of its non-critical function, location, mass and familiar use in reconstructive operation the latissimus dorsi muscle has been the muscle of choice for most of the experimental studies. The latissimus dorsi is large and flat; it is easy to mobilize into the thoracic cavity and can be moulded into various shapes. Its principal function of LD is adduction of the forelimb. Other muscles used have included the rectus abdominus, quadriceps femoris, pectoralis major, gluteus maximus, psoas, and diaphragm (Ghosh, 1989).

To construct an SMV, the latissimus dorsi is freed from its attachments to the chest wall, sacrificing penetrating collateral vessels but preserving the thoracodorsal nerve and blood vessels. The muscle is then wrapped around a Teflon P.T.F.E. mandrel of a given shape and size in an overlapping spiral (see Fig.2.5). The mandrel is either conical, when forming pouch-type ventricles, or cylindrical, to produce tube-type or flow-through ventricles. Generally, 1.5-2.5 muscle wraps are obtained. The SMV can be placed inside the thoracic cavity or left on the chest wall under the skin and subcutaneous tissue. Electrodes are placed in position for subsequent stimulation of the thoracodorsal nerve and the wound is closed. The muscle can be stimulated either directly, through the muscle body, or indirectly through the thoracodorsal motor nerve (Khalafalla and Malek, 1989). However nerve stimulation allows a complete uniform transformation of the muscle fibres to the fatigue resistant state by electrical preconditioning, where direct stimulation promotes transformation segmentally in the area of the wire electrode (Macoviak et al., 1982).

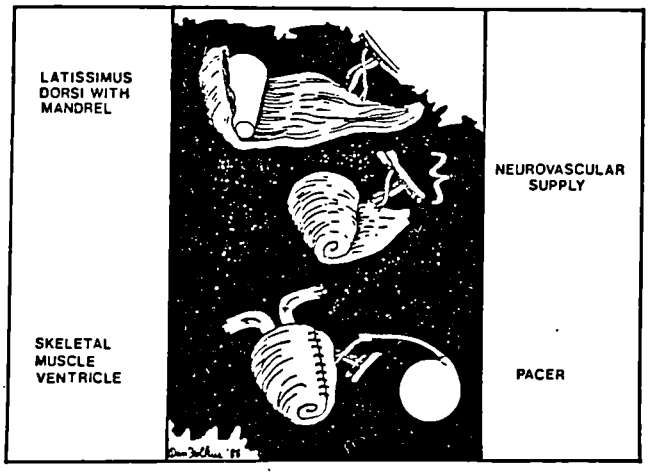


Figure 2.5 Schematic representation of the skeletal muscle ventricle construction from latissimus dorsi. From Anderson et al. (1989)

Loss of the collateral vessels renders the distal portion of the muscle ischaemic and it has been found beneficial to introduce a post-operative delay of at least 3 weeks during which a collateral circulation is allowed to develop (Mannion et al., 1986a). The conditioning pattern of stimulation can be commenced at this stage, although preconditioning of the graft has been found not to be strictly necessary in dogs (Acker et al., 1987b). The electrical preconditioning process takes approximately 6 weeks. The muscle is stimulated

to contract isometrically against the rigid Teflon mandrel at a rate of 54 contractions per min at 25 Hz (Acker et al., 1986). At the time the SMV is to be used, the mandrel is replaced by a bladder of synthetic material in a second operation; this is then connected to an apparatus for measuring pressure and flow or to the animal's own circulation.

The combination of a vascular delay period and electrical preconditioning allows the SMV to be essentially fatigue resistant. Using radiolabeled microspheres, Mannion et al. (1986b) demonstrated that all layers of an SMV receive substantial blood flow following the vascular delay period while the ventricles are pumping in the circulation.

#### 2.3.2.2 In Vivo Assessment of Skeletal Muscle Ventricles

Skeletal muscle ventricles have been constructed by several investigators, and they reported encouraging results. Stevens and Brown for example (Stevens and Brown, 1986) formed cylindrical pouches from the unconditioned canine rectus abdominus muscle and connected it to a mock circulation device. Although it had been known for some time that skeletal muscles transformed by chronic stimulation showed a high resistance to fatigue, the tests had always been conducted under isometric conditions. Acute experiments with conditioned SMVs showed that they were in fact capable of generating significant pressures and flows for several hours (Mannion et al., 1987).

Most of the experiments in vivo have been performed on dogs. The main reason for selecting this species is the observation that the latissimus dorsi muscle and the heart are comparable both in size and anatomy to the human equivalents. However, compared with the human LD muscle, canine skeletal muscle has a high basal level of oxidative metabolism in which no increase is seen after electrical stimulation. The species that is used to perform the experimental (in vivo) part of this study is the sheep. The reason for this is that sheep are even closer than dogs to humans in size and other parameters (Thoma et al., 1991).

An implantable mock circulation circuit used in the Philadelphia laboratory has enabled long-term evaluation of the capabilities of SMVs to be undertaken without the potential complexities of actually pumping blood. Coneshaped SMVs of 17 ml were tested in the mock circulation device shown in Fig.2.6. This device provided for manipulation of both SMV preload and afterload as well as SMV output. Skeletal muscle ventricles underwent a 3-week vascular delay followed by a 6-week electrical preconditioning period; they functioned for up to 9 weeks in conscious animals (Acker et al., 1986; Acker et al., 1987b). In these experiments, it was arranged for the SMVs to pump against a pressure of 80 mmHg with a preload of 40 mmHg. A subsequent study was designed to determine functional characteristics of SMVs during the electrical conditioning process (Acker et al., 1987a).

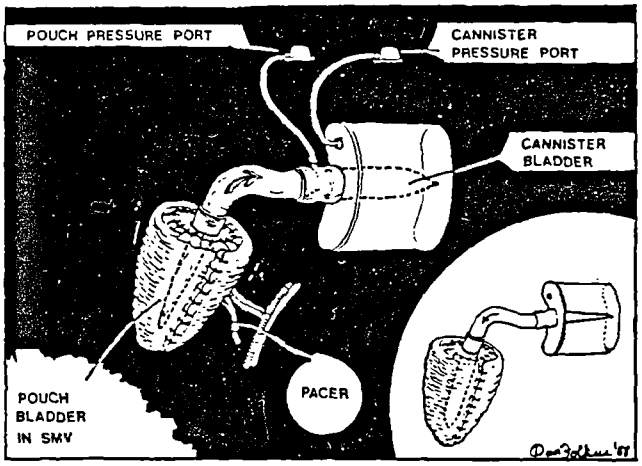


Figure 2.6 Schematic representation of the mock circulation device. From Anderson et al. (1989)

Similar experiments were conducted by the same group to prove that continuous work is performed while skeletal muscle is undergoing adaptive transformation at the level needed for an auxiliary cardiovascular pump. No period of electrical preconditioning was applied to the SMVs, which were stimulated to contract immediately. The work generated was intermediate between the work of the canine right and left ventricle. After one week of continuous pumping, the performance of muscle conditioned and electrically preconditioned muscle was essentially identical. After two months few animals were still generating significant work. In subsequent experiments larger mandrels were used to form the SMV, with a considerable improvement in performance under physiological conditions of preloads (Bridges et al., 1989). Further evidence that a skeletal muscle can acquire the capacity for sustaining continuous tetanic, cardiac-like work, after the second week of muscle conditioning is reported from the experimental results carried out by Carraro et al. (1991). Animal have survived up to two years with skeletal muscle ventricles without thromboembolism (Mocek et al., 1992).

#### 2.3.2.3 Skeletal Muscle Ventricles as Diastolic Counterpulsators

Skeletal muscle ventricles can be configured in series with the descending aorta as shown in type A of Fig.2.7, in parallel as in type C, or in an adjacent configuration as in type B. Skeletal muscle ventricles configured (type B) to function as diastolic counterpulsators are connected in series with the thoracic aorta. These SMVs are designed to pump blood, augment aortic diastolic blood pressure , and reduce mean systemic afterload during systole. They have shown to produce significant diastolic augmentation for many weeks with a substantial reduction in left ventricular stroke work and augmentation of coronary blood flow.

The Philadelphia research group headed by Dr. Stephenson has tested SMVs in series and in parallel to the heart (Anderson et al., 1989). Mannion demonstrated electrically preconditioned SMVs working as diastolic counterpulsators were able to function well in the circulation for many hours (Mannion et al., 1986a; Mannion et al., 1987). Acker et al. (1987b) demonstrated that skeletal muscle ventricles could function as long-term diastolic counterpulsators, pumping blood in the circulation. In order to obtain experience of the operation of such devices in the canine systemic circulation, a tubular ventricle (SMT) was interposed in the descending aorta and stimulated in counterpulsation with the heart. In fact this configuration would be less likely to precipitate thromboembolic events. These SMTs produced significant diastolic augmentation for several weeks (Acker et al., 1987a).

The performance of the ventricles, and their response to different frequencies of stimulations was documented by the work of Salmons and Stephenson (1989). Recently, long-term aortic diastolic counterpulsation has been achieved with SMVs of improved design lined with pleura or pericardium (Anderson et al., 1991).

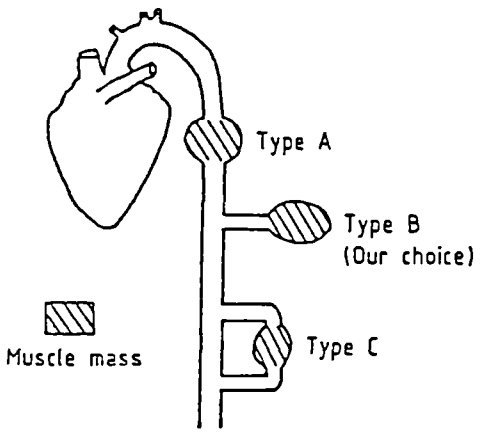


Figure 2.7 Possible configurations of a SMV in the circulation. From Khalafalla and Malek (1989)

### 2.3.2.4 Skeletal Muscle Ventricles in-parallel with the Left Ventricle

As mentioned above the first skeletal muscle pouches were constructed from canine rectus by Spotnitz et al. (1974). As said earlier, the research group in Philadelphia has directed effort toward using skeletal muscle to form pouch-shaped or tube-shaped ventricles in parallel to the heart which when placed in the circulation can pump blood effectively for at least several days (Andersen et al., 1989). The biomedical engineering research group at Purdue University (West Lafayette, USA), has studied the in vivo application of skeletal muscle ventricles in parallel to the heart in dogs (see Fig.2.8). An SMV was constructed by wrapping the untrained rectus abdominus muscle around a valved compressible pouch that was inserted into the left ventricular apex (with no valve) and to the aorta via a one-way valve. Consequently, the pressure in the SMV

pouch is always equal to LV pressure. This configuration allows for (i) a low pouch diastolic pressure, which together assures a high muscle capillary blood flow, and (ii) a high precontraction pressure , which assure a forceful muscle contraction.

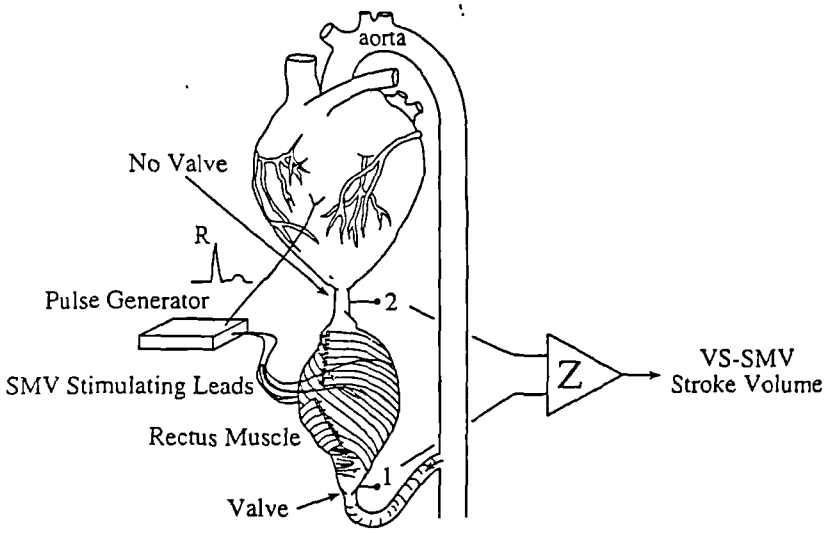


Figure 2.8 SMV in parallel connected between the left ventricle without a valve and the aorta with an outlet valve. From Geddes et al. (1993)

The first to connect a double valved, air-compressed pouch between the left ventricle and aorta in a chronic calf study was LaFarge et al (1968). Similar double-valved pouches were powered by skeletal muscle in the experimental studies conducted in dogs by (Drinkwater et al., 1980; Neilson et al., 1985; Badylack et al., 1989). Wessale et al. (1991) showed that there was an increased cardiac output during SMV assistance, with an unloading of the left ventricle. Stimulation parameters have been optimized for specific studies (Geddes et al., 1993) in terms of pulse duration, frequency and delay to the ventricle contraction, those being a function of the fluid dynamics of the pumping system, which in turn depends on the geometry and size of chamber and conduits.

## 2.4 MUSCLE MECHANICS

Muscle is a generator of mechanical work from chemical fuel. In order to understand the mechanisms of this generation first muscle structure will be analyzed at macro- and micro-anatomic level, then muscle mechanics will be introduced pointing out differences between skeletal muscle and cardiac muscle.

There are three kinds of muscle: skeletal, heart, and smooth muscles. Skeletal muscle makes up a major part of the animal body. It is the prime mover of animal locomotion, and is controlled by voluntary nerves. It has the feature that if it stimulated at a sufficiently high frequency, it can generate a maximal tension, which remains constant in time. It is then said to be tetanized. Since a resting skeletal muscle is a visco-elastic

material with quite ordinary properties, the really interesting part of the properties of skeletal muscle is the contraction. Hence skeletal muscle is often studied in the tetanized condition. Heart muscle is also striated like skeletal muscle, but in its normal function it is never tetanized. Smooth muscles are not striated, and are not controlled by voluntary nerves. There are many kinds of smooth muscles, with widely different mechanical properties.

### 2.4.1 Skeletal Muscle Structure

Most mammalian muscles contain a mixture of fibre types and motor units. Generally, whole muscles contain a heterogeneous mixture of fast-contracting and slow-contracting fibres, as well as fibres with high endurance and low endurance. The organization of skeletal muscles is hierarchic and is shown in Fig.2.9.

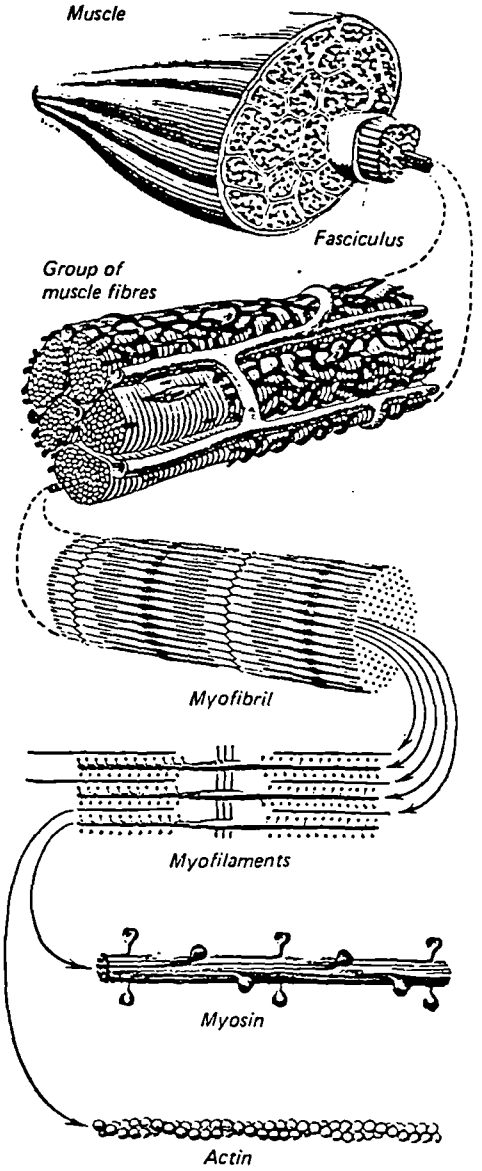


Figure 2.9 The organizational hierarchy of skeletal muscle. From Gray's Anatomy, 35th edn. (1973), Warwick and William (eds).

### 2.4.1.1 Skeletal Muscle Fibres

The following discussion on skeletal muscle fibres is largely based on the material published by Lieber (1992). Skeletal muscle fibres are cells that, in many ways, are like any other body cell. However, because muscle cell function is highly specialized to produce force and movement, the cellular components are also specialized (Fig.2.10). Muscle cells (fibres) are cylindrical, with a diameter ranging from about 10 $\mu m$ to about 100 $\mu m$.

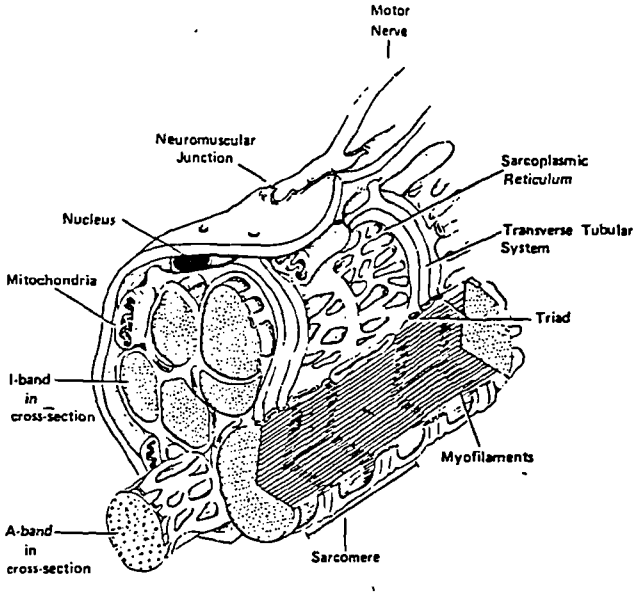


Figure 2.10 Schematic representation of the muscle cell. From Lieber (1992)

The muscle fibre diameter determines its strength and use. Muscle fibre length is highly variable, depending on the muscle architecture. This plays an important role in the attainment of fibre contraction velocity and distance over which the fibre can shorten. The muscle cell contains an array of filamentous proteins as well as other subcellular organelles such as mitochondria, nuclei, sarcoplasmic reticulum, and the transverse tubular system.

*Nuclei* are located at intervals along the cell length. These, as cell nuclei, control the scheduling and type of cell material that must be distributed throughout the cell. Protein synthesis is coordinated by the nucleus and performed on ribosomes. The amount and type of muscle proteins present confer on the cell its strength, speed, and endurance properties.

Muscle *mitocondria* are responsible for the aerobic generation of the main cellular energy molecule, adenosine triphosphate (ATP). ATP is used throughout the cell, for example, for muscle contraction, ion transport, protein syntesis, and cellular repair. The location and distribution of mitocondria are dependent on the particular muscle fibre type. Mitocondria density is important in determining the muscle fibre's endurance properties. The actual amount of mitocondria in the highly oxidative fibres may exceed 20% of the total cell volume (Einsenberg, 1983).

The most distinctive feature of the muscle is the ordered array of contractile filaments that are arranged throughout the cell. A well-defined hierarchy of filament organization proceeds from large (the order of microns) to a small scales of angstrom dimensions.

The largest functional unit of contractile filaments is the *myofibril.* Myofibrils are simply a string of sarcomeres arranged in series. The myofibrils are arranged in parallel (side by side) to make up the muscle fibre; thousands of myofibrils can be packed into a single fibre. The functional consequence of this arrangement is that the various myofibrils may not act completely independently during normal contraction.

Myofibrils can also be subdivided into *sarcomeres* arranged in series. The total distance of myofibrillar shortening is equal to the sum of the individual shortening distances of the individual sarcomeres. Sarcomeres are composed of contractile filaments termed *myofilaments.* Two major sets of contractile filaments exist in the sarcomeres (Fig.2.11). They represent large polymers of the proteins *myosin* (thick filament) and *actin* (thin filament). These filaments interdigitate to generate muscle shortening and form a hexagonal lattice. This interdigitated pattern gives the muscle its striated appearance observable microscopically by virtue of the dark and light banding pattern. The sarcomere region containing the myosin filaments is known as the A-band and that containing the actin filament the I-band. The region of the A-band where there is not actin-myosin overlap is called the H-zone. The dark narrow line that bisects the I-band is the Z-band. If the muscle contracts greatly, the I and H bands may narrow to extinction, but the A bands remain unaltered. Finally, the relatively dense structures noted in the centre of the A-band are known as the M-band. The distance from one Z-band to the next is defined as the sarcomere length, which is an important variable relevant to force generation. The hexagonal pattern of arrangement of these filaments is shown in Fig.2.11.

While the myosin-containing filament *generates* tension during the muscle contraction, the actin-containing filament *regulates* tension generation. Actin monomers are relatively small and roughly spherical in shape; their arrangement creates a long groove along the filament's length where the regulatory protein (tropomyosin) fits. At intervals along the filament the protein troponin (Tn) is located. This is responsible for turning on the contraction.

A meshlike sheath of collageneous tissue, called endomysium, surrounds the muscle fibre. This plays some role in the passive mechanical properties of the fibre. Bundles of fibres, each surrounded by endomysial tissue, are organized into muscle fascicles, each surrounded by a more stout perimysial tissue. Finally, bundles of fascicles are organized into muscles, surrounded by epimysial connective tissue. Finally, the macroscopic organization of the muscle fibres also determines a muscle's contractile properties.

In addition to the well-defined arrangement of force-generating components present in muscle cells, there is an intricate membrane system for causing these force generators to act. This is composed of two main components: the transverse tubular system (T-system) and the sarcoplasmatic reticulum (SR). The function of the T-system is to convey an activation signal to the myofibrils, which are themselves not in direct contact with the motorneuron. The SR has the main function to release and take up calcium during contraction and relaxation, respectively. As such, the SR envelops each myofibril to permit intimate contact between the activation and force-generation systems. The SR

is also in contact with the T-system and therefore acts as the 'middleman' in skeletal muscle activation and relaxation.

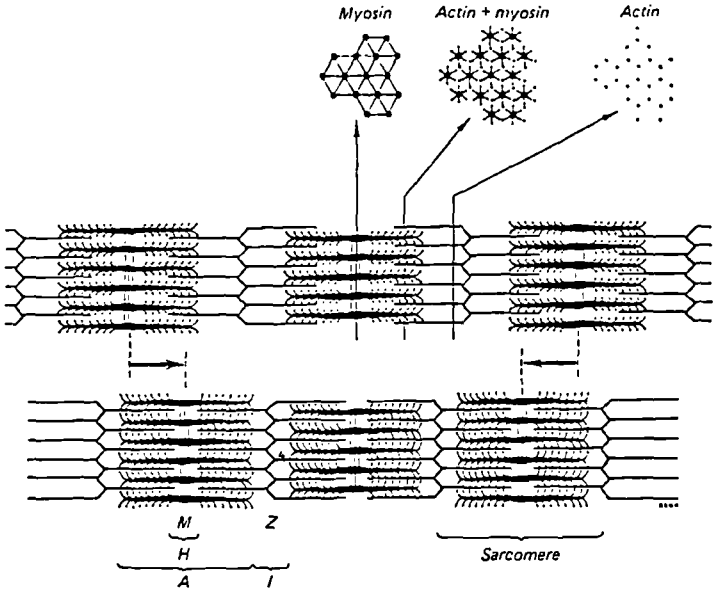


Figure 2.11 The structure of a myofilament, showing the spatial arrangement of the actin and myosin molecules. From Gray's Anatomy, 35th edn. (1973), Warwick and William (eds).

Numerous microscopic methods have been used to examine skeletal muscle structure. Early light microscopes did not provide a great deal of insight into the structure of the living muscle fibre due to its translucency. The interference microscope developed by A. Huxley (1952) allowed the striated appearance of the muscle fibre to be seen. During a similar period, H. Huxley and Hanson (1954) developed preparative methods for the then-new electron microscope, and observed the hexagonal lattices and the actin and myosin filaments. The X-ray diffraction method provided the muscle structural changes during contraction (Huxley et al., 1981).

### 2.4.2 Activation Process

Peripheral nerves innervate skeletal muscles so that neural activation precedes muscle contraction. This process is known as *excitation-contraction coupling* (EC coupling), and comprises a sequence of events. The first step in the EC coupling chain is the generation of the peripheral nerve action potential that arrives at the neuromuscular junction, that is the interface between muscle and nerve. The end of the nerve contains packets of the neurotransmitters acetylcholine (ACh), which causes muscle fibre excitation. The action potential is conducted deep into the fibre by the T-system, by signalling the SR to release calcium in the regions of myofilaments. The calcium ions bind to troponin, which in turn releases the inhibition on the actin filament, permitting interaction with the myosin filament and resulting in cross-bridge cycling, i.e. force generation.

When the neural impulse ceases, calcium is pumped back into the SR by the calcium-activated adenosine triphosphatase (ATPase) enzyme. Calcium levels in the region of the myofilaments drop below a critical level, thin filament inhibition again resumes, and actin-myosin interaction is prevented. This inhibition is manifested externally as muscle fibre relaxation. The time required for activation, contraction, and then relaxation to occur is finite. Excitation (with accompanying calcium release) is relatively rapid (about 5 ms), while contraction and relaxation are relatively slow (of the order of about 100 ms).

Successive twitches may act additively to produce a stronger action. A critical frequency is reached at which the successive contractions fuse together. This is the *tetanized state*. For frequencies higher than the critical frequency further increase in the force of contraction is slight.

### 2.4.3 The Cross-Bridge Cycle and Skeletal Muscle Energetics

Much of our understanding of the mechanism of muscle contraction has come in large part from the excellent biochemical studies performed from the 1950s to the mid-1970s, see for example (Mommaerts, 1969). It was during this period that methods for isolating specific muscle proteins were developed as well as the methods for measuring their physicochemical and biochemical properties. In its simplest form, the cross-bridge cycle can be envisaged as actin combining with myosin and ATP to produce force, adenosine diphosphate (ADP), and inorganic phosphate, $P_i$. ATP serves at least two functions in skeletal muscle systems: 1) it disconnects and 2) reconnects actin and myosin. In more detail, in contracting skeletal muscle, ATP binds to the actin-myosin complex, causing actin and myosin to dissociate. When it does, ATP is hydrolyzed by the S-1 portion of the myosin molecule into ADP and $P_i$, which then allows actin and myosin to reassociate.

Muscle cells require energy to perform their normal functions and force generation. Glucose serves as the major energy source of the cell. There are two main processes by which glucose can be oxidized to yield energy that is useable by the cells: glycolysis, and oxidative phosphorylation. Glycolysis does not require oxygen and occurs within the soluble cytoplasm of the cell; oxidative phosphorylation requires oxygen and occurs within the mitocondria. ATP is the primary energy molecule used in the cross-bridge cycle. In the glycolysis process for every molecule of glucose metabolized, two ATP molecules are created. While glycolysis can supply the energy needs of the cell, it is not extremely efficient. Lactate buildup after glycolysis can alter the intracellular pH, thus changing cellular contractile and metabolic activity. In addition, lactate clearance requires further bodily energy. When oxygen is present, the preferable pathway for glucose metabolism is to oxidize glucose completely by oxidative phosphorylation. This process yields 32 ATP per glucose molecule.

### 2.4.4 Skeletal Muscle Mechanics

The following discussion is based on the approach used by Noordergraaf (1978). During most of the nineteenth century, activated muscle was regarded in mechanical sense as a stretched spring with a store of potential energy. Shortening was then looked upon as a release of this energy. The concept of the stretched spring was found inadequate when Fick (1891) discovered that the stored energy during stretching

$$\int_{l_0}^{l_1} K(l - l_0)dl \tag{2.2}$$

in which K is the spring constant, $l$ the instantaneous and $l_0$ the initial length, was less than the energy released by shortening over the same distance $l_1 - l_0$

$$\int_{l_0}^{l_1} Fdl + \Delta Q \tag{2.3}$$

where $F$ is the force exerted by the muscle and $\Delta Q$ the heat generated during shortening.

This discrepancy led to the introduction of the viscoelastic model by Hill (1922). This model considers an elastic force in combination with a viscous force which opposes the shortening. However, upon inspection of the thermodynamics aspects, Fenn (1923) found Hill's ideas unacceptable, and discovered that the 'Fenn effect', namely the sum of the external work performed, $\Delta E$, and the dissipated heat $\Delta Q$,

$$\Delta E + \Delta Q = \int_{l_0}^{l_1} Fdl + \Delta Q \tag{2.4}$$

is not constant, but a function of the speed with which the distance $l_1 - l_0$ is covered. It transpired gradually that the contractile force $F$ was a function of the speed of the contraction $v$ (Fenn and Marsh, 1935). This understanding was crystallized in Hill's now classic model of skeletal muscle, which marked a new era in muscle research (Hill, 1938; Hill, 1949-1950; Hill, 1950; Hill, 1953). Hill's model consists of two elements in series (Fig.2.12): a passive elastic (nonlinear) element (SE) and a contractile element (CE). These obey the relationship:

$$(P + a) \times v = b \times (P_0 - P) \tag{2.5}$$

or its equivalent

$$(P + a)(v + b) = constant \tag{2.6}$$

where a and b are constants[1]derived experimentally (usually about 0.25), P is the muscle force, $P_0$ the maximum tetanic tension, and $v$ the muscle velocity of contraction. This equation can be used to determine the relative muscle force that occurs as a muscle is allowed to shorten. Roughly, if we ignore the constants a and b the equation states that the rate of work done, and thus the rate of energy conversion from chemical reaction, is a constant. This seems reasonable in the tetanized condition, for which the equation was



[1]Dimensions of $a$ and $b$ are N and m/s, respectively.

derived. This equation is in contrast to the viscoelastic behaviour of a passive material, for which the higher velocity of deformation calls for higher forces that cause the deformation. Therefore, the active contraction of a muscle has no resemblance to the viscoelasticity of a passive material. The original derivation of Hill's equation is presented in APPENDIX A.

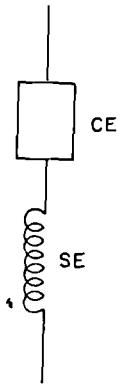


Figure 2.12 Hill's two-element model of skeletal muscle consisting of a passive elastic element SE and a contractile element CE. From Noordergraaf (1978)

### 2.4.4.1 Length-Tension Relationship: Isometric Muscle Contraction

Since the late 1800s, it has been known that the force developed by a muscle during isometric contraction (when the muscle is not allowed to shorten) varies with its starting length (see review by Podolsky and Shoenberg, 1983). The isometric length-tension curve is generated by maximally stimulating a skeletal muscle at a variety of discrete lengths and measuring the tension generated at each length. When maximum tetanic tension at each length is plotted against length, a relationship such as that shown in Fig.2.13 is usually obtained. While a general description of this relationship was established early in the history of biological science, the precise structural basis for the length-tension relationship in skeletal muscle was not elucidated until the sophisticated mechanical experiments of the early 1960s. These experiments defined the precise relationship between myofilament overlap and tension generation, which we refer to today as the *length-tension relationship*. In its most basic form, this relationship states that tension in skeletal muscle is a direct function of the magnitude of overlap between the actin and myosin filaments.

In the late 1950s and early 1960, Gordon et al.(1966), and Edman (1966) proposed that in order to determine the detailed structural basis for the length-tension relationship, isolated, intact, single skeletal muscle fibres are required. The mechanics of the sarcomere is the foundation on which the mechanics of muscle bundles can be built by the addition of other constituents. A. Huxley (1957) designed a mechanical apparatus to

keep a small segment of the fibre at a constant length, that is, to keep a region of the fibre at a constant sarcomere length.

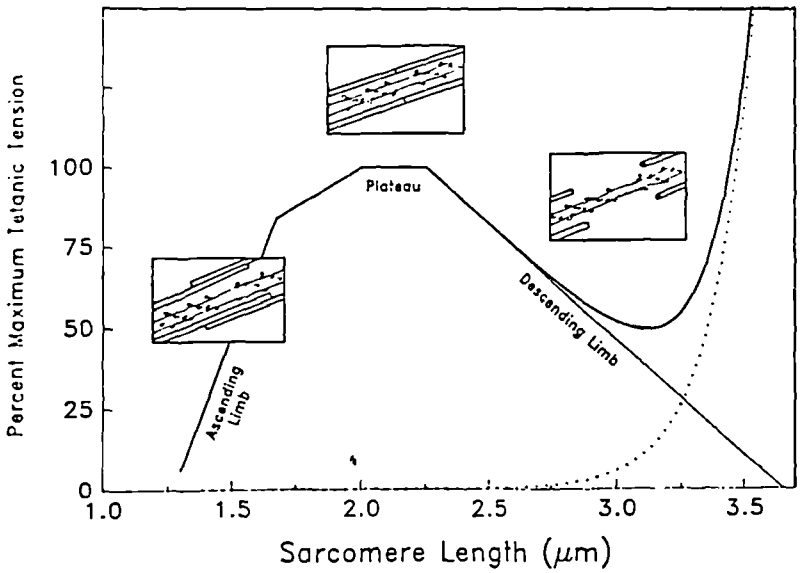


Figure 2.13 The sarcomere length-tension curve for frog skeletal muscle. Insets show schematic arrangement of myofilaments in different regions of the length-tension curve. Dotted line represents passive muscle tension. From Lieber (1992)

The results of the classic experiments by Gordon, Huxley and Julian (1966) are summarized in Fig.2.13, where muscle relative tetanic tension (as a percentage of maximum) is plotted as function of sarcomere length ($\mu$m). During the extreme stretching of the muscle to a sarcomere length of 3.65 $\mu$m, the latter developed no active force. In fact, since the myosin length is 1.65 $\mu$m long and the actin filament is 2.0 $\mu$m in length, at a sarcomere length of 3.65 there is no overlap between the actin and myosin filaments, that is no myosin cross-bridges are in the vicinity of the actin active sites. Hence, no force generation may occur. During shortening of the muscle, overlap between actin and myosin was possible, and the amount of force generated by the muscle increased as sarcomere length decreased (because the number of cross-bridges between actin and myosin increased) until the muscle sarcomere length reached length of 2.2 $\mu$m. This region of the length-tension curve is known as the 'descending limb'.

As the length of sarcomere changed from 2.0 to 2.2 $\mu$m, the muscle force remained constant. This was because no additional cross-bridge connections were made. In fact, there exists a bare region of the myosin molecule that is devoid of cross-bridges, as a result of the myosin molecules coming together in the centre of the myosin filament. This region of the curve is known as the plateau region. The length at which the maximum tetanic tension ($P_0$) is obtained is known as the optimal length ($L_0$).

It might be predicted that shortening past the sarcomere length of 2.0 $\mu$m would be impossible. However, after this point actin filaments from one side of the sarcomere double overlap with the actin filaments on the opposite side of the sarcomere. The actin filament from one side interferes with the cross-bridge formation on the other side of the sarcomere, and this results in decreased muscle force output (shallow ascending limb). At shorter lengths the myosin filament actually begins to interfere with shortening as it

abuts on the sarcomere Z-disk, reducing force precipitously (steep ascending limb).

The dotted line in Fig.2.13 represents the tension generated if a muscle is stretched to various lengths without stimulation. Near the optimal length, passive tension is almost zero. However, as the muscle is stretched to greater lengths, passive tension increases dramatically. This means that passive tension can play a role in providing resistive force even in the absence of muscle activation. Recent studies performed by Magid and Law (1985) on chemical stripping of sarcolemma have demonstrated that the source of the passive tension is a new structural very large protein (titin) which connects the thick myosin filaments end to end. This is very fragile and thus has probably been missed in earlier studies. In addition to passively supporting the sarcomere, titin stabilizes the myosin lattice so that high muscle forces do not disrupt the orderly hexagonal array.

#### 2.4.4.2 Force-Velocity Relationship: Isotonic Muscle Contraction

Unlike the length-tension relationship, the force velocity relationship does not have a precise, anatomically identifiable basis. The force-velocity relationship states that the force generated by a muscle is a function of its velocity, or conversely, that the velocity of muscle contraction is dependent on the force resisting the muscle. This relationship was historically also used to define the kinetic properties of the cross-bridges.

Experimental elucidation of the force-velocity relationship was first presented by Hill and Katz in their classic papers (Hill, 1938; Katz, 1939). The current description has been ascribed to Hill (1970), who, in his decades of important muscle studies, generated an equation for the muscle force-velocity relationship that is still in use today.

Experimentally, the force-velocity relationship is a curve that actually represents the results of many experiments plotted on the same graph. A muscle is stimulated maximally and allowed to shorten (or lengthen) against a constant load. The muscle velocity during shortening (or lengthening) is measured and then plotted against the resistive force. The general form of this relationship is plotted in Fig.2.14. The horizontal axis represents the ratio of muscle velocity relative to maximum velocity ($V_{max}$), while the vertical axis is the ratio of muscle force relative to maximum force ($P_0$).

When a muscle is activated and required to lift a load that is less than its maximum tetanic tension, the muscle begins to shorten. Contractions that permit the muscle to shorten are called concentric contractions. In this case, the force generated by the muscle is always less than the maximum $P_0$. As the load that the muscle is required to lift decreases, contraction velocity increases. This occurs until the muscle reaches its maximum contraction velocity $V_{max}$. The mathematical form of the force-velocity relationship is a rectangular hyperbola and is given by eq.(2.5).

The physiological basis of the force-velocity relationship is determined by the fact that the cross-bridges between actin and myosin both attach and detach at certain rates. These rates are referred to as 'rate constants'. At any point in time, the force generated

by a muscle depends on the number of cross-bridges attached. Because it takes a certain amount of time for the cross-bridges to attach (based on the rate constant of attachment), when the filaments slide past one another increasingly rapidly (i.e. as the muscle shortens with increasing velocity), the force decreases due to the lower number of cross-bridges attached. Conversely, as the relative filament velocity decreases (i.e. as muscle velocity decreases), more cross-bridges have time to attach and to generate force, and thus force increases.

As the load on the muscle increases, it reaches a point where the external load is greater than the load which the muscle itself can generate. Thus the muscle is activated, but it is forced to lengthen due to the high external load. This is referred to as eccentric contraction (contraction does not necessarily imply *shortening*). The absolute tensions are very high relative to the muscle's maximum tetanic tension generating capacity, and it is independent of lengthening velocity. Hence, skeletal muscles are very resistant to lengthening.

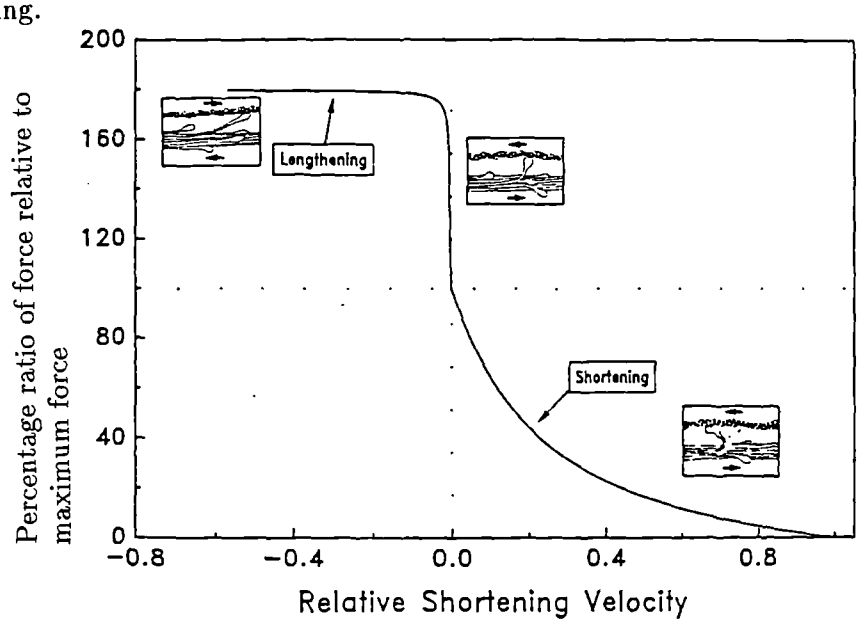


Figure 2.14 The muscle force-velocity curve for skeletal muscle. Insets show schematic representation of cross-bridges. From Lieber (1992)

### 2.4.4.3 Length-Tension-Velocity Relationship

The muscle force changes with changes in length and/or due to changing velocity. This means that when muscle length and muscle velocity change simultaneously, it is still possible to define the muscle force produced. The length-tension experiment can be viewed simply as a series of length-force-velocity experiments at constant velocity (zero), and the force-velocity relationship can be viewed as a series of length-force-velocity experiments performed at constant length $L_0$. The point shared bewteen the classic force-velocity and length-tension curves is the point of maximum isometric tension ($L_0$ at zero velocity, resulting in a tension $P_0$).

The appearance of the length-tension-velocity relationship is shown in Fig.2.15. If the muscle velocity is very high, the force will be independent of length. This means that at high velocity length is not very important. At low concentric velocities, muscle length becomes an important force modulator. At eccentric velocities, again muscle velocity dominates length as the determinant of force.

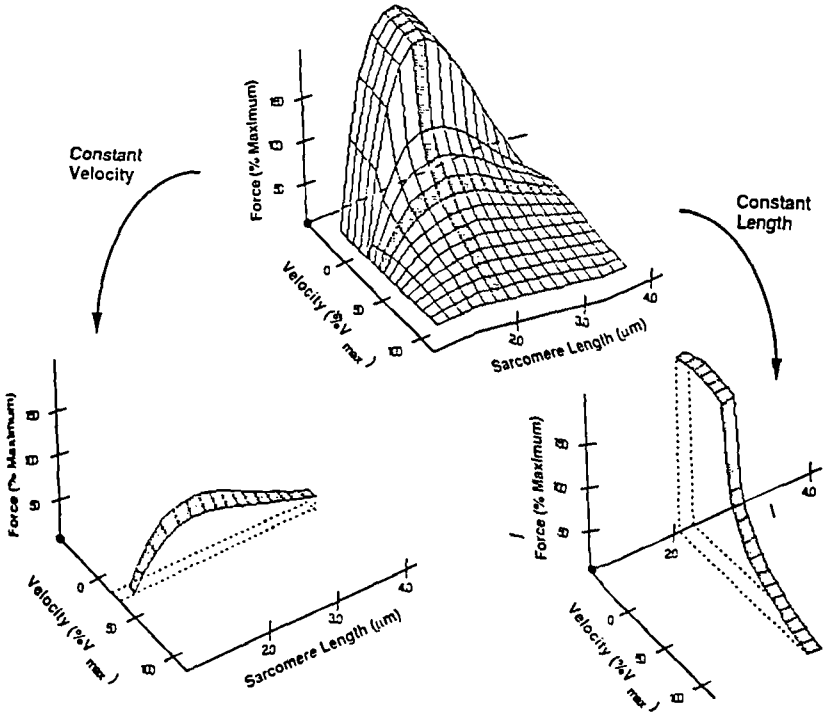


Figure 2.15 The hypothetical muscle length-force-velocity surface for skeletal muscle. Shaded regions represent a slice of the surface at either constant length or velocity. From Lieber (1992)

### 2.4.4.4 Hill's Three-Element Model

Hill's equation was derived from quick-release experiments on frog muscle in tetanized condition. It reveals only one aspect of the muscle behaviour. To be able to model situations where a slow release occurs or strain varies with time, or where a muscle is unstimulated a comprehensive approach is necessary. Several methods have been proposed, the best known being 'Hill's three-element model'. Two alternative configurations of three-element models have been proposed: the *Voigt Model* and *Maxwell Model* (Fig.2.16). That favoured by Hill was the Maxwell model. Brankov and Petrov (1978) demonstrated that if a nerve signal is used as a physiological parameter, instead of $Ca^{++}$ concentration, Hill's three-parametric model should be replaced by a five-parameter model.

The muscle is regarded as an accumulation of identical sarcomeres. The model (Fig.2.17) represents an active muscle as composed of three elements. Two elements are arranged in series: (a) a contractile element, which at rest is freely extensible (zero tension), but when activated is capable of shortening; and (b) an elastic element arranged

in series with the contractile element. To account for the elasticity of the muscle at rest, a 'parallel elastic element' is added. The passive tissue state is modelled by substituting a viscous element for the contractile element.

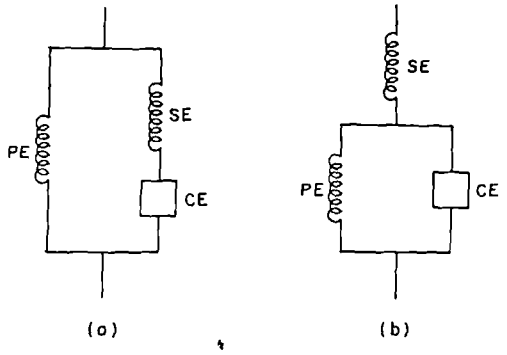


Figure 2.16 Alternative configurations of the three-element models. From Noordergraaf (1978)

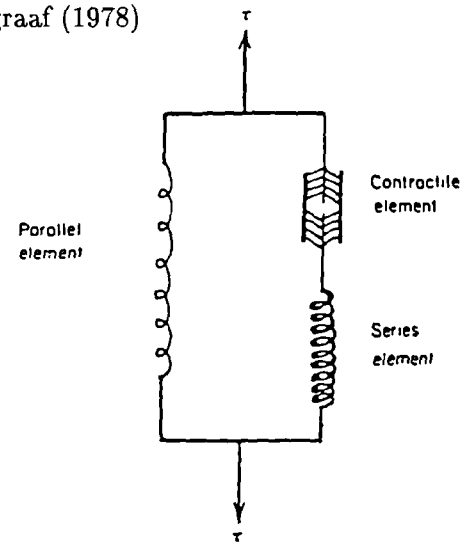


Figure 2.17 Hill's functional model of the muscle. From Fung (1981)

Most authors would identify the contractile element with the sliding actin-myosin molecules, and generation of active tension with the number of active cross-bridges between them. The series elasticity may be due to the intrinsic elasticity of the actin and myosin molecules and cross-bridges, and of Z band and connective tissues. It may arise also from the nonuniformity both of the sarcomeres and of activation of the myofibril filaments. The parallel elasticity may be due to connective tissues, cell membranes, mitochondria and collageneous sheaths.

Assuming that the contractile element contributes no tension in a resting muscle, then the stress-strain-history relationship of a resting muscle determines the constitutive equation of the parallel element. The difference between the mechanical properties of the whole muscle and those of the parallel element then characterizes the contractile and series elastic elements in combination, whose division of the total strain is not uniquely identifiable. However, a model may be postulated by assuming that the contractile element is tension-free when the muscle is in the resting state (resting state is unique), and that

the series elastic element is truly elastic (not viscoelastic). The mathematical derivation of the basic dynamic equations for this model are in APPENDIX B. Modifications have been proposed to make the series and parallel elements viscoelastic. Other approaches result in different configurations for these elements, with one element parallel with the contractile, and another in series with the combination. The basic difficulty with Hill's model and all its modifications is that the division of forces between the parallel and contractile elements, and the series elastic, is made by introducing auxiliary hypotheses on which depend the experimental evaluation of the properties of the elements.

#### 2.4.4.5 Distribution-Moment Model

The models discussed above employ a functional formulation of the state variables of the closed system of thermodynamics. Extraordinary advances have been made in recent years in understanding the mechanism of muscular contraction at the molecular level applying increasingly sophisticated experimental methods, such as diffraction analysis, micromechanical perturbations, microcalorimetry, and fast time resolution of chemical kinetics. These advances, however, appear to have had little impact on macroscopic biomechanics. Although biophysical theories of molecular contraction dynamics admit of precise mathematical formulation and analysis, even in the simplest versions the resulting equations are too complex for direct application. Recently, a muscle contraction model based on the molecular structure (the open system of thermodynamics) has been proposed by Zahalak (1986; 1990; 1994), as a reasonably close connection between the simplified muscle models employed by the biomechanicists and the more complex models of the biophysicists. His technique, dubbed the 'Distribution-Moment (DM) Approximation', uses simple state-variable models of muscle extracted from A.Huxley's cross-bridge theory (Huxley, 1957), and also developed in detail in (Peskin, 1973-74).

The DM theory focuses on the low order moments of the actin-myosin bond-distribution function, as these moments are related directly to important macroscopic variables of muscle function namely stiffness, force, and elastic energy. This approach has been used to develop a muscle-fibre model that encompasses the salient features of activation, contraction, energetics, and metabolism. Although the DM approach suffers the disadvantage of complexity with respect to the Hill-type models, it offers the advantage of simplicity with respect to the Huxley-type kinetic-molecular models.

### 2.4.5 Heart Muscle Structure

Myocardial cells are also striated in the same way as skeletal muscle cells, and their ultrastructure is also very similar. While the basic mechanism of contraction is the same,

important differences do, however, exist. The most significant difference between skeletal and cardiac muscle is the semblance of a syncytium in cardiac muscle with branching interconnecting fibres. The myocardium is not a true anatomical syncytium. At the ends, each myocardial cell is separated from its neighbour by dense structure, intercalated discs, which are continuous with the sarcolemma. Nevertheless, cardiac muscle functions as a syncytium, since a wave of depolarization is followed by contraction of the entire myocardium when a suprathreshold stimulus is applied to any one focus in the atrium. Graded contraction, as seen in skeletal muscle by activation of different numbers of cells, does not occur in heart muscle. All cells of the heart act as a concerted whole (all-or-none-response).

The second difference is the abundance of mitochondria in cardiac muscle as compared with their relative sparsity in skeletal muscle. The heart muscle relies on the large number of mitochondria to keep pace with its energy needs. The skeletal muscle is called on for relatively short periods of repetitive or sustained contraction, and relies only partly on the immediate supply of energy by mitochondria, the remaining energy being supplied by anaerobic metabolism, which builds up a substantial oxygen debt. In contrast, cardiac muscle has to contract repetitively for a lifetime, and is incapable of developing a significant oxygen debt.

A third difference is the abundance of capillary blood vessels in the myocardium as compared with their relatively sparse distribution in the skeletal muscle. This is consistent with the greater need of the myocardium for an immediate supply of oxygen and substrate for its metabolic machinery. The exchange of substances between the capillary blood and myocardial cells is helped further by a system of longitudinal and transverse tubules (T tubules), that play a part in excitation-contraction coupling.

Recent studies have revealed an extensive network of connective tissue in the myocardium, see for example (Robinson et al., 1987). This extracellular matrix is organized into a distinct hierarchy of different structures. Robinson classified these structures using a terminology associated with the organization of connective tissue network in skeletal muscle. The connective tissue network surrounding individual myocytes or coupling adjacent myocytes is called *endomysium*; *perimysium* is the collagen network surrounding groups or bundles of fibres and linking contiguous bundles; and *epymysium* is the connective tissue coat surrounding the entire muscle. This scheme, generally accepted, works well for papillary muscle and trabeculae, the myocardium which most closely resembles skeletal muscle, but is less appropriate for ventricular myocardium.

### 2.4.6 Cardiac Muscle Mechanics

Mechanically, the most important difference between cardiac and skeletal muscles lies in the importance of the resting tension in the normal function of the heart. However, other differences like the time dependence of the active state, the dependence of the active

state on the mechanical history of the contraction, the length-dependence of developed tension in the physiological range of lengths, need to be take into account in a muscle mechanics study.

Fig.2.18 shows the relationship between the end-diastolic volume and the end-diastolic and peak systolic pressure in the left ventricle of a dog. If the tension is computed from the pressure and is plotted against the length of muscle fibres, a diagram similar to Fig.2.13 will be obtained with the ordinate and abscissa giving respectively muscle tension and muscle length. When such a diagram is compared with Fig.2.13 for the skeletal muscle, two observations can be made: (a) in the normal (physiological) range of muscle length, the resting tension is entirely negligible in the skeletal muscle, but is significant in the heart muscle; (b) because of the resting tension, the operational range of the length of the heart muscle is quite limited, whereas that of the skeletal muscle can be larger.

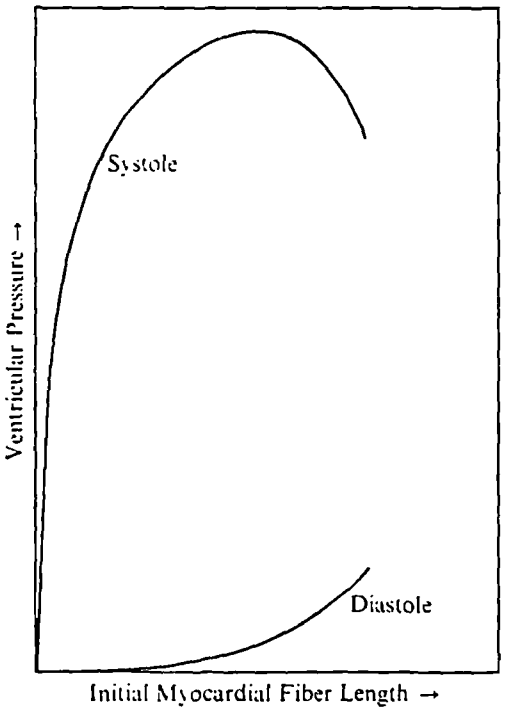


Figure 2.18 Relationship of the left ventricular end-diastolic volume to end-diastolic and peak systolic ventricular pressure in intact dog heart. From Fung (1981)

Initial studies of cardiac mechanics concentrated on the active state, and the passive state was ignored. The first attempts to characterize fully the mechanical properties of passive myocardium are due to Pinto and Fung (1973). From the mechanical point of view, a heart muscle in the passive state is an inhomogeneous, anisotropic, and incompressible material. Its properties change with temperature and other environmental conditions. It exhibits stress relaxation under maintained stretch, and creep under maintained stress (Fung, 1970). It dissipates energy and has a hysteresis loop in cyclic loading and unloading. Thus, heart muscle in the resting state is viscoelastic (Pinto and Patitucci, 1980). When a heart muscle is subjected to a cyclic loading and unloading at a constant strain rate, the stress-strain curve stabilizes into a unique hysteresis loop,

which is independent of temperature (in the range 5-37$^0$ C) and is affected by the strain rate only in a minor way. Thus the pseudoelasticity concept is applicable (see section 2.8.1)(Fung, 1981).

The differences in properties between skeletal and cardiac muscle have compounded the difficulties encountered in quantitative studies of cardiac muscle. In spite of this, the pattern followed by researchers of skeletal muscle has been adopted by several workers in the field of cardiac muscle. Roughly speaking, Hill-like models are similarly applicable. The only modification that is needed is to introduce a factor of an 'active state' to relate the maximum force and the maximum velocity that occur in Hill's equation with the time after stimulation. The confirmation is quite good if the muscle is tested at a length so small that the resting tension in the parallel element is negligible compared with the active tension. The existence of the rest tension requires that a model for heart muscle behaviour must consist of at least three elements.

In consistency with the above, the Voigt and Maxwell models have been proposed. Hefner and Bowen (1967) adopted a three-element model identical to the one denoted in Fig.2.16(a) (parallel resting tension). Brady (1967) selected an alternative (Fig.2.16(b))(series resting tension), while Parmley and Sonnenblick (1967) concluded that neither sufficed, and, in fact, that a four-element model was required. Although many multi-element models have been developed, the most useful current model of the mechanical properties of the heart muscle considers each muscle fibre as composed of two elements (Fig. 2.17). In this case, if the series element is assumed elastic, then its elastic characteristics can be determined by the methods described in APPENDIX B. Extensive work on the series element has been reported by Parmley and Sonnenblick (1967), Edman and Nilsson (1968; 1972), and others.

For cardiac muscle of such a length that the resting tension must be taken into account, the analysis of the experimental data according to the three-element model becomes complex. Many authors have looked into this problem, and varying results are reported. Hefner and Bowen (1967) found bell-shaped force-velocity curves and concluded that the maximum velocity of shortening occurs for loads appreciably larger than zero. They found near-hyperbolic behaviour, however, for large resting tension. Experimental results demonstrated non-unique model-dependence. Since all these complications are associated with attempts to take the parallel element into account, it was concluded that identifying this element with the unstimulated resting muscle was not successful. Also the assumptions concerning the contractile element may not be valid. Then perhaps, having considered these difficulties, the three-element model severely limited in empirical value. An alternative more general approach was proposed by Fung (1981), called *fading memory theory*, which could accomodate any experimental results.

Recently, Lacker and Peskin (1986) developed a cross-bridge model with a very simple relation between actin activation and tension development during isometric contraction. Their model is general enough to fit the complete force-velocity relation observed in isolated cardiac muscle. This model was used by Guccione and McCulloch (1993c) to

develop the constitutive relations for active stress in cardiac muscle.

Active work has continued in the application of the principles of muscle mechanics derived from isolated preparations to the analysis of function in the intact heart. The mechanism which determines the contraction of isolated cardiac muscle affects the contraction of the whole heart. However, in order to know how the entire muscle contracts, the fluid mechanical equations for the blood, together with the solid mechanical equations for the wall, need to be coupled to the muscle mechanics of the single fibre presented so far. This discussion will be faced in section 2.7 when ventricular modelling will be reviewed.

## 2.5 HARNESSING SKELETAL MUSCLE POWER FOR CARDIAC ASSISTANCE

There is a long history of attempts to use skeletal muscle power for cardiac assistance. Compared to myocardium, normal skeletal muscle is far less resistant to fatigue, and the problem is exacerbated when the muscle is activated via the unphysiological route of electrical stimulation. This susceptibility to fatigue thwarted the pioneering attempts to harness skeletal muscle to the performance of cardiac patterns of work. In 1969, Salmons and Vrbova (1969) discovered that chronic indirect electrical stimulation produce in skeletal muscle a complete transformation in which the fast muscle acquires all the physiological, biochemical, and morphological attributes of a slow-twitch, fatigue resistant muscle. In terms of the mechanical behaviour of the muscle, the overall response to chronic stimulation is a reduction in contractile speed.

In this section, we will discuss the physiological, biochemical, and engineering problems related to the fatigue resistant property of normal skeletal muscles, the conditioning process, the mechanical properties and the power generating capacity of the conditioned muscle compared to the normal skeletal muscle.

### 2.5.1 Skeletal Muscle Fatigue

As discussed in section 2.4.5, skeletal muscle and cardiac muscle share many similarities, but they differ in several important physiological and histological properties. Cardiac muscle functions as an electrical syncytium, while skeletal muscle fibres are arranged into motor units that contract individually, as each unit contains its own nerve ending. An electrical stimulus applied to a skeletal muscle motor nerve may be sufficient for contraction of some, all, or none of the motor units. In this way, the strength of a contraction is a function of the number of motor units activated as well as of the rate of recruitment. A single twitch generated by a single electrical stimulus is usually not sufficient to cause skeletal muscle to generate cardiac-type work. A burst stimulation leads

to rapid mechanical summation of motor units and generation of substantial contractile force, whose magnitude and duration can be modified by varying the burst stimulation parameters.

Histologically, cardiac muscle cells are relatively uniform while in skeletal muscle two basic fibre types may be distinguished. Type-I fibres are oxidative fatigue resistant like cardiac muscle fibres, use aerobic metabolism and contract slowly. Type-II fibres are glycolitic fatigue sensitive fibres, use anaerobic metabolism and contract rapidly. These are more plentful than type-I. The relative number of each fibre type varies in response to the work with which a particular muscle is required to perform. Histochemical study of skeletal muscle shows specific myosin isotypes correlating with each of the differing fibre types. Type-I fibres have a specific 'slow' isoform of myosin, while type-II fibres have an analogous 'fast' myosin isoform. *Fatigue* occurs when the high-energy phosphate reserves of skeletal muscle have been used up and the muscle is no longer able to replenish high-energy phosphates at the rate that is being utilized.

Salmons and Vrbova (1969) found that 'it was the pattern of the stimulation through the motor nerve which governed the ultimate definition of muscle type, and not the motor neuron characteristic'. Slow-twitch muscles are subjected to chronic low-frequency stimulation. If fast-twitch skeletal muscle undergoes a similar stimulation, an orderly sequence of changes occurs, which results in the transformation of a fast-twitch muscle into a slow-twitch muscle. Whereas some features of this response are seen in the muscles of athletes undergoing endurance training, chronic electrical stimulation can accomplish the complete spectrum of adaptive changes in a matter of weeks.

### 2.5.2 Skeletal Muscle Adaptation to Electrical Stimulation: Conditioning Process

The discussion that follows is based on the material published by Lieber (1992). Skeletal muscle is one of the most adaptable (plastic) tissues in the body. This includes architecture, fibre type distribution, tendon length, fibre diameter, myosin profile, mitochondrial distribution, capillary density, and fibre length. Chronic electrical stimulation produce this sort of adaptive transformation. If the stimulator is activated at a nominal frequency of about 10 Hz and allowed to operate 24 hours a day, a well-defined progression of changes is observed whereby the fast muscle first changes its metabolic and then its contractile properties to transform completely into a slow muscle.

The histochemical assay for myofibrillar ATPase is used to distinguish between fast - and slow- contracting muscle fibres. In fact, Barany (1967) found that $V_{max}$ and myosin ATPase activity were directly proportional. Myosin activity ATPase is a rate expressed in units of moles of product per unit mass per time interval, that is millimoles protein per minute in the case of the myosin ATPase assay.

Experimental data from a number of laboratories including the work of Eisenberg

(Chicago), Pette (Konstantz), and Salmons (Liverpool) have documented transformation in a number of different muscles and species. The fast-to-slow transformation that occurs is detectable using modern techniques such as measurement of muscle contractile, ultrastructural, histochemical, biochemical, and morphological properties. In all cases, following transformation, the new slow fibres are almost completely indistinguishable from normal slow skeletal muscle fibres (Einsenberg and Salmons, 1981; Eisenberg et al., 1984; Salmons and Henriksson, 1981; Pette, 1980; 1990).

If low-frequency stimulation is applied 24 hours a day, the total transformation process requires only about 8 weeks. The earliest observed changes occur within a few hours after the onset of stimulation, when the sarcoplasmic reticulum begins to swell (Fig.2.19). Within the next 2-12 days, increases are measured in the volume percent of mitocondria (Eisenberg and Salmons, 1981), oxidative enzyme activity (Henriksson et al., 1990), in capillaries (Brown et al., 1976), total blood flow, and total oxygen consumption, reflecting the increased metabolic activity of the muscle (Fig.2.19(B) and (C)). The increase in oxidative enzymes and capillary density is manifested as a decrease in muscle fatiguability. At this point, the width of the Z-band begins to increase toward the wider value observed for normal slow muscle (Fig.2.19(D)). The amount and activity of the calcium transport adenosine triphosphatase (ATPase) decreases and changes its particle distribution within the SR layer (Fig.2.19(E)). This decrease in the amount and activity of the calcium (ATPase) to levels approaching those of slow-twitch type-I fibres can be detected as prolonged time-to-peak twitch tension and a prolonged relaxation time of a muscle twitch, or as a decrease in the fusion frequency. There is a decrease in the tetanus-twitch ratio and the rate of tension development. This slowing is also a consequence of the changes in the myosin isoforms which result in less rapid cycling of the cross-bridges formed between the thick and the thin filaments (Brown et al., 1983). As a result the muscle can develop substantial forces at much lower frequencies of activation, and the energy cost of those contractions is substantially reduced (Crow and Kushmerick, 1982). Finally, after about 4 weeks of continuous stimulation, an alteration in the myosin light chain profile is observed whereby the muscle contains light chains characteristic of slow fibres. By this time, muscle fibre cross-sectional area, maximum tetanic tension, and muscle weight have decreased significantly (Fig.2.19(G)). The Z-band is now the full width of that normally observed in a slow fibre, and the density of the T-system is greatly decreased (Fig.2.19(H)). In every respect, the muscle is indistinguishable from a normal slow skeletal muscle. Under such conditions skeletal muscle never becomes cardiac muscle, but it can become functionally indistinguishable from the myocardium in terms of its ability to deliver significant pumping work indefinitely without fatigue.

As a result of this *conditioning* process, as Dr. Stephenson coined it, the muscle is potentially capable of performing cardiac work. Such muscles show more efficient coupling between the development and maintenance of tension and the consumption of oxygen (Acker et al., 1987d), and a production of ATP that can match even extreme increases in its utilization during high-intensity repetitive contractions (Clark et al., 1988).

This set of phenomena may be interpreted as evidence of a natural adaptive capacity of skeletal muscle (Salmons, 1971; Salmons and Stephenson, 1989). In the absence of activity, differentiation is oppositely directed, so that the mucles tend to retain, or revert to, a native fast state. Changes due to chronic stimulation have been found to undergo complete reversal after stimulation has been discontinued (Brown et al., 1989; Salmons, 1990b). There is growing evidence that the changes seen during stimulation and recovery suggests that there is a threshold which must be exceeded for these changes to take place. This *threshold* concept has been discussed in Salmons (1980). A general feature of the recovery process is that changes tend to take place on a 'first-in, last-out' basis, so that the earlier a parameter changes during the course of stimulation, the later it returns to control level during recovery.

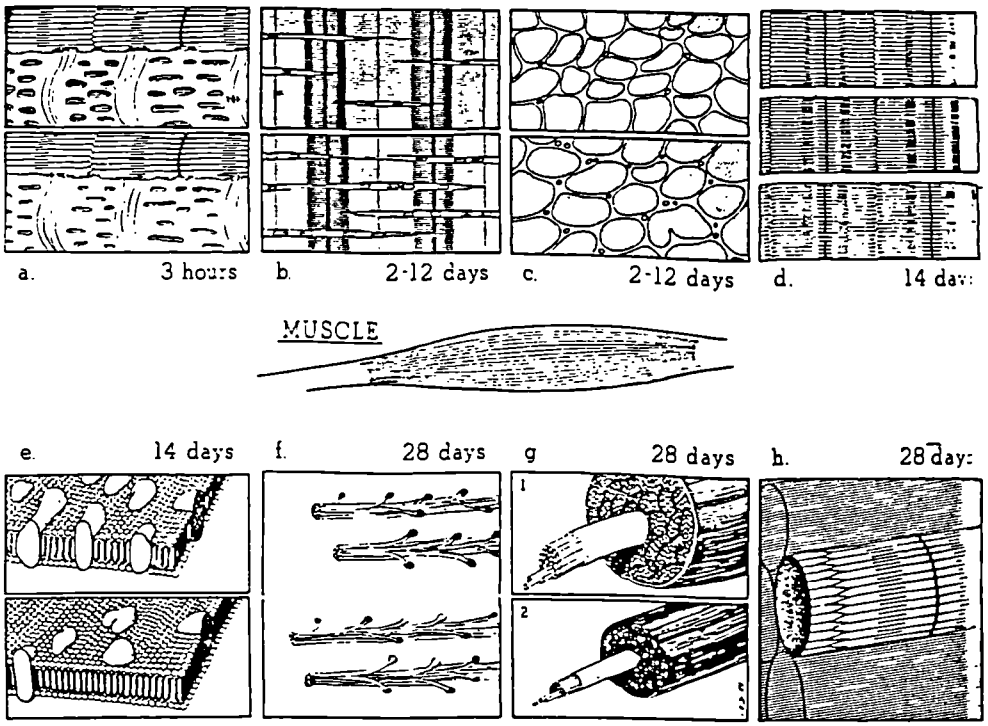


Figure 2.19 Schematic representation of the time course of muscular adaptation to chronic stimulation trasforming a fast to slow fibre. In each panel the normal fibre is shown in the upper panel and the stimulated fibre in the lower panel. From Lieber (1992)

Optimal stimulation regimes are a key area of research and development, fundamental to the successful use of skeletal muscle for long term cardiac assistance. Macoviak et al.(1982) first showed that direct electrical conditioning at 10 Hz of the canine diaphragm after five weeks results in nearly a complete transformation to a slow-twitch, fatigue resistant muscle in areas adjacent to the stimulating electrode. Armenti et al. (1984) extended this work to show that the entire muscle could be converted using indirect stimulation of the phrenic nerve. As LD is used infrequently, it is a relatively

fast twitch muscle and fatigues rapidly. Mannion and co-workers (Mannion et al., 1986c) demonstrated that the latissimus dorsi could be preconditioned at stimulation frequency of either 2 or 10 Hz, while the same effect was obtained on the canine diaphragm with stimulation frequencies of 2 and 4 Hz (Acker et al., 1987c). Further work by Acker et al. showed that near complete transformation of LD could be accomplished after several weeks of electrical preconditioning using intermittent burst stimulation at a frequency of 25 Hz, and a yielded contraction of 54/min. The preconditoning process was completed in a 6 week period of isometric contractions, followed by a period of contraction against a mock circulation device for measurement of stroke work and power output (Acker et al., 1986). A second similar experiment demonstrated that the preconditioning process could be accomplished while the muscle was performing useful-type work and contracting against the mock circulation device (Acker et al., 1987a). Total conversion of muscle fibre types of LD muscles stimulated in situ with a continuous 2 Hz pattern was obtained by Carraro et al. (1990).

### 2.5.3 The Power-Generating Capacity of Skeletal Muscle

The following discussion is largely based on the material published by Salmons and Jarvis (1992) and summarized as below.

The maximum value of the power required for pumping in cardiac assistance is given by:

$$P = Q \times P' \tag{2.7}$$

where Q is the mean flow rate, and P' the average systemic pressure. This is estimated for a normal 70 kg subject at rest (Q=6 l/min, P=100 mm Hg) to be about 1.3 W. In order to support activities such as walking and climbing stairs, the pump should have a short term capacity of 10 l/min, and therefore a power capability of 3 W. These levels are necessary when most of the power required for producing the systemic blood flow is provided by the assist device. For partial assistance lower levels of operation are acceptable.

Skeletal muscle represents a particularly attractive biological source, as it is capable of converting the small amount of energy required to stimulate the motor nerve into mechanical work with great efficiency. The power available is determined by: (i) the mass of well-vascularized tissue that can be recruited for the purpose, (ii) the sustainable power per gram of tissue, and (iii) the way in which power is to be coupled to the circulation. Configurations requiring the muscle to be diverted entirely from its normal function and transposed into a new position would have the benefit of a high efficiency in the utilization of the energy available; while configurations where the muscle operates in situ would have the benefit ofa major freedom in the choice of the suitable muscle, but a poorer efficiency.

The power produced by the human left ventricle at rest is about 4 W/kg of muscle tissue. The average mass of an adult male latissimus dorsi muscle is 600 g. For a sustainable pumping power of 1.3 W, with a reserve capacity for short-term use of 3 W, the power required would be 2.1 W/kg of muscle tissue, with a short-term capability of 5 W/kg.

In order to analyse the capacity of continuous power production of a single skeletal muscle Prof. Salmons and Dr. Jarvis at the University of Liverpool (Jarvis, 1990; Salmons and Jarvis, 1992) have performed experiments using the rabbit tibialis anterior muscle to measure the effects of long artificial electronic activation. An ergometer has been designed to facilitate the investigation of the relationships between force, velocity, power, and endurance in the rabbit tibialis muscle (Jarvis and Salmons, 1990). Fig.2.20 shows the force-velocity and power-velocity curves for such a muscle. The curves show the rate of work output at any velocity of shortening between zero, where the force is maximal but the power (force $\times$ velocity) is zero, and the maximum unloaded shortening velocity, where all the force produced is used to achieve shortening within the muscle, and the external output is also zero. Between these extremes of zero power output, there is a velocity ($V_{opt}$) for which the power output is maximal.

The curves of characteristics show very clearly that the power output of skeletal muscle is highly dependent on the load and that for a muscle to deliver its maximum power it must work against a load which allows it to shorten at a velocity near to $V_{opt}$. In cardiomyoplasty or in the construction of skeletal muscle ventricles, the relationship between the geometrical configuration of the muscle graft and the imposed load should be considered so that the surgical technique can be optimised mechanically within the anatomical limits. This is not a simple task, and require the use of numerical modelling of the solid mechanics to predict the performance of skeletal muscle as a hydraulic pump, after having duly taken into account the fundamental properties of the muscle fibres.

In Fig.2.20, $V_{opt}$, expressed in fibre lengths per second, varies between fibre types. Chronic stimulation of fast-twitch skeletal muscle produces a transformation towards slow muscle characteristics. Fast-twitch fibres produce their maximal power output at about 2 fibre lengths/s and slow-twitch fibres at 0.5 fibre lengths/s. For an unconditioned rabbit TA muscle, the maximum acute power output is about 300 W/Kg. After 8-10 weeks of continuous stimulation at a frequency of 10 Hz, the mass falls to 50% of control and $V_{opt}$ to 25% of control values. The combined effect of these losses is a reduction in power output to about 10% of control values (Fig.2.20, lower curve), that is the maximal acute power output of the stimulated muscle is still 30-40 W/kg, close to the systolic power of the left ventricular myocardium. These power outputs refer only to the rate at which work is performed during contraction. In any practical application, the muscle spends at least as much time in relaxation as in contraction, and since work is available only during contraction the maximum power output is about 20 W/kg. At the specified work rates of 2.1-5 W/kg, then, the stimulated muscle would be working at 10-20% of the maximum.

The characteristic curves only describe the behaviour of muscles in single maximally

activated contractions and do not therefore give any direct information concerning the contraction duration and the endurance of the muscle. Optimal timing of conditioned skeletal muscle contraction is essential for effective cardiac augmentation, and, unlike mechanical devices, skeletal muscle requires time to develop a peak of tension. Recently. Letsou et al. (1994) found that conditioned skeletal muscle needed, on average, 0.35 sec to develop peak tension and 0.20 sec for 90% relaxation. Thus, 0.55 sec of muscle contraction/relaxation cycle was devoted to development of peak tension and successive relaxation.

Fatigue tests performed on the same muscles have shown that conditioned muscles working under conditions in which they were constrained to perform external work at 10 W/kg, were able to maintain this level of work for many hours whereas control muscle showed progressive fatigue at the same initial work rate, even though their maximum power capacity was much greater. The induction to fatigue resistance to the power requirement appears to occur early in the sequence of the progressive changes of the transformation. After 2 weeks of stimulation at 10 Hz, for example, the contractile apparatus itself is little changed and the acute output power is still 50% of control but there is a large increase both in the extent of the vascular bed in the capacity of the aerobic pathways of ATP production. The fatigue resistance of muscles in this state is not significantly different from muscles in the extreme state of transformation. This 'ideal' intermediate state with good power output and high fatigue resistance would appear to be much better suited for use in cardiac assistance. Fibres with these properties exist in normal muscles, and are called 2A type.

Experiments have been conducted at lower stimulation frequencies by the Liverpool research group to see if these properties could be maintained stably. These experiments showed that skeletal muscle could become sufficiently fatigue-resistant to perform cardiac work without concomitant induction of slow myosin heavy chain isoforms by continuous stimulation at 2.5 Hz (Jarvis et al., 1991a; Jarvis et al., 1991b). Analysis of metabolic changes in muscles stimulated for 10 months at 2.5 Hz showed no secondary decline in oxidative enzyme activity as shown in muscles stimulated at 10 Hz. Current experimental research is being carried out in which these patterns of stimulation are maintained for nearly one year, in order to examine the long-term stability of the changes. The challenge will be to devise stimulation regimes that fulfil the functional requirements of the cardiac assistance application while still maintaining in the long term an appropriate combination of muscle properties.

Conventional, constant-frequency burst stimulation is unphysiological and wastful of energy. New approaches are being developed based on the changing interpulse intervals found in motorneurone firing patterns. A comprehensive study of the relationship of force and force-time integral to the interpulse intervals contained in the stimulating pattern have been performed for determining the optimum pulse train for muscles of given contractile speed. Optimized pulse trains should enable the cost of contraction to be reduced, so that effective stimulation can be introduced at an earlier stage of conditioning; the

reduced number of impulses will also be important for minimizing the tendency to induce slow contractile characteristics.

A new promising technique for providing powerful cardiac assistance avoiding the disadvantages of muscle conditioning (loss of power, mass, contractile speed) from skeletal muscle has recently been developed by Guldner and his group (Guldner et al., 1994). This method consists of the initial combination of electrical conditioning with dynamic training of the SMVs against an elastic compliant afterload (obtained with the opposition of the flow direction in the SMVs using special heart valves), which resulted in a strong muscle pump that did not develop fatigue. The elastic training device is removed once the electrical and dynamic training has been completed.

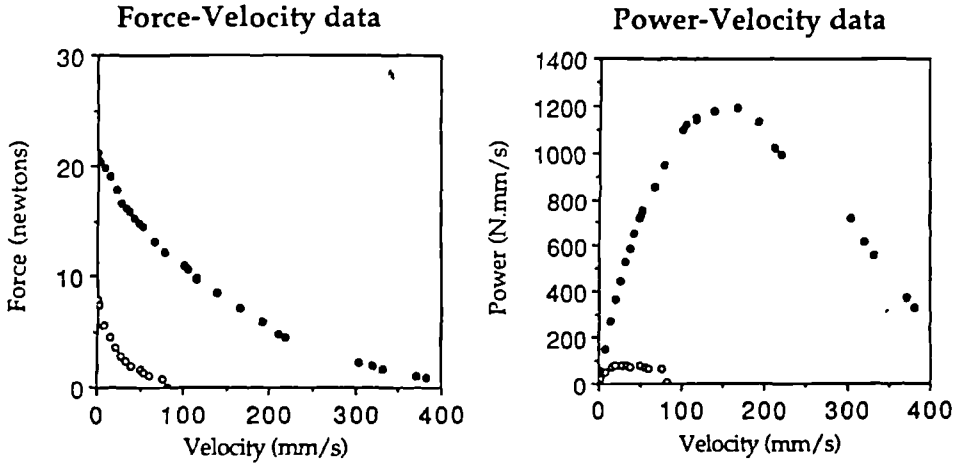


Figure 2.20 Force-velocity and power-velocity curves for a control rabbit tibialis anterior muscle (filled circle) and its contralateral muscle that has been stimulated at 10 Hz for 8 weeks (open circles). From Jarvis (1990)

### 2.5.4 Harnessing Skeletal Muscle Power

A power-generating capacity per muscle mass unit of 10 W/kg has to be regarded as an overestimate because it is based on rabbit muscle; the specific power of human muscle is intrinsically less, because of its slower contractile characteristics (Faulkner et al., 1992). However it would be sensible to allow for a reduction to 8W/kg. The actual mass will also be less than the starting one (from 600 g to 225 g), for several reason (transformation, grafting procedure, ischaemic damage). The power available would therefore be unlikely to exceed 1.8 W. Since the power requirement for cardiac assistance is 1.3-3 W, this estimated power available could be harnessed to provide a substantial assist (8 l/min) (Salmons and Jarvis, 1992).

As seen in section 2.3, two main approaches are available to couple skeletal muscle to the circulation:

1. direct coupling to the circulation;
2. indirect coupling to the circulation.

Direct mechanical linkage (Fig.2.3(F)) would be moderately efficient, especially if the muscle were allowed to operate in its normal line of action and without disturbance to its vascular supply. Problems would compromise the need for the assist device to be close to the muscle, and the difficulty of creating a strong and reliable junction between a muscle and a non-biological surface. A hydraulic link could be established by wrapping a muscle around a fluid-filled bladder (Fig.2.3(G)) (Anderson et al., 1988b) or, more conservatively, by arranging for the bladder to divert the muscle from its normal line of action, so that it would be compressed when the muscle contracted (Li et al., 1990). This approach would give a little more freedom in the placement of the assist device relative to the muscle, at the cost of some resistive energy losses in the coupling lines. However, all existing biopolymers are permeable to some extent, so that in the present state of development it would be possible to avoid a progressive escape of fluid from the system.

An indirect approach (Fig.2.3(H)), in which contraction of the muscle was coupled to the generation of electricity, has several advantages - flexible placement, broad choice of assist devices - accompanied by the disadvantages of the technological problems and the high cost. Estimating a 50% rate of energy conversion, the maximum pumping power available from human muscle working at 8 W/kg would be 0.9 W, equivalent to 4 l/min for the mechanical and hydraulic approaches. The electromechanical approach involves two conversions, and the maximum pumping power available would therefore be 0.45 W, equivalent to 2 l/min. Thus partial assistance of the resting heart function borders on feasibility with this technique, but the reserve capacity would be limited (Salmons and Jarvis, 1992).

In section 2.7 possible approaches for ventricle modelling will be presented with the purpose of providing an adequate background for the future coupled solid-fluid modelling to be used in the modelling of skeletal muscle ventricles. This discussion will be preceded by a review on blood flow modelling presented in the next section.

## 2.6 BLOOD FLOW MODELLING

As mentioned above, for the purposes of formulating a comprehensive approach of fluid and solid mechanics to be applied in the modelling of SMVs, the fluid-dynamics and solid mechanics equations have to be coupled. In this section applications of the former (fluid dynamics) to blood flow modelling will be reviewed and discussed.

The three-dimensional and unsteady characteristics of blood flow throughout the cardiovascular system make the mathematical analysis a challenging problem. The analysis is complicated by the compliant nature of the vessels in which the blood flows, and by the rheological properties of blood. Powerful Computational Fluid Dynamics (CFD) codes developed in the last few years allow the modelling of realistic geometries with moving walls. This is an important feature of physiological flows, which are mostly driven by the periodical motion of the blood vessels at each cardiac cycle.

The rheological properties of blood and its constituents play an important role in the physiology of the circulation of the blood. In large vessels, blood can reasonably be considered a homogeneous incompressible fluid, although non-Newtonian effects become significant in the pulsatile flow (Liepsch, 1986). Kobayashi and Pereira (1994) demonstrated that blood cannot be considered Newtonian for separated flows, even in large vessels. Nevertheless, it has been shown that basic features of the flow are not affected (Perktold et al., 1991; Xu and Collins, 1994) and it may be concluded that non-Newtonian effects can be considered a 'third-order' effect after geometry and wall distensibility effects. A discussion on blood rheology and its interactions with the flow will be given in section 2.6.1. A discussion on blood flow modelling, concentrating on blood flow in the large vessels, will follow in section 2.6.2, where applications to arterial wave propagation, bifurcations, stenoses and grafts will be briefly reviewed. These have been extensively studied in the context of the work on blood flow modelling developed in the Biomechanical Research Group at City University over the last decade and satisfying results have been achieved. In this discussion, particular attention will be paid to natural and artificial ventricles, that is artificial hearts and assist devices. Finally, cardiovascular diseases and blood trauma caused by fluid-dynamics factors will be discussed in section 2.6.4.

### 2.6.1 Rheological Properties of Blood

The rheological properties of blood and its flow in the cardiovascular system of humans have posed a serious challenge to researchers through the ages. Efforts have been made and theories postulated, yet even today, with the most modern sophisticated equipment and methods available, this fluid has defied attempts at a completely satisfactory solution (Rodkiewicz et al., 1990).

Human blood is a suspension of cells in a complex acqueous solution called *plasma*. The plasma is about 90% water by weight, 7% plasma protein (mainly fibrinogen, globulin and albumin), 1% inorganic substances, and 1% other organic substances. The cellular contents are essentially *red cells* (erythrocytes), occupying 97% of the total particle volume, with *white cells* (leukocytes) of various categories, and *platelets*. For a normal human body the value of hematocrit (concentration of cells in the total volume of the suspension) is around 45% in large vessels, and 25% in small arterioles or venules (Cokelet, 1972). Human red cells are biconcave disk shaped, white cells are more rounded and there are many types. Platelets are much smaller and they play a significant role in the formation of blood clots.

The mechanical properties of blood are determined by those of plasma, the rheological properties of the red cells, and the distribution and interaction of individual cells. Whole blood has a density between 1.05 and 1.06 $\times$ $10^3$ Kg/m$^3$. Plasma behaves like a homogeneous Newtonian viscous fluid (Merrill et al., 1965), and its viscosity varies with temperature. Blood behaves as a non-Newtonian fluid, due to the presence of suspended

cells. Its apparent viscosity varies with the rate of shear (pseudoplastic fluid), with the hematocrit, the temperature, the vessel diameter and eventual desease state (Chien et al., 1966). Fig.2.21 shows the variation of blood viscosity with the shear rate and the temperature. In addition to its pseudoplastic behaviour, it was observed that under static conditions whole blood exhibits a *Bingham plastic* behaviour. This means that a certain minimum force (yield stress) is necessary to initiate flow. However, it should be pointed out that the yield stress for blood is extremely small (of the order of 0.05 dyn/cm$^2$), and that it is doubtful that a yield stress would exist in dynamic situations. The non-Newtonian behaviour becomes insignificant when the shear rate is greater than 1000 s $^{-1}$, and the apparent viscosity approaches an asymptotic value of $4 \times 10^3$ Kg/ms. As the shear rate decreases the apparent viscosity increases slowly, until at a rate less than 1 s $^{-1}$ it rises extremely steeply. Experimental studies have shown that at hematocrit up to about 12%, a suspension of red cells in plasma behaves like a Newtonian fluid at all shear rates, although it has a higher viscosity than plasma. As the hematocrit increases, not only does the viscosity of the suspension increase, but also non-Newtonian behaviour is evidenced.

There are two primary reasons for the characteristic behaviour of whole blood. First, red blood cells deform at high shear rates in such a way as to reduce the resistance to flow. Second, at low shear rates, red blood cells aggregate and form rouleaux which increase apparent viscosity (Chien, 1970). The existence of rouleaux is related to the presence of the proteins fibrinogen and globulin in the plasma. The slower the blood flows, or rather, the smaller the shear rate, the more prevalent are the aggregates. When the shear rate increases, blood aggregates tend to be broken up, and the viscosity of blood is reduced. As the shear increases further, the deformation of the red cells becomes more evident, and the cells tend to become elongated and line up with the streamlines. This further reduces the viscosity. Also tumbling of suspended particles (red cells) while flowing disturbs the flow and requires expenditure of energy, which is revealed in viscosity. Detailed studies of the tumbling and deformation of red cells and rouleaux in shear flow have been made by Goldsmith and co-workers (Goldsmith and Marlow, 1972). It has also been pointed out by different investigators that when blood flows in a tube, red cells tend to move toward the axis of the tube, leaving a marginal zone of plasma, increasing in width with increasing shear rate. Goldsmith (1972) found that the deformability of the particle appears to be the reason for lateral migration. Observations of flow containing rouleaux of red cells show that the rouleaux migrate to the tube axis faster than individual red cells. When the cell concentration is high (45% hematocrit), the crowding effect acts against migration away from the wall into the crowded centre. The plasma-rich zone near the solid wall, although very thin, affects blood viscosity, especially in small blood vessels.

In large vessels, blood can reasonably be considered a homogeneous incompressible fluid. It is universally agreed that at very high shear rate ($> 1000\ s^{-1}$) blood can be assumed to be Newtonian. However, recent experimental studies (Liepsch, 1986) showed

that blood may behave as a non-Newtonian fluid, even in large arteries (femoral artery). The normal arterial blood flow is subjected to some cyclic peak shear-rates, and at such shear-rates blood behaves like a Newtonian fluid (Caro et al., 1978). However, high shear-rates occur only during a relatively short part of the cycle period, and predominantly close to the wall. Therefore, it would be more appropriate to consider that blood behaves predominantly as a non-Newtonian fluid (Rodkiewicz et al., 1990), and that for a realistic modelling of blood (even in large arteries) appropriate constitutive equations for the viscous behaviour of blood should be incorporated in accordance with the levels of shear rates established. However, this effect is not considered primary in blood flow modelling.

Furthermore, when blood is tested dynamically, it exhibits viscoelastic characteristics, which change with the level of strain and strain history (that is, a thixotropic fluid). A thixotropic fluid is characterized by the breakdown of structure by shear. Rouleaux disaggregation is the primary cause of this behaviour. Blood, however, is different from some other non-Newtonian fluids in that its thixotropic behaviour is reversible. While the breakdown of rouleaux happen almost instantaneously, the reaggregation time depends on hematocrit, plasma composition, and shear rate.

In the numerical simulations performed in model SMVs, non-Newtonian behaviour of blood was not taken into consideration for simplicity. On the other hand, since the *in vitro* experiments on model SMVs have been carried out using Newtonian fluids, the validation of the numerical predictions had to be performed modelling the fluid as Newtonian. Further *in vitro* and numerical studies on the investigation of the shear rates that establish throughout the cardiac cycle in the whole volume of the ventricle, will show whether it is necessary to use constitutive equations for modelling the non-Newtonian viscosity of blood.

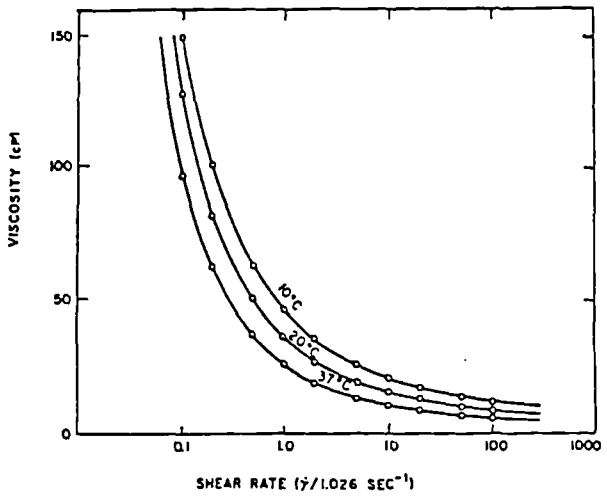


Figure 2.21 Variation of the viscosity of human blood with shear rate and temperature at the hematocrit 44.8%. From Merrill et al. (1965)

#### 2.6.1.1 The Constitutive Equation

Several functional forms for the constitutive equation have been proposed to models the non-Newtonian behaviour of blood, such as the general power law, Bingham model, Casson model, biviscosity model, and Walburn and Schneck model. These are discussed in more detail by Xu (1992) and their mathematical formulations are summarized in APPENDIX C. The Walburn and Schneck model has been shown to be the most appropriate in modelling pulsatile flows in a conduit (Rodkiewicz et al., 1990). However, it was developed for low shear rates, and has been found to be invalid for high shear rates. A separate issue is that these models have validity based on steady flow problems. In reality, blood in the cardiovascular system is changing constantly in chemical composition and shear rate and the interrelations are many and complex. Despite this, the models do offer reasonable and practical constitutive equations for human blood.

The above discussion may be expressed algebraically. For a given sample of blood the stress tensor in its most general form is a function not only of the strain rate tensor and time, but the time history of the strain rate tensor

$$\tau = \tau(\dot{\gamma}(t))$$

The several steady state models represent a simplification of the shear stress expression to

$$\tau = \tau(\dot{\gamma}).$$

#### 2.6.1.2 Effects of Blood Rheology on the Flow

The potential importance of non-Newtonian effects in various physiological flows has been demonstrated by several pioneering experiments. Liepsch and his co-workers found striking differences in flow patterns and calculated wall shear stress in arterial bifurcation models between Newtonian and non-Newtonian fluids. Moravec and Liepsch (1983) found that significant effects of the non-Newtonian behaviour of the blood are likely to occur where separation and reverse flow are manifested even in large blood vessels. Similar conclusions were reported by Ku and Liepsch (1986). Numerical analysis of the effect of the non-Newtonian characteristics of blood was conducted by Dr Xu (1992) on 3-D bifurcation problems. Newtonian and non-Newtonian flow has also been investigated in an artificial ventricle (Mann et al., 1987), and in straight and curved arterial models (Mann and Tarbel, 1990). Differences were found. Kobayashi and Pereira (1994) showed that a non-Newtonian fluid produces higher levels of shear stress, and therefore is prone to produce early damage to the vessels. However, most of the findings have shown that the overall features of the flow appear to be little affected by the choice of the rheological

model, although they could have local significance. These findings agree with the results presented by Perktold et al. (1991).

Analytical and numerical studies relating to non-Newtonian blood flow are more sparse. Pulsatile flow of non-Newtonian and viscoelastic fluids in simple geometries is discussed in Joseph (1990). Pulsatile physiological flows of several constitutive blood models in a straight rigid tube have been compared by Rodkiewicz et al. (1990). Blood rheology substantially influences flow in some modelling conditions in cardiovascular devices and arteries. Sharp (1994) calculated the effect of blood viscoelasticity on velocity profiles and shear stress in flows representative of those in large arteries, such as the ascending aorta and femoral artery. He used an analytical solution for pulsatile flow of a generalized Maxwell fluid in straight rigid tubes, and found small differences in velocity and shear stress, comparing viscous and viscoelastic flow. He concluded that blood behaves nearly as a Newtonian fluid when arteries are approximated as straight tubes, but suggested, however, that viscoelasticity is an important factor where stagnant flows occur and in regions not washed out at each heart beat. This situation, likely to occur in assist devices, would encourage red blood cells aggregation and hence a change in blood viscosity.

### 2.6.2 Blood Flow Modelling

Blood pumped from the left ventricle into the circulatory system creates a change in pressure and results in flow along the aorta and throughout the circulatory system. At any given point pressure and velocity change periodically, and the flow is pulsatile and associated with propagation of a pressure wave. The complete cardiovascular system is far too complex to be amenable to a comprehensive analytical treatment, and the purpose of most of the analyses has focused on the specific aspect of interest.

An extensive account of the early historical development of ideas concerning the circulation is given by Fishman and Richards (1964). The pioneer worker concerning the laminar flow of blood in its vessels was Poiseuille (1846). Interest in arterial blood flow started with Womersley (1955) and McDonald (1960). They developed an analytical linearized solution to calculate the pulsewave propagation for an oscillatory flow of a Newtonian fluid in a circular tube. In the early theoretical studies, linear and non linear theories were extensively used in the mathematical analysis of wave propagation in arterial blood flow. Recently, theory of unsteady flow in collapsible tubes has been developed to model blood flow in veins. In the last three decades, progress has been made in describing blood flow at junctions, through stenoses, in bends and in capillary blood vessels. More recently (in the last two decades), extensive treatments of blood flow problems have been made by solving numerically the Navier-Stokes equations. Early numerical studies were performed using the vorticity stream function method. In order to model 3-D situations primitive variables were used with finite difference or finite element techniques.

### 2.6.2.1 Arterial Flow

Flow and pressure at one point in the arterial tree behave in the manner shown in Fig.2.22. Although the increase in flow starts more or less synchronously with the pressure rise, the peak flow velocity precedes the peak pressure. This is explained by the fact that it is the pressure gradient that determines pulsatile flow. The first derivation of the velocity of propagation of the pulse wave in blood flow was given by Young (1808). Womersley (1955; 1957) found the mathematical solution of an oscillatory laminar flow in a compliant tube when the pressure gradient varied periodically in the form of a sine wave, and for a homogeneous Newtonian fluid. The flow is related to any periodic pressure gradient with a Fourier series. To reproduce the pulsatile nature of arterial flow, oscillatory flow and higher order harmonics of flow may be superimposed on a steady flow.

Greenfield and Fry (1965) derived a pressure-flow relation that is simpler than the more general form of the Womersley theory. Under simplifying assumptions the one dimensional flow equations can be linearized, the resulting equations being analogous to those for electric transmission lines (pressure and volume flow rate are analogous to voltage and current respectively). Advantages associated with the use of this method are its versatility in superposing a partial solution, and analogy with electric transmission lines. However, the linearization process may well introduce errors. In modelling the arterial system wave propagation, the best representation of the pulse wave is given by the application of non linear theories. Anliker et al. (1971) made a significant development of the *method of characteristics* applied to the Navier-Stokes and continuity equations, to model a major canine arterial pathway. The flow is treated as quasi-one-dimensional but the nonlinear terms of the equations are retained.

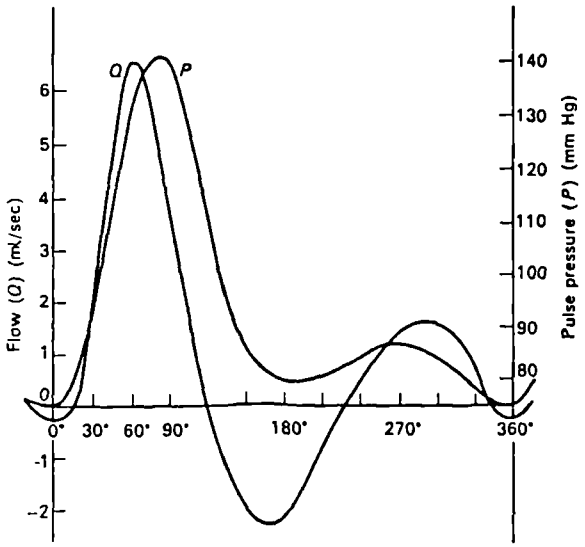


Figure 2.22 A flow velocity pulse (Q) and the arterial pressure pulse (P) recorded simultaneously in the femoral artery of a dog. From Nichols and O'Rourke (1992).

The two techniques discussed above can be applied to a segment of the arterial tree

or to the entire arterial system, and are used either separately or in combination. However, since the flow is treated as one-dimensional, they do not give information on the local flow. The effect of the geometric complexity of the arterial system has been explored recently. A principal effect of the geometric transition of the arterial system is the generation of partial reflections of the pulse wave. While the linear theory of wave reflections has provided considerable insight, in order to provide a more accurate mathematical description of the observed phenomena, several studies have included the effects of transition in the nonlinear theories of blood flow (Jones et al., 1992). Comprehensive theories of wave propagation in the circulatory system based on regarding it as a system of elastic tubes, have been developed in the past three decades. Details on blood *vessel* modelling will be discussed in section 2.6.3.

#### 2.6.2.2 Flow at Arterial Bifurcations

The study of blood flow through arterial bifurcations has been driven to a large extent by the fact that these areas of the cardiovascular system appear to be preferred sites for atheroma. There is evidence that due to the complex nature of the flow occurring in arterial bifurcations the walls in these regions experience low and fluctuating shear stress. Modelling of flow in bifurcations involves treating the complex three-dimensional geometry of the bifurcation, the pulsatile nature of the flow, the distensibility of the arterial wall and the non-Newtonian characteristics of the blood.

A study on the development of numerical models for the analysis of flow in arterial bifurcations is given by Xu (1992). Initial studies were confined to two-dimensions in the 1970s. However, three dimensional modelling is virtually essential, due to the presence of such phenomena as secondary flows. Three-dimensional pulsatile flow simulations in realistic geometrical models of arterial bifurcations have become possible with the latest CFD codes and computers. These simulations are expected to clarify the role played by haemodynamics in the formation of atheromatous plaques. In the last couple of years, Perktold and co-workers (Perktold et al., 1991) have studied three-dimensional, pulsatile flow in realistic models of the human carotid artery bifurcation. He used a newly developed pressure correction finite element method, which includes a realistic velocity waveform and consideration of non-Newtonian effects. Xu et al. (1992) have performed three-dimensional simulations of the flow through canine femoral bifurcations. Geometry and inlet velocity waveforms were based on in vivo measurements.

Few attempts have been made to model pulsatile flow through compliant bifurcations. Reuderink (1991) presented a decoupled model; Xu and Collins (1994 a) have successfully simulated flow in a compliant T-junction; and Perktold and Rappitsch (1993) used a coupled approach to calculate the pulsatile, non-Newtonian flow field and the wall shear stress distribution in a distensible human carotid artery bifurcation.

#### 2.6.2.3 Flow through Stenoses

Atheromatous lesions within the intimal layers of arteries grow to the extent that they protrude in to the lumen of the artery, thus forming a stenosis. Understanding of local flow behaviour in the vicinity of an arterial stenosis has proceeded from both theoretical and experimental research. Several numerical treatments have considered symmetric constrictions in rigid axisymmetric conduits, both steady (Luo and Kuang, 1992), and pulsatile (Tu, 1992). However, arterial stenoses are unlikely to be axisymmetric and a number of researchers have considered more physiologically realistic models.

Pulsatile flows through a plane channel with an indentation on one side (Tutty, 1992) exhibit trains of counter-rotating vortices whose effect is to produce periodically changing shear stresses at the wall. However, Ojha et al. (1990) found experimentally that flow downstream of an asymmetric stenosis in a circular tube does not exhibit an axially periodic shear stress distribution. This finding was confirmed by the numerical study performed by Henry and Collins (1993a; 1994) of the flow through axisymmetric and asymmetric stenoses.

#### 2.6.2.4 Flow through Bypass Graft Anastomoses

Bypass grafts, used to alleviate chronic ischaemic heart disease and restore blood supply to the distal areas of stenosed arteries, often fail due to the formation of atheromatous plaques in the anostomosis region. Local flow dynamics may play a role in the formation of atheromatous lesions. Numerical simulations of flows in proximal and distal anastomosis models have helped in the understanding of the important factors governing these flows. Analysis of the predicted wall shear stress and separation sites can be used to determine the optimal anastomosis angle and graft to artery diameter ratio for the particular flow situation in the presence of moderate shear levels and minimum blood damage.

Most of the models reported in the literature are two-dimensional - see for example Kim and Chandran (1992). *In vitro* studies of steady and pulsatile flow in proximal and distal end-to-side anastomoses by Hughes and How (1994) have showed the highly three-dimensional nature of these flows. Recent calculations on three-dimensional distal anastomoses were published by Perktold et al. (1993). Proximal and distal steady anastomosis models were investigated by Henry and co-workers (Henry et al., 1992a; 1994b, 1995a). The numerically predicted flow patterns compared well with the *in vitro* measurements of Hughes and How (1994). An interesting feature of the flow in the graft tube is the occurrence of two counter-rotating vortices, roughly aligned with the mean flow direction. Similar streamwise vortex pairs have been seen in the daughter vessels of arterial bifurcations.

#### 2.6.2.5 Flow in the Heart, and through Natural and Prosthetic Valves

Modelling of the flow in the heart is one of the most challenging problems of the current generation of blood flow modellers. Due to the complex geometry and flow features, analytical approaches are not accurate and numerical modelling is the only method which can be pursued by researchers.

The shape and orientation of the atrio-ventricular valves, and the fibrous threads, the chordae tendinae, attached to them, which are in turn attached to the papillary muscles protruding from the ventricular wall must all affect the flow within the ventricle. A simplified mathematical model of potential flow in a pulsating bulb was presented by Jones (1970). However, a more complete analysis of the flow in the heart can be obtained using numerical methods applied to realistic or simplified geometries of the heart and left ventricle. Accurate representation of these characteristics require a grid size which is beyond current capabilities. The first comprehensive time-dependent 3-D model of flow through the left side of the heart was developed by Peskin and McQueen (1993). Peskin's group have worked in the last 20 years in the development of a coupled approach for modelling cardiac wall and blood flow where the cardiac wall is modelled as a system of fibres immersed in the blood fluid (Immersed Boundary Method). Details of this method will be given in section 2.9.1 where solid-fluid coupling approaches are discussed. The model included the elastic fibres of the heart, a Newtonian model for the blood, the left atrium, ventricle, natural mitral valve and natural aortic valve (massless). However, even this comprehensive model does not show the correct contraction of the heart when compared with a real human heart.

Georgiadis et al. (1992) have recently demonstrated that computational fluid dynamics techniques can be a valuable tool for simulating heart flow problems. They have developed an elliptical axisymmetric model for the left ventricle assuming inviscid flow. This assumption was justified by the fact that during ejection the flow is dominated by the inertia effects. The stream function method was used to solve the Navier-Stokes equations, and the alternating-direction-implicit (ADI) algorithm. Taylor et al. (1993; 1994) have recently developed a realistic 3-D model to solve the LV ejection flow using a CFD package, made in Japan (SCRYU). This is based on a finite volume integration method of the three-dimensional Navier-Stokes equations. The SIMPLE pressure/velocity coupling algorithm is used with body-fitted coordinates. The blood flow was assumed to be Newtonian, homogeneous and incompressible. A preliminary spherical model was considered. The time course of the ventricular wall changes were assumed to vary as a trigonometric function. The modelling framework of this model was used to construct a realistic model using a cast from a dog heart which was in diastole. The left ventricular wall motion was assumed to follow the blood flow.

The most interesting fluid-dynamical events in the heart are the filling and ejecting of blood in the ventricles associated with the motion of the heart valves. Details of the dynamics of the opening and closing of the valves will be given in section 2.7.1, and flow

dynamics characteristics will be summarized briefly as follows. During systole, the aortic valve is opened, while the mitral valve is closed. The flow issuing from the ventricle immediately upon opening of the aortic valve at the inception of systole is split into two streams at each valve cusp. Part of the flow is directed into the sinus behind the valve cusp, where it forms a vortical flow before re-emerging to rejoin the main stream in the ascending aorta. When the aortic pressure rises sufficiently so that deceleration of the flow occurs, an adverse pressure gradient is produced, which causes a greater flow into the sinus and carries the cusps toward apposition. During diastole, the deceleration of the jet and the associated adverse pressure gradient are the mechanisms responsible for valve closure. The opening of the mitral valve occurs when the pressure in the left ventricle is low. The vortical motion prevents valve cups from bulging outwards to contact the walls of the sinuses (Fung, 1981).

Modelling of the fluid through natural and prosthetic valves has also been the subject of many theoretical investigations (Lee and Talbot, 1979; Peskin, 1977; 1982), and more recently numerical modelling (Peskin, 1992; King, 1994). Lee and Talbot (1979) formulated a mathematical theory to calculate the valve cusp motion from the velocity-time history of the flow through the valve, under the assumption that valve cusps are massless and passive, and the velocity in the valve cross section is uniform.

Numerous investigators have considered flow downstream of tilting disk, ball and cage, and ball and disk mechanical heart valves using a variety of 2-D, 3-D, time-dependent and steady state flow, Newtonian and non-Newtonian blood models, turbulent and laminar flow using numerical methods (CFD). Numerical simulations were being performed as early as the 1970s (Peskin, 1977). Some years later McQueen and Peskin (1985) used CFD methods to give concepts for the design of bileaflet valves (mechanical heart valves) obtained from the numerical parametric study of a two-dimensional model. However, experimental findings showed the occurrence of vortical 3-D structures of the flow past the bileaflet valve. Currently, the most commonly implanted heart valve is the bileaflet heart valve and yet a detailed knowledge of the flow characteristics of this valve is not available. Experimental findings have shown flow disturbance and probable turbulence leading to high shear stresses and risks of thrombogenic events (Stein and Sabbah, 1980). Use of CFD models combined with experimental verification will permit greater understanding of the flow mechanisms downstream of the valve, and the performance of parametric design studies (King, 1994). Eilers et al. (1994) have recently found that small differences occur when non-Newtonian blood models are applied to the flow at mechanical heart valve prostheses, while an opposite conclusion was reported by Kobayashi and Pereira (1994).

#### 2.6.2.6 Flow in Cardiac Assist Devices

Enormous research effort is involved in the quite difficult task of establishing the crucial fluid dynamics factors which is why cardiac assist device implantation is still not

satisfactory from the clinical point of view. High shear rates and extended residence times causing haemolysis and platelet activation developing in the pump or in the cannula when inferior flow conditions are established may severely limit clinical applications. A large number of investigators have worked in the field of determination of the optimal haemodynamic conditions in which assist devices should operate, and although considerable progress has been made, few have achieved the actual goal. In this discussion, only a brief review of the experimental studies will be reported. Major attention will be addressed to the numerical studies.

Experimental techniques have extensively been used to test *in vitro* and *in vivo* artificial ventricle models, and improve the blood pump characteristics. Several investigators performed experiments on LVAD, BVAD, and TAH devices to measure the flow characteristics using polystyrene tracer techniques, pulsed Doppler ultrasound velocimetry and Laser Doppler Anamometry (Araki et al., 1993; Baldwin et al., 1990; Goldman et al., 1991). The LDA technique has become a popular tool for assessing haemocompatibility by measuring flow induced shear stresses. This method can provide three-dimensional maps of stresses which can be used to predict potential areas for blood trauma. It has been argued that the expensive and time consuming LDA technique makes its use more appropriate in the final stages of confirmation of a design. Simple and inexpensive flow visualization techniques may be used for qualitative analysis. Mulder et al. (1993) used for example this technique to study the effectiveness and haemocompability of a magnetically suspended centrifugal pump impeller for use in assist devices. Jin and Clarke (1993) have used both the LDA and flow visualization techniques to carry out an experimental investigation of the unsteady non-Newtonian flow behaviour within a sac-type ventricular device. Good 'wash-out' of the mural peripheral parts and central parts of the chamber were observed. This was caused by the main vortex developed during filling. Flow recirculation regions developed at junctions may lead to fluid particle deposition and indicates a risk of thrombus formation which may be reduced by modifying the device design.

Experimental techniques require geometrically accurate models for testing to be carried out in every new prototype. In researching the requirements of the optimal design, numerical techniques present several advantages. They provide detailed information even in points not accessible to experimental measurements, and hence may be used to test local areas. They also permit parametric study of the geometric design. Jin and Clarke's research group, for example, is currently using CFD methods to improve design features of their model. Despite so, very few numerical studies have been reported in the literature. This lack of numerical simulation studies may be due to difficulties encountered when modelling realistic cardiac assist devices models. Generally, flows inside cardiac assist devices are three-dimensional, time-dependent, and often turbulent. An essential feature is the capability to accomodate the geometries of moving boundaries. This has been introduced very recently in the computational fluid dynamic packages and still has not been sufficiently tested against experimental evidence. Another important feature is

the three-dimensionality of the problem, which requires very powerful grid capabilities, with special attention on the refinements necessary where boundaries are in motion. Furthermore, the grid has to undergo changes for each time step, which in turn has to allow for the 'accurate' solution to be established without bordering the calculation too much. Flows inside these assist devices are often turbulent, and this is another open problem in fluid dynamics modelling. On the one hand, the new generation of supercomputer hardware has increased remarkably the computer power and is combined with new computational fluid dynamics algorithms with the ability of modelling anything which has an engineering interest. On the other hand however, a lot of work still needs to be done to validate the newly available facilities against experimental evidence, and thus a close collaboration between experimental researchers and haemodynamics specialists has to be established.

Chesler and Kamm (1994) developed an approach to mechanical heart assist design and evaluation, which resulted in an efficient procedure to find the optimum for a single chamber mechanical ventricle with fixed stroke volume and ejection time. This procedure involved the use of a finite element 'rubber mesh' template and the spectral solver provided by the commercial code NEKTON. The problem was modeled as an unsteady, incompressible three-dimensional flow with moving boundaries. Despite the good promise offered by their software, they have not carried out validation studies to the best of our knowledge. Hence some doubt exists as to the accuracy of their application.

Experimental and numerical studies were conducted by Amling et al. (1990) on a 'teaspoon pump' (nutating centrifugal pump) to test the risk of damage to red blood cells in this new type of centrifugal pump. The flow in the pump was found to be highly turbulent. The numerical solution was based on the 2-D time-dependent Navier-Stokes equations solved using a discrete vortex method. This method allows the strong shear layers generated in the gap between impeller and annular passage wall to be computed with greater resolution than is possible with conventional grid-based methods. The flow is represented by a collection of vortex 'blobs' that yield an associated velocity field. Results showed the persistent occurrence of a recirculation area behind the impeller, which was not seen in the experiments.

In order to understand the problems of damage to constituent elements of the blood due to the flow dynamics within the chamber, several experimental studies have been reported on the measurement of turbulent shear stresses within a TAH. Due to the practical limitations of measurements there, especially in the vicinity of the inflow and outflow valves, data obtained from experimental measurements appear to be limited. Computational fluid dynamics again has provided an alternative technique in which more detailed analysis of fluid dynamic effects of the flow within a TAH can be evaluated. Rogers et al. (1989) solved the 3-D Navier-Stokes equation for steady and time-dependent flows in a Penn state artificial heart. This involved a relatively low Reynolds number. Kim et al. (1992) have tested a total artificial heart model using a steady two-dimensional numerical model in conditions of both laminar and turbulent flows. The governing equations

were solved using the Finite Analytic method of Chen and Chen (1984) on a staggered cartesian grid. This method derives the necessary algebraic equations from local analytical solutions of the governing equations at each cell. Pressure-velocity de-coupling was accomplished using the SIMPLER algorithm, and the $k$-$\epsilon$ turbulence model was used. Kim et al. (1992) reported reasonable agreement with available experimental data, but recognized the need to extend their model to pulsatile 3-D flows, and to include body-fitted moving grids to allow the modelling of the moving valve leaflets, and the pump diaphragm. Their results suggested a correlation between high turbulent stresses and presence of thrombus in the vicinity of the valves in the total artificial heart, and that a tilting disk valve produces preferential flow dynamics characteristics relative to those is the trileaflet valve.

Another important problem in the analysis of flow in assist devices is the choice of the working fluid to use in the *in vitro* and numerical studies. Experimental investigation of the effect of non-Newtonian fluids on flow in artificial ventricles has been carried out by Mann et al. (1987) and Pohl et al. (1990). Mann et al. (1987) investigated blood rheology effects on the flow inside the Penn State Electric Ventricular Device (EVAD) using Pulsed Doppler Ultrasound Velocimetry. They concluded that rheological properties of the working fluid are very important in the experimental simulation studies. The same conclusion was reported by Pohl et al. (1990). They performed experiments using hot film anemometry to investigate the influence of the rheological properties of the fluids on flow patterns inside artificial ventricles. They found significant qualitative and quantitative differences in the flow characteristics especially in areas of low shear stresses, and concluded that blood-analogous fluid is important in *in vitro* investigations.

### 2.6.3 Blood Vessel Modelling

For the purpose of blood flow modelling it is important also to consider wall distensibility of blood vessels. Experimental results have shown that mechanical properties of blood vessels are characterized by a high deformability, a non-linear stress-strain relationship and the existence of viscoelastic time-dependent behaviour, such as hysteresis, creep and stress relaxation. These effects are determined by the properties of the tissues that compose vessels, and their arrangement in the wall.

Blood vessels are composed of viscoelastic inhomogeneous multi-layered tissues. These are mainly composed of endothelial lining, elastin and collagen fibres, and smooth muscles, arranged in three concentric layers - the intima, the media and adventia. Arterial walls are considerably thicker than the walls of veins, and although composed of the same tissues, they have different architecture. In this discussion attention will only be paid to arterial vessels. In the mathematical formulation, the arterial wall can be assumed as a homogeneous, incompressible and non-linearly elastic material which can be modelled as an orthotropic thin-walled cylinder undergoing finite deformation.

#### 2.6.3.1 Mechanical Properties of Blood Vessels

The mechanical properties of the wall are mainly determined by the connective tissue and smooth muscle of the media. The endothelial lining is the innermost layer of the vessel wall that comes into contact with the flowing blood. It provides a smooth surface and offers a selective permeability to various substances carried in the blood stream but is too soft to contribute to the elastic properties of the wall. It is therefore omitted from the discussion on the overall elastic performance. Elastin fibres are highly elastic, while collagen is much stiffer. The modulus of smooth muscle varies in the passive and the active states. It has been shown that the most significant effect of smooth muscle is on the circumferential properties. At low strains the collagen fibres are slack and most of the load is borne by elastin fibres. At higher strains, however, the collagen fibres straighten out, causing the arterial wall to become relatively inextensible. Thus the response of the arterial wall to transmural pressure is highly nonlinear, being strongly compliant at low pressure but increasing in stiffness with rising pressure.

The overall properties of blood vessels result from its complex multicomponent structure and are characterized by an anisotropic behaviour, with orthotropic symmetry. This implies that only normal strains are present in arteries and the mathematical treatment can be considerably simplified (Patel and Vaishnav, 1972). Young's modulus of the arterial wall is in the range $2 - 8 \times 10^5$ $Nm^{-2}$. Although uniaxial and biaxial tests on flat specimens are performed to determine mechanical properties of arterial walls, pressure-diameter data obtained from *in vitro* and *in vivo* tubular segments are more informative and realistic (Hayashi, 1993).

#### 2.6.3.2 Mathematical Models for the Stress-Strain Relationship

A variety of analytical approaches have been proposed to model arterial wall with different assumptions about the wall behaviour. Generally, in order to simplify analysis arterial vessels are assumed to be homogeneous. This is reasonably valid in the circumferential and longitudinal directions, but not strictly radially because of the layered structure. Furthermore, it can be assumed incompressible and approximated by a thin-walled cylinder model (11% of error) (How, 1990). Membrane and shell theories have been applied. For the constitutive models linear and non-linear elastic, and viscoelastic behaviour has been variously assumed, with uniaxial, biaxial, or triaxial laws. When the *uniaxial elastic model* is applied, the wall motion will be assumed to have a preferential radial direction due to the longitudinal tethering inhibition. For this reason the mechanical properties of arteries are commonly defined in terms of distensibility $D$ ($D = (dA/dp)/A$). Uniaxial elastic models have extensively been used in both linear and non-linear arterial wave propagation theories (McDonald, 1960).

It has been found that when subjected to physiological loads an arterial segment deforms circumferentially by 2 - 5 %. When the artery is excised, it shortens by up to

60%. It is therefore under considerable initial strain (How, 1990). During the heartbeat, however, the longitudinal deformation is small. In the radial direction, deformation is compressive and stresses are usually much smaller than those in the circumferential and longitudinal directions. These findings imply that a finite deformation approach should be used for the stress-strain relationship. However, in the past more simplified models, such as *small strain analysis* and *incremental analysis* have been applied. Patel and Vaishnav (1972) and others have treated the arterial tissues as non-linear viscoelastic. However, they found that viscosity can be considered as a second-order effect, and therefore it is reasonable to treat the arterial tissue as a nonlinear elastic material.

When applying small stress analysis the wall material is assumed to be isotropic and linearly elastic. For a thin-walled tube, the radial stress is much smaller than the circumferential and longitudinal stresses and may be ignored. The incremental analysis is an approximate analysis of nonlinear finite elasticity. It is based on the use of linear small strain theory to describe non-linear stress-strain behaviour. The *finite deformation analysis* can be applied to finite non-linear elastic deformations. It is based on the assumption that the work done in deforming an elastic body is stored as strain energy expressed as a function of strains only. Polynomial (Patel and Vaishnav, 1972) and exponential (Fung et al., 1979) strain functions have been used. Polynomial functions are more general and simple to use. A third order polynomial function gives a satisfactory fit with experimental data.

The group at City are working on the problem of flow through compliant arterial models. Henry and Collins have developed a technique to couple solid and fluid equations simultanously and applied it to a tube (Henry and Collins, 1993b). Xu and Collins (1994a) have successfully simulated flow in a compliant T-junction, using a simplified pressure/diameter relationship. Perktold and Rappitsch (1993) modelled the artery segment as a thin shell applying non-linear shell theory and incrementally linear elastic wall behaviour. The structural problem and the flow problem were solved in a coupled approach using finite element techniques. Reuderink et al. (1993) developed an uncoupled approach to solve the fluid flow and the wall motion in non-uniform distensible tubes. Coupled approaches reported in the literature will be described in more detail in section 2.9.

### 2.6.4 Haemodymanics and Flow-Induced Diseases

Fluid-dynamic factors exert pivotal influence upon prothrombotic and atherogenetic reactions, both of which occur under conditions associated with deviations from strictly laminar Poiseuille-flow. The mechanical environment imposed by the haemodynamics of the vascular system have wide ranging effects, which may be divided into:

(i) the effects on blood (haemolysis and thrombosis)

(ii) effects on blood vessels (atherosclerosis), and

(iii) interaction of blood with the non-endothelialized artificial surface.

### 2.6.4.1 Effects of Flow on Blood

Substantial evidence exists that indicates that abnormal flow phenomena, such as elevated shear stress, high turbulence levels, prolonged stasis, cavitation and rapid changes in shear, form substantial obstacles to routinely successful application of many cardiovascular devices and treatments. Lysis of blood cells has been observed at shear stresses in the range of 1500 dyn/cm$^2$ for erythrocytes, 300 for leukocytes and 100-150 for platelets (Sutera, 1977). The threshold values depend upon the nature and duration of shear. Similarly, large shear stresses in the fluid domain can lead to blood cell damage, activation of the clotting cascade and thrombosis (Sutera, 1977).

The *thrombosis* process represents a very complex blood coagulation sequence. The biochemical reactions of the clotting mechanism have been studied extensively, and it has been universally agreed that a number of proenzymes and enzymes are involved in blood clotting. At each stage, the product of one triggers the next, and as a biochemical amplifier, leading to the formation of a greater weight of protein than at the earlier step.

Analysis of the blood damage caused by the implantation of a total artificial heart have shown a deposition of thrombi concentrated in the vicinity of inflow and outflow valves (Levinson et al., 1986). Hung et al. (1991) found increased blood viscosity, erythrocyte rigidity, plasma fibrinogen concentration, platelet aggregation and thrombus formation around valves in a study of Jarvik-7 total artificial heart and Novacor left ventricular assist device recipients. Previous investigators (Chandran et al., 1984) have suggested that haemolysis and/or subhaemolytic damage to red blood cells may occur due to turbulent stresses in the downstream wake of prosthetic valves even though mean velocity shear rates are low. Much lower values of shear stress cause aggregation and adhesion of platelets (Brown et al., 1975). Moderate shear stress results in aggregation of white cells (Dewitz et al., 1977). Shear stresses lower than 0.1 dyn/cm$^2$ have been observed to cause deformation of red cells (Goldsmith, 1972). Hence, since white cells
are much more deformable than red cells and since many of the functions of these cells are membrane related, it follows that the processes leading to thrombus formation may be sensitive to increases in shear stress of quite a small magnitude. Indeed, the release of serotonin, an activator of thrombogenesis, from platelets has been shown to increase with an applied average oscillatory shear stress of only 16.5 dyn/cm$^2$ (Goldsmith, 1974).

Implantable artificial heart and assist devices have been more prone to infection than other prosthetic devices, due to the number of possible pathways. The incidence of infection occurring inside the blood pump has been connected with the presence of thrombi. Since thrombus formation, propagation, composition and disintegration may be substantially flow-induced (Goldsmith and Turrito, 1986), improved flow dynamics

in the device may result not only in reduced damage to blood components and reduced thrombus formation with its associated effects, but also in reduced *infection*. Mixing structures such as vortices may be of value to the long term patency of SMVs by increasing local mixing of the blood constituents and decreasing peak residence times.

### 2.6.4.2 Effects of Flow on Blood Vessels

Today, atherosclerosis is the main cause of death in the western world. It has been recognized that a correlation exists between the disease processes and fluid-dynamic aspects of the blood flow (Nerem, 1992). The initial stage of the development of atheromatous lesions in the walls of arteries (atherogenesis) involves truly nano-scale phenomena and microhydronamics with the accumulation in the intimal layers of the wall of lipoproteins and other blood-borne materials, and changes in both the cellular and connective tissue components of the wall. The basic lesions (atheroma) may lead to narrowing (stenoses) and hardening of the arterial wall and so to further pathological complications. Localisation of atherosclerosis lesions is preferential in geometrically contorted sites such as bifurcations and bends, where flow separation and recirculation regions occur.

Wall shear stresses have received most attention in the analysis of atherosclerosis causes due to the flow-induced changes of the endothelial cells. *In vitro* studies using cell cultures exposed to defined laminar flow have demonstrated that time history of shear stress can influence cell shape and metabolism. The mechanism of the transduction of the mechanical signals into chemical are not yet well understood, different hypotheses having been postulated. Initially, Fry (1972) proposed that atheromatous lesions were more likely to be found in regions of high wall shear stress. However, Caro et al. (1981) concluded that low wall shear stress was the cause of the atheromatous lesions. This hypothesis has gained much support from other laboratories and theoretical investigations, and has suggested that the development of atheroma is associated with shear dependent mass transport phenomena rather than wall damage due the motion of blood. Ku and Giddens (1985) confirmed these findings, but also indicated that marked oscillations in the wall shear stress may enhance atherogenesis.

### 2.6.4.3 Interaction of Blood with Artificial Surfaces

Blood/foreign surface interaction phenomena affect significantly the *in vivo* performance of cardiac assist devices. In contrast to the living intact endothelium, all other surfaces induce interactions in blood the extent of which varies from the tolerable to the detrimental. The scheme in Fig.2.23 summarizes the essential pathways of these interactions under physiological conditions. The end result of contact between blood and artificial surfaces is thrombus formation. When synthetic smooth surfaces come into contact

with blood, most of them absorb a thin layer of proteins after the initial contact (Brash, 1989). The nature of this absorption phenomenon under *in vivo* physiological conditions and the subsequent changes that occur in the absorbed proteins are both influenced by several factors, including surface smoothness, chemical structure and haemorheologic factors. As a consequence, the prerequisite for blood compatibility with synthetic solids is the adsorption of specific plasma proteins. The adsorption process is frequently accompanied by adsorption of blood components, which may affect not only blood compatibility but the physical properties of biomaterials (Bruck, 1989). Platelet-surface interactions are involved directly in initiation of thrombosis at polymer surfaces. This is accomplished via platelet adhesion, release of constituent granules, and formation of surface-localized aggregates, which eventually involve red cells and fibrin mesh (Baier, 1977).

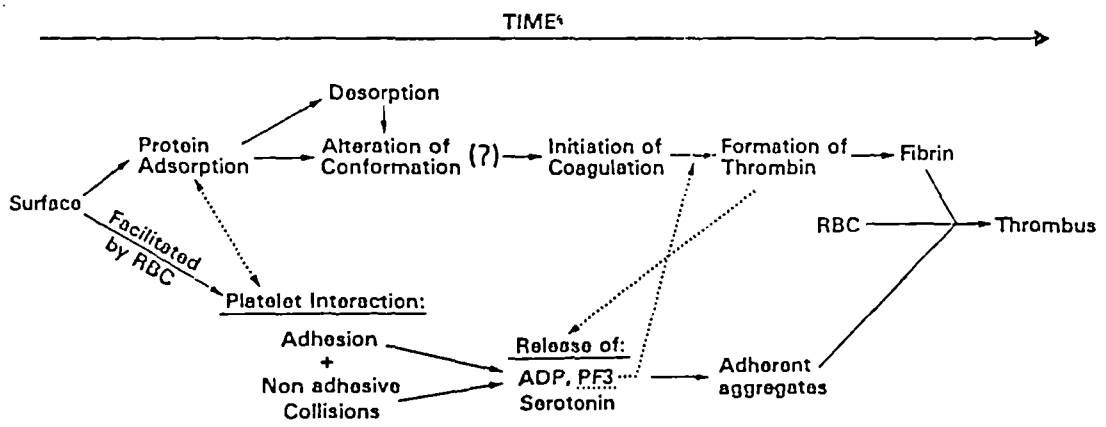


Figure 2.23 Sequence of events leading to thrombus formation on artificial surfaces. From Brash (1989).

In contrast to most synthetic biomaterials, there is no evidence that the living endothelium absorbs proteins in the blood under physiological conditions. The endothelial layer maintains an active secretory process that prevents platelet activation and creates an effective 'renewing' surface.

In the design of assist devices stagnant flows are to be avoided. Prolonged exposure of blood constituents to non-endothelialized surfaces entails a risk of thrombus formation. Regions of low shear stress, which are are associated with blood stasis, are implicated in the development of stable mural thrombi on artificial surfaces (Hashimoto et al., 1985). Regions of stagnant or recirculating flows near walls within an artificial ventricle can also cause calcification of the artificial surface (Harasaki et al., 1985). Calcification occurring especially in the moving portion of a blood pump can cause diaphragm perforation and serve as nuclei for embolism. The process is initiated by nonviable and degraded cells and subcellular components. It has been hypothesized that a rotational flow leading to a 'wash-out' of the pump chamber is advantageous in reducing thrombus formation and possibly blood sac calcification.

Preliminary *in vitro* and numerical simulation studies are in this context essential. In the next section modelling reported in the literature for the left ventricle will be discussed with the objective of defining the solid mechanics problems that very probably

would apply to the modelling of SMVs.

## 2.7 VENTRICLE MODELLING

For the purposes of the coupled solid-fluid model of an SMV, fluid mechanics equations should be coupled together with solid mechanics equations. Besides, since muscles are not passive tissues, muscle mechanics equations should be coupled to the fluid and solid equations. In this section ventricle modelling approaches will be discussed with the objective of providing a suitable approach for the coupled solid-fluid system outlining the requirements for the solid mechanics equations, in order to give a valid representation of the mechanics of the ventricle.

Ventricle modelling has been applied to the heart left ventricle to date. Geometric and physiological features in model SMVs would, in fact, be quite different. However, provided that these differences are duly taken into account, methods for left ventricle modelling would constitute an approach also applicable to the SMV modelling. A more specific literature review on solid-fluid coupled approaches will be given in section 2.9.

Firstly, a brief description of the dynamics of the pumping function of the heart in the systemic circulation will be presented in section 2.7.1. This will help in finding general criteria that allow the global pumping function characteristics of a ventricle to be related to its modelling at the muscle fibre level. It will also give an overview of the cardiac dynamics, and an outline of the interactions of the potential use of an assist device such as an SMV in the circulatory system dynamics. Then, section 2.7.2 will deal with the mechanical properties of the intact heart. Determining the relationship between stress and strain in the myocardium poses the principal challenge to the study of heart mechanics due to the non-linear time-dependent constitutive law. Finally, the most relevant left ventricle models documented in the literature will be described in section 2.7.3.

### 2.7.1 Cardiac Dynamics

The heart is the prime mover of blood. By periodic stimulation of its muscles it contracts rhythmically and pumps blood throughout the body. The heart contains two sections: the right side, which receives deoxygenated blood from the body and pumps it to the lungs; and the left side, which receives oxygenated blood from the lungs and pumps it out around the body. The flow of blood through the heart is controlled by four one-way valves which open when there is a positive pressure drop across them and close when an negative pressure difference is applied. As shown in Fig.2.24, at each cycle in the diastolic phase the left and right ventricles are filled with blood from the left and right atria, respectively. Then by the deceleration of the blood stream a pressure field

is generated, which closes the valves between the atria and ventricles (tricuspid in the right side, and mitral in the left side). The contraction of the heart muscle begins and the pressure in the ventricles rises. When the pressure in the left ventricle exceeds that in the aorta, and the pressure in the right ventricle exceeds that in the pulmonary artery, the aortic valve in the left and the pulmonary valve in the right are pushed open, and blood is ejected into the aorta and the lung. The ejection in the systolic phase continues until the deceleration of the jets of blood creates pressure fields which close the valves. Then the muscle relaxes, the pressure decreases, and the diastolic phase begins.

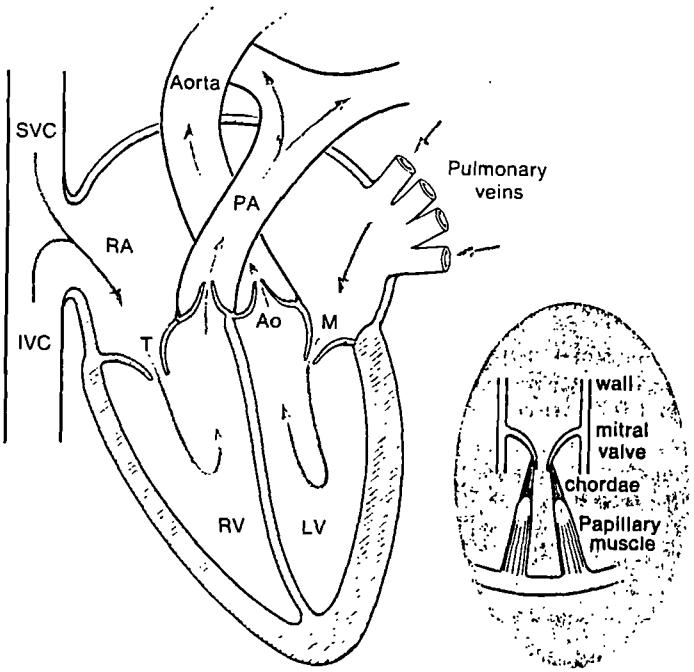


Figure 2.24 Blood flow through the heart. The arrows show the direction of blood flow. From Folkow and Neil (1971).

The pressure in the left ventricle fluctuates from a low of nearly zero (i.e. atmospheric) to a high of 120 mm Hg or so. In the aorta, the pressure fluctuation is much less because of its distensibility. The pressures acting on the pericardium and in the ventricles are unsteady with respect to time and nonuniform with respect to space. These pressures together with the inertial forces due to acceleration, and with the elastic, viscoelastic, and active contraction stresses in the muscle, determine the dynamics of the heart. On the other hand, a feedback mechanism is in operation due to the pressure of the fluid in the heart cavities and determined by the movement of the walls.

#### 2.7.1.1 Geometry and Material of the Heart

The four chambers of the human heart constist of two thin-walled atria separated by an interatrial septum, and two thick-walled ventricles separated by an interventricular septum. The muscles of the atria and ventricles are joined to a skeleton of fibrous tissue

on which the rings of the four valves are seated. The valves are seated in a plane (see Fig.2.24). The mitral and tricuspid valves are relatively large in area: they are opened to fill the ventricles when the blood pressure is low and its velocity is small. The aortic and pulmonary valves, through which blood is pumped out of the ventricles at high velocity, are smaller. The mitral and tricuspid valves are attached to papillary muscles, which contract in systole, pull down the valves to generate systolic pressure rapidly, and prevent the valves from any danger of inversion into the atrium. The aortic and pulmonary valves have no such strings attached.

Fig.2.25 shows the ejection pattern of the two ventricles. The left ventricle remains nearly ellipsoidal in shape. The right ventricle appears as a bellows, which is a geometry ideally suited to the ejection of a large volume of fluid at a low pressure. In both ventricles, there is also some shortening of the longitudinal axis. *In vivo* studies on dogs showed that during ejection the minor axis of the inner wall of the chamber shortens by about 25% and the major axis by 8%, increasing the wall thickness by about 20-25% (Fung, 1984).

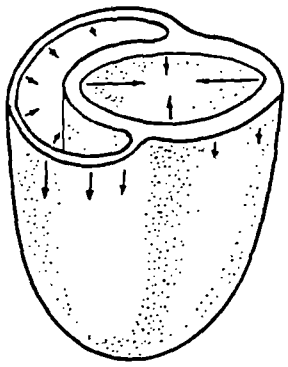

Figure 2.25 Patterns of ventricular contraction. From Fung (1984).

The model often used when considering the left ventricle is a thick-walled ellipsoid of revolution. In longitudinal section, the left ventricle has been geometrically described as somewhat egg shaped. The equatorial plane divides the LV into apical and basal ports. The shape of the apex is between a cone and an ellipsoid. The basal portion can be regarded as a truncated version of the apical. This approximation applies to both contracted and distended states. Because the LV wall is thick, epi- and endo-cardial shells can be considerably different in shape. Although the cone and ellipsoid are possible representations of ventricular wall in various states of contraction, empirical methods of representation are often used (Streeter and Ramon, 1983). Fully three-dimensional reconstructions of left ventricular geometry have been obtained using a variety of imaging methods, such as biplane cineangiography, two-dimensional ultrasound, and tomography.

### 2.7.1.2 Muscle Fibre Orientation

Fibre orientation has been studied by many investigators. The most extensive

analysis was performed by Streeter and co-workers (Streeter et al., 1969; Streeter et al., 1973; Streeter and Ramon, 1983), who measured fibre orientation in dogs and found a systematic orientation through the wall. In the epicardium, the muscle fibres are oriented from the apex to the base and are arranged in the direction of the longitudes. Away from the epicardium the muscle fibre orientation changes continuously. At the midwall the fibres are oriented parallel to the base, i.e., in the direction of the latitudes. The rotation continues until the fibres become longitudinal again in the endocardium.

The principal fibrepaths tend to follow a geodesic path on the surface of the dissected heart wall in both ventricles, see Fig.2.26; and in addition they 'burrow' into the wall in a continuous fashion such that they make a 'figure 8' path and returns to the equator. Thus a muscle fibrepath can be represented by a helical path from epi- to endo-cardium in both ventricles. The helix angle changes in each section quite smoothly, progressively changing from a somewhat large negative angle at the pericardial surface, through zero degrees near midwall, to an increasingly positive angle towards the endocardium (Streeter and Ramon, 1983).

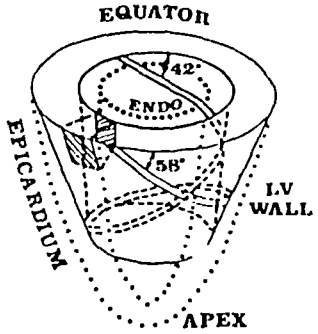


Figure 2.26 Schematic representation of the left ventricle of the heart with muscle fibrepath plotted on it. From Streeter and Ramon (1983).

### 2.7.1.3 The Pumping Function of the Heart: Pressure-Volume Curve

The heart is a pump that provides the blood with energy to circulate through the body's vascular network. Its energy output is roughly the product of mean pressure and flow. Because mean systemic arterial pressure is maintained within a relatively narrow range by various mechanisms, cardiac pump function is often evaluated in terms of flow output per minute, or simply 'cardiac output'. Under different loadings, the heart may provide the blood with an identical amount of mechanical energy while consuming vastly different amounts of total chemical energy for contraction. The working conditions imposed on the heart before and after the onset of contraction have been called 'preload' and 'afterload'.

The pressure volume diagram enables an evaluation to be made of the pumping function of the heart. The first pressure-volume diagram of the heart (Frank-Starling law of the heart) was published by Frank (1895), and later by Starling (1918). They wanted

to use the knowledge of the length-tension relationship gained in isolated skeletal muscle studies in the attempt to interpret the pressure-volume relationship data measured in the ventricle. Similarly, many recent investigators have attempted to understand the basic characteristics of ventricular contraction by focusing on the tension-velocity relationship.

Fig.2.27 shows a left ventricular pressure-volume diagram obtained from the time function curves of pressure and volume. The pressure-volume loop (shaded in Fig.2.27) represents the energy imparted to the blood by contraction of the ventricle. More conventionally the loop area represents the stroke work,

$$SW = -\int_{EDV}^{EEV} p(t)dv$$

of the ventricle on the external (arterial) system, from the end-diastolic volume (EDV) to end-ejection volume (EEV).

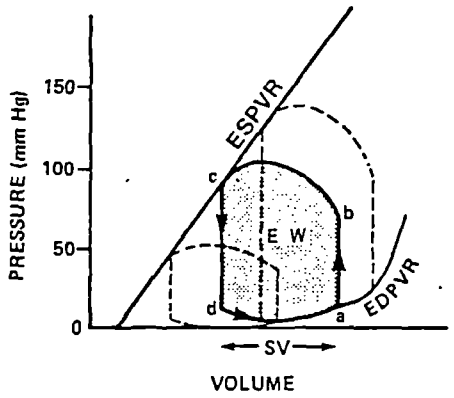


Figure 2.27 Pressure-volume loop diagram of the ventricle. Point a indicates the pressure and volume at which the ventricle begins its contraction. The isovolumic period is represented by the vertical segment of line a-b. The aortic valve opens in point b. The ventricle ejection occurs in segment b-c. From Sagawa et al. (1988).

The end-systolic pressure-volume relationship (ESPVR) and the end-diastolic pressure-volume relationship (EDPVR) of the ventricle in a given contractile state can also be inserted in the pressure-volume diagram, as indicated in Fig.2.27. These curves represent the mechanical properties of the fully contracted ventricle at end-systole and fully relaxed ventricle at end diastole. Both ESPVR and EDPVR relationships shift with changes in the contractile state of the myocardium, or with changes in the ratio of the wall thickness to the cavity radius.

#### 2.7.1.3.1 Pressure-Volume Curve in model SMVs

According to the Frank-Starling relationships, cardiac muscle is like skeletal muscle in that the energy of contraction is a function of the length of the muscle fibre before contraction. As the fibre length increases, the energy of contraction also increases up

to an optimal length, above which lengthening will cause the energy of contraction to decrease. Stroke volume is a function of the extent of ventricular shortening at any level of diastolic length and contractility.

Results from experiments on models SMVs in mock circulations showed that like the heart, the SMV has an inverse relationship between afterload and stroke volume. Stroke work (stroke volume × pressure) of the SMV remained relatively unchanged over the ranges of afterloads studied (Acker et al., 1986). The stroke volume was high at low afterloads and low at high afterloads, which resulted in little change in total stroke work. As with the heart, stroke work did decline sharply when, at very high afterloads, little or no flow was generated. Ejection fraction of the SMV compares favourably with the ejection fraction of the left ventricle. (Ejection fraction, like stroke volume, is inversely related to afterload).

When SMVs are used as diastolic counterpulsators, the preload pressure is equivalent to aortic diastolic pressure, typically 60-100 mm Hg. In the early mock circulation studies, (Acker et al., 1986), preload was set at 40 mm Hg. Bridges et al. (1989) demonstrated that preconditioned SMVs in dogs can be constructed that have the pressure-volume characteristics appropriate for pumping blood under the physiological conditions that pertain to the left and right ventricles.

P-V curves of SMVs, when configured as (rectus muscle wrapped) pouches in parallel to the left ventricle (Geddes et al., 1993), are shown in Fig.2.28 (see also section 2.3.2.4). Fig.2.28 illustrates two P-V diagrams A and B for the SMV in which instantaneous pouch pressure is plotted against instantaneous pouch volume, detected by impedance, for non-contracting and contracting rectus muscle respectively.

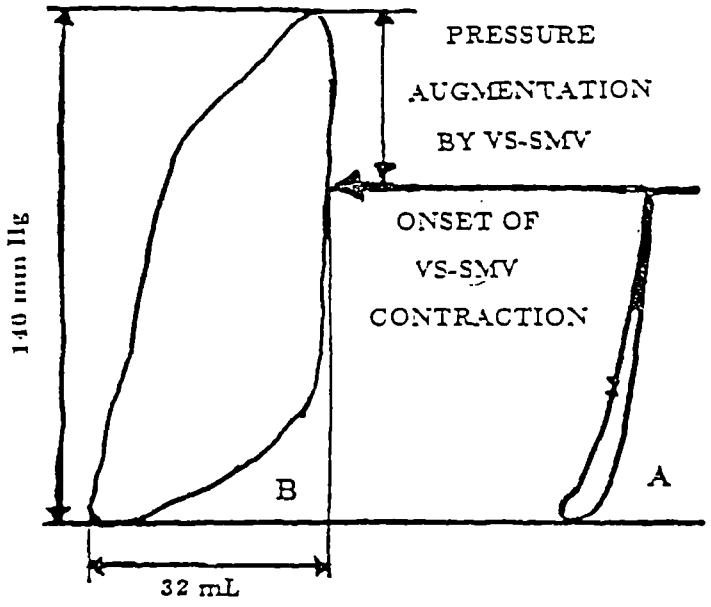


Figure 2.28 Pressure-volume loops for an SMV in parallel, not activated in A, and activated in B. From Geddes et al. (1993).

### 2.7.2 Mechanical Properties of the Intact Heart

Mechanical analysis of myocardium is in general required to compute the wall stresses, strains, and their variation during the cardiac cycle. For several decades researchers have been attempting to understand the mechanics of the heart. In spite of the considerable effort no unified description of heart mechanics has emerged. This is because of the complexity of the geometry of the heart, of its structure, and of the material behaviour of its musculature. In addition, the large number of variables entering a given experimental situation and their complex interaction make the interpretation of experimental data difficult. To circumvent these difficulties many researchers have focused their attention on the study of muscle bundles, such as the papillary muscle.

The performance of the whole heart is affected by the mechanism of contraction of isolated cardiac muscle. Pinto discussed the relevance of the constitutive law of papillary muscle to the mechanics of intact heart in a fairly recent paper (Pinto, 1987). However, it is evident that there are important structural differences between papillary muscle and ventricular myocardium. Other factors such as the shape of the ventricles, the muscle fibre orientation, and the thickness of the ventricular wall all determine the distribution of forces within the ventricular myocardium.

The myocardial connective structure plays an important role in the characterization of the mechanical properties of the myocardium both in the active and passive state. Both the fibrous structure of cardiac muscle and the organization of its extracellular connective tissue matrix indicate that the mechanical properties of passive myocardium are anisotropic. Humphrey and Yin (1987) demonstrated that, although cardiac tissue possesses a complex deformation-dependent anisotropy, the assumption of *transverse isotropy* with respect to a local muscle fibre direction (orthotropy) appears to be reasonable. Uniaxial laws implemented in ventricular models may be extended to two or three dimensions only under conditions of isotropy. Therefore, the three-dimensional material properties cannot be fully characterized by one-dimensional mechanical tests.

#### 2.7.2.1 Biaxial Testing

It is possible to characterize the three-dimensional material properties of incompressible anisotropic membranes using biaxial mechanical testing procedures. Yin et al. (1987) proposed biaxial exponential laws which fits very well with the experimental results. Stress-strain curves for myocardial sections taken from midway through the left ventricular free wall are shown in Fig.2.29. In the fibre direction, stress-strain relations exhibited the non-linear characteristics of passive papillary muscle with low stiffness at small extensions but which increased sharply, as maximum extensions were approached. Stress-strain relations in the cross-fibre direction exhibited creep and rate dependent

hysteresis. These findings show a clear anisotropy associated with the fibre direction, depending on the transmural site from which the myocardial section is removed.

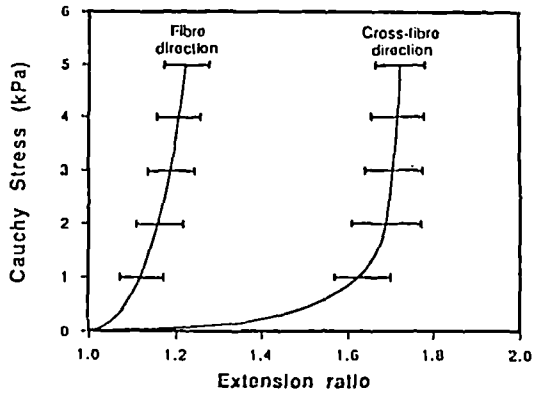


Figure 2.29 Stress vs extension ratio under equibiaxial loading for left ventricular midwall specimens. Bars represent errors. From Hunter and Smaill (1988).

### 2.7.2.2 Relation between isolated muscle and intact heart mechanics

Numerous investigators have used the one-dimensional models to interpret data collected on the intact three-dimensional left ventricle, such as the pressure-volume curve. Fry et al. (1964) were among the first investigators to use a lumped parameter model to analyze experimental data obtained from the intact left ventricle. Grood et al. (1979) demonstrated that the one-dimensional model of the isolated muscle is not adequate to describe the behaviour of the 3-D ventricular wall. They developed a composite model of the heart muscle consisting of active uniaxial contractile filaments embedded in a passive 3-D elastic binder. Equations were developed to relate the average contractile filament force to the stress in the muscle tissue.

In a qualitative sense, the ventricle does behave in a manner similar to the isolated muscle. The ventricular wall exhibits a roughly inverse hyperbolic relationship between stress and shortening velocity. Further, contractile force increases with an increase in length up to a maximum value as in the isolated muscle (Starling effect). This seems to show that there is a similarity between ventricular pressure $p(t)$ and myocardial force $F(t)$, and between ventricular volume $V(t)$ and muscle length $L(t)$. However, an accurate reinterpretation of the ventricular variables (P-V) into muscle variables (F-L) is a very difficult task, because of the complex shape, non-uniform thickness and fibre orientation of the ventricular wall. If cardiac wall is assumed as a homogeneous medium with isotropic properties, the internal pressure $p$ is related to the mean wall circumferential stress $T$ through the relationship

$$p = f(V)T \tag{2.8}$$

where the so-called 'shape factor' $f(V)$ depends on the particular representation adopted

for the LV geometry. In any case, it decreases with the inner volume $V$. Some biomedical engineers incorporated the concept of time-varying elastance for modelling the ventricle at the muscle level (Sagawa, 1978), assuming a load-independence of the volume elastance $E(t)$, or Pressure:Volume ratio,

$$p(t) = E(t)V(t) \tag{2.9}$$

Recent experimental evidence, however, demonstrates that the tension-length/(muscle) and pressure-volume/(ventricle) relationships are load dependent. These findings have led to the addition to the ventricular model of internal viscous resistance in series to the elastance (Sagawa et al., 1988).

### 2.7.3 Approaches to Ventricle Modelling

Realistic modelling of the complex three-dimensional geometry and fibre architecture, the large deformations and the non-linear elastic, anisotropic, time-dependent material properties is extremely difficult. Therefore, most models of the heart have been restricted to the passive left ventricle and have relied either on simplified geometric representations, such as cylinders or spheres, or on linear approximations to the governing equations when reproducing global pressure-volume relationships. Under these conditions mathematical sophistication is not required. Even linear models based on cylindrical or spherical approximations are able to produce the diastolic filling curve to within 20% (Janz et al., 1974). However, the importance of accounting for large deformations of the passive left ventricle when predicting stress distributions has been demonstrated when finite element models are used (Janz et al., 1974). This is supported by experimental measurements of myocardial fibre stretches that may exceed 20% at physiological filling pressures.

Numerous models dealing with the mechanical activity of the heart ventricles have been published in the more recent past. These models can be divided into two main groups:

1. **phenomenological models**, which utilize material laws in the form of general mathematical expressions, and
2. **structural models**, that are based on the microstructure of the heart.

Experience has shown that it is difficult to account for the complex three-dimensional, anisotropic properties of the myocardium using phenomenological material laws. A more realistic analysis of the deformation pattern of the ventricle or the intramyocardial pressure and stress, can be carried out with models utilizing microstructural material laws (Lanir, 1983). In the phenomenological approach the myocardium mechanics is modelled using the equations for continuum mechanics. This approach avoids a detailed representation of the complex structure of the myocardium, and hence has the benefit of a greater simplicity.

The structural approach considers basic elements with known properties. Their contributions are integrated to obtain the behaviour of the whole system. The integration process is based upon the morphological structure of the myocardium, particularly the ordered pattern of muscle fibres, as described by Streeter et al. (1969). Most of the published structural models consider the basic myocardial element as an isolated cardiac muscle, and then define a pattern to these fibres across the ventricle wall. The Immersed Boundary Method developed by Peskin and co-workers will be discussed in detail in section 2.9.1 with the solid-fluid coupled models.

When studying the dynamics of the left ventricle, the choice of the geometry of the left ventricle model is rather important because the relation between wall stress and left ventricle pressure depends on the geometry. From Back's analysis (Back, 1977), for example, it can be concluded that the calculated wall stress is approximately 50% less if a spherical rather than an ellipsoidal geometry is assumed. The most realistic results for the relation between left ventricular pressure and wall stress are obtained when ellipsoidal geometry is assumed. Cylindrical geometry approximates these results closely, within 10%, and significantly better than when spherical geometry is assumed.

Numerous ventricle models in the literature use a cylindrical geometry to approximate the shape of the left ventricle. Besides its inherent simplicity, the thick-walled cylinder is the only geometry in which an anisotropic structure can be described with one single spatial parameter, the radial coordinate. Solving the mechanics of a fibrous thick-walled sphere or ellipsoid is substantially more complicated as each more realistic rotationally symmetric geometry involves loss of symmetry after deformation. In the ellipsoidal case, the corresponding solution of the problem has two dimensions in space, the radial and axial coordinate. In an asymmetric geometry, a third, tangential coordinate has to be added.

#### 2.7.3.1 Phenomenological Approach

The phenomenological approach uses the equations of the continuum mechanics for deformable material to model the mechanics of the ventricle. The result of a set of forces acting on a deformable material is a time-varying displacement field. Each material point moves a certain distance depending both on its position relative to the applied forces and on the mechanical properties of the material. The derivation of the equations governing the motion of deformable materials is considered in the following steps:

(i) kinematic relations, which define the components of strain in terms of displacement gradients and, in the case of incompressible materials, define the compressibility constraint;

(ii) stress equilibrium, or equations of motion, derived from the laws of conservation of linear momentum and conservation of angular momentum;

(iii) constitutive relations, which express the relationship between stress and strain

and must be established from experimental data characterizing the non-linear anisotropic material properties of cardiac muscle;

(iv) boundary conditions, which specify the external loads or displacement constraints acting on the deforming body.

In mechanical studies, an efficient representation of the geometry of the cardiac structure should consider the three-dimensional geometry of the right and left ventricles and the complex pattern of muscle fibre orientations. An accurate three-dimensional reconstruction of the ventricular geometry is not an easy task. The instantaneous three-dimensional ventricular geometry was estimated from biplane cineventriculograms by Pao et al. (1974) and Yettram et al. (1982), and used to develop finite element models. Recent advances in cardiac imaging have been spectacular and it seems likely that sequential high-resolution reconstruction of three-dimensional ventricular structure will soon become available. In the following discussion, analytical ventricle models are reviewed.

#### 2.7.3.1.1 Left Ventricle Analytical Models

A considerable number of analytical models of the mechanics of the left ventricle have been described in the literature due to the great interest in the study of the wall stresses of the myocardium. Ventricular wall stress is, in fact, a primary determinant of myocardial oxygen consumption and coronary blood flow, and local stress and strain give an indication of myocardial ischemia. Direct information on the distribution of myocardial stresses is not available because intramural force gauges have proved to be unreliable (Huisman et al., 1980). In order to calculate wall stresses indirectly, assumptions for the of the ventricle need to be made.

The earliest attempt was by Woods (1892), who calculated wall tension $\sigma_w$ for the thin-spherical geometry from cavity pressure $p$ and radius $R$ using the classical Laplace membrane solution ($\sigma_w = R \times p/2$). Calculations on ellipsoidal *thin-walled* models were carried out by Sandler and Dodge (1963), Streeter et al. (1969) and Falsetti et al. (1970). However, as the left ventricular wall is of comparable thickness to the ventricular radius, the absence of any shear stress in these models severely limited their application.

*Thick-walled* models with linear material properties originate from Lame's classical solution for the stress distribution in an inflated thick-walled and a basical spherical geometry was proposed by Sokolnikoff (1956), and applied by Hanna (1973) and Mirsky (1973). Vito (1979) proposed a more complex version of the Mirsky model (1973), which was recently reassessed by Shivakumar et al. (1989); they modelled the heart with the pericardium as two concentric spheres. A more accurate description of the ventricular geometry is a prolate ellipsoid as proposed by Hood et al. (1969), Mirsky (1969), Wong and Rautaharjiu (1968), Ghista and Sandler (1969), and Streeter et al. (1973). They all used ellipsoidal geometries with sufficient simplification to the stress distributions to enable an analytical solution to be obtained. Streeter et al. (1973) considered anisotropy

of the myocardial material and changing of fibre orientation across the wall. In their model, however, large deformations, which occur during ventricular ejection, could not be described adequately because of the applied mathematics.

Any attempt to discuss here details on the mathematical formulation of the calculation of exact stress distribution in the ventricular wall for the model mentioned above would represent a cumbersome discussion, even considering the simplifying assumptions used. However, to give a representative example the thick-walled ellipsoidal model by Wong and Rautaharju (1968) is reported in detail in APPENDIX D.

With the advent of the Finite Element Method, stress analysis of complex geometry together with constitutive models became possible. Extension to more complex axisymmetric shapes using finite element models, but still with linear elastic material properties were made by Gould et al.(1972) and Pao et al. (1974). All these models use the infinitesimal elasticity theory.

The first model to offer real insight into myocardial stress distribution were those of Mirsky (1973), who used the large elastic deformation solutions of Green and Zerna (1968) for the inflation of a thick-walled sphere, and Janz et al. (1974), who used finite deformation theory with an axisymmetric finite element model having isotropic properties. These studies showed circumferential stress and strain distribution at end-diastole to be much higher in the subendocardium than in the subepicardium. Chen et al. (1980) using finite elements, modelled a 3-D active LV as a non-liear elastic orthotropic material having long and layered fibres allowing large deformations. An evaluation of several geometric assumptions for the estimation of left ventricular circumferential wall stress was given by McHale and Greenfield (1973). A recent evaluation of the above analytical models was presented by Eberhardt and Sanford (1993). They also compared finite element models of passive linear elastic ellipsoids with experimental results.

The calculated stress distribution across the myocardial wall depends also on the mechanical properties of the myocardial material as introduced in the model. Many authors (Hood et al., 1969; Janz and Grimm, 1972; Mirsky, 1969; Pao et al., 1974; Wong and Rautohaju, 1968) assumed isotropy of the myocardial material. Models based on isotropic material introduce large errors in describing the process of ejection and the transmural distribution of stresses (Arts and Reneman, 1977). During ejection the simulated, isotropic left ventricle appears three times stiffer than the real ventricle in a dog. An anisotropic asymmetric model based on finite deformation theory was developed by McCulloch et al. (1992). The basic equations for the solution of the solid mechanics under the assumptions of interest - large deformation and strains, non-linear elastic behaviour and anisotropy of material - will be discussed in section 2.8.

Among the modelling approaches documented in the recent literature, some seem to have gained substantial success in the valid representation of the mechanics of the left ventricle, although their complete development is still in progress. These include:

- the **global body force approach**, developed by Shoucri;
- the **finite element approach**, developed by Hunter and co-workers in collabora-

tion with Guccione and co-workers; and

- the **nonlinear, laminated-muscle-shell theory approach**, developed by Taber.

#### 2.7.3.1.1.1 Global Body Force Continuum Mechanics Approach

The concept of a active body force in an elastic model of the left ventricle was developed by Pierce (1981) and later by Shoucri (1991a). In Pierce's model, the active myocardium fibres create a body force proportional to the divergence of the tension direction vector, and a second equal to the tension divided by the radius of curvature. Explicit solutions to isotropic linearly elastic tensor equations with these body forces are found for a axisymmetric thick-walled spherical ventricle with radial body force.

Shoucri proposed a global continuum mechanics approach in which the active force of the myocardium is represented by three components of a body force along three orthogonal coordinate axes. These components are included in the equations that describe the mechanics of cardiac contraction. The concept of body force is used to model the active state of myocardium in the same way that the laws of the theory of elasticity are employed. The concept of strain energy density function is used. This had already been applied to biological tissues by Fung et al. (1979), for instance. The theory of large elastic deformation was used as discussed in Green and Adkins (1970).

The myocardium is represented as a thick-walled elastic cylinder with transverse isotropy contracting symmetrically. Bending and twisting of the cylinder are neglected, as are the inertia. The myocardium was assumed to be incompressible. Fibres lie on cylindrical surfaces and wind around the surface in a helical manner. The relation between body force and tension is derived from Peskin's formulation (Peskin, 1973-74). Shoucri used this approach to derive an equation for the P-V relation in the left ventricle from the calculation of the radial force per unit area (Shoucri, 1991a), and to evaluate the pump function of the left ventricle (Shoucri, 1991b).

#### 2.7.3.1.1.2 Finite Element Continuum Mechanics Approach for the Left Ventricle

A numerous group of investigators comprising a collaborative activity between the Guccione and Hunter groups have been working in the recent past on the modelling of the myocardium using a finite element continuum mechanics approach. Guccione and his collaborators have developed the mathematical formulation of the passive and active properties of the myocardium and have recently modeled the heart (Guccione et al., 1993a) using the finite element techniques developed by Hunter et al. (1988). Previous

studies on the passive myocardium properties were performed in a thick-walled cylindrical model of the left ventricle representing the equatorial region. The myocardium was modeled as a homogeneous incompressible hyperelastic material possessing curvilinear aelotropy with respect to the local muscle fibre axis. The stress-free state of the left ventricle was assumed to be a warped cylindrical arc. Residual stress and strain are modelled by prescribing displacements in two steps. First, the cylindrical arc is deformed from the stress-free state to the intact unloaded configuration. Then displacement are prescribed to model the deformation of the cylinder during the passive loading.

The finite element method developed specifically for the heart by Hunter and his co-workers (Hunter and Smaill, 1988) uses the Galerkin finite element equations for three-dimensional finite elasticity derived in prolate spheroidal coordinates. Orthotropic constitutive equations derived from biaxial testing of myocardial sheets are defined with respect to the microstructural axes of the tissue. Muscle fibre orientation is identified throughout the myocardium using finite element fields with nodal parameters fitted by least squares to comprehensive measurements of these variables. The material anisotropy of the ventricular wall was defined by referring the stress tensor components at every point in the element to an orthogonal system of local material coordinates, having one axis aligned with the fibre direction. An elastance model for active fibre stress was incorporated in a three-dimensional model that included an accurate representation of the left ventricular free wall geometry and fibre angle distribution in the dog heart, and a nonlinear constitutive equation for the resting myocardium, that was transversely isotropic with respect to the local fibre axis. Details on the method development are given in APPENDIX E.

Grid generation included the generation of nodal coordinates for the finite element mesh and the generation of orthotropic material axes at each computational point. Solution of the governing equations on the computational mesh required the material constitutive laws to be defined at the Gaussian quadrature or collocation points of the mesh. Thus, the spatially varying material coordinate axes needed to express the constitutive laws, may be defined mathematically by finite element basis functions and nodal parameters in a manner analogous to the decription of mesh geometry.

This model was used to simulate a canine heart with the purpose of analyzing the local sarcomere length and the active fibre stress during ejection (Guccione et al., 1993a). It was able to reproduce experimental data very well using a uniform stress-free sarcomere length distribution, the same transmural fibre angle distribution in all regions, and homogeneous material properties.

#### 2.7.3.1.1.3 Nonlinear Laminated-muscle-shell Theory Approach

While many researchers have modelled the left ventricle as a 'shell' few have used 'shell theory' to analyze their models. In general, researchers have used membrane the-

ory, and three-dimensional elasticity theory. Using the recent advances in nonlinear theory (Libai and Simmonds, 1988), Taber has developed laminated-shell equations that account for large-strain geometric and material nonlinearities, thick-shell effects, anisotropy, muscle activation, and residual stress (Taber, 1991a); and has modelled the canine left ventricle as a thick-walled laminated cylinder (Taber, 1991b).

Each layer is composed of an incompressible, orthotropic, pseudoelastic material with principal material directions that lie along helices whose orientation is based on anatomical data for the muscle fibres. The shell was moderately thick (ratio of radius to thickness greater than 10). Bending and transverse shear strains were considered moderately large. Surface shear stresses were neglected. In each lamina, shear strains due to residual strains and muscle activation were considered small to the principal material directions. Dynamic effects (inertia and muscle contraction velocity) were neglected. The governing equations were expressed in general lines-to-curvature coordinates and include axisymmetric deformation with torsion due to off-axis orthotropy. A single pseudostrain-energy density function with time-varying coefficients was used to describe the passive and active behaviour of the cardiac muscle for uniaxial, biaxial, and intact physiological loading conditions. For each layer of the shell three states were defined: zero-stress state, unload physiological state, and loaded state. Residual strain and muscle activation were treated in a unified manner, through shifts across the zero-stress configuration. The model predicted strain distributions that agree fairly well with published experimental measurements.

#### 2.7.3.2 Structural Approach

The most popular structural methods that use analytical techniques are the nested shell approach, known as Arts's approach, and the Fluid-fibre approach. Both methods use cylindrical geometries to model the left ventricle. A nested shell spheroidal shape with a realistical distribution of muscle fibres in the wall was used by Beyar and Sidenam (1986).

##### 2.7.3.2.1 Arts's Approach

Arts and his group have worked in the last twenty years in the development of a mathematical model for the mechanics of the left ventricle, which relate instantaneous values of left ventricular volume, pressure and dimensions as well as the transmural course of stress and sarcomere length in the left ventricle (Arts et al., 1979). They have simulated the left ventricle with a thick-walled cylinder composed of eight concentric shells. The ejecting ventricle was analyzed without considering the strain rate effect. The myocardial

tissue is assumed to be anisotropic, and consisting of a contractile fibre structure embedded in a soft incompressible material. The sarcomere length changes during the cardiac cycle as a function of the degree of activation of the cardiac muscle. Fibre orientation and sarcomere length change across the wall, and the spread of activation was considered to proceed only in the radial direction. Within a cylindrical shell all fibres have the same orientation, the same load, the same sarcomere length and similar degree of activation. Transmural gradients of these quantities are presented as stepwise changes from shell to shell. A similar model was developed by Feit (1979), who confined his analysis to the end-diastolic passive state and used an exponential stress-strain relation.

The calculation was performed following an iterative procedure starting on estimated height and torsion angle of the cylinder. Condition of equilibrium was applied to the total axial force and torque, acting on the upper surface of the cylinder including the cavity, and calculated taking into account the left ventricular pressure and the axial stresses. Iterations were stopped when the deviations from the equilibria were sufficiently small. Details of the calculation procedures are given in Arts et al. (1979). Recently, the mitral valve papillary muscle was incorporated in the model (Arts and Reneman, 1989).

The model presented above has given realistic results as global hemodynamics parameters and also in respect of the torsional deformation. It revealed that, when torsion is admitted, the transmural course of sarcomere length and tensile muscle stress are rather uniform. This result is essentially different from the results of studies on ventricular mechanics as performed by Wong and Rautaharju (1968) and Hood et al. (1969), who found a subendocardial stress in systole approximately twice as high as subepicardial stress. This discrepancy can be explained by the fact that the latter assumed isotropic cardiac muscle material.

#### 2.7.3.2.2 Fluid-Fibre Approach

The linear continuum mechanics methods in which the myocardium is represented in a way that can be interpreted as a fluid-fibre continuum was first proposed by Chadwick (Chadwick, 1981; Chadwick, 1982). Anisotropic elastic effects due to the fibre direction field are incorporated (Streeter, 1973). The model consists of a thick-walled cylindrical shaped ventricle in which fibres spiral on helical paths and terminate on planar end surfaces. The helix pitch angle varies continuously through the wall. Tozeren (1983) presented a similar model, but used nonlinear continuum mechanics to account for the large deformations which occur during myocardial contraction.

The myocardium is seen as a mixture of fluid and elastic components, where muscle fibres are embedded in a continuum. Fibres carry tensile stresses, while the fluid matrix sustain only hydrostatic pressure. A stress tensor is used, which accounts for the pressure in the fluid and the tensile stress produced by the action of the fibres. The quasi-static equilibrium approximation is used at each instant of time. That is, the ventricular cycle

is idealized as a sequence of mechanical equilibrium states and the effect of inertia is neglected. Moskowitz (1981) demonstrated that the difference between dynamic and quasi-static stresses is not significant for the case of late rapid-filling stage. A linear relation between fibre stress and linearized fibre strain was used. The instantaneous elastic modulus includes a time-dependent activation function to account for the heartbeat. Strain rate or other pathdependent effects are omitted. These assumptions lead to a theory which is consistent with the observation of Sagawa (1978), namely that over a significant physiological range there exists an essentially linear relationship between end systolic chamber pressure and chamber volume, and that this relationship is independent of preload and path. Nonlinear effects, such as finite deformation and a stress-dependent elastic modulus are quantitatively important during diastole (Mirsky, 1979). To include such effects more complex theory has to be applied.

The model was applied by Chadwick (1982) to a cylinder that is allowed to deform longitudinally in one direction while maintaining the cylindrical shape radially. The 'four corners' of the pressure-volume loop were analyzed. Ohayon and Chadwick (1988) used the same thick-walled cylindrical model to consider the effect of isotropic collagen matrix and the sheath surrounding a myocite. Their analysis is for infinitesimal deformations and uses the phenomenological isotropic Hooke's law for the collagen matrix.

Recently, a similar model for nonlinear finite deformations of the left ventricle has been developed by Nevo and Lanir (1989), based on a three-dimensional micro-structure of the myocardium which consists of helical muscle fibres interconnected by transverse collagen fibres. Muscle and collagen fibres are embedded in a fluid matrix. The collagen fibres form two distict networks: transverse collagen bundles interconnecting adjacent muscle fibres, and collagen fibres parallel to muscle fibres, forming collagenous sheaths around muscle cells. The uniaxial properties of the collagen fibres and those of the muscle fibres during the active phase are based on the experimental studies performed with passive and active isolated papillary muscles, respectively. Based on the findings of Horowitz et al. (1988), the passive stiffness of the myocardium is entirely represented by the collagen fibres.

From the extensive literature on ventricle modelling discussed in this section, it is possible to conclude that, in order to have reasonably realistic modelling of an SMV, the solid mechanics equations to be used in the coupled approach should generally be formulated for *large deformation*, *non-linear elastic* and *viscoelastic* material with *orthotropic* properties. The formulation of these equations will be addressed in the next section.

The final goal of this research is the achievement of a coupled solid-fluid ventricle models to be applied to model SMVs. Numerical modelling of fluid-solid coupling was initially carried out by our Biomedical group treating the solid as a quasi-fluid along the lines of Peskin's approach. Few pioneering approaches have coupled continuum solid equations to the fluid equations, and they are under investigation by our group. Details of these approaches are given in section 2.9.

## 2.8 SOLID MECHANICS

In this section, the basic equations are presented for a comprehensive solid mechanics model applicable to ventricle modelling. A realistic modelling of the ventricle dynamics should include the following aspects:

(i) reasonably faithful three-dimensional geometric representation
(ii) time-dependent analysis
(iii) large deformation analysis
(iv) non-linear constitutive relations
(v) anisotropy of the material
(vi) viscoelastic effects
(vii) inertia effects
(viii) large strain analysis

Table 2.1 summarizes the most relevant approaches reported in the literature to model the solid mechanics of the left ventricle pointing out the various approximations made to the geometry, material behaviour, and type of deformation analysis. As mentioned in the previous section, initial models were derived from the exact solution of the linear elasticity equations for small deformations and isotropic material. The mathematical formulation of a thick-walled ellipsoidal model is reported in APPENDIX D. More realistic models require a greater mathematical effort. As Janz et al. (1974) demonstrated from the analysis of available experimental data showing peak fibre stretches of about 20 %, finite deformation analysis is required. In addition, due to the nature of the constitutive equations both in the passive and active states of muscles, the analysis should consider viscoelastic and non-linear elastic terms. The structure of the muscle can be assumed homogeneous, but anisotropic effects cannot be neglected. However, the analysis is in part simplified by the fact that transverse isotropy (orthotropy) can be assumed. Inertia effects are usually neglected, reducing the problem to a quasi-static case.

It has to be pointed out that fibre organization when using the latissimus dorsi as powering muscle for SMVs does not have the same configuration encountered in the cardiac muscle. It is admitted that it should be borne in mind that a certain degree of orientation with respect to the longitudinal axis will be presented in the *in vivo* harnessed SMV. For muscle modelling in the immediate future, however, a simplified approach is intended where the orientation of the fibres is mainly circumferential and uniform throughout the wall thickness.

An important issue to consider is the separate behaviour of the muscle in the passive and active states. In the passive state, anisotropy cannot be neglected. In the active state, body forces have to be included in the equilibrium equations. Passive constitutive relations consider viscoelastic effects. As discussed in the previous section, when the muscle is operating passively the connective structure of the fibres determine the mechanical behaviour. Experimental data seem to fit well with exponential curves although

biaxial testing is needed to take into account the anisotropy of the muscles. When the muscle is operating actively, the constituive equations are represented by force-length, and force-velocity relations available from experimental data.

Table 2.1

Summary of ventricle models reported in literature

| Reference | Geometry | Elasticity Theory | Anisotropy | Deformation Analysis |
|---|---|---|---|---|
| Sandler and Dodge (1963) | thin-walled ellipse | linear | isotropic | small |
| Streeter et al. (1969) | thin-walled ellipse | linear | isotropic | small |
| Wong & Rautahaju (1968) | thick-walled ellipse | linear | isotropic | small |
| Sandler and Ghista (1969) | thick-walled ellipse | linear | isotropic | small |
| Mirsky (1969) | thick-walled ellipse | linear | isotropic | small |
| Gould et al. (1972) | realistic model | linear | isotropic | small |
| Hanna (1973) | thick-walled sphere | linear | isotropic | small |
| Streeter et al. (1973) | thick-walled ellipse | linear | anisotropic | small |
| Mirsky (1973) | thick-walled sphere | linear | isotropic | large |
| Pao et al. (1974) | realistic model | linear | isotropic | small |
| Janz et al. (1974) | thick-walled cylinder | linear | isotropic | large |
| Vito (1979) | thick-walled sphere | linear | isotropic | large |
| Chen et al. (1980) | ring strip | non-linear | isotropic | large |
| Shivakumar et al. (1989) | thick-walled sphere | linear | orthotropic | large |
| Shoucri (1991) | thick-walled cylinder | linear | orthotropic | large |
| Taber (1991b) | thick-walled cylinder | non-linear | orthotropic | large |
| Guccione et al. (1993c) | thick-walled cylinder | non-linear | orthotropic | large |
| Guccione et al. (1993a) | thick-walled prolate spheroid | non-linear | orthotropic | large |

The basic solid mechanics equations for large deformation problem are discussed in section 2.8.1. Numerical methods are presented in section 2.8.2.

### 2.8.1 Basic Equations

From an estimate of the deformations that model SMVs may experience, it is possible to conclude that *finite deformation* equations have to be considered for the purpose of modelling the solid mechanics of the ventricle. The discussion that follows refers to Fung's approach as it is described in (Fung, 1990, 1981), and based on the

*non-linear elastic theory* as treated by Green and Adkins (Green and Adkins, 1970). This approach has been extensively used in biomechanics by many ventricle modellers. In order to know the deformation of a body, stresses and strains are to be found first, then the deformation gradient, and finally, the functions that describe the deformation of each point.

Large Deformation Analysis

To describe the deformation of a body we need to know the position of any point in the body with respect to an initial configuration termed the *reference state*. When considering Lagrangian formulation, stresses and strains are referred to the initial configuration. Positions are described with respect to a fixed *frame of reference*, represented by the rectangular cartesian coordinate system. Every point in the body at the reference state has three coordinates $x_1$, $x_2$, $x_3$. When the body is deformed, the point $P$, having coordinates $x_i$ in the reference state, will have new coordinates $y_i$. The deformation of the body is known completely when the relationship

$$y_i = y_i(x_1, x_2, x_3) \qquad i = 1, 2, 3 \tag{2.10}$$

is known, or its inverse

$$x_i = x_i(y_1, y_2, y_3) \qquad i = 1, 2, 3 \tag{2.11}$$

for every point in the body. These relations are single-valued functions possessing a unique inverse and continuous derivatives. They represent the final goal to which stress analysis leads once stress and strain are calculated. To describe the deformation in the immediate neighbourhood of a point, the *deformation gradient* tensors are used:

$$\partial y_i/\partial x_j, \qquad \partial x_i/\partial y_j \qquad i, j = 1, 2, 3$$

These deformation gradients enable the description of the change in distance between two neighbouring points such as $P(x_i)$, $P'(x_i + dx_i)$ after deformation to $Q(y_i)$, $Q'(y_i + dy_i)$. Using the summation convention, these distances $PP'(dx_i)$ and $QQ'(dy_i)$ can be written as

$$ds_0^2 = \delta_{ij} dx_i dx_j, \qquad ds^2 = \delta_{ij} dy_i dy_j$$

where $\delta_{ij}$ is the Kronecker delta. The difference is given by

$$ds^2 - ds_0^2 = \delta_{ij}(dy_i dy_j - dx_i dx_j) \tag{2.12}$$

Substituting the derivatives of the deformation expressions:

$$ds^2 - ds_0^2 = \left(\frac{\partial y_i}{\partial x_l}\frac{\partial y_i}{\partial x_k} - \delta_{lk}\right) dx_l dx_k = \left(\delta_{lk} - \frac{\partial x_i}{\partial y_l}\frac{\partial x_i}{\partial y_k}\right) dy_l dy_k \tag{2.13}$$

leads to the form:

$$ds^2 - ds_0^2 = 2E_{ij}dx_i dx_j = 2e_{ij}dy_i dy_j$$

where $E_{ij}$ is the *Green's strain tensor* and $e_{ij}$ the *Almansi strain tensor*. These latter can also be written as

$$E_{ij} = \frac{1}{2}\left(\frac{\partial u_i}{\partial x_j} + \frac{\partial u_j}{\partial x_i} + \frac{\partial u_k}{\partial x_i}\frac{\partial u_k}{\partial x_j}\right) \tag{2.14}$$

and

$$e_{ij} = \frac{1}{2}\left(\frac{\partial u_i}{\partial y_j} + \frac{\partial u_j}{\partial y_i} - \frac{\partial u_k}{\partial y_i}\frac{\partial u_k}{\partial y_j}\right) \tag{2.15}$$

where $u_i = y_i - x_i$.These tensors allow the calculatiion of distances between two neighbouring points in a deformed body, and from these the calculation of the deformation functions. For small deformations the square of an infinitesimal can be neglected and the *Cauchy's infinitesimal strain tensor* is obtained

$$\epsilon_{ij} = \frac{1}{2}\left(\frac{\partial u_i}{\partial y_j} + \frac{\partial u_j}{\partial y_i}\right) = \frac{1}{2}\left(\frac{\partial u_i}{\partial x_j} + \frac{\partial u_j}{\partial x_i}\right) \tag{2.16}$$

The use of curvilinear coordinates system $(a_i)$ can be advantageous when considering a local coordinate system. In this case, the square of length of a differential element can be written as

$$ds_0^2 = g_{ij}^{(0)}dx_i dx_j, \qquad ds^2 = g_{ij}dy_i dy_j$$

where $g_{ij}^{(0)}$ and $g_{ij}$ are *metric tensors* defined as

$$g_{ij}^{(0)} = \frac{\partial x_k}{\partial a_i}\frac{\partial x_k}{\partial a_j}, \qquad g_{ij} = \frac{\partial y_k}{\partial a_i}\frac{\partial y_k}{\partial a_j}$$

Thus the strain tensor may be expressed as:

$$E_{ij} = \frac{1}{2}\left(g_{ij} - g_{ij}^{(0)}\right)$$

Stress State Analysis

The state of stress at a point in the deformed body, referred to a cartesian system is determined by the symmetric *Cauchy's stress tensor* $\sigma_{ij}$. Stresses may, like strains, be expressed with respect to the original configuration. Consider an element in the *original* state and in the *deformed* state. A force vector $d\mathbf{T}$ acts on a surface of the deformed element with a unit outer normal $\mathbf{n}$, with a corresponding force vector $d\mathbf{T}_0$ acting in the original configuration on a surface with area $dS_0$ and unit outer normal $\mathbf{n}_0$. The assignment of a correspondence rule between $d\mathbf{T}$ and $d\mathbf{T}_0$ is arbitrary, but must be mathematically consistent. According to Cauchy's relation:

$$dT_i = \sigma_{ji}n_j dS$$

According to the Lagrangian rule, the force vector is transformed without change of direction and magnitude from the surface element in the deformed configuration. If $T_{ij}$ is the *Lagrangian stress tensor*, it follows that

$$dT_{0_i}^L = T_{ji} n_{0_j} dS_0 = dT_i$$

An alternative is the Kirchhoff's rule. This requires a change of magnitude and direction of the force vector, and states

$$dT_{0_i}^K = \frac{\partial x_i}{\partial y_\alpha} dT_\alpha = S_{ji} n_{0_j} dS_0$$

$S_{ij}$ is called the *Kirchhoff's stress tensor*. The following relationships between $\sigma_{ij}$, $T_{ij}$, and $S_{ij}$ are given in standard textbooks:

$$T_{ji} = \frac{\rho_0}{\rho} \frac{\partial x_j}{\partial y_m} \sigma_{mi} \tag{2.17}$$

and

$$S_{ji} = \frac{\rho_0}{\rho} \frac{\partial x_i}{\partial y_\alpha} \frac{\partial x_j}{\partial y_\beta} \sigma_{\beta\alpha} \tag{2.18}$$

The Eulerian stress tensor $\sigma_{ij}$, and the Kirchhoff's stress tensor $S_{ij}$ are symmetric. The Lagrangian stress tensor $T_{ji}$ is not necessarily symmetric. This implies that the Lagrangian stress tensor is inconvenient to use in a stress-strain law in which the strain tensor is always symmetric; the Kirchhoff stress tensor is more suitable. From eqs.(2.17) and (2.18), we have

$$S_{ji} = \frac{\partial x_i}{\partial y_\alpha} T_{j\alpha} \tag{2.19}$$

$$\sigma_{ji} = \frac{\rho}{\rho_0} \frac{\partial y_i}{\partial x_p} T_{pj} = \frac{\rho}{\rho_0} \frac{\partial y_i}{\partial x_\alpha} \frac{\partial y_j}{\partial x_\beta} S_{\beta\alpha} \tag{2.20}$$

$$T_{ij} = S_{ip} \frac{\partial y_j}{\partial x_p} \tag{2.21}$$

Equilibrium Equation

In the Eulerian description, the external loads consist of a body force $\mathbf{F}$ per unit mass, and a surface traction $\tilde{\mathbf{T}}$ per unit area acting on a surface element $dS$ whose unit outer normal is $\mathbf{n}$. In the Lagrangian description, the focus is on the body force per unit mass $\mathbf{F}_0$ (with $F_i = F_{0_i}$). By considering the resulting forces acting on the volume and on the surface and using Gauss's theorem, the following equation of static equilibrium can be written in Lagrangian terms:

$$\frac{\partial T_{ji}}{\partial x_j} + \rho_0 F_{0_i} = 0 \tag{2.22}$$

If the body is in motion, we can apply D'Alembert's principle to reduce an equation of motion to an equation of equilibrium by applying the inertial force, as an external load. Hence $F_{0_i}$ includes the inertial force. The equation of equilibrium, expressed in terms of

the Kirchhoff stress tensor is:

$$\frac{\partial}{\partial x_j}\left(S_{jk}\frac{\partial y_i}{\partial y_k}\right)+\rho_0 F_{0_i}=0 \tag{2.23}$$

The well known equation of equilibrium expressed in terms of Cauchy stress can easily be written in the deformed state as:

$$\frac{\partial \sigma_{ji}}{\partial y_j}+\rho_0 F_i=0 \tag{2.24}$$

Strain Energy Function

One of the best known approaches to the elasticity of bodies capable of finite deformation is to postulate the form of an elastic potential, or strain energy function $W$. If a material (tissue) is *elastic*, a *strain energy function* per unit mass $W$ exists, which is an analytical function of the strain components measured with respect to the stress-free state, with the property that the rate of change of strain energy per unit mass is equal to the power of the stresses. This definition expressed in terms of Eulerian variables, gives

$$\frac{D}{Dt}W=\frac{1}{\rho}\sigma_{ij}V_{ij} \tag{2.25}$$

where $D/Dt$ is the substantial derivative and $V_{ij}$ is the rate of deformation defined as

$$V_{ij}=\frac{1}{2}\left(\frac{\partial v_i}{\partial y_j}+\frac{\partial v_j}{\partial y_i}\right) \tag{2.26}$$

where $v_i$ is the velocity field. In terms of Lagrangian variables, we have

$$\frac{D}{Dt}W=\frac{1}{\rho_0}S_{ij}\frac{D}{Dt}E_{ij}=\frac{1}{\rho_0}S_{ij}\frac{\partial}{\partial t}E_{ij} \tag{2.27}$$

Among the salient properties of the strain energy function $\rho_0 W$ are:

(i) the Kirchhoff's stress tensor can be expressed as

$$S_{ij}=\frac{\partial(\rho_0 W)}{\partial E_{ij}} \tag{2.28}$$

(ii) the Lagrangian stress tensor can be expressed as

$$T_{ij}=\frac{\partial(\rho_0 W)}{\partial(\partial y_i/\partial x_j)}=\frac{\partial(\rho_0 W)}{\partial(\partial u_i/\partial x_j)} \tag{2.29}$$

If the material is incompressible, then $\partial v_i/\partial y_i = V_{ii} = 0$. This condition can be expressed in terms of $DE_{ij}/Dt$, and writing

$$\frac{\partial x_i}{\partial y_r}\frac{\partial x_j}{\partial y_r}=B_{ij} \tag{2.30}$$

we have

$$B_{ij}\frac{DE_{ij}}{Dt} = 0 \tag{2.31}$$

$B_{ij}$ is called Finger's strain tensor. From this follows that for an incompressible material:

$$S_{ij} = \frac{\partial \rho_0 W}{\partial E_{ij}} - pB_{ij} \tag{2.32}$$

where $p$ is an arbitrary scalar which can be identified with pressure. Known strain energy functions of biological tissue are reported by Fung (1981). Guccione et al. (1991) have found a strain energy function to be used in modelling of the passive state of the myocardium. Details are in APPENDIX E.

Strain-Rate Effects and Pseudo-Elasticity

Mechanical properties of soft tissues, such as arteries and muscles, are qualitatively similar. They are inelastic in that there is not a single-valued relationship between stress and strain. They show hysteresis, relaxation, and creep. They are anisotropic, and their stress-strain-history relationships are nonlinear. When hysteresis can be ignored, nonlinear elasticity can be approached using the incremental laws of elasticity. Since these laws represent the behaviour of a nonlinear viscoelastic material subjected to oscillations of small amplitude, they may be strain-rate dependent. If hysteresis is not ignored but the loops remain small, then one may consider *incremental laws of viscoelasticity* (Patel and Vaishnav, 1972). The stress-strain relationship of muscle is rather insensitive to strain rate (Fung et al., 1979).

If a tissue is able to be preconditioned, the stress-strain relationship for the loading and unloading branches separately is unique. Then the material can be treated as *pseudo-elastic*, and a *pseudo strain energy function* can be used. The concept of pseudo-elasticity is very useful because of its insensitivity to the strain rate.

Stress-Strain Relation for a Transverse Isotropic Material

Suppose that the material is transversely isotropic with respect to the direction parallel to $x_3$, in the cartesian coordinate system. The strain invariant expressions for an incompressible body are

$$I_1 = 3 + 2E_{rr}, \qquad I_2 = 3 + 4E_{rr} + 2(E_{rr}E_{ss} - E_{rs}E_{rs}), \qquad I_3 = 1 \tag{2.33}$$

Let us define $K_1$, and $K_2$ as

$$K_1 = E_{33}, \qquad K_2 = E_{3\alpha}E_{3\alpha} \tag{2.34}$$

where $\alpha$ represents the orientation angle in the plane orthogonal to the fibre direction. The strain energy function can be expressed as

$$W = W(I_1, I_2, K_1, K_2) \tag{2.35}$$

The stress tensor $\tau^{ij}$, measured per unit area of the deformed body, and referred to curvilinear coordinates, is expressed by:

$$\tau^{ij} = \Phi g_{ij} + \Psi B^{ij} + p g_{ij}^{(0)} + \Theta M^{ij} + \Lambda N^{ij} \tag{2.36}$$

where

$$\Phi = 2\frac{\partial W}{\partial I_1}, \qquad \Psi = 2\frac{\partial W}{\partial I_2}, \qquad \Theta = \frac{\partial W}{\partial K_1}, \qquad \Lambda = \frac{\partial W}{\partial K_2}, \tag{2.37}$$

$$B^{ij} = I_1 g_{ij} - g_{ir} g_{is} g_{rs}^{(0)}, \qquad M^{ij} = \frac{\partial a_i}{\partial x_3}\frac{\partial a_j}{\partial x_3}, \tag{2.38}$$

$$N^{ij} = \left(\frac{\partial a_i}{\partial x_3}\frac{\partial a_j}{\partial x_\alpha} + \frac{\partial a_j}{\partial x_\alpha}\frac{\partial a_i}{\partial x_3}\right) E_{\alpha 3} \tag{2.39}$$

$p$ is an unknown scalar invariant function of the curvilinear coordinate system.

### 2.8.2 Numerical Methods

A complete analytical solution for the displacement, stresses or strains in a body subjected to internal and external forces, can be found only in a limited number of examples. Numerical methods overcome these difficulties by giving an approximate solution to the governing differential equations. These are replaced by a set of algebraic simultaneous equations which allow the calculation of the variables of the problem at discrete nodes. Two approaches are available: the Finite Difference Method and the Finite Element Method. The older Finite Difference Method is based on a differential formulation, while the Finite Element Method is based on integral formulations. The earliest mathematical formulations for finite element models were based on variational techniques. This was followed by the more recent weighted residual techniques, among which the most common are the Galerkin method, collocation methods, and subdomain methods. Other details of the Finite Element Method are given in section 3.4.2, where major attention is paid to its use in the solution of fluid-dynamics problems.

Application of Finite Element Analysis (FEA) to structural problems has proved to be successful in many cases, and biomechanics applications have also been performed (Reuderink, 1991; Perktold and Rappisch, 1993). They have been developed to the point where theoretical analyses for more complex situations and constitutive material laws have been directly developed for the use in finite element analysis. Recently the modelling has been extended to finite deformation, and more latterly to large strain problems, and this has made the approach very promising in modelling biological tissues mechanics. A discussion on the equations to be used for finite deformation and finite strain in the finite element context is given below, followed by an outline of the solution algorithm. For a background to general finite element procedures see Zienkiewicz (1977).

Formulation of Finite Element Equations

In the following derivation the equations will be written for a single element. The equilibrium equation in Lagrangian variables expressed in terms of the Finite Element is formulated by considering a continuum occupying a region $V$ with a boundary surface S in the deformed state, which corresponds to a region $V_0$ with a boundary surface $S_0$ in the original state. The body is subjected to external loads, consisting of a body force $\mathbf{F}^0$ per unit mass, and a surface force $\mathbf{T}^0$ per unit area acting on a surface element $dS_0$. The equilibrium equation referred to the initial configuration is:

$$\int_{S_0} \mathbf{T}^{0^T} \mathbf{v} dS_0 + \int_V \mathbf{F}^{0^T} \mathbf{v} dV_0 = \int_{V_0} \mathbf{S}^T \dot{\mathbf{E}} dV_0 \tag{2.40}$$

where $\mathbf{v}$ is the velocity field within the region referred to the current geometry. $\mathbf{S}$ is the Kirchhoff stress, and $\dot{\mathbf{E}}$ the time rate change of Green's strain. If the displacement field is $\mathbf{u}$ this becomes

$$\int_{S_0} \mathbf{T}^{0^T} d\mathbf{u} dS_0 + \int_V \mathbf{F}^{0^T} d\mathbf{u} dV_0 = \int_{V_0} \mathbf{S}^T d\mathbf{E} dV_0 \tag{2.41}$$

This leads to the equilibrium equation in finite element form:

$$\mathbf{P} = \int_{V_0} \bar{\mathbf{B}}^T \mathbf{S} dV_0 \tag{2.42}$$

In this equation the surface traction and body forces have been lumped together in $\mathbf{P}$ which is the vector of equivalent nodal loads. $\mathbf{B}$ is the matrix which relates an increment of Lagrange strain to the nodal displacement increments. By taking derivatives the incremental stiffness equations are obtained which relate displacement increments to load increments:

$$d\mathbf{P} = \left[ \int_{V_0} \bar{\mathbf{B}}^T \mathbf{D} \bar{\mathbf{B}} dV_0 + \int_{V_0} \mathbf{G}^T \mathbf{M} \mathbf{G} dV_0 \right] d\mathbf{a} \tag{2.43}$$

where $\mathbf{D}$ is the constitutive matrix relating stress increments to strain increments, $\mathbf{G}$ the matrix relating displacement derivatives to nodal displacement increments, $\mathbf{M}$ the matrix of Kirchhoff stress components, and $\mathbf{a}$ the vector of nodal displacement increements. This formulation is valid for small strain. If large strains are to be considered, then the matrix $\mathbf{D}$ has to be defined so that increments of Kirchhoff stress are related to increments of Lagrange strain. In order to do so, other stress definitions have to be introduced, such as the Jaumann stress.

The solution to a problem is achieved by applying the load as a series of increments. Within each load increment iterations are performed to establish equilibrium. A full tangent stiffness is evaluated for each iteration, allowing increments of maximum size to be used.

Current FEA programs (Puttre', 1991) offer extensive features for non-linear dynamic analysis and finite strains (Harper, 1984). Whereas available CFD codes can adequately represent all the large scale phenomena of blood flows, to simulate the various aspects of the compliance and muscle behaviour require the most comprehensive solid

mechanics stress modelling available today. Among the current FEA packages for structural analysis used in the modelling of biomechanics problems are ABAQUS, used by Perkold and co-workers (Perktold and Rappisch, 1993), and MARC used by Reuderink (Reuderink, 1991). Some of these packages - FEAT for example - allow a comprehensive solid-fluid analysis, being then suitable for application in solid-fluid interaction modelling. More details on these packages are discussed in section 3.6, where other FEM CFD packages are described.

## 2.9 COUPLED SOLID-FLUID APPROACHES

Much of the interest in blood flow modelling is focused on the conditions prevailing at the interface between blood and vessel wall. The latter constitues a rather complex, fibrous, compliant material which interacts mechanically and chemically with blood. In addition, when modelling the wall motion of a ventricle, the active muscle behaviour in contraction has to be addressed. The total load acting on the wall consists of the fluid pressure (acting normally) and of the wall shear stress (acting tangentially). These two distend and distort the wall which in turn reacts producing stresses and strains. Although, microscopically, both the pressure and the shear stress are important, macroscopically it is the pressure that plays the principal role.

Numerical modelling of a coupled solid-fluid model is complicated by the necessity of solving the equations of motion for the flow and wall simultaneously. Very few researchers have simulated the interaction of fluid with cardiovascular tissue. The Immersed Boundary Method developed by Peskin (1977) represents a comprehensive approach in the modelling of the complex structure of the heart. Despite several years of research aiming at defining the most realistic and sophisticated approach, fulfilment of expectations has been elusive. Reuderink (1991) developed an uncoupled approach to solve the equations for the solid and for the fluid separately. As mentioned previously, Xu and Collins (1994) have modelled the wall distensibility in an arterial bifurcation using a simple pressure-diameter relationship incorporated in the wall boundary routine of CFDS-FLOW3D. Perktold and Rappisch (1993) have developed a coupled approach using the FEM method to solve the flow and solid mechanics problems. A number of groups are actively working on the development of coupled fluid/solids numerical codes. The Biomechanical Research group at City University are currently engaged in two projects aimed at developing numerical codes capable of solving the coupled problem (Xu et al., 1994c). The first is based on the finite volume code CFDS-FLOW3D, modified to allow the modelling of the solid wall. The second project is based on the use of a FEM code called FEAT, developed by Nuclear Electric's Engineering Analysis Group. Coupled calculations of flow in a compliant artery using infinitesimal strain theory have been successfully conducted using both codes. We now look at various approaches in detail.

Of less interest, the uncoupled approach by Reuderink can be summarized as follows. First the time-dependent pressure distribution due to wave propagation (1-D) is determined. Next the wall motion due to this pressure distribution is calculated. Finally, the wall motion is prescribed as a boundary condition for the solution of the fluid motion. This approach is valid when the pressure distribution causing the wall motion is indeed mainly dependent on wave phenomena and not on 'local flow effects'. Reuderink (1991) applied this approach to a 3-D distensible model of the carotid bifurcation (Reuderink), and to a distensible non-uniform tube (Reuderink et al., 1993). The Boundary Immersed Method is discussed in section 2.9.1, followed by a brief description of Perktold's approach in section 2.9.2. The two approaches that are being developed at City are presented in sections 2.9.3 and 2.9.4.

### 2.9.1 The Immersed Boundary Method

The Immersed Boundary approach treats the fluid-structure system as two separate subsystems, those of the fluid and the structure. Each subsystem is solved separately at each time step. The results of the previous solution of one subsystem are used to solve the other. The fluid velocity field is used to deform the moving structure (cardiac tissue). Once deformed, the structural forces associated with the new configuration are computed, ignoring the fluid flow field. In reality, the boundary force would be in equilibrium with the fluid force; a weakly coupled method only approximates equilibrium. These forces are then applied to the fluid field, and a new fluid velocity field is computed. In the immersed boundary method, a semi-implicit estimate of the boundary forces improves the estimate of the structural forces in equilibrium with the fluid forces. The effect of the fluid inertia is included in the computation of the boundary forces.

For the Immersed Boundary Method, the cardiac tissue is represented as a system of totally immersed, neutrally buoyant, infinitely thin springs. Elastic and/or contractile fibres are immersed in a viscous incompressible fluid. The cardiac tissue has a Lagrangian representation, while the fluid has an Eulerian representation. An interpolation function rather than a Jacobian matrix is used to convert a Lagrangian variable to a Eulerian variable, and viceversa. The interaction between the fluid and the tissue is described by using local body forces on the fluid at the location of the contact point with the surface, rather than by prescribing boundary conditions at the contact point. The magnitude and direction of the body forces are determined by the tissue strain. Because the fluid is viscous, the velocity field cannot have discontinuities, and since the structure is assumed infinitely thin and moves at the velocity of the adjacent fluid, no slip can occur on either side of the tissue.

The three-dimensional Navier-Stokes equations are solved by an extension of Chorin's projection method (Chorin, 1967). Peskin extended the algorithm to include a body force term (Peskin, 1977). Fluid equations are solved using a finite difference method on a fixed

regular computational lattice. Fibre points move freely through this lattice without being constrained to lie at the lattice intersections. Communication between fibres and fluid involves interpolation of the fluid velocity to the fibre points and spreading of the fibre forces to the computational lattice of the fluid. Details of the governing equations and the computational method are described in Peskin and McQueen (1989), McQueen and Peskin (1989), and Peskin (1992), Peskin and McQueen (1993), and are reported in APPENDIX F. Yoganathan et al. (1994) have used this approach to model a 3-D thin-walled left ventricle during isovolumic contraction and early systolic ejection. The numerical predictions, have been compared with available clinical data.

### 2.9.2 Perktold's Approach

Perktold and co-workers have developed a coupled approach to model the flow in distensible artery bifurcations. The mathematical description of the flow field uses time-dependent Navier-Stokes equations to calculate pulsatile, non-Newtonian flows. The flow equations are solved numerically using their recently developed pressure-velocity correction method and finite element techniques. The artery segment is modelled as a thin shell where geometrically non-linear shell theory and incrementally linear elastic wall are applied. The wall calculations are carried out applying the finite element program package ABAQUS version 4.9 (Hibbit, 1989). The numerical scheme at a time level consists of the following steps:

1. Calculation of the wall displacements
2. Calculation of the wall velocity
3. Updating of the geometry and the finite element mesh
4. Calculation of the flow velocity and the pressure with the updated boundary conditions
5. Iteration of the scheme until convergence is obtained.

Application of this approach to a human carotid bifurcation is reported in Perktold and Rappisch (1993).

### 2.9.3 The Finite Volume Method Approach

The application of the Finite Volume (FV) method to solid mechanics is quite novel. The advantage of this approach is that coupled wall-fluid problems of blood flow can be investigated using conventional CFD codes with relative ease. The model is able to predict the full, time-dependent displacement and stress within the wall as well as to solve the flow problem. The model has been applied to simple compliant-wall flows giving reasonable agreement with available analytical solutions.

The equation of motion is derived for a tube in cylindrical coordinates. The wall is assumed to be isotropic, linearly elastic, and incompressible. The governing equation of

the unsteady, axisymmetric flow for a Newtonian fluid are solved using CFDS-FLOW3D. The standard version of CFDS-FLOW3D requires the position of the moving surface to be a known function of time. Because, in this coupled approach the interface position is part of the solution, it was necessary to modify CFDS-FLOW3D so that the routine defining the wall position could be called repeatedly, until the predetermined convergence condition is achieved. This allowed the interface position to be found using a predictor/corrector scheme as follows:

1. An initial wall position is defined.
2. Using the current wall position, the flow field is calculated. The predicted distributions of pressure and shear stress at the wall provide an estimate of the wall loading.
3. Using the current guess of wall loading, the equation of motion and volumetric invariance equation are solved to give an updated guess of the interface configuration.
4. The current interface configuration is compared with the preceding guess, and the procedure is repeated from step 2 if convergence is not achieved.
5. Steps 2, 3, and 4 are repeated for each time step. The interface configuration at time T is used as the initial guess for the configuration at T+$\Delta$T.

A discrete formulation of the equations of motion is obtained using the finite volume method. The solution procedure mirrors that used to solve the flow field. Each variable is decomposed into a guessed, or predicted, value and a correction. Following the SIMPLEC approach, correction equations are formulated from reduced forms of the momentum equations. The equation for the pressure correction is derived from the equation of volumetric invariance. Values of all variables (except displacement) and coefficients on the control volume boundaries are estimated as averages of the two nodal values either side of the relevant boundary. Details of the formulation of the equations and the numerical procedure to solve them can be found in Henry and Collins (1993b).

### 2.9.4 The Finite Element Method Approach

In this approach three sets of equations are solved: (1) the full time-dependent Navier-Stokes equations for a non-Newtonian fluid, (2) the linear elastic small displacement stress equations for the wall, and (3) the mesh displacement equations. The flow equations are solved in moving boundary grids. The grid velocity is determined by solving the mesh displacement equations. As a starting point, simpler models have been considered solving the equations governing the motion of a linearly elastic, incompressible, isotropic solid undergoing small deformations. The three sets of equations are solved simultaneously together with appropriate boundary conditions. Details of these equations are reported in Xu and Collins (1995).

The coupled solution procedure has been implemented in the FE-based computational fluid-dynamics code FEAT (Anonymous, 1991a), a code extensively used in the nuclear industry. The momentum equations for both the fluid and the wall are discretised using the Galerkin finite element method, with the continuity equations being incorporated by a penalty-augmented Lagrangian-multiplier (PALM) method. An implicit predictor/corrector method is used to solve the fully-coupled time-dependent equations. The predictor is the second order explicit Adams-Bashforth method and the corrector is the implicit Crank-Nicholson scheme, which is non-dissipative, completely stable and second order accurate. The non-linear system of algebraic equations is solved using the Newton-Raphson iteration algorithm. The mesh displacement equations are solved separately at each time step to obtain updated grid velocities, which will then be used to calculate the transformation matrix introduced in the modified fluid equations. By doing so , the transformed fluid equations are always solved on the original computational mesh, regardless of the fact that the physical grid is moving.

In order to validate the two approaches under investigation in our research group, tests have been performed in three stages: (1) decoupled solution for wall displacement, (2) decoupled solution for flow field with moving boundary, and (3) coupled solution for wall motion and fluid flow. For each case, numerical predictions have been attempted using both the FV and the FE codes, and good agreement has been demonstrated. Future work will include modifying the model wall used in the current codes to allow more complex stress-strain relationships. Both these two techniques are very promising for the purpose of muscle modelling.

In chapter 4, the first validation exercise, for the problem of decoupled flow with moving boundary, will be discussed in detail. This has been found to be essential as an initial validation of the numerical solution calculated by CFDS-FLOW3D, details of which are discussed in the next chapter, but leading towards the full qualitative and quantitative validation of the flows in realistic *in vitro* model SMVs. This procedure will be discussed in the chapters that follow.

# CHAPTER 3

# NUMERICAL METHODS FOR COMPUTATIONAL FLUID DYNAMICS

## 3.1. INTRODUCTION

This chapter describes the mathematical model equations for fluid flow and heat and mass transfer used in Computational Fluid Dynamics, and the numerical methods for solving these equations. Discretization methods, advection schemes, time differencing schemes and pressure/velocity coupling algorithms are discussed. Commercially available CFD software packages are reviewed and CFDS-FLOW3D is described in detail.

Flows inside model Skeletal Muscle Ventricles are laminar, axisymmetric, time-dependent and incompressible. Furthermore, these flows are driven by the wall motion and, therefore, are characterized by moving boundaries.

The governing equations are complex non-linear partial-differential equations, which can be solved using numerical approaches. The next section is intended to give a brief historical background of the numerical methods in Computational Fluid Dynamics. The third section of this chapter is dedicated to the governing equations; while numerical methods are discussed in the fourth section. Grid generation techniques are reviewed in the following section. Commercially available codes, and a code overview of CFDS-FLOW3D are presented in the sixth and seventh section respectively.

## 3.2 BRIEF HISTORICAL PERSPECTIVE

Until the end of World War II, most fluid dynamics problems were solved using methods that were either analytical or empirical. Few pioneers used numerical methods and a single solution of a problem represented a monumental amount of work since calculations were performed by hand. Most people attribute the first important work on CFD to Richardson (Richardson, 1910), who introduced Finite Difference approximations to the governing differential equations. He used point iterative schemes to solve Laplace's equation applied to an elastic model of an ideal beam. The invention of relaxation methods by Southwell (1946) allowed many practical solutions to be achieved. Sometimes the beginning of numerical analysis is attributed to a famous paper by Courant, Friedrichs and Lewy (1928), where the stability requirement was assessed for the numerical solution of hyperbolic partial differential equations.

During the World War II and immediately following, a great deal of research was done on the use of numerical methods for solving problems in fluid dynamics. J. Von Neumann developed a method to evaluate stability of numerical methods for solving

time-marching problems (O'Brien et al., 1950). This method is the most widely used technique in CFD for determining stability. At the same time, progress was being made on the development of methods for both elliptic and parabolic problems. Frankel (1950) presented the first version of the Successive Over-Relaxation scheme (SOR) for solving Laplace's equation. Peaceman, Douglas, and Rachford (Douglas and Rachford, 1956) developed a new family of implicit methods for parabolic and elliptic equations. These methods are referred to as Alternating Direction Implicit (ADI) schemes and are used extensively today.

Various aspects of CFD began to be treated in the late fifties and early sixties starting with the early book of Richtmyer (1957). During the past 25 years, the progress made and the number of researchers working in CFD has expanded at an ever increasing rate. For this reason, it would be difficult to provide a short history of the significant contributions. A comprehensive review was summarized by Hall (1981), while Levine (1982) gave details of the potential of computational methods in prospective of the supercomputer generation. Even since then, there has been a virtual revolution in the range of applicability of CFD to engineering problems.

## 3.3 GOVERNING EQUATIONS

The fundamental equations of fluid dynamics are based on the universal laws of conservation of mass, momentum (Newton's second law), and, in a non-isothermal flow, energy (first law of thermodynamics). Applying these conservation laws to a fluid flow, the continuity equation, the momentum equations, and the energy equation are derived. The derivation of these equations may be found in a variety of sources, as for instance, Collins and Ciofalo (1991).

For unsteady, compressible flow, these equations are written, using an Eulerian approach and a vector notation, as follows:

(a) Continuity Equation

$$\frac{\partial \rho}{\partial t} + \nabla \cdot (\rho \mathbf{u}) = 0 \tag{3.1}$$

where $\rho$ is the fluid density, $\mathbf{u} = (u, v, w)$ is the fluid velocity vector, and t is time;

(b) Momentum Equations

$$\frac{\partial (\rho \mathbf{u})}{\partial t} + \nabla \cdot (\rho \mathbf{u} \otimes \mathbf{u}) = \mathbf{B} + \nabla \cdot \sigma \tag{3.2}$$

where $\mathbf{B}$ is the body force and $\sigma$ is the stress tensor;

(c) Energy Equation

$$\frac{\partial(\rho H)}{\partial t} + \nabla \cdot (\rho \mathbf{u} H) - \nabla \cdot (\lambda \nabla T) = \frac{\partial p}{\partial t} \tag{3.3}$$

where $H$ is the total enthalpy given in terms of static enthalpy $h$ as $H = h + \frac{1}{2}\mathbf{u}^2$; p is the pressure, T the temperature and $\lambda$ the thermal conductivity.

The main advantage of using a vector notation is that the equations apply to any coordinate system. The five equations above ( the momentum equations represent three equations in three dimensions), in seven unknowns $u$, $v$, $w$, $\rho$, $p$, $t$, $H$, are completed by the equation of state $\rho = \rho(T, p)$ and the constitutive equation $h = h(T, p)$.

Since no heat transfer is usually involved in the flows in the cardiovascular system, the energy equation can be omitted. Therefore, the transport equations in index notation using (Einstein's) summation convention that repeated indices are summed over, using a cartesian coordinate system are:

$$\frac{\partial \rho}{\partial t} + \frac{\partial(\rho u_i)}{\partial x_i} = 0 \tag{3.4}$$

$$\frac{\partial(\rho u_k)}{\partial t} + \frac{\partial(\rho u_i u_k)}{\partial x_i} = B_k + \frac{\partial \sigma_{ik}}{\partial x_i} \tag{3.5}$$

For a Newtonian fluid the stress tensor $\sigma_{ij}$ is given according to Schlichting (1968) as:

$$\sigma_{ij} = -p\delta_{ij} + \mu' S_{kk}\delta_{ij} + 2\mu S_{ij} \tag{3.6}$$

where $S_{ij}$ is the strain rate tensor defined as:

$$S_{ij} = \frac{1}{2}\left(\frac{\partial u_i}{\partial x_j} + \frac{\partial u_j}{\partial x_i}\right) \tag{3.7}$$

$\mu$ is the coefficient of dynamic viscosity of the fluid and $\mu'$ is its second coefficient of viscosity. The two coefficients of viscosity are related to the coefficient of bulk viscosity $K$ by the expression

$$K = \frac{2}{3}\mu + \mu'$$

Because the coefficient of bulk viscosity is negligible except in the study of the structure of shock waves, the second coefficient of viscosity becomes $\mu' = -\frac{2}{3}\mu$ and the tensor stress may be written as

$$\sigma_{ij} = -p\delta_{ij} + \mu[2S_{ij} - \frac{2}{3}S_{kk}\delta_{ij}] \tag{3.8}$$

Substituing eq. (3.8) into eq. (3.5) the famous Navier-Stokes equation is obtained:

$$\frac{\partial(\rho u_j)}{\partial t} + \frac{\partial(\rho u_i u_j)}{\partial x_i} = B_j - \frac{\partial p}{\partial x_j} + \frac{\partial}{\partial x_i}\{\mu[(\frac{\partial u_i}{\partial x_j} + \frac{\partial u_j}{\partial x_i}) - \frac{2}{3}\delta_{ij}\frac{\partial u_k}{\partial x_k}]\} \tag{3.9}$$

It is common practice to include the continuity equation in the Navier-Stokes equations. Body forces, consisting mainly of inertial forces due to gravitational acceleration, are considered negligible in medical applications. However, there is some evidence that the flow in coronary arteries, for example, is affected by the cyclic motion of the heart wall (Moore et al., 1992).

For a constant-density fluid (incompressible fluid) the continuity equation takes the simplified form:

$$\frac{\partial u_i}{\partial x_i} = 0 \tag{3.10}$$

and the stress tensor becomes:

$$\sigma_{ij} = -p\delta_{ij} + 2\mu S_{ij} \tag{3.11}$$

Then, the momentum equation is:

$$\frac{\partial u_i}{\partial t} + u_j \frac{\partial u_i}{\partial x_j} = -\frac{1}{\rho}\frac{\partial p}{\partial x_i} + \frac{\mu}{\rho}\frac{\partial^2 u_i}{\partial x_j \partial x_j} \tag{3.12}$$

In the general case of three-dimensional flows we have four equations (3.10 and 3.12) in four variables (velocity components and pressure), which are solvable with appropriate initial and boundary conditions.

If the fluid is non-Newtonian, its viscosity will be a function of the second invariant of the strain rate tensor, i.e.,

$$J_2 = \frac{1}{2} S_{ij} S_{ji}$$

and the stress tensor will be:

$$\sigma_{ij} = -p\delta_{ij} + 2\mu(J_2) S_{ij}.$$

In order to solve the governing equations (3.10 and 3.12), the constitutive equations for the non-Newtonian fluid must also be specified.

The above equations (3.12) can also be expressed as a scalar transport advection-diffusion equation in the independent variable $\phi = \phi(x, y, z, t)$, given in vector notation by:

$$\frac{\partial \rho\phi}{\partial t} + \nabla\cdot(\rho \mathbf{u}\phi - \Gamma\nabla\phi) = S \tag{3.13}$$

and in index notation by:

$$\frac{\partial \rho\phi}{\partial t} + \frac{\partial}{\partial x_i}(\rho u_i \phi \; - \Gamma\frac{\partial \phi}{\partial x_i}) = S \tag{3.14}$$

The four terms are the unsteady term, the convection term, the diffusion term and the source term. $\Gamma$ is the diffusion coefficient, and S is a source or sink term representing

creation or destruction of $\phi$. In addition to this equation the continuity equation has to be satisfied (it is a case of eq.(3.14) where $\phi = 1$).

## 3.4 NUMERICAL METHODS FOR THE SOLUTION OF THE NAVIER-STOKES EQUATIONS

The Navier-Stokes equations can exhibit different mathematical characteristics, depending on the nature of the particular problem. They may represent a parabolic, hyperbolic or elliptic set of equations, or they can be a mixed set of those. The unsteady incompressible Navier-Stokes equations are a mixed set of elliptical-parabolic equations where the unknowns are the velocity vector $\mathbf{u}$ and the pressure $p$.

As in the experimental fluid-dynamics, the continuous problem domain is 'discretized' so that the solution of the basic equations represent sets of data found at discrete points in the flow field. Numerical methods used to discretize the Navier-Stokes equations are referred to as 'discretization methods' and fall into three main categories: (a) Finite Difference Methods (FDMs), (b) Finite Element Methods (FEMs), and (c) Spectral Methods.

Historically, the preferred approach has been the finite difference method; however, more recently finite element methods have been used particularly in the field of the blood flow, see for example (Perktold et al. 1994; Perktold and Rappitson, 1994). The difference between the three methods results from the ways of deriving the discretization equations. The discretization of the space and of the dependent variables allow the governing equations to be replaced with simple non-linear algebraic equations, consisting of four equations, three for the velocities and one for the pressure for each control volume.

### 3.4.1 Finite Difference Methods

In the Finite Difference approach, the dependent variables are considered to exist only at discrete points of the problem domain which has been discretized by a finite-difference mesh. Several procedures are available for developing finite difference equations. Among these are: (i) the Taylor-series expansions technique, (ii) the Polynomial fitting technique, (iii) the Integral method, and (iv) the Control-volume approach.

The most commonly used procedure to solve the basic equations with the finite difference method is the *control volume approach*, or *finite volume method.* The control volume formulation can be regarded as a spectral version of the finite element method. The calculation domain is divided into a number of non-overlapping control volumes, generally hexahedral. The conservation equations are then integrated over each control

volume. Gauss's theorem is invoked, and the resulting convective and diffusive fluxes across the volume's faces are approximated by the values of the flow variables at discrete points (volume centroids) at neighbouring volumes.

In practice, this method has a history of leading quickly to expressions that prove to be more accurate than others near boundaries, probably because the method keeps the discrete nature of the solution method in view at all times. This ensures that the physical law is satisfied over a finite region rather than only at a point.

One of the most attractive feature of finite difference methods is their relatively smaller computer cost. However, they are less amenable to irregular-shaped geometries. Generalized grid techniques have been developed for the FDM, and such body-fitted curvilinear coordinate systems, have contributed to an accurate representation of complex geometries also. More details on these methods will be presented in section 3.5 of this chapter.

### 3.4.2 Finite Element Methods

In the Finite Element methods the problem domain is subdivided into a number of non overlapping subdomains, called finite elements, and the mesh can be 'arbitrarily' irregular. These elements are triangular and quadrilateral-shaped in 2-D, and tetrahedric, pentahedric and hexahedric-shaped in 3-D.

Each flow variable is approximated by a 'shape function' and the differential equations are solved for each element using the method of weighted residuals, or variational principle (Finlayson, 1972). The local equations are then collected together to form a global system of ordinary differential equations or algebraic equations, usually non linear, including a proper account of the boundary conditions. The nodal values of the dependent variables are determined from the solution of this system of equations using direct or indirect methods. Different versions of the method result from the choice of different classes of weighting functions among which is the Galerkin method (Galerkin, 1915).

Finite element methods were originally developed by engineers in the 1950s for stress and strain analysis in large structural systems for aircrafts; they are now routinely used in structural mechanics to perform analysis of complex structures. Applications to non structural problems, such as elementary flow and electromagnetism, were first reported by Zienkiewicz and Cheung (1965). Although several weighted-residuals criteria were employed in the pioneering research, the Galerkin criterion is the most representative of a direct extension from the classical variational calculus and Rayleigh-Ritz methods (Rayleigh, 1877; Ritz, 1909).

Recently FEM has received an increased attention in CFD. Whereas most finite-element methods are based on the variational principle, Baliga and Patankar (1983) have developed a method based on the control volume approach. This employs triangular grids with unequal-order interpolation, a shape function based on the local velocity vector, and

a solution scheme that is similar to SIMPLER. For a natural convection problem, a mixed solution method has been proposed by McDonough and Catton (1982), who employed the Galerkin technique in the horizontal direction and finite difference in the vertical.

FEM are computationally more expensive than standard finite difference methods despite the efforts of Gresho (1984) and others to produce new algorithms for the solution of Navier-Stokes equations for time-dependent flows and incompressible fluid. The finite volume method is a variant of the finite element method when the simplest weighting function (the Dirac delta) is used. A survey of past work and prospects for the future are reported by Hutton et al. (1987).

### 3.4.3 Spectral Methods

These methods were originally developed and used for many years by meteorologists. They have become recently the prevailing numerical technique for large-scale calculations in certain areas of computational fluid dynamics such as direct simulation of homogeneous turbulence, computation of transition in shear flows, and global weather modelling.

Spectral methods have been a standard analytical tool in the solution of linear differential equations since the last century. The eventual difficulties represented by the non-linearity of certain problems were surmounted effectively in the early 1970s. Methods prior to 1970 were termed Garlekin methods; after the 1970s the advent of computers made feasible an alternative discretization, termed the spectral collocation technique, also used in FEM. Many useful versions of spectral methods have been used since then and especially during the 1980s. The book by Canuto et al. (1987) contains a detailed description of many spectral algorithms and presents an exhaustive discussion of the theoretical aspects of these numerical methods. Also Hussaini and Zang (1987) have reviewed recent developments in this field with special attention to the fluid-dynamics applications, where spectral methods have recently been developed to the point where they can be applied to problems with complex geometries and general boundary conditions. They have shown to be more accurate compared with finite difference methods although they have difficulties in handling general boundary conditions.

Each flow variable is expanded in a truncated series of global and, usually orthogonal, polynomials, which possess attractive approximation properties for use in numerical calculations, and the coefficients of which are determined by a weighted-residual projection technique. In fact, these functions are infinitely differentiable, and converge rapidly. This convergence is referred to as infinite-order accuracy, exponential convergence, or spectral accuracy. The expansion functions have to be appropriate to the boundary conditions. For example, Fourier series would be appropriate for problems with periodic boundary conditions, while in general non periodic cases, Jacobi polynomials, normalized to [-1,1], such asChebishev or Legendre functions, are used. For time-evolution

problems, a spectral discretization of the spatial derivatives is combined with a standard finite-difference technique for the time derivatives. The Leap Frog, Adams-Bashforth, Crank-Nicolson, and Runge-Kutta schemes are those most commonly used (Canuto et al., 1987). The stability regions of these schemes depend upon the spatial operators.

The recent development of the multidomain technique has advanced this method to the stage of use for more realistic engineering problems having the benefit of the geometric flexibility of FEM and the accuracy of the spectral method. Multidomain techniques allow geometries to be treated for which a simple, global expansion is either impossible or inadvisable. The domain is partitioned into subdomains that may overlap or be patched together at interfaces. Interface conditions may be expressed as continuity conditions, may arise from a variational principle (Patera, 1984), or may be enforced by a penalty method. Patera's method is to date the most highly developed of these. An attractive approach to very large problems is to combine a less accurate but more ready preconditioning with multigrid techniques so that one combines iterations on the desired grid with much cheaper iterations on successively coarser grids.

Several computations are reported in the literature which use mixed spectral/finite difference methods, i.e. algorithms with spectral discretizations in some directions and finite differences in the others. Among these are the large eddy simulations of turbulent channel flow of Moin and Kim (1982). A recent application of this technique to biomedical flows is reported by He and Ku (1992). They have used the same method that Patera (1984) applied to time-dependent laminar flow problems. A more recent application of spectral methods to the simulation of the fluid-dynamics of an artificial heart pumping chamber has been reported by Chelser and Kamm (1994). As said in section 2.6.2.6, the spectral element solver NEKTON was used to treat the problem involving unsteady flows with moving boundaries in a 3-D geometry.

### 3.4.4 Pressure/Velocity Coupling Procedures

The process of discretization of the governing differential equations leads to a set of non-linear, coupled algebraic equations, which are solved using iterative methods. Methods for two-dimensional Navier-Stokes equations have been reviewed by Cebeci et al. (1981). One of the most popular early techniques for solving the 2-D incompressible Navier-Stokes equations is the *Vorticity-Stream Function Method* (Gosman et al., 1969). The main attraction to this approach is the fact that pressure does not appear in the formulation; however, difficulties in specifying the vorticity at boundary conditions at sharp corners may cause problems in obtaining a converged solution.

A change of variables is made replacing the velocity components with the vorticity $\zeta$ and the stream function $\psi$. Using these new dependent variables, the two momentum equations can be combined to lead to the parabolic vorticity transport equation and an elliptic PDE in the form of a Poisson equation. This allows the separation of the

mixed elliptic-parabolic PDE into one parabolic and one elliptic, that can be solved with any standard iterative method such as SOR (Successive Over-Relaxation). In order to determine the pressure an additional equation, referred to as a Poisson equation for pressure, is solved.

The extension of the vorticity-stream function approach to three-dimensional problems is complicated by the fact that a stream function does not exist for a truly three-dimensional flow. However, using a velocity-potential vector, it is possible to have a vector Poisson equation and a vector vorticity transport equation, which must be separated into three parabolic and three elliptic PDEs. As a result, it does not appear that the vorticity-stream function approach offers any advantage over the *primitive-variable approach* when solving a 3-D problem (Roache, 1972). The latter uses the incompressible Navier-Stokes equations in the primitive-variable form, and then non-dimensionalizes them.

The artificial compressibility method of Chorin (1967) is one of the early techniques proposed for solving the incompressible Navier-Stokes equations in the primitive-variable form. An artificial compressibility is introduced which vanishes when the steady-state solution is reached and makes the differential equations a mixed set of hyperbolic equations which can be solved using a standard time-dependent approach.

The most common *primitive-variable approach*, however, involves the use of a Poisson equation in place of the continuity equation in order to separate the pressure effects into a single equation. This technique was first used by Harlow and Welch (1965) in conjunction with their Marker-and-Cell (MAC) method, for solving the incompressible Navier-Stokes equations for transient flows. Approximate initial values are given to the pressure gradients to find the velocities from the momentum equation and the pressure from the Poisson equation. This procedure is repeated until the solution converges. The ADI scheme is applied to the momentum equations (Ghia et al., 1981) and a SOR method is then used to solve the Poisson pressure equation.

#### 3.4.4.1 SIMPLE Algorithms

All the above methods were slowly converging, suffered from stability problems and were very difficult to use in 3-D flows. In the early 1970s a pressure-correction technique, referred to as SIMPLE (Semi-Implicit Method for Pressure-Linked Equations) procedure was developed by Patankar and Spalding (1972). The SIMPLE procedure marked a significant improvement and is currently used, in one of its many forms, in all general purpose CFD codes.

This procedure is based on a cyclic series of guess-and-correct operations to solve the governing equations and is, with its variants SIMPLER and SIMPLEC, the most widely used in solving for the pressure field. It was first proposed for parabolic flows, and then was soon adapted to general 3-D elliptic problems. The velocity components

are first calculated from the momentum equations using a guessed pressure field. The pressure and the velocities are then corrected so as to satisfy continuity. This process continues until the solution converges.

The actual pressure $p$ at the generic iteration step is written as

$$p = p_0 + p'$$

where $p_0$ is the estimated (or intermediate) value of pressure and $p'$ is the pressure correction. Similarly in 2-D

$$u = u_0 + u' \qquad \text{and} \qquad v = v_0 + v'$$

where $u_0$ and $v_0$ are estimated values, and $u'$ and $v'$ are the velocity corrections.

Using these equations and approximate forms of the momentum equations, we obtain a pressure correction equation which is a Poisson equation in the pressure correction $p'$ and the estimated velocity vector. Once the first guess of the pressure is made and the velocities are then estimated by the momentum equations, the pressure-correction equation is solved to find $p'$, then $p$, and finally $u$, $v$ using the approximate form of the momentum equations. These new values are then used as estimated values and the process is repeated until the solution converges.

Because the pressure correction equation tends to overestimate the value of $p'$ in certain cases, the rate of convergence was found to be unsatisfactory. Under-relaxation techniques were used to improve the convergence properties. A new technique was then proposed by Patankar (1981), called SIMPLER (SIMPLE Revised), where initially the velocity field is guessed. Velocity corrections are computed in the same manner as in SIMPLE, but a complete Poisson equation is used to compute pressure. With this procedure the need of under-relaxation is greatly reduced and a converged solution is obtained with fewer iterations, although more computational effort is involved per iteration. The original implementation of this scheme required the use of staggered grids in order to prevent a numerical instability known as 'checkerboarding', which occurred on a single grid because the velocities were insensitive to small oscillations in the pressure solution, and vice versa.

The SIMPLEST method (Spalding, 1980) is based on an explicit treatment of convective terms and implicit treatment of diffusive terms in the momentum equations. The SIMPLEC method, proposed by Van Doormal and Raithby (1984), uses consistent under-relaxation for the momentum and pressure corrections. This method has been shown to allow faster convergence in pressure gradient-dominant and drag forces-dominant problems.

#### 3.4.4.2 PISO Algorithms

An alternative pressure-correction scheme was proposed by Issa (1985) as a Pressure-Implicit with Splitting of Operators (PISO) technique. In order to remove completely

the need to iterate between pressure and velocity equations, a second pressure-correction equation is solved in each iteration, much like SIMPLER yielding pressure and velocity fields that are second-order accurate in time. This allows its use as a non-iterative method (one cycle per time step), but it requires an accurate solution of the linearized equations.

Although this method appear to be preferentially indicated for problems where conservation of mass and momentum are particularly important, it does require pressure and velocity equations to be solved to tight convergence tolerances, and in practice the scheme is often implemented in an iteration loop similar to that used for SIMPLE. It was proved to be faster than SIMPLE for transient problems in which the flow field varies markedly at each step, but not for 'smooth' time-dependent flows (Ciofalo and Collins, 1988). At last, in the PISOC method similar modifications to SIMPLEC are applied to PISO.

A review of pressure-velocity coupling algorithms is given by Latimer and Polland (1985). The SIMPLE-like and PISO-like methods have all been implemented in the previous versions of CFDS-FLOW3D (single-block versions). Only SIMPLE and SIMPLEC methods are available in the more recent multi-block versions of CFDS-FLOW3D. In fact, these are the only ones that prove to be robust for more general purpose applications.

#### 3.4.4.3 Pressure/Velocity Coupling Techniques for FEMs

As in FDM, early calculations using FEM circumvented the pressure/velocity coupling problem by using the vorticity-stream function formulation. Techniques in use to date for handling the coupling between velocity and pressure are the *Penalty Method*, the *Lagrange Multiplier Method* or a combination of these, and the *PALM Method* (Smith, 1985). In other cases either the momentum and continuity equations are solved directly or a SIMPLE-like iterative procedure is devised.

The *Penalty Method*, first presented by Zienkiewicz (1977), uses a penalty parameter which, multiplied by the pressure, is introduced in the right-hand side of the continuity equation, which should be zero for the continuity condition. This parameter is very small so that the continuity equation is nearly satisfied. The pressure, given as the ratio of the divergence of the velocity vector and the vanishing penalty parameter, is substituted into the momentum equation, thereby eliminating pressure. A general discussion of the penalty method is given by Reddy (1982), while Baker (1984) has described the use of the penalty method in three-dimensional parabolic flows. In the *Lagrange Multiplier Method*, the pressure is considered as a linear function or piecewise constant over quadratic or linear velocity elements respectively (Gresho et al., 1980). That is, the approximation for pressure has to be of lower degree than that used for velocity.

Solution existence can be only guaranteed for those velocity/pressure element nodal arrangements that satisfy the Babuska-Brezzi condition (Babuska and Aziz, 1982; Brezzi, 1974). That is, on a triangular element it is required to have velocity on more than each

vertex (for example also on the medians), and pressure at more than at the centroid (for example, at three internal point centroids).

Recently Hilbert (1987) and Perktold (1989) have proposed a scheme which uses simple hexahedral elements that are linear in velocity and constant in pressure in a manner similar to the pressure correction scheme used in FDM codes. Perktold and his collaborators have successfully applied this method to a variety of blood flow problems, although the need to filter the pressure to suppress checkerboarding was reported by Perktold et al. (1991).

#### 3.4.4.4 Rhie-Chow Interpolation Method

In order to prevent a 'checkerboard' pressure field that may develop when velocity components and pressure are located at the same grid point and FDM are applied, a common approach has been the use of 'staggered grids'. In this case pressure and scalars are defined at the centroids of control volumes, while the velocities are defined at the centroids of the faces to which they are normal. However, this approach may become quite cumbersome in the presence of non-orthogonal, body-fitted grids.

The Rhie-Chow algorithm (Rhie, 1981; Rhie and Chow, 1983) allowed the required velocity components on the cell faces to be computed from the values of velocity and pressure at the cell centroids in non-staggered grids without inducing checkerboarding. It works on 3-D body-fitted grids, and allows a natural application of SIMPLE-like algorithms. The Rhie-Chow algorithm has been incorporated into CFDS-FLOW3D since its Release 2 version; and it is also implemented into most last-generation computer codes.

An improvement to this algorithm has been carried out within the latest versions of CFDS-FLOW3D to allow applications to be treated where large pressure gradients occur which balance strongly varying body forces. Details on this formulation are in the user manuals (Anonymous, 1994a; 1994b).

### 3.4.5 Advective-term Methods

In recent years, a significant amount of research effort has been directed toward discretization of the combined convection and diffusion fluxes. Inaccurate modelling of these terms can seriously degrade overall accuracy and stability of the solution. In many cases, it is almost impossible to refine the grid sufficiently so that the numerical errors will reduce to acceptable levels. Thus, it is essential to have a convection-diffusion formulation that leads to a stable and accurate solution with grids of modest fineness. Whereas many methods have been formulated, there exists no clear consensus about a preferred method. The more accurate schemes tend to be less robust and slower.

In order to help subsequent discussion, some of the more common models will be described. We shall consider a simple situation of steady one-dimensional flow where only convection and diffusion terms are present. If $\phi$ is the variable advected at a constant velocity $u$, then, integrating the relevant advection term over the control volume shown in Fig.3.1 gives

$$\int u\frac{\partial \phi}{\partial x} = u \times (\phi_e - \phi_w)$$

As values of $\phi$ are only known at the centre of each control volume, a linear profile can be taken to estimate $\phi_e$ and $\phi_w$. The result is the Central Difference Scheme (CDS):

$$\phi_e = \tfrac{1}{2}(\phi_E + \phi_P) \qquad \text{and} \qquad \phi_w = \tfrac{1}{2}(\phi_P + \phi_W)$$

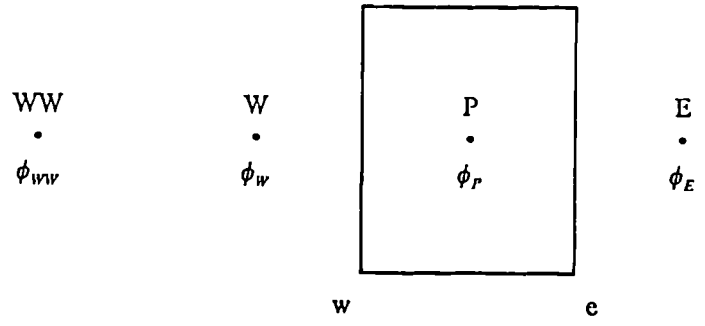


Figure 3.1 Typical control volume

The factor 1/2 arises from the assumption of the interfaces being midway. This scheme is formally second-order accurate, but can lead to spurious spatial oscillation ('wiggles') of the solution (Roache, 1972) or physically non-realistic solutions unless the cell Peclet number ( $Pe = \rho \times u\Delta x/\Gamma$, where $\Delta x$ is the cell width, and $\Gamma$ is the diffusion coefficient ) is less than 2. There has been some misunderstanding in the literature as to the nature of these oscillations; however, it is now accepted that they are related to an accuracy problem rather than to a stability problem (Vreugdenhil, 1989). It is also relevant that, when CDS is used and the cell Peclet number is high, the linearized governing equations lose diagonal dominance. This makes the CDS algorithm lose its 'robustness', and very small under-relaxation factors, or very small time steps, are needed to converge or converge easily.

An unconditionally stable but rather 'crude' approximation is to assume that the value at the face is the same as the nodal value upstream of the face. This technique is the basis of the Upwind-Difference Scheme (UDS). It was first put forward by Courant et al. (1952) and subsequently reinvented by Gentry et al. (1966). This scheme introduces a false 'numerical diffusion' and produces a result that is actually the solution to a different problem.

The exponential scheme which uses the exact solution profile would give a highly desirable behaviour, but at very high computational cost and without being able to

to be applicable to more general situations. An easy-to-compute scheme that has the qualitative behaviour of the exponential scheme is Hybrid Difference Scheme (HDS). It was developed by Spalding (1972), and applies a central-difference scheme for the Peclet-number range $-2 \leq Pe \leq 2$ and an upwind-difference outside this range by ignoring diffusion. This advection model is used as a default model in many FDM programs. It is again first-order accurate and cannot eliminate false diffusion errors, but it is slightly better than upwind differencing because second-order central differencing will be result across streams and in regions of low flow.

Since it is the grid Peclet number that decides the behaviour of the numerical schemes, it is, in principle, possible to refine the grid (i.e., to use smaller $\Delta x$) until $Pe$ is small enough ( $< 2$ ) for the central difference scheme to yield a reasonable solution. In most practical problems, however, this strategy requires excessively fine grids, which are usually not feasible on economic grounds.

A large number of differencing schemes have been proposed to prevent numerical diffusion while preserving robustness and avoiding 'wiggles'. They include the following approaches:

(a) Higher-order upwind schemes, based on the use of more than one grid point value in the finite-difference expression of the advective fluxes, such as the second-order upwind, third-order upwind (QUICK), or the related 'power-law' schemes (Patankar, 1980)(PLDS), 'Hermitian Polynomial' schemes (Glass and Rodi, 1982), and 'spline' methods (Rubin and Graves, 1975).

(b) 'Skew' schemes, such as the 'skewed upwind' (SUDS) and 'skewed upwind weighted' (SUWDS) schemes (Raithby, 1976), the 'mass flow weighted' (Hassan et al., 1983), the 'vector upstream' (Lillington, 1981), 'bounded skew upwind' (BSUDS) (Syed and Chiappetta, 1985), and 'flux bending' schemes (Gosman and Peric, 1985): they all take some account of the angle at which the fluid crosses the coordinate lines.

(c) Methods based on a locally exact solution of the governing equations, such as the 'finite analytic' method (Chen et al., 1981), and the 'locally analytic' scheme (LOADS) (Wong and Raithby, 1979). These formulations do give stable and accurate results but are rather complex and expensive for regular use.

(d) Modified-central differencing schemes, such as CONDIF (Runchal, 1987), and NONDIF (Hedberg, 1989).

Among these we give some details of advection schemes available in CFDS-FLOW3D and used, in particular, in the parametric studies carried out in the numerical simulations to be presented in the next chapters.

The Higher-order Upwinding scheme (HUW) represents a more accurate upwind scheme, which uses an additional nodal value further from the face. Assuming equal

spatial increments, $\phi_w$ is given by:

$$\phi_w = \tfrac{3}{2}\phi_W - \tfrac{1}{2}\phi_{WW}$$

A formally more accurate scheme than HUW is the quadratic upwinding scheme known as QUICK (Leonard, 1979). This is an upwinded scheme which is third-order accurate for the advection and second-order accurate for the diffusion terms. This scheme uses two upstream points and one downstream point, which makes it slightly unstable:

$$\phi_w = \tfrac{3}{8}\phi_P + \tfrac{3}{4}\phi_W - \tfrac{1}{8}\phi_{WW}$$

The higher order upwinded schemes can suffer from non-physical overshoots in their solutions. For example, turbulent kinetic energy can become negative. The CCCT scheme is a modification of the QUICK scheme which is bounded, eliminating these overshoots. The scheme has:

$$\phi_w = (\tfrac{3}{8} - \alpha)\phi_P + (\tfrac{3}{4} + 2\alpha)\phi_W - \tfrac{1}{8}\phi_{WW}$$

where $\alpha$ is a parameter that depends on the curvature of the variable $\phi$. Full details of the calculation of $\alpha$ are given by Alderton and Wilkes (1988).

CONDIF is a modification of central differencing in which the coefficients are written in such a way as to be diagonally dominant, and upwind differencing is used at any points at which the solution may have a non-physical overshoot. Again full details are given by Alderton and Wilkes (1988).

A survey of comparative studies on advection schemes is given by Patankar (1988). While some reviewers are in favour of the QUICK scheme, others report over- and undershoots, oscillations and convergence problems, and conclude in favour of HUW or even UDS. Also, higher-order schemes imply a significant increase in computational complexity. Burns and Wilkes (1987) handled this problem using the 'deferred correction approach', that is, they included the extra terms on the right hand side of the equations in the source term.

Convection-diffusion formulations in *Finite Element* methods have followed a similar pattern, and various comparable upwinding schemes have been proposed. Because of the non-linearity of the advection terms, Newton-Raphson or Picard iteration methods are commonly used. A control-volume formulation was introduced by Baliga and Patankar (1980), who used a shape function based on the direction of the local velocity vector. In the Galerkin formulation of the finite-element method, a streamline upwind procedure was employed by Brooks and Hughes (1982).

### 3.4.6 Time Stepping Procedures

In steady-state problems, the generic transport equation for the variable $\phi$ can be written as:

$$F(\phi) = S_\phi \tag{3.15}$$

In time-dependent problems this equation becomes:

$$\frac{\partial \phi}{\partial t} + F(\phi) = S_\phi \tag{3.16}$$

The time derivative of the flow variable $\phi$ can be discretized with a degree of implicitness $\chi$ $(0 < \chi \leq 1)$ as:

$$\frac{1}{\Delta t}(\phi^{n+1} - \phi^n) + \chi F(\phi^{n+1}) + (1-\chi)F(\phi^n) = S \tag{3.17}$$

which can be written in the same form as the steady-state equation (3.15):

$$F(\phi^{n+1}) = S \tag{3.18}$$

Thus the same basic algorithms can be used, though some extra storage is required for the values of the variables at step $n$. For a degree of implicitness $\chi = 1.0$ we have, for example, the fully implicit backward time differencing scheme; for $\chi = 0.5$ there is the time-centred time differencing scheme of Crank and Nicolson and for $\chi$=0.0 the scheme is fully explicit. The fully implicit and the Crank-Nicolson schemes are unconditionally stable in the mathematical sense, while the explicit method is subject to the Courant stability criterion, e.g., the Courant number $Cr \leq 1$, (where $Cr = \frac{c}{\Delta x/\Delta t}$ , with c as celerity of propagation in the analytical solution and $\Delta x$ the width of the smallest cell).

In the Finite Element Methods, Crank-Nicolson or backward Euler time stepping may be used. However, more general time-splitting techniques are becoming popular, some of which have recently been reviewed by Glowinski and Pironneau (1992).

### 3.4.7 Solution Techniques for the Linearized Equations

The discretization/linearization techniques described above lead, at the generic inner iteration (SIMPLE iteration), to very large systems of linear equations representing either the scalar transport equation or the pressure correction equation, having the general form:

$$\mathbf{Ax} = \mathbf{b} \tag{3.19}$$

In the pressure correction case, the coefficient matrix is symmetric. In all cases, if the 'deferred correction technique', described above, is used, the matrix **A** contains only seven non-zero diagonals ( in 3-D problems) and is efficiently stored as a $N \times 7$ array, N being the overall number of control volumes in the grid.

To solve such a large systems only iterative methods, such Gauss-Seidel and Successive Over-Relaxation (SOR) methods, are applicable. These consist in guessing and solving the equations repetitively until the iterative procedure converges.

Whereas the Gauss-Seidel (point-by-point, line-by-line or ADI) methods have been commonly used for the solution of linear algebraic equations, these methods converge

very slowly, especially when a large number of grid points are involved. For large three dimensional problems, it has been found that a more reliable technique is the Strongly Implicit Procedure (SIP) proposed by Stone (1968); this was also strongly indicated for problems with internal blockages (Burns et al., 1987). This technique has proved to be the best in the solution of the pressure correction equation having a high degree of accuracy. It applies a 'factorization' strategy, which consists in replacing the original sparse matrix **A** by a modified matrix **A+T**, such that it can be decomposed into upper and lower triangular matrices. The matrix **T** has to be selected so that the ADI procedure can be applied.

Recently, new techniques have been proposed, some of which are extensions of the SIP method. Lin (1985) has proposed the use of three free parameters to accelerate the convergence of Stone's method. In the methods formulated by Schneider and Zedan (1981) and Peric (1987), the five diagonal matrix in Stone's method is replaced by a nine-diagonal matrix. As a result, these modified methods (Modified Strongly-Implicit, MSI) are applicable to the discretization formulations that lead to nine-diagonal matrices; they have also been shown to be more efficient when applied to five-diagonal systems as well.

## 3.5 THE COMPUTATIONAL GRID AND GRID GENERATION TECHNIQUES

One of the main problems in computing numerical solutions of PDE is the generation of the mesh for the solution domain. The grid has to be well-constructed otherwise it may lead to an instability or lack of convergence. Numerical grid generation has now become a fairly common tool in the numerical solution of PDEs on arbitrarily shaped regions and several commercial packages are available (Thompson, 1988). A comprehensive survey of procedures and applications has been given by Thompson et al. (1982; 1984).

Body-fitted curvilinear coordinate systems - used in modern CFD codes - generated to maintain coordinate lines coincident with the boundaries were introduced to extend the capabilities of FDMs to deal with complex geometries and assist in the imposition of boundary conditions without the need of special procedures at the boundaries. Motion of the boundaries is also possible, the coordinate system adjusting to follow variations developing in the evolving physical solution. In any case, the numerically-generated grid allows all computations to be done on a fixed square grid in the computational field which is always rectangular by construction. However, the cost of the greater flexibility afforded by the use of body-fitted grids and general coordinates is an increase in complexity of the equations to be solved, due to the non-linear coordinate transformation.

The first step in the generation of the grid is the transformation of the physical space (complex-geometry domain) into a computational domain (simple-rectangular domain), where all numerical algorithms, finite difference or finite element, are implemented. Numerical grid generation techniques may be roughly classified into three categories:

(a) Complex variable methods

(b) Algebraic methods

(c) Differential Equation Techniques

*Complex Variable Methods* are restricted to two dimensional problems and so their applicability is very limited. These techniques have the advantage that the transformations used are analytic or partially analytic as opposed to the other methods that are entirely numerical. Algebraic and differential equation techniques can be used on complicated three-dimensional problems. In the next sections we present the main approaches to the generation of meshes for structured grids. Then, special techniques for gridding complex geometries will be discussed.

### 3.5.1 Algebraic Methods

Algebraic mesh generation methods determine the coordinate positions by interpolation among boundaries and/or intermediate surfaces using known functions or sets of data points. The main advantages of algebraic mappings are that they are direct and the metrics of the transformation can be analytically computed; however, since inherent smoothing properties are missing, discontinuities can arise in the mesh.

Several interpolation methods are used, and are classified as *unidirectional* and *multidirectional* methods. In the unidirectional interpolation method, the interpolation, in one curvilinear coordinate direction only, occurs between points. These points can, however, lie on boundary (or interior) curves of surfaces, and in this sense the unidirectional interpolation can be considered to be between these curves or surfaces. Several interpolation techniques are available (Lagrange, Hermite, Splines), the most general procedure being the 'multi-surface procedure' (Eiseman, 1979) of which Lagrangian or Hermitian interpolations are special cases. This procedure is constructed from an interpolation of a specified vector field, defined from piecewise-linear curves determined by the boundaries and successive intermediate control surfaces. These vectors are taken to be tangential to the coordinate lines intersecting the surfaces, so that integration of this vector field produces the position vector field for the grid points.

Multi-directional interpolation involves interpolation among functions of curves or surfaces. The most general method used is the 'transfinite', described in detail by Rizzi and Eriksson (1981). The interpolation generates the mapping by combining unidirectional interpolation with Boolean sums, and matches the function at any number of points.

### 3.5.2 Partial Differential Equation Methods

These techniques are the most highly developed for generating grids. The grids are

the solution of a set of partial differential equations, which can be *hyperbolic*, *elliptic* or *parabolic*. If the coordinate points are specified on the entire closed boundary of the physical region, the equations must be elliptic, while if the specification is on only a portion of the boundary the equations would be parabolic or hyperbolic.

The use of elliptic PDEs to generate grids has been extensively treated by Thompson et al. (1974). This procedure transforms the physical space into the computational space where the mapping is controlled by general Poisson-type systems. The generation system guarantees a one-to-one mapping for boundary-conforming curvilinear coordinate systems on general closed boundaries. The advantages of using this technique are to generate a smooth grid, complex boundaries being easily treated, without overlap of grid lines (extremum principles). However, grid point control on the interior is difficult to achieve, and if boundaries are changing in time, since the grid has to be computed for each time step, large amounts of computer time may be consumed.

The most simple elliptic partial differential system is the Laplace equation:

$$\nabla^2 \xi^i = 0 \qquad (i = 1, 2, 3) \tag{3.20}$$

where $\xi^i$ is the coordinate vector in the computational domain.

This system exhibits an extremum principle and considerable smoothness. Control of the coordinate line distribution in the field can be obtained by generalizing the elliptic generating system to the Poisson equations:

$$\nabla^2 \xi^i = P^i \qquad (i = 1, 2, 3) \tag{3.21}$$

in which the 'control functions', $P^i$, can be fashioned to control the spacing and orientation of the coordinate lines. In the absence of the control functions, the coordinate lines will tend to be generally equally spaced away from the boundaries regardless of the boundary point distribution. Variations of elliptic systems are noted in Thompson et al. (1982; 1984).

A number of different algorithms have been used for the solution of these equations, including point and line SOR, ADI (Thompson et al., 1982; Thompson, 1984). The convergence can be accelerated by using multiple grid iteration (Forsey and Billing, 1988). For general configurations, point SOR is certainly the most convenient to code and has been found to be rapid and dependable, using over-relaxation, for a wide variety of configurations. Since the system is nonlinear, convergence depends on the initial guess in iterative solutions. Algebraic grid generation procedures may be used to generate this initial guess. Transfinite interpolation generally produces a more reliable initial guess than unidirectional interpolation does because of its reduced skewness.

A fundamental development of the hyperbolic generation system was made by Starius (1977). Hyperbolic systems are applicable to domains in which the inner boundary is specified but the surrounding outer boundary is arbitrary, and is therefore of interest only for use in calculation on physically unbounded regions where the precise location of a

computational outer boundary is not important. The parabolic system can be applied to generate the grid between the two boundaries of a doubly-connected region with each of these boundaries specified. The grid control is generally weak and difficult compared with the elliptic methods. However the weakest method in the grid control is the hyperbolic grid generation method. Both parabolic and hyperbolic grid generation systems have the advance of being generally faster than elliptic generation systems, but, as just noted, are applicable only to certain configurations. Hyperbolic generation systems are faster than elliptic by one or two orders of magnitude, and can be used to generate orthogonal grids.

Orthogonality is one of the most desirable properties in grid generation techniques. Orthogonal coordinate systems produce fewer additional terms in transformed partial differential equations, and thus reduce the amount of computation required. It also makes the application of boundary conditions more straightforward, and permits a greater degree of vectorization on supercomputers. A severe departure from orthogonality will introduce truncation error in 'difference expressions'. Orthogonality in three dimensions is difficult to achieve, and only exists when the coordinates lines on the bounding surfaces follow lines of curvature, i.e., lines in the direction of maximum or minimum curvature of the surface. It is possible, however, to have the system locally orthogonal at boundaries, and/or to have orthogonality of surface coordinates. Since a part of the truncation error decreases as the grid becomes more orthogonal, it is of interest to generate grids which are 'nearly-orthogonal'. Various generation procedures of orthogonal systems are surveyed in Thompson (1980).

### 3.5.3 Adaptive Grids

Adaptive grids are generated with the objective of directing the distribution of grid points so that a functional relationship on these points may represent the physical solution with sufficient accuracy. As the physical solution develops, grid points move concentrating in regions of large gradients in the solution as they emerge. Movement of grid points is coupled to their neighbours, and cannot be too far or too fast, otherwise oscillations may occur.

Different techniques for constructing adaptive grids have been proposed. Brackill and Saltzman (1980) have developed a technique for constructing an adaptive grid using a *variational approach*. It offers a powerful method for constructing computational grids; however, a considerable effort must be expended in solving the equations which govern the grid generation. Many applications of adaptive grids require grid motion along one coordinate. The *equidistribution scheme* is a minimisation process applied in a one-dimensional form, and the grid points are distributed so that the weight function is equally distributed over the field. A number of applications of the use of one-dimensional equidistribution are cited in the survey on adaptive grids given by Thompson (1984). The *grid speed scheme*, developed by Hindman and Spencer (1983) also incorporates

the idea of equidistribution. The grid speeds are established by differentiating the steady grid equation, and solving the resulting equation. To advance the grid to the next time level the grid speeds are integrated. Several other approaches are discussed by Thompson (1984).

Once adaptivity criteria have been formulated, it is necessary to move points around the domain so that the flow solution has a minimum error. Three basic strategies may be employed to do so: (i) redistribution of a fixed number of points, (ii) local refinement of a fixed set of points, (iii) local increase in algorithm order.

Solutions to PDEs obtained using numerical methods in conjunction with adaptive grids show significant improvements in either accuracy or resolution. Oscillations associated with cell Reynolds number and with shocks in fluid mechanics computations have been shown to be eliminated with adaptive grids. The adaptive grid is most effective when it is dynamically coupled with the physical solution, so that solution and grid are solved together in a single continuous problem. The development and application of adaptive grids have been surveyed by Eiseman and Eriebacher (1987).

### 3.5.4 Moving Boundary Grids

Moving Boundary procedures have recently been developed by a number of research groups and are included in the most advanced commercially available CFD codes. Moving boundaries are a chief feature of the flow in the cardiovascular system where the blood flow is driven by the motion of the wall at each cardiac cycle throughout the arterial and venous systems (Henry and Collins, 1994b; Henry and Collins, 1995; Xu and Collins, 1995). Also in lungs air flow is generated by the motion of the alveoli (Henry et al., 1994c; 1994d).

Details of the application of the moving boundaries procedures to the Navier-Stokes equations are given by Demirdzic and Peric (1990), and Hawkins and Wilkes(1991). The validation of the moving-grid capabilities in CFDS-FLOW3D will be presented in chapter 4, together with further discussion of this issue.

### 3.5.5 Computational Grids for Complex Geometry Domains

There are three basic types of computational grid in current use:

(i) Single-block, fully structured grids,
(ii) Multi-block grids,
(iii) Unstructured grids.

Single-block, fully structured grids, discussed above, are traditionally used in FDMs. As shown in Fig.3.2, they transform the physical space into a rectangular (or hexahedronal

in 3-D) computational space. In complex geometry domains, to have accurate solutions of the flow, special techniques are required for gridding, such as multi-block and unstructured grids.

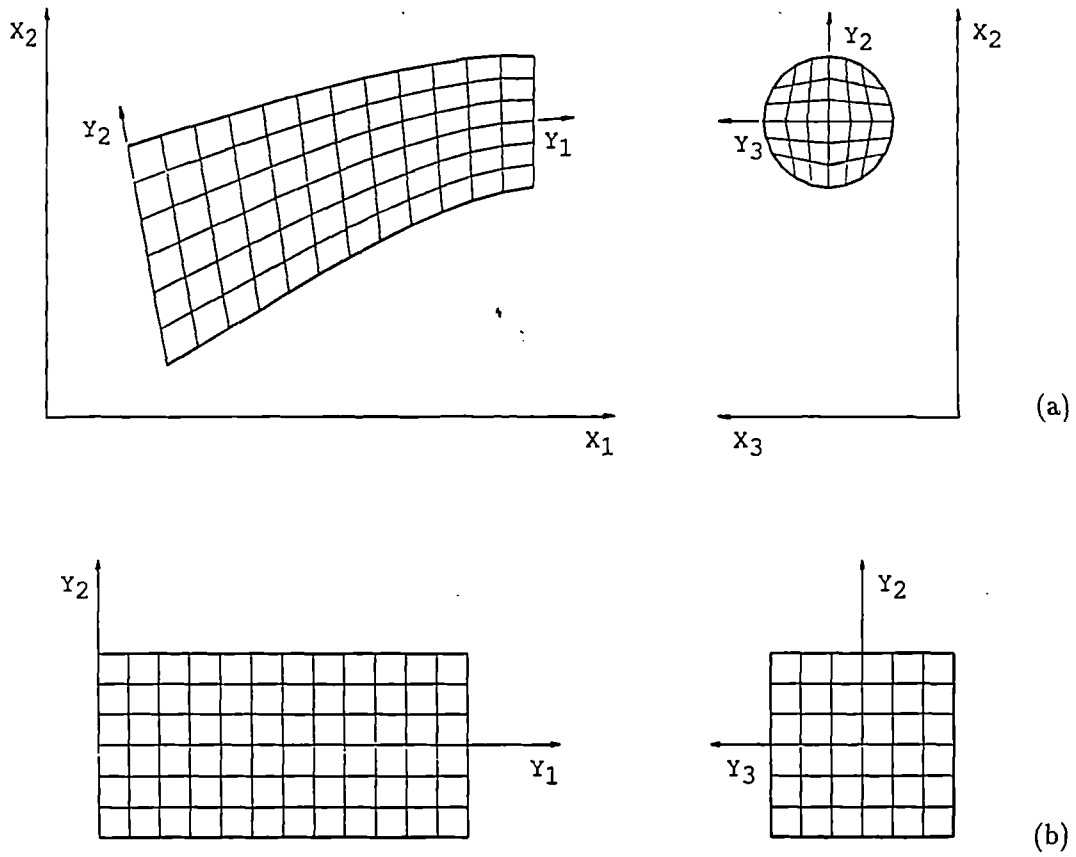


Figure 3.2 Sample of a single-block grid. (a) Physical domain. (b) Computational domain.

### 3.5.5.1 Multi-block Grids

The Multi-block approach is a very popular method of applying structured grids to complex geometrical regions. The physical domain is segmented into sub-regions, which constitute contiguous blocks. Each block has to transform into a hexahedron, so that several local curvilinear systems are constructed and connected together. However, the global distortion of the grid is relatively less accentuated. Grid points at block interfaces have to be treated so that points at the common edge of any two adjacent blocks are continuous and so that slope continuity may be enforced.

Multiblock grids are very powerful in that they allow the use of a wide range of mesh topology for a given configuration and different coordinate systems are allowed in each block. They are restricted to the grid generation technique - algebraic or partial differential equations. Although the concept of multiblock mesh is very attractive from

a mesh generation point of view, additional complexities are intoduced in the solution procedures, that involve a slow-down of the calculation time.

Examples of three-dimensional multi-block grids applied to complex geometry are given in the literature by Weatherill and Forsey (1984), and are noted in the survey given by Thompson and Warsi (1983). Multi-block grids have been implemented in the latest Releases (3.1.2, 3.2, and 3.3) of CFDS-FLOW3D which will be discussed in section 3.7.

#### 3.5.5.2 Unstructured Grids

Unstructured meshes, traditionally used in FEM, are generally composed of triangles and/or arbitrary quadrilaterals in 2-D, and tetrahedra and/or hexahedra in 3-D. Therefore, the number of cells surrounding a typical node of the mesh is not constant. Techniques for the generation of unstructured meshes are discussed in detail by Peraire et al. (1990). It was found that to have an adaptive mesh triangulation is necessary to allow easy transition between small and large elements.

The unstructured nature of the mesh requires a local coordinate system of each element. The resultant mesh, therefore, is poorly ordered and less amenable to the use of vectorization algorithms. Also larger computer time and storage are required in comparison with structured grids. However, unstructured meshes are more efficient in complex geometry domains, and offer the possibility of incorporating adaptivity. In order to minimize computer time requirements, renumbering strategies for unstructured grids have been proposed.

## 3.6 COMMERCIALLY AVAILABLE CODES

Computational Fluid Dynamics has been used for numerical prediction of fluid flows and heat transfer since the 1960s. With the development of computer hardware, computational techniques have been vigorously proposed, tested and refined to the point that these are recognized as cost-effective and convenient means of obtaining detailed data for complex physical situations. Many powerful CFD programs are available based on the three above-mentioned (3.4) numerical methods with varying degrees of modelling capabilities. Among these, commercially available codes based on (i) FDM are for example CFDS-FLOW3D, FLUENT, PHOENICS, STAR-CD, ASTEC, FIRE; while codes based on (ii) FEM are for example FIDAP, FEAT, P/FLOTRAN; an available package which uses spectral methods is NEKTON.

Grid generation and post-processing packages are often included. Pre- and post-processing packages are also available from specialized companies and referred to as visualisation software, such as CAD, PATRAN, FEMVIEW, UNIRAS, and AVS. The power

and flexibility of the CFD packages available today are such that there is now little need to develop purpose-built programs for specific problems.

Vector-processing and parallel-processing capabilities of new supercomputers have made some impact both on computer programming and on the development of numerical algorithms that have been specifically designed to achieve a high degree of vectorization and speed up computational time. A recent survey of a number of CFD codes has been presented by Wolfe (1991) and by Collins and Ciofalo (1991).

(i) Finite Difference Codes. TEACH (Gosman and Pun, 1974) can be considered the 'ancestor' of many CFD codes based on FDMs. It was developed in the early 1970s at Imperial College, and could handle problems of 2-D flows; it employed a $\kappa$-$\varepsilon$ turbulent flow model and the SIMPLE algorithm. Several last-generation codes, such as PHOENICS (Anonymous, 1990b), CFDS-FLOW3D, STAR-CD (Anonymous, 1990a) and ASTEC, can be considered as 'offsprings' of TEACH. These codes solve 3-D flows in laminar and turbulent regimes, with steady and time-dependent conditions, in complex geometries treated by body-fitted grids. PHOENICS and CFDS-FLOW3D are based on *structured* grids, while STAR-CD and ASTEC can use *unstructured* grids. Details of CFDS-FLOW3D, which was used throughout this research, are given in the next section.

(ii) Finite Element Codes. FEAT, developed at the Berkeley Nuclear Laboratories, is a 'classic' finite element code for CFD and heat transfer problems. Also FIDAP is widely used. In addition to these, most general purpose FE packages such as MSC/NASTRAN, ADINA/ANSYS, NISA-II and ABAQUS, include CFD modules although they are less advanced than specialized CFD codes. A review of FE methods for CFD problems is given by Lohner (1987).

## 3.7 CFDS-FLOW3D: CODE OVERVIEW

CFDS-FLOW3D, also known as HARWELL-FLOW3D up to a few years ago, is a general purpose thermofluid-dynamic computer code born, as other computer codes of the same family, in the early seventies and developed from the research work at Imperial College. The original version of FLOW3D was limited to simple staggered and rectilinear grid, cartesian or cylindrical coordinates, (Wilkes et al. 1985, Jones et al. 1985, 1986). HARWELL-FLOW3D was marketed with the Release 2 of the code (Burns et al., 1986, 1987). A body-fitted coordinate system was implemented in a structured non-staggered grid, and the Rhie-Chow algorithm (Rhie and Chow, 1983) was used to prevent 'chequerboarding'. The pressure/velocity coupling algorithm was a SIMPLE-family algorithm. Linear equations solvers were used (Kightley and Jones, 1985), and higher-order advection treatment schemes (including HUW and QUICK) (Thompson and Wilkes (1982)). Adaptive gridding, combustion models, coupling with radiation codes, some two-phase flow capabilities, and new advection treatment schemes were introduced, like CCCT and CONDIF, (Anonymous, 1990c).

The first predictions and code validation presented in this work were carried out using Release 2.4 of the code (Anonymous, 1991). In this version, moving grid facilities (essential in the simulation of model SMVs) were introduced (Hawkins and Wilkes, 1991). While this work was in progress, the code's capabilities were being extended. The current release of the code renamed as CFDS-FLOW3D, Release 3, has extended the geometric capabilities of the code by introducing the facility of multi-block grids. The first version of release 3, Release 3.1.2 (Anonymous, 1992), did not allow for moving gridding and was not used in this work. The following release, Release 3.2.1 (Anonymous, 1993), allowed for moving gridds, and was used largely in this work. The current release, Release 3.3 (Anonymous, 1994a), is currently used in this research work, and also by the biomechanical, mechanical and aeronautical research groups at City University. Details presented below relate to this last version.

### 3.7.1 Description of the code

The suite of CFDS programs consists of a number of modules: (i) Pre-Processing Modules, or Geometry and Grid Generators; (ii) Interactive Frontend; (iii) Frontend Module of CFDS-FLOW3D; (iv) Solution Module of CFDS-FLOW3D; (v) Post-Processing, or Graphics Modules.

The Geometry and Grid Generators may be used to define the finite difference grid. The grid coordinates are dumped to disk in a form readable by the Frontend. Through the use of a flag in the Frontend, the program is informed that the grid information is to be read in from disk. Use of these modules is optional. The grid can also be defined within the Frontend. The Geometry and Grid Generators include the interactive grid generator, SOPHIA, which may also be used to specify some of the topological features of the geometry, and the finite element to multi-block grid converter FEF3D, which are described in the ENVIRONMENT User Guide (Anonymous, 1994b). Body-fitted Grids are generated using transfinite interpolation.

The Frontend takes the input specification of the problem and converts it from a form convenient for the user into a form designed for efficient execution. Detailed error checking is performed. Facilities are available to provide a database which calculates the physical properties of some common fluids. The problem is specified in a single data file using the Command Language, that is a set of English-like commands, subcommands, and associated keywords. In the Interactive Frontend, this data file is constructed automatically via a series of displays on the screen. User-defined Fortran routines may be included for features that are too complex to be described using the Command Language.

The Solution Module solves the discretized representation of the problem. It receives the information in a form that permits maximum efficiency to be obtained on different types of computer including vector processors. The Solution Module has only a few output facilities - for, example, for printing and dumping the solution to disk files.

The Graphics Modules produce the main graphics output, interrogating the disk files written by the Solution Module. Interfaces to other post-processing packages have been constructed, and there are a number of post-processing options available for various workstations. Use of these modules is optional, and described in the ENVIRONMENT User Guide.

In the present work no use was made of the pre-processing facilities such as the interactive grid generator (SOPHIA), since this so far does not allow for transient grids automatically. In fact, it would have been necessary to construct the grid for each time step. Use of the Fortran user subroutine USRGRD was found to be more flexible to define a time dependent grid. Problem specifications were made using the Command Language File. Calculations of local velocity vectors, pressure, and shear stresses were also carried out using the user subroutine USRTRN. This routine can be used to monitor the calculation, or to produce special output for each time step. The output produced can be used by graphics packages, such as GINO-GRAF, to plot velocity patterns, or any other solution variables.

The main features of the code are summarized in Table 3.1.

Table 3.1
Main features and capabilities of CFDS-FLOW3D, Release 3

1. Physical Models and Geometry

| | |
|---|---|
| Physical Space Coordinates: | Cartesian / Cylindrical |
| Type of Flow: | Laminar / Turbulent |
| | Steady / Unsteady |
| | 2-Dimensional / Three-Dimensional |
| | Incompressible / Compressible |
| | Isothermal / Non-Isothermal |
| | Forced / Natural Convection |
| | Buoyant: Boussinesq approximation or fully compressible |
| | Multiphase flow: multi-fluid model / homogeneous model |
| Boundary Conditions: | Solid Walls |
| | Symmetry or Periodicity Surfaces |
| | Inlet / Outlet Faces |
| | Pressure Boundary |
| | Mass Flow Boundary |
| Turbulence Models: | $\kappa$-$\varepsilon$ for high Reynolds number / |
| | Low Reynolds number model |
| | Higher order turbulence models: |
| | Algebraic Reynolds Stress Model (ASM) / |
| | Differential Reynolds Stress Model (RSM) / |
| | Differential Reynolds Flux Model |
| Combustion Models: | Two gaseous models: |
| | eddy break-up model / mixed-is-burnt model |
| Particle Transport Models: | Lagrangian |
| Grid: | Rectangular / body-fitted |
| | Multi-block |

| | |
|---|---|
| | Rotating coordinate system |
| | Adaptive Grids |
| Other Options: | Solids / Thin Walls / Porous Regions |
| | Heat Conduction in Solids |
| | Radiative Heat Transfer (via RAD3D code) |
| | Chemical Kinetics for single-phase chemical reactions |
| | Additional Scalar Transport Equations for fluid mixture |

2. Numerical Methods

| | |
|---|---|
| Finite Volume Discretization: | multi-block unstructured, non-staggered grid |
| Time-Differencing: | Fully Implicit Backward Euler Differencing[a] |
| | Crank/Nicolson (central) differencing |
| Pressure/Velocity Coupling: | SIMPLE / SIMPLEC [b] |
| Advection Algorithm Schemes: | Central / Upwind / Hybrid / HUW / |
| | QUICK / CONDIF /CCCT |
| Linear Equation Solver: | Line Relaxation / |
| | Preconditioned Conjugate Gradient (ICCG) / |
| | Full field Stone's Method/ |
| | Block Stone's Method/ |
| | Algebraic Multi-Grid |

[a]This option should not be used with transient gridding
[b]PISO and PISOC are not available in Release 3 of the code

### 3.7.2 Computational Domain

The generic computational domain in 2-D is shown in Fig.3.3.

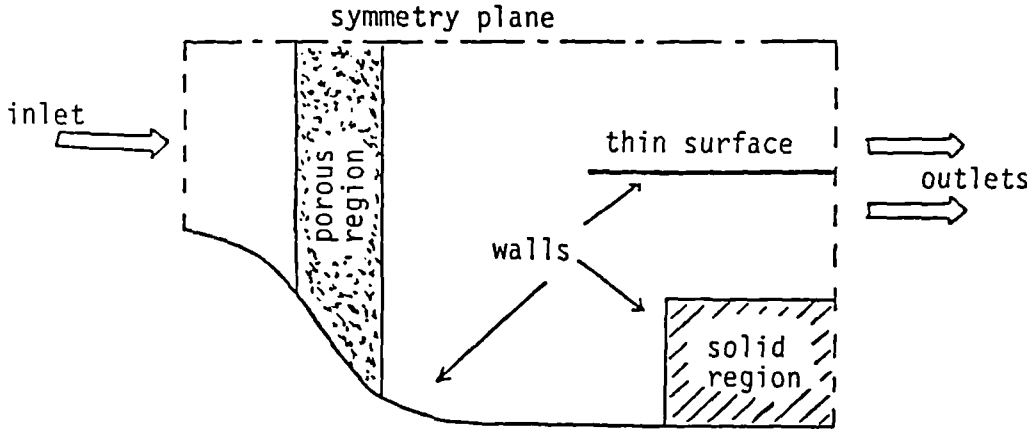


Figure 3.3 Generic CFDS-FLOW3D 2-D computational domain and structures which can be defined within it.

Multi-block grids are constructed by patching together a number of simple, rectangular grids to form a grid that is not restricted to be topologically rectangular. Topological

features within the domain of each block are described using patches (Boundary condition surfaces and interblock boundaries). The generic block grid include NI, NJ, NK volumes along the 'intrinsic' directions I, J, K, respectively. The grid is defined by specifying the coordinates of the grid vertices in physical space, arbitrarily oriented.

The generic control volume, shown in Fig.3.4, appears like a distorted 'brick'. The corners of the volume are numbered, and 'intrinsic' directions are indicated following the usual 'compass rose' convention. In order to invoke boundary conditions the control volumes lying on the perimeter of a grid block, considered outside the solution domain, are added (automatically in the multi-block version) to constitute dummy control volumes. The interior control volumes are called active control volumes. Two dimensional problems are treated as three-dimensional with two symmetry or periodicity planes. If cylindrical coordinates are used, a special treatment is implemented to deal with the singularity created by the fact that the axis is included in the computational domain.

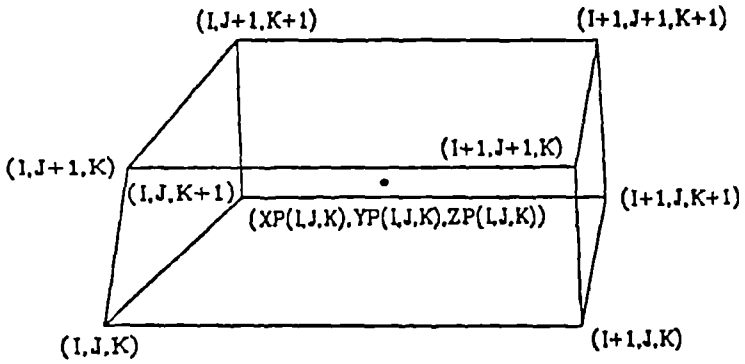


Figure 3.4 Generic control volume. Indices of corners are shown.

The Dirichlet boundary condition (flow variables) is specified at the inlets. For the outlets the Neumann boundary condition is specified by giving the normal derivatives of all flow variables. Symmetry plane boundary conditions are imposed by setting as *opposite* the values of the normal velocity components, and as *identical* the values of tangential velocity components and all scalars. Periodicity boundary conditions are allowed by imposing on each variable $\phi$ the double condition:

$$\phi_{1,j,k} = \phi_{NI-1,j,k} \qquad \text{and} \qquad \phi_{2,j,k} = \phi_{NI,j,k}$$

A summary of CFDS-FLOW3D commands and keywords are reported in the manual (Anonymous, 1994a). The schematic flow chart for the code is shown in Fig.3.5. The 'inner' iterations of the linear solvers, are nested in the loop of 'outer' iterations, which in turn are nested in the time stepping loop. The 'outer' iteration process is stopped either completely or for the current time step of a transient problem, when the chosen convergence criteria are satisfied. These criteria are for example: maximum number of outer iterations, the tolerance on a residual, the CPU limit. In the tolerance on a residual criterion, iterations are stopped when the overall residual mass source $\varepsilon_m$ (the sum of

the absolute mass source residual in all control volumes) falls below a prescribed value SORMAX.

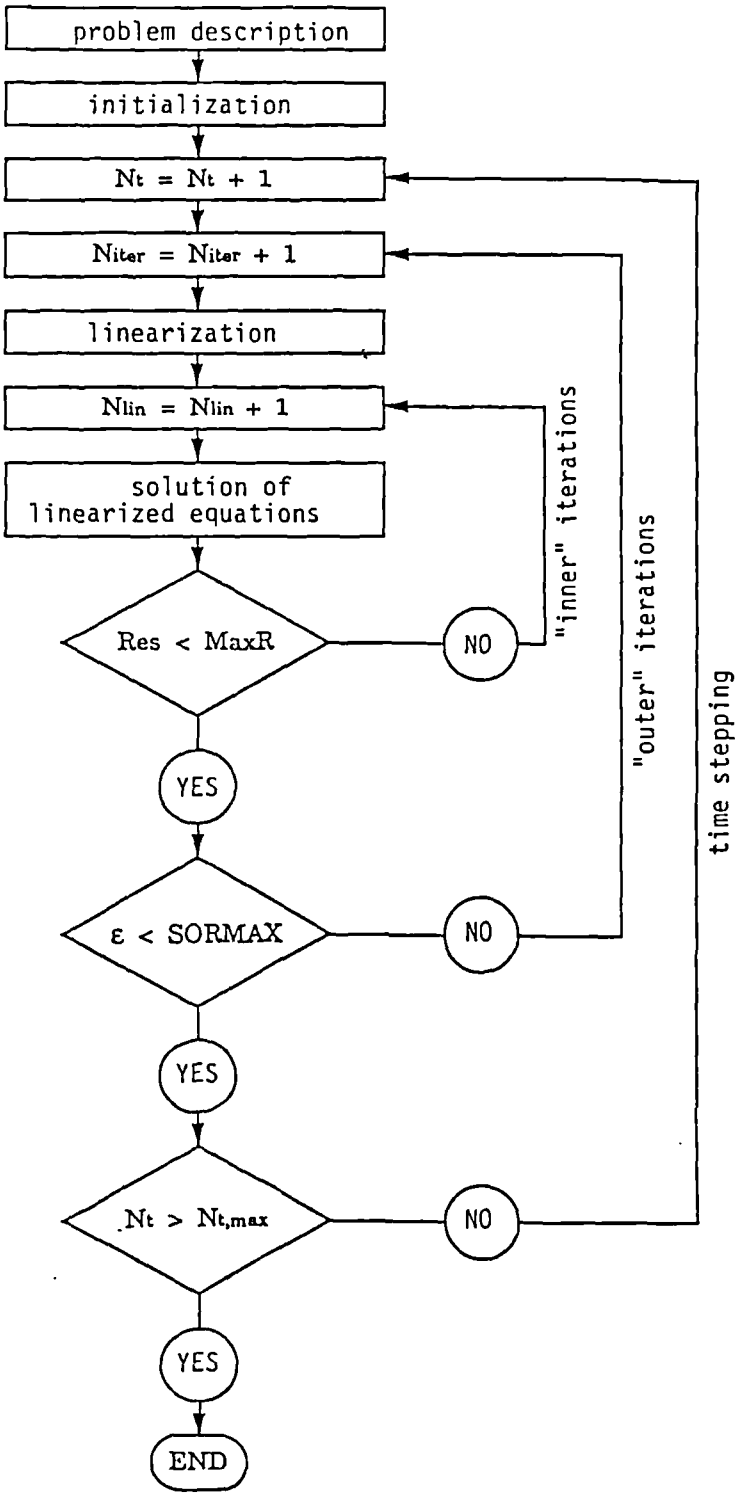


Figure 3.5 Schematic flow chart of CFDS-FLOW3D.

### 3.7.3 Applications

A survey of the applications and validation tests of CFDS-FLOW3D is given by Jones (1991). Recent applications may also be found in the Proceedings of the last two CFDS conferences (1993; 1994). They range from numerical simulations of indoor air-flows and tunnel fires to two-phase flow in a vapour generator, and a steam condensor. Extensive applications and tests on CFDS-FLOW3D have been performed at City University and at the University of Palermo since 1986 by Dr. M. Ciofalo and Prof. Collins on a wide range of problems concerning turbulent flows (Ciofalo and Collins, 1988; Ciofalo and Collins, 1989; Ciofalo and Karayiannis, 1991; Ciofalo et al., 1991; Ciofalo and Collins, 1992), and are reported in the bibliography of Ciofalo's Ph.D. thesis (Ciofalo, 1992). Other tests of the $\kappa$-$\varepsilon$ turbulence model against experimental data have been performed by Dr. Henry and Prof. Collins for the prediction of flow over rib-roughened surfaces (Henry and Collins, 1991) relevant to the Advanced Gas Cooled Reactor (AGR).

A number of numerical studies are now in progress at City University, which are supported by the predictions of CFDS-FLOW3D. Among them, in the Department of Mechanical Engineering and Aeronautics, Dr. Henry has studied a numerical model of boundary layer flows over flat plates, generated by pitched and skewed air jets (Henry and Pearcey, 1994). Since Dr. Xu started the first approach to biomechanical problems in 1988, followed by work of Dr. Henry in these topics, several biomechanical applications have been carried out. Dr. Xu has used computational fluid-dynamics codes, such as ASTEC, FLOW3D and FEAT to study predicted flows in arterial bifurcations. This has led to a considerable experience in the numerical predictions of flows in blood vessels (Xu and Collins, 1990; Collins and Xu, 1990; Xu, 1992; Xu and Collins 1994a). In parallel Dr. Henry, who has used CFDS-FLOW3D for a number of applications in engineering (as above) has achieved substantial results in modelling of several cardiovascular vessels, such as flow in graft bypasses (Henry et al., 1992a; 1994b; 1995a), in stenoses (Henry and Collins, 1993a; 1994) and air flow in lung alveoli (Henry et al., 1994c; 1994d). Also he has studied the flow inside SMVs (Henry et al., 1992b).

Nowdays, much of the interest in blood flow modelling is focused on the fluid-srtucture interactions occuring at interface between blood and vessel wall. The research at City is currently engaged in two projects aimed at developing codes capable of solving the coupled problem. The first involves solving for the wall motion in a special subroutine within CFDS-FLOW3D. In this case, the equations of motion of an incompressible solid are solved using the techniques employed by CFDS-FLOW3D to solve the Navier-Stokes equations. The second project is being carried out in conjunction with researchers at Nuclear Electric's Engineering Analysis Centre, and will be based on their FEM FEAT.

Recent validations of CFDS-FLOW3D against experiments have been published. Among these are Fletcher et al. (1993), Oakley and Bahn (1993), and Graham et al. (1992). In the next chapter, the numerical analysis conducted to validate the moving grid/boundary capability of CFDS-FLOW3D is presented.

# CHAPTER 4

# VALIDATION OF THE MOVING GRID/BOUNDARY CAPABILITY IN CFDS-FLOW3D

## 4.1 INTRODUCTION

In this chapter a validation of the moving grid/boundary capability of the code CFDS-FLOW3D is presented. Numerical predictions of the flow created by a closed-end pipe expanding or contracting radially are compared with an analytical solution. The main purpose of this numerical study has been to test whether CFDS-FLOW3D can predict accurately physiological types of flows that are driven by the movement of the walls, and that are of relevance to the SMV modelling.

As discussed in the introductory chapter, the numerical studies carried out on model SMVs have as a major objective the provision of a powerful comprehensive analysis tool for the design of model SMVs. However, before being able to use the numerical predictions in the design process, a comprehensive set of validations needs to be carried out. Most of the work presented in this thesis has been focused on the validation of the numerical predictions computed by CFDS-FLOW3D. Firstly, the validation of the predictions will be discussed for a simple problem of unsteady flow with moving boundaries against the analytical solution. Then numerical models undergoing an analytical wall motion will be presented (Chapter 5) and the flow fields compared to similar experimental models. Numerical simulations of the flow within model SMVs where experimental data have been used to drive the wall motion are discussed in Chapters 6 and 7. Finally, some numerical designs for the modelling of SMVs are presented in Chapter 8.

As discussed in chapter 2, the simplest geometry used in the ventricle modelling is a cylindrical vessel which produces flows by alternate contraction and expansion of its wall. During systole, contracting muscles in the wall of the left ventricle reduce the vessel's internal volume and force the blood through the aortic valve into the aorta. Throughout this pumping stage, the mitral valve is closed, and hence, the ventricle resembles a closed-end cylinder which is contracting radially. In diastole, the muscles relax, the aortic valve closes, the mitral valve opens, and the ventricle refills. Again, the ventricle resembles a closed-end cylinder, but now it is expanding radially.

Similar physiological flows occur in a cardiac assist device such as a skeletal muscle ventricle. As in the case of the left ventricle, the flow in an SMV is driven by the wall movement, and hence, in modelling such flows it is essential to take into account the moving boundaries. As indicated above, a possible model for an SMV, or the left ventricle, is a semi-infinite pipe with one end closed. An analytical solution for such a pipe has been given by Uchida and Aoki (1977). Their solution is based on the full Navier-Stokes equation for unsteady flow in a semi-infinite contracting or expanding pipe and

low Reynolds numbers. The closed end of the pipe is idealized as a compliant membrane which prevents axial motion of the fluid, but allows radial motion.

It is admitted that Uchida and Aoki's model is restricted to a type of wall motion that does not represent well that seen in an SMV; i.e., it is not periodic, but is either expanding or contracting, and the Reynolds numbers considered are rather low. Despite these, it does offer some definitely useful features. For instance, it is not restricted to small wall displacements, in contrast to Secomb's (1977) solution of a flow in a channel with pulsating walls. Also, being a solution of the Navier-Stokes equations, it more faithfully represents the viscous nature of blood flow than does that given by Jones (1970) for the unsteady flow of an inviscid fluid in pulsating bulbs. Finally, being an analytical solution, it can be used to validate the numerical predictions more easily than could another numerical prediction, such as the two-dimensional prediction by Tsangaris and Koufopoulos (1990) of pulsating flows induced by the wall motion of an arbitrarily shaped left ventricle.

In this chapter numerical predictions, using the code CFDS-FLOW3D, are compared with an analytical solution of a flow that has some common features to those occuring in model SMVs. The flow simulated is that studied by Uchida and Aoki (1977), and their solution is used to validate the predictions of both single-block (Release 2.4), and multi-block (Release 3.2) versions of FLOW3D. In the following, the analytical solution is first described. Brief details of the numerical solution procedure follow, and then the numerical predictions are compared with the analytical solution. The chapter concludes with an assessment of the importance of the present findings to the simulation of flow in an SMV.

## 4.2 ANALYTICAL SOLUTION

In the work presented by Uchida and Aoki (1977) an analytical solution was developed for unsteady flow produced by a single contraction or expansion of the wall of a semi-infinite pipe with a closed end (see Fig.4.1). The no-flow end condition was modelled by dividing the infinite circular pipe into two parts by an elastic membrane perpendicular to the axis of the pipe. Mathematically this was modelled as a symmetry plane at $x = 0$.

If $u$ and $v$ are the axial and radial components of the velocity respectively, the equations of continuity and motion in cylindrical coordinates for axisymmetric unsteady flow are:

$$u_x + v_r + v/r = 0 \tag{4.1}$$

$$u_t + uu_x + vu_r = -p_x/\rho + \nu(u_{xx} + u_{rr} + u_r/r) \tag{4.2}$$

$$v_t + uv_x + vv_r = -p_r/\rho + \nu(v_{xx} + v_{rr} + v_r/r - v/r^2) \tag{4.3}$$

where $p$, $\rho$ , $\nu$ are pressure, density and kinematic viscosity of the fluid respectively.

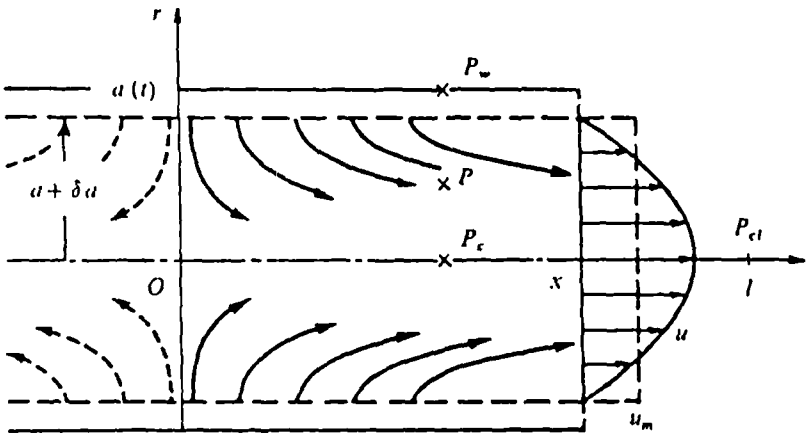


Figure 4.1 Representation of the semi-infinite pipe and flow patterns in a contracting pipe. From Uchida and Aoki (1977).

As the wall moves only in the radial direction, the radial velocity at the wall, $v_w$, is the wall velocity $da/dt = a'$. Therefore, the boundary conditions are:

$$\begin{cases} \text{x} = 0 & u = 0 \\ \text{r} = 0 & v = 0 \quad u_r = 0 \\ \text{r} = \text{a(t)} & u = 0 \quad v = v_w = a' \end{cases}$$

Eliminating the pressure from the equation of motion and introducing the Stokes stream functions defined by: $\psi_x = -vr$ and $\psi_r = ur$, the vorticity equation is

$$\zeta_t + u\zeta_x + v\zeta_r - v\zeta/r = \nu(\zeta_{xx} + \zeta_{rr} + \zeta_r/r - \zeta/r^2) \tag{4.4}$$

where $\zeta = v_x - u_r$ is the vorticity component normal to the meridian plane.

Assuming the variation of the radius to be independent of $x$ it is possible to find a similar solution, and as the problem has not been linearized, a full solution similar in both space and time can be found. Therefore, introducing the non-dimensional variable $\eta = r/a$, the stream function can be written

$$\psi = \nu x F(\eta, t) \tag{4.5}$$

and then the axial and radial velocities are respectively:

$$u = (\nu x/a^2)(F_\eta/\eta); \qquad v = -(\nu/a)F/\eta \tag{4.6}$$

As $v$ is independent of $x$, $\zeta = -u_r$, and using the continuity equation, the vorticity equation becomes:

$$[\nu(u_{xx} + u_{rr} + u_r/r) - (u_t + uu_x + vu_r)]_r = 0 \tag{4.7}$$

Uchida and Aoki showed that a full solution similar in both space and time can be

obtained by assuming $F_{\eta t} = 0$ and $\alpha = constant$. The value of $\alpha$ is set to its initial value

$$\alpha = a'a/\nu = a'_0 a_0/\nu$$

The parameter $|\alpha|$ represents the Reynolds number and its sign indicates whether the pipe is contracting or expanding; e.g., it is negative when the pipe is contracting.

Integrating $\alpha = a'a/\nu = a'_0 a_0/\nu$ the temporal function of the radius of the pipe is obtained as

$$a/a_0 = \sqrt{1 + 2\alpha(\nu t/a_0^2)} \tag{4.8}$$

Substituting eq.(4.6) in eq.(4.7) we have the differential equation for $F(\eta)$

$$[G(\eta)]' = 0$$

and integrating

$$G(\eta) = (F'/\eta)'' + (1/\eta + F/\eta + \alpha\eta)(F'/\eta)' - (F'/\eta - 2\alpha)F'/\eta = K \tag{4.9}$$

The transformed boundary conditions for the new variable $\eta$ are:

$$\begin{cases} \eta = 0 & F/\eta = 0 \quad (F_\eta/\eta)_\eta = 0 \\ \eta = 1 & F/\eta = -\alpha \quad F_\eta/\eta = 0 \end{cases}$$

Integrating numerically equation (4.9), we can obtain $F(\eta)$. Since there is a singularity at the origin, $F(\eta)$ is expanded in a power series in the region $0 < \eta < 0.01$ as:

$$F(\eta) = b_0 + b_2\eta^2 + b_4\eta^4 + b_6\eta^6 + b_8\eta^8 \ldots \tag{4.10}$$

where

$$b_4 = \frac{1}{16}[K + 4(b_2 - \alpha)b_2]; \quad b_6 = \frac{1}{12}(b_2 - 2\alpha)b_4; \quad b_8 = -\frac{1}{72}(9\alpha b_6 - 2b_4^2);$$

$$b_{2n+4} = -[[(2n-4)b_2 + (2n+2)\alpha](2n+2)b_{2n+2} + B_n]/[(2n+2)^2(2n+4];$$

and

$$B_n = \sum_{m=1}^{n-1} (2n - 2 - 4m)(2n + 2 - 2m)b_{2m+2}b_{2n+2-2m} \qquad n \geq 2$$

The coefficients $b_2$ [$b_2 = (F'/\eta)/2$] and K are determined to satisfy the boundary conditions. Uchida and Aoki gave values of $b_2$ and K for certain values of $\alpha$ and these are reproduced in Table 4.1.

Table 4.1

Numerical values of the constant K and of the functions at the boundary.
From Uchida and Aoki (1977).

| $\alpha$ | $K$ | $(F'/\eta)_{\eta=0}$ | $(F'')_{\eta=1}$ |
|---|---|---|---|
| -10.0 | -1267 | 26.90 | -175.36 |
| -5.0 | -369.7 | 14.6 | -69.23 |
| -1.0 | -29.93 | 3.620 | -9.788 |
| -0.1 | -1.744 | 0.3944 | -0.8192 |
| 0.0 | 0.0 | 0.0 | 0.0 |
| 0.1 | 1.451 | -0.4055 | 0.7792 |
| 1.0 | -1.107 | -4.839 | 5.291 |
| 1.2 | -7.281 | -6.289 | 5.335 |
| 1.4 | -17.13 | -8.072 | 4.528 |
| 1.6 | -35.73 | -10.84 | 1.697 |
| 1.67 | -54.75 | -13.33 | -2.156 |

To calculate $F(\eta)$ the Runge-Kutta method was applied to the system of first-order differential equations obtained from equation (4.9); i.e.,

$$\begin{cases} F' = A \\ A' = B \\ B' = \eta k + \frac{2}{\eta}\left(B - \frac{A}{\eta}\right) - \left(\frac{1}{\eta} + \frac{F}{\eta} + \alpha\eta\right)\left(B - \frac{A}{\eta}\right) + \left(\frac{A}{\eta} - 2\alpha\right)A \end{cases}$$

The boundary conditions at $\eta = 0.01$ are derived from equation (4.10). From the calculated $F(\eta)$ it is possible to find:

$$\frac{u}{u_m} = -\frac{F'/\eta}{2\alpha} \tag{4.11}$$

$$\frac{v}{v_w} = -\frac{F/\eta}{\alpha} \tag{4.12}$$

where $u_m$ is the mean velocity.

Typical flow patterns from Uchida and Aoki for contracting and expanding pipes are shown in Fig.4.2. Axial and radial velocity distributions given by (4.11) and (4.12) are shown in Fig.4.3. For a very low Reynolds number, the axial velocity distribution is parabolic for both expansion and contraction. For a contracting pipe the effects of viscosity are limited to a thin boundary layer attached to the wall, which becomes thinner for higher values of the Reynolds number. For an expanding pipe and high Reynolds number, the axial velocity distribution contains higher harmonics, the flow adjacent to the wall is retarded, and reverse flow occurs in the wall region for Reynolds number above

a critical value of $\alpha = 1.644$. The magnitude of the radial velocity increases from the centre of the pipe to a peak value at about $\eta = 0.5$, which is always larger than its value at the wall. It then decreases monotonically to the wall value. In the case of the expanding pipe, where reverse flow occurs, the maximum value of $v/v_w$ is approximately 40% larger than at the wall.

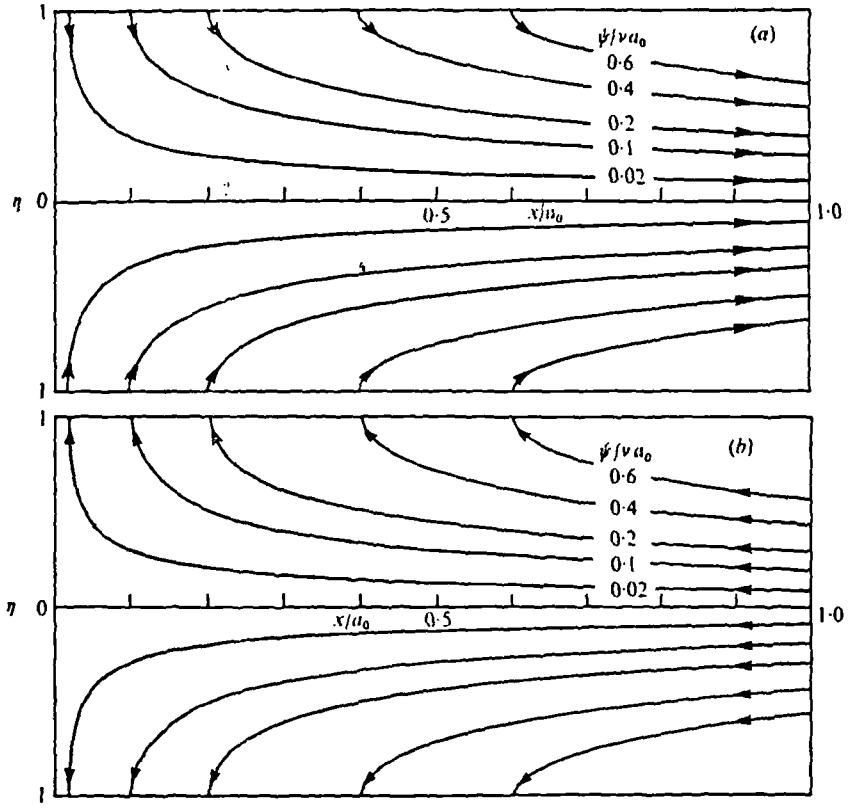


Figure 4.2 Streamlines. (a) Contracting pipe ($\alpha = -1$). (b) Expanding pipe ($\alpha = 1$). From Uchida and Aoki (1977).

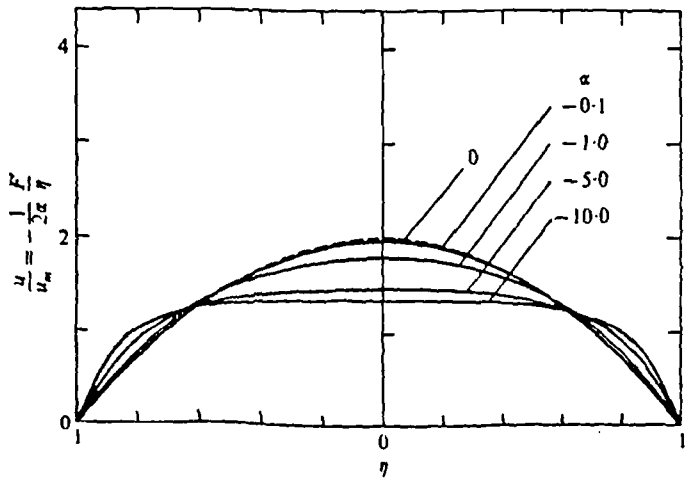


(a)

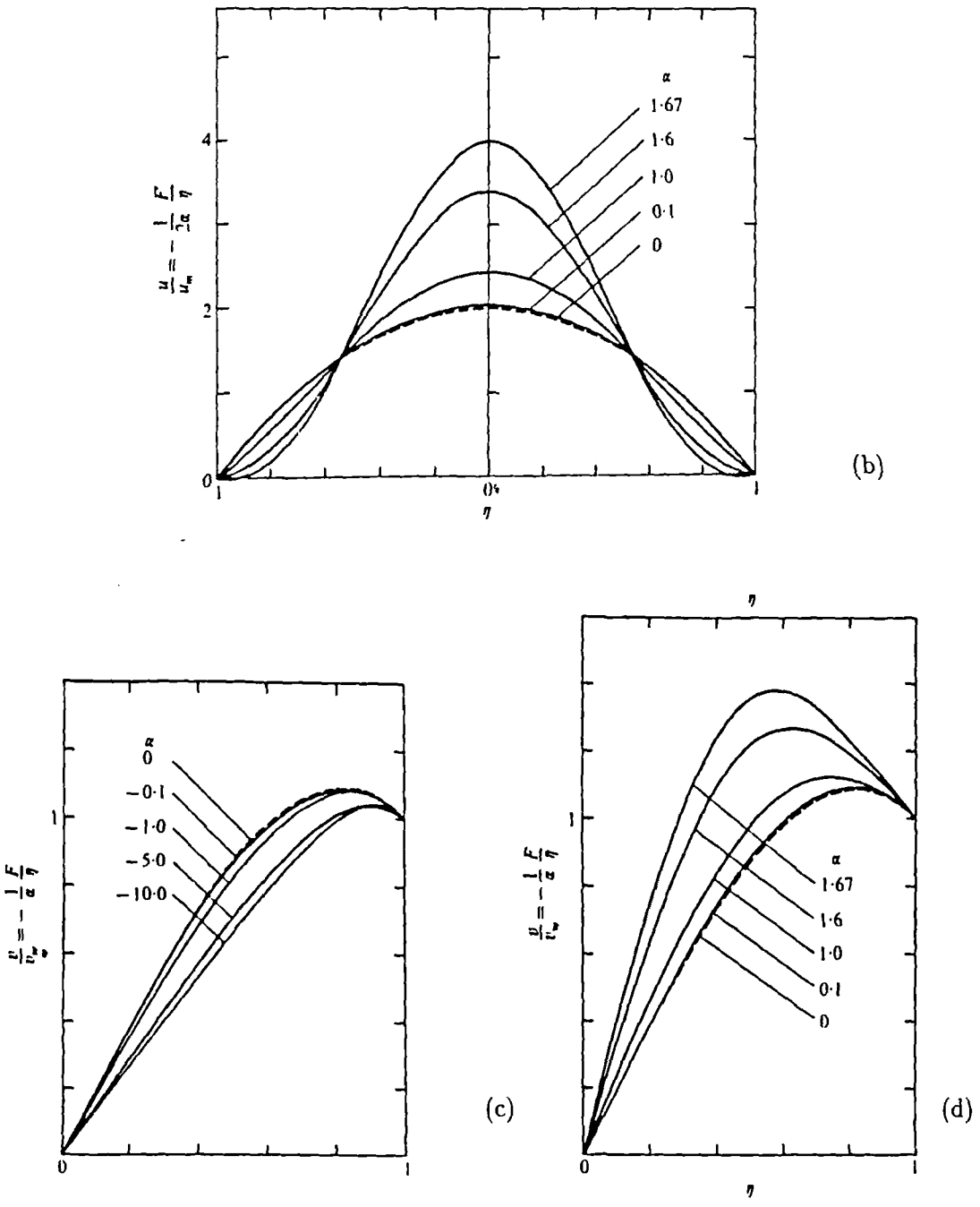


Figure 4.3 Distributions of axial velocity ((a) and (b)), and radial velocity ((c) and (d)). (a) and (c) Contracting pipes. (b) and (d) expanding pipes. From Uchida and Aoki (1977).

## 4.3 TREATMENT OF THE MOVING WALL IN CFDS-FLOW3D

The governing equations for the fluid are the equations for the conservation of momentum and mass. For unsteady, laminar, axisymmetric flow these are given by equations (4.1), (4.2) and (4.3).

The solution algorithm for the calculation of unsteady flows with moving boundaries

has been provided by Demirdzic and Peric (1990) and is concisely summarized as follows:

1. Provide the initial grid and the solution for the initial time $t_0$.

2. Determine the location of the boundary grid points for the time $t_0 + \delta t$ and move the new grid to fit the new boundaries at the new prescribed position.

3. Calculate iteratively the new solution employing the currently available pressure and mass fluxes until the sum of the absolute residuals in the momentum and continuity equations are satisfactory reduced.

4. Advance the time by another increment $\delta t$ and return to step 2.

In order to allow the boundaries and the grid to move in the prescribed manner, the momentum and mass equations have been modified. If the physical grid is moving the time derivatives have to be modified so that in computational space the grid is fixed. This has the effect that the convective term

$$\frac{\partial \phi}{\partial t} + \frac{\partial (\phi u_j)}{\partial x_j}$$

becomes, following Thompson et al. (1985),

$$\frac{1}{\sqrt{g}} \frac{\partial (\sqrt{g}\phi)}{\partial t} + \frac{\partial}{\partial x_j} \phi \left( u_j - \frac{\partial x_j}{\partial t} \right)$$

where $g$ is the determinant of the metric tensor which represents the square of the volume in physical space and corresponds to unit volume in computational space. In addition, an equation for the conservation of space

$$\frac{1}{\sqrt{g}} \frac{\partial \sqrt{g}}{\partial t} - \frac{\partial}{\partial x_j} \left( \frac{\partial x_j}{\partial t} \right) = 0$$

has to be solved simultaneously with mass, momentum and energy equations, as it is pointed out by Demirdzic and Peric (1988).

Full details are given in Hawkins and Wilkes (1991), while the user interface is given in FLOW3D Release 2.4 and Release 3.2 user manuals (Anonymous, 1991b; 1993)

## 4.4 NUMERICAL MODEL

Validation exercises have been carried out for both single-block (Release 2.4) and multi-block versions (Release 3.2). The semi-infinite pipe of the analytical solution has been simulated as a pipe with a symmetry plane at the closed-end and a pressure

boundary condition ( $p = 0$ ) at the inlet/outlet. The pipe diameter is $10.0 \times 10^{-3} m$ and has a length of 15 diameters. The wall moves in a manner defined by equation (4.8). The kinematic viscosity $\nu$ has been taken as $4 \times 10^3\ m^2/s$ ( the viscosity of the liquid used in the *in vitro* work).

Because of the simplicity of the solution domain, a grid comprising only a single axisymmetric block was in fact used in the multi-block calculations, which meant that the grids used in the two versions were identical. Also, polar coordinates were used in physical space in both versions. The grid, as shown in Fig. 4.4, expands in $r$ from the wall and in $x$ from the symmetry plane. The cyclic contraction and expansion occuring in cardiovascular pumps and in particular in the model SMVs used in the *in vitro* experimental study and in the corresponding numerical analysis, have, for obvious reasons, a period about 1.0 $s$. A value of 1.0 $s$ for the time of simulation has been used as the reference value. This has been chosen mainly to see whether a similar solution could be achieved over the time scale of the cardiac cycle period.

The choice of the simulation parameters set for the reference case, see Table 4.2, has been reached after a suitable parametric study on the geometric features (length and initial diameter of the pipe), number of cells in the radial and axial directions, time stepping and number of iterations. For this set, the predictions have shown good convergence.

In this study two speeds of expansion and one of contraction have been modelled:

1. A slow expansion with $\alpha = 0.1$
2. A relatively fast contraction with $\alpha = -10$
3. A faster expansion with $\alpha = 1.67$

An initial study has been performed with the single-block version and subsequently the same study has been carried on for the multi-block version. Thus three comparisons have been possible: the predictions with the analytical solutions for both versions, and between the predictions from different versions.

Table 4.2

Simulation parameters

| | |
|---|---|
| Number of cells in radial direction | $NJ = 20$ |
| Number of cells in axial direction | $NI = 50$ |
| Total number of cells | $NC = 1000$ |
| Time step | $DT = 10\ ms$ |
| Number of iterations per time step | $IT = 20$ |

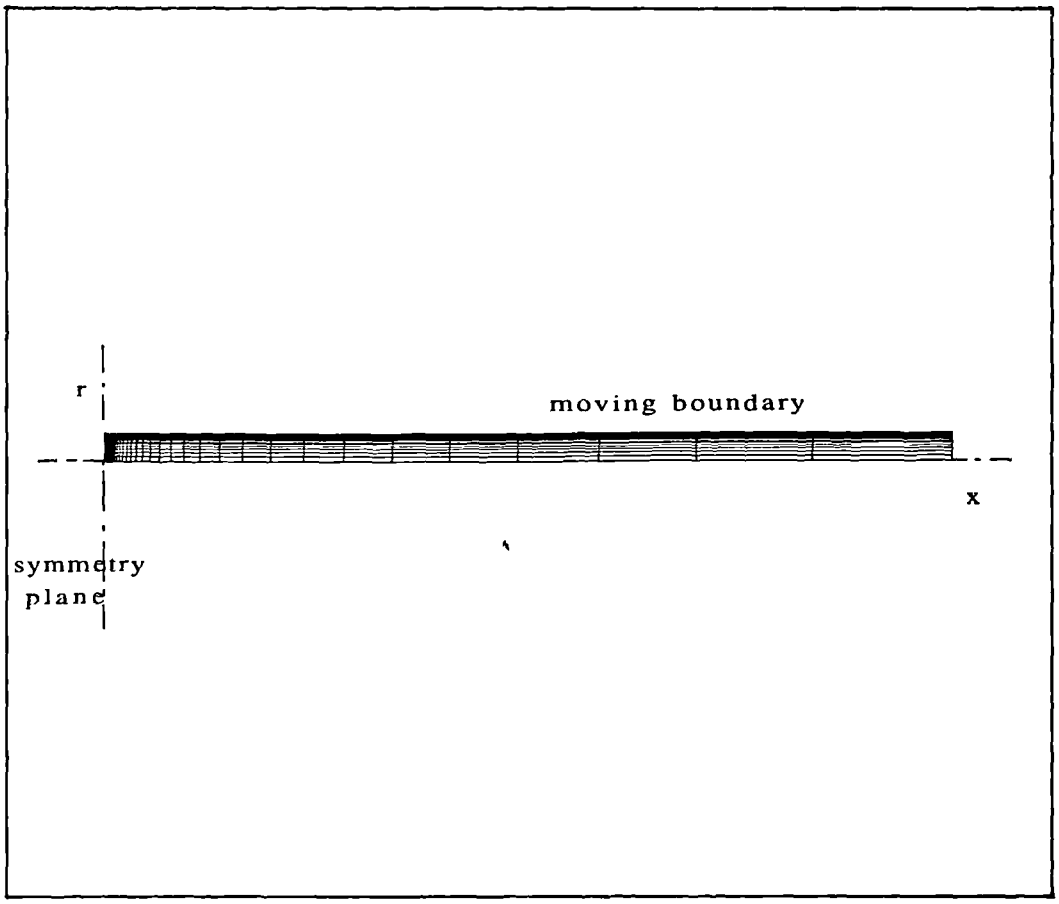


Figure 4.4 Grid used to model the semi-infinite pipe.

## 4.5 COMPARISON BETWEEN NUMERICAL AND ANALYTICAL SOLUTION

### 4.5.1 Single-block Version (Release 2.4)

1. Expansion with Reynolds number, $Re = 0.1$

For this case, the set of parameters given in Table 4.2 has been used. Very good agreement between the predicted and analytical results has been achieved, as can be seen in Fig.4.5. It can be seen that for low Reynolds number the axial velocity distribution is parabolic, while the radial distribution increases from the wall and falls to zero at the centre of the pipe. The predicted results have been plotted for an axial position of $x/d = 0.9$. This has been found to be sufficiently far from the outlet to ensure the numerical solution to be similar. It is noted that the constant pressure boundary condition used is not consistent with the analytical solution. Hence, the predictions close to this boundary can be expected to be in error. As an alternative, a fully-developed flow boundary condition has been tried at the outlet of the pipe without any reasonable results. However, this was not unexpected as the flow cannot be fully developed, in the usual sense, when the pipe wall is moving.

2. Contraction with $Re = 10$

Again the parameters given in Table 4.2 have been used for the contraction case with an initial diameter equal to $30.0 \times 10^{-3}m$. Also for this case the agreement is very satisfactory as shown in Fig.4.6. The distribution of the axial velocity is monotonic and the effect of viscosity is limited to a thin layer attached to the wall.

3. Expansion with $Re = 1.67$

This expansion represents an interesting case as reverse flow is seen in the analytical solution, and it proved a more difficult flow to simulate. Use of the parameter set in Table 4.2 has not produced the expected characteristics of the flow; comparisons between predictions and analytical solutions for this set are shown in Fig.4.7. The axial velocity distribution is underpredicted near the centreline and overpredicted approaching the wall. This would appear to indicate that the time required to establish similar velocity profiles is larger than the simulation time used in the standard parameter set. The radial velocity distribution is underpredicted in most of the central region although the values at the centre and at the wall are predicted correctly.

It has been found possible to achieve improvement by increasing the time of simulation and decreasing the time step. Comparisons between numerical and analytical results are given in Fig.4.8 for this study from which it may verified that the best agreement is reached for a time of simulation of 3.0 s and a time step $DT = 5ms$ (Fig.4.8(d)). In this case reverse flow has been predicted. The main factor influencing the numerical solution appears to be the time of simulation.

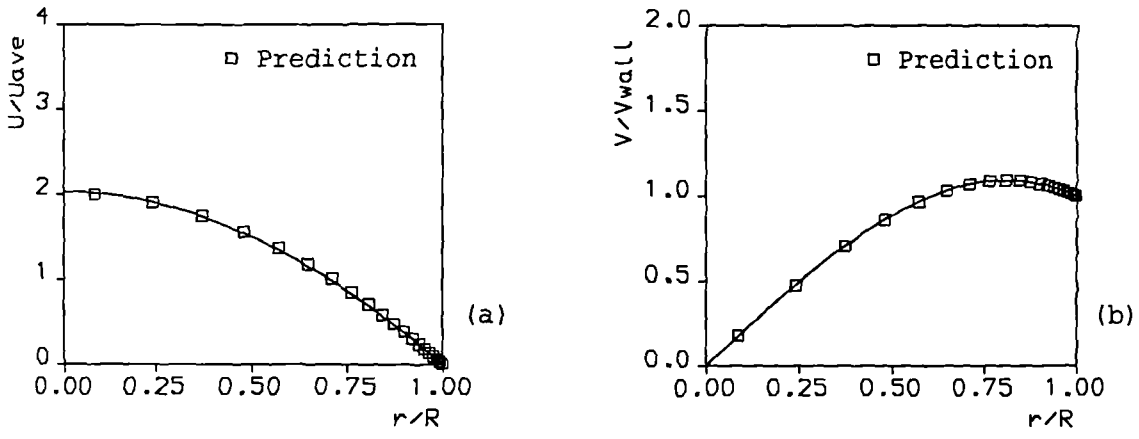


Figure 4.5 Comparisons of the distributions of (a) axial and (b) radial velocities. Expansion at $Re = 0.1$. Single-block version.

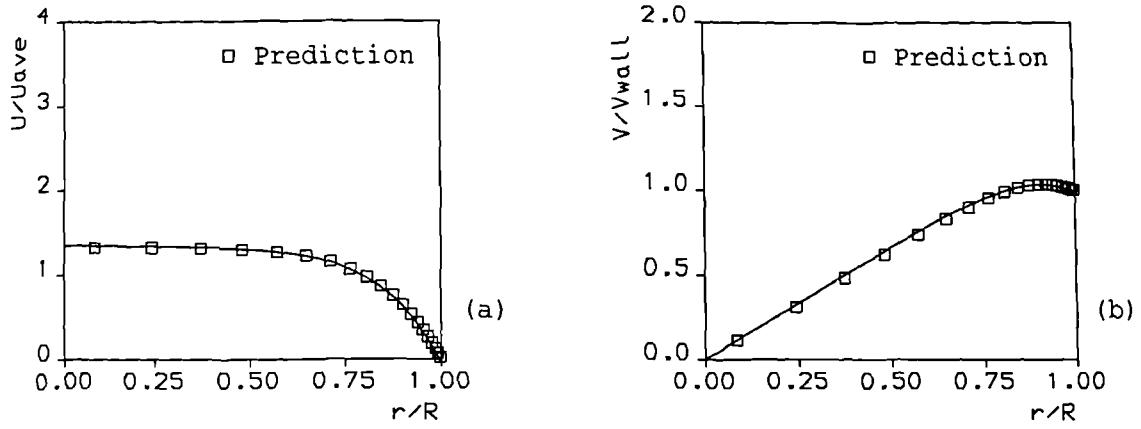


Figure 4.6 Comparisons of the distributions of(a) axial and (b) radial velocities. Contraction at $Re = 10$. Single-block version.

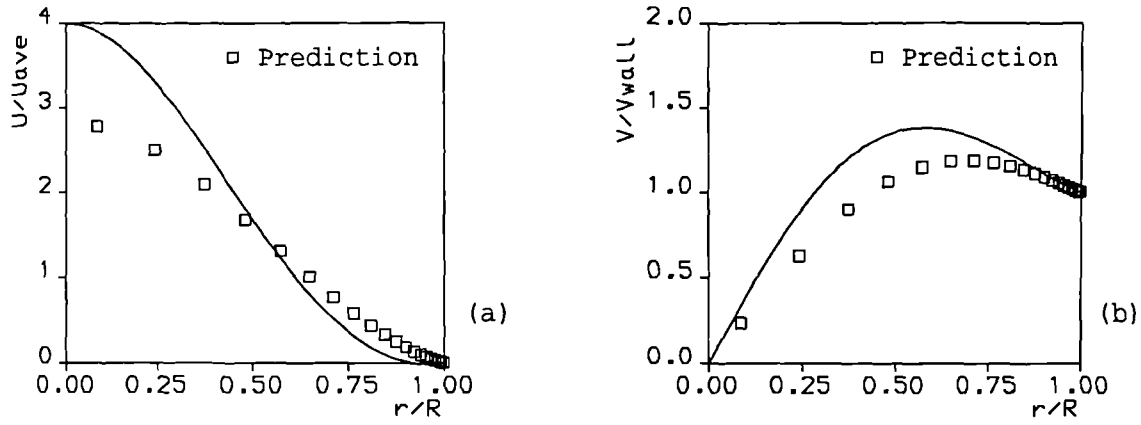


Figure 4.7 Comparisons of the distributions of (a) axial and (b) radial velocities. Expansion at $Re = 1.67$. Single-block version.

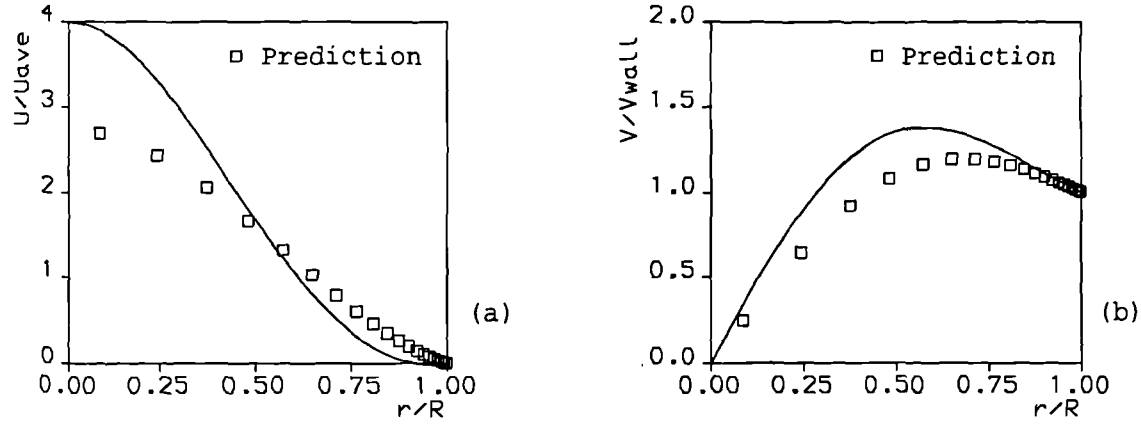


Figure 4.8(a) Comparisons of the distributions of (a) axial and (b) radial velocities. Expansion at $Re = 1.67$. DT = 5 ms. Single-block version.

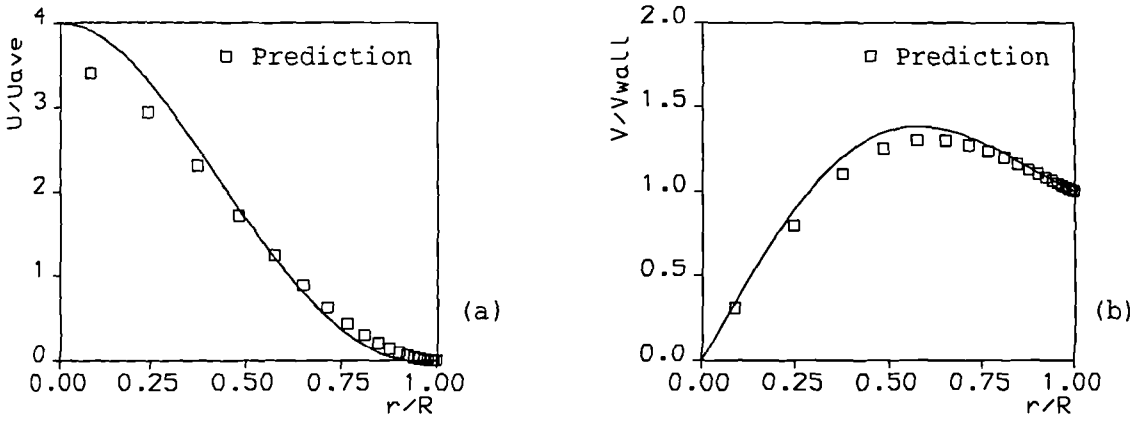


Figure 4.8(b) Comparisons of the distributions of (a) axial and (b) radial velocities. Expansion at $Re = 1.67$. Simulation time 2 s. Single-block version.

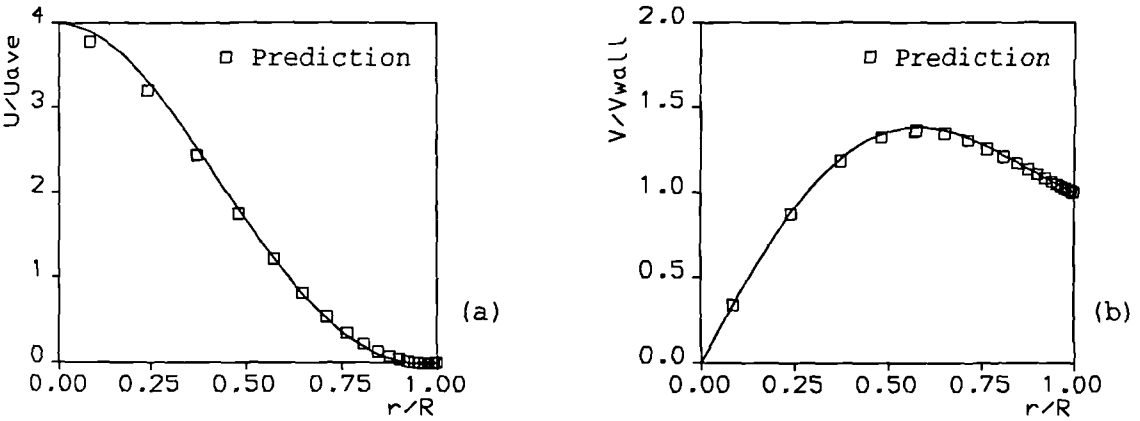


Figure 4.8(c) Comparisons of the distributions of (a) axial and (b) radial velocities. Expansion at $Re = 1.67$. Simulation time 3 s. Single-block version.

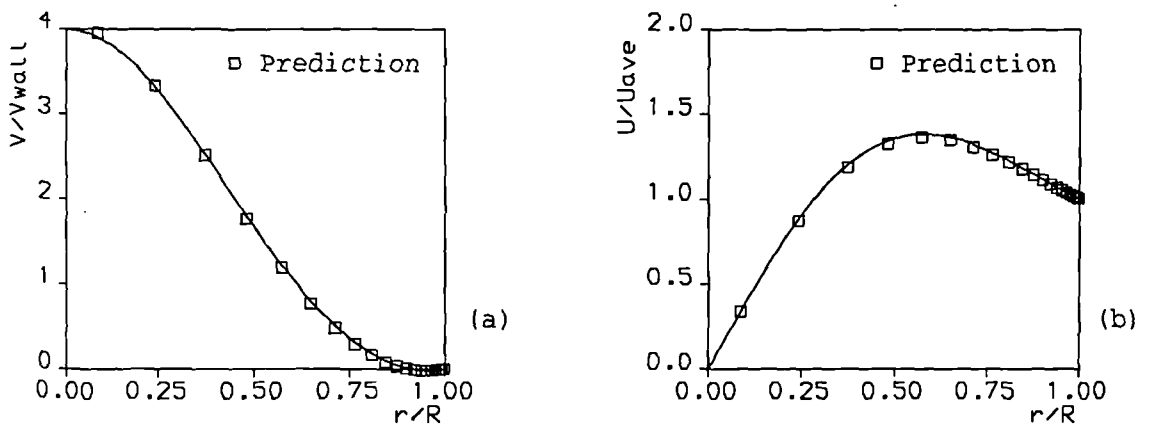


Figure 4.8(d) Comparisons of the distributions of (a) axial and (b) radial velocities. Expansion at $Re = 1.67$. Simulation time 3 s. DT= 5 ms. Single-block version.

### 4.5.2 Multi-block Version (Release 3.2)

The same set of calculations as described above has been performed for the multi-block version of the code. The grid is composed of one axisymmetric block and polar coordinates are used in physical space. The set of parameters used for the reference case is the same as that used for the single-block version.

Comparison between predictions and analytical solution are given in Figs.4.9(a) and (b) for $\alpha = 0.1$ and $\alpha = -10$, respectively. As can be seen, the results show good agreement for both expansion and contraction. The graphs in Fig.4.10 show the axial and radial velocity distribution for $Re = 1.67$ when the parameter set of the reference case is used. In this case, the same disagreement can be seen as has been found in the single-block version for a time of simulation 1.0 s.

It is shown in Figs.4.11 and 4.12 that using a larger time of simulation has produced predictions that approached the analytical solution in a manner similar to that found with the single-block version. Also, the effect of time stepping is comparable with the effect seen in the single-block version. The graphs in Fig.4.13 show the best agreement reached with a time of simulation of 3.0 s and $DT = 5ms$.

The above indicates that, for the problem studied, the multi- and single-block moving grid facilities produce comparable results and that each is able to match well the analytical solution.

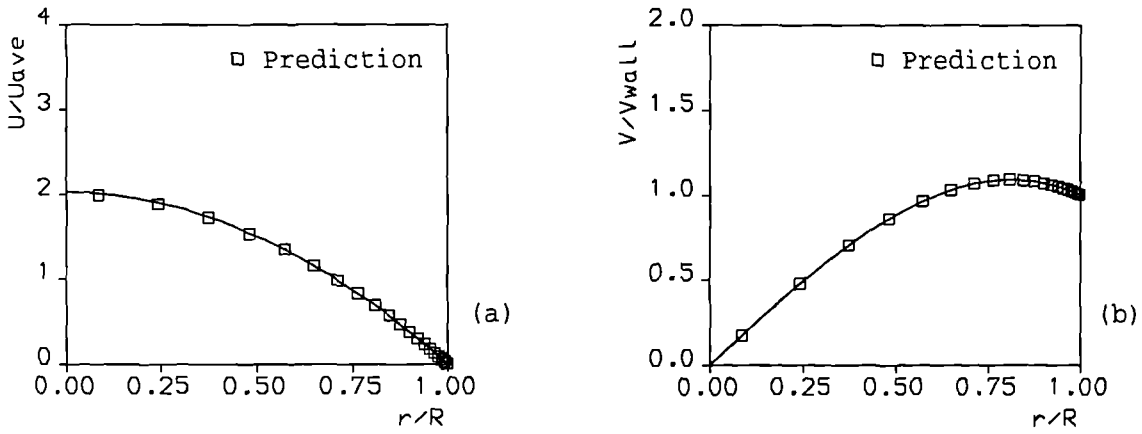


Figure 4.9(a) Comparisons of the distributions of (a) axial and (b) radial velocities. Expansion at $Re = 0.1$. Multi-block version.

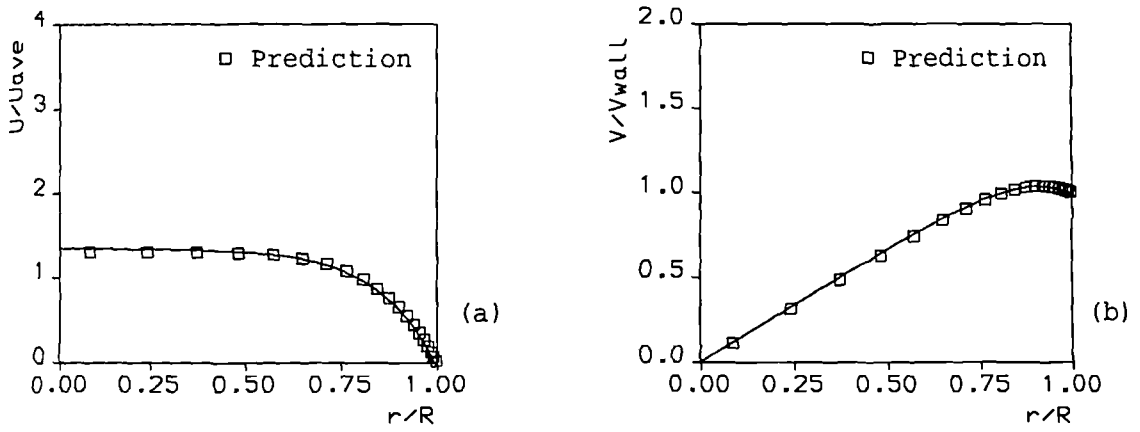


Figure 4.9(b) Comparisons of the distributions of (a) axial and (b) radial velocities. Contraction at $Re = 10$. Multi-block version.

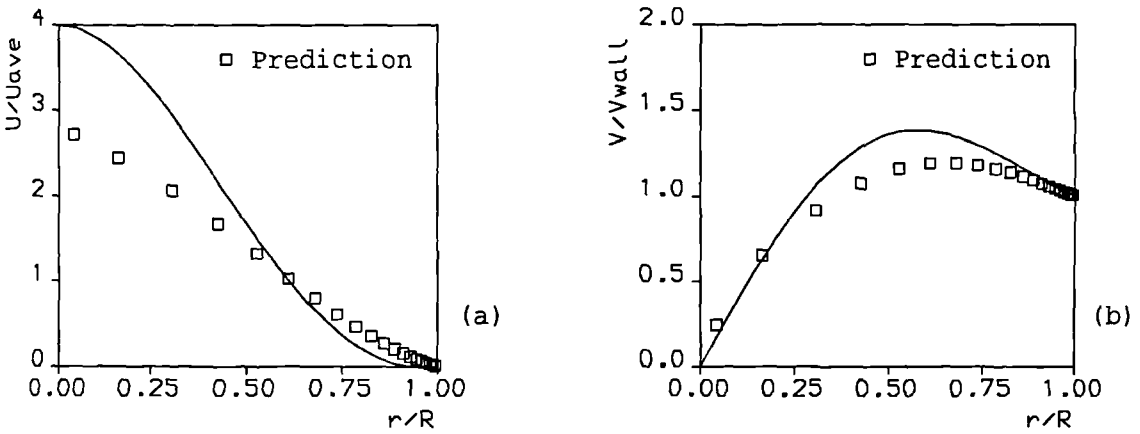


Figure 4.10 Comparisons of the distributions of (a) axial and (b) radial velocities. Expansion at $Re = 1.67$. Multi-block version.

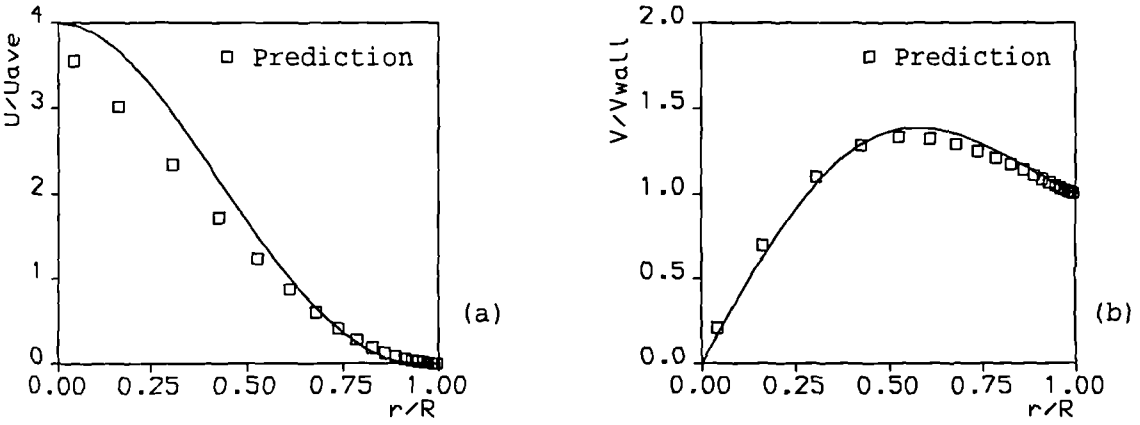


Figure 4.11 Comparisons of the distributions of (a) axial and (b) radial velocities. Expansion at $Re = 1.67$. Simulation time 2 s. Multi-block version.

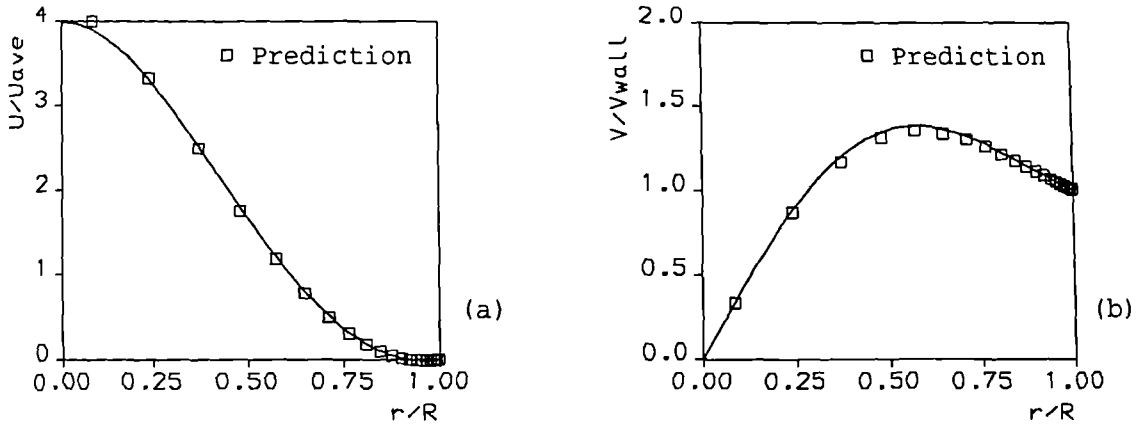


Figure 4.12 Comparisons of the distributions of (a) axial and (b) radial velocities. Expansion at $Re = 1.67$. Simulation time 3 s. Multi-block version.

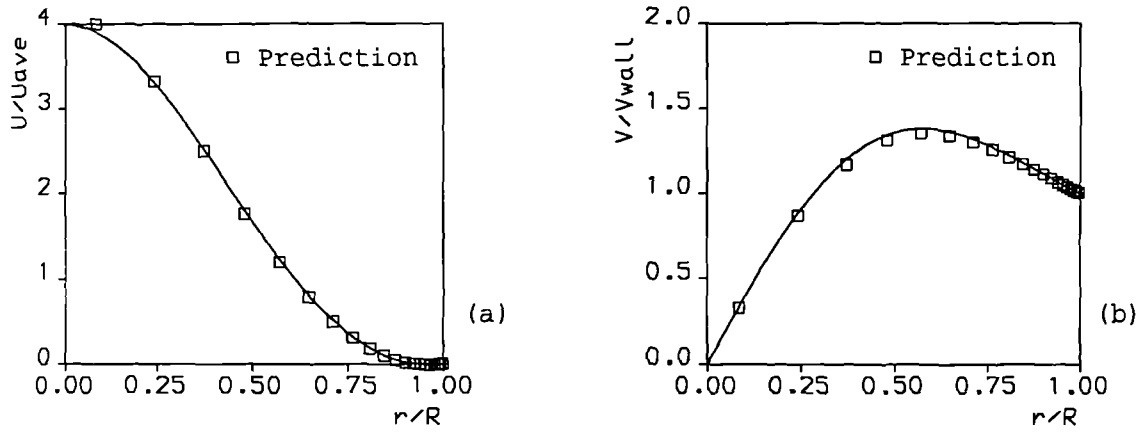


Figure 4.13 Comparisons of the distributions of (a) axial and (b) radial velocities. Expansion at $Re = 1.67$. Simulation time 3 s. DT= 5 ms. Multi-block version.

## 4.6 DISCUSSION OF RELEVANCE TO SMV SIMULATIONS

The results presented above are important in that they are the first comparison, carried out by the City University group, between numerical predictions and an analytical solution with some flow features common to those in an SMV. While the good agreement between predictions and analytical solution is encouraging, it is should be remembered that there are many points of difference between the flow studied here and that in an SMV.

The first and most obvious difference is that the physiological flow is periodic, and hence, the flow cannot be similar in time. Also, the time taken by the numerical model to reach a similar solution has been of the same order as the period of the SMV flow. It is therefore unlikely that a similar solution could be established even over part of the cycle.

Further, the Reynolds number, $\alpha$ , for the SMV is at least an order of magnitude larger than has been considered here (a typical peak value is about 200). Finally, all the SMVs studied to date have rigid inlet tubes, and hence, over part of the cycle at least, the flow geometry resembles that of a sudden pipe expansion. As would be expected, this produces flow separation and recirculation. The primary recirculation is usually accompanied by a second and possibly a third recirculating region. Hence, the flows are far from similar in the axial direction. In the next chapter the numerical model has been extended by adding a rigid section to the pipe in order to see whether recirculation regions can be predicted similar to those seen experimentally.

## 4.7 SUMMARY

In this chapter, a validation exercise of the moving wall capability of both single- and multi-block versions of CFDS-FLOW3D has been presented. Predicted flows in an expanding or contracting semi-infinite pipe have been compared with the analytical solution due to Uchida and Aoki (1977). Very good agreement between the predictions of both versions of the code and the analytical solution have been achieved. Only minor differences have been observed between the predictions using the single-block version of the code, and those produced using the multi-block version. More 'realistic' mathematical models for the SMV are presented in the next chapter.

# CHAPTER 5

# NUMERICAL MODEL SKELETAL MUSCLE VENTRICLES: RIGID/COMPLIANT MODELS

## 5.1 INTRODUCTION

In this chapter a numerical study on rigid/compliant model SMVs is presented. The obvious limitation of the model considered in the previous section is that an SMV has a finite length, and hence a similarity solution in $x$ cannot be developed. Also, the pulsatile motion of the SMV wall means that a similarity solution in time is not possible. Further, it is likely that the SMV will be fed by a rigid tube. While an analytical solution encompassing the preceding features is almost certainly unattainable, *in vitro* data are available with which numerical predictions can be compared. The model presented in the preceding chapter has been modified to include a rigid inlet/outlet tube, and the wall motion has been made sinusoidal. This will be referred to as the *rigid/compliant model.*

The essential features of the flow in an SMV are (i) flow separation and (ii) regions of recirculation. Similar features have been shown to exist, both experimentally (Sobey, 1985) and numerically (Tutty, 1992), in pulsatile flows in channels with rigid constrictions. These flow fields show trains of counter-rotating vortices whose features are related to the frequency and Reynolds number of the upstream flow.

Preliminary studies on model SMVs were reported by Henry et al. (1992). In this chapter, predicted flow patterns in two numerical model SMVs are presented: (i) a simple rigid/compliant model, and (ii) a spherical-end rigid/compliant model. Calculations have been performed using both single- and multi-block versions of FLOW3D. The ventricle wall has been prescribed to move in a simple sinusoidal manner. Different structures of the flow field can be seen for different frequencies of the cycle considered. This is relevant in that similar flow behaviour has been revealed in the *in vitro* study. A brief description of the experimental flow patterns is given in the next section; a more detailed discussion on the *in vitro* experimental setup is presented in the two chapters that follow where a validation of the numerical results against the experimental data is presented. The two numerical models presented in this chapters are reported in the sections 5.3 and 5.4; predicted results are then presented and discussed in the following sections; the chapter concludes with a summary.

## 5.2 BRIEF DESCRIPTION OF THE EXPERIMENTAL FLOW FIELD

In the *in vitro* studies, the flow fields inside elastomer models are visualized throughout the cycle using a plane of laser light illuminating suspended particles in the

fluid, and photographs were taken in diametral planes. One *in vitro* model SMV is shown in Fig.5.1. All the model SMVs studied to date have rigid inlet tubes, and hence, over part of the cycle at least, the flow geometry resembles that of a sudden pipe expansion. As would be expected, this produces flow separation and recirculation. The primary recirculation, which consists of a vortex ring close to the inlet wall and symmetrical to the axis, is accompanied by a second vortex ring further in the ventricle when the volume of the model is approaching its maximum value. Eventually a third recirculation region can be seen close to the closed end of the model at high frequencies of the cycle.

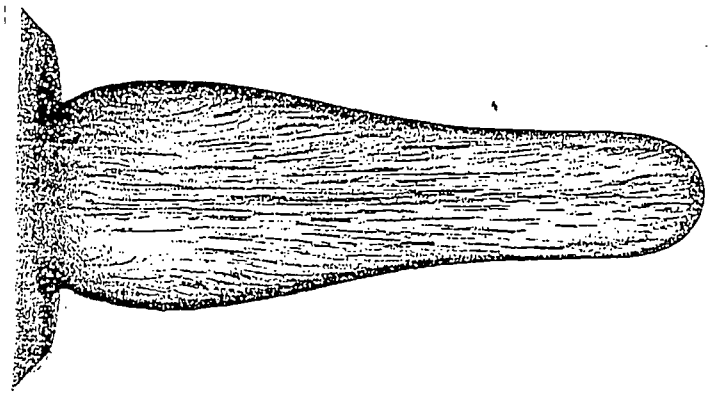

Figure 5.1 *In vitro* model SMV

## 5.3 SIMPLE RIGID/COMPLIANT MODEL

The simple model comprises a compliant closed-end cylinder attached to a rigid inlet tube, as illustrated in Fig.5.2 for the maximum volume configuration. The walls of the compliant section are prescribed to expand and contract radially in a simple sinusoidal fashion with a variation of the radius of 40%. The radius changed from a minimum of 11.5 mm, to a maximum of 16.1 mm, while the length was fixed at 30 mm. The ejected volume was approximately 28% of the minimum ventricular volume. The predicted flow field in this model is shown in Fig.5.3. Fig. 5.4 shows a model of twice the length of the model in Fig.5.2, while Fig.5.5 shows the predicted flow field.

The flow fields shown in Figs.5.3 and 5.5 have been predicted using the single-block version of FLOW3D, and represents the flow at maximum ventricular volume, that is, at the time when the ventricle is passing from the filling to the pumping phase. The cycle frequency is 1.33 $Hz$. A clear two vortex structure is visible, while a third weaker vortex ring is shown close to the wall of the straight compliant tube. This configuration has not been significantly affected by a change in frequency between 1.0 and 2.0 $Hz$. Fig. 5.6 shows that the same results have been predicted by the multi-block version of the code (compare with Fig.5.3) with the same grid and simulation parameters. Comparing the numerical results with the experimental flow patterns (Fig.5.1)[1], a clear similarity in the features of the flow field can be seen.



[1]Flow patterns of the model in Fig.5.1 at the maximum volume are shown in Fig.6.2(c)

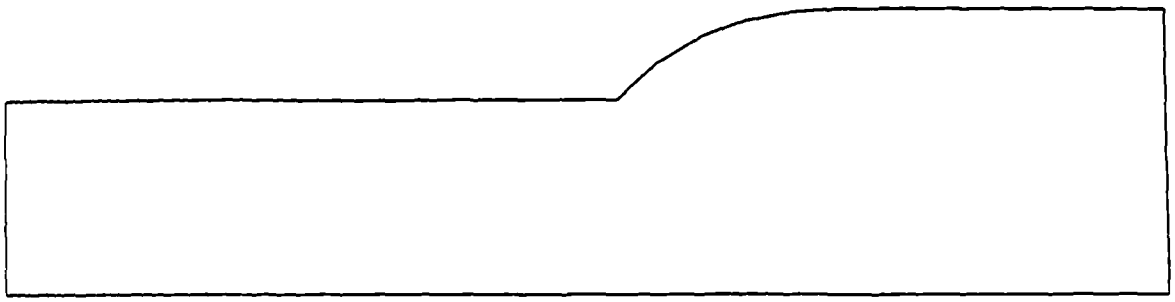

Figure 5.2 Simple rigid/compliant model ($L_{ventricle} = 3 \times R_{inlet}$)

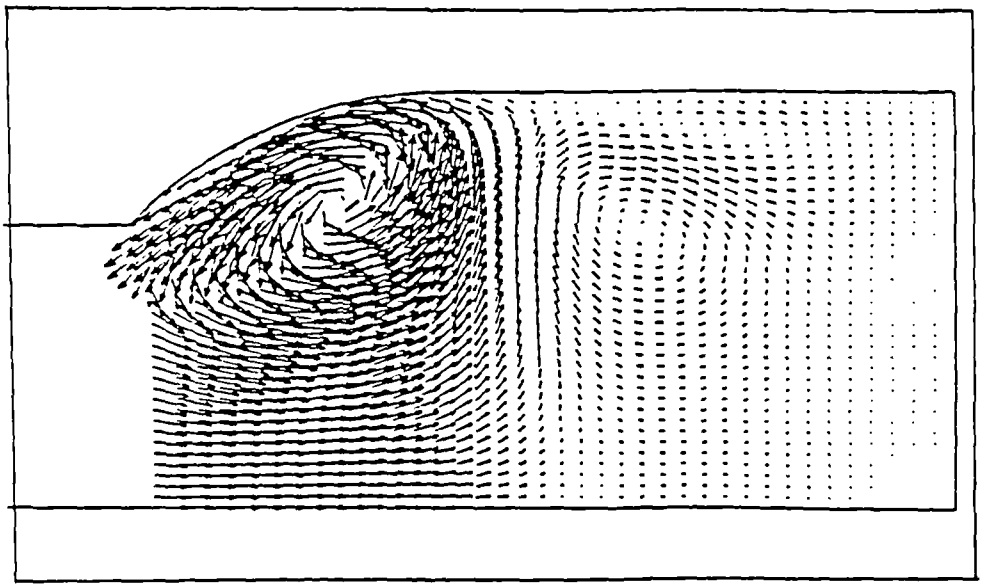

Figure 5.3 Flow structure predicted at the maximum volume for the simple rigid/compliant model ($L_{ventricle} = 3 \times R_{inlet}$)

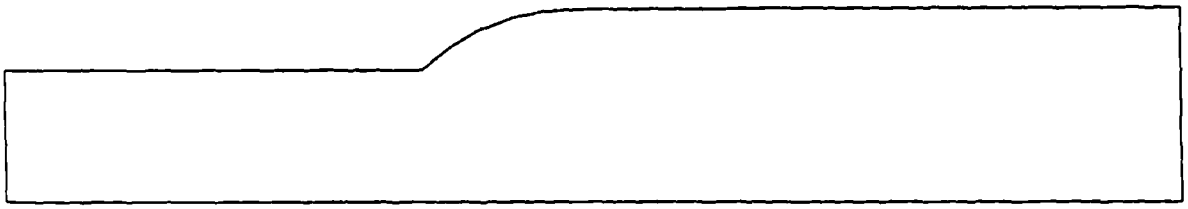

Figure 5.4 Simple rigid/compliant model ($L_{ventricle} = 6 \times R_{inlet}$)

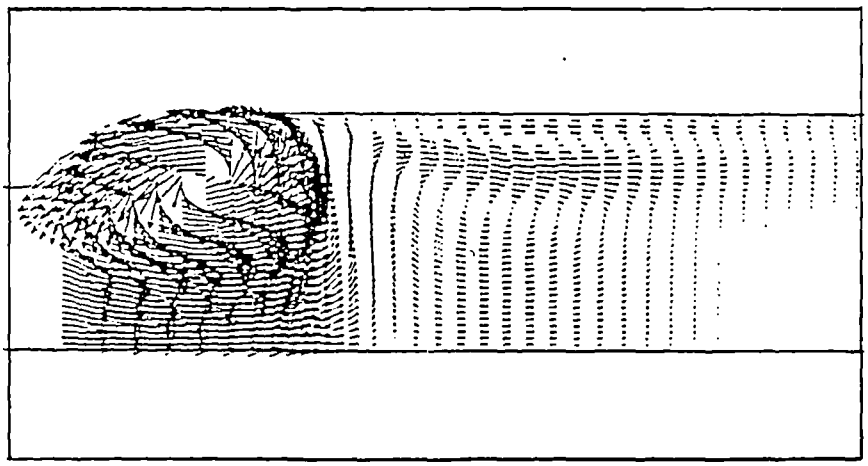

Figure 5.5 Flow structure predicted at the maximum volume for the simple rigid/compliant model ($L_{ventricle} = 6 \times R_{inlet}$)

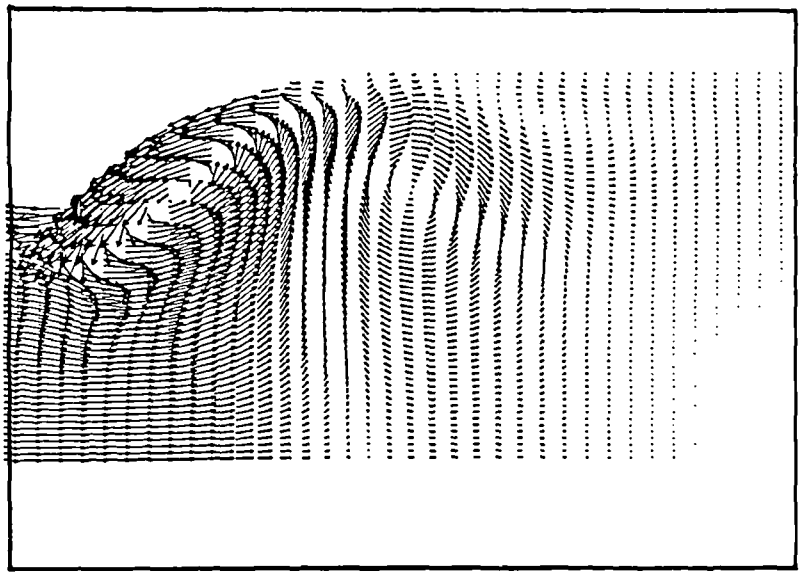

Figure 5.6 Flow structure predicted at the maximum volume for the simple rigid/compliant model ($L_{ventricle} = 3 \times R_{inlet}$) obtained using the multi-block version CFDS-FLOW3D

## 5.4 SPHERICAL-END RIGID/COMPLIANT MODEL

The spherical-end rigid/compliant model has been constructed by information available from the *in vitro* studies (Shortland et al., 1993). Fig.5.7 shows a photograph of the *in vitro* model at its maximum volume. The model is similar to the above simple model, but it has a spherical rather than a square end. The geometric features of the model, assumed in the numerical analysis, are summarized in Table 5.1.

Table 5.1
Geometric features of the model

| | |
|---|---|
| Inlet pipe diameter | $D_{in} = 22$ mm |
| Inlet pipe length | $L_{in} = 30$ mm |
| Minimum SMV diameter | $D_{min} = 23$ mm |
| Maximum SMV diameter | $D_{max} = 32$ mm |
| SMV length | $L_{SMV} = 31$ mm |

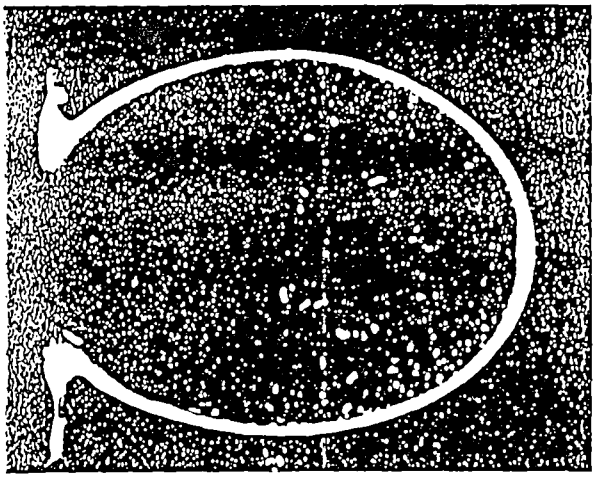

Figure 5.7 *In vitro* model SMV

Throughout the cycle the model undergoes a significant change in shape from a cylindrical central region configuration, at minimum volume to a totally spherical shape, at maximum volume, as in Fig. 5.8. This has been taken into account in the numerical modelling. The grid used to model the ventricle is shown in Fig.5.9. The same grid was used for both single- and multi-block versions of the code. The wall has been assumed to move sinusoidally in the axial direction with $\Delta r = 40\%$. The boundary condition is constant pressure at the inlet of the duct: $p = 1.3332 \times 10^4 N/m^2$. The density and the viscosity assumed for the fluid are respectively: $\rho = 1176 kg/m^3$; $\nu = 4.0 \times 10^{-3} Ns/m^2$. These values are taken from the values of density and viscosity used in the *in vitro* experiments. Note that the experimental fluid is Newtonian.

The choice of simulation parameters was reached after a suitable parametric study. The parameter set used in the simulation, for which the predictions show good convergence, is shown in Table 5.2. The flow was assumed to be laminar and axisymmetric.

Table 5.2
Simulation Parameters

| | |
|---|---|
| Number of cells in radial direction | NJ=24 |
| Number of cells in axial direction | NI=50 |
| Total number of cells | NC=1200 |
| Time step | DT=10 ms |
| Number of iterations per time step | IT=50 |
| Pressure/velocity coupling | SIMPLEC |
| Advection algorithm | HIGHER UPWIND |

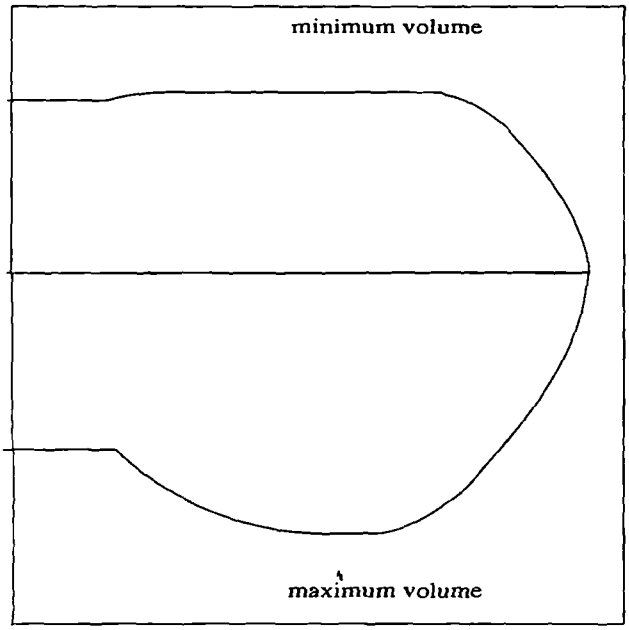


Figure 5.8 Spherical-end model at minimum and maximum volume

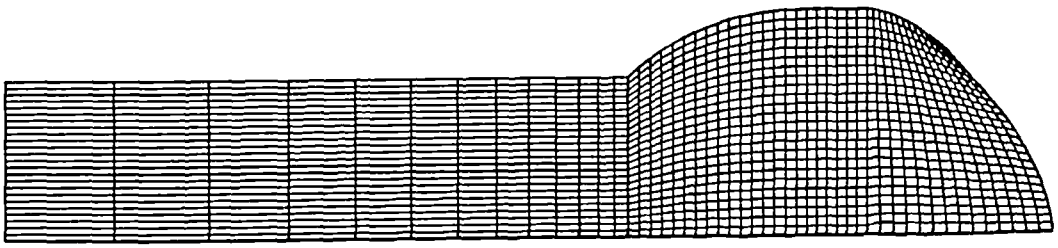

Figure 5.9 Grid used for the spherical-end model

## 5.5 NUMERICAL RESULTS

As in the previous case, the chief feature of the predicted flows in the spherical-end model is the formation of recirculation regions, or vortex rings, at the time of maximum ventricular volume. In this case, however, different flow structures are predicted as the frequency of the wall motion varies. Different frequencies of the cycle were tested within a range of 0.3-3.0 Hz.

Fig. 5.10. shows the temporal sequence of the flow field in the model SMV for $f = 1.0Hz$ over the whole cycle. For this case the predicted flow develops within the ventricle in the same manner as in the typical *in vitro* model. For all the frequencies considered a 'vortex structure' is clearly visible at the time coincident with the maximum

volume of the ventricle.

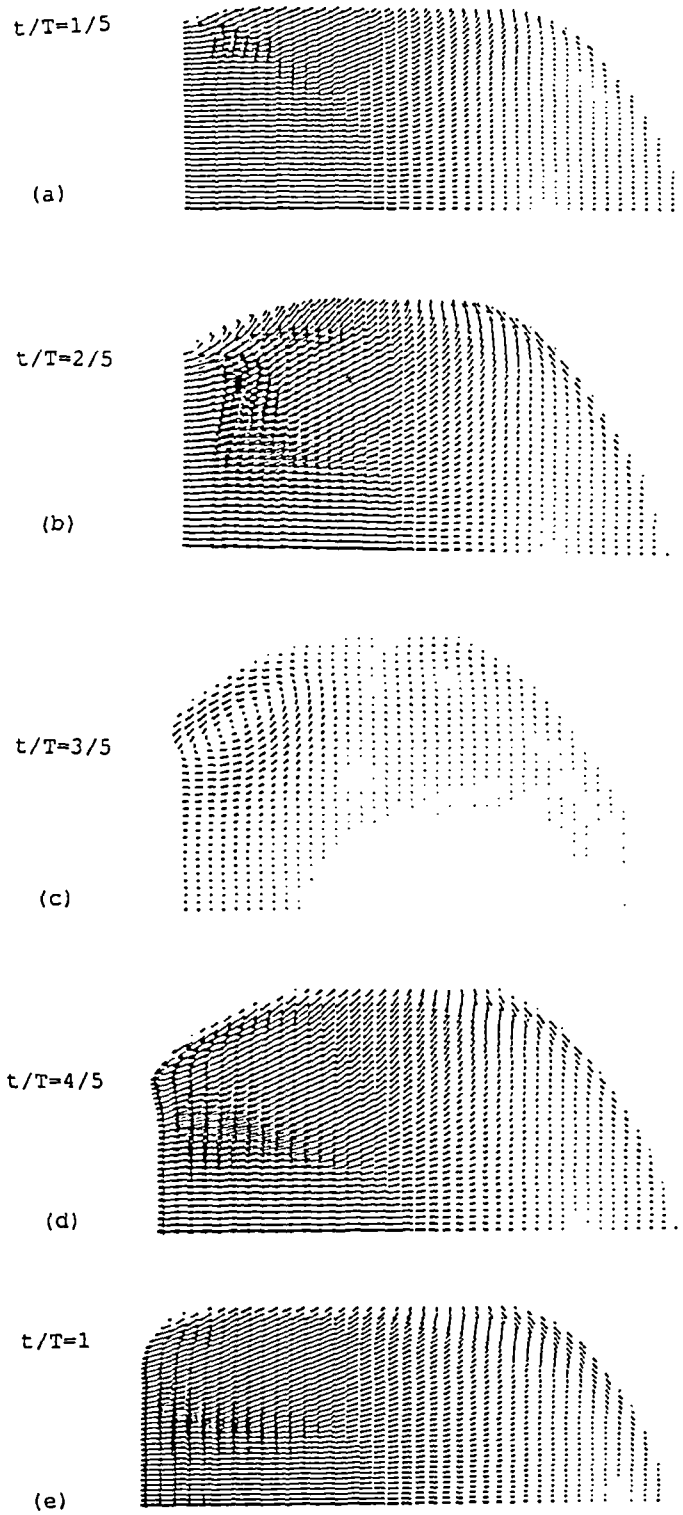


Figure 5.10 Predictions of the flow field inside the spherical-end model: (a), (b), (c), (d), (e) show the temporal sequence over one period

At low frequencies only primary recirculations can be seen. This is shown in the flow field given in Fig.5.11, which represents the flow structure at the time of maximum ventricular volume with the ventricle driven at a frequency of 0.3 $Hz$. Above this frequency, a second recirculation forms. Two vortex rings can be seen in the flow field given in Fig.5.12, which represents the flow in the ventricle at a frequency of 1.25 $Hz$. At a frequency between 1.25 and 1.33 $Hz$, a third vortex is formed. The three-vortex flow structure can be seen in Fig. 5.13, for a frequency of 1.33 $Hz$. The frequency has been increased to 3.0 $Hz$ without further vortices appearing. The flow field for a frequency of 3.0 $Hz$ is shown in Fig.5.14.

The flow fields presented in Figs.5.11 to 5.14 have been predicted using the multi-block version of the code. Predictions using the single-block version have been performed for the same frequency range and are shown in Figs. 5.15 to 5.18. While the predicted flow fields have agreed in general, the frequency at which three vortices form has been found to be somewhat lower than in the multi-block version. Table 5.3 summarizes the predicted results for the flow structures over the frequency range 0.3-3.0 $Hz$ for both versions of the code. The reason for the differences is as yet unexplained.

Table 5.3

Vortex structures over the frequency range

| Number of vortices | 1 | 2 | 3 |
|---|---|---|---|
| Single-block version | below 0.3 $Hz$ | 0.3-1.38 $Hz$ | 1.38-3.0 $Hz$ |
| Multi-block version | below 0.3 $Hz$ | 0.3-1.25 $Hz$ | 1.25-3.0 $Hz$ |

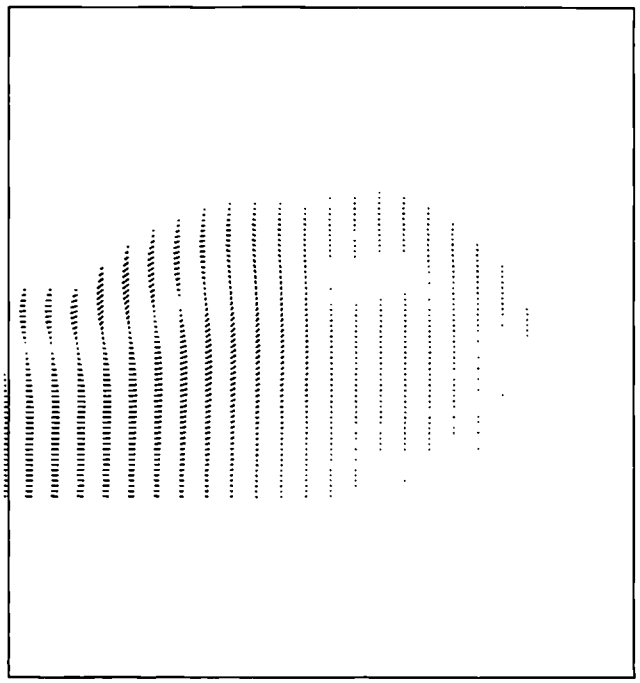

Figure 5.11 Flow structure predicted at the maximum volume for the spherical-end rigid/compliant model for $f$=0.3 Hz and using the multi-block version of CFDS-FLOW3D

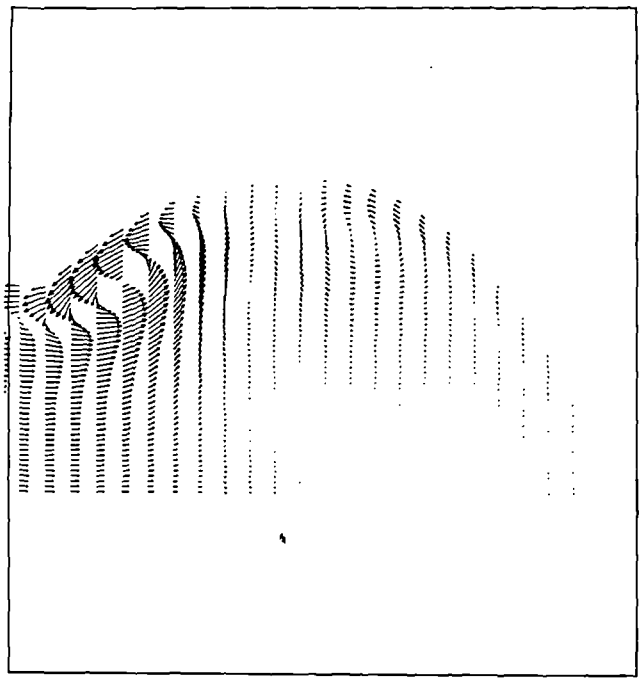

Figure 5.12 Flow structure predicted at the maximum volume for the spherical-end rigid/compliant model for $f$=1.25 Hz and using the multi-block version of CFDS-FLOW3D

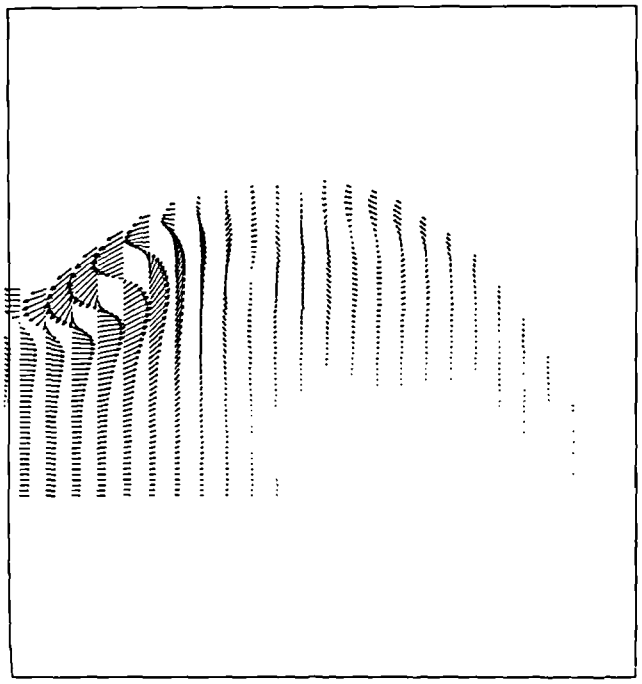

Figure 5.13 Flow structure predicted at the maximum volume for the spherical-end rigid/compliant model for $f$=1.33 Hz and using the multi-block version of CFDS-FLOW3D

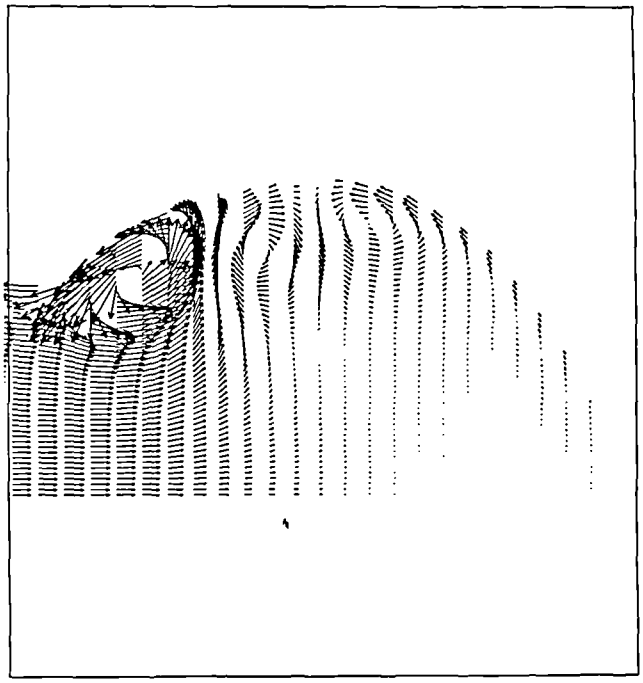

Figure 5.14 Flow structure predicted at the maximum volume for the spherical-end rigid/compliant model for $f$=3.0 Hz and using the multi-block version of CFDS-FLOW3D

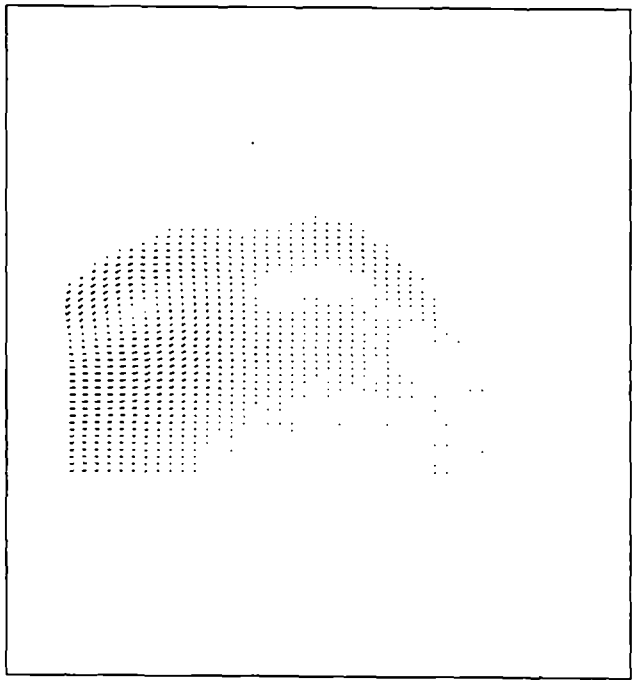

Figure 5.15 Flow structure predicted at the maximum volume for the spherical-end rigid/compliant model for $f$=0.3 Hz and using the single-block version of CFDS-FLOW3D

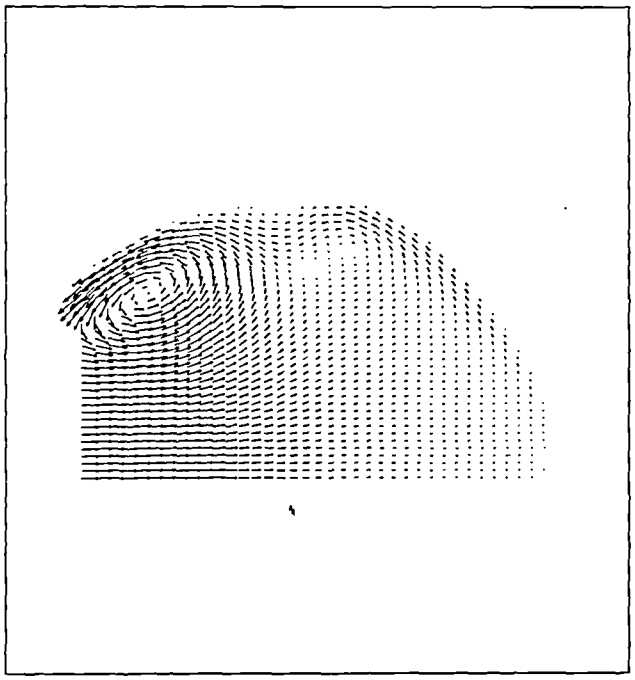

Figure 5.16 Flow structure predicted at the maximum volume for the spherical-end rigid/compliant model for $f$=1.33 Hz and using the single-block version of CFDS-FLOW3D

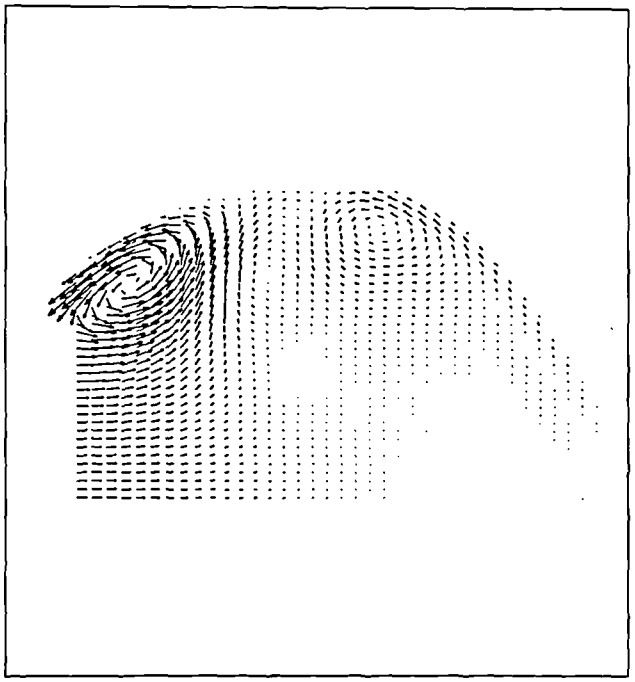

Figure 5.17 Flow structure predicted at the maximum volume for the spherical-end rigid/compliant model for $f$=1.66 Hz and using the single-block version of CFDS-FLOW3D

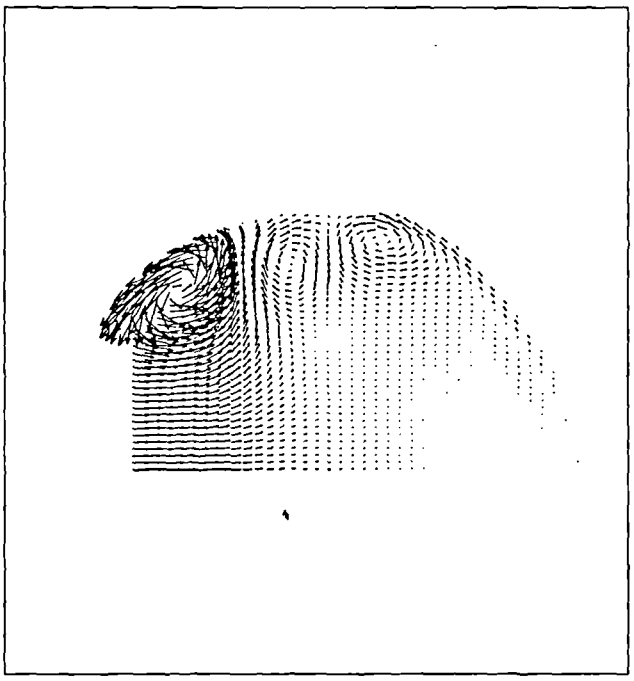

Figure 5.18 Flow structure predicted at the maximum volume for the spherical-end rigid/compliant model for $f$=3.0 Hz and using the single-block version of CFDS-FLOW3D

## 5.6 DISCUSSION

A mathematical model for unsteady flow and inviscid fluid in pulsating bulbs was proposed by Jones (1970). Recently Tsangaris and Koufopoulos (1990) presented numerical simulations of pulsating viscous flow induced by sinusoidal motion of the wall in a ventricle model similar to that presented above. In their work the predicted flow field were not compared with experimental results and, as the rate of wall motion was slower, their data could not form a basis of comparison with the present work.

The essential features of the model SMV can be compared with a channel with a symmetrical indentation. Several numerical and experimental studies have been reported on flow in such channels: Tutty (1992) studied pulsatile flows through a plane channel with an indentation and his predicted results are supported by the experimental findings of Sobey (1985). The flow field show trains of counter-rotating vortices demonstrating different features for different frequencies and Reynolds numbers of the upstream flow. Furthermore, experimental and theoretical two-dimensional unsteady flows in a channel with a time-dependent indentation which moves sinusoidally are described by Pedley (1985); similar numerical predictions are also presented by Demirdzic and Peric (1990).

In the light of these findings we can try to characterize the behaviour of the flow in the model SMV studied above. In fact, we can reasonably conclude that the formation of

the train of vortices is determined by the features of the flow filling the ventricle during its expansion. If the rate of this expansion is low, as it is at low frequencies of the cycle, the separation of the entering flow establishes only a single recirculation region inside the ventricle; if this is higher a second or even third recirculation can be established.

## 5.7 SUMMARY

In this chapter, two numerical model SMVs have been discussed. For the simple rigid/compliant model, the predicted flow fields have shown good agreement over the cycle with the experimental flow fields from the *in vitro* study for a similar model. For the spherical-end rigid/compliant model, the predicted flow structures have shown that the number of vortex rings formed at the time of maximum ventricular volume is a function of the frequency of the wall motion. The number of vortices increases with the frequency. A similar connection between vortex structure and frequency has been seen in the *in vitro* model SMVs. These results have indicated that modern CFD codes, such as CFDS-FLOW3D, are probably capable of simulating physiological flows in actual SMVs.

In the next chapter, a numerical analysis will be presented where experimental data for the motion of the wall are incorporated in the calculations to drive the grid boundary at each time step throughout the cycle.

# CHAPTER 6

# NUMERICAL SIMULATION OF THE FLOW IN A MODEL SMV WITH EXPERIMENTAL WALL MOTION

## 6.1 INTRODUCTION

In this chapter, a numerical analysis is presented of the flow inside a model SMV with wall motion prescribed experimentally. The predicted results are qualitatively compared with the corresponding experimental *in vitro* data. The calculations have been carried out on ventricles whose wall motion is defined by experimental data, and undergoing identical boundary conditions. These data were provided by Dr. Shortland at the University of Liverpool, and consisted of radial and axial coordinates of points along the ventricle wall. Numerical results have shown that while the predictions agreed in general with the experimental data, differences can be seen about the time of maximum ventricular volume.

The chapter begins with a brief description of both the experimental set up and the data provided. Predictions of the *in vitro* cases are then presented and discussed.

## 6.2 IN VITRO STUDIES

### 6.2.1 Experimental Apparatus

The *in vitro* model SMVs are thin-walled, translucent elastomer ventricles made from silicone rubber (Dow Corning, MDX4-4410). The ventricle, fitted inside a perspex fluid-filled tank, is attached to a rigid inlet/outlet tube. The tube has a length of 30 cm and a diameter of 22 mm, and is attached to a constant head tank. Wall motion is generated by a computer controlled piston pump attached to the fluid-filled chamber. A sketch of the flow apparatus is shown in Fig.6.1. The pump can be programmed to provide a wide range of waveforms. In the case to be discussed, it is assumed that the ventricle is activated in a pulsatile mode at each cardiac cycle.

As can be seen in Fig.6.2, the general shape of the ventricle is that of a closed-end cylinder. The fluid used (Newtonian) is a 36% sucrose solution with a viscosity and density of $4.0 \times 10^{-3} Ns/m^2$ and $1176.0 kg/m^3$, respectively. A small amount of 80-150 micron diameter polymethyl methacrylate particles are introduced to the fluid to enhance flow visualization. Planar illumination of the longitudinal mid-plane is provided by a 16 mW Helium Neon laser. Streak-line images of 80 ms duration are captured by a modified charge coupled device (CCD) video camera capable of integration on its sensor. Video images were collected by a framegrabber and recorded on video tape.

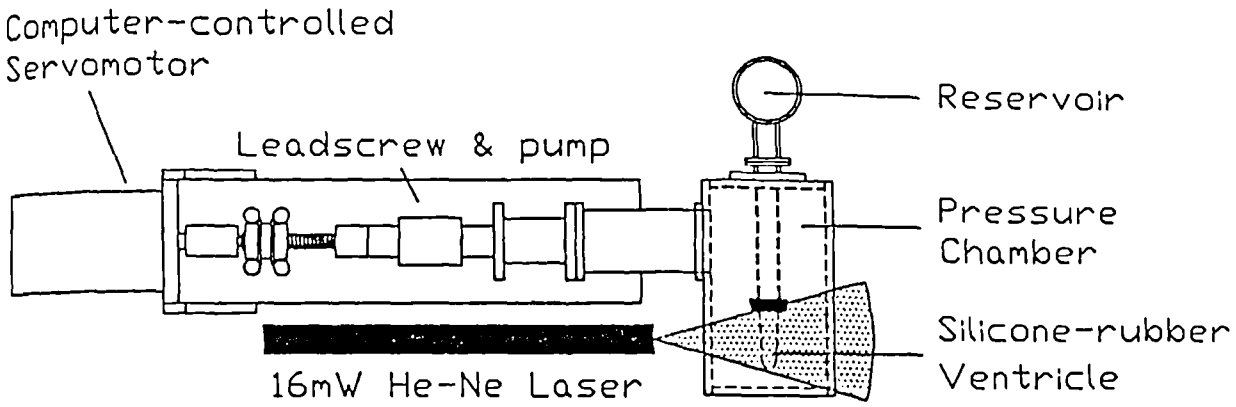


Figure 6.1 Experimental apparatus

### 6.2.2 General Features of the Flow in the *in vitro* Model SMV

The basic features of the flow are shown in the sequence of photos shown in Fig.6.2. As the ventricle fills, Fig.6.2(a), its radius increases, and eventually the flow situation is similar to that of a sudden expansion in a pipe. That is, the flow separates at the step formed at the inlet and reattaches further into the ventricle, forming a recirculating region. As the flow is axisymmetric, the two vortices shown in Fig.6.2(b) are actually cross sections of the same vortex ring. This ring grows in size and strength as the ventricle continues to expand. Eventually, the radial motion produced by the vortex ring on the fluid passing through its centre is sufficient to produce a second vortex ring, of opposite sense, as can be seen in Fig.6.2(c). Each ring produces an induced motion in the other such that the initial ring reduces in diameter while the second ring increases in diameter. This can be seen by comparing Fig.6.2(d) with Fig.6.2(c). As flow starts to be forced out of the ventricle, the second vortex ring disappears almost immediately, while the first persists a little longer. This sequence appears to be relatively insensitive to changes in the length of cycle period or the precise value of ejected volume.

### 6.2.3 Wall Movement Data

A number of data sets of wall movement were produced for use in the numerical simulations. The data consist of subsets of radial and axial coordinates of 40 equispaced

points along the ventricle wall. The interval between subsets is fixed at $40ms$. Hence, the number of subsets in a set depends on the cycle period. In this description two sets of data will be discussed, termed the *B data set* and the *D data set*. It is believed that the latter set is more accurate.

The B set comprises four subsets; B1010, B1015, B1215, and B1515. Each subset has a different combination of ejected volume and frequency, which is signified by the numbers following the letter used to designate to which data set the subset belongs. The first two digits are a code for the frequency; for instance, B1215 has a frequency of $1.2Hz$. The second two digit are a code for the amplitude of the stroke of the pump, in term of D/A converter units, and hence, they are related to the ejected volume. The essential point to note is that the larger the second of the two digits, the larger is the ejected volume. That is, B1015 has a larger ejected volume than does B1010. The D data set in fact has only one subset, D1010.

The temporal behaviour of the radial and axial position of three points along the ventricle is given in Figs 6.3, 6.4, 6.5, for the B1515, B1010, and D1010 data, respectively. Note that the axial movement has been magnified by 10. In order to allow the computational time step to be reduced if necessary, a Fourier decomposition has been applied to the original data to produce data sets with a desired subdivision of the original time step. Examples of regenerated data sets with a time step of one quarter the original; i.e., 10 ms, are also given in Figs.6.3, 6.4, 6.5. The corresponding variation in the total volume of the ventricle for each of the three data sets is given in Fig.6.6. It is evident from a comparison of Figs.6.4 and 6.5, and 6.6(b) and 6.6(c) that the D data set changes more smoothly than does the B set. The higher frequencies seen in the B set are believed to be largely due to experimental error. The D set has been produced using a more sophisticated data gathering system, and hence it is believed that this set is relatively free of error.

Characteristic values of mean, maximum, minimum and ejected volume are given in Table 6.1 for some of the sets analyzed. This table also shows the maximum estimated Reynolds number, based on the inlet tube diameter. The Reynolds numbers for the B data set have been obtained by averaging the surrounding points at maximum volume variation rate, and omitting the obviously erroneous points. Without this averaging process, the maximum Reynolds number occurs at the 'bump' seen after the maximum volume in Fig.6.6(b). The artificially large value of the derivative of volume with respect to time caused by this bump produces an exceptionally large flow down the inlet pipe.

Table 6.1

Values of mean, maximum, minimum and ejected volume, and maximum estimated Reynolds number for some data sets.

B1515 data set

| | |
|---|---|
| Mean volume | $V_m = 33ml$ |
| Maximum volume | $V_{mx} = 46ml$ |
| Minimum volume | $V_{mn} = 21ml$ |
| Ejected volume | $V_{ej} = 25ml$ |
| Maximum estimated Reynolds number | $Re = 2000$ |

B1010 data set

| | |
|---|---|
| Mean volume | $V_m = 28ml$ |
| Maximum volume | $V_{mx} = 37ml$ |
| Minimum volume | $V_{mn} = 20ml$ |
| Ejected volume | $V_{ej} = 17ml$ |
| Maximum estimated Reynolds number | $Re = 900$ |

D1010 data set

| | |
|---|---|
| Mean volume | $V_m = 24ml$ |
| Maximum volume | $V_{mx} = 31ml$ |
| Minimum volume | $V_{mn} = 17ml$ |
| Ejected volume | $V_{ej} = 14ml$ |
| Maximum estimated Reynolds number | $Re = 900$ |

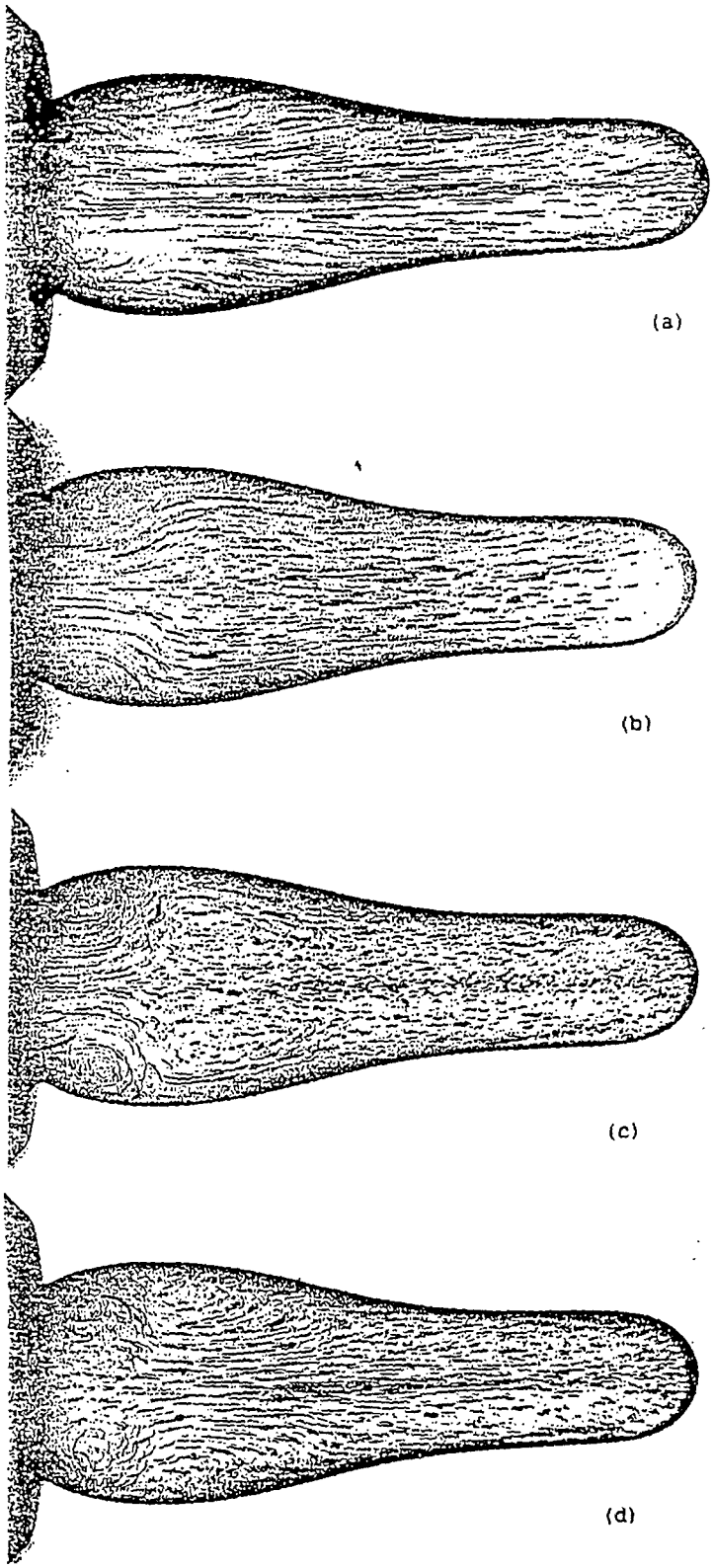


Figure 6.2(a-d)Experimental flow field at four characteristic times of the period in the *in vitro* model SMV

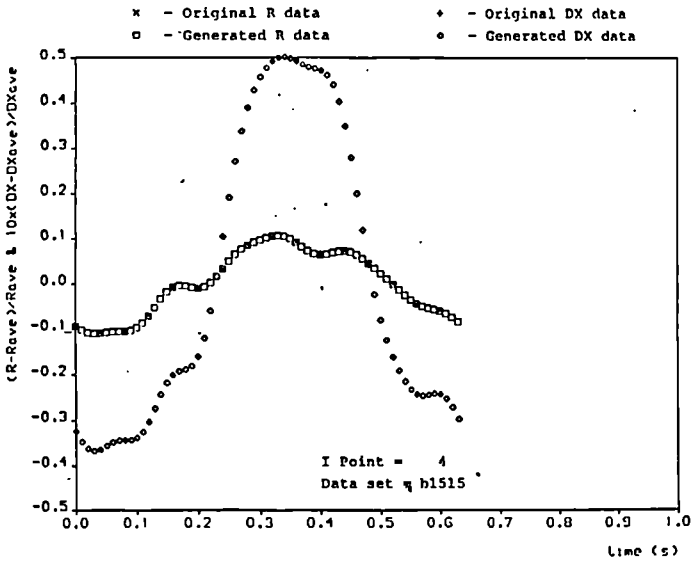


(a)

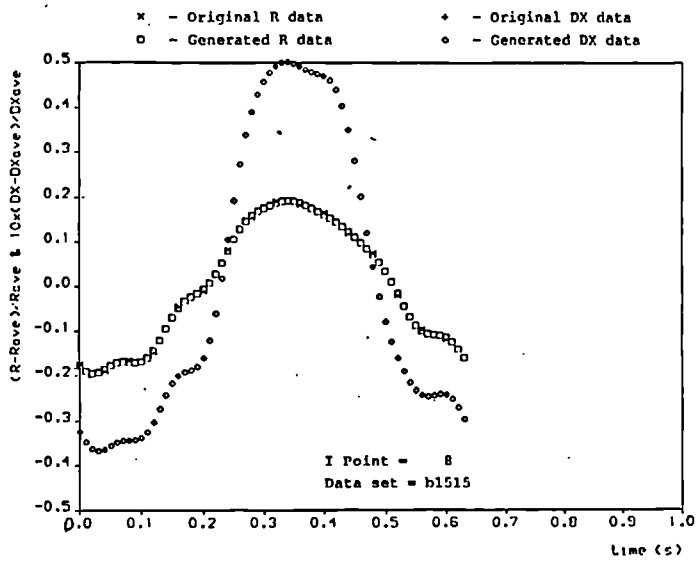


(b)

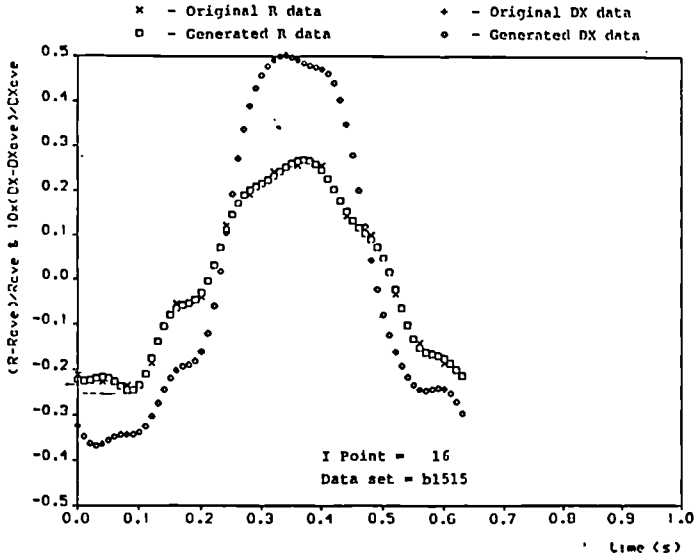


(c)

Figure 6.3(a-c) Temporal behaviour of dx and dr at different axial points for the b1515 data set.

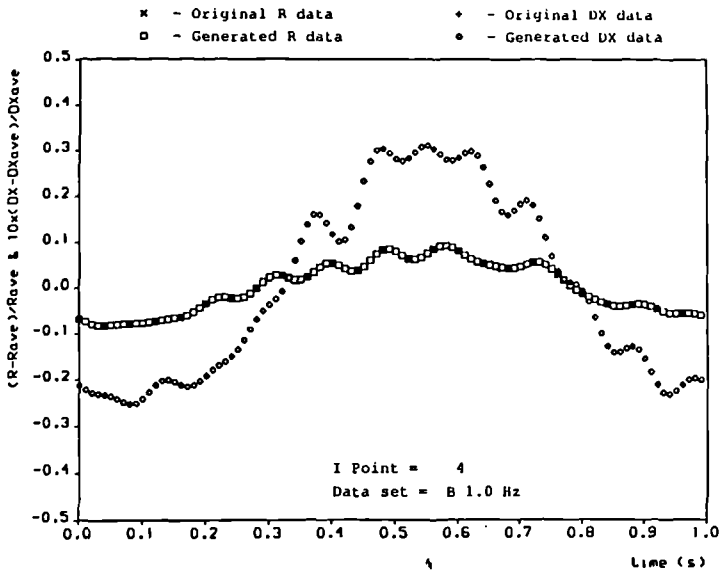


(a)

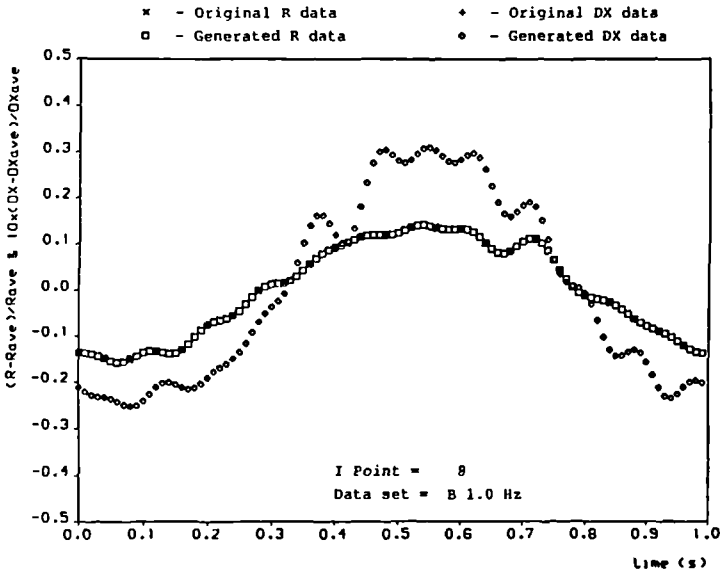


(b)

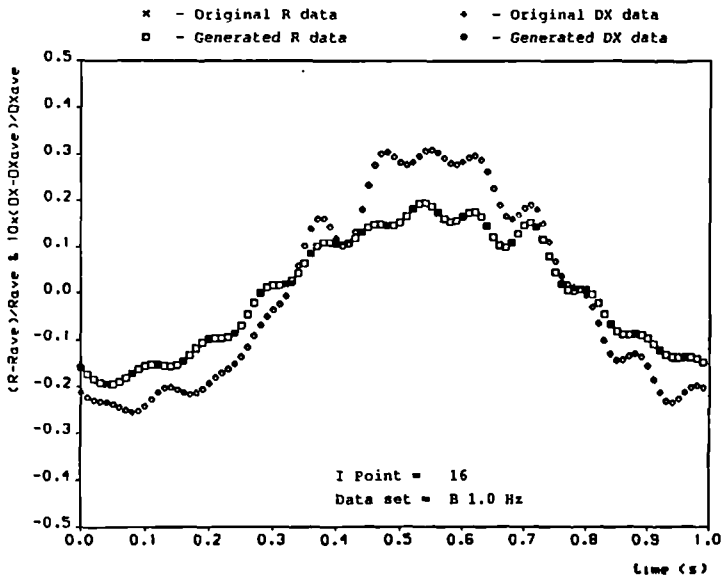


(c)

Figure 6.4(a-c)Temporal behaviour of dx and dr at different axial points for the b1010 data set.

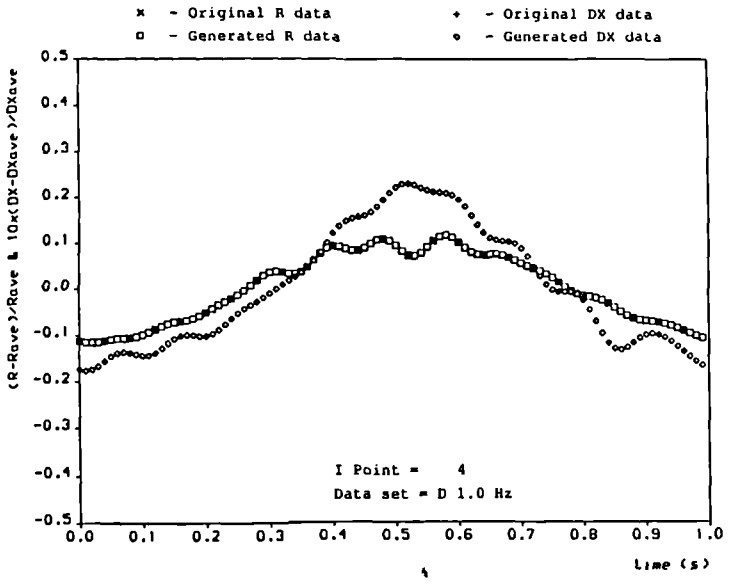


(a)

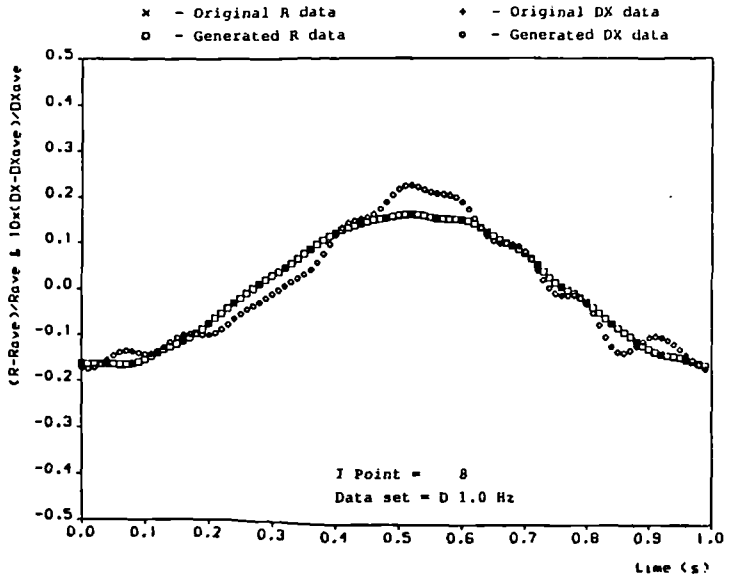


(b)

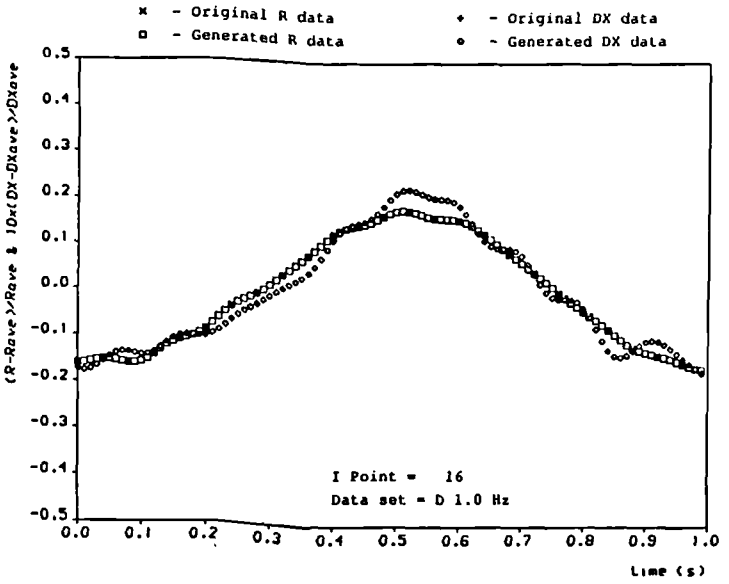


(c)

Figure 6.5(a-c)Temporal behaviour of dx and dr at different axial points for the d1010 data set.

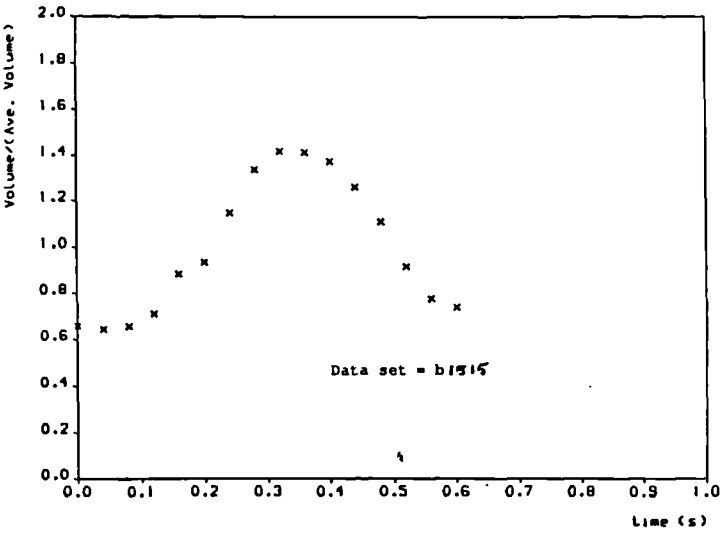


(a)

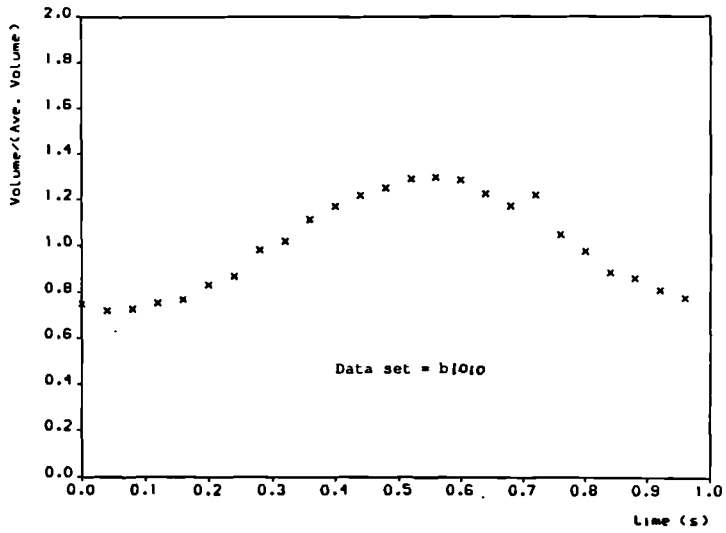


(b)

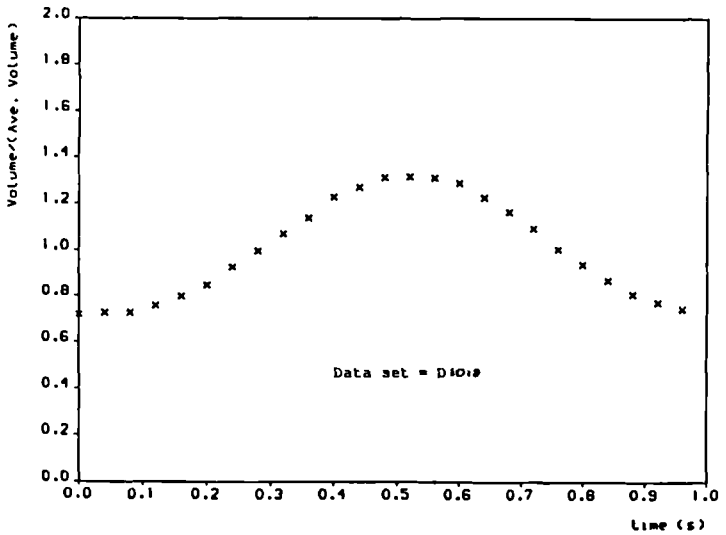


(c)

Figure 6.6 Volume variation function of the SMV in time: (a) b1515 data set; (b) b1010 data set; (c) d1010 data set.

## 6.3 NUMERICAL RESULTS

### 6.3.1 Numerical Grid

The axial spacing of the grid given by the experimental data was fixed. Grid refinement in the axial direction was achieved by linearly interpolating the original data at the time each grid was produced. The original grid data placed no restriction on the radial grid spacing. Both equispaced grids and those expanding away from the wall have been used in the radial direction. The rigid $30cm$ inlet pipe was also modelled. To reduce the number of control volumes used in the inlet tube, the grid was made to expand away from the ventricle.

### 6.3.2 Original Data

All sets of data have been simulated using the single-block version of FLOW3D; Release 2.4. Predicted flow fields for equispaced times in the period are given in Fig.6.7 for the B1010 data. Although the predicted flow fields agree with the experimental data over a large part of the cycle, they do not predict the occurrence of the second vortex ring. It can be seen that at the inlet a powerful jet is predicted to exist at the time of maximum volume with one vortex close to the wall. Further into the ventricle, the maximum velocity in the predicted flow is near the centreline, whereas in the experimental flow, the maximum velocity is in the area close to the wall. Both grid refinement and reductions in time step have failed to make any significant difference to the predicted flow field. The results presented above were in fact for a refined time step of one quarter of the original. A sample refined-grid prediction, for set B1010, is given in Fig.6.8.

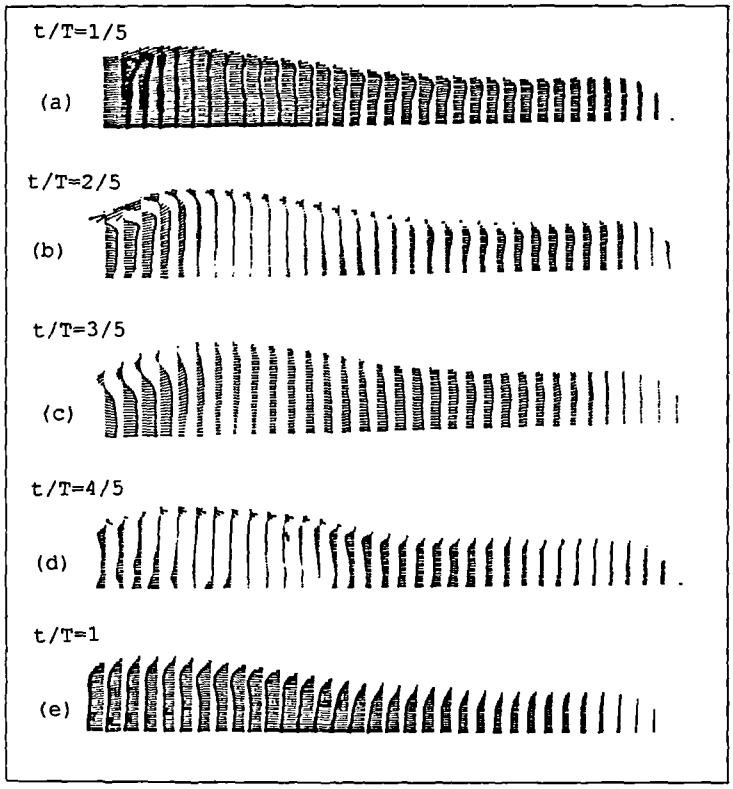


Figure 6.7 Predictions of the flow field inside the SMV for the b1010 data; (a), (b), (c), (d), (e) show the temporal sequence over one period. NI=51, NJ= 18, DT= 10 ms

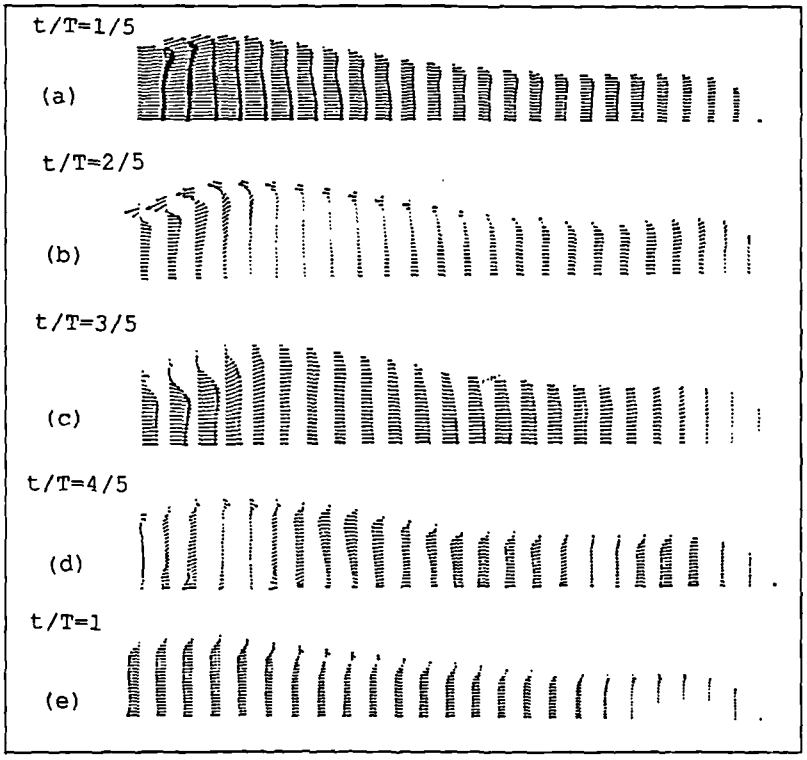


Figure 6.8 Predictions of the flow field inside the SMV for the b1010 data; (a), (b), (c), (d), (e) show the temporal sequence over one period. NI=51, NJ= 24, DT= 10 ms

### 6.3.4 New Data

It was felt that the known inaccuracies in the B data set might be responsible for the inability of the numerical model to predict the second vortex ring. In order to test this hypothesis, a new set of data, the D set, was produced using a more accurate data gathering procedure. Unfortunately, as can be seen in Fig.6.9, simulations using the new data also failed to predict the second vortex ring. In fact, it could be argued that not even the primary vortex is predicted.

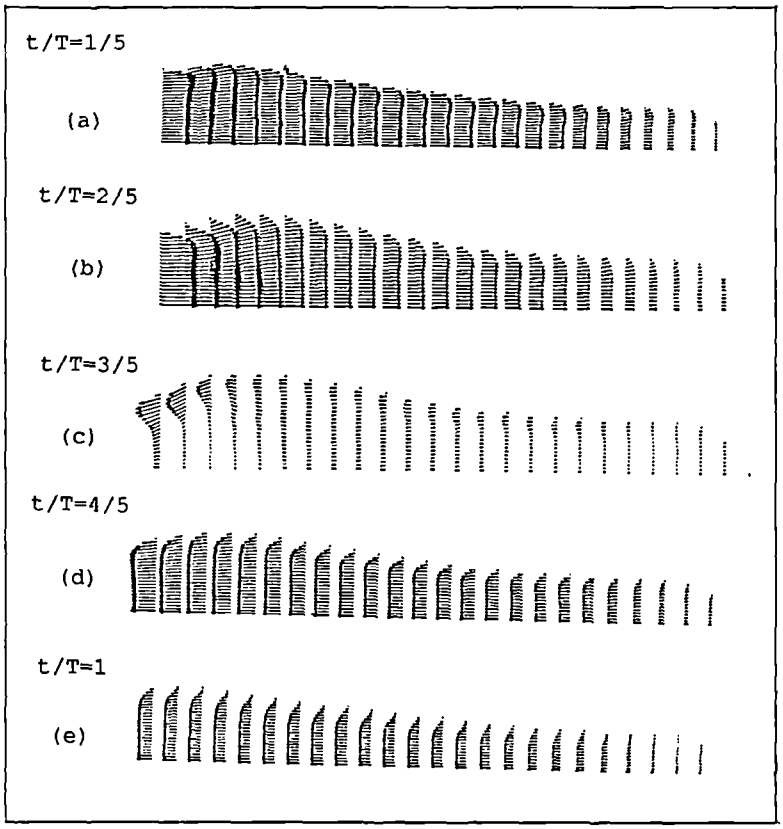


Figure 6.9 Predictions of the flow field inside the SMV for the d1010 data; (a), (b), (c), (d), (e) show the temporal sequence over one period. NI=51, NJ= 18, DT= 10 ms

### 6.3.4 Advection Models

The default scheme used to model the advection terms in the governing equations in FLOW3D is the HYBRID scheme. This scheme uses central differences when the cell Peclet number is below 2, and first-order Upwind Differences otherwise. While this scheme is extremely robust, it is known to introduce numerical dissipation which tends to 'smear' the solution. As mentioned in chapter 3, FLOW3D offers several other options,

including the second-order accurate Higher-order Upwind scheme (HUW) and the third-order accurate QUICK scheme. Simulations using both schemes were performed to check whether, in this case, the advection model had any influence on the predicted flow fields.

The advection algorithm study was carried out using the B1515 data set. In Fig.6.10 are given predicted flow fields for eight equispaced times in the cycle using the HYBRID scheme. Plots are given for predictions using HUW and QUICK in Figs.6.11 and 6.12, respectively, for four equispaced times close to the time of maximum volume. While, differences in the flow fields produced using the various advection algorithms are apparent, those produced using HUW and QUICK are quite similar. Both predict the centre velocity to be a little stronger than does the HYBRID scheme. However, neither HUW nor QUICK predicts the second vortex.

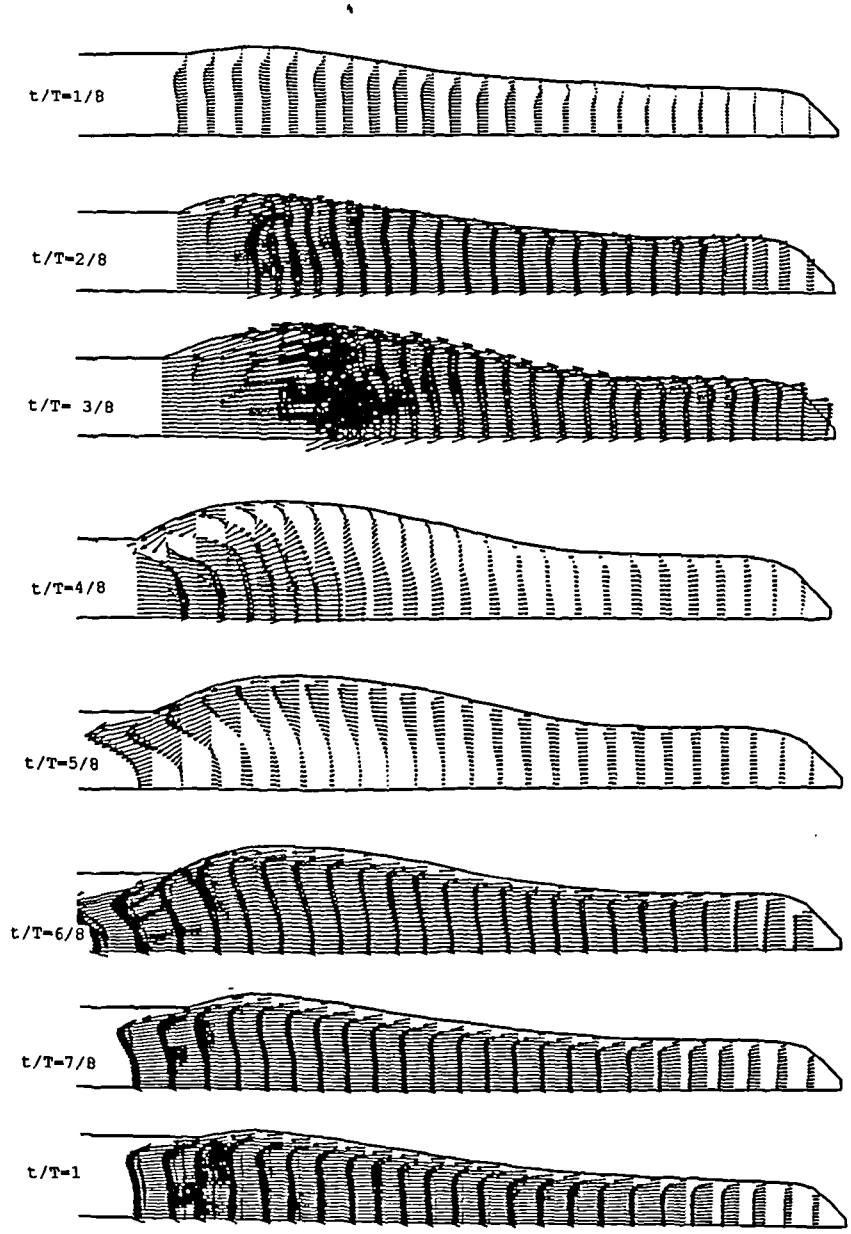


Figure 6.10 Predictions of the flow field inside the SMV for the b1515 data using HYBRID advection algorithm. NI=51, NJ= 18, DT= 10 ms

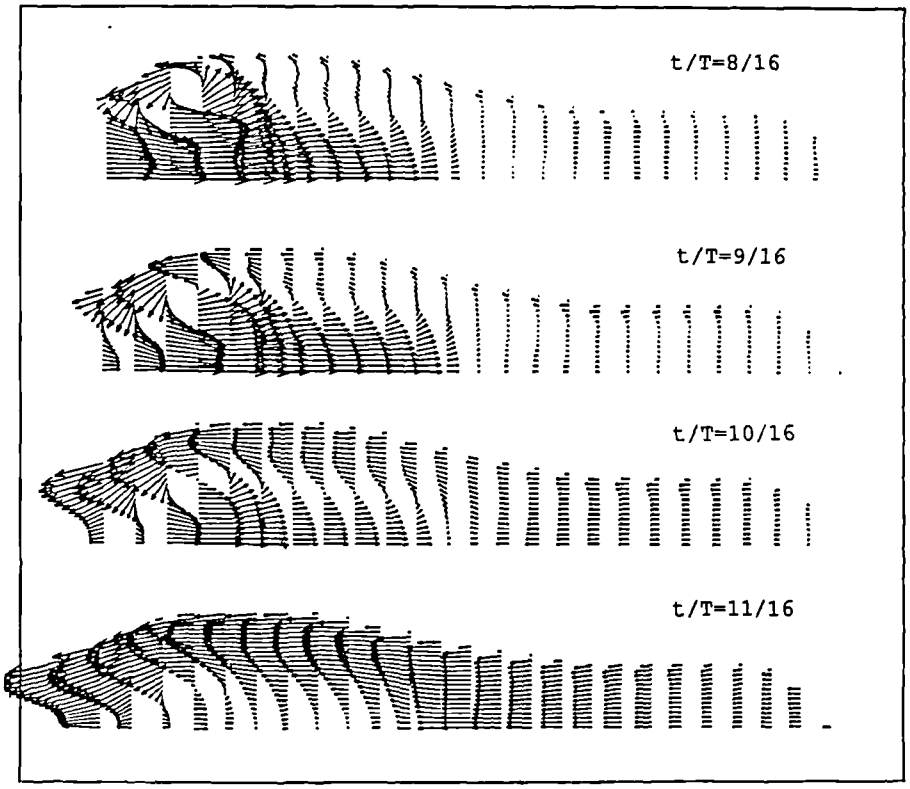


Figure 6.11 Predictions of the flow field inside the SMV for the b1515 data using QUICK advection algorithm.

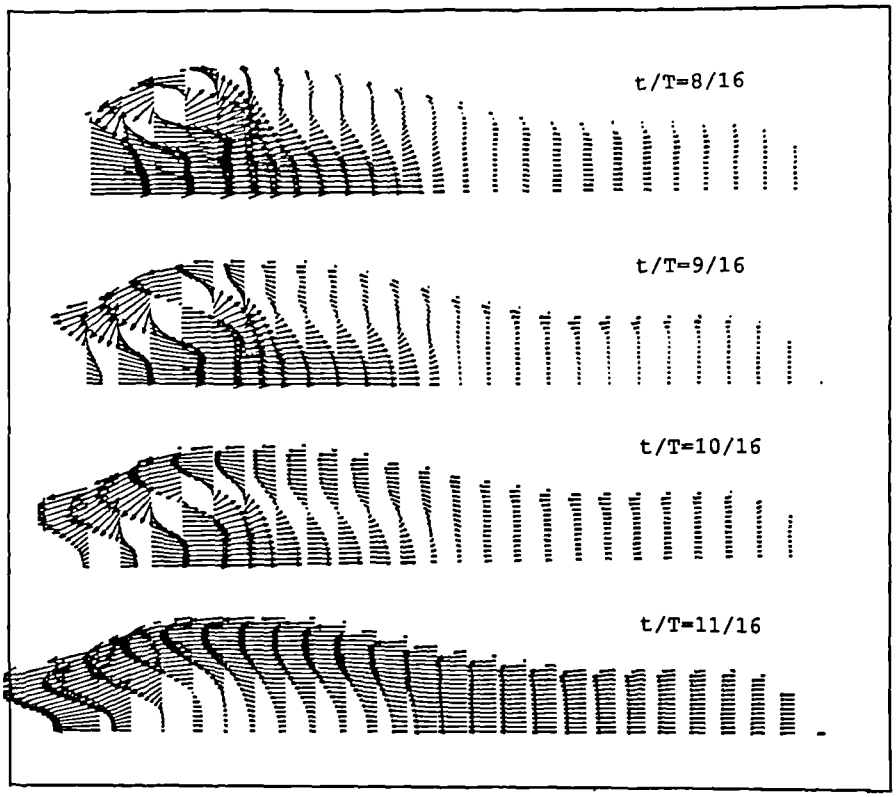


Figure 6.12 Predictions of the flow field inside the SMV for the b1515 data using HIGHER UPWIND advection algorithm.

### 6.3.5 Pressure/Velocity Coupling

FLOW3D (Release 2.4) provided four different pressure/velocity coupling algorithms; SIMPLE, SIMPLEC, PISO and PISOC. The default was SIMPLEC, and this scheme was used in the predictions discussed above. SIMPLEC is a modified version of SIMPLE, and the former has been shown to have better convergence properties. PISOC is a similarly modified version of PISO. As PISO was designed specifically for transient flow calculations, it was decided to see whether its use (actually, PISOC) would have any affect on the prediction. In Fig.6.13 is given the predicted flow field for a time close to maximum ventricle volume using the D data set. It can be seen that the predicted flow is significantly different from that produced using SIMPLEC. Specifically, it contains a double vortex ring structure similar to that seen in the experimental data. However, in the predicted field, the primary vortex, the one closest to the inlet, is much smaller than in the experimental case. Also, while not obvious from the given figure, the second vortex in the predicted field was observed to persist for a longer period of time than was seen in the experimental case. Further, there is some question as to the accuracy of the PISOC solution, as convergence was never fully achieved. There is no reason to expect that solutions produced using SIMPLEC and PISOC should be significantly different, providing each has converged sufficiently. Hence, the PISOC solution must be viewed with some caution.

It should be noted that in this case, the grid was slightly modified at the closed end. While in most of the grid the gridlines in the radial direction were normal to the centreline, at the closed end of the ventricle, the grid was made more non-orthogonal in order to more accurately model the rounded end. An example of the grid is shown in Fig.6.14.

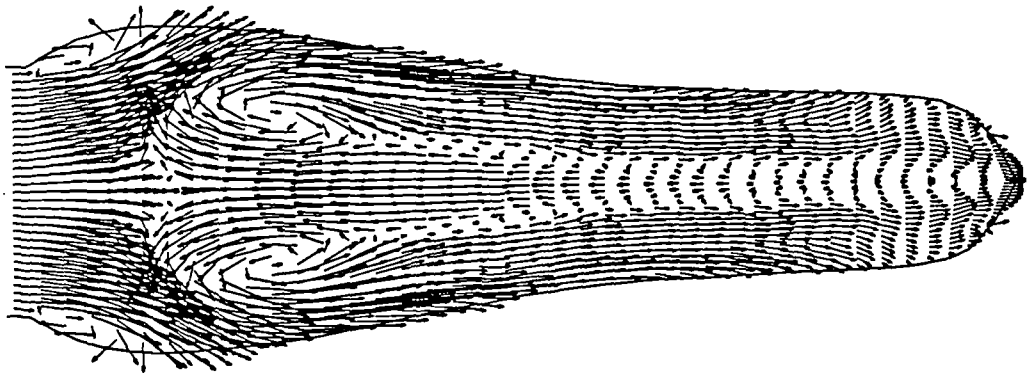

Figure 6.13 Predictions of the flow field inside the SMV for a particular time in the period using PISOC

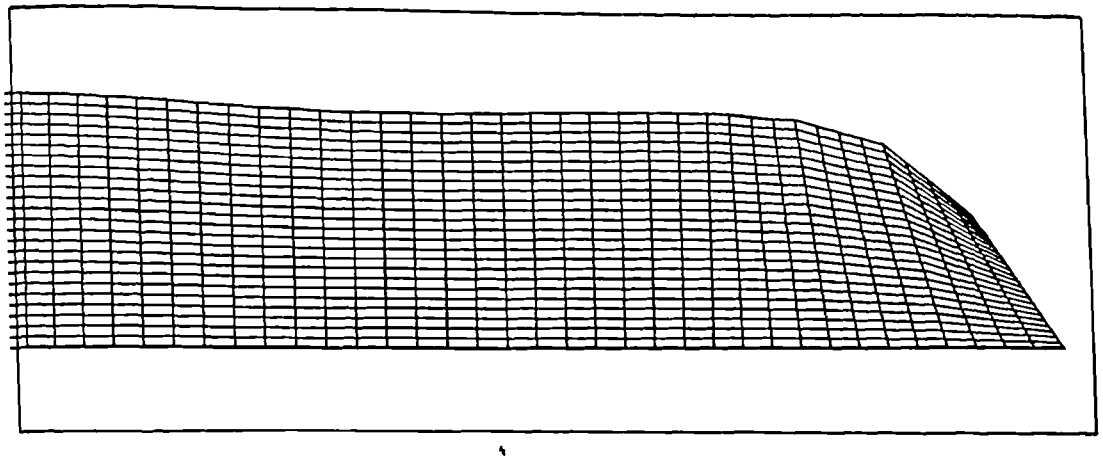

Figure 6.14 Particular of the grid used at the closed end of the ventricle.

## 6.4 SUMMARY

In this chapter, the numerical predictions of model SMVs driven by experimental wall motion have been qualitatively compared with the general features of the flow patterns in the experiments. While the predictions agreed in general with the experimental data, differences were seen about the time of maximum ventricle volume. Specifically, the predicted flow fields exhibited one vortex ring close to the inlet, while the experimental flows had at least two counter rotating vortices. Various refinements of the numerical model, such as increasing the grid density, and using more accurate advection algorithms failed to produce the second vortex. For a possible explanation of this disagreement there is a further discussion in the next chapter where qualitative and quantitative comparisons for another model SMV with experimental wall motion will be discussed.

A flow field that was seemingly better was achieved using PISOC, but as convergence was poor in this case, it is believed that this can not be taken as a true solution. Hence, the reason for this difference has yet to be determined.

# CHAPTER 7

# NUMERICAL SIMULATION OF THE FLOW IN MODEL SKELETAL MUSCLE VENTRICLES WITH SIGMOIDAL[1] FILLING

## 7.1 INTRODUCTION

In this chapter, the numerical predictions of the flow in model SMVs with sigmoidal filling are compared with the experimental data. Three cases with different combinations of filling volume and filling duration are discussed. Qualitative and quantitative comparisons are analysed for two models: (i) an *experimental wall motion model*, and (ii) an *analytical wall motion model.*

Besides the validation exercise of the numerical predictions against the experiments, the study of the dynamics of the flow inside model SMVs has been carried out on physical and numerical models with the objective of analysing the effect of the size and shape of the ventricle and inlet/outlet orientation of the duct. Due to the physiological limit on the power available to pump the blood out of the ventricle, the efficiency of these potential assistance devices has to be maximized. It is also necessary to minimize the risks of haemolysis and thrombogenesis, which are both related, in different ways, to the level of shear stress on the wall and within the flow.

A common feature of the flow in model SMVs is the formation of vortex rings. Vortices enhance mixing, and this is a useful process to encourage in an SMV, as it could assist in the mixing of the blood components and in the reduction of the apical residence time. Being able to predict accurately the dynamics of the vortices is therefore important, as this will affect the prediction of residence times and shear stresses at the wall and within the flow. Therefore, it is very important to know whether CFD codes can predict vortex ring dynamics from both qualitative and quantitative points of view. In order to study the dynamics of the formation of these vortices, sigmoidal filling curves have been used in two *in vitro* models. Vortex rings have been observed in the experiments and vortex core paths have been estimated from the recorded video images. Details of the experimental study are given by Shortland et al (1995). The numerical simulation of these flows is the main topic of this chapter.

The chapter briefly reviews the experimental studies carried out by Dr. Adam Shortland of the University of Liverpool, discussing the important features of the flow patterns in the *in vitro* models. The numerical predictions of the *in vitro* flows in the two models mentioned above will then be discussed. Calculations of instantaneous streamlines and particle pathlines are also analysed. These are very important in the calculation of

[1]Sigmoidal indicates the type of filling curve used to vary the injected volume in the filling phase. The curve is expressed by the function $V(t) = 1 - cos(\omega t)$

residence times to be carried out in the near feature. Finally predicted wall shear stresses are discussed. An initial calculation of the fluid shear stresses concludes the chapter.

## 7.2 EXPERIMENTAL STUDIES

The experimental apparatus has been discussed in detail in the previous chapter. Details of the experiments carried out on model SMVs with sigmoidal filling are given in Shortland et al. (1995). The fluid used is a 40% aqueous-glycerol solution with a density, $\rho$, of $1158 kg/m^3$ and viscosity, $\nu$, of $3.3 mPas$. Injection volumes ranged between 5 and 60 ml, and filling times ranged between 300 and 800 ms. Streak-lines were analysed off-line using a frame grabber together with a computer-generated cursor to measure vortex extent, position, and ventricular dimensions.

### 7.2.1 Description of the Flow Patterns

The dominant feature observed in the ventricle for the case of sigmoidal filling was the formation of a vortex ring, and its subsequent motion towards the apical end. The development of a region of flow separation creates a vortex ring. Then the vortex becomes more voluminous and it is bounded by the incoming jet. When the wall velocity decreases and the jet weakens, the vortex ring diameter decreases and its axial progress slows. Also, the core of the vortex ring increases to occupy the radial extent of the ventricle, and later, the axial velocity increases to approach the same value it had during the filling phase. In some cases, soon after the wall stops moving, a counterrotating vortex ring forms behind the primary vortex.

Vortices were observed to form for nearly all the conditions studied. Usually, the vortex reached the end of the ventricle. The influence of various factors on the characteristics of the vortex formation and travel; e.g., the axial velocity and the diameter of the ring, were all investigated (Shortland et al., 1995).

### 7.2.2 The Experimental Data

The experimental data were provided in the form of recorded radial and axial positions of the ventricle wall measured at 40 ms time intervals. Vortex core positions were also provided. Three different filling curves for the model ventricle shown in Fig.7.1 were simulated numerically. Details of the filling curves are given in Table 7.1.

Table 7.1

Details of filling curves

| CASE | Filling volume (ml) | Filling time (ms) | Average inlet $Re$ | Maximum inlet $Re$ | Average wall $Re$[1] | Maximum wall $Re$ |
|---|---|---|---|---|---|---|
| I | 30 | 500 | 1233 | 1928 | 94 | 154 |
| II | 20 | 800 | 604 | 947 | 48 | 79 |
| III | 20 | 400 | 1191 | 1840 | 89 | 155 |

[1] wall $Re$ is $\frac{|\dot{a}|a}{\nu}$, where a is the current ventricular radius (Uchida and Aoki, 1977).

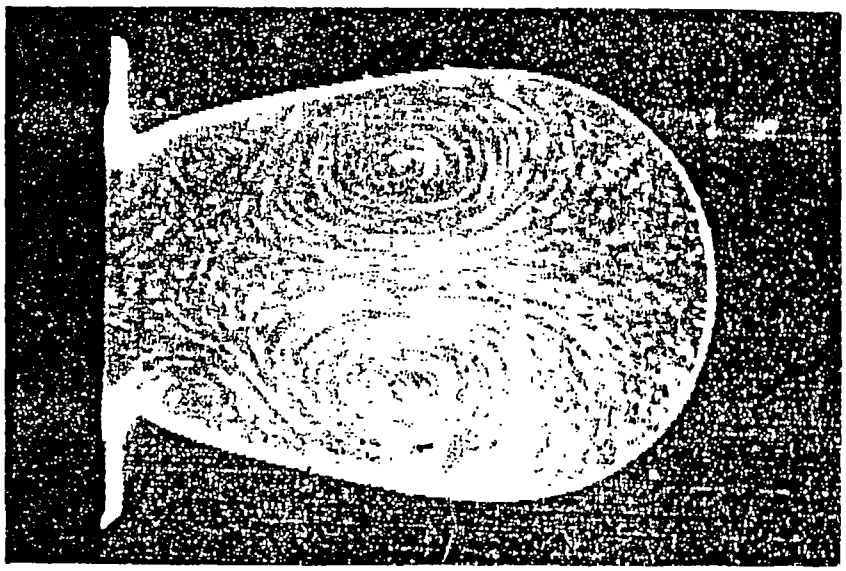

Figure 7.1 Physical model and flow patterns at t=760 ms for CASE I

## 7.3 EXPERIMENTAL WALL MOTION MODEL

Measured wall profiles were used to define the ventricle shape at each time step. Like the *in vitro* case, the numerical model of the ventricle was assumed to be attached to a 30 cm long rigid tube. The other end of this tube was also defined to be at a fixed pressure.

Experimental measurements of the flow in various diametral planes revealed the flow to be axisymmetric, and to remain laminar. Hence the numerical flow was defined to be axisymmetric and laminar. The fluid was assumed to be incompressible and Newtonian. The density was set to be $1.158 \times 10^3 kg/m^3$, and the viscosity to be $3.6 \times 10^{-3} m^2/s$.

The grid comprised three blocks. The multi-block grid allowed a better description of the spherical end of the ventricle than would be possible with a single block. The grid spacing was decreased near solid surfaces, the centre line, and the interface plane between

the rigid tube and the ventricle. This ensured a high grid density in areas of the flow expected to have high gradients.

### 7.3.1 CASE-I: Filling Volume 30 ml - Filling Duration 500 ms

In the first case studied, a volume of 30 ml was drawn in over a period of 500 ms. The flow patterns were observed for a further 500 ms for a total time of observation of 1 s. The experimental wall position data were recorded as described above in the form of 15 data sets (representing 14 time steps) of axial and diametral positions of the wall for each time interval. The numerical model uses these sets to drive the wall motion for 560 ms. (The wall actually stops moving at 500 ms; i.e., between the 12th and 13th time step). Then, without changing the configuration of the compliant wall further, the computation is continued for another 440 ms. The variation of the wall position in the time is shown in Fig.7.2 in terms of axial and radial movement at the axial position I=22 for a data set of 40 equi-spaced points along the ventricle wall. More accurate data were produced with more grid points in the inlet: one with '54 points', and a even more refined set of '103 points'. These refined sets were produced by curve fitting the original 40 equi-spaced points.

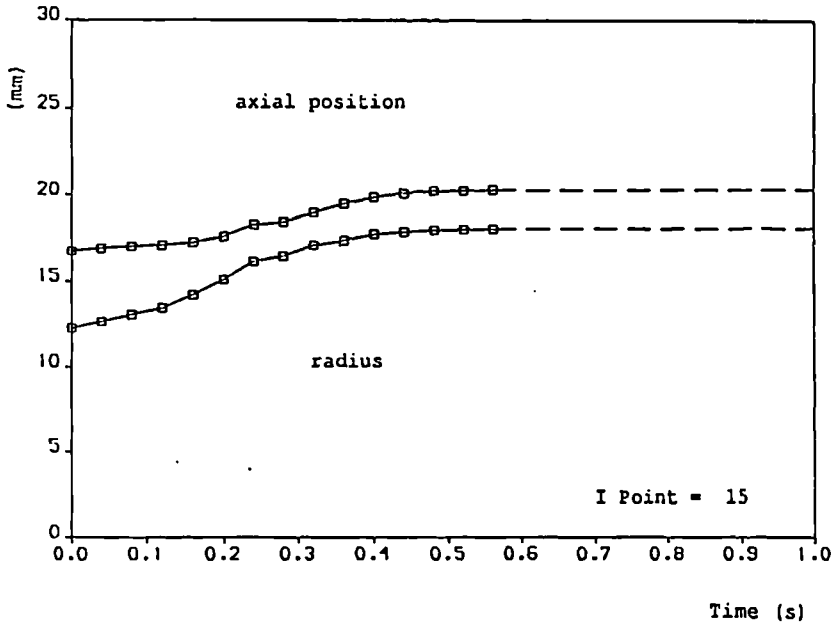


Figure 7.2 Time history of a typical wall point

A parametric study was performed on the '40 point' basic set. An attempt was made to achieve a numerical solution which was independent of all simulation parameters. This is of course a key issue in numerical studies, and comprised the effects of

(i) the grid density,

(ii) the relative radial position of the blocks,

(iii) the time stepping,

(iv) the advection algorithm,

and (v) the inaccuracies of measurement of the density and viscosity.

Also, this study represents a good test of the CFDS-FLOW3D capabilities in simulating the kind of flows in question against experimental solutions.

### 7.3.2 Parametric Study

A summary of the study is shown in the following Table 7.2.

Table 7.2
Parametric Study on the Simulation Parameters.

| Grid Density | | | | |
|---|---|---|---|---|
| $N^0$ of cells | 671 | 1388 | 1908 | 2120 |
| Time Stepping | | | | |
| $\Delta T$=40 ms | YES | YES | YES | YES |
| $\Delta T$ =10 ms | NO | YES | YES | YES |
| Advection Algorithm | | | | |
| HIGHER UPWIND | YES | YES | YES | YES |
| HYBRID | NO | YES | YES | YES |
| CENTRAL | NO | YES | NO | NO |
| UPWIND | NO | YES | NO | NO |
| CONDIF | NO | YES | NO | NO |
| QUICK | NO | YES | NO | NO |

Initially a grid of 671 cells was used. With this grid only the second-order upwind advection model known as HUW was used as previous results had showed it to be satisfactory (see chapter 5). The time step was set to 40 ms, and 100 iterations per time step were found necessary to reach satisfactory convergence. Then, the grid was refined in the radial direction. The resulting grid had 1388 cells (see Fig.7.3). Initial calculations with the new grid again used HUW, $\Delta T = 40ms$ and 100 iterations per time step. Predicted flow patterns are shown in Fig.7.4 at relevant times in the simulation and these will be discussed in the next section. The vortex ring travels towards the apical end of the ventricle in a similar fashion to that seen in the *in vitro* simulations. The predicted and experimental axial positions of the vortex core at each time step is given in Fig. 7.5(a), and the corresponding variation of radial position, which also represents the vortex ring radius, is given in Fig. 7.5(b). The two are combined in Fig.7.6 to give the time history of the vortex core; i.e., the path the vortex core would be seen to take in the experimental rig. The vortex core position at each time step was determined using a program which calculates the location of the minimum velocity in a certain specified domain assuming that locally the velocity behaves as a biquadratic function of the computational space. Details are presented in APPENDIX G.

As can be seen in the plots of Fig.7.5, significant differences between experiment and prediction exist, and several refinements to the numerical model were performed. The grid refinement produced an improvement of the results both in the prediction of the qualitative features of the flow field development and the evaluated position of the vortex core with time (compare Fig.7.5 with Fig.7.7). However, an error of about 40% in the radial predicted position against the experimental data still existed. A time step of 10 ms was tried. In order to use a smaller time step than that of the wall data, some form of interpolation had to be performed. In this case linear interpolation was used. The predictions were found to be sensitive to the grid density but not to the time step.

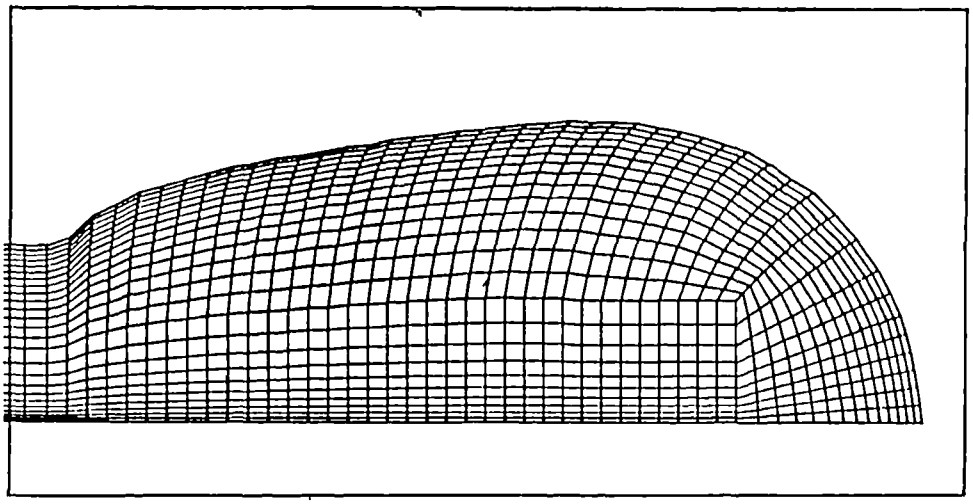

Figure 7.3 Grid (1388 cells) used in the numerical model at maximum volume

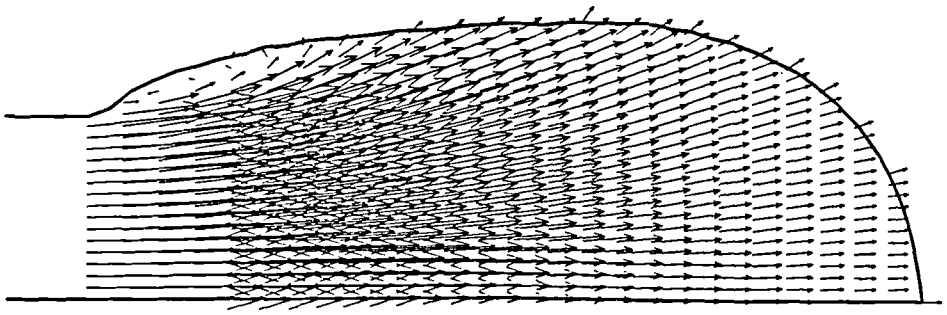

(a)

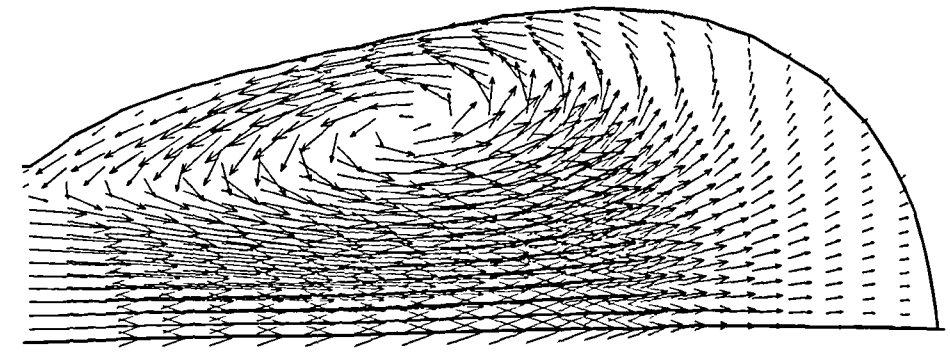

(b)

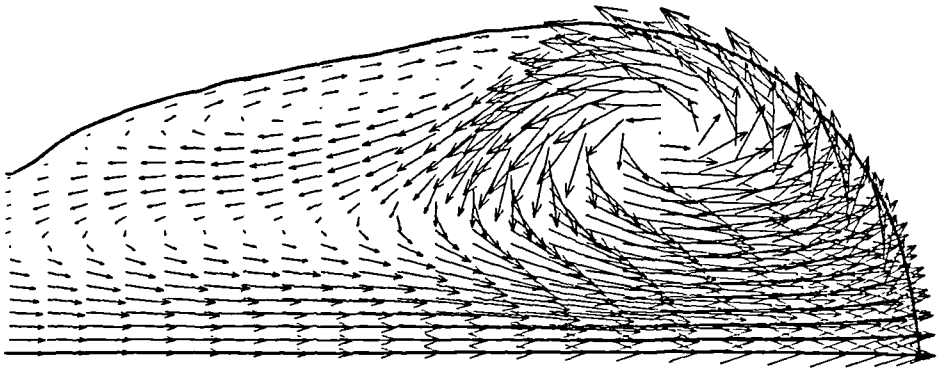

(c)

Figure 7.4 Predicted flow patterns at relevant times in the simulation (a) 240 ms; (b) 480 ms; (c) 1.0 s

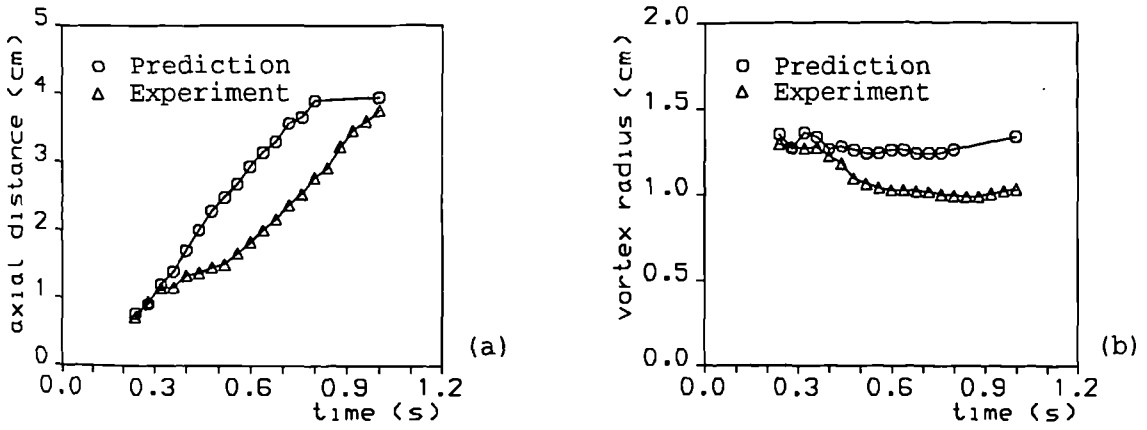


Figure 7.5 (a) Axial position of vortex core and (b) Vortex ring radius over simulation time; 1388 cells, HUW, DT=40 ms, Iterations/time step=100

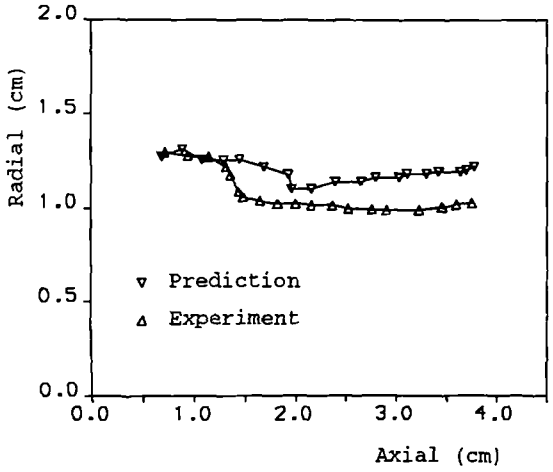


Figure 7.6 Vortex core path; 1388 cells, HUW, DT=40 ms, Iterations/time step=100

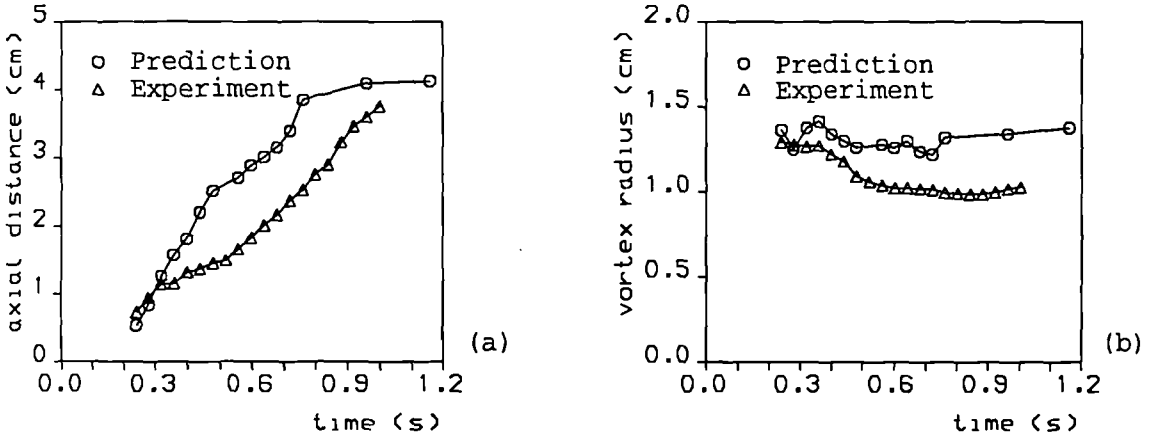


Figure 7.7 (a) Axial position of vortex core and (b) Vortex ring radius over simulation time; 671 cells, HUW, DT=40 ms, Iterations/time step=100

Various advection models were also tested. All the advection algorithms available in FLOW3D were tried: CENTRAL, UPWIND, HYBRID, HIGHER UPWIND, CONDIF, QUICK. In all cases a 1388 cell grid, $\Delta T = 40ms$, and 100 iterations per time step were used. A non-divergent solution could not be obtained with Central differencing. However, CONDIF, QUICK, and HUW all converged and produced more or less the same flow patterns, as can be seen in Fig. 7.8. The predictions using HYBRID showed a very different result, and, somewhat surprisingly, were the closest to the experimental data in terms of vortex core positions. It is known that the HYBRID scheme uses central-differencing for a cell Peclet number between -2 and 2, and that outside this range it reduces to (first-order) Upwinding (Patankar, 1980). Comparison of the plots for HYBRID and (first-order) Upwinding in Fig. 7.9 suggest that the HYBRID calculation used Upwinding for the first 360 ms of simulation. At later times, the two predictions were not identical, suggesting that, at least in some areas, HYBRID was central-differencing. The comparisons between the numerical and experimental solutions are in Figs. 7.10 and

7.11, while the predicted flow patterns are in Fig.7.12.

Further tests were made with a grid of increased density in the radial direction and in the axial direction in the inlet/outlet tube, using the HYBRID scheme, but no significant change in the resulting flow fields were found. Also reducing the time step to 10 ms and changing the relative radial position of the blocks led to the same results. Using finer grids of 1908 and 2120 cells gave the same results as before, even with HUW.

In order to test the effects of possible inaccuracies in the measurement of the viscosity and density on the resulting computed flow field, the values provided were varied by $\pm 5\%$ and then by $\pm 25\%$. A variation of $\pm 5\%$ produced no noticeable change. A slight change was found for larger variations; however, this large an error would almost certainly not occur in practice. Also, it can be expected that the dynamics of filling the ventricle with a fluid with such different properties would result in a different wall motion. Hence, the validity of predicting the dynamics of filling using ventricle wall profiles taken for a fluid of significantly different properties is questionable. Examples of the flow field at the end of the running time are shown in Figs. 7.13 to 7.16.

QUICK

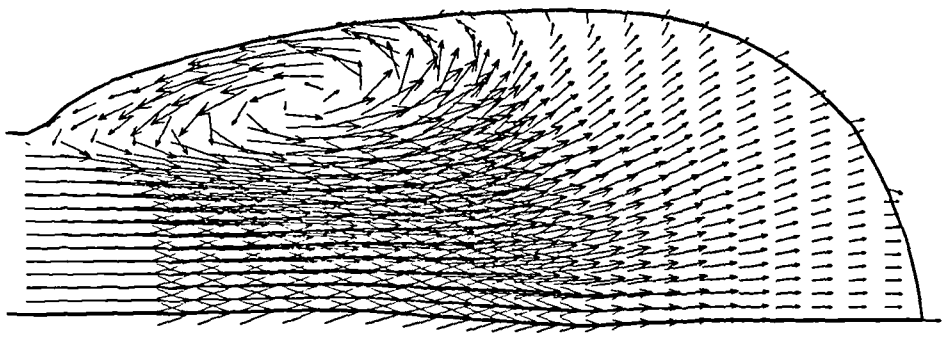

(a)

CONDIF

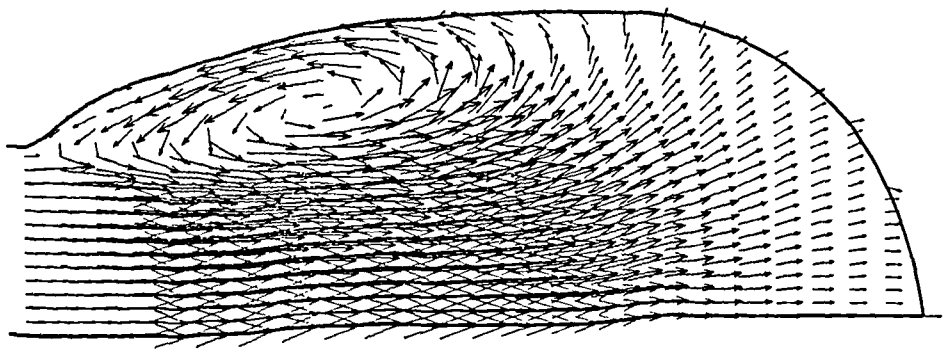

(b)

HUW

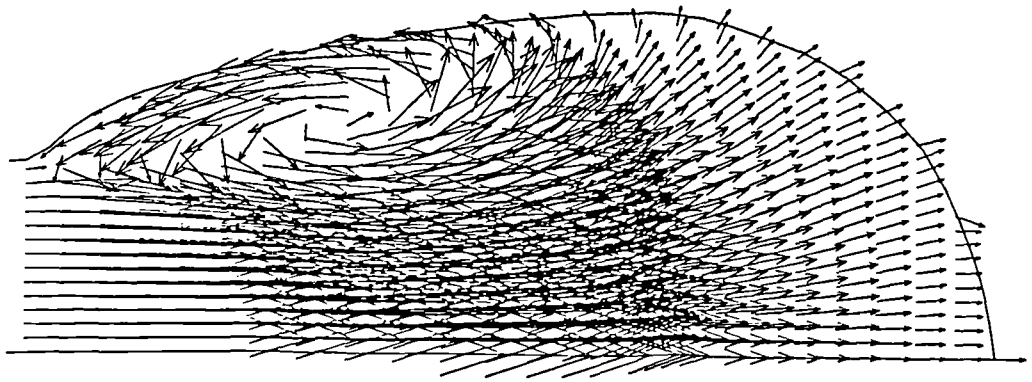

(c)

Figure 7.8 Comparison of the flow field using (a) QUICK; (b) CONDIF; (c) HUW

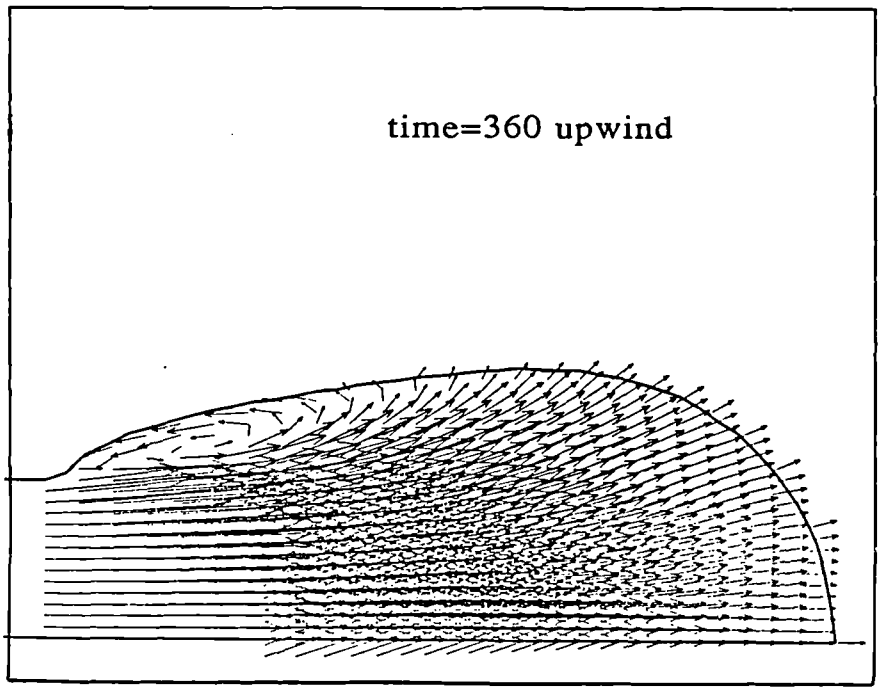


Figure 7.9 Predicted flow patterns at 360 ms using UPWIND advection algorithm

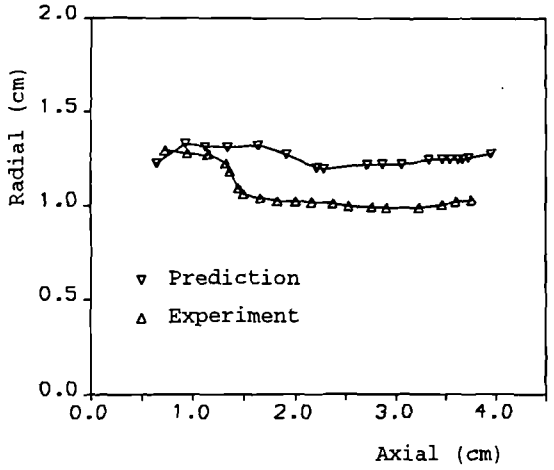


Figure 7.10 Vortex core path; 1388 cells, HYBRID, DT=40 ms, Iterations/time step=100

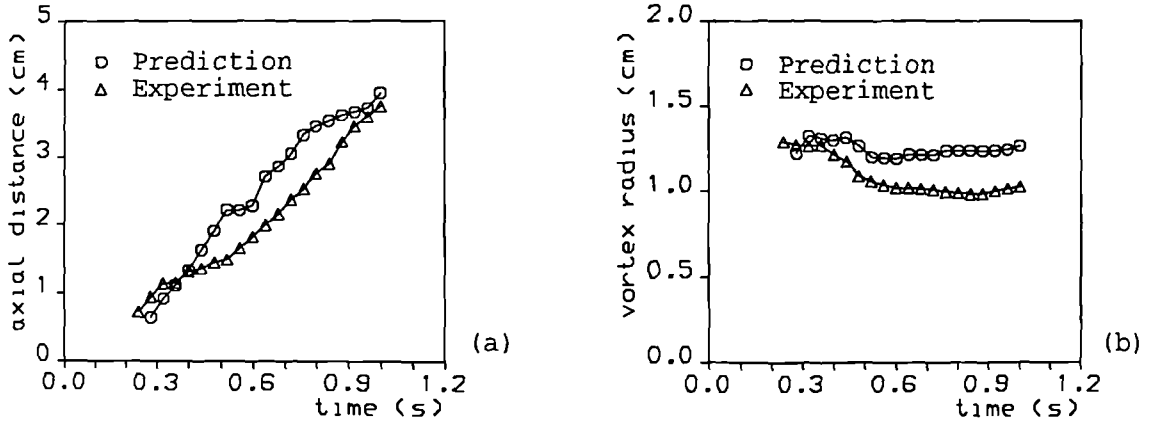


Figure 7.11 (a) Axial position of vortex core and (b) Vortex ring radius over simulation time; 1388 cells, HYBRID, DT=40 ms, Iterations/time step=100

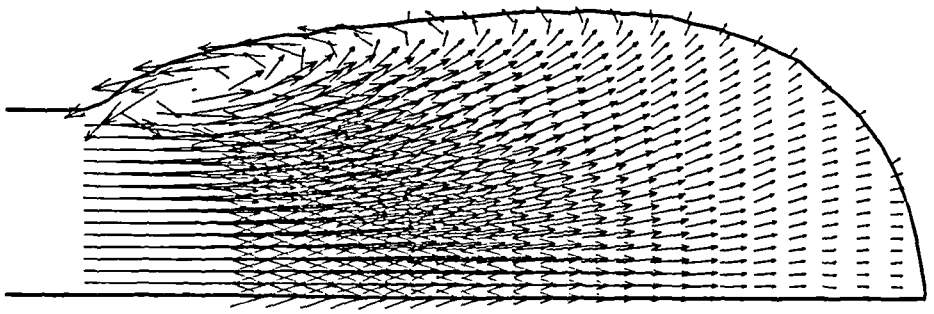

(a)

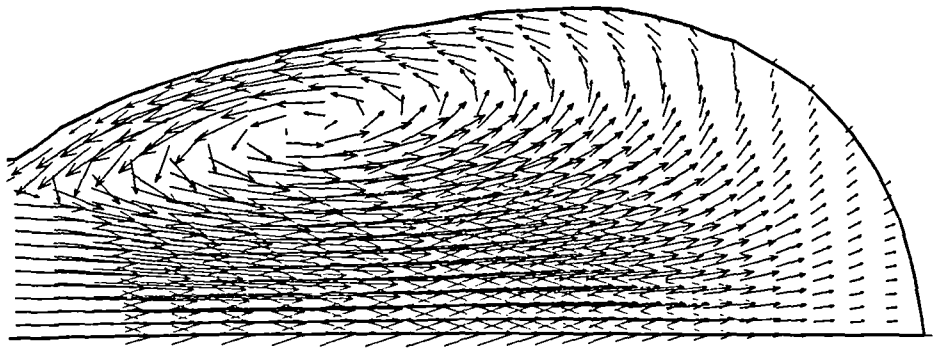

(b)

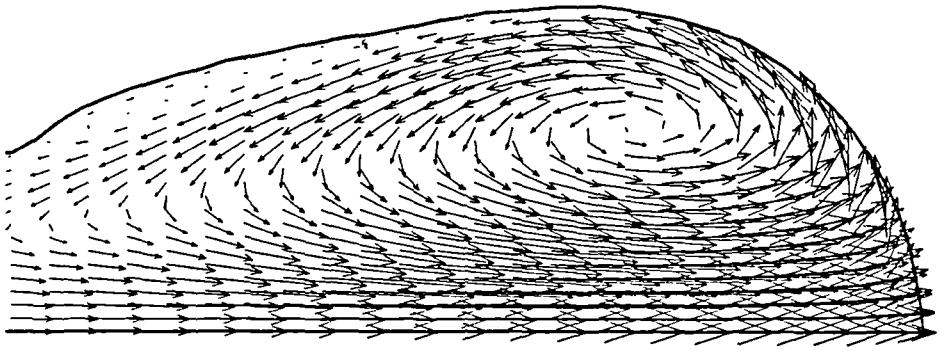

(c)

Figure 7.12 Predicted flow patterns using HYBRID at relevant times in the simulation (a) 280 ms; (b) 480 ms; (c) 1.0 s

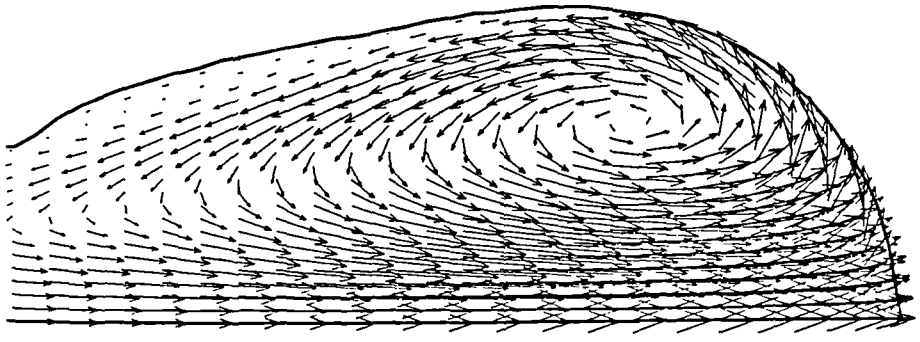

(a)

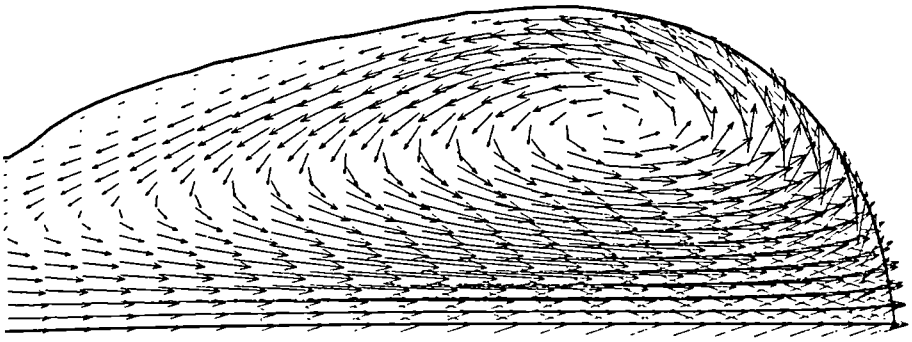

(b)

Figure 7.13 Predicted flow patterns for variation of the fluid properties (a) $\rho$=1.1172×10$^3$ kg/m$^3$ (b) $\rho$=1.2348×10$^3$ kg/m$^3$

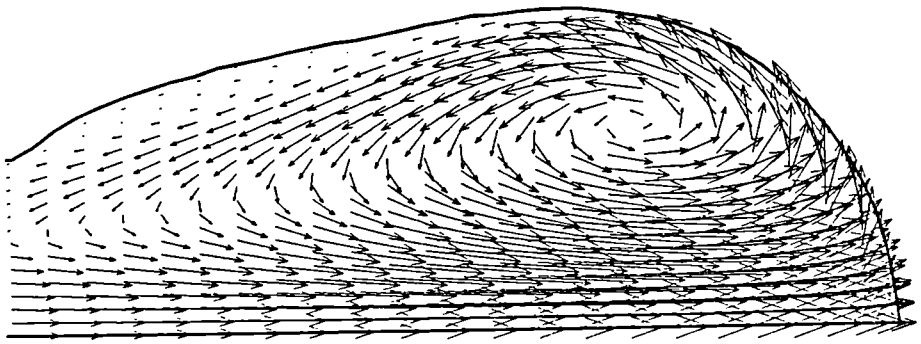

(a)

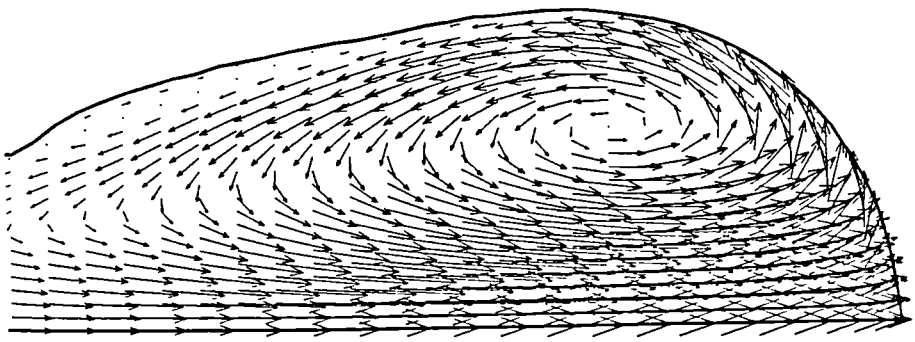

(b)

Figure 7.14 Predicted flow patterns for variation of the fluid properties (a) $\rho$=0.882×10$^3$ kg/m$^3$ (b) $\rho$=1.47×10$^3$ kg/m$^3$

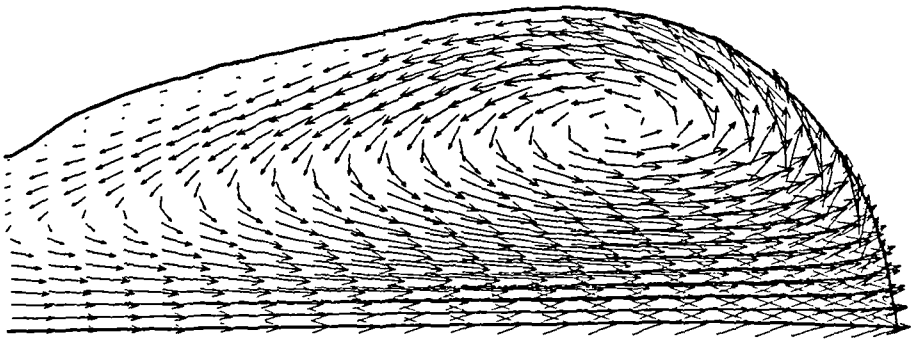

(a)

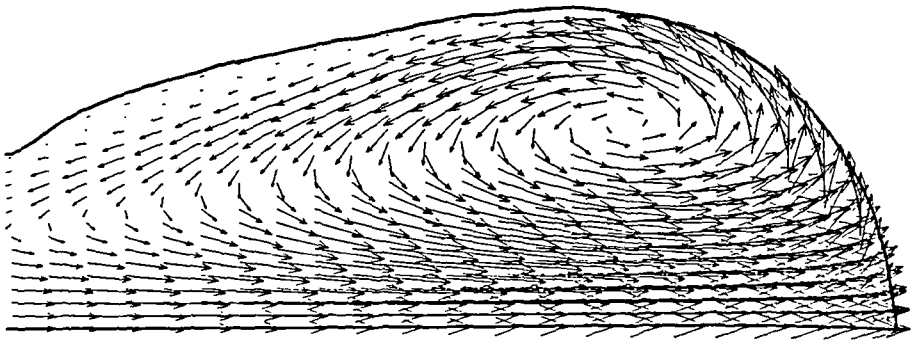

(b)

Figure 7.15 Predicted flow patterns for variation of the fluid properties (a) $\mu$=3.42×10$^{-3}$ Pa s (b) $\mu$=3.78×10$^{-3}$ Pa s

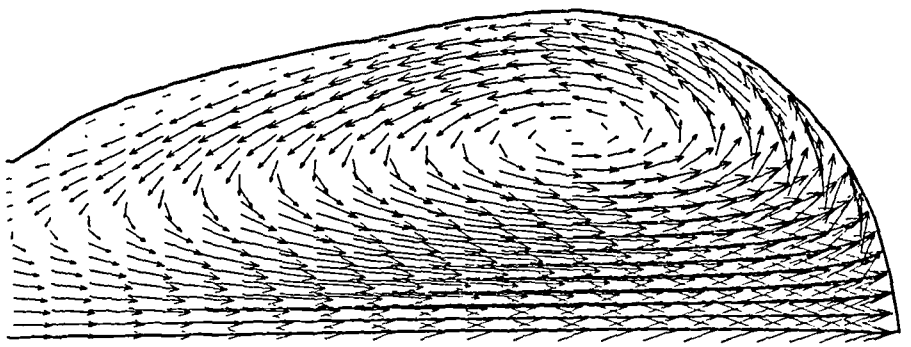

(a)

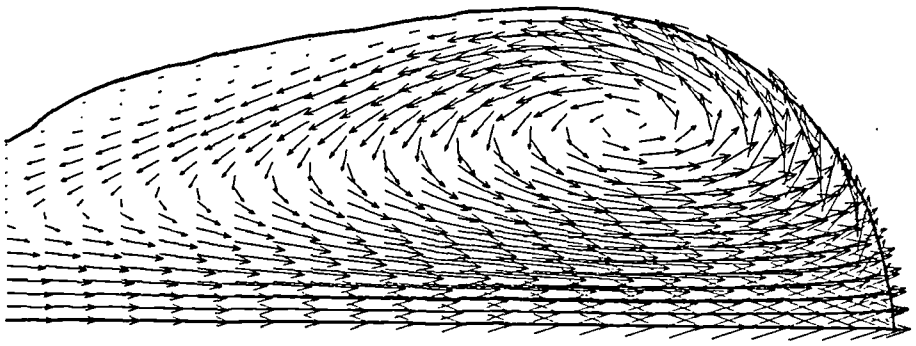

(b)

Figure 7.16 Predicted flow patterns for variation of the fluid properties (a) $\mu$=1.8×10$^{-3}$ Pa s (b) $\mu$=4.5×10$^{-3}$ Pa s

### 7.3.3 Refinement of the Experimental Data

A refinement of the experimental data was required in order to have a larger number of data points at the entrance of the ventricle. In fact, it was found that the accuracy of the outlines at the inlet of the expanding section, and then of the velocity of the wall, were important in predicting the dynamics of the vortex formation and, hence, of its motion. Two sets were provided; termed '54 points' data set and '103 points' data set. At the initial stages of vortex formation the shape of the vortex resembled more closely that seen in the experiments. However, the overall results of this refinement only slightly changed the flow patterns at later times.

The predicted results seem to have a slight change in the flow patterns with data sets of 54 and 103 points. The flow field is more circular and especially with the first set ('54 points') a better matching of the vortex path was seen. Comparison between predictions and experimental data are given in Figs 7.17 to 7.20 for '54 data' case and in Figs. 7.21 to 7.24 for '103 data' case. Comparisons for different grids are given in Fig.7.25.

Using the '54 points' data set, the grid had 1724 cells ( see Fig. 7.26) and 100 iterations per time step were necessary to achieve convergence. However, the '103 points' data set produced a grid of 2900 cells (Fig. 7.27), and convergence was obtained with 200 iterations per time step.

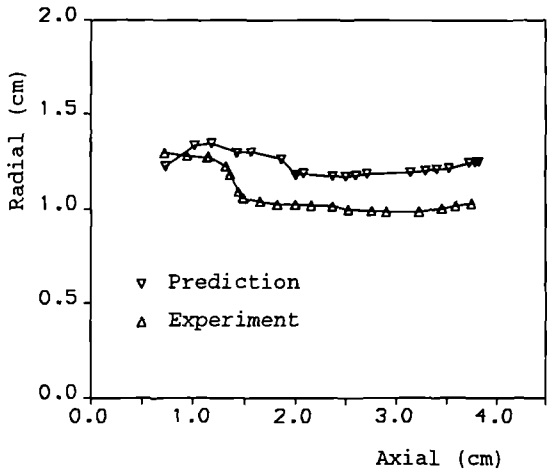


Figure 7.17 Vortex core path; 1724 cells, HYBRID, DT=40 ms, Iterations/time step=100

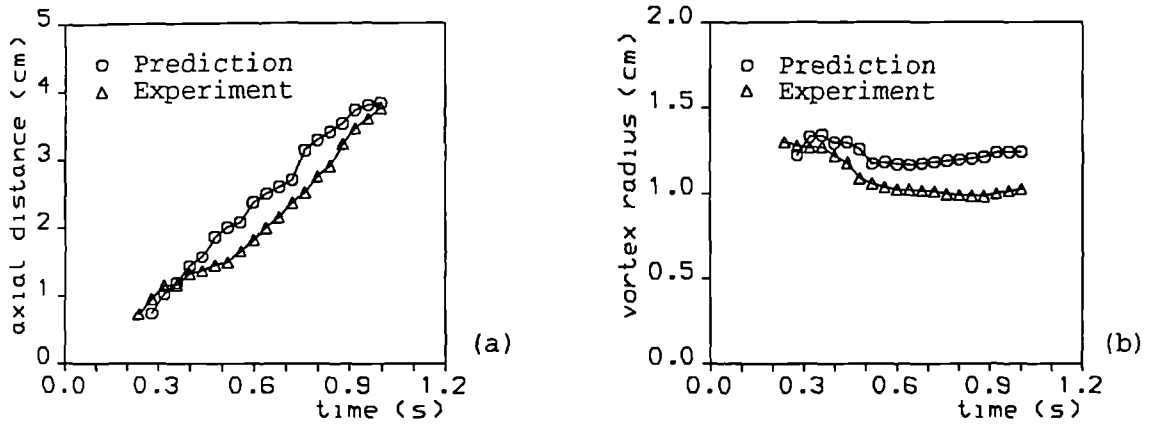


Figure 7.18 (a) Axial position of vortex core and (b) Vortex ring radius over simulation time; 54 data points; 1724 cells, HYBRID, DT=40 ms, Iterations/time step=100

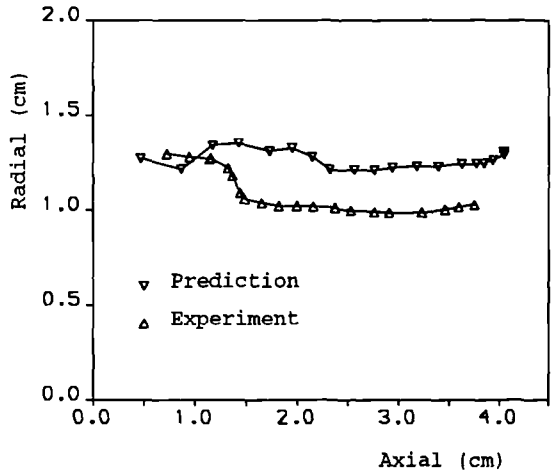


Figure 7.19 Vortex core path; 1724 cells, HUW, DT=40 ms, Iterations/time step=100

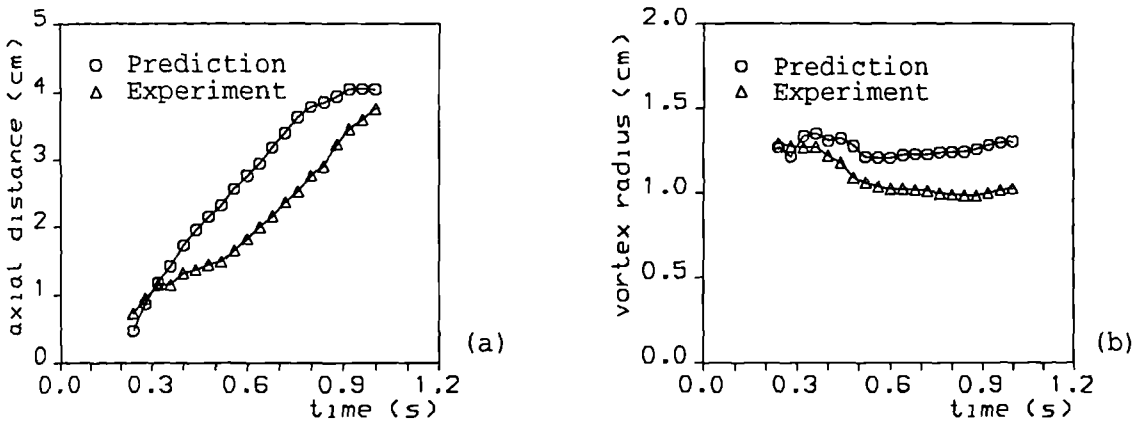


Figure 7.20 (a) Axial position of vortex core and (b) Vortex ring radius over simulation time; 54 data points; 1724 cells, HUW, DT=40 ms, Iterations/time step=100

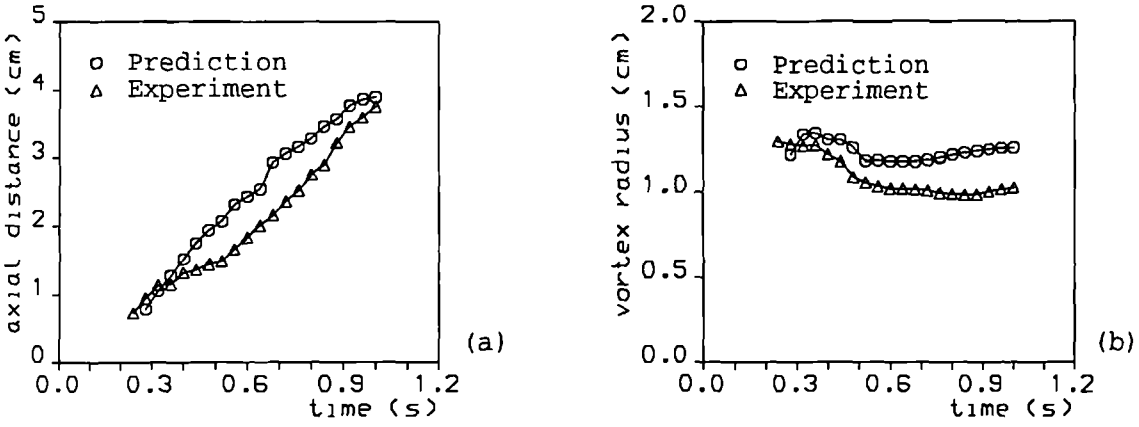


Figure 7.21 (a) Axial position of vortex coreand (b) Vortex ring radius over simulation time; 103 data points; 2900 cells, HYBRID, DT=40 ms, Iterations/time step=200

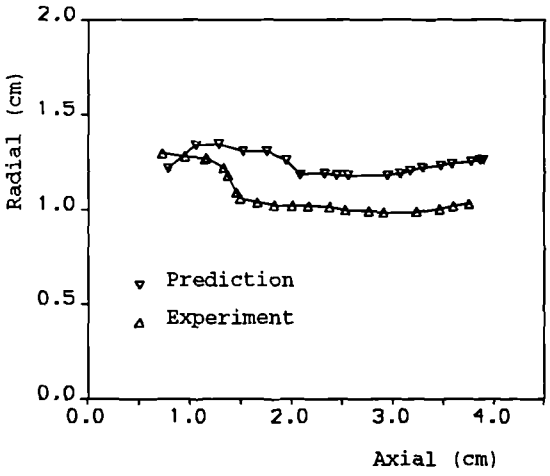


Figure 7.22 Vortex core path; 2900 cells, HYBRID, DT=40 ms, Iterations/time step=200

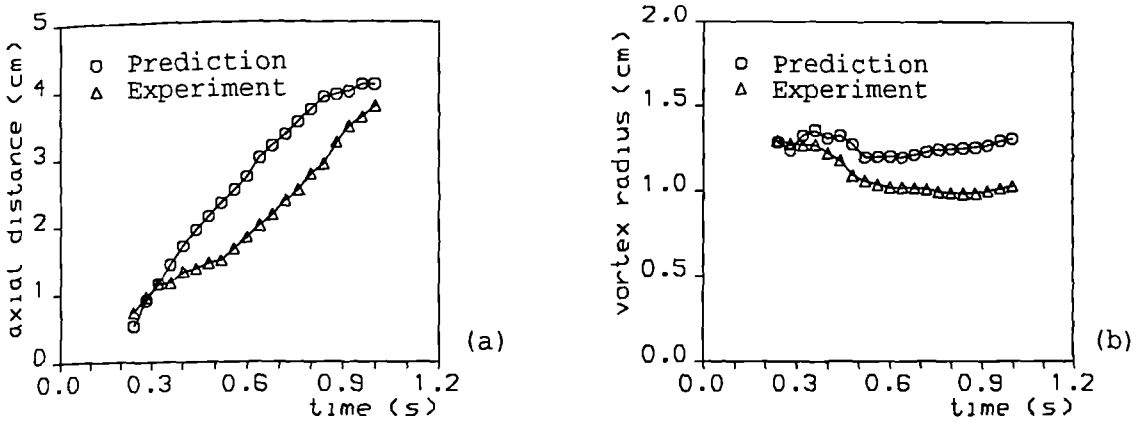


Figure 7.23 (a) Axial position of vortex core and (b) Vortex ring radius over simulation time; 103 data points; 2900 cells, HUW, DT=40 ms, Iterations/time step=200

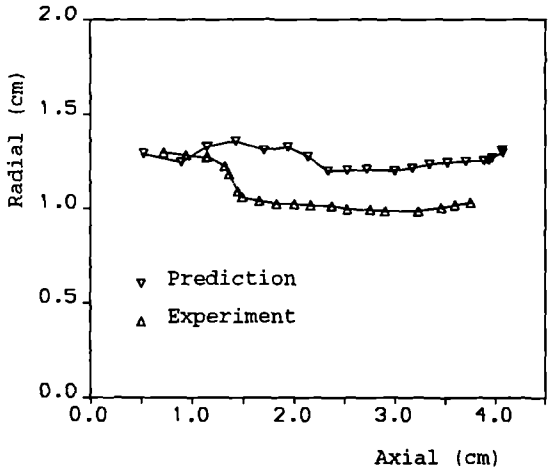


Figure 7.24 Vortex core path; 2900 cells, HUW, DT=40 ms, Iterations/time step=200

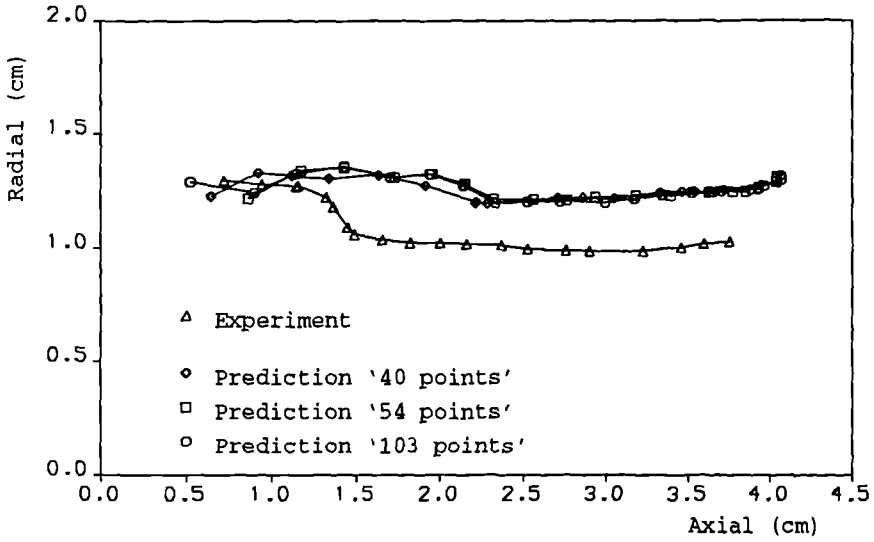


Figure 7.25 Vortex core path for different grids HYBRID, DT=40 ms

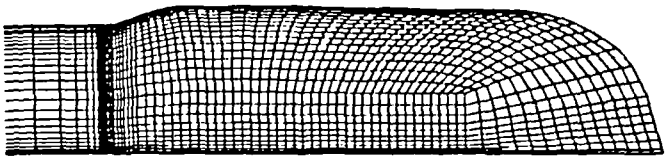

Figure 7.26 Grid for '54 data points' at minimum volume

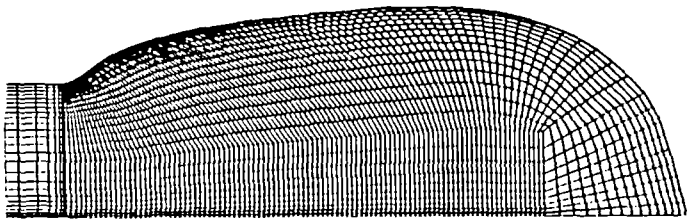


Figure 7.27 Grid for '103 data points' at t=280 ms

### 7.3.4 Discussion of the Results

CASE-I

From the comparisons between experimental and numerical results, it appears that the code predicts the general features of the flow driven by the wall motion; however, the dynamics of the vortex rings have not been well predicted, in general. Travelling velocity, core position and the flow patterns are still not very satisfactorily predicted; however the time of formation of the vortex was predicted with reasonable accuracy.

It is possible to distinguish, from the parametric study just presented, that the code used can give two numerical solutions: one using HUW and another using HYBRID. The former predicts the formation of the first vortex at 240 ms, which is the same as that observed in the experiments; and the latter predicts the vortex appearing 40 ms later, that is, at 280 ms. Also, the vortex ring seen in the experiments looks very circular

and large while the one predicted in the HYBRID case is more elliptical and smaller at the beginning. However, later, it becomes larger and appears to fill all the volume of the ventricle. This is not seen in the experiments. The vortex is always circular and compact. The shape and extent of the vortex are obviously relevant in residence time calculations.

Unfortunately, at the moment, we do not have any measure of the velocity patterns inside the *in vitro* ventricle nor of the shear stresses involved. If the predicted flow patterns agreed with the experiment, then we would have had confidence that the predictions of shear stress were reasonably accurate. But we cannot say that the velocities are the same in our case because the vortex dynamics are different. The fact that the predicted vortices are elliptical suggests an effect of numerical diffusion in the axial direction. In any case it is not desirable from the hemodynamic point of view to have such a flow field for a skeletal muscle ventricle. Plots of instantaneous streamlines are in Fig. 7.28 for certain times in the filling. These clearly show the more elliptical shape of the vortex produced. Inspection of the results generated with HUW, shows the predicted vortex to be more circular and to appear at the same time as that seen in the experiments. However it is very fast and its radius is larger (see Fig.7.4). The appearance of the second vortex is predicted correctly again, while it is late with HYBRID.

If we examine the dynamics of the vortex from the time it appears to when the wall stops moving, we can see that, in the experiments and in the numerical predictions, the vortex appears approximately in the same place. While the wall is moving, the vortex is predicted to travel faster towards the apical end than in the experimental case. The predicted radial position is always above the measured values. When the wall stops, the measured vortex changes its axial and radial velocity. The vortex core, which was midway between the jet and the wall, is not now supported by the jet, and so it reduces its radius. The radius starts decreasing when the velocity of the wall is very small and then it remains relatively unchanged, slightly increasing following the shape of the ventricle end. The axial velocity of the vortex ring is almost constant, but it decreases at the end of the simulation because it nears the end of the ventricle.

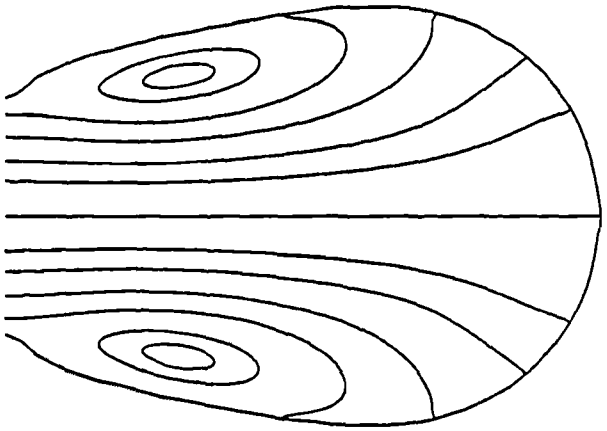

(a)

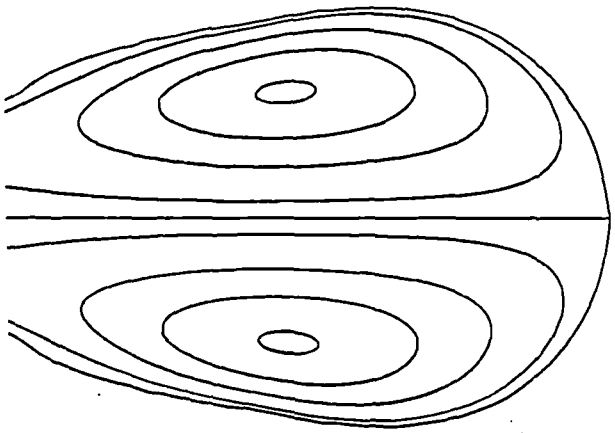

(b)

Figure 7.28 Instantaneous Streamlines at (a) t=0.44 s; and (b) t=0.64 s

In the numerical predictions it seems that the overall flow is affected by the reduction of the velocity with a certain delay. This is clearly shown in the HYBRID case where the axial and radial velocities of the vortex change with a certain delay with respect to the experimental data. When HUW was used, the velocity of the vortex core seemed to be unaffected by the reduction in wall speed. At later times in the simulation the predicted experimental vortices travel at approximately the same speed, but as the predicted vortex had a higher initial speed it is always ahead of the experimental vortex. Hence it travels with a constant velocity, but it is sited in different places at equal times in the numerical predictions and in the experiments. The radial position of the vortex is predicted to be above the position assumed in the experiments, although the same velocity can be assumed. A better numerical prediction of the step in velocity, occurring at the time the wall motion arrests, is obtained with the more refined sets. In this case the step is very clear even though still late and less sharp.

### 7.3.5 CASE-II: Injection Volume 20 ml - Filling Duration 800 ms

In this case the mean velocities are smaller, but qualitatively, the resulting flow fields are similar to the previous case. An experimental data set of 54 points was used in the numerical simulations. The first vortex is predicted to appear later than seen in experiment (at 320 ms with HYBRID and HUW). Between 320 ms and 520 ms, the vortex is weak and unstable (it is seen to go forwards and backwards); after which it is clearly distinguishable. It is not evident whether this is seen in the experiments. As in the other case, the predicted vortex is quicker in the axial direction compared with the experimental data, and after the wall stops, the radial position reflects the step more smoothly and late. These features are more accentuated for the prediction using HUW, when a second vortex appears just at the end of the time of simulation of 1 s. This was

not seen using HYBRID. Results are compared in Fig. 7.29 to 7.32. The predicted flow field at the end of the time of simulation is shown in Figs.7.33 and 7.34 for HYBRID and HUW respectively.

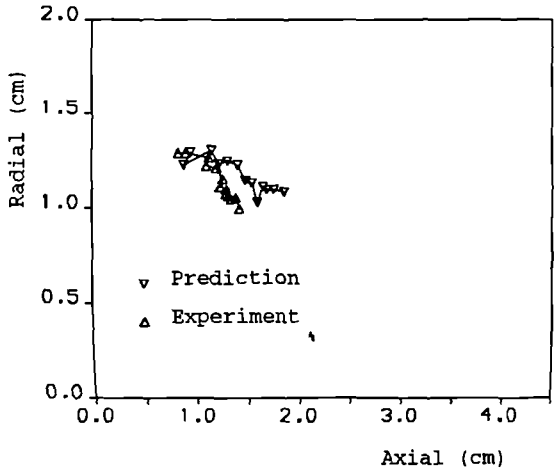


Figure 7.29 Vortex core path: CASE II; 1724 cells, HYBRID, DT=40 ms, Iterations/time step=100

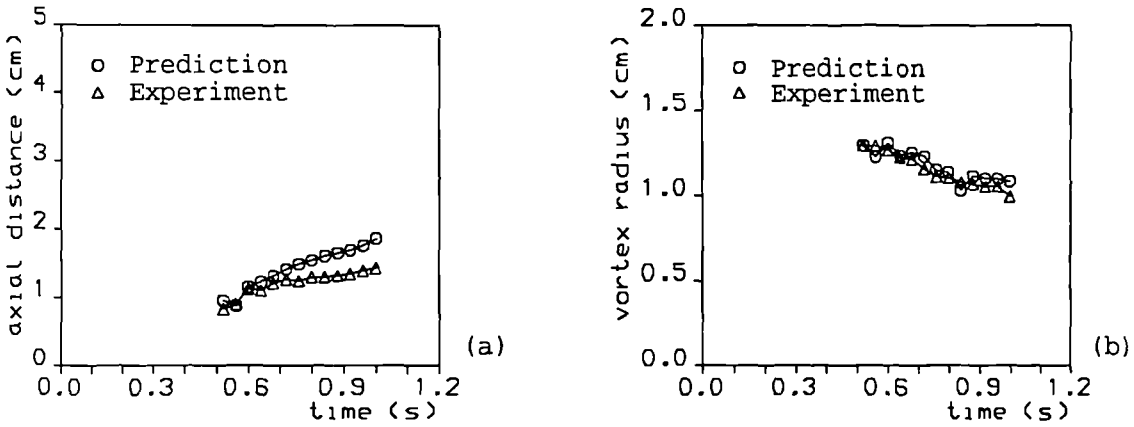


Figure 7.30 (a) Axial position of vortex core and (b) Vortex ring radius over simulation time. CASE II; 1724 cells, HYBRID, DT=40 ms, Iterations/time step=100

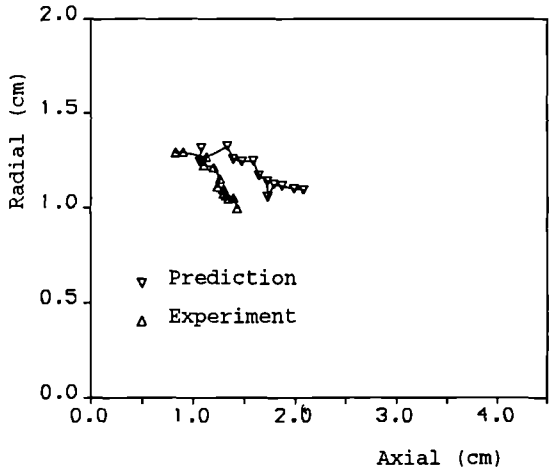


Figure 7.31 Vortex core path: CASE II; 1724 cells, HUW, DT=40 ms, Iterations/time step=100

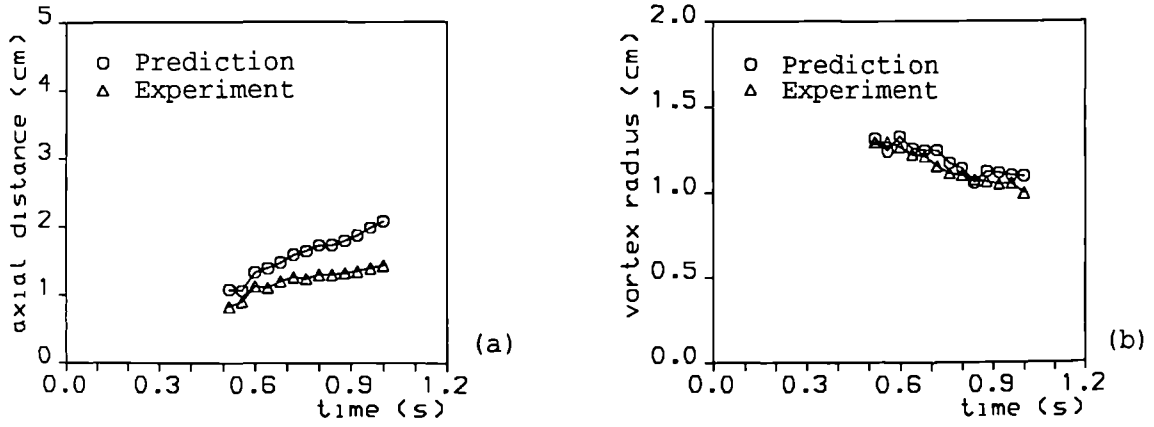


Figure 7.32 (a) Axial position of vortex core and (b) Vortex ring radius over simulation time. CASE II; 1724 cells, HUW, DT=40 ms, Iterations/time step=100

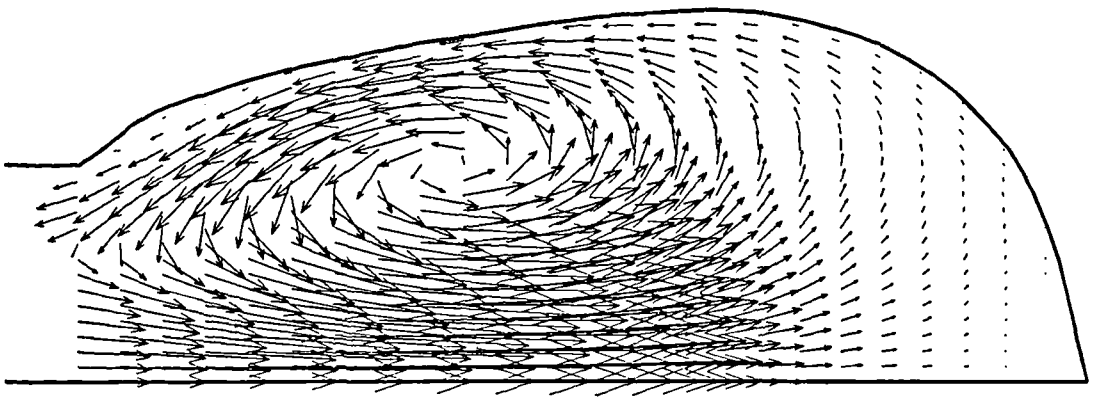

Figure 7.33 Predicted flow patterns for CASE II; HYBRID; t=1.0 s

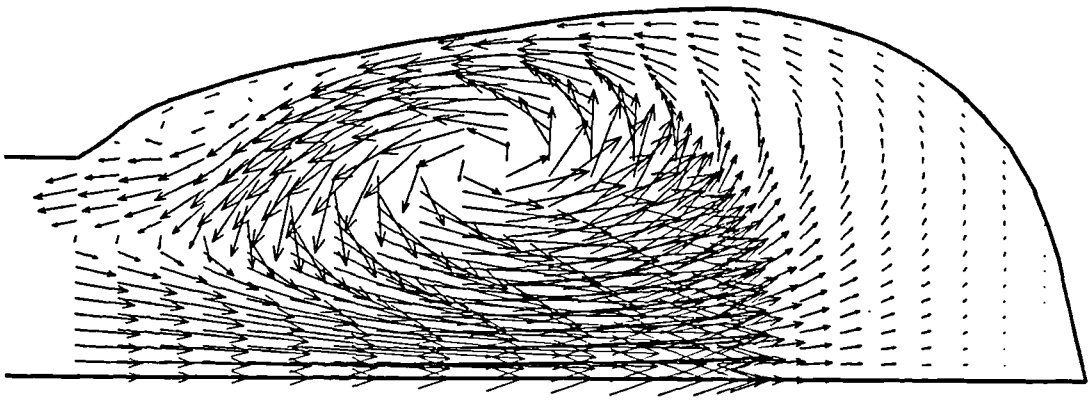

Figure 7.34 Predicted flow patterns for CASE II; HUW; t=1.0 s

### 7.3.6 CASE-III: Injection Volume 20 ml - Filling Duration 400 ms

In the last case simulated, the mass of liquid drawn in was the same as in CASE-II, but the duration of the filling was halved. This caused a very fast filling of the ventricle. While the average rate of filling was as in Case I, maximum instantaneous values were

higher. However, the formation of the vortex, both in the experiment and in the numerical predictions, was at 240 ms, which is the same time as CASE-I. This would suggest that 240 ms might be a minimum time required for vortex formation for any injected volume and duration of the filling, at least in the range of values used.

It seems also that the faster the filling, the better the numerical solution can approximate the time of formation of the vortex ring. In fact both HYBRID and HUW advection algorithms predicted that the vortex appeared at 240 ms.

Unfortunately, later in the simulation, the predictions do not match well the experimental results. In fact, the vortex is predicted to speed up either using HYBRID or HUW with a much higher velocity toward the end of the ventricle, so that, at the end of the simulation of 1 s, the vortex ring has reached the apical end of the ventricle, while in the experiments it is only just past the middle of the ventricle.

A second vortex was predicted to form at the back of the main one after 520 ms with HUW and after 680 ms with HYBRID. Experimental evidence of this occurence is inconclusive. In the HUW prediction, a third recirculation region is established at the end of the time of simulation, as can be seen in Fig.7.35. This is not present in the HYBRID prediction, see Fig.7.38.

Other comparisons of the vortex path are shown in the plots of Figs.7.37-40. The predicted results displayed for this case reported the maximum disagreement with the experimental data. This is thought to be due to the fact that, in the last case, the filling velocity is higher than in the other cases and CFDS-FLOW3D is not capable of predicting very well, quantitatively, flows with boundaries moving at high speed. Although predicting flow patterns very similar to HUW, the CONDIF advection algorithm predicted slight differences in the patterns of the vortex motion, as may be seen in Figs.7.41 and 7.42.

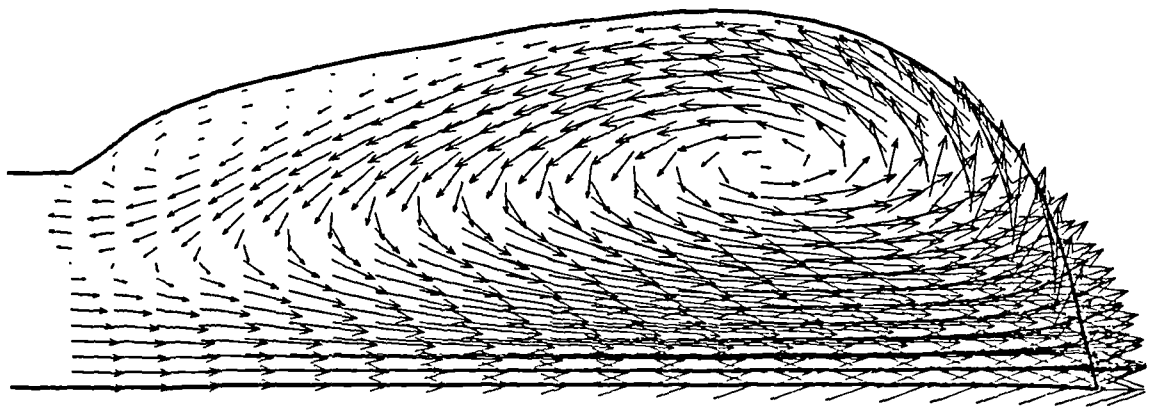

Figure 7.35 Predicted flow patterns for CASE III; HYBRID; t=1.0 s.

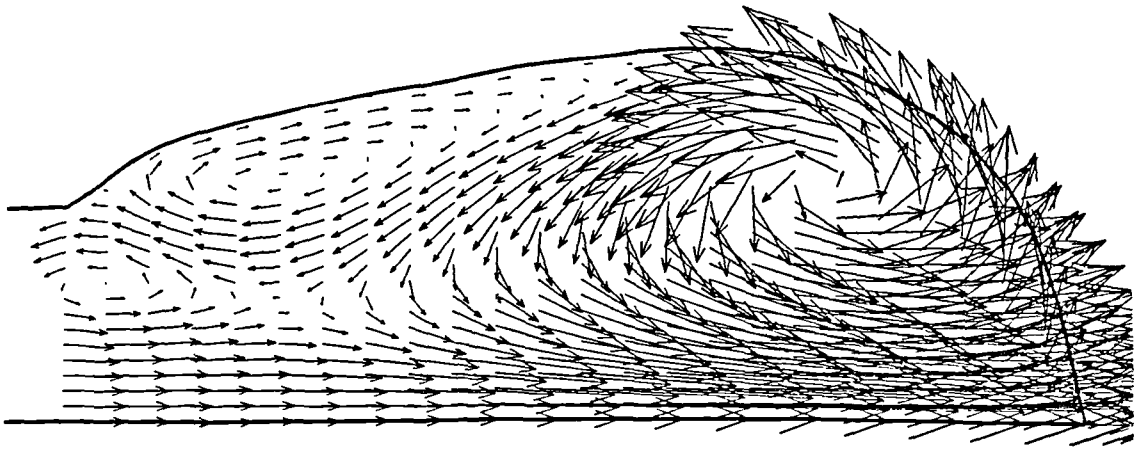

Figure 7.36 Predicted flow patterns for CASE III; HUW; t=1.0 s.

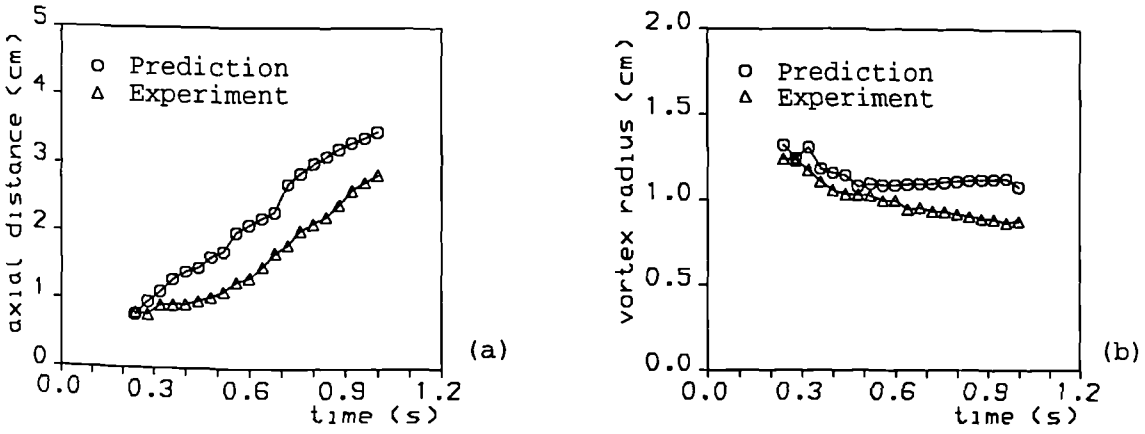


Figure 7.37 (a) Axial position of vortex coreand (b) Vortex ring radius over simulation time. CASE III; 1724 cells, HYBRID, DT=40 ms, Iterations/time step=100

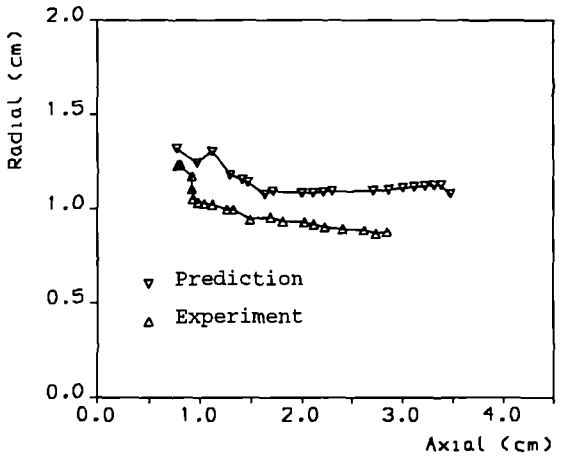


Figure 7.38 Vortex core path: CASE III; 1724 cells, HYBRID, DT=40 ms, Iterations/time step=100

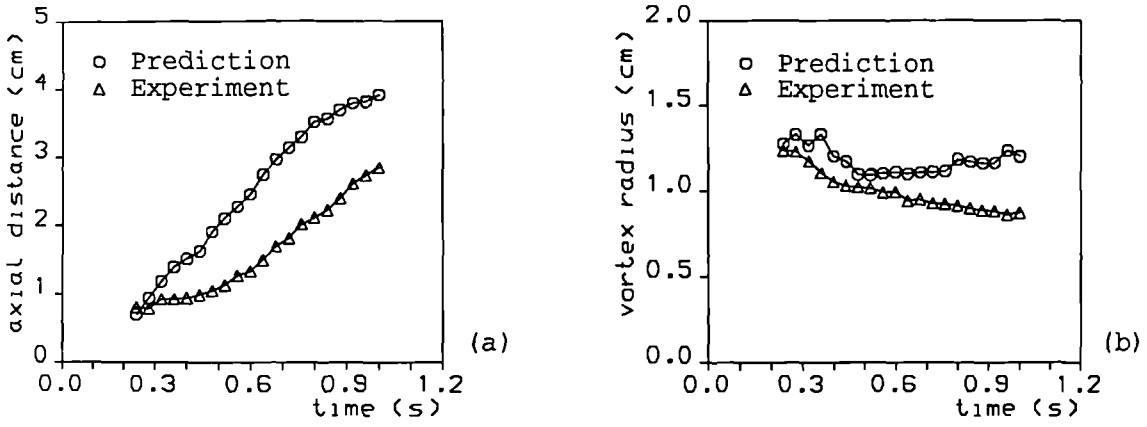


Figure 7.39 (a) Axial position of vortex core and (b) Vortex ring radius over simulation time. CASE III; 1724 cells, HUW, DT=40 ms, Iterations/time step=100

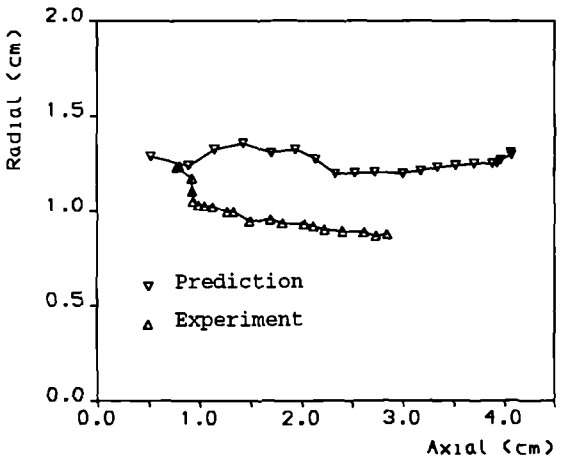


Figure 7.40 Vortex core path: CASE III; 1724 cells, HUW, DT=40 ms, Iterations/time step=100

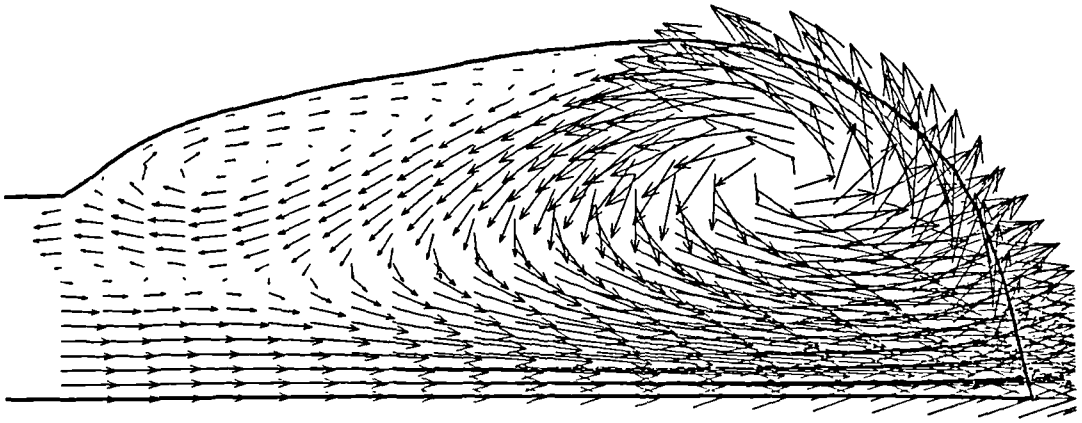

Figure 7.41 Predicted flow patterns for CASE III; CONDIF; t=1.0 s

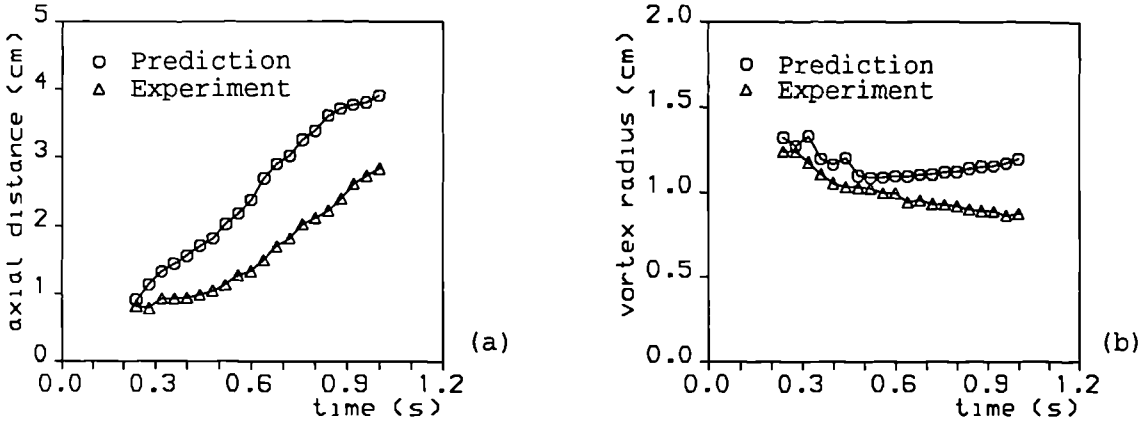


Figure 7.42 (a) Axial position of vortex core and (b) Vortex ring radius over simulation time. CASE III; 1724 cells, CONDIF, DT=40 ms, Iterations/time step=100

## 7.4 ANALYTICAL WALL MOTION MODEL

The principal reason that led to the idea of the development of a model with analytical wall motion was the fact that in the experimental wall motion model the predicted shear stresses at the wall behaved discontinuously. This was due to the method

used to take the experimental points on the ventricular wall. The points, at which axial and diametral positions are taken, are not always the same material points. They are taken by dividing the ventricular extension into forty equal parts, but an uniform expansion at each time of all the forty intervals is not very likely to occur. This may cause a relative motion of the fluid to the wall which is not real.

Another reason for constructing a model with analytical motion but still matching the experimental outlines in space and in time, was the attempt to overcome the discontinuities presented by the experimental data (see Fig.7.2). In fact, although accurate methods were used to interpolate the experimental data, they appeared to be smooth in space but not always in time. Details of the construction of this model are given below.

### 7.4.1 The Numerical Model

The analytical wall motion model (Fig. 7.43) was constructed from the experimental outlines. This was achieved by defining as boundary conditions analytical outlines matching the *in vitro* outlines of the ventricle at minimum and maximum values. Intermediate outlines were found by iterations of the geometric variables shown in Fig.7.43, and were based on the *in vitro* ventricular volume (sigmoidally varying) at each time. Fig. 7.44 shows the analytical outlines matching the experimental wall data at minimum and maximum volumes. Fig. 7.45 shows the time history of the radial and axial positions at one point along the ventricular wall. Note the smoothness of two variables in time compared with Fig. 7.2.

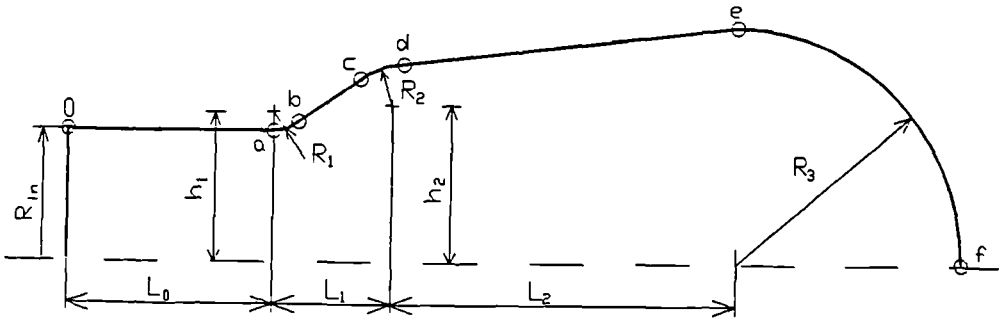


Figure 7.43 Construction of the analytical wall motion model

A parametric study on the grid density and time stepping was carried out. This study led to the grid shown in Fig. 7.44 for which the numerical solution appeared to be independent of the grid density. The final grid was composed of 2352 active volumes. The parametric study performed on the time stepping showed that the comparisons between the experimental and numerical results did not improve significantly for a time step less than 10 ms.

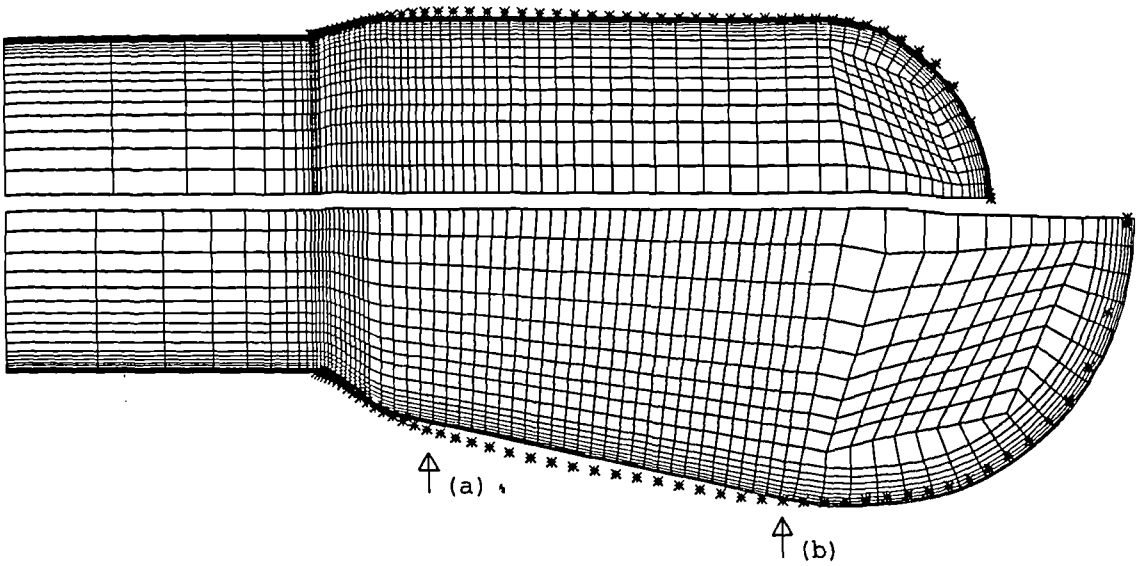


Figure 7.44 Comparison between wall outlines derived from video (indicated by *) and computational grid at minimum and maximum volumes.

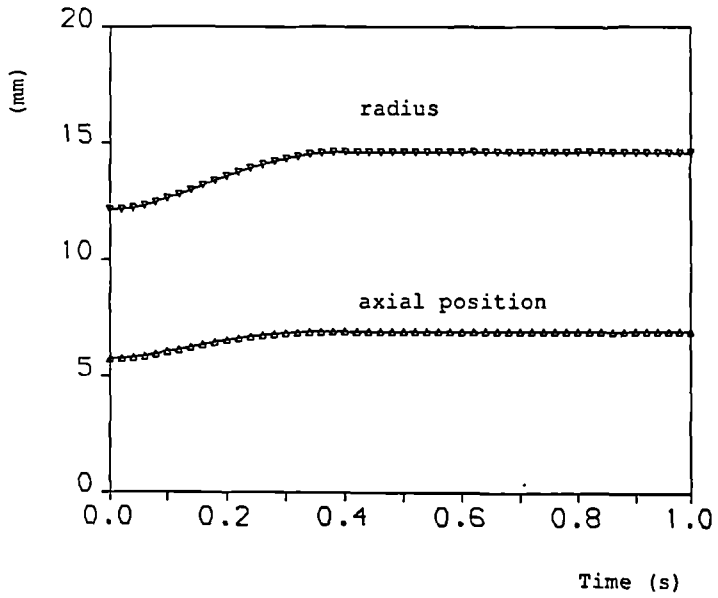


Figure 7.45 Time history of the radial and axial positions at one point (I=50, see Figure 7.44) along the ventricular wall

### 7.4.2 Predicted Results

Qualitative Comparisons

As in the previous model the general features of the predicted flow were in good

agreement with the flows observed in the experiments. The vortex appeared more circular and similar to the one seen in the experiments when HUW was used. When HYBRID was used, the vortex filled all the ventricle, and appeared less circular. This is confirmed by the comparison of the streak lines derived from particle pathlines over a period of 80 ms and the flow visualization images for the same nominal time after the initiation of the filling, as shown in Fig.7.46. However, quantitative comparisons showed that the solution obtained using HYBRID matched closer the experimental data.

Quantitative Comparisons

Figs. 7.47 - 7.49 show the comparisons of the vortex trajectories for the three cases considered. As can be seen, the quantitative agreement between predictions and experiments improved significantly with the new model. They were obtained using HYBRID. The maximum discrepancy was estimated to be 8% for the axial trajectories and 10% in diameter in Case III.

Plots of the trajectories of the vortex obtained using HUW are compared with the experimental data in Fig.7.50. This shows that the quantitative agreement using HUW did not improve to the same extent as when using HYBRID.

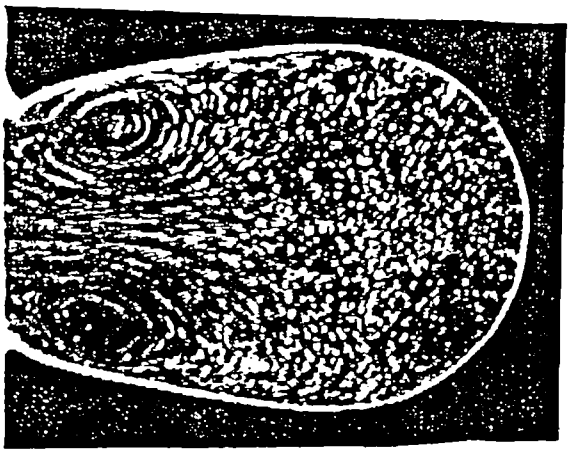

(a)

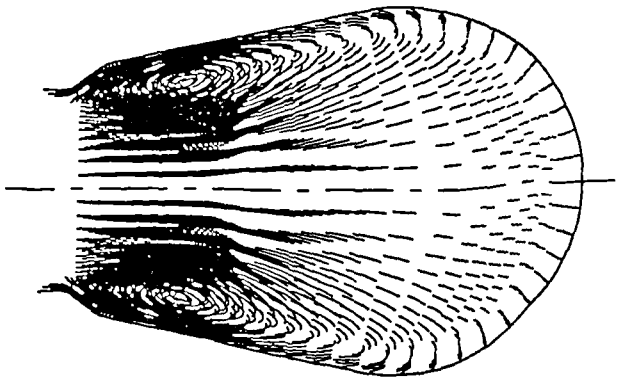

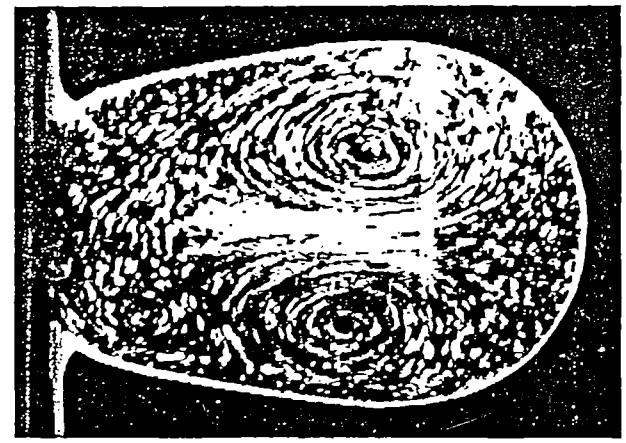

(b)

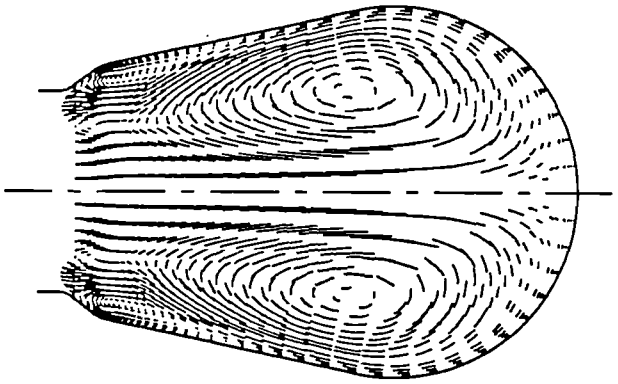

Figure 7.46 Experimental and predicted flow particle streaklines for Case I: (a) experimental, and (b) predicted - 0.44 s; (c) experimental, and (d) predicted - 0.92 s

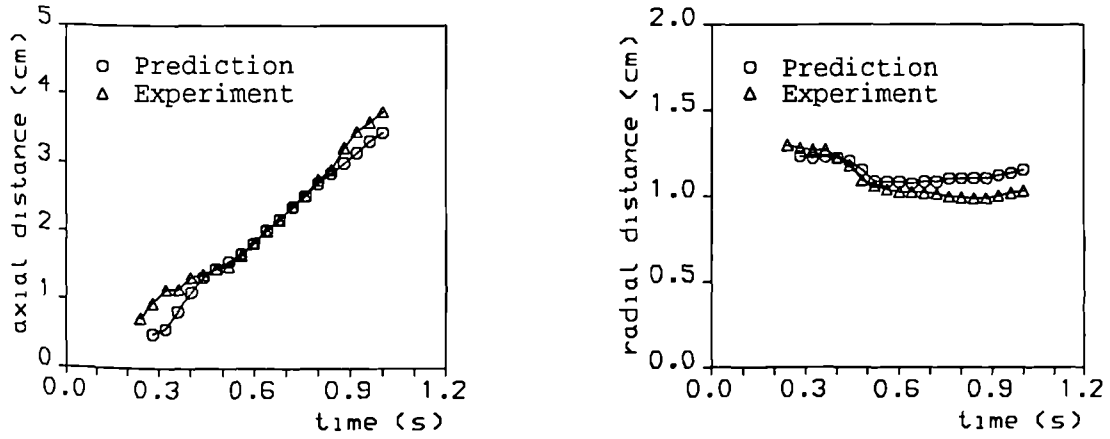


Figure 7.47 Vortex centre trajectories for Case I

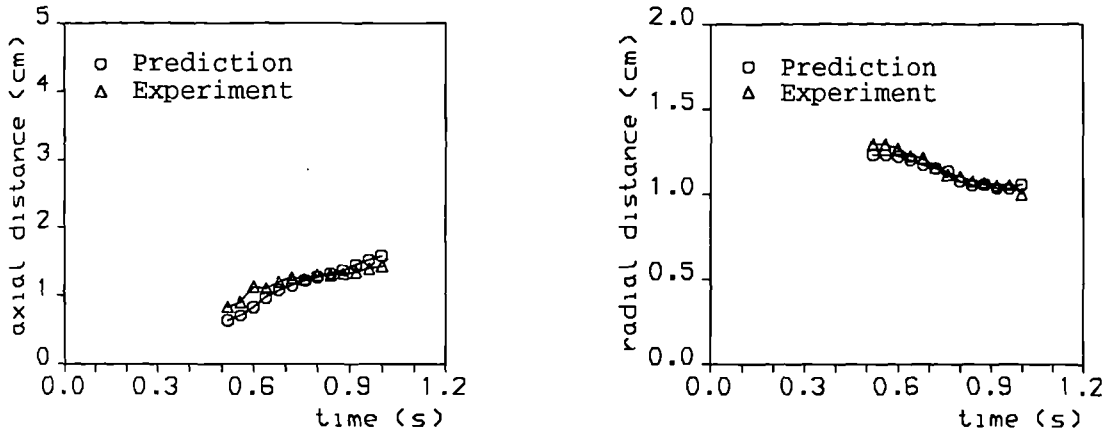


Figure 7.48 Vortex centre trajectories for Case II

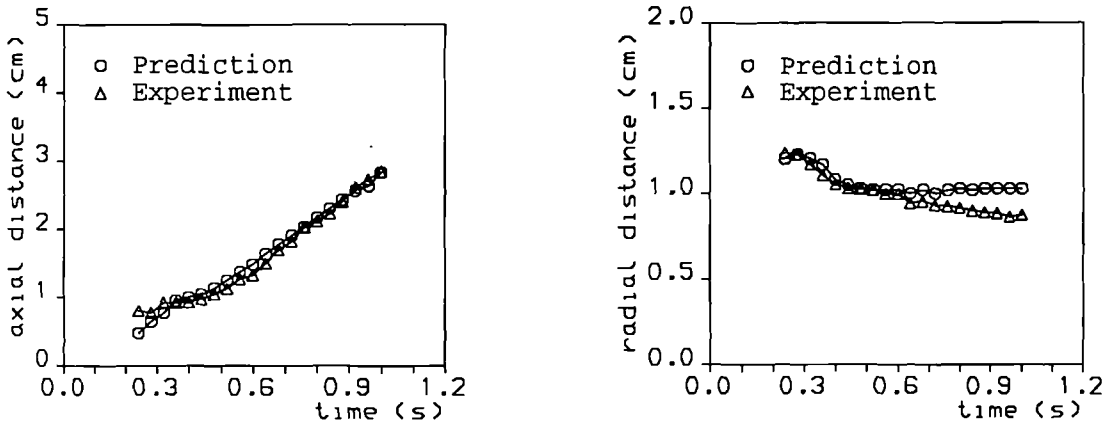


Figure 7.49 Vortex centre trajectories for Case III

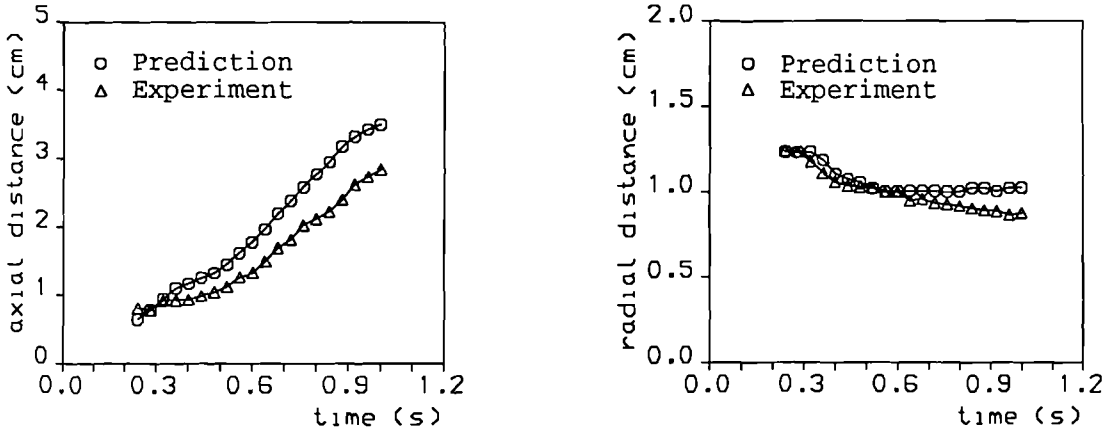


Figure 7.50 Vortex centre trajectories for Case III - HUW

### 7.4.3 Tank Model Test

In order to study the influence of the boundary condition on the predicted flows, a tank upstream of the rigid tube was modelled as shown in Fig.7.51. The tank was $20\times20$ cm$^2$ and had a pressure boundary condition (p= $1.333\times10^4$ Pa) at its top surface. An example of the predicted flow patterns in Case III and at t=1.0 s is shown in Fig. 7.52. Vortex core trajectories are compared with the experimental data in Fig. 7.53. Comparing those with the ones shown in Fig. 7.49, it may be concluded that there is no difference in the predictions when upstream the boundary conditions are changed.

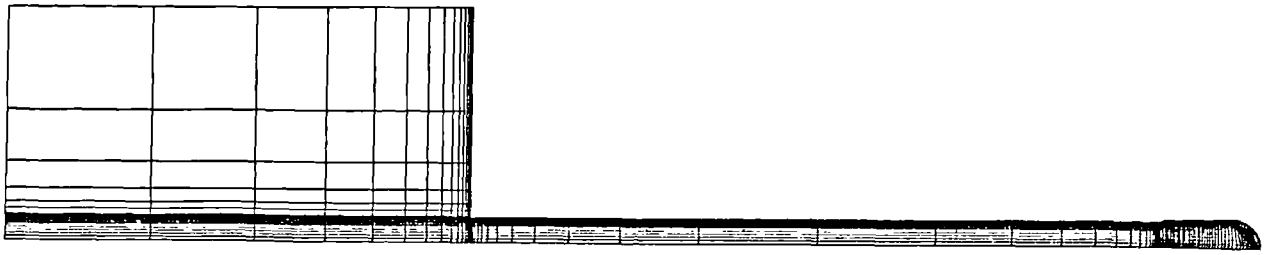

Figure 7.51 Model used when a tank upstream of the tube was considered

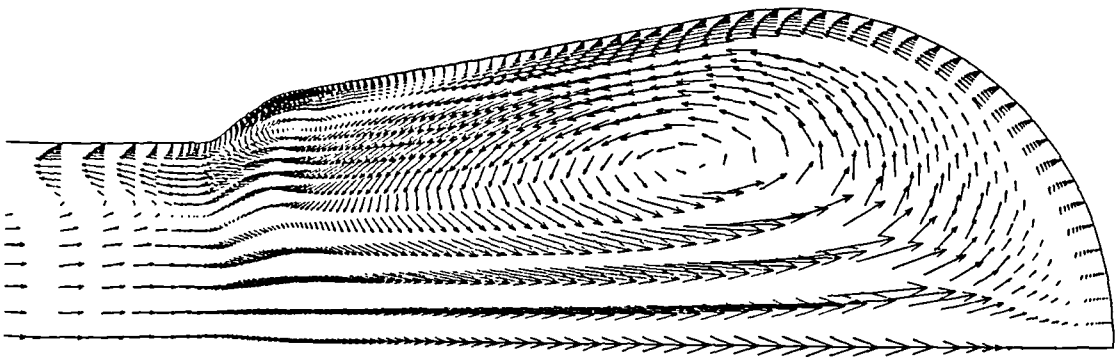

Figure 7.52 Predicted flow pattern for the tank model test

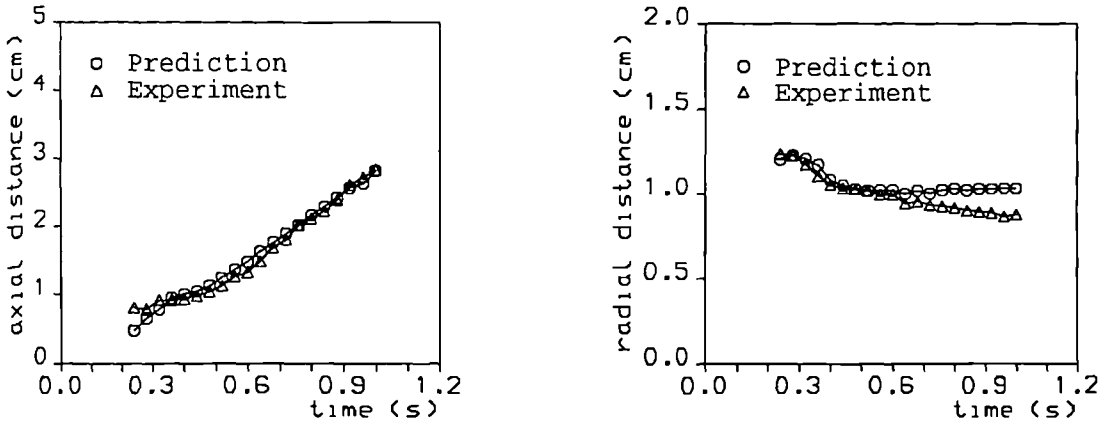


Figure 7.53 Vortex centre trajectories for Case II for the tank model test

## 7.5 CALCULATION OF THE STREAMLINES AND PARTICLE TRACKING

Particle tracking calculation is very important in the design of the SMV, as it allows the estimation of residence times of particles inside the ventricle. Instantaneous streamlines and particle tracking have been calculated from the velocity vector field using a program developed by Dr. Henry. The program is suitable for 2-D geometries, and allows for moving boundaries. Instantaneous streamlines were also used to test the validity of the method presented in APPENDIX G in finding the vortex core positions. Fig. 7.54 shows a plot of streamlines at the end of the run (1.0 sec) for Case III using the upstream tank as a boundary condition. Similar plots have already been discussed previously for the experimental wall motion model in Fig. 7.28.

Fig. 7.55 shows two sets of the predicted particle pathlines over a period of 1.0 for Case I. Figs. 7.56 and 7.57 show the same set of predictions for Case II and III respectively. The vortex travelling induces the trasport of particles from the inlet of the ventricle or at its vicinity in the tube to the apex. The velocity of the vortex is proportional to the mean flow velocity during filling (Shortland et al., 1995). Particle traces are longer in the case with the largest mean volume flow rate. Therefore, it can be expected that the fluid dynamics of the particles inside the ventricle is determined by the vortex dynamics.

The above plots show that particles which are at the inlet when the expansion begins do not reach the apical end of the ventricle in the period of 1 s. Particle at the inlet near to the wall return towards the inlet after having travelled for a short length in the ventricle. Particle in the apex area (Figs.7.55 (b), 7.56 (b) and 7.57 (b)) travel very little unless the vortex is in the vicinity. These results indicate that the presence of the vortex travelling along the ventricle length enhances the mixing properties and reduces

the residence time of the fluid within the ventricle.

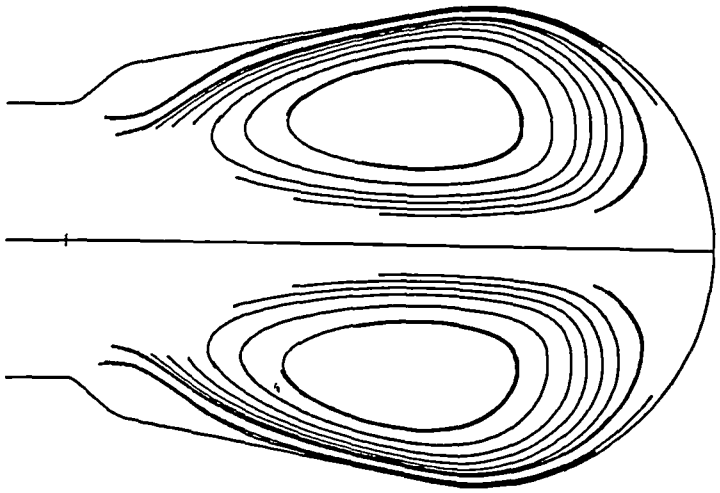

Figure 7.54 Instantaneous streamlines for the tank model test at 1.0 s

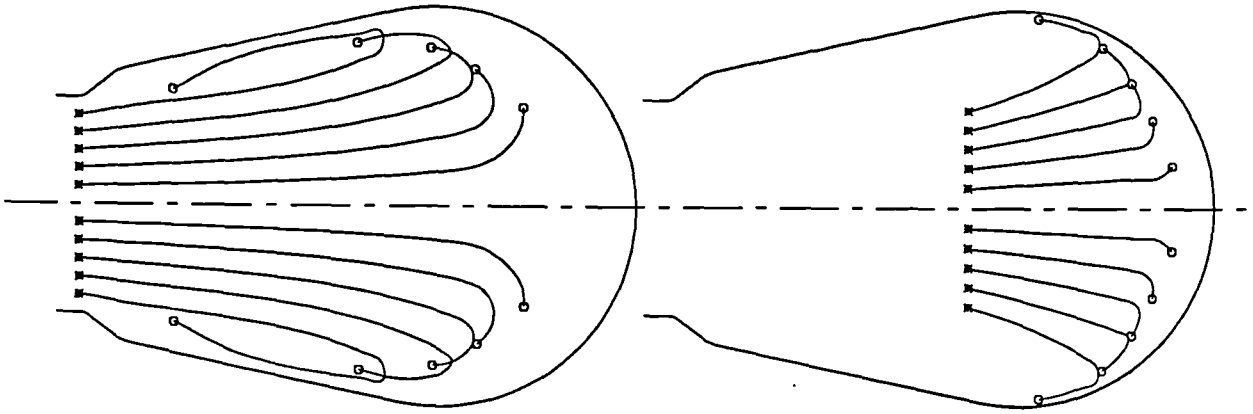

Figure 7.55 Particle pathlines during filling for case I (* indicates initial position; o indicates final position)

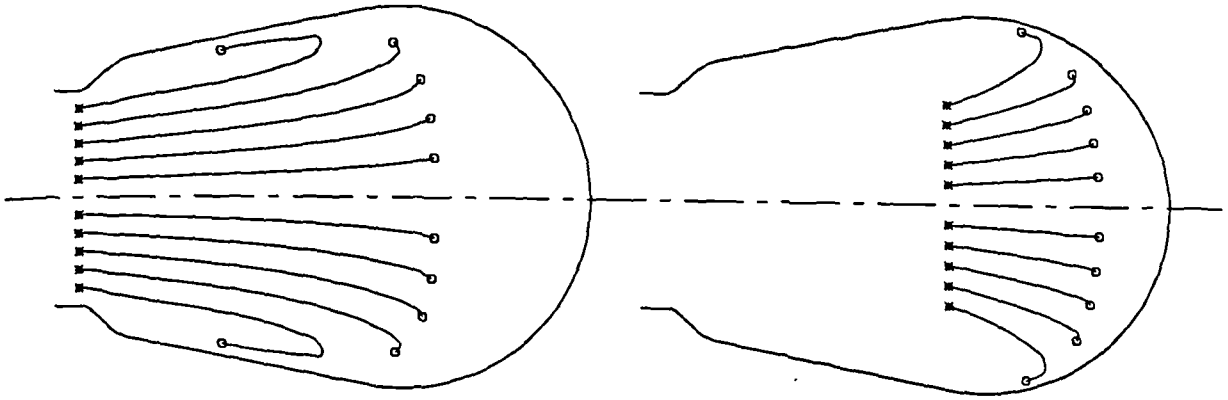

Figure 7.56 Particle pathlines during filling for case II (* indicates initial position; o indicates final position)

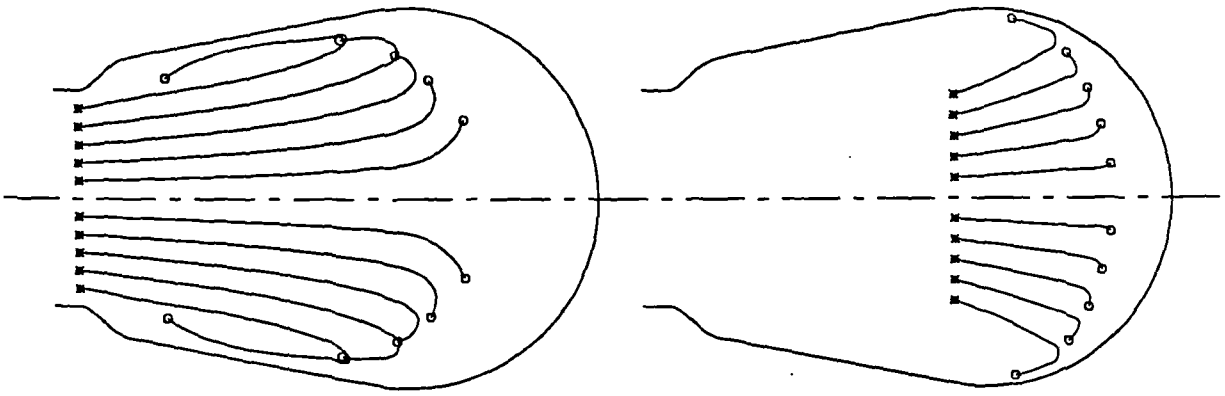

Figure 7.57 Particle pathlines during filling for case III (* indicates initial position; o indicates final position)

## 7.6 CALCULATION OF THE WALL SHEAR STRESSES

Wall shear stresses were calculated using a subroutine provided by CFDS-FLOW3D staff. The routine was modified slightly to allow a dump of the shear rates at each time step and to include the dumping of position variables. This subroutine uses the velocity gradients at the wall to calculate the tangential stresses. A form-factor takes into account the surface deformation at the wall. This routine produced values of wall shear stress that matched analytical predictions.

Time histories of wall shear stress are shown in Fig. 7.58 at two points along the ventricular wall for the cases considered. Positive values of shear indicate that flow in the immediate vicinity of the wall is moving away from the inlet. As the vortex passes, the sign of the shear stress changes. In the apical volume the flow is towards the inlet for most of the time simulated. The maximum value of shear is experienced in Case III ($\tau_w$= 2.0 Pa). In the other two cases the maximum level of shear is about 1 Pa.

In the calculation of the wall shear stress, it is important to define the wall grid points so that there is no relative motion to each other when the curve defining the grid boundary is changing in length. The grid points are assumed to be fixed to material points in the wall, and therefore they must expand in the wall in a similar fashion, otherwise the resulting shear stresses will include a component due to their relative motion.

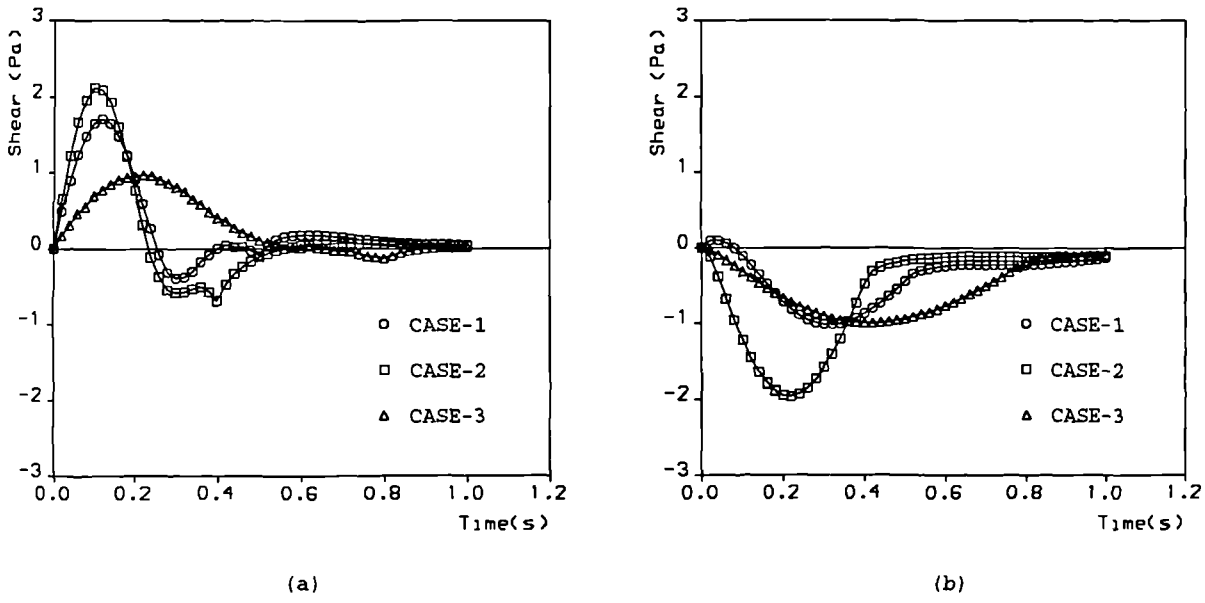


Figure 7.58 Time history of wall shear stress at two sites on the ventricular surface. See Figure 7.44 for location of sites

## 7.7 INITIAL CALCULATION OF THE FLUID SHEAR STRESS FIELD

The calculation of the shear stress field within the flow is not a default output parameter in CFDS-FLOW3D. The calculation, in fact, requires some user input. As measurement of shear stress is not feasible with the current experimental setup, the numerical predictions of such cannot be validated against experimental data. Therefore as an initial approach for their calculation in a model SMV, numerically predicted distributions of shear stress have been compared with corresponding analytical data for:

(i) fully-developed flow of a Newtonian fluid through a circular tube,
and (ii) the flow in a seminfinite expanding/contracting pipe.

This study was performed to check the ability of CFDS-FLOW3D to predict shear stress fields, particularly over grid inter-block boundaries. The computational grid used for these calculations was topologically similar to that used for the SMV predictions. Particular attention was paid to conditions at the interfaces of the grid blocks.

The shears were calculated at the centre of each control volume using initially the utility subroutine GRADDV, which calculates the spatial gradients of a specified velocity component from which the components of the shear are calculated. Predictions obtained with this method showed significant differences compared with the analytical solution at grid block interfaces. The main reason for the inaccuracy at the interfaces is believed to be due to the way in which cell information is interpolated over the interfaces, and how this affects the calculation of velocity gradients. To resolve this problem, a routine to calculate the shear stress on a uniformly spaced computational space, and perform a variable transformation, was written by Dr. Henry. This allowed interpolation inaccuracies related to the grid topology to be reduced when the gradients are calculated directly on the physical space. Details of this study are given in APPENDIX H.

In order to validate this method for problems of flow with moving boundaries, such as the expanding/contracting pipe of Uchida and Aoki (1977), numerical predictions were compared with the available analytical solution. Comparisons have been made for the case of 'one-block' grid topology as used in Chapter 4 to validate velocity profiles, and for the case of 'three-block' grid topology as used for the simulations discussed in this chapter. In Fig.7.69 the comparisons are shown for the case of the 'three-block' grid configuration. Predicted results are shown to be in good agreement with the analytical solution. Results obtained for the 'one-block' grid topology are reported in APPENDIX H, together with the other details of the validation. Slight differences can still be seen at grid block interfaces with respect to the 'one-block' grid. These results lead to the conclusion that flow shear stresses predicted by CFDS-FLOW3D agree with the analytical solution for simple cases. However, some care has still to be taken at grid-block interfaces. Validation against experimental measurements is still required to be carried out in the next feature.

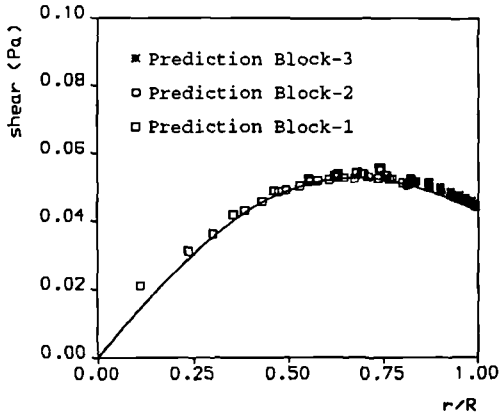


(a)

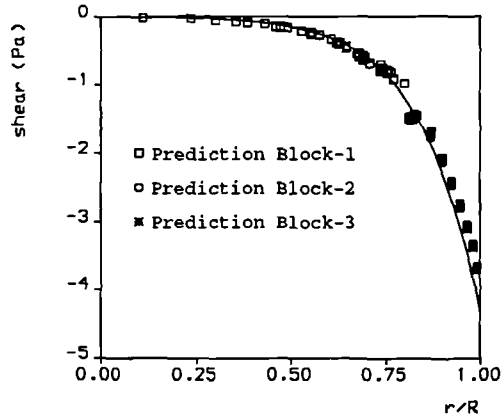


(b)

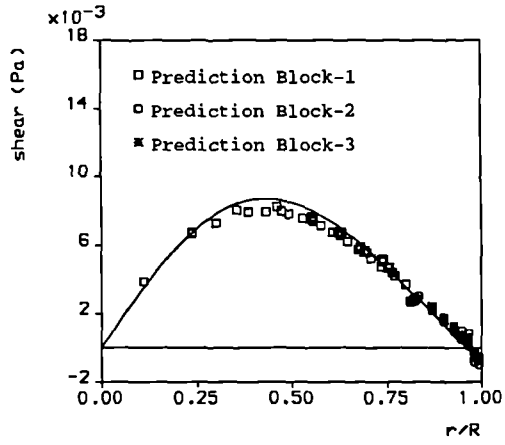


(c)

Figure 7.59 Comparisons of the distributions of flow shear stress. (a) Expansion at $Re$=1.0; axial location X=0.046 m; time of simulation T=1.0 s. (b) Contraction at $Re$=10; X=0.13 m; T=1.0 s. (c) Expansion at $Re$=1.67; X=0.128 m; T=3.0 s. Three-block grid topology.

## 7.8 SUMMARY

A range of numerical simulations has been performed in order to validate the numerical solution against the experimental *in vitro* data of the flow inside a ventricle into which fluid was drawn following a sigmoidal filling curve. Qualitative and quantitative comparisons have been analysed for two models: 1) an experimental wall motion model, and 2) an analytical wall motion model. Simulation parameters have been tested; e.g., grid density, time step and advection algorithm. A typical simulation took 90 min on a Convex C3860 supercomputer.

Although the basic features of the flow patterns revealed in the experiments are predicted by FLOW3D, the numerical solutions have to be viewed with some caution. The best agreement was obtained for slow filling of the ventricle. Predicted results have shown that the numerical solution is most sensitive to the way in which the wall motion is defined. The development of an analytical wall motion model with smooth wall motion profiles in space and in time, has produced a closer quantitative agreement of the predictions with the experimental data.

It could be argued that the assumed axisymmetry of the flow should be investigated by modelling the full ventricle, and not a two-dimensional slice; however, this would increase the size of the grid to such an extent that the cost of the computation would be high and the scope for grid or time stepping refinement would be limited. In the design of model SMVs, however, it is very important to consider its three-dimensionality. Some 3-D models, proposed as potential designs for an SMV, are presented in the next chapter.

# CHAPTER 8

# NUMERICAL SIMULATION OF THE FLOW IN 3-D MODEL SKELETAL MUSCLE VENTRICLES

## 8.1 INTRODUCTION

In this chapter some numerical 3-D model SMVs are analysed. These may be taken into consideration in the design of the SMV. Computational Fluid Dynamics represents a powerful method of research into blood flow in the cardiovascular system. Numerical simulations of flows in cardiac assist devices can be used to study the effect on the flow of the shape and size of the device, and of the orientation of inlet and outlet ducts. The objective is to optimize the performance, in terms of maximum efficiency of the blood pump for the limited (physiologically provided) power, while at the same time minimizing the risk of haemolysis and thrombogenesis.

A three dimensional analysis of the flow inside SMVs is very important in order to have a reliable estimate of the variables of medical relevance, and consequently to be able to contribute to the design of model SMVs. It is very likely that in the final design the duct that feeds the SMV is not a straight tube. This implies that in the numerical modelling two dimensional cylindrical models cannot be taken into consideration. When the duct is a curved cylinder or is a T-junction a truly 3-D model has to be considered.

The models discussed in this chapter are characterized by two different inlet configurations: (i) a straight inlet tube, as for the models previously considered, and (ii) a curved inlet tube. These will be referred to as the straight inlet model, and the curved inlet model. For each of these, a number of models have been analysed. They are characterized by their shape, and referred to as flask models and spherical models. Both of them have been analysed for the above two inlet configurations. Some of the models have been treated for a circumferential range of $180^0$, others for a circumerential range of $360^0$, the formers being modelled with a symmetry plane at the diametral plane. This simplification is justified by the high computer cost involved when the size of the grid is doubled.

The calculations were performed using the multi-block version of CFDS-FLOW3D. The multi-block grid capability allows the simulation of flows in solution domains with significantly more complex geometries than can be achieved with a single-block grid. Specifically, non-axisymmetric geometries such as curved inlet tubes can be considered with relative ease. Also, the spherical end of the ventricle can be modelled more accurately. In all the cases to be discussed in this chapter, the base geometry and the wall movement were defined analytically.

The chapter begins with the analysis of the flow inside straight inlet models, flask- and spherical-shaped. Then curved inlet models are analysed, again considering flask and spherical models. A summary concludes the chapter.

### 8.2.1 Flask Models

The general geometrical features are as shown in Fig.8.1. The ventricle starts with a diverging section, continues with a section of constant diameter, and ends hemispherically. The geometric features used for the reference case are in Table 8.1. The density and the viscosity of the fluid are respectively: $\rho = 1.0 \times 10^3 kg/m^3$, $\nu = 4.0 \times 10^{-3} Ns/m^2$. A constant pressure boundary condition was specified at the inlet of the duct: $p = 1.3332 \times 10^4 N/m^2$. All points on the wall are assumed to move radially in a pure sinusoidal manner about a mean position. The amplitude of the wall movement was defined to be 20% of the mean diameter. The period of oscillation was taken to be 0.75 seconds, and unless otherwise stated, the time step was set to one twenty-fourth of the period.

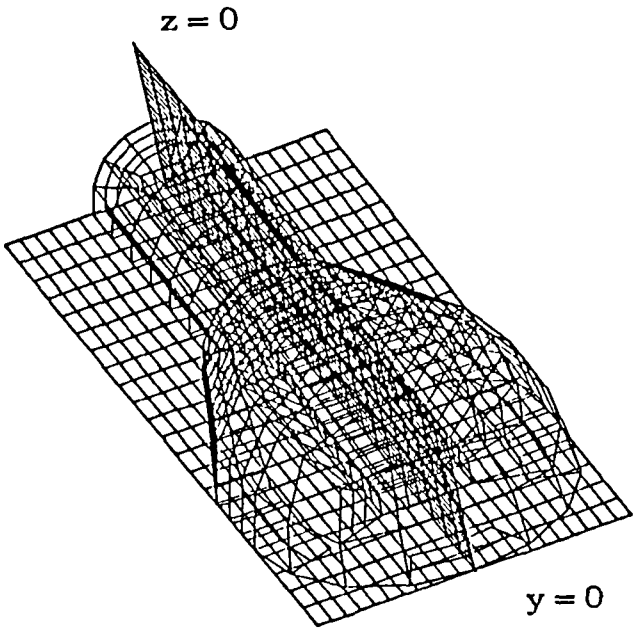


Figure 8.1 Straight inlet flask model

The predicted velocity fields for various times in the cycle for SMVs are given in Fig. 8.2. In order to study the effect of shape on the predicted flow, various changes to the basic geometry were considered. Grid refinement and advection model studies were also performed. The various geometries, grids and advection models used are specified in Table 8.2. In Fig.8.3 are given predicted velocity fields for the base model, referred to

as case I in Table 8.2. The two plots are for times just before and just after maximum volume respectively.

t/T=0.25

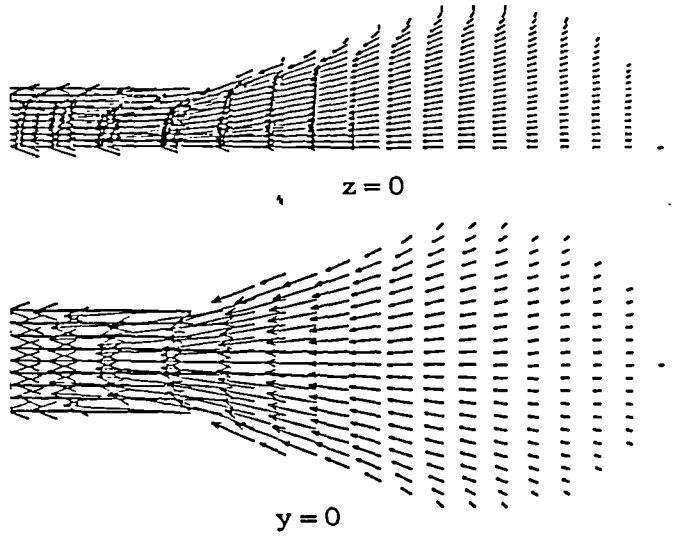


t/T=0.5

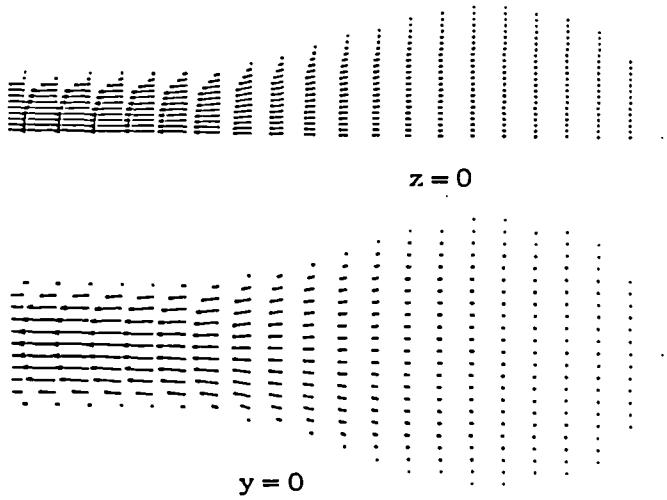

t/T=0.75

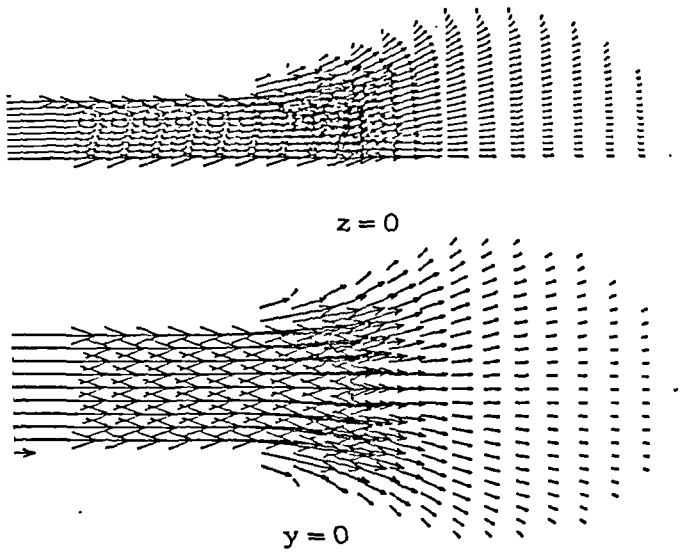


t/T=1.0

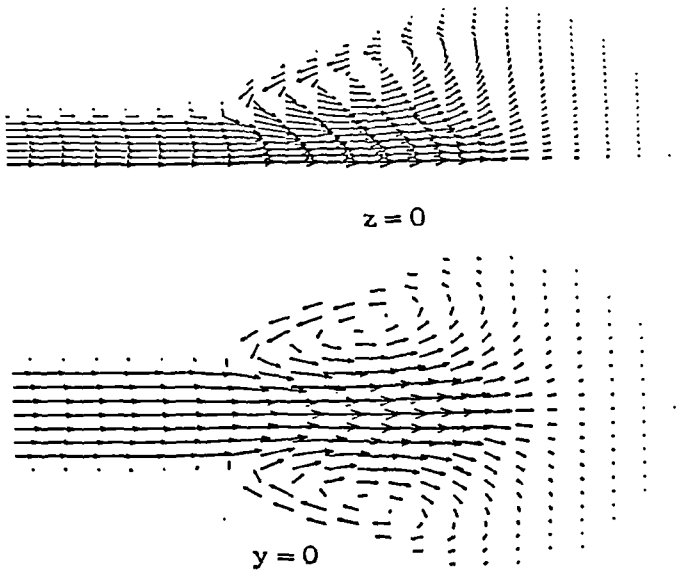


Figure 8.2 Predicted flow fields at four times of the cycle.

Table 8.1

Geometric features of the reference case

| | |
|---|---|
| Inlet pipe diameter | $D_{in}$ = 20 mm |
| Inlet pipe length | $L_{in}$ = 30 mm |
| Straight pipe length | $L_s$ = 10 mm |
| Divergent pipe length | $L_{div}$ = 20 mm |
| Maximum SMV diamter | $D_{max}$ = 30 mm |

Table 8.2

Details of the parametric study

| Case | Number of axial cells | Number of radial cells | Total number of volumes | Geometric ratio | Advection algorithm |
|---|---|---|---|---|---|
| I | 23 | 5 | 664 | 1 : 1 | HYBRID |
| II | 33 | 5 | 984 | 1 : 1 | HYBRID |
| III | 23 | 7 | 1392 | 1 : 1 | HYBRID |
| IV | 26 | 5 | 760 | 2 : 1 | HYBRID |
| V | 29 | 5 | 856 | 3 : 1 | HYBRID |
| VI | 29 | 7 | 1788 | 3 : 1 | HYBRID |
| VII | 29 | 7 | 1788 | 3 : 1 | QUICK |
| VIII | 29 | 7 | 1788 | 3 : 1 | HIGHER UPWIND |

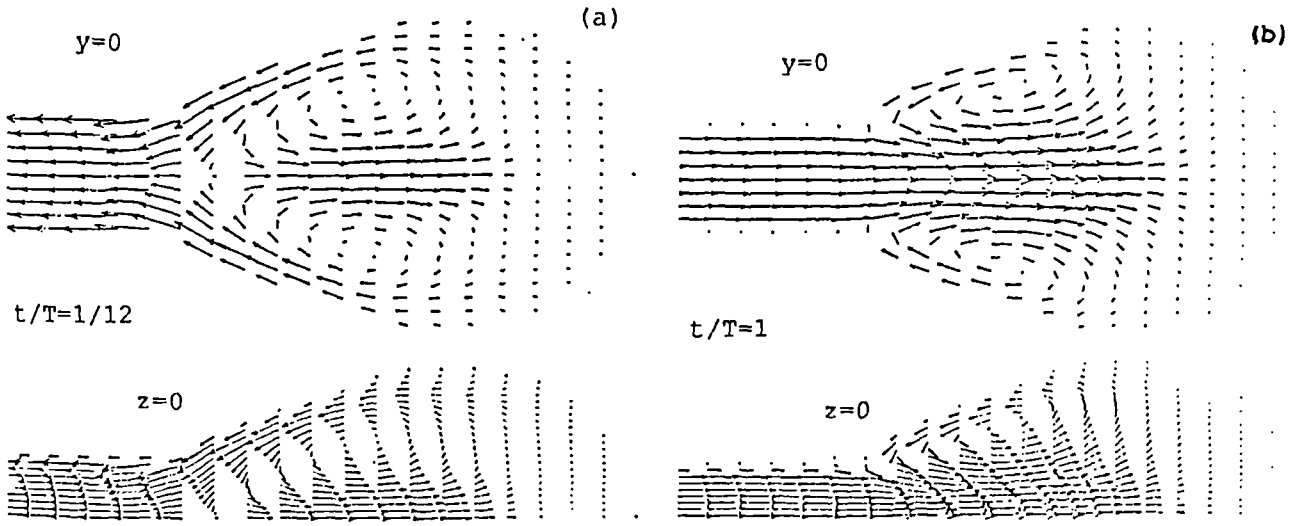


Figure 8.3 Predicted flow fields for two stages near maximum volume: (a) emptying, (b) filling. Case I

Grid Refinement

In Fig.8.4 are given predictions of velocity for the same times as in Fig.8.3. In this case, (Case II) the number of control volumes in the axial direction has been changed from 23 to 33. Similar plots are given in Fig.8.5 for a case of grid refinement in the radial direction (Case III). Only minor differences can be seen in the three cases.

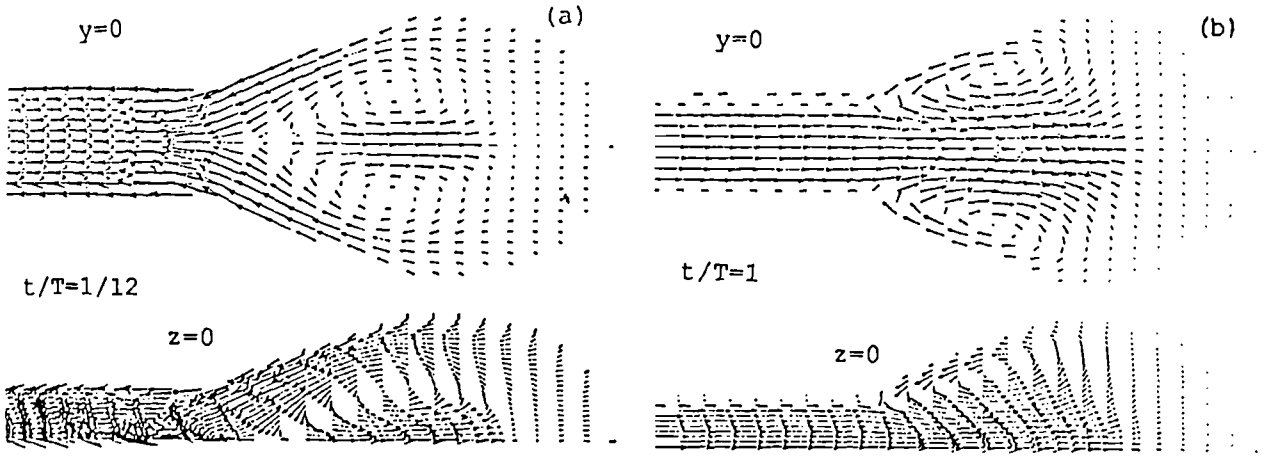


Figure 8.4 Predicted flow fields for two stages near maximum volume: (a) emptying, (b) filling. Case II

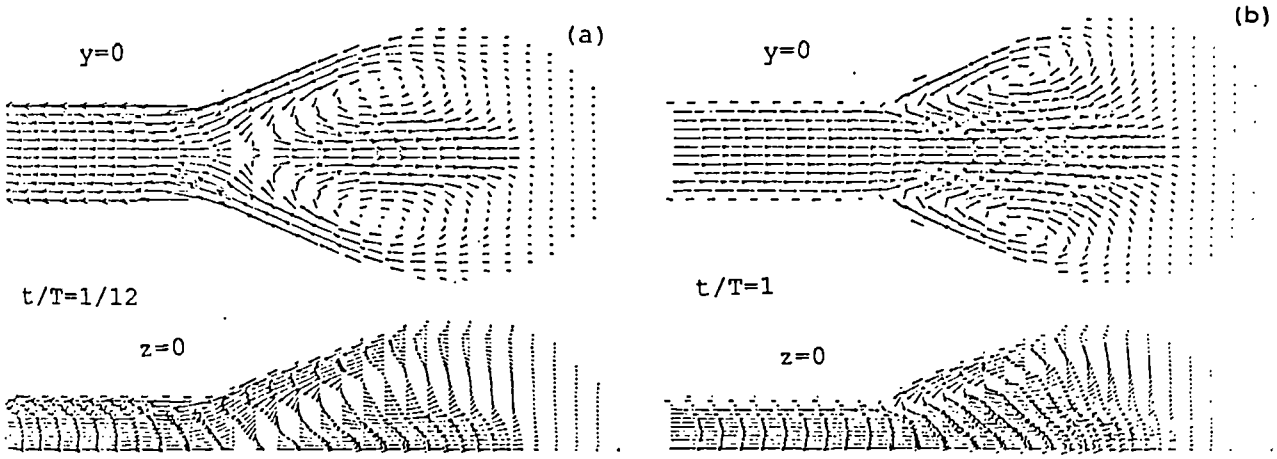


Figure 8.5 Predicted flow fields for two stages near maximum volume: (a) emptying, (b) filling. Case III

Changes in Geometry

The effect of ventricle geometry on the resulting flow fields was restricted to changing the length of the straight section. Two cases were considered; one (Case IV) with a

straight section twice as long as the base case, and one (Case V) with the section three times as long. Sketches of the grids used for Cases IV and V are given in Figs.8.6 and 8.7, respectively. The corresponding flow fields, for the same times as in Fig.8.3, are given in Figs.8.8 and 8.9. It can be seen that as the length is increased, the vortex moves towards the closed end, and closer to the wall. However, the basic flow pattern is similar to the base case. That is, the flows are characterized by a single vortex ring forming within the first half of the ventricle, and flow in the second half being relatively quiescent.

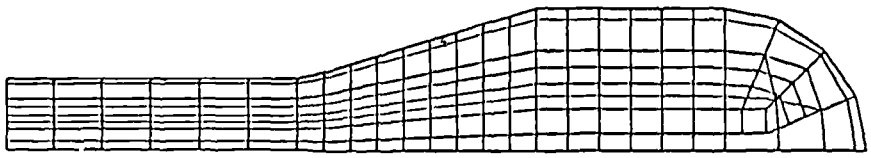

Figure 8.6 Grid used in Case IV

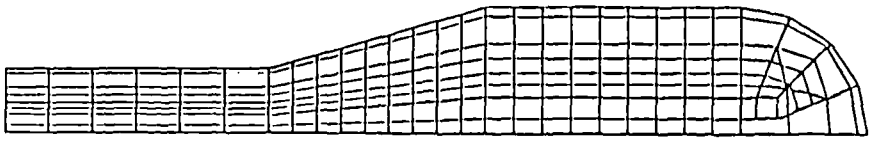

Figure 8.7 Grid used in Case V

The effect of refining the grid in the radial direction for Case VI is shown in Fig.8.10. It can be seen that grid refinement does not produce any dramatic changes in the resulting flow field. It should be noted that the plots in Fig.8.10 have more vectors both in the radial and axial directions than do the plots in Fig.8.9. This gives the impression that the two flow fields differ more than actually is the case.

A flask model with a geometry similar to the models analysed in chapter 5 is in Fig.8.11. The predicted flow for this model is given in Fig.8.12. In this case the time step was halved. Flow patterns show the formation of one vortex ring only during the whole cycle. This seems to lead to the conclusion that the particular shape of the flask model,

together with a smaller expansion, may affect the type of flow in terms of the number of the vortices formed.

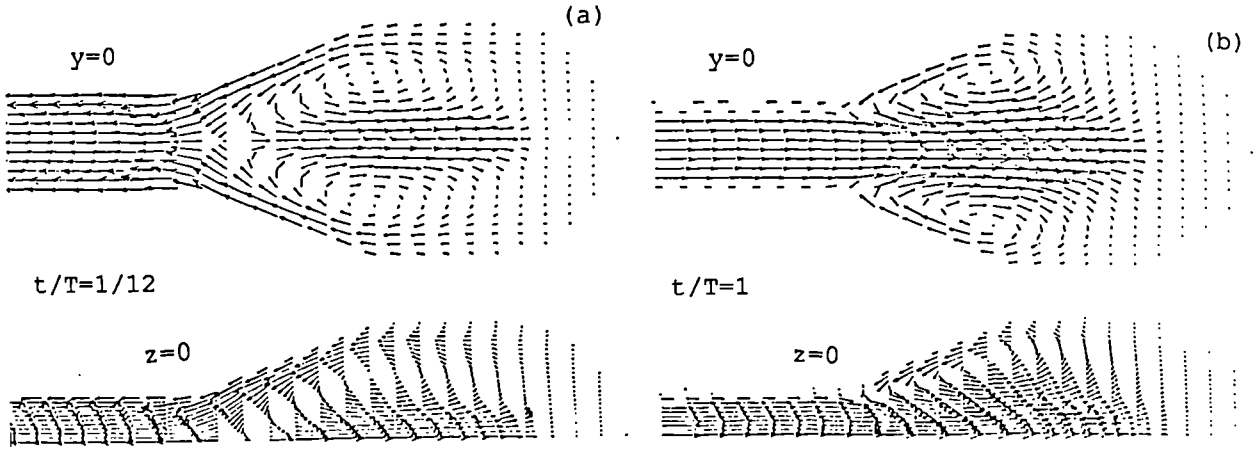


Figure 8.8 Predicted flow fields for two stages near maximum volume: (a) emptying, (b) filling. Case IV

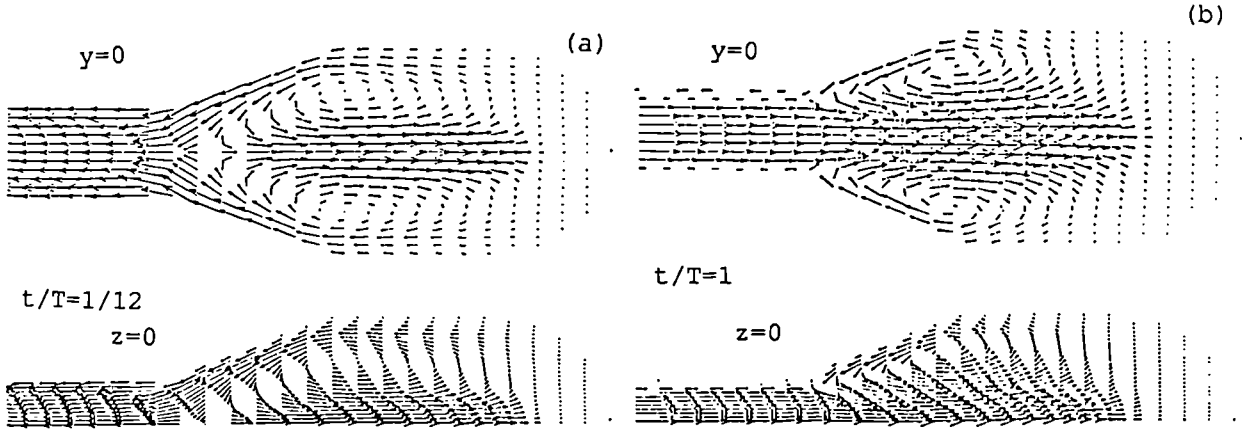


Figure 8.9 Predicted flow fields for two stages near maximum volume: (a) emptying, (b) filling. Case V

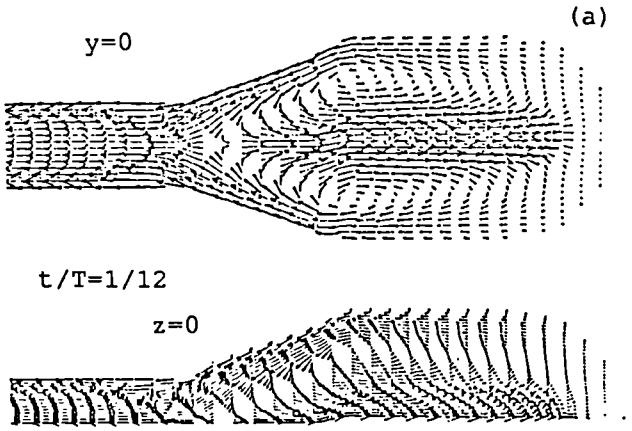

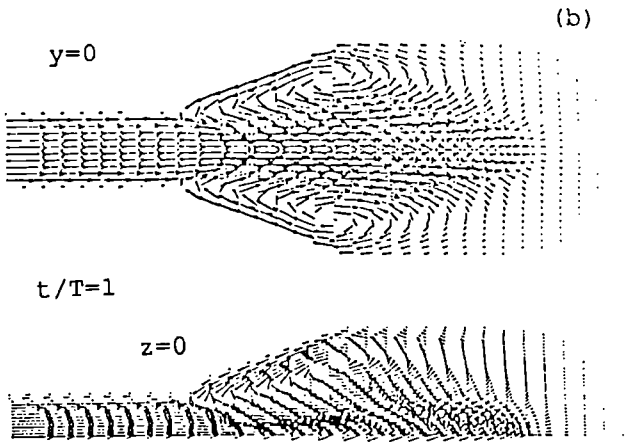


Figure 8.10 Predicted flow fields for two stages near maximum volume: (a) emptying, (b) filling. Case VI

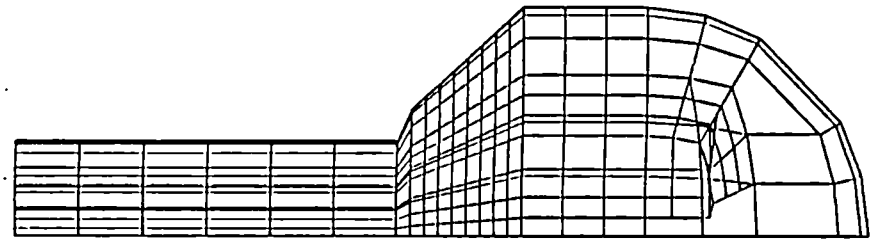

Figure 8.11 Other flask model

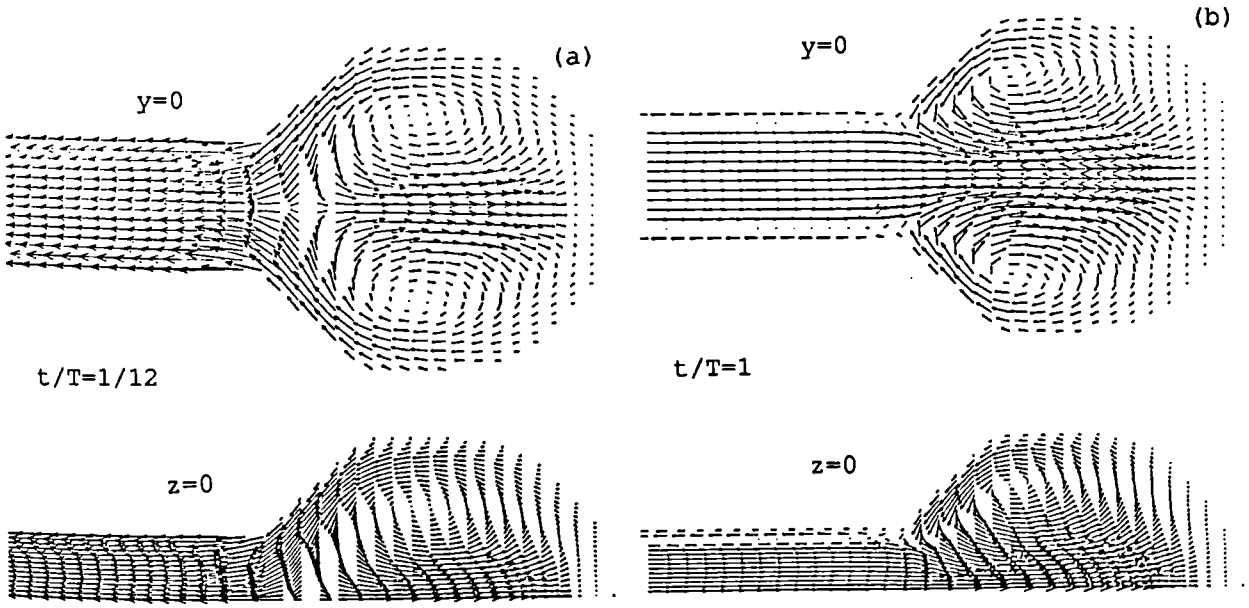


Figure 8.12 Predicted flow fields for two stages near maximum volume: (a) emptying, (b) filling. Other flask model.

Predictions of the flow using the QUICK advection model are given in Fig.8.13. The geometry and grid were the same as those used for the predictions given in Fig.8.9. It can be seen that QUICK produces a vortex that is longer than that predicted using the HYBRID scheme. This results in a more energetic flow in the closed-end region, both in filling and emptying. Predictions using HUW, at identical times to those in Fig.8.9, are given in Fig.8.14. It can be seen that HUW predicts a vortex that almost completely fills the ventricle.

All the models presented above exhibit essentially the same flow structure, namely the occurrence of one large vortex ring. The predictions differ only in the extent to which this vortex approaches the closed end. This may be taken into account in the design considerations. Geometries where vortices occupy part of the ventricle volume promote stagnant flows in the apical region. Geometries where vortices occupy most of the ventricle volume allow good mixing and prevent flow stagnations.

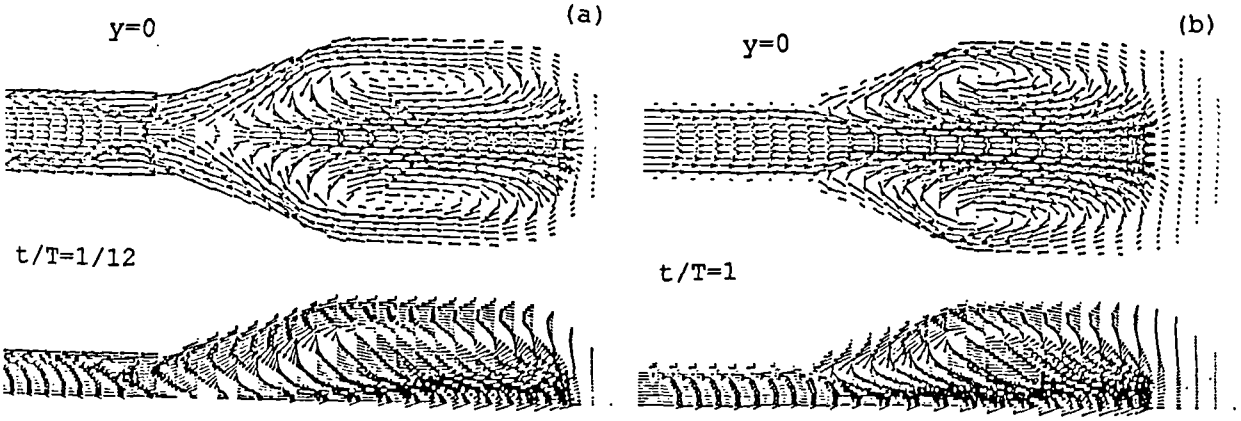


Figure 8.13 Predicted flow fields for two stages near maximum volume: (a) emptying, (b) filling. Case VII

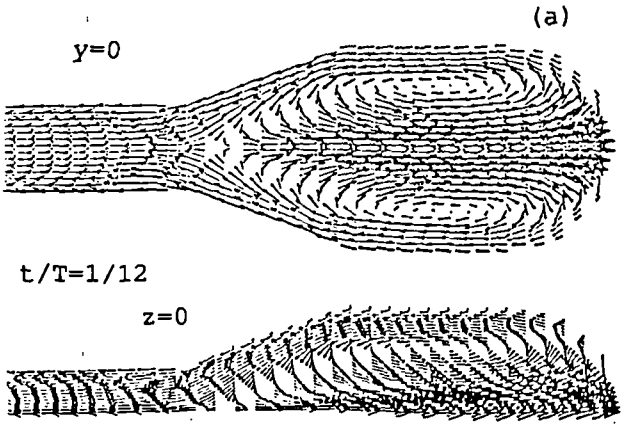

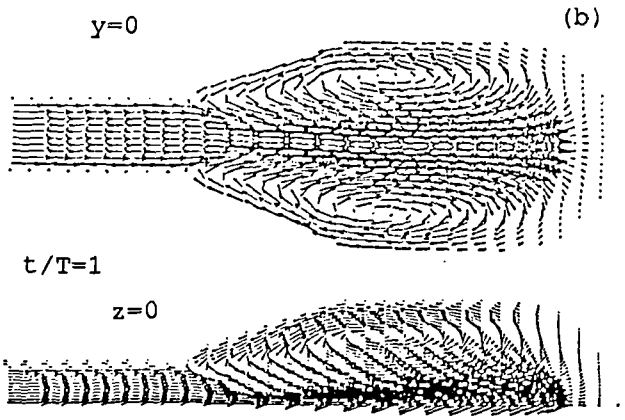


Figure 8.14 Predicted flow fields for two stages near maximum volume: (a) emptying, (b) filling. Case VIII

### 8.2.2 Spherical Models

In order to have a complete analysis of the problem $360^0$ models are required. This is not an easy task since the number of cells involved may lead to a prohibitive CPU time. The spherical model considered in this section has the same geometric features of the spherical-end rigid/compliant model analysed in chapter 5 to which I return for more details. Also the analytical function used to drive the wall motion is identical.

The three-dimensional grid used for the model is shown in Fig.8.15. Different frequencies of the cycle were considered. Preliminary studies for the refinement of the grid and time stepping were carried out. Then simulations for the analysis of the solution over the frequency range were performed. This required a considerable amount of CPU time. Calculations for this preliminary study were performed by the supercomputer Convex C3860 at University of London Supercomputer Centre (ULCC). The final grid used in the frequency study had 21500 active volumes. The time step varied for each of the frequencies considered. It was found that this would save a quantity of CPU time.

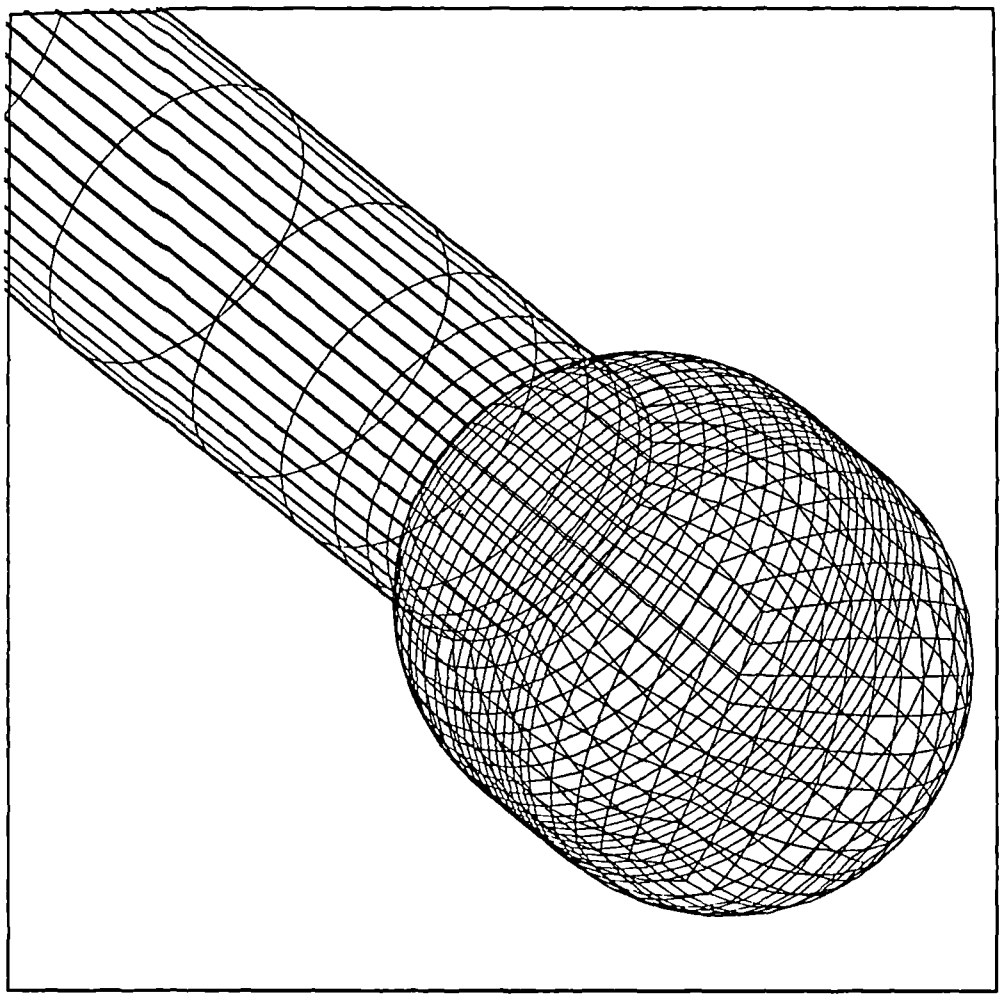

Figure 8.15 Straight inlet spherical model

Before a steady periodically repeating solution was achieved, the model ventricle had to undergo three cycles of numerical computations. The calculations required 32 hours of CPU time in the Convex for each cycle. Successive cycles were simulated using successive restarts. Because of the limited CPU time granted by ULCC, it was neccessary to run the cases locally at City University on a SUN sparcstation 5. Each cycle required between four days and one week to run, depending on the number of contemporary users.

For the above reasons, only two frequencies were tested. The predicted flow patterns at maximum volume for a frequency of 1.33 Hz are shown in Fig.8.16. Fig. 8.17 shows the predicted flow patterns for a frequency of 0.33 Hz. A striking feature of the predicted flow is that the vortex structure (two-vortex rings at $f$=1.33 Hz, and one-vortex ring at $f$=0.33 Hz, as predicted in the 2-D model) is not symmetric with respect to the axis of the ventricle. This feature cannot be easily evidenced in the experimental flows. As can be seen, the asymmetry is less evident at lower frequencies. It can be expected that for even lower frequencies flows are symmetric. Such simulations will be performed soon.

Having reported the asymmetric characteristic of the flow to mathematicians, we have learned of the symmetry-breaking bifurcation problem, considerations on which are

summarized below.

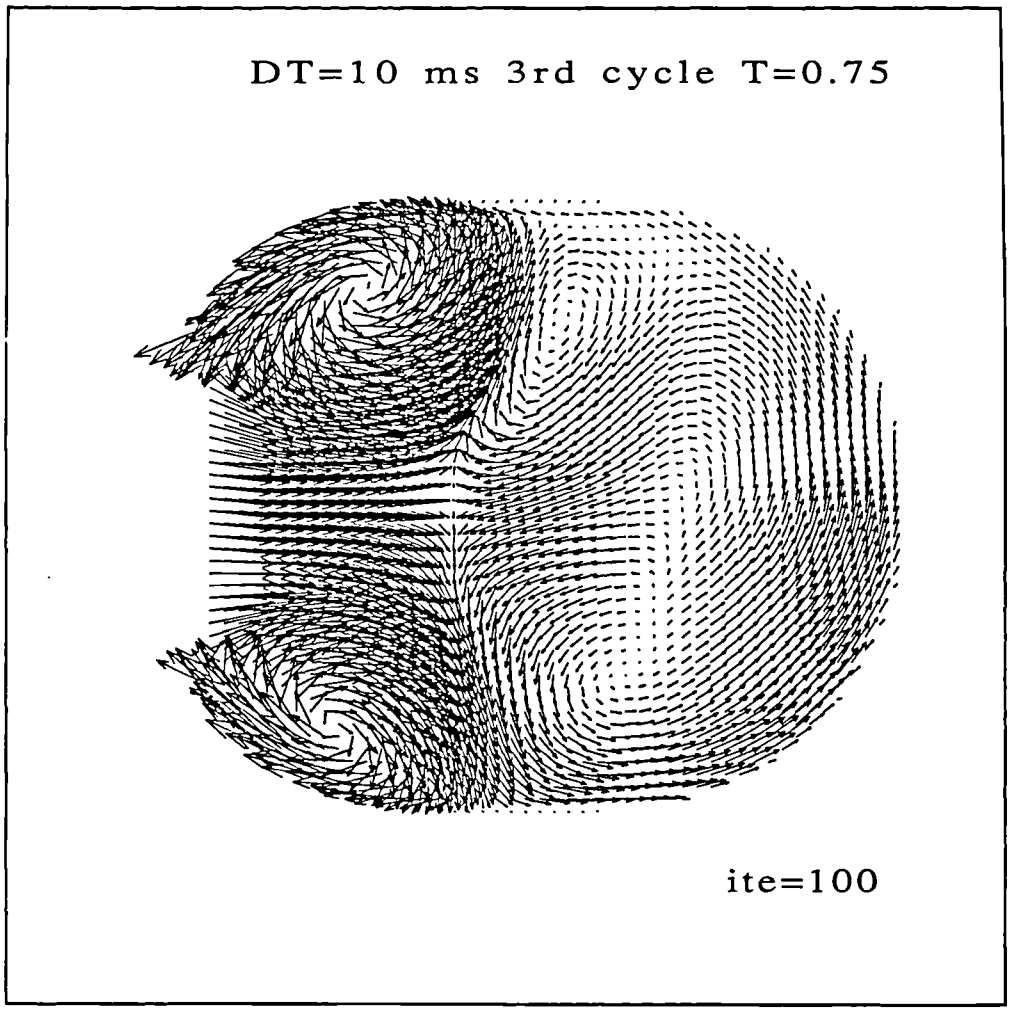


Figure 8.16 Predicted flow patterns at maximum volume $f$=1.33 Hz

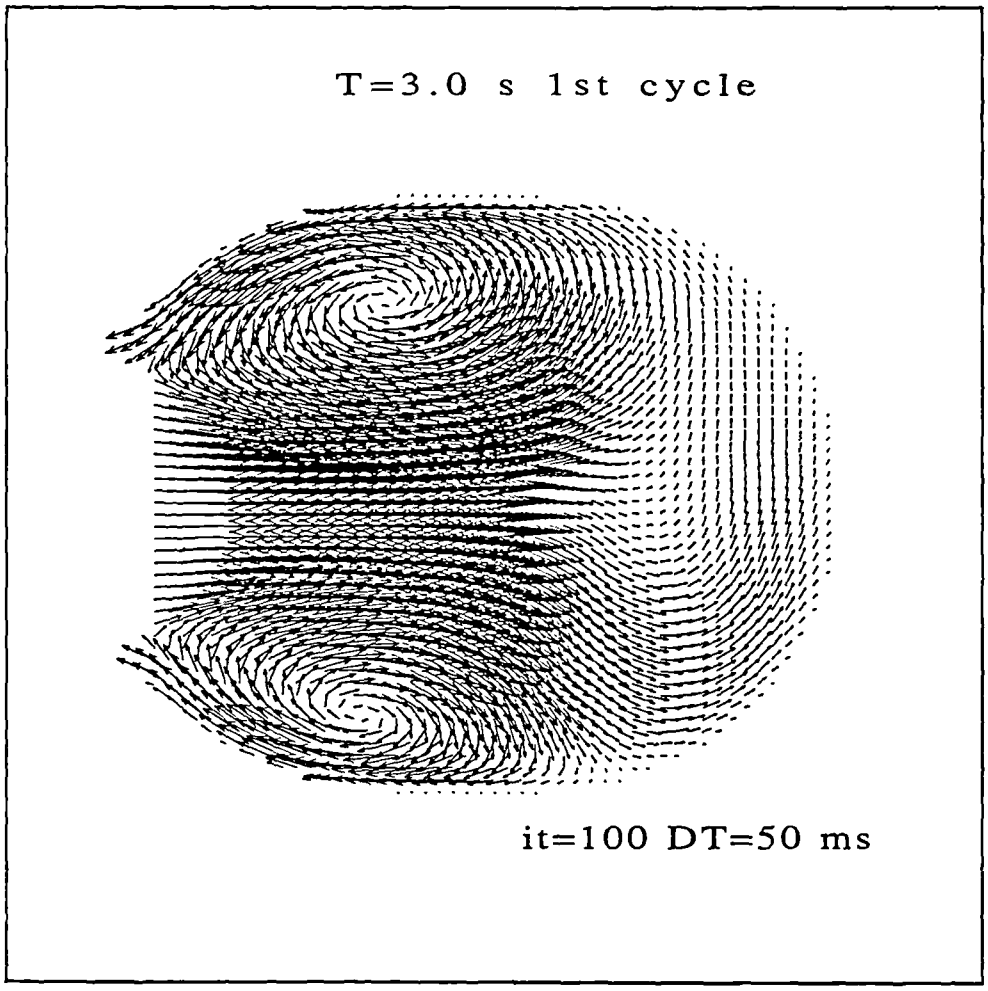


Figure 8.17 Predicted flow patterns at maximum volume $f$=0.33 Hz

#### 8.2.2.1 Considerations on symmetry-breaking bifurcation problems

Experimental observations and numerical analysis of the flow through a symmetric channel expansion have shown the following features. Initial flow at low Reynolds number is symmetric, becomes unstable in the proximity of a critical $Re$, and then becomes asymmetric. As $Re$ is increased further, various events may occur according to the channel configuration. The flow may become first three-dimensional and then time-dependent or viceversa.

Experimental studies on the above problem were performed by many investigators, see for example Sobey (1985). Numerical and experimental studies were carried out by Fearn, Mullin and Cliffe (1990). They showed that the asymmetry arises at a symmetry-breaking bifurcation. The numerical results predict that the unique solution to the steady two-dimensional Navier-Stokes equation loses stability at a critical value of $Re$, via symmetry-breaking bifurcation. Above this value of $Re$, the equations have

three solutions, of which the original solution is now unstable. As a consequence of the symmetry in the geoemtry of the problem, the two stable solutions *above the critical Re* are a pair of asymmetric solutions of opposite senses with respect to the line of symmetry. Analysis of the flow at higher *Re* is still under investigation, and will be discussed by Tavener and Cliffe in a paper in preparation.

Unfortunately, CFDS-FLOW3D is not suitable for investigating instabilities phenomena such as those above, and other packages, which use a finite element formulation, should be used to ascertain instabilities and bifurcations of the numerical solutions. However, since FLOW3D generates only stable solutions in the context of the symmetry-breaking bifurcation problem, an investigation on the stable solutions only can be carried out by performing a large number of simulations at different *Re* (e.g. frequency of the cycle), and analysing the flow symmetry. When by decreasing *Re* (or the frequency) the flow becomes symmetric, it is possible to extrapolate to the critical *Re*. This study requires an enormous CPU time and the use of powerful supercomputers. Future analysis will be carried out using the CRAY Y-MP machine at the ATLAS centre Cray (Rutherford).

## 8.3 CURVED INLET MODELS

As part of design considerations of the flask model discussed in the previous section, the requirement of preventing stagnant flows in the apex of the ventricle has been pointed out. In order to allow a good wash-out of the flow within the ventricle, Prof. Collins and Dr. Henry thought that a curved inlet could produce a flow field that would *'flush out'* the ventricle in a way that could not be achieved with a straight inlet, and thus reduce haemodynamic residence times. Two models are presented, a flask model and a spherical model. They both have a circumferential range of $180^0$.

### 8.3.1 Flask Models

The curved inlet flask model is shown in Fig.8.18. Geometric features of the ventricle are identical to those used for the straight inlet flask model as summarized in Table 8.1. The angle of curvature of the tube was $60^0$. The number of active volumes was 664, and the time step was one twenty-fourth of the period (T=0.75 s). Fig.8.19 shows the predicted flow patterns for various times in the cycles. As can be seen, the whole ventricular volume is 'washed' by a single vortex, which is established early in the expansion and disappears late during the contraction.

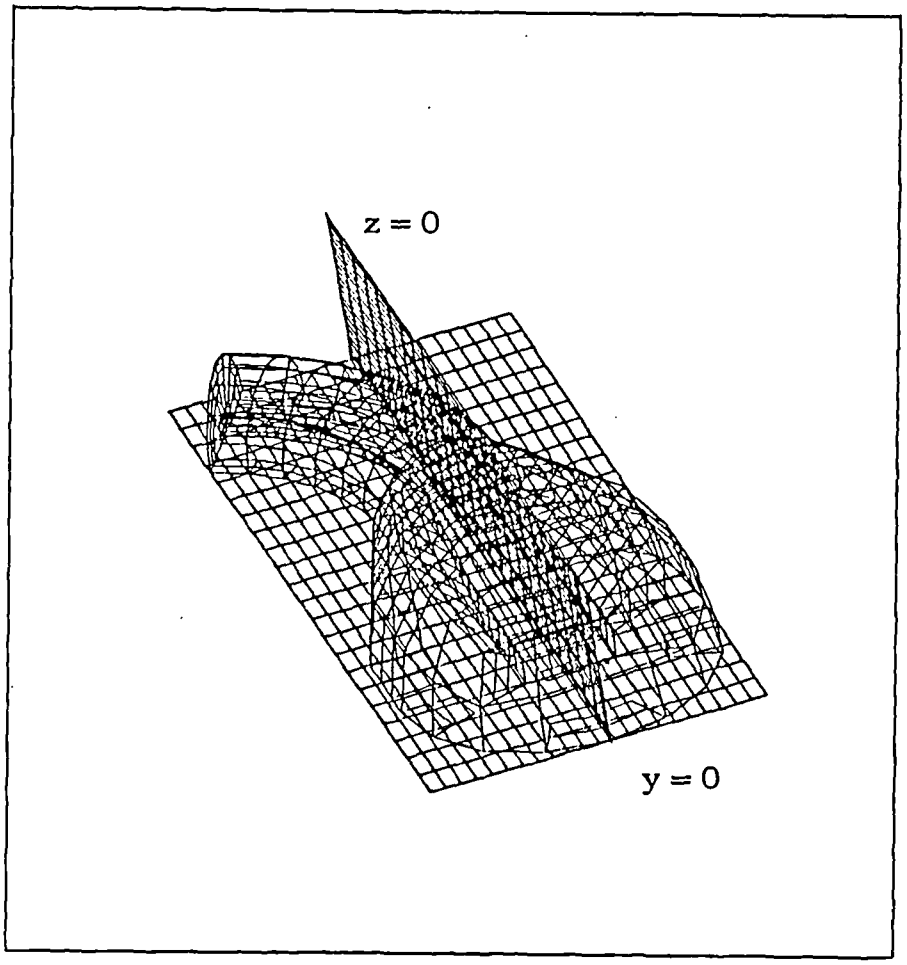


Figure 8.18 Curved inlet flask model

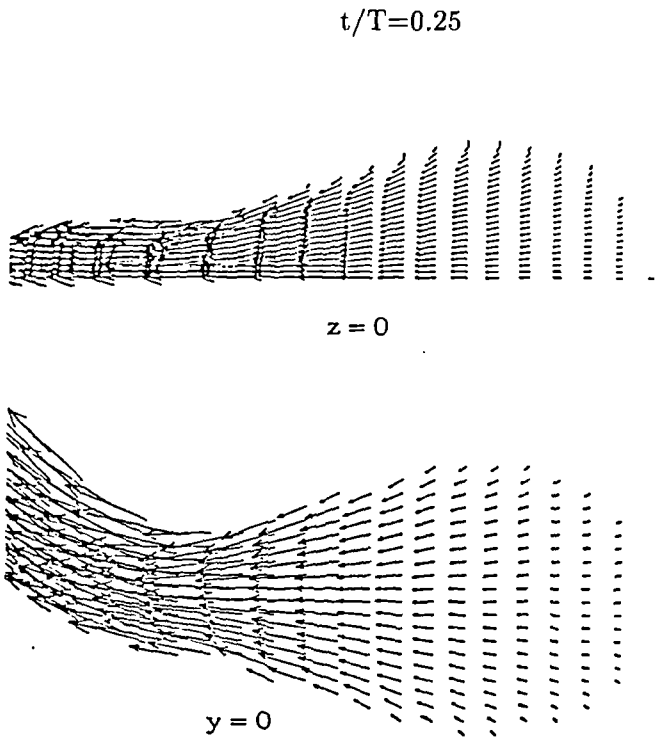

t/T=0.5

z = 0

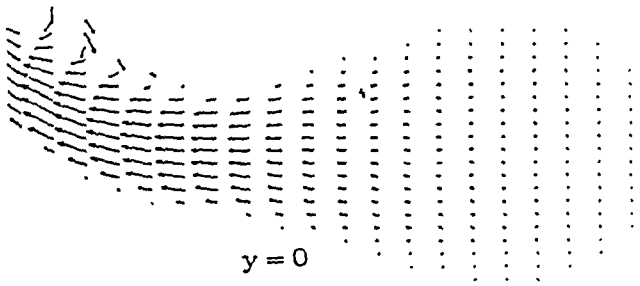

y = 0

t/T=0.75

z = 0

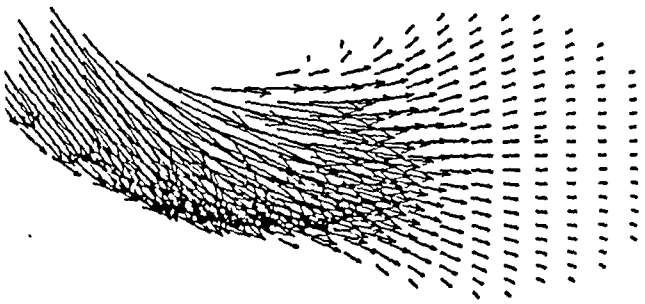

y = 0

t/T=1.0

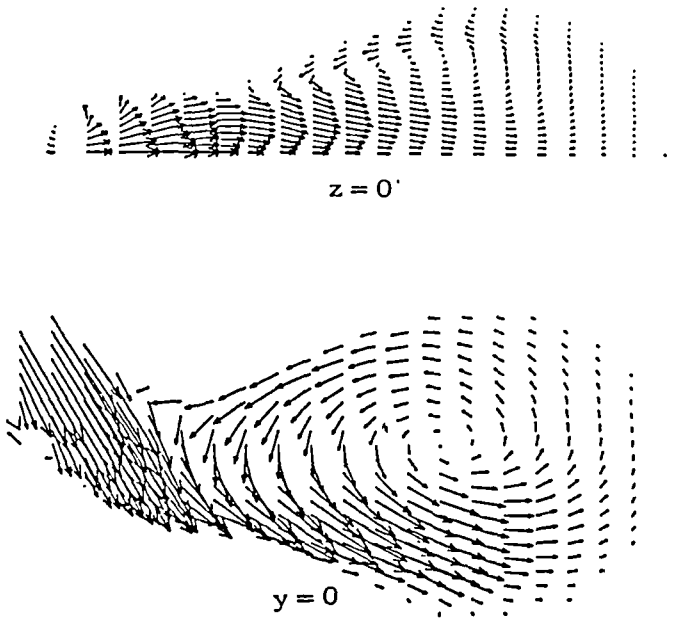


Figure 8.19 Predicted flow fields at four times of the cycle.

### 8.3.2 Spherical Models

The curved inlet spherical model is shown in Fig.8.20. Geometric features of this model are assumed to be the same as those for the straight inlet spherical model. The inclination angle of the tube was $60^0$. The number of active volumes was 568, and the time step was one twenty-fourth of the period (T=0.75 s). Fig.8.21 shows the predicted flow patterns for various times in the cycle. They show the formation of a vortex close to the inlet in the top side, which grows and moves around the ventricle up to its bottom side where it disappears just before the minimum volume is reached. This vortex travelling around the ventricular wall promotes a good wash-out of the ventricle again. However, before a complete evaluation of this model versus the straight inlet equivalent can be made, the levels of shear established during the cycle and the residence times values require consideration. This will be done in the near future.

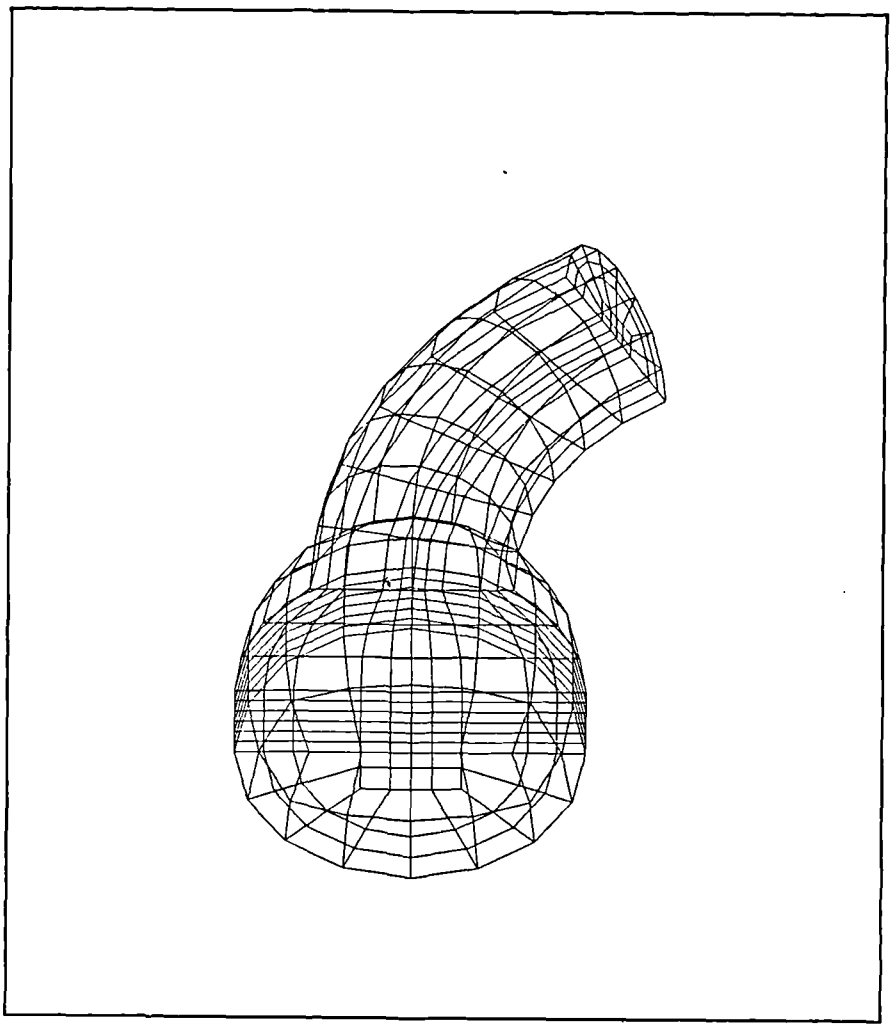

Figure 8.20 Curved inlet spherical model

t/T=0.25

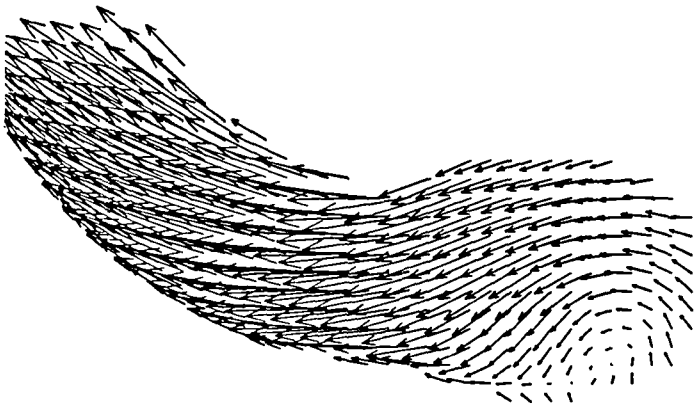

t/T=0.5

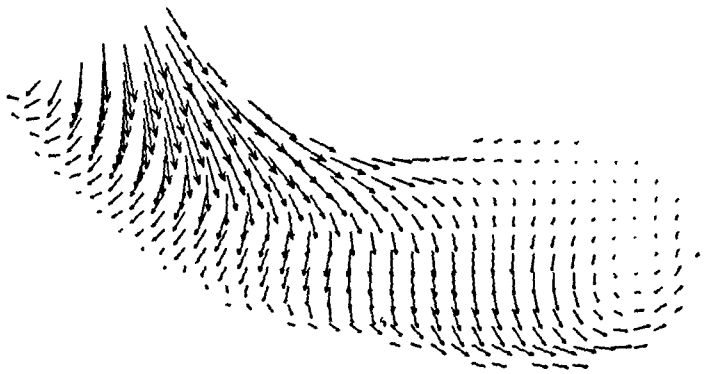

t/T=0.75

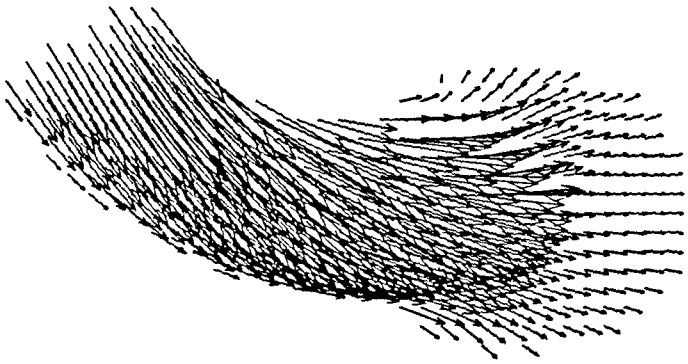

t/T=1.0

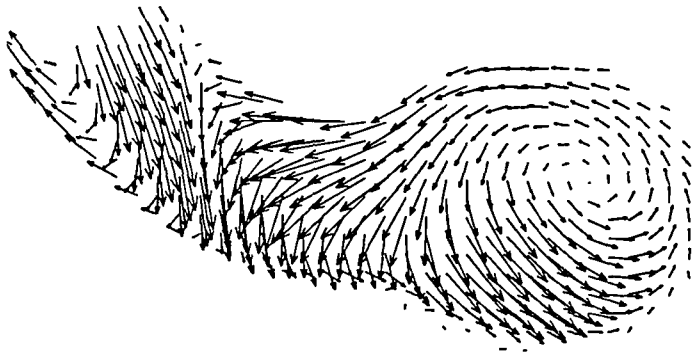

Figure 8.21 Predicted flow fields at four times of the cycle.

## 8.4 SUMMARY

The purpose of the numerical study presented in this chapter has been to ascertain how changes in shape and inlet/outlet configuration affect the resulting flow fields for design considerations. One significant finding with respect to inlet geometry is that a curved inlet appears to produce in the SMV a purging type of flow, similar to that seen in the normal left ventricle. This would promote mixing of the blood components and reduce significantly the residence times of particles. However, before a thorough evaluation of the design is made, analysis of levels of the shear (at the wall, and within the flow) requires further investigation. This will be carried out in the near future.

An interesting feature of the predicted flows inside axisymmetric $360^0$ models is that the flow patterns assume asymmetric characteristics which may be attributed to a mathematical bifurcation occurring in the numerical solution. To investigate this phenomenon a large number of simulations over the frequency range needs to be performed. Because of the prohibitive computer cost only a few frequency values have been investigated so far. Further studies will be carried out using a new Supercomputer Resource Grant recently awarded.

# CHAPTER 9

# CONCLUSIONS AND FUTURE WORK

In the present thesis, numerical studies have been carried out on model SMVs with the major objective of providing a powerful and reliable comprehensive analysis tool for the design of model SMVs. Most of the work presented in this Thesis has been focused on the validation of the numerical predictions computed by CFDS-FLOW3D. A comprehensive set of validations has been carried out.

Firstly, a validation exercise of the moving wall capability of both single- and multi-block versions of CFDS-FLOW3D has been presented. Predicted flows in an expanding or contracting semi-infinite pipe have been compared with an available analytical solution of good validity. Very good agreement between the predictions of both versions of the code and the analytical solution have been achieved.

Subsequently, two numerical model SMVs have been studied. For the simple rigid/compliant model, the predicted flow fields have been shown to be in good agreement over the cycle with the experimental flow fields from the *in vitro* study for a similar model. For the spherical-end rigid/compliant model, the predicted flow structures have shown that the number of vortex rings formed at the time of maximum ventricular volume is a function of the frequency of the wall motion. The number of vortices increases with the frequency. A similar connection between vortex structure and frequency has been seen in the *in vitro* model SMVs. These results have indicated that modern CFD codes, such as CFDS-FLOW3D, are probably capable of simulating physiological flows in actual SMVs.

As a next step, the numerical predictions of model SMVs driven by experimental wall motion have been qualitatively compared with the general features of the flow patterns in the experiments. In order to study the dynamics of the formation of the vortices (the striking feature of the flow inside model SMVs), sigmoidal filling curves have been used to drive the ventricular wall motion. A range of numerical simulations has been performed in order to validate the numerical solution against the experimental *in vitro* data of the flow inside a ventricle into which fluid was drawn following a sigmoidal filling sequence. Qualitative and quantitative comparisons have been analysed for two models: 1) an experimental wall motion model, and 2) an analytical wall motion model.

Although the basic features of the flow patterns revealed in the experiments are predicted by FLOW3D, the numerical solutions have to be viewed with some caution. The best agreement was obtained for slow filling of the ventricle. Predicted results have shown that the numerical solution is most sensitive to the way in which the wall motion is defined. The development of an analytical wall motion model with smooth wall motion profiles in space and in time, has produced a closer quantitative agreement of the predictions with the experimental data.

It could be argued that the assumed axisymmetry of the flow should be investigated by modelling the full ventricle, and not a two-dimensional slice; however, this would increase the size of the grid to such an extent that the cost of the computation would be high and the scope for grid or time stepping refinement would be limited. In the design of model SMVs, it is very important to consider its three-dimensionality. Some 3-D models have been presented as proposals for potential designs for an SMV. Different shapes and inlet/outlet configurations have been analysed and resulting flow fields have been discussed in the light of design considerations. One significant finding with respect to inlet geometry is that a curved inlet appears to produce in the SMV a purging type of flow, similar to that seen in the normal left ventricle. This would promote mixing of the blood components and reduce significantly the residence times of particles.

An interesting feature of the predicted flows inside axisymmetric 3-D models is that the flow patterns assume asymmetric characteristics which may be attributed to a mathematical bifurcation occurring in the numerical solution. To investigate this phenomenon a large number of simulations over the frequency range needs to be performed. Because of the prohibitive computer cost only a few frequency values have been investigated so far. Further studies will be carried out using a new Supercomputer Resource Grant recently awarded.

From the results discussed in the preceding chapters, we can conclude that both qualitative and quantitative aspects of reliability of the numerical predictions have been established by critical validation against experimental data. This agreement was only reached after considerable effort spent varying several computational parameters, including grid density and time step. Validation with geometry of a more complex character (not axisymmetric and hence only with 3-D models) will require further investigation. Also prediction of residence times and shear stresses will require the development and use of new programs. A critical evaluation of the predicted results may be obtained by a validation of the shear stresses against *in vitro* measurements. In order to investigate particle tracks and residence times, which are clinically relevant, a visualization of the predicted results is intended to be performed using the most advanced visual techniques.

Finally, in this thesis numerical studies have modelled only the fluid dynamics of model SMVs, the wall motion being prescribed by analytical functions or experimental data. However, the SMV behaviour is a solid-fluid coupled problem. The review has included consideration of the solid-fluid coupled approaches and of ventricle modelling with special attention paid to muscle modelling. Muscles are not passive tissues, and therefore, in a coupled approach, not only are the fluid and solid mechanics equations coupled, but so also are the muscle mechanics equations. Following Peskin's approach our initial thoughts on solid-fluid coupling modelling involved considering the solid as a quasi-fluid. However, more recently other approaches have been tested in our group where the solid behaviour is based on classical solid mechanics equations. Modelling the solid-muscle behaviour in this way is felt to be very promising for coupled solid-fluid modelling in the future.

## REFERENCES AND BIBLIOGRAPHY


Acker M.A., Hammond R., Mannion J.D., Salmons S., Stephenson L.W. (1986): An autologous biologic pump motor. J. Thorach. Cardiovasc Surg. vol.92 pp.733-46

Acker M.A., Hammond R., Mannion J.D., Salmons S., Stephenson L.W. (1987a): Skeletal muscle as the potential power source for a cardiovascular pump:Assessment in vivo. Science vol. 236 pp.324-327

Acker M.A., Anderson W.A., Hammond R., Mannion J.D., Chin A.J., Buchaniam J.W., Morse C.C., Kelly A.M., Stephenson L.W. (1987b): Skeletal muscle ventricles in circulation: one to eleven week's experience. J. Thorach. Cardiovasc. Surgery. vol.94 pp.163-74

Acker M.A., Mannion J.D., Brown W.E., Salmons S., Henriksson J., Bitto T., Gale D.R., Hammond R., Stephenson L.W. (1987c): Canine diaphragm after one year of continuous electrical stimulation: its potential as a myocardial substitute. J. Appl. Physiol. vol.62 pp.1264-70

Acker M.A., Anderson W.A., Hammond r.L., DiMeo F., McCullum J., Staum M., Velchik M., Brown W.E., Gale D., Salmons S., Stephenson L.W. (1987d): Oxygen consumption of chronically stimulated skeletal muscle. J. Thorac. Cardiovasc. Surgery vol. 94 pp.702-9

Akatsu T., W.J. Kolff (1958): Permanent substitutes for valves and heart. Trans. Am. Soc. Artif. Intern. Organs vol.4 p.230

Alderton J.H., Wilkes N.S. (1988): Some applications on New Finite Difference Schemes for Fluid Flow Problems. Harwell Report AERE-R 13234

Amling A., Yamada N., Hokimoto T., Akamatsu T. (1990): Experimental and numerical investigation of the performance and shear stresses in a nutating centrifugal blood pump In: Biofluid Mechanics, Blood Flow in Large Vessels. Proc. of the 2nd International Symposium in Biofluid Mechanics and Biorheology Liepsch D. (ed) pp.343-349

Andersen J.S., Bridges C.R., Anderson W.A., Acker M.A., Hammond R.L., DiMeo F., Chin A., Stephenson L.W. (1989): In: Assisted Circulation, ed. by F. Unger, Innsbruck, Austria. Springer-Verlag, pp.490-511

Anderson D.A., Tannehill J.C., Pletcher R.H. (1986): Computational Fluid Mechanics and Heat Transfer. McGraw-Hill Book Company

Anderson W.A., Andersen J.S., Acker M.A., Hammond R.L., Chin A.J., Douglas P.S., Khalafalla A.S., Salmons S., Stephenson L.W. (1988a): Skeletal muscle grafts applied to the heart: a word of caution. Circulation (Suppl. III) vol.78 pp.180-90

Anderson W.A., Bridges C.R., Chin A.J., Andersen J.S., Acker M.A., Hammond R.L et al. (1988b): Long-term neurostimulation of skeletal muscle: its potential for a tether-free biologic cardiac assist device. PACE vol. 11 pp. 2128-34

Anliker M., Rockwell R.L., Odgen E. (1971): Nonlinear analysis of flow pulses and shock waves in arteries. Part I: derivation and properties of mathematical model. Part II: Parametric study related to clinical problems. J. Applied Mathematics and Physics (ZAMP) vol.22 pp.217-246 (part I) vol. 22 pp.563-81 (part II)

Anderson D.R., Pochettino A., Hammond R.L., Hohenhause E., Spanta A.D., Bridges C.R. (1991): Autogenously lined skeletal muscle ventricles in circulation. Up to nine month's experience. J. Thorach. Surg. vol. 101 pp.661-70

Anonymous (1990a): STAR-CD Manual, Computational Dynamics, London, 1990

Anonymous (1990b): The PHOENICS Reference Manual. Report CHAM/TR/100. CHAM Ltd, London 1990

Anonymous (1990c): Harwell-FLOW3D, Release 2.3: User Manual. Harwell Laboratory, 1990

Anonymous (1991a): User guide to FEAT. Engineering Analysis Centre, Nuclear Electric Plc, UK

Anonymous (1991b): FLOW3D Relėase 2.4: User Manual. AEA Ind-Tech, Harwell Laboratory, Oxfordshire U.K., 1991

Anonymous (1992): FLOW3D Release 3.1.2: User Manual. AEA Ind-Tech, Harwell Laboratory, Oxfordshire U.K., 1992

Anonymous (1993): FLOW3D Release 3.2: User Manual. AEA Ind-Tech, Harwell Laboratory, Oxfordshire U.K., 1993

Anonymous (1994a): FLOW3D Release 3.3: User Manual. AEA Ind-Tech, Harwell Laboratory, Oxfordshire U.K., 1994

Anonymous (1994b): ENVIRONMENT User Guide Release 1,5 AEA Ind-Tech, Harwell Laboratory, Oxfordshire U.K., 1994

Araki K., Taenaka Y., Masuzawa T., et al. (1993): A flow visualization study of centrifugal blood pumps developed for long term usage. Artificial Organs vol. 17 pp. 307-12

Armenti F., Bitto T., Macoviak J.A. et al. (1984): Transformation of skeletal muscle for cardiac replacement. Surg. Forum vol. 35 pp.258

Arts M.G.J. (1978): A mathematical of the dynamics of the left ventricle and the coronary circulation. Thesis, University of Limburg, The Netherlands, 1978

Arts T., Reneman R.S. (1977): Analysis of intramyocardial pressure (IMP). A model study. Bibl. Anat. vol. 15 pp.103-7

Arts T., Reneman R.S., Veenstra P.C. (1979): A model of the mechanics of the left ventricle. Annals of Biomedical Engineering vol. 7 pp.299-318

Arts T., Reneman R.S. (1989): Dynamics of the left ventricular wall and mitral valve mechanics- A model study. J. Biomechanics vol.22 n.3 pp.261-71

Babuska I., Aziz A.K. (1972): Survey lectures on the mathematical foundation of the finite element method. In: Mathematical Foundation of the Finite Element Method. Ed. A.K. Aziz. Academic Press, New York

Back L. (1977): Left ventricular wall and fluid dynamics of cardiac contraction. Math. Biosc. vol. 36 pp.257-97

Baker A.J. (1983): Finite Element Computational Fluid Mechanics. McGraw-Hill

Baker A.J. (1984): A Finite Element Penalty Algorithm for the Parabolic Navier- Stokes Equations for Turbulent Three Dimensional Flows. Computer Methods in Applied Mechanics and Engineering Vol. 46 pp. 277-93

Badylack S.F., Stevens L., Janas W., Gray M.H., Geddes L.A., Voorhees W.D. (1989): Cardiac assitance with electrically stimulated skeletal muscle. Medical & Biological Engineering & Computing pp. 159-162

Baier R.E. (1977): The organization of blood components near interfaces. Ann. N.Y. Acad. Sci. vol.293 pp. 17-36

Baldwin J.T., Deutch S., Geselowitz D.B., Tarbell J.M. (1990): Estimation of Reynolds stresses within the Penn State left vehtricular assist device. ASAIO Trans. vol. 35 pp. M274-M278

Baliga B.R., Patankar S.V. (1980): A New Finite Element Formulation for Convection-Diffusion Problems. Num. Heat Transfer Vol.3 pp.393-409

Baliga B.R., Patankar S.V. (1983): A Control Volume Finite Element Method for Two Dimensional Fluid Flow and Heat Transfer. Num. Heat Transfer Vol.6 pp.245-61

Barany M. (1967): ATPase activity of myosin correlated with speed of muscle shortening. J. Gen. Physiology vol.50 pp.197-216

Baratta R.V., Solomonow M. (1992): The dynamic performance model of skeletal muscle. Critical Review in Biomedical Engineering vol.19 n.6 pp.419-454

Barnard C.N. (1968): Human cardiac transplanation. Am. J. Cardiology vol.22 p.584

Beck C.S. (1935): A new blood supply to the heart by operation. Surg. Gynecol. Obstet. Vol.1 pp.407-10

Bernhard W.F., C.G. Lafarge, T. Robinson, I. Yun, K. Shirahige (1968): An improved blood-pump interface for left ventricular bypass. Ann. Surg. vol. 168 pp. 750-64

Bernstein E.F., F.D. Dorman, P.L. Blackshear, D.R. scott (1970): An efficient compact pump for assisted circulation. Surgery vol.68 p.105

Beyar R., Sydeman S. (1986): The dynamic twisting of the left ventricle: A computer study. Ann. Biomed. Eng. vol.14 pp.547-62

Brackill J.U., Saltzman J. (1980): An Adaptive Computation Mesh for the Solutionof Singular Perturbation Problems. In: Numerical Grid Generation Techniques. NASA Conference Publication 2166 pp.193-96

Brady A.J. (1967): Three element model for muscle mechanics. Its applicability to cardiac muscle. Physiologist vol.10 pp.75

Brankov G., Petrov N. (1978): A thermodynamic model of biological body: muscle mechanics. Trans ASME J. Biomech Eng vol.100 pp.14-19

Brash J.L. (1989): Hydrophobic polymers as materials for interfacing with blood. In: Assisted Circulation, ed. by F. Unger, Innsbruck, Austria. Springer-Verlag, pp.506-519

Brezzi F. (1974): On the Existence, Uniquess, and Approximation of Saddle-Point Problems arising from Lagrange Multipliers. R.A.I.R.O., Numerical Analysis, Vol.8 pp. 128-51

Bridges C.R., Brown W.E., Hammond R.L., Anderson D.R., Anderson W.A., DiMeo F., Stephenson L.W. (1989): Skeltal Muscle Ventricles: improved performance at physoilogical preloads. Surgety vol.106 pp.275-82

Brooks A.N., Hughes T.S.R. (1982): Streamline Upwind/Petrov-Galerkin Formulations for Convection Dominated Flows with Particular Emphasis on the Incompressible Navier-Stokes Equations. Comp. Meth. Appl. Mech. Eng. Vol.32 pp.199-259

Brown C.H., Leverett L.B., Lewis C.W. et al. (1975): Morphological biochemical and functional changes in human platelets subjected to shear stress. J. Lab. Clin. Med. vol.86 pp.462

Brown M.D., Cotter M.A., Hudlicka O., Vrbova G. (1976): The effects of different patterns of muscl activity on capillary density, mechanical properties and structure of slow and fast rabbit muscles. Pflugers Arch. vol. 361 pp.241-50

Brown W.E., Salmons S., Whalen r.G. (1983): The sequential replacement of myosin subunit uniform during muscle type transformation induced by long-term electrical stimulation. J. Biol. Chem. vol. 258 pp.14686-14692

Brown J.M.C., Henriksson J., Salmons S. (1989): Restoration of fast muscle characteristics following cessation of chronic stimulation: physiological, histochemical and metabolic changes during slow-to-fast transformation. Proc. R. Soc. B vol.235 pp.321-46

Bruck S.D. (1989): Some current problems and new dimensions of polymeric biomaterials for blood contact applications. In: Assisted Circulation, ed. by F. Unger, Innsbruck, Austria. Springer-Verlag, pp.497-505

Burns A.D., Wilkes N.S., Jones I.P., Kightley J.R. (1986): FLOW3D: Body-Fitted Coordinates. AERE-R 12262

Burns A.D., Wilkes N.S. (1987): A finite Difference Method for the Computation of Fluid Flows in Complex Three-Dimensional Geometries. UKAEA Report AERE-R 12342

Canuto C., Hussaini M.Y., Quarteroni A., Zang T.A. (1987): Spectral Methods in Fluid-Dynamics. Berlin. Springer-Verlag

Caro C.G. (1981). Arterial fluid mechanics and atheorgenesis. Recent Advances in Cardiovascular D vol. 2 pp.6-11

Caro C.G., Pedley T.J., Schroter R.C., Seed W.A. (1978). In: The Mechanics of the Circulation. Chapter 10, Oxford University Press pp. 177

Carpantier A., Chachques J.C. (1985): Myocardial substitution with a stimulated skeletal msucle: first successful clinical case (Letter). Lancet vol. 1 pp. 267

Carraro U., Catani C., Rizzi C., Danieli-Betto D., Arpesella G., Mikus P.M., Cirillo M., Parlapiano M., Senni M., Pierangeli A. (1991): Muscle conditioning for circulatory assist-

ance: an effective protocol using continuous or cyclic stimulation. In: Harnessing skeletal muscle power for cardiac assistance. Proc. of the expert meeting held in Liverpool. Salmons and Jarvis (ed), May 8-12, 1990, pp.55-59

Casson N. (1959): A flow equation for pigment-oil suspension of the printing ink type. In: Rheology of Disperse Systems. Pergamon Press, Oxford pp. 84-104

Cebeci T., Hirsh R.S., Keller H.B., Williams P.G. (1981): Studies of Numerical Methods for the Plane Navier-Stokes Equations. Computer Methods in Applied Mechanics and Engineering Vol. 27 pp.13-44

Chachques J.C., Grandjean P.A., Schwartz K., Mihaileanu S., Fordeau M., Swynghedaw B. Fontaliran F., Romero N., Wisnewsky C., Perier P., Chanvand S., Bourgeois I., Carpentier A. (1988): Effect of latissimus dorsi dynamic cardiomyoplasty on ventricular function. Circ. (Suppl. III) vol.78 pp.203-16

Chachques J.C., Grandjean P.A., Bourgeois L., Carpentier A. (1989): Dynamic cardiomyoplasty to improve ventricular function In: Assisted Circulation, ed. by F. Unger, Innsbruck, Austria. Springer-Verlag, pp.525-541

Chachques J.C., Grandjean P.A., Cabrera Fischer E.I., Latremouille C., Jebara V.A., Bourgeois I., Carpentier A. (1990): Dynamic aortamyoplasty to assist left ventricular failure. Ann. Thorach. Surg. vol.49 pp.225-30

Chadwick R.S. (1981): The myocardium as a fluid-fiber continuum: passive equilibrium configurations, Advances in Bioengineering. ASME. New York pp.135-138

Chadwick R.S. (1982): Mechanics of the left ventricle. Biophys. J. vol.39 pp. 279-88

Chagas A.C.P., Moreira L.F.P., Da Luz P.L., Camarano G.P., Leirner A., Stolf N.A.G. (1989): Stimulated preconditioned skeletal muscle cardiomyoplasty. An effective means of cardiac assist. Circulation vol. 80 (Suppl III) pp. 202-8

Chandran K.B et al. (1984): Pulsatile flow past aortic valve bioprostheses in a model human aorta. J. Biomech. vol. 17 pp.9

Chen C.J., Chen H.C. (1984): Finite analytic numerical method for unsteady two-dimensional navier stokes equations. J. Comp. Physics vol. 53 pp. 209-226

Chen C.-J, Naseri-Neshat H., Ho K.-S (1981): Finite Analytical Numerical Solution of Heat Transfer in Two-Dimensional Cavity Flow. Numerical Heat Transfer Vol.4 pp.179-97

Chen J.C., Kwak B.M., Rim K., Falsetti H.L. (1980): A model an active left ventricle deformation-formulation of a nonlinear, quasi-steady finite element analysis for oethotropic, three-dimensional myocardium. Proc. Intern. Conf. on Finite Elements in Biomechanics, University Arizona Press pp.639-55

Chesler N.C., Kamm R.D. (1994): A Systematic Method for Design and Evaluation of Cardiac Pumping Chamber. Advances in Bioengineering ASME 1994 BED Vol.28 pp. 401-2

Chien S. (1970): Shear dependence of effective cell volume as a determinant of blood viscosity. Science vol.168 pp. 977

Chien S., Usami S., Taylor H.M., Lundberg J.L., Gregersen M.I. (1966): Effects of hematocrit and plasma proteins on human blood rheology at low shear rates. J. Applied Physiol. vol. 21 pp.81-87

Chorin A.J. (1967): A Numerical Method for Solving Incompressible Viscous Flow Problems. J. Comput. Phys. Vol.2 pp. 12-26

Ciofalo M., Collins M.W. (1988): Time-Dependent Numerical Simulation of the Starting Flow of an Incompressible Fluid past a Backward-Facing Step. In: Proc. Agard Symposium Validation of CFD, Lisbon, 1988 Vol.36 pp 1-16

Ciofalo M., Collins M.W. (1989): $\kappa - \varepsilon$ Predictions of Heat Transfer in Turbulent Recirculating Flows using an Improved Wall Treatment. Numerical Heat Transfer, Part B Vol.15 pp 21-47

Ciofalo M., Collins M.W., Perrone G. (1991): Turbulent Flow and Heat Transfer Predictions for Cross-Corrugated Rotary Regenerators. Procs EuroTech - Direct 91, Thermofluids Engineering, Birmingam, U.K. 2-4 July 1991, Paper c413/041

Ciofalo M., Karayiannis T.G. (1991): Natural Convection Heat Transfer in a Partially -or Completely- Partined Vertical Rectangular Enclosure. Int. J. Heat and Mass Transfer Vol.34 pp.167-79

Ciofalo M. (1992): Large-Eddy Simulation of Turbulent Flows with Heat Transfer in Simple and Complex Geometries. Ph.D. Thesis, Dept of Mechanical Engineering and Aeronautics, City University, London, U.K.

Ciofalo M., Collins M.W. (1992): Large-Eddy Simulation of Turbulent Flow and Heat Transfer in Plane and Rib-Roughened Channels. Int. J. Numeric. Methods in Fluids Vol. 15 pp.453-89

Clark J. (1994): CFD brings more Power to the Design Elbow. Professional Eng. Vol. 7 N.6 p.16

Clark B.J. III, Acker M.A., McCully K., Subramanian H.V., Hammond R.L., Salmons S., Chance B., Stephenson L.R. (1988): In vivo $^{31}$P-NMR spectroscopy of chronically stimulated canine skeletal muscle. Am. J. Physiol. vol.254 pp. C258-66

Cokelet G.R. (1972): The rheology of human blood. In: Biomechanics - Its foundations and Objectives. Vol. II. Fung, Perrone, Anliker (eds). Prentice Hall p.63-103

Collins M.W. (1980): Finite Difference Analysis for Developing Laminar Flow in Circular Tubes Applied to Forced and Combined Convection. Int. J. Numeric. Methods in Engineering Vol.15 pp.381-404

Collins M.W., Xu X.Y. (1990): A Predective Scheme for Flow in Arterial Bifurcations: Comparisons with Laboratory Measurements. Biomechanical Transport Processes. Ed. by Mosora F., Caro C., et al. Plenum Press pp. 125-33

Collins M.W., Ciofalo M. (1991): Computatiional Fluid-Dynamics and its Appilcation to Transport Processes. J. Chemical Technology and Biotechnology Vol.52 pp.5-47

Cooley D.A. (1969): First human implantation of cardiac prosthesis for staged total replacement of the heart. Trans. Am. Soc. Artif. Intern. Organs vol.15 p.252

Courant R., Friedrichs K.O., Lewy H. (1928): Uber die Partillen Differenzengleinchungen der Mathematischen Physik. Mathematische Annalen Vol. 11 pp. 32-74. Translated to: On the Partial Difference Equations of Mathematical Physics, IBM J. Res. Dev. Vol.11 pp.215-234 1967)

Courant R., Isaacson E., Rees M. (1952): On the solution of Non-Linear Hyperbolic Differential equations by Finite Differences. Comm. Pure Appl. Math. Vol. 5 p.243

Creswell L.L., M. Rosenbloom, J.L. Cox, T.B. Ferguson, N.T. Kouchoukos, T.L. Spray, M.K. Pasque, T.B. Ferguson, T.H. Wareing, C.B. Huddleson (1992): Intraaortic Balloon Counterpulsation: Patterns of usage and outcome in cardiac surgery patients. Annals of Thorachic Surgery vol.54 n.1 pp.11-20

Crow M.T., Kushmerick M.J. (1982): Chemical energetics of slo- and fast-twitch muscles of the mouse. J. Gen. Physiol. vol.79 pp.147-166

Cumming D.V.E., Pattison C.W., Yacoub M.H. (1991): Wrapping the aorta. In: Harnessing skeletal muscle power for cardiac assistance. Proc. of the expert meeting held in Liverpool. Salmons and Jarvis (ed), May 8-12, 1990, pp.31-33

De Bakey M.E. (1934): A single continuous flow blood transfusion instrument. New Orlans Med. Surg. I vol.87 p.386

De Bakey M.E. (1971): Left ventricular bypass pump for cardiac assistance. Am. J. Cardilogy vol.27 p.3

De Jesus F.R. (1931): Breves consideraciones sobre un case de herida penetrante del corazon. Bol. Assoc. Med. PR vol. 23 pp.380-382

Demirdzic I., Peric M. (1988): Space conservation law in finite volume calculations of fluid flow. Intern. J. Numerical Methods in Fluids vol.88 pp. 1037-58

Demirdzic I., Peric M. (1990): Finite volume method prediction of fluid in arbitrarily shaped domains with moving boundaries. Intern. J. Numerical Methods in Fluids vol.88 pp. 771-790

Dennis C., A. Senning, D.P. Hall, J.R. Moreno (1962): An experimental study of prolonged left heart bypass without thoracotomy. Ann. Surg. vol.156 p.190

De Vries W.C., Anderson J.L., Joyce L.D., Anderson F.L., Hammond E.L., Jarvik R.K., Kollf W.J. (1984): Clinical Use of Total Artificial Heart. N. Engl. J. Med. Vol 310 pp. 273-278

Dewitz T.S. et al. (1977): Mechanical trauma in leukocytes. J. Lab. Clin. Med. vol. 86 pp.462

Douglas J., Rachford H.H. (1956): On the Numerical Solution of Heat Conduction Problems in two and three Space Variables. Trans. AMer. Math. Soc. Vol.82 pp.421-39

Douglass R.W., Ramshaw J.D. (1994): Future Research Directions in Computational Fluid-Dynamics. J. Fluids Eng. ASME Vol. 116 pp. 212-5

Drinkwater D.C., Chiu C.-J., Modry D., et al. (1980): Cardiac assist and myocardial repair with synchronously stimulated skeletal muscle. Surg. Forum vol. 31 pp. 271-4

Eberhardt A.W., Sanford J.A. (1993): An experimental and finite element study of ventricular wall stress models. ASME Advances in Bioengineering BED-Vol.26 pp.563-566

Edman K.A.P. (1966): The relation between sarcomere length and active tension in isolated semitendinosus fibres of the frog. J. Physiology vol.183 pp. 407-417

Edman K.A.P., Nilsson E. (1968): The mechanical parameters of myocardial contraction studied at a constant length of the contractile element. Acta Physiol. Scand. vol.72 pp.205-219

Edman K.A.P., Nilsson E. (1972): Relationship between force and velocity of shortening in rabbit papillary muscle. Acta Physiol. Scand. vol.85 pp.488-500

Eilers R., Ritter C., Reul H., rau G. (1994): Influence of non-Newtonian blood properties on numerical flow simulation at mechanical heart valve prostheses. Proc. of the 3rd International Symposium in Biofluid Mechanics and Biorheology July 16-19, 1994. Liepsch D. (ed) pp.693-700

Einsenberg B.R., Salmons S. (1981): The reorganization of subcellular structure in muscle undergoing fast-to-slo type transformation. A stereological study. Cell. Tissue Research vol. 220 pp.449-71

Einsenberg B.R. (1983): Quantitative ultrastructure of mammalian skeletal muscle. In: Peachy L.D., Adrian R.H., and Geiger S.R. (eds). Handbook of Physiology. Bethesda, MD:Amarican Physiological Society. pp.73-112

Einsenberg B.R., Brown J.M.C., Salmons S. (1984): Restoration of fast muscle characteristics following cessation of chronic stimulation. Cell. Tissue Research vol. 238 pp.221-30

Eiseman P. (1979): A Muilti-Surface Method of Coordinate Generation. J. Comp. Phys. Vol.33 pp. 118-150

Eiseman P.R., Eriebacher G. (1982): Grid Generation for the Solution of Partail Differential Equations. NASA Contract Report 178365

Evans R.W., Manninen D.L., Garrison L.P., Maier A.M. (1986): Donor availability as the primary determinant of the future of heart transplantation. JAMA vol.255 pp.1892-1898

Falsetti H.L., Mates R.E., Grant C., Green D.G., Bunnell I.L. (1970): Left ventricular wall stress calculated from one-plane cineangiography: An approach to force-velocty relationship in man. Circ. Res. vol. 26 n.1 pp.71-83

Faulkner J.A., Claflin D.R., Brooks S.V., Burton H.W. (1992): Power output of fiber segments from human latissimus dorsi muscles: implications for heart assist devices. In: Basic and Applied Myology: Perspective for the 90's, Carraro U., Salmons S. (eds). Padua Unipress pp. 31-38

Fearn R.M., Mullin T., Cliffe K.A. (1990): Nonlinear flow phenomena in a symmetric sudden expansion. J. Fluid Mech. vol.211 pp.595-608

Feit T.S. (1979): Diastolic pressure-volume relations and distribution of pressure and fiber extension across the wall of a model left ventricle. Biophysics J. vol.28 pp. 143-166

Fenn W.O. (1923): Quantitaive comparison between energy liberated and work performed by isolated sartorious muscle of the frog. J. Physiol. (London) vol.58 pp.175

Fenn W.O., Marsh B.S. (1935): Muscular force at different speeds of shortening. J. Physiology vol.85 pp.277

Fick A. (1891): Neue beitrage fur kenntniss von der warmeentwicklung im muskel. Pfluegers Arch. Gesamte Physiol. Menschen Tiere vol. 51 pp.541

Finlayson B.A. (1972): The Method of Weighted Residuals and Variational Principles. Academic Press, New York

Fishman A.P., Richards D.W. (1964): Circulation of the blood: men and ideas Oxford University Press New York.

Fletcher D.F., Mccaughey M., Hall R.W. (1993): Numerical Simulation of a Laminar Jet Flow - A Comparison of 3 CFD Models. Computer Physics Communications Vol. 78 n.1-2 pp. 113-20

Folkow B., Neil E. (1971); Circulation. Oxford University Press, New York

Forsey C.R., Billing C.M. (1988): Some Experiences with Grid Generation on Curved Surface using Varational and Optimmization Techiques. In: Numerical Grid Generation Methods for Fluid Dynamics (3).Ed. by K.W. Morton and M.J. Baines, Oxford University Press

Frank O. (1895): Zur Dynamik des Herzmuskels, Z. Biol. (Munich) vol.32 p.370. Traslated by Chapman C.B. and Wasserman E. (1959): On the dynamics of the cardiac muscle. Am. Heart J. vol. 58 n.2 pp.282-317; vol.58 n.3. pp.467-78

Frankel S.P. (1950): Convergence Rates of Iterative Treatments of Partial Differential Equations. Mathematical Tables and other Aids to Computation Vol.4 pp.65-75

Frey M., Thoma H., Gruber., Stohr H., Havel M. (1986): The Chronically Stimulated Psoas Muscle as an Energy Source for Artificial Organs: An Experimental Study in Sheep. In: Chiu R.C.J. (ed.) Biomechanical Cardiac Assist. Futura, Mount Kisco, N.Y., pp.179-191

Fry D.L. (1972): Localising factors in arteriosclerosis. In: Atherosclerosis and coronary heart disease. Likoff W. et al. (eds). Grune and Stratton New York pp 85-104

Fry D.L., Griggs D.M., Greenfield J.C. (1964): Myocardial mechanics: tension-velocity relationships of the heart muscle. Circ. Rec. vol. 14 pp.73-85

Fung Y.C. (1970): Mathematical representation of the mechanical properties of the heart muscle. J. Biomechanics vol.3 pp.381-404

Fung Y.C. (1981): Biomechanics: Mechanical properties of living tissues. Springer-Verlag. New York

Fung Y.C. (1984): Biodynamics: Circulation. Springer-Verlag. New York

Fung Y.C. (1990): Biomechanics: Motion, flow, stress, and Growth. Springer-Verlag. New York

Fung Y.C., Fronek K., Patitucci P. (1979): Pseudoelasticity of arteries and the choise of its mathematical expression. Am. J. Physiol. vol. 237 H620-31

Galerkin B.G. (1915): Series occuring in some Problems of Elastic Stability of Rods and Plates. Engineering Bulletin Vol.19 pp.897-908

Geddes L.A., Janas W., Hinds M., Badylack S.F., Cook J. (1993): The Ventricular-Syncronous Skeletal muscle ventricles: preliminary feasibility studies. Pace-pacing and clinical electrophysiology vol.16 n.6 pp.1310-22

Gentry R.A., Martin R.E., Daly B.J. (1966): An Eulerian Differencing Method for Unsteady Compressible Flow Problems. J. Comput. Phys. Vol.1 p.87

Georgiadis J.G., Wang M., Pasipoularides A. (1992): Computational fluid dynamics of left ventricular ejection. Annals of Biomed. Engng vol. 20 pp.81-97

Ghia U., Ghia K.N., Rubin S.G., Khosla P.K. (1981): Study of Incompressible Flow Separation using Primitive Variables. Comput. Fluids Vol.9 pp.133-42

Ghista D.N., Sandler H. (1969): An analytic elastic-viscoelastic model for the shape and the forces in the left ventricle. J. Biomechanics vol. 2 pp.35-47

Ghosh P.K. (1989):Precedents and perspectives. In: Assisted Circulation, ed. by F. Unger, Innsbruck, Austria. Springer-Verlag, pp.8-45

Gibbon J.H. (1954): The application of the mechanical heart and lung apparatus to cardiac surgery. Minn. Med. vol.37 p.171

Glass J., Rodi W. (1982): A Higher Order Numerical Schemes for Scalar Transport.Comput. Mech. Appl. Mech. Engin. Vol.337-58

Glowinski R., Pironneau (1992): Finite Element Methods for Navier-Stokes Equations. Ann. Rev. of Fluid Mechanics Vol. 24 pp.167-204

Goldman P.R., Hansen A.C., Mohammad S.F., Olsen D.B. (1991): Early results from flow measurements in a Utah-100 ventricle. ASME Advances in Bioengineering vol. 20 pp. 477-80

Goldsmith H.L. (1972): The flow of model particles and blood cells and its relation to thrombogenesis. In: Progress in Hemostasis and Thrombosis Chap 4. Spaet Th (ed), Grune and Stratton, New York p.97

Goldsmith H.L. (1974): The effects of the flow and fluid mechanical stress on red cells and platelets. Trans ASAIO vol. 20 pp. 21-26

Goldsmith H.L., Marlow J. (1972): Proc. Roy. Soc. London B182 pp.351-84

Goldsmith H.L., Turritto V.T. (1986): Rheologic aspects of thrombosis and haemostasis: basic principles and applications. Thromb. Haemost. vol.55 pp.415-35

Gordon A.M., Huxley A.F., Julian F.J. (1966): The variation is isometric tension with sarcomere length vertebrate muscle fibers. J. Physiology vol.184 pp.170-192

Gosman A.D., Pun W.M., Runchal A.K., Spalding D.B., Wolfshtein M. (1969): Heat and Mass Transfer in Recirculating Flows. Academic, New York

Gosman A.D., Pun W.M. (1974): Lecture Notes for a Course Entitled " Computation of Recirculating Flows". Heat Transfer Sec. Report HTS/74/2, Imperial College, London, 1974

Gosman A.D., Peric M. (1985): A Flux Bendin Scheme for Reducing Numerical Diffusion in Convective Transport. Mech. Eng.Dept. Report, Imperial College, London

Gould P., Ghista D., Brombolich L. (1972): In vivo stresses in the human left ventricular wall: analysis accounting for the irregular 3-dimensional geometry and comparison with idealised geometry analyses. J. Biomechanics vol. 5 pp. 521-539

Graham and Lewis (1990): Lining artificial ventricles - status 1990. In: Harnessing skeletal muscle power for cardiac assistance. Proc. of the expert meeting held in Liverpool. Salmons and Jarvis (ed), May 8-12, 1990, pp.45-53

Graham D.I., Jawes P.W., Jones T.E.R., Davies J.M., Delo E.A (1992): Measurement and Prediction of Surface Shear-Stress in Annular Flume. J. of Hydraulic Engineering ASCE Vol. 118 n.9 pp.1270-86

Green A.E., Zerna W. (1968): Theoretical elasticity. 2nd Edn, Oxford University Press, London.

Green A.E., Adkins J.E. (1970): Large elastic deformations. Oxford UK: Clarendon

Greenfield J.C., Fry D.L. (1965): Relationship between instantaneous aortic flow and the pressure gradient. Circ. Res. vol.17 pp.340-8

Gresho P.A. (1984): A Modified Finite Element Method for Solving the Time- Dependent Incompressible Navier-Stokes Equations. Part I: Theory. Int. J. Mathematics in Fluids Vol.4 pp.557-98

Gresho P.M., Lee R.L., Sani R.L. (1980): On the Time Dependent Solution of the Incompressible Navier-Stokes Equations in Two and Three Dimensions In: Recent Advances in Num. Methods in Fluids. Eds. C. Taylor and K. Morgan. Pineridge Press, Swansea, Vol1

Grood E.S., Phillips C.A., Mates R.E. (1979): Contractile filament stress in the left ventricle and its relationship to wall stress. J. Biomech. Engineering ASME vol. 101 pp.225-31

Guccione J.M., McCulloch A.D., Waldman L.K. (1991): Passive material properties of intact ventricular myocardium determined from a cylindrical model. J. Biomech. Engineering ASME vol. 113 pp.42-55

Guccione J.M., McCulloch A.D., Hunter W.C. (1993a): Three-dimensional finite element analysis of anterior-posterior variations in local sarcomere length and active fiber stress during left ventriculat ejection. Advances in Bioengineering ASME BED-VOL.26 pp.571-4

Guccione J.M., McCulloch A.D. (1993b): Mechanics of active contraction in cardiac muscle: Part I -Constitutive relations for fiber stress that describe deactivation. J. Biomech. Engineering ASME vol. 115 pp.72-81

Guccione J.M., Waldman L.K., McCulloch A.D. (1993c): Mechanics of active contraction in cardiac muscle: Part II -Cylindrical Models of the systolic left ventricle. J. Biomech. Engineering ASME vol. 115 pp.82-90

Guldner N.W., Eichstaedt H.C., Klapproth P., Tilmans M.H.I., Thuaudet S., Umbrain V., Ruck K., Wyffels E., Bruyland M., Sigmund M., Messmer B.J., Bardos P. (1994): Circ. vol.89 n. 3 pp. 1032-40

Hagege A.A., Desnos M., Chacques J.C., Carpentier A., Fernandez F., Fontaliran F., Guerot C. (1990): Preliminar report: follow-up after dynamic cardiomyoplasty. Lancet vol. 335 pp.1122-4

Hall M.G. (1981): Computational Fluid-Dynamics - A Revolutionary Force in Aero-Dynamics. AIAA Paper 81-1014, Palo Alto, California

Hanna W.T. (1973): A simulation of human heart function. Biophys. J. vol. 13 pp. 603-21

Harasaki H., McMahon J., Richards T., Goldamp J., Kiraarly R. Nose Y. (1985): Calcification in cardiovascular implants: degraded cell related pheomena. ASAIO Trans. vol.31 pp.489-94

Hardy J.D., C.M. Chavez (1968): The first heart transplant in man: developmental animal investigations with analysis of 1964 case in the light of current clinical experience. Am. J. Cardiology vol.22 pp. 772-781

Harlow F.H., Welch J.E. (1965): Numerical Calculation of Time-Dependent Viscous Incompressible Flow of Fluid with Free Surface. Phys. Fluids Vol.8 pp.2182-9

Harper P.G. (1984): Large strain analysis in BERSAFE. CEGB report.

Hashimoto S., Maeda H., Sasada T. (1985): Effect of shear rate on clot growth at foreign surfaces. Artificial Organs vol.9 pp.345-50

Hassan Y.A., Rice J.G., Kim J.H. (1983): A Stable Mass-Flow-Weighted Two-Dimensional Skew Upwind Scheme. Num. Heat Transfer Vol.6 pp.395-408

Hawkins I.R., Wilkes N.S. (1991): Moving Grids in Harwell FLOW3D. UKAEA Report AEA-In Tech-0608

Hayashi K. (1993): Experimental approaches on measuring the mechanical properties and constitutive laws of arterial walls. ASME J. Biomech. Engng vol.115 pp.481-88

He X., Ku D.N. (1992): Entrance flow development for pulsatile flow in a straight tube. In: Advances in Bioengineering ASME (ed. by M.W. Bidez) 461-64

Hedberg P.K.M. (1989): NONDIF: A Method to Avoid Numerical Diffusion and over- and under-shoots. Proc. $6^{th}$ Int. Conf. Num. Meth. Lam. Turb. Flow. Swansea UK, 11-15 July 1989 Ed. by C. Taylor, P. Gresho, P.L. Sani and J. Hauser. Pineridge Press,

Swansea pp.193-202

Hefner L.L., Bowen T.E. (1967): Elastic components of cat papillary muscle. Am. J. Physiol. vol.212 pp.1221

Henriksson J., Nemeth P.M., Borg K., Salmons S., Lowry O.H. (1990): Fibre type-specific enzyme activity profiles. A single fibre study of the effectss of chronic stimulation on the rabbit fats-twitch tibialis anterior muscle. In: The Dynamic State of Muscle Fibres, Pette D. (ed) Berlin, Walter de Gruyter pp.385-398

Henry F.S., Collins M.W. (1991): Prediction of Flow over a Helically Ribbed Surfaces. Int. J. Numeric. Methods in Fluids Vol.13 pp.321-40

Henry F.S., Collins M.W., and How T.V. (1992a): Numerical Analysis of the Flow in an End-to-side Bypass Anastomosis. Advances in Bioengineering, M.W. Bidez, ed., BED-Vol 22 pp. 227-228, ASME

Henry F.S., Jalili V., Jarvis J.C., Black R.A., Shortland A., Collins M.W., Salmons S. (1992b): Numerical Modelling of the Flow in Skeletal Muscle Ventricles: A Preliminary Study. Advances in Bioengineering ASME Vol.22 pp.223-5

Henry F.S. and Collins M.W. (1993a): Computations of Flow Distal of Axisymmetric and Asymmetric Stenoses. Advances in Bioengineering, J.M. Tarbell, ed., BED-Vol 26 pp.87-90, ASME

Henry F.S., and Collins M.W. (1993b): A Novel Predictive Model with Compliance for Arterial Flows. Advances in Bioengineering, J.M. Tarbell, ed., BED-Vol 26, pp. 131-135, ASME

Henry F.S., Pearcey H.H. (1994): Numerical Model of Boundary-Layer Control using Air-Jet Generated Vortices. AIAA J. vol.32 n.12 pp.2415-25

Henry F.S. and Collins M.W. (1994): Numerical Predictions of Post-stenotic Flow using a Compliant Artery Model. Proc. Int. Conference on Biomedical Engineering BME'94, Hong Kong, Biomedical Division- The Hong Kong Institute of Engineers, pp. 22-25

Henry F.S., Xu X.Y., Collins M.W., Jones C.J.H., Griffith T.M., and Tardy Y. (1994a): Predictions of Wall Shear Stress with Application to Atherosclerosis and EDRF Release. Clinical Hemorheology, Vol. 14, No. 3, p. 430

Henry F.S., Hughes P.E., How T.V. and Collins M.W. (1994b): Flow Details and Fluid Particle Paths in Model By-pass Grafts. Biofluid Mechanics: Proceedings of the 3rd International Symposium. July 16-19, 1994, Munich, (D. Liepsch, ed.) Vol 17, No. 107, pp. 497-507, VDI-Verlag, Du@EAsseldorf

Henry F.S., Butler J.P., and Tsuda A. (1994c): Acinar Fluid Mechanics in Alveolar Expansion and Contraction. Fed. Proc. Vol. 8, no.5, p.4005

Henry F.S., Tsuda A., and Butler J.P.(1994d): Acinar Flow Patterns in a Rhythmically Expanding Alveolated Duct. 1994 Advances in Bioengineering, M.J. Askew, ed., BED-Vol 28, pp. 377-378, ASME

Henry F.S., Iudicello F., Shortland A., Black R.A., Jarvis J.C., Collins M.W., Salmons S. (1994): Modelling Wall Driven Cardiovascular Flows. Submitted to International Mech-

anical Engineering Congress & Exposition, Nov 6-11 1994, Chicago

Henry F.S., Collins M.W. (1995): Numerical Modelling of Blood Flow. In: Advances in Heamodynamics and Haemorology. Ed. by T.V. How. JAI Press London

Henry F.S., Collins M.W., Hughes P.E., How T.V. (1995a): Numerical investigation of the flow in proximal and distal end-to-side anastomoses. Submitted to ASME J. Biomech. Engng

Henry F.S., Shortland A., Iudicello F., Black R.A., Jarvis J.C.,Collins M.W., Salmons S. (1995): Flow in a simple ventricle: Comparison between numerical and physical simulations. Submitted to ASME Journal of Biomechanical Engineering. Previsionally accepted.

Hibbit, Karlsson & Sorensen Inc. (1989): ABAQUS (version 4.9). 100 Medway Street, Providence R.I. 02906

Hilbert D. (1987): An efficient Navier-Stokes Solver and its Application to Fluid Flow in Elastic Tubes. In: Numerical Methods, Colloquia Societatis Janos Bolyai Vol.50 pp.423-31, North Holland Amsterdam

Hindman R.G., Spencer J. (1983): A New Approach to Truly Adaptive Grid Generation. AIAA Paper 83-0450, Reno, Nevada

Hill A.V. (1922): The maximum work and and mechanical efficiency of human muscles, and their most economical speed. J. Physiol. (London) vol.56 pp.19

Hill A.V. (1938): The heat of shortening and the dynamic constants of muscle. Proc. R.Soc.London B vol.126 pp.136-195

Hill A.V. (1949-1950): The abrupt transition from rest to activity in muscle. Proc. R.Soc.London B vol.136 pp.399-420

Hill A.V. (1950): Mechanics of the contractile element of muscle. Nature n.4219 pp.415-419

Hill A.V. (1953): The "instantaneous " elasticity of active muscle. Proc. R.Soc.London B vol.141 pp.161-178

Hill A.V. (1970): First and last experiments in muscle mechanics. Cambridge. Cambridge University Press

Hill J.D. (1988): Bridges to Cardiac Transplantation. Ann. Thorac. Surg. Vol.46 pp.131-132

Hood W.P. Jr., Thomson W.J., Rackley C.E., Rolett E.L. (1969): Comparison of calculations of left ventriuclar wall stress in man from thin-walled and thick-walled ellipsoidal models. Circ. Res. vol. 24 pp.575-82

Hooper T.L., Salmons S. (1993): Skeletal muscle assistance in heart failure. Cardiovasc Research vol.27 pp.1404-06

Horowitz A., Lanir Y., Yin F.C.P., Perl M., Sheinman I., Strumpf R.K. (1988): Structural three-dimensional constitutive law for the passive myocardium. ASME J. Biomechanics

Engineering vol.110 pp.200-7

How T.V. (1990): Modelling mechanical properties of arteries and arterial prostheses In: Harnessing skeletal muscle power for cardiac assistance. Proc. of the expert meeting held in Liverpool. Salmons and Jarvis (ed), May 8-12, 1990, pp.81-89

Hughes P.E., How T.V. (1994): Flow structures in models of distal end-to-side anastomis. Influence of geometry and flow division on flow. J. Biomech. Engng

Huisman R.M., Elzinga G., Westerhof N., Sipkema P. (1980): Measurement of left ventricular wall stress. Cardiovascular Res. Vol.14 pp.142-53

Humphrey J.D., Yin F.C.P. (1987): On constitutive relations and finite deformations of passive cardiac tissue: I. A pseudostrain-energy function. ASME J. Biomech. Engineering vol. 109 pp.298-304

Hung T.C., Butter D.B., Yie C.L., Sun Z., Borovetz H.S., Kormos R.L., Griffith B.P. Dardasty R.L. (1991): Interim use of Jarvik-7 and Novacor artificial heart: Blood rheology and transient ischemic attacks (TIA's). Biorhelogy vol.28 pp. 9-25

Hunter P.J., Smaill B.H. (1988): The analysis of cardiac function: a continuum approach. Prog. Biophys. Molec. Biol. vol.52 pp.101-64

Hunter P.J., Nielsen M.F., Smaill B.H., LeGrice I.J., Hunter I.W. (1992): An anatomical heart model with application to myocardial activation and ventricular mechanics. Critical Rev. Biomed. Engineering vol. 20 n.5,6 pp.403-426

Hussaini M.Y., Zang T.A. (1987): Spectral Methods in Fluid-Dynamics. Ann.Review Fluid Mech. Vol.19 pp. 339-67

Hutton A.G., Smith R.M., Hickmott S. (1987): The Computation of Turbulent Flows of Industrial Complexity by the Finite Element Method - Progress and Prospects. Int. J. for Numerical Methods in Fluids Vol.7 pp.1277-98

Huxley A.F. (1952): J. Physiology vol.117 pp.52

Huxley A.F., Hanson J. (1954): Changes in the cross-striation of muscle during rapid contraction and stretch, and their structural interpretation. Nature vol. 173 pp.973-6

Huxley A.F. (1957): Muscle structure and theories of contraction. Progr. Biophys. vol.7 pp.255-318

Huxley A.F. (1969): The mechanism of muscular contraction. Science vol. 164 pp. 1356

Huxley A.F., Simmons R.M., Faruqi A.R., Kress M., Koch M.H.J. (1981): Millisecond time-resolved changes in x-ray reflections from contracting muscle during rapid mechanical transients, recorded using syncrhotron radiation. Proc. Natl. Acad. Sci. vol.78 pp. 2297-2301

Issa R.I. (1985): Solution of Implicitily Discretised Fluid Flow Equations by operator Splitting. J. Computatonal Physics Vol.61 pp.40

Iudicello F., Henry F.S., Collins M.W, Shortland A., Jarvis J.C., Black R.A., Salmons S. (1993): Numerical Simulation of the Flow in Model Skeletal Muscle Ventricles. Proc.

Computers in Cardiology, London 1993 pp.377-380

Iudicello F., Henry F.S., Collins M.W., Shortland A.P., Jarvis J.C., Black R.A., Salmons S. (1994): Flow Structures Predicted in Model Skeletal Muscle Ventricles. BME 1994, Hong Kong pp.13-16

Janz R.F., Grimm A.F. (1972): Finite-element model for the mathematical behaviour of the left ventricle. Circ. Res. vol. 30 pp. 224-52

Janz R.F., Grimm A.F. (1973): Deformation of the diastolic left ventricle. I. Nonlinear elastic effects. Biophys. J. vol.13 pp.689-704

Janz R.F., Grimm A.F., Kubert B.R., Moriarty T.F. (1974): Deformation of the diastolic left ventricle. I. Nonlinear geometric effects. J. Biomechanics vol.7 pp.509-16

Jarvis J.C. (1990): The power-generating capacity of normal and conditioned skeletal muscle. In: Harnessing skeletal muscle power for cardiac assistance. Proc. of the expert meeting held in Liverpool. Salmons and Jarvis (ed), May 8-12, 1990, pp.15-19

Jarvis J.C., Salmons S. (1990): An electrohydraulic apparatus for the measurement of static and dynamic properties of rabbit muscles. J. Appl. Physiol. vol. 70 pp.938-41

Jarvis J.C., Mayne C.N., Salmons S. (1991a): Basic studies on skeletal muscle for cardiac assistance. J. Cardiac Surg. vol.6 n.1 SUPPL. pp.204-9

Jarvis J.C., Brownson C., Sutherland H., Salmons S. (1991b): Comparison between the effects of continuous long-term stimulation of rabbit skeletal muscle at 2.5 Hz and 10 Hz. In: Basic and Applied Myology: Perspectives for the 90's, Carraro U., and Salmons S. (eds), Padua Unipress, 1991, pp.109-113

Jarvis J.C., Mayne C.N., Little P., Sutherland H., Brownson C., Salmons S. (1991c): Use of 2.5 Hz and 10 Hz stimulation to examine coordination in the phenotypic response of of fast skeletal muscle to increased use. Muscle Res. Cell Motility vol.13 pp. 237

Jarvis J.C., Sutherland H., Kwende M.M.N, Gilroy S., Salmons S. (1994): To what extent can we engineer the properties of skeletal muscle for cardiac assistance. J. Muscle Research & Cell Motility vol. 15 n. 2 pp.178

Jin W., Clark C. (1993): Experimental investogation of unsteady flow behaviour within a sac-type ventricular assist device (VAD). J. Biomechanics vol.26 n.6 pp.697-707

Jones T.R. (1970): Motions of a liquid in a pulsating bulb with application to problems of blood flow. Medical and Biological Engng vol.8 pp.45-51

Jones I.P., Kightley J.R., Thompson C.P., Wilkes N.S. (1985): FLOW3D, a Computer Code for the Prediction of Laminar and Turbulent Flow and Heat Transfer Release 1. Harwell Report AERE-R 11825, 1985

Jones I.P., Kightley J.R., Thompson C.P., Wilkes N.S. (1986): FLOW3D Release 1: User Manual. Harwell Report AERE-R 11893, 1986

Jones I.P. (1991): CDFS Software - Validation Report: Part I. AEA-InTech Report Harwell Laboratory, Nov 1991

Jones C.J.H., Parker K.H., Hughes R., Sheridan D.J. (1992): Nonlinearity of human arterial pulse wave transmission. ASME J. Biomechanical Engineering vool. 114 pp. 10-4

Joyce L.D., Johnson K.E., Pierce W.S. (1986): Summary of the world experience with clinical use of the total artificial hearts as heart support devices. J. Heart Transplant vol.5 pp. 229-35

Joseph D.D. (1990): Fluid dynamics of viscoelastic liquids. Springer-Verlag NY

Kantrowitz A., A. Kantrowitz (1953): Experimental augmentation of coronary flow by retardation of arterial pressure pulse. Surgery vol.34 p.678

Kantrowitz A., W.M.P. McKinnen (1958): Experimental use of diaphragm as experimental myocardium. Surgery Forum vol.9 pp.266-68

Kantrowitz A., F. Gradel, T. Aktusu (1965): The auxiliary ventricle. IEEE Int. Convent. Rec. Part 12, p.20

Kantrowitz A., J. Krakauer, J.L. Sherman (1968): A permanent mechanical auxiliary ventricle. J. Cardivascular Surgery (Torino) vol.9 p.1

Kantrowitz A.(1989): Intra-aortic Balloon Pumping: Clinical aspects and prospects In: Assisted Circulation, ed. by F. Unger, Innsbruck, Austria. Springer-Verlag, pp.52-73

Katz B. (1939): The relation between force ans speed in muscular contraction. J. Physiology vol.96 pp.45-64

Khalafalla A.S. (1986): Muscle mass and design requirements for cardiac assist systems. cardiac assist systems. In: Biomechanical cardiac assist. Chiu R.C.-J (ed), Futura p 151

Khalafalla A.S., Malek A.M. (1989): Design and Stimulation of biological cardiac assist systems. In: Assisted Circulation, ed. by F. Unger, Innsbruck, Austria. Springer-Verlag, pp.512-24

Kightley J.R., Jones I.P. (1985): A Comparison of Conjugate Gradient Preconditioning for Three-Dimensional Problems on a CRAY-1. Comp. Physics Commun. Vol. 37 pp.205-14

Kim S.H., Chandran K.B. (1992): A numerical study of steady flow across end-to-side vascular bypass grafts anastomeses. ASME Advances in Bioengineering Bidez M.W. (ed) pp.233-6

Kim S.H., Chandran K.B., Chen C.J. (1992): Numerical simulation of steady flow in a two-dimensional total artificial heart. ASME J. Biomech. Engng vol. 114 pp. 497-503

King M.J. (1994): Computational and experimental studie of flow through a bileaflet mechanical heart valve. Ph.D. Thesis. University of Leeds

Kobayashi M.H., Pereira J.C.F. (1994): A computational method for solving arbitrary two-dimensional physiological flows. ASME J. Biomechanical Engineering vol. 116 pp.315-7

Kochamba G., Desrosiers C., Dewar M., Chiu R.-C. (1988): The muscle powered dual-chamber counterpulsator: rheologically superior implantable cardiac assist device. Ann.

Thorach. Surg. vol.45 pp.620-5

Kollf W.J., Akutsu T., Dreyer B., Norton H. (1959): Artificial in the Chest and the Use of Polyurathane for Making Hearts, Valves and Aortas. Trans. Am. Soc. Artif. Intern. Organs vol.15 pp. 298-300

Ku D.N., Liepsch D. (1986): The effects of non-Newtonian viscoelasticity and wall elasticity on flow at a 90 degree bifurcation. Biorheology vol.23 pp.359-70

Kusaba E., Schraut W., Satwatani S., Jaron D., Freed P., Kantrowitz A. (1973): A diaphragmatic graft for augmenting left ventricular function: a feasibility study. Trans. Am. Soc. Artif. Intern. Organs Vol.19 pp. 251-57

Kusserow B.K., Clapp J.F. III (1964): A small ventricle-type pump for prolonged perfusions: construction and initial studies including attempts to power a pump biologically with skeletal muscle. Trans. Am. Soc. Artif. Intern. Organs vol.10 pp.74-78

Lafarge C., Bernhard W.F., Robinson T.C.,, et al. (1968): Physiological consequences of acutely and chronically implanted left ventricular-aortic assist device. Trans ASAIO vol. 14 pp. 316-33

Lacker H.M., Peskin C.S. (1986): A mathematical method for unique determination of cross-bridges properties from steady-state mechanical and energetic experiments on macroscopic muscle. In: some mathematical questions in biology-muscle physiology. Miura R.M. (ed) American Math. Soc, Providence, RI pp.121-153

Lanir Y. (1983):Constitutive equations for fibrous connective tissue. J. Biomechanics vol. 16 pp.1-12

Latimer B.R., Pollard A. (1989): Comparison of Pressure-Velocity Coupling Algorithms. Num. Heat Transfer Vol.8 pp. 635-52

Lee C.S.F., Talbot L. (1979): A fluid mechanical study on the closure of heart valves. J. Flui Mechanics vol. 91 n.1 pp.41-63

LeGallois C.J.J. (1813): Experiences on the principle of life. Thomas, Philadelphia. Translation of: LeGallois C.J.J. (1812) Experiences sur le principle de la vie. Paris

Leonard B.P. (1979): A Stable and Accurate Convective Modelling Procedure based on Quadratic Upstream Interpolation. Comp. Meth. Appl. Mech. Eng. Vol.19 pp.59-98

Leriche R., Fontaine R. (1933): Essai experimental de traitment de certain infarctus du myocarde et de l'aneurisme du coeur par une greffe de muscle strie. Bull. Soc. Nat. Chir. vol.59 pp.229

Letsou G.V., Zarif A., Smith A., Hogan J., Lee P., Ariyan S., Baldwin J.C., Elefteriades J.A. (1994): Latency of skeletal muscle contraction after pulse train stimulation: an important factor in correct timing of skeletal muscle cardiac assist devices. J. Surg. Res. vol. 57 pp.672-6

Levine R.D. (1982): Supercomputers. Sc. Am. Vol.246 pp.118-135

Levinson M.M., Smith R.G., Cork R.C., Galoo J., Emery R.W., Icenogle T.B., Ott R.A., Burns G.L., Copeland J.G. (1986): Thromboembolic complications of the Jarvick-7 total

artificial heart: Case Report. Artificial Organs vol.10 pp.236-44

Li C.M., Hill A., Colson M., Desrosiers C., Chiu R.C.-J. (1990): Implantable rate-responsive counterpulsation assist system. Ann. Thorac. Surg. vol. 49 pp.356-62

Lieber R.L. (1992): Skeletal muscle structure and function. Williams & Wilkins

Liepsch D.W. (1986): Flow in tubes and arteries - A comparison. Biorheology vol. 23 pp.395

Lillington J.N. (1981): A Vector Upstream Differencing Schemes for Problems in Fluid Flow involving Significant Source Term in Steady-Linear Systems. Int. J. Num. Meth. Fluids Vol.1 pp 3-6

Lin A. (1985): The Parameterized Strongly Implicit Method for Solving Elliptic Difference Equations. Int. J. Num. Meth. in Fluids Vol.1 pp.3-6

Liotta D., C.W. Hall, W.S. Henly, A.C. Beall, D.A. Cooley, De Bakey M.E. (1963): Prolonged assisted circulation during and after heart or aortic surgery. Trans. Am. Soc. Artif. Intern. Organs vol.9 pp.182-85

Litwak R.S., R.S. Koffsky, S.B. Lukban, R.A. Jurado, S.K. Elster, F. Lajam, R.W. Brancato (1974): Implanted heart assist device after intracardiac surgery. N. Engl. J. Med. (291): 1341

Lohner R. (1987): Finite Elements in CFD: What lies Ahead ?. Int. J. Numer. Meth. Engng Vol.24 pp.1741-56

Luo X.Y., Kuang Z.B. (1992): Non-Newtonian flow patterns associated with an arterial stenosis. ASME J. Biomech. Engng vol.114 pp.512-4

Macoviak J.A., Stephenson L.W., Armenti F., Kelly A.M., Alavi A., Mackler T., Cox J., Palatianos G.M., Edmunds L.H. (1982): Electrical conditioning of in situ skeletal muscle for replacement of myocardium. J. Surgery Res. vol.34 pp.429-39

Magid A., Law D.J. (1985): Myofibrils bear most of the resting tension in frog skeletal muscle. Science vol.230 pp.1280-1282

Mann D.E., Tarbell J.M. (1990): Flow of non-Newtonian blood analog fluids in rigid curved and straight artery models. Biorheology vol.27 pp.711-33

Mann K.A., Deutsch S., Tarbell J.M., Geselowitz D.B., Rosenberg G., Pierce W.S. (1987): An experimental study of Newtonian and non-Newtonian flow dynamics in a ventricular assist device. ASME J. Biomech. Engng vol. 109 pp. 139-47

Mannion J.D., Hammond R.L., Stephenson L.W. (1986a): Hydraulic pouches of canine latissimus dorsi. J. Thorach. Cardiovasc. Surg. vol.91 pp.534-44

Mannion J.D., Bitto T., Hammond R.L., Rubinstein N., Stephenson L.W. (1986b): Histochemical fatigue characteristics of conditioned canine latissimus dorsi muscle. Circ. Res. vol. 58 pp.298-304

Mannion J.D., Velchik M.A., Acker M., Hammond R.L., Staum M., Alavi A., Duckett S., Stephenson L.W. (1986b): Transmural blood flow of multi-layered latissimus dorsi

skeletal muscle ventricles during circulatory assistance. Trans. AM. Soc. Artoif. Intern. Organs vol.32 pp.454-60

Mannion J.D., Acker M.A., Hammond R.L., Falteyer W., Duckett S., Stephenson L.W. (1987): Power output of skeletal muscle ventricle in circulation: short term studies. Circulation vol.76 pp.155-62

MARC K.3 (1988): Manuals A-E, Marc Analysis Research Corporation , Palo Alto, USA

McCulloch A.D., Guccione J.M., Waldman L.K., Rogers J.M. (1992): Large-scale finite element analysis of the beating heart. Critical Reviews in Biomedical Engineering vol.20 pp.427-49

McDonough J.M., Catton I. (1982): A mixed Finite Difference-Galerkin Procedure for Two-Dimensional Convection in a Square Box. Int. J. Heat and Mass Transfer Vol.25 pp.1137-46

McHale A., Greenfield J.C. (1973): Evaluation of several geometries models for estimation of left ventricular circumferential stress. Circ. Res. vol.33 pp.303-12

McQueen D.M., Peskin C. (1985): Computer-assisted design of butterfly bileaflet mechanical heart valves for the mitral position. J. Computational Fluids vol. 82 pp. 289-7

McQueen D.M., Peskin C. (1989): A three-dimensional computatinal method for blood flow in the heart. 2. Contractile fibers. J. Computational Physics vol. 82 pp.289-97

Merrill E.W., Benis A.M., Gilliland E.R., Shewood T.K., Salzman E.W. (1965): J. Appl. Physiology. vol. 20 pp. 954-67

Millner R., Guvendik L., Clarke T., Hynd J. and Pepper J. (1991): Improved right ventricular function after cardiomyoplasty. In: Harnessing skeletal muscle power for cardiac assistance. Proc. of the expert meeting held in Liverpool. Salmons and Jarvis (ed), May 8-12, 1990, pp.27-30

Mirsky I. (1969): Left ventricular stresses in the intact human heart. Biophys. J.. vol.9 pp.189-208

Mirsky I. (1973): Ventricular and arterial wall stresses based on large deformation analysis. Biophys. J.. vol.13 pp.1141-59
Mirsky I., (1979): Elastic properties of the myocardium: a quantitative approach with physiological and clinical applications. In: Handbook of Physiology, Sec. 2, Vol.I. The Heart. Berne R.M., Sperelakis N. (eds). American Physiological Society, Bethesda, Md., pp.497-531

Mocek F.W., Anderson D.R., Pochettino A. et al. (1992): Skeletal muscle ventricles long term: 191-836 days. J. Heart Lung Tranplant vol.11 pp s334-40

Moin P., Kim J. (1982): Numerical Investigation of Turbulent Channel Flow. J. Fluid Mech. Vol.118 pp. 341-77

Mommaerts W.F.H.M., Seraydarian K., Wallner A. (1962): Demonstration of phosphocreatine splitting as an early reaction in contracting frog sartorius muscle. Biochim. Biophys Acta vol. 63 pp.75-81

Moore Jr J., Delfino A., Meister J.-J. (1992): Preliminary Analysis of the effect of Blood Vessel Movement on Blood Flow Patterns. In: Advances in Bioengineering ASME (ed. by M.W. Bidez) pp.537-39

Moravec S., Liepsch D. (1983): Flow investigation in a model of a three-dimensional human artery with Newtonian and non-Newtonian fluids. Part I. Biorheology vol.20 pp.745-59

Moskowitz S.E. (1981): Effects of inertia and viscoelasticity in late rapid filling of the left ventricle. J. Biomechanics vol.14 pp. 443-445

Moulopoulos S.D., S.R. Topaz, W.J.Kaff (1962): Extracorporeal assistance to the circulation and intra-aortic balloon pumping. Trans. Am. Soc. Artif. Intern. Organs vol.8 p.85

Moulopoulos S.D. (1989): Systolic counterpulsation. In: Assisted Circulation, ed. by F. Unger, Innsbruck, Austria. Springer-Verlag, pp.86-93

Mulder M.M., Hansen C., Olsen D.B. (1993): Development of an experimental model to investigate henocompatibility of a centrifugal blood pump. ASME Advances in Bioengineering. Tarbell J.M. (ed) BED-Vol.26 pp. 443-6

Nakamura M., Sawada J. (1987): Numerical study on the laminar flow of slurries. J. non-Newtonian Fluid Mechanics vol.22 pp.191-206

Neilson I.R., Brister S.J., Khalafalla A.S., et al. (1985): Left ventricular assistance in the dog using a skeletal muscle powered device for diastolic augmentation. J. Heart Transp. vol. 4 pp.343-7

Nerem R.M. (1992): Vascular fluid dynamics, the arterial wall, and atherosclerosis. ASME J. Biomech. Engng vol. 114 pp. 274-82

Nevo E., Lanir Y. (1989): Structural finite deformation model of the left ventricle during diastole and systole. J. Biomech. Engineering ASME vol. 111 pp.342-9

Nichols W.W., O'Rourke M.F. (1990): McDonald's Blood Flow in Arteries. Third Ed. Edward Arnold, London

Noordergraaf A. (1978): Circulatory System Dynamics. Academic Press New York

Oakley D.E., Bahn R.E. (1993): Compuational Modelling of Spray Dryers. Computers & Chemical Engineering Vol. 17 n.ss pp.s493-s498

O'Brien V., Ehrlich L.M. (1977): Simulation of unsteady flow at renal branches. J. Biomechanics vol. 10 pp.623-31

Ohayon J., Chadwick R.S. (1988): Effects of collagen microstructure on the mechanics of the left ventricle. Biophysical J. vol. 54 pp. 1077-88

Ojha M., Cobbold R.S.C., Johnston K.W., Hummel R.L. (1990): Detailed visualization of pulatile flow fields produced by modelleed arterial stenoses. J. Biomed. Engng vol. 12 pp. 463-9

Pao Y.C., Ritman E.L., Wood E.H. (1974): Finite element analysis of left ventricular myocardial stresses. J. Biomechanics vol. 7 pp.469-77

Parmley W.W., Sonnenblick E.H. (1967): Series elasticity in heart muscle: Its relation to contractile element velocity and proposed muscle models. Circ. Res. vol.20 pp.112

Patankar S.V., Spalding D.B. (1972): A Calculation Procedure for Heat, Mass and Momentum Transfer in Three-Dimensional Parabolic Flows. Int.J. Mass Transfer Vol.15 pp.1787-1806

Patankar S.V. (1980): Numerical Heat Transfer and Fluid Flow. McGraw-Hill Book Company

Patankar S.V. (1981): A Calculation Procedure for Two-Dimensional Elliptic Situations. Numerical Heat Transfer Vol.4 pp.409-25

Patankar S.V. (1988): Recent Developments in Computational Heat Transfer. ASME J. Heat Transfer Vol.110 pp. 1037-45

Patel D.J., Vaishnav R.N. (1972): Rheology of large blood vessels. In: Cardiovascular Fluid Mechanics. vol.2 Bergel D.H. (ed) Academic Press Inc. New York pp.1-64

Patera A.T. (1984): A Spectral Method for Fluid Dynamics: Laminar Flow in a Channel Expansions. J. Comp. Phys. Vol.54 pp.468-88

Pattison C.W., Cumming D.V.E., Williamson A., Clayton-Jones D.G., Goldspink G., Yacoub M. (1991): J. Thorach. Cardiovasc. Surg. vol.101 pp.766-73

Pedley T.J. (1980): The fluid mechanics of large blood vessels. Cambridge University Press

Pedley T.J. (1985): Flow along a channel with a time-dependent indentation in one wall: the generation of vorticity waves. J. Fluid Mech. vol.160 pp. 337-367

Peraire J., Morgan K., Peiró J. (1990): Unstructured Mesh Methods for CFD. Von Karman Institute for Fluid Dynamics. "Numerical Grid Generation" Lecture Notes

Peric M. (1987): Efficient Semi-Implicit Solving Algorithm for Nine-Diagonal Coefficient Matrix. Numerical Heat Transfer Vol.11 pp. 251-79

Perktold K. (1989): On Numerical Simulation of Three-Dimensional Physiological Flow Problems. Ber. Math.-Stat. Sektion, Furshungsges, Joanneum Graz Nr.280, Graz

Perktold K., Peter R.O., Resch M., Langs G. (1991): Pulsatile non-Newtonian blood flow in three-dimensional carotid bifurcation models: a numerical study of flow phenomena under different bifurcation angles. J. Biomech. Engng vol.13 pp.507-15

Perktold K., Resch M., Peter R.O. (1991): Three Dimensional Numerical Analysis of Pulsatile Flow and Wall Shear Stress in the Carotid Arterial Bifurcation. J. Biomechanics Vol.24 pp.409-20

Perktold K., Tatl H., Schima H. (1993): Computer Simulation of hemodynamic effects in distal casular graft anastomeses. ASME Advances in Bioengineering. Tarbell J.M. (ed)

BED-Vol.26 pp. 91-94

Perktold K., Rappitsch G.R. (1993): Numerical analysis of arterial wall mechanics and local blood flow phenomena. ASME Advances in Bioengineering. Tarbell J.M. (ed) BED-Vol.26 pp. 127-30

Perktold K., Rappitch G. (1994): Mathematical Modelling of Local Arterial Flow and Vessel Mechanics. In: Computational Methods for Fluid-Structure Interaction. J.M.Crolet, R. Ohayon ed.Longman Scientific & Technical Vol.306 pp.230-45

Perktold K., Rappitch G., Liepsch D. (1994): Flow and Wall Shear Stresses in the Human Carotid Artery Bifurcation: Computer Simulation under Anatomically Realistic Conditions. In: Advances in Bioengineering ASME BED Vol.28 pp.437-8

Peskin C.S. (1973-1974): Mathematical aspects of heart physiology. Courant Institute of Mathematical Sciences. New York University

Peskin C.S. (1977): Numerical analysis of blood flow in the heart. J. Computational Physics vol.25 pp.220-52

Peskin C.S. (1982): The fluid-dynamics of heart valves: experimental, theoretical, and computational methods. Annual Review of Fluid Mechanics vol. 14 pp. 235-59

Peskin C.S., McQueen D.M. (1989): A three-dimensional computatinal method for blood flow in the heart. 1. Immersed elastic fibers in a viscous incompressible fluid. J. Computational Physics vol. 81 pp.372-405

Peskin C.S. (1992): Cardiac Fluid Mechanics. Critical Review in Biomedical Engng chapter 17 vol 20 n. 5-6 pp. 451-9

Peskin C.S., McQueen D.M. (1993): In: Cardiac Fluid Dynamics. High Performance Computing in Biomedical Research, Pilington T. et al. (eds) CRC Press, Boca Raton, FL pp.51-9

Petrovsky B.V. (1966): Surgical treatment of cardiac aneurysms. J. Cardiovasc. Surgery vol.2 pp.87-91

Peters J.L., J.C. McRea, H. Fukumasu, T. Li, R. Waeckerlin (1977): Single and biventricular bypass (BVP) of the natural heart. Proc. $12^{th}$ AAMI. San Francisco

Pette D. (1980): Plasticity of Muscle. New York. Walter de Gruyter

Pette D. (1990): The dynamic state of muscle fibers. Berlin. Walter de Gruyter

Pette D., Vrbova G. (1992): Adaptation of mammalian skeletal muscle fibers to chronic electrical stimulation. Rev. Physiol. Biochem. Pharmacol. vol.120 pp.115-202

Pierce W.H. (1981): Body Forces and Pressures in elastic models of the myocardium. Biophysical J. vol.34 pp. 35-59

Pinto J.G. (1987): A Constitutive description of contracting papillary muscle and its implications to the dynamics of the heart. Biomech Engineering ASME vol.109 pp.181-91

Pinto J.G., Fung Y.C. (1973): Mechanical properties of the heart muscle in the passive state. J. Biomechanics vol. 597-616, 617-630

Pinto J.G., Patitucci P.J. (1980): Visco-elasticity of passive cardiac muscle. J. Biomech Engineering ASME vol.102 pp.57-61

Pinto J.G., Boe A. (1991): A method to characterize the passive elasticity in contracting muscle bundles. J. Biomech Engineering ASME vol.113 pp.72-78

Podolsky R.J., Shoenberg (1983): Force generation and shortening in skeletal muscle. In: Peachy L.D., Adrian R.H., and Geiger S.R. (eds). Handbook of Physiology. Bethesda, MD:Amarican Physiological Society. pp.173-187

Pohl M., Wendt M.O., Lerche D. (1990): The influence of rheological properties of test fluids on the flow pattern inside the artificial ventricle (Type Rostok) and in the aortic outflow tract. In: Biofluid Mechanics, Blood Flow in Large Vessels. Proc. of the 2nd International Symposium in Biofluid Mechanics and Biorheology Liepsch D. (ed) pp.381-389

Poiseuille J.M.L.C.R. (1846): Recherches experimentales sur le movement des liquides dans les tubes de tres petits diametres. Mem. Savant Etrangers vol.9 pp.433-544

Proceedings of the First CFDS International User Conference 6-7 May 1993, Eynsham Hall, Oxford

Puttre' M. (1991): FEA programs band together. ASME Mech. Engng vol.113 pp.77-80

Rai M.M., Anderson D.A. (1982): Application od Adaptive Grids to Fluid Flow Problems with Asymptotic Solutions. AIAA J. Vol.20 pp.496-502

Raithby G.D. (1976): Skew Upwind Differencing Schemes for Problems involving Fluid Flow. Comp. Meth. Appl. Mech. Eng. Vol.9 pp. 153-65

Rayleigh J.W.S. (1877): Theory of Sound. 1st ed.. Revised, Dover, New York 1945

Reddy J.N. (1982): On Penalty Function Methods in the Finite Element Analysis of Flow Problmes. Int. J. Num. Metho. in Fluids Vol.2 pp.151-71

Reuderink P.J. (1991): Analysis of the flow in 3-D distensible models of the carotid bifurcation. Ph.D. Thesis, Eindhoven University of Technology, the Netherlands

Reuderink P.J. (1993): Incompressible low-speed-ratio flow in a non-uniform distensible tube. Inter. J. Numer. Methods in Fluids vol.16 pp.597-612

Richtmyer R.D. (1957): Difference Methods for Initial-Value Problems. 2nd ed. Interscience Publisher, Wiley, New York

Richardson L.F. (1910): The approximate arithmetical solution by finite differences of physical Problems involving Differential Equations with an application to theStresses in a Masonry Dam. Phylos. Trans. Roy.Soc. London Ser. A Vol.210 pp. 307-57

Rhie C.M. (1981): A Numerical Study of the Flow Past an Isolated Airfoil with Separation. Ph.D. Thesis Dept Mech. and Industrial Engineering University of Illinois at Urbana-Champaign

Rhie C.M., Chow W.L. (1983): Numerical Study of the Turbulent Flow Past an Airfoil with Trailing Edge Separation. AIAA J. Vol.21 pp.1527-32

Ritz W. (1909): Uber Eine Neue Methode zur Losung Gewisser Variations-Probleme der Mathematischen Physik. J.Reine Angew. Math. Vol.135 N.1 pp.1

Rizzi A. Eriksson L.E. (1981): Transfinite Mesh Generation and Damped Eulerian Equation Algorithm for Transonic Flow around Wing-Body Configurations. Proc. AIAA $5^{th}$ Computational Fluid Dynamics Conference, Palo ALto, California pp.43-69

Roache P.J. (1972): Computational Fluid Dynamics. Hermosa Publishers

Robinson T.F., Factor S.M., Capasso J.M., Wittenberg B.A., Blumenfeld O.O., Selfter S. (1987): Morphology, composition, and function of struts between cardiac myocytes of rat and hamster. Cell tissue Reg. vol. 249 pp.247-55

Rodkiewicz C.M., Sinha P., Kennedy J.S. (1990): On the application of a constitutive equation for whole human blood. ASME J. Biomech. Engineering vol. 112 pp. 198-206

Rogers S., Kutler P. Kwak D., Kiris C. (1989): Numerical simulation of flow through an artificial heart. Proc. 4th Intern. Conf. on Supercomputing, Karatashev L., Karateshev S. (eds) Intern. Supercomputing Institute Inc. St. Peterburg pp. 1-20

Rosenberg G. (1994):Design Philosophy of Penn State Cardiovascular Devices. Advances in Bioengineering ASME 1994 BED-Vol.28 pp.27-28

Rubin S.G., Graves R.A. Jr. (1975): Viscous Flow Solutions with a Cubic Spline Approximation. Comput. Fluids Vol.3 pp.1-36

Runchal A.K. (1987): CONDIF: A Modified Central-Difference Scheme for Convective Flows. Int. J. Num. Meth. Eng. Vol.24 pp.1593-608

Sagawa K. (1978): The ventricular pressure-volume diagram revisited. Circ. Res. vol. 43 pp.677-87

Sagawa K., Maugman L., Suga H., Sunagawa K. (1988): Cardiac contraction and the pressure-volume relationship. Oxford University Press, New York, Oxford

Salmons S. (1971): Skeletal Muscle - an adaptive machine?. British Science News (Spectrum) vol. 83 pp.2-4

Salmons S. (1980): The response skeletal muscle to different pattern of use - some new developemnts and concepts. In: Plasticity of Muscles, Pette D. (ed), Berlin: Walter de Gruyter 1980 pp.387-399

Salmons S. (1990a): The resistance to fatigue of normal and conditioned skeletal muscle. In: Harnessing skeletal muscle power for cardiac assistance. Proc. of the expert meeting held in Liverpool. Salmons and Jarvis (ed), May 8-12, 1990, pp.11-4

Salmons S. (1990b): On the reversibility of stimulation-induced muscle trasnformation. In: The Dynamic State of Muscle Fibres, Pette D. (ed), Berlin: Walter de Gruyter 1990 pp.401-414

Salmons S (1994): Exercise, stimulation and type transformation of skeletal muscle. International Journal of Sports Medicine vol.15 n. 3 pp.136-141

Salmons S., Sreter F. (1967): Significance of impulse activity in transformation of skeletal muscle type. Nature Vol.263 pp.30-34

Salmons S., Vrbova G. (1969): The influence of activity on some contractile characteristics of mammalian fast and slow muscle. J. Physiology (London) vol.210 pp.535-49

Salmons S., Henriksson J. (1981): The adaptive response of skeletal muscle to increased use. Muscle & Nerve vol.4 pp.94-105

Salmons S., Stephenson L.W. (1989): Adaptive capacity of skeltal muscle and its therapeutic applications. In:Neuromuscular Stimulation. Basic Concepts and Clinical Implications, Rose F.C., Jones R., Vrbova G. (eds), New York: Demos, 1989 pp.203-15

Salmons S., Jarvis J.C. (1990): The working capacity of skeletal muscle transformed for use in a cardiac assist role. In: Transformed Skeletal Muscle for Cardiac Assistance, Chiu R.C.-J., Bourgeois I.M. (eds). Mount Kisco, NY, Futura Publishing Company pp.89-104

Salmons S., Jarvis J.C. (1991): Cardiompyoplasty: a look at the fundamentals. In: Cardiomyoplasty, Carpantier A., Chachques J.-C., Grandjean P. (eds). Mount Kisco, NY, Futura Publishing Company pp.3-17

Salmons S., Jarvis J.C. (1992): Cardiac assistance from skeletal muscle: a critical appraisal of the various approaches. British Heart J. vol. 68 pp. 333-8

Sandler H., Dodge H.T. (1963): Left ventricular tension and stress in man. Circ. Res. vol.13 pp.91-104

Schlichting H. (1968): Boundary Layer Theory. $6^{th}$ ed., translated by J. Kestin. McGraw-Hill, New York

Schneider G.E., Zedan (1981): A Modified Strongly Implicit Procedure for the Numerical Solution of Field Problems. Num. Heat Transfer Vol.4 pp. 1-19

Secomb T.W. (1977): Flow in a channel with pulsating walls. J. Fluid Mechanics Vol. 88 pp. 273-288

Sharp M.K. (1994): The effect of blood viscoelasticity on pulsatile flow in straight tubes. In: Biofluid Mechanics, Blood Flow in Large Vessels. Proc. of the 3rd International Symposium in Biofluid Mechanics and Biorheology July 16-19, 1994. Liepsch D. (ed) pp.663-80

Shepherd M.P. (1969): Diaphragmatic muscle and cardiac surgery. Ann. R. Cool. Surg. Engl. vol.45 pp.212-31

Shettigar U.R., Dropmann M., Christian P.E., Kolff W.J. (1989): Residence time distributions in artificial ventricles. ASAIO Trans. vol.35 pp. 708-12

Shivakumar P.N., Man C.-S., Rabkin S.W. (1989): Modelling of the heart and pericardium at end-diastole. J. Biomechanics vol.22 n.3 pp.201-209

Shortland A., Iudicello F., Jarvis J.C., Henry F.S., Black R.A., Collins M.W. and Salmons S. 1993): Physical and numerical simulation of blood flow within a skeletal muscle ventricle.Proceedings of the World Symposium of Cardiomyoplasty and Biomechanical Assist, Paris (1993)

Shortland A.P., Black R.A., Jarvis J.C., Henry F.S., Iudicello F., Collins M.W., Salmons S. (1995): Flow Visualization of Vortex Formation and Travel in a Model Ventricle: Application to the Design of a Skeletal Muscle Ventricle, 1994. Journal of Biomechanics. In Press

Shoucri R.M. (1991a): Theoretical study of pressure-volume relation in left ventricle. Am J. Physiol. vol.260 pp. H282-291

Shoucri R.M. (1991b): Pump function of the heart as an optimal control problem. J. Biomed. Engineering vol.13 pp. 384-90

Smith R.M. (1985): The current Status of Turbulence Modelling in the Fluid Flow Code Feat. CEGB Report TPRD/B/0591/N85

Sobey I.J. (1985): Observation of waves during oscillatory flow. J. Fluid Mech. vol. 151 pp.395-426

Sokolnikoff I.S. (1956): Mathematical Theory of Elasticity. 2nd Edn, McGraw-Hill, New York

Southwell R.V. (1946): Relaxation Methods in Theoretical Physics. Claredon Press, Oxford

Spalding D.B. (1972): A novel Finite Difference Formulation for Differential Expressions Involving both First and Second Derivatives. Int. J. Num. Meth. Eng. Vol.4 pp.551-9

Spalding D.B. (1980): Mathematical Modelling of Fluid Mechanics, Heat Transfer and Mass Transfer Processes. Imperial College, London, Mech. Eng. Dept. Rep.n. HTS/80/1

Spotnitz H.M., Merker C., Malm J.R. (1974): Applied physiology of the canine rectus abdominis force-length curves correlated with functional characteristics of a rectus powered "ventricle": potential for cardiac assistance. Trans Am Soc. Artif. Intern. Organs vol.20 pp747-55

Starling E.H. (1918): The Linacre lecture on the law of the heart. Delivered at St. John's College, Cambridge, 1915. Longmans, Green, London, 1918

Starius G. (1977): Construction of Orthogonal Curvilinear Meshes by Solving Initial Values Problems. Num. Math. Vol.28 pp.25-48

Stein P.D., Sabbah H.N. (1980): Hemorheology of turbulence. Biorheology vol.17 pp.301-19

Stevens L., Brown J. (1986): Can noncardiac muscle provide useful cardiac assistance? Am Surg. vol.52 pp.423-7

Stone H.L. (1968): Iterative Solution of Implicit Approximations of Multi-Dimensional Partial Differential Equations. SIAM J. Num. Anal. Vol. 5 pp. 530-58

Streeter D.D., Spotnitz H.M., Patel D.P., Ross J., Sonnenblick E.H. (1969): Fiber orientation in the canine left ventricle during diastole and systole. Circ. Res. vol.24 pp. 339-47

Streeter D.D., Spotnitz H.M., Patel D.P., Ross J., Sonnenblick E.H. (1973): Fiber orientation in the canine left ventricle during diastole and systole. Circ. Res. vol.33 pp. 656-64

Streeter D.D., Ramon C. (1983): Muscle pathway geometry in the heart wall. ASME J. Biomechanical Engineering vol.105 pp. 367-73

Sutera S. (1977): Flow-induced trauma to blood cells. Circulation. vol. 41 pp. 2-8

Syed S., Chiappetta L. (1985): Finite Difference Methods for Reducing Numerical Diffusion in TEACH-Type Calculations. AIAA Paper 85-0056

Taber L.A. (1988): On a theory for large elastic deformation of shells of revolution including torsion and thick-shell effects. Inter. J. Solids and Structures vol. 24 pp.973-85

Taber L.A. (1991a): On a nonlinear theory for muscle shells: part I - Theoretical development. ASME J. Biomechanical Engineering vol. 113 pp.56-62

Taber L.A. (1991b): On a nonlinear theory for muscle shells: part II - Application to the beating left ventricle ASME J. Biomechanical Engineering vol. 113 pp.63-71

Takahashi R., Yozu R., kurosaka Y., Kawada S. (1993): Assisted circulation using cardiomyoplasty together with aortomyoplasty. Artificial Organs vol. 17 pp.914-18

Tarbell J.M., Gunshinan J.P., Geselowitz D.B., Rosenburg G., Shung KK., Pierce W.S. (1986): Pulsed Doppler velocity measurements inside a left ventricular assist device. ASME J. Biomech. Engng vol. 108 pp. 232-8

Taylor T.W., Okino H., Yamaguchi T. (1993): Realistic three-dimensional left ventricular ejection determined from computational fluid dynamics. ASME Advances in Bionengineering BED-vol.26 pp. 119-122

Taylor T.W., Okino H., Yamaguchi T. (1994): Three-dimensional analysis of left ventricular ejection using computational fluid dynamics. ASME J. Biomech. Engng vol.116 pp. 127-30

Termet H., Chalencon J.L., Estour F. (1966): Transplantation sur le myocarde d'un muscle strie exciete par pacemaker. Ann. Chir. Thorac. Cardiovasc. vol.5 pp.260-3

Thoma H., W. Fasching, H. Enekel, E. Wolner, K.J. Polzer, J. Nevrotil (1973): Ein neues Konzept mechanischen Unterstutzung des Kreislaufes. Proceedings of the Austrian Society Surgery, $14^{th}$ Annual Meeting

Thoma H., Frey M., Girsch W., Happak W., Losert U., Mayr W., Gruber H. (1991): The sheep as a model for skeletal muscle assist: Fibre-selective stimulation via epineural electrodes. Harnessing skeletal muscle power for cardiac assistance. Proc. of the expert meeting held in Liverpool. Salmons and Jarvis (ed), May 8-12, 1990, pp.65-71

Thompson J.F., Thames F.C., Mastin C.W. (1974): Automatic Numerical Generation of Body-Fitted Curvilinear Coordinate System for Field Containing Any Number of Arbit-

rary Two-Dimensional Bodies. J. Computational Phys. Vol. 15 pp. 299-319

Thompson J.F. (1980): Numerical Solution of Flow Problems using Body Fitted Coordinate Systems. Int. Computational Fluid Dynamics Vol.1. Ed. by W. Kollmann. Hemishpere Washington. D.C.

Thompson J.F., Warsi Z.U., Mastin C.W. (1982): Boundary Fitted Cooridnate Systems for Numerical Solution of Partial Differential Equations- A Review. J. Comp. Phys. Vol.47 pp.1-108

Thompson J.F., Wilkes N.S. (1982): Experiments with Higher-Order Finite Defference Formulae. AERE 10493

Thompson J.F., Warsi Z.U.A. (1983): Three Dimensional Grid Generation from Elliptic Systems. AIAA -83-1905. AIAA $6^{th}$ Computational Fluid Dynamics Conference, Danvers, Massachussettes

Thompson J.F. (1984): Grid Generation Techniques in Computational Fluid-Dynamics. AIAA Journal Vol.22 n.11 pp.1505-23

Thompson J.F. (1984): A Survey of Dynamically-Adaptive Grids in the Numerical Solution of Partial Differential Equations. J. of Numerical Mathematics

Thompson J.F., Warsi Z.U., Mastin C.W. (1985): Numerical Grid Generation. Elsevier Science Publishing

Thompson J.F. (1988): A Composite Grid Generation Code for General 3-D Regions -The Eagle Code. AIAA J. Vol.26 pp. 271-2

Tozeren A. (1983): Static Analysis of the left ventricle. ASME J. Biomech. Engineering vol. 105 pp. 39-46

Tsangaris S., and Koufopoulos N. (1990): Internal flows with moving boundaries and applications in ventricular ejection. In: Biomechanical Transport Processes, Edited by F.Mosora et al, Plenum Press, New York; pp. 77-85

Tu C., Deville M., Dhuer L., Vanderschuren L. (1992): Finite-Element simulation of pulsatile flow through arterial stenosis. J. Biomechanics vol.25 n.10 pp.1141-2

Turner M., Clough R., Martin H., Topp L. (1956): Stiffness and Deflection Analysis of Complex Structures. J. Aero. Sci. Vol.23 n.9 pp.805-23

Tutty O.R. (1992): Pulsatile flow in a constricted channel. ASME J. Biomech. Engng vol. 114 pp.5–54

Uchida S., Aoki H. (1977): Unsteady flows in a semi-infinite contracting or expanding pipe. Journal of Fluid Mechanics Vol. 82 pp.371-387

Ugolini F. (1986): Skeletal Muscle for Artificial Heart Drive: Theory and in Vivo Experiments. In: Chiu R.C.J. (ed.) Biomechanical Cardiac Assist. Futura, Mount Kisco, N.Y., pp.193-210

Umezu M. (1994): Design Optimization of Artificial Heart Blood Pumps Based on Hemolysis Testing. Advances in Bioengineering ASME 1994 BED-Vol.28 pp.33-34

Unger F. (1979): Assisted Circulation, ed. by F. Unger, Innsbruck, Austria. Springer-Verlag

Unger F. (1984): Assisted Circulation, ed. by F. Unger, Innsbruck, Austria. Springer-Verlag

Unger F. (1989): Assisted Circulation, ed. by F. Unger, Innsbruck, Austria. Springer-Verlag

Van Doormal J.P., Rairhby G.D. (1984): Enhancements of the SIMPLE Method for Predicting Incompressible Fluid Flow. Heat Transfer Vol.7 pp. 147-63

Vito R.P. (1979): The role of the pericardium in cardiac mechanics. J. Biomechanics vol. 12 pp.587-592. Corrections to this paper published under the title 'Response to the letter of H.A.Puryear and R.A. Casper' appeared in J. Biomechanics vol.13 p.636 (1980)

Von Recum A., Stulc J.P., Hamada O., Baba H., Kantrowitz A. (1977): Long-term stimulation of a diaphragm muscle pouch. J. Surg. Res. Vol.23 pp. 422-27

Vreugdenhil C.B. (1989): Computational Hydraulics. Springer-Verlag, Berlin
Walburn F.J., Schneck D.J. (1976): A constitutive equation for whole human blood. Biorheology vol. 13 pp.201-10

Weatherill N.C., Forsey C.R. (1984): Grid Generation and Flow Calculations for Complex Aircrafts Geometrics using a Multiblock Scheme. AIAA -84-1665. AIAA $17^{th}$ Fluid Dynamics, Plasma Dynamics, and Lasers Conference, Snowmass, Co

Weber K.T., J. Janicki (1974): Intraaortic balloon conterpulsation. Ann. Thorachic Surgery vol.17 p. 602

Wessale J.L., Geddes L.A., Badylack S.F., Janas W. (1991): Use of electrical impedance for continuous measurement of stroke volume of skeletal muscle-powered cardiac assist device. Medical & Biological Engineering & Computing pp. 207-211

Wilkes N.S., Thompson C.P., Kightley J.R., Jones I.P., Burms A.D. (1985): On the Numerical Solution of 3-D Incompressible Flow Problems. Harwell Report AERE-CSS 179, 1985

Withmore R.L. (1968): Rheology of the circulation. Pergamon Press

Wolfe A. (1991): CFD Software: Pushing Analysis to the Limit. Mechanical Engineering pp.48-54

Womersley J.R. (1955): Method for the calculation of velocity, rate of flow and viscous drag in arteries when pressure gradient is known. J. Physiol. vol. 127 pp.55-63

Womersley J.R. (1957): Oscillatory flow in arteries: the contrained elastic tube as a model of arterial flow and pulse transmission. Phys. Med. Biol. vol.2 pp.178-87
Woods R.H. (1892): A few applications of a physical theorem to membranes in the human body in a state of a tension. J. Anat. Physiol. vol. 26 pp.362-70

Wong A.Y.K., Rautoharju P.M. (1968): Stress distribution within the left ventriuclar wall approximated as a thick ellipsoidal shell. Am. Heart J. vol. 755 pp.649-61

Wong H.H., Raithby G.D. (1979): Improved Finite Difference Methods Based on a Critical Evaluation of the Approximation Errors. Num. Heat Transfer Vol.2 pp.139-63

Xu X.Y., Collins M.W. (1990): A review of the numerical analysis of blood flow in arterial bifurcations. Proc Instn Mech Engrs vol. 204 pp.205-16

Xu X.Y. (1992): Numerical analysis of blood flow in 3-D arterial bifurcations. Ph.D. thesis, City University, London

Xu X.Y., Collins M.W., Jones C.J.H. (1992): Flow studies in canine artery bifurcations using a numerical simulation method. ASME J. Biomech Engng vol. 114 pp.504-11

Xu X.Y., Collins M.W., Griffith T.M., Jones C.J.H. and Tardy Y. (1993): Coupled Modelling of Blood Flow and Arterial Wall Interactions by the Finite Element Method. In: Computers in Cardiology 1993, IEEE Computer Society Press, Washington, Brussels, Tokyo, pp.687-690

Xu X.Y., Collins M.W. (1994a): Studies of blood flow in arterial bifurcations using computational fluid dynamics. Proc Instn Mech Engrs vol. 208 pp.163-75

Xu X.Y. and Collins M.W. (1994b): Particle Flow Behaviour and Pressure Distribution in a 3-D T-junction. In: Biofluid Mechanics, Proc.of 3rd International Symposium. Ed. by D.Liepsch (VDI-Verlag), pp.489-496

Xu X.Y., Henry F.S., Collins M.W., Griffith T.M., GRiffith T.M., Tardy Y. (1994c): Numerical predictions - an effective research method for haemodynamic wall-fluid interaction problems. Presented at 2nd World Congress of Biomechanics.

Xu X.Y. and Collins M.W. (1995): Numerical Modelling of Blood Flow in Compliant Arteries and Arterial Bifurcation. In: Biofluid Mechanics, Ed. by H.Power, Computational Mechanics Publications, pp. 55-94

Yettram A.L., Vinson C.A., Gibson D.G. (1982): Computer modeling of the human left ventricle. ASME J. Biomechanical Engineering vol.104 pp.148-152

Yin F.C.P., Strumpf R.K., Chew P.H., Zeger S.L. (1987): Quantification of the mechancial properties of non-contracting canine myocardium under simultaneous biaxial loading. J. Biomechanics vol. 20 pp. 577-89

Yoganathan A.P., Lemmon J.D. Jr., Kim Y.H., Walker P.G., Levine R.A., Vesier C.C. (1994): A computational study of a thin-walled three-dimensional left ventricle during early systole. ASME J. Biomech. Engng vol.116 pp. 307-14

Young T. (1808): Hydraulic Investigations - subservient to an intended Cronian lecture on the motion of blood. Phil. Trans. Roy. Soc. (London) vol. 98 pp.164-86

Zahalak G.I. (1986): A comparison of the mechanical behaviour of the cat soleus muscle with a distribution-moment model. Trans. ASME J. Biomech. Engineering vol.108 pp.131-140

Zahalak G.I., Ma S.-P. (1990): Muscle activation and contraction: constitutive relations based directly on cross-bridge kinetics. Trans. ASME J. Biomech. Engineering vol.112

Zahalak G.I., Ma S.-P. (1990): Muscle activation and contraction: constitutive relations based directly on cross-bridge kinetics. Trans. ASME J. Biomech. Engineering vol.112 pp.52-62

Zahalak G.I. (1994): From molecules to movement: translating muscle biophysics into muscle biomechanics. Abstracts from 8th International Conference on mechanics in medicine and biology. L. Blankevvort and J.G.M. Kooloos (eds). July 10-15, 1994, Amsterdam, The Netherlands vol.1 p.7

Zhang H., Reggio M., Trepanier J.Y., Camarero R. (1993): Discrete Form of the CGL for Moving Meshes and its Implementation in CFD schemes. Computers Fluids Vol.22 N.1 pp.9-23

Zienkiewicz O.C., Cheung Y.K. (1965): Finite Elements in the Solution of Field Problems. The Engineer pp.507-10

Zienkiewicz O.C. (1977): The finite element method. Third Edition, McGraw-Hill

Zwart H.J. (1966): Complete left heart bypass without thoracotomy. Proefschrift, University of Amsterdam: S.O.C. Offsetdruck - Amsterdam 1966

Ku D.N., Giddens D.P., Zarins C.K., Glakov S. (1985): Pulsatile Flow and atherosclerosis in the human carotid bifurcation - Positive correlation between plaque location and low and oscillating shear stress. Atherosclerosis vol.5 n.3 pp.293-392

Libai A., Simmonds J.G. (1988): The nonlinear theory of elastic shells. Academic Press Boston

McDonald D.A. (1960): Blood flow in arteries. William and Wilkins Co. Baltimore

Mommaerts W.F.H.M. (1969): Energetic of muscular contraction. Physiol. Reviews vol.49 n.3 pp. 428-508

O'Brien G.G., Hyman M.A., Kaplan S. (1950): A study of the numerical solution of partial differential equations. J. Math. Phys. vol.29 pp.223-251

Oda T., Miyamoto A.-T., Okamoto Y., Ban T. (1993): Skeletal muscle-powered ventricle. Effects of size and configuration on ventricular function. J. Thorachic and Cardiac Surgery vol.105 pp.68-77

Proceedings of the Second CFDS International User Conference November 1994, Pittsburg, USA

# APPENDIX A
## Derivation of Hill's Equation

The original derivation of Hill's equation for characterization of the mechanical properties of muscles comes from the equation of balance of energy:

$$E = A + S + W$$

where E is the rate of energy release,
A is the activation or maintenance heat per unit of time,
W is the rate of work done, equal to $P \times v$,
S is the shortening heat.

In the isometric condition the rate of energy release is equal to the activation energy (E=A). When the muscle contracts, an additional chemical reaction takes place, and it releases an amount of 'extra energy' equal to the sum of the shortening heat and the work done (S=W). By measuring E and A, Hill identified the term S+W, and showed that it is represented by the empirical equation

$$S + W = b(P_0 - P) \qquad (A-1)$$

He asserted further that empirically

$$S = av \qquad (A-2)$$

where $a$ and $b$ are the same constants defined in section 2.4.4.
Combining equations (A-1) and (A-2) and rearranging terms we obtain eq. (2.5). Hill's major contribution lies in his ingenious methods for accurately measuring the heats E, A, S, W.

To describe muscle mechanics, other equations have been proposed in the past. However Hill's equation remains the most popular. Many years later, Hill (1970) admitted that it is better to think of eq. (2.5) directly as a force-velocity relationship, and not as a thermomechanical expression, because improved experiments do not always support eqs. (A-1) and (A-2).

# APPENDIX B

## Derivation of the Basic Dynamic Equations for Hill's Three-Element Model

Mathematical derivation of the basic dynamic equations for Hill's three-element model follows. We may express the geometric change of a muscle sarcomere in terms of the actin and myosin fibres as shown in Fig.B-1 where

M is myosin filament length

C is actin filament length

$\Delta$ is insertion of actin filaments (overlap between actin and myosin filaments)

H is H-band width

I is I-band width

L is total length of sarcomere

$L_0$ is length of sarcomere at zero stress

$\eta$ is extension of the series elastic element in a sarcomere

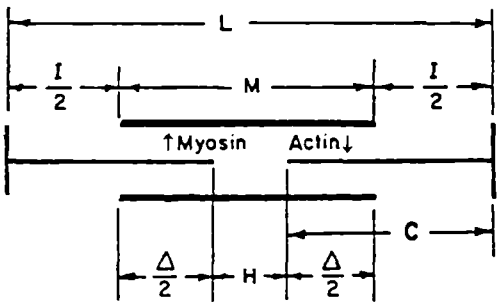


Figure B-1 Geometric nomenclature of various elements of a muscle sarcomere unit. From Fung (1981)

The insertion $\Delta$ is defined by the equation

$$\Delta = M - H = 2C - I$$

and the length L without elastic extension

$$L = M + I = M + 2C - \Delta$$

and with elastic extension

$$L = M + I + \eta = M + 2C - \Delta + \eta \qquad (B-1)$$

On differentiating eq. (B-1) with respect to time, we obtain the basic kinematic relation

$$\frac{dL}{dt} = -\frac{d\Delta}{dt} + \frac{d\eta}{dt} \qquad (B-2)$$

The strain in the parallel elastic element can be defined as $(L - L_0)/L_0$; but since $L_0$ is constant, the stress contributed by the parallel elastic element is:

$$\tau^{(P)} = P(L)$$

Similarly the stress contributed by the activated actin-myosin filaments is:

$$\tau^{(S)} = S(\eta, \Delta)$$

and

$$S(\eta, \Delta) \gtrless 0 \qquad \eta \gtrless 0$$

$$S(\eta, \Delta) = 0 \qquad \eta = 0$$

The total tensile stress is the sum of the contributions from the series and parallel elements:

$$\tau = \tau^P + \tau^S = P(L) + S(\eta, \Delta)$$

If the stress varies with time, we have:

$$\frac{d\tau}{dt} = \frac{dP}{dL}\frac{dL}{dt} + \left(\frac{\partial S}{\partial \eta}\right)_\Delta \frac{d\eta}{dt} + \left(\frac{\partial S}{\partial \Delta}\right)_\eta \frac{d\Delta}{dt} \qquad (B-3)$$

On substituting eq.(B-2) into eq.(B-3) we obtain the basic dynamic equation

$$\frac{d\tau}{dt} = \frac{dP}{dL}\frac{dL}{dt} + \left(\frac{\partial S}{\partial \eta}\right)_\Delta \left(\frac{dL}{dt} + \frac{d\Delta}{dt}\right) + \left(\frac{\partial S}{\partial \Delta}\right)_\eta \frac{d\Delta}{dt}$$

$$= \left(\frac{dP}{dL} + \left(\frac{\partial S}{\partial \eta}\right)_\Delta\right)\frac{dL}{dt} + \left(\left(\frac{\partial S}{\partial \eta}\right)_\Delta + \left(\frac{\partial S}{\partial \Delta}\right)_\eta\right)\frac{d\Delta}{dt}$$

Two special cases of great interest are:

1. *Isometric contraction*: L=constant, and dL/dt=0

$$\frac{d\tau}{dt} = \left(\left(\frac{\partial S}{\partial \eta}\right)_\Delta + \left(\frac{\partial S}{\partial \Delta}\right)_\eta\right)\frac{d\Delta}{dt}$$

2. *Isotonic contraction*: $\tau$=constant, and $d\tau/dt = 0$

$$\left(\frac{dP}{dL} + \left(\frac{\partial S}{\partial \eta}\right)_\Delta\right)\frac{dL}{dt} + \left(\left(\frac{\partial S}{\partial \eta}\right)_\Delta + \left(\frac{\partial S}{\partial \Delta}\right)_\eta\right)\frac{d\Delta}{dt} = 0$$

Experimental methods to determine the characteristics of the series elastic element are discussed in more detail in (Fung, 1984).

# APPENDIX C
## Constitutive Models for Blood Rheology

Functional forms for the constitutive equation of blood to model its non-Newtonian behaviour as discussed above, are: the general power law, Bingham model, Casson model, biviscosity model, and Walburn and Schneck model.

Power Law

The expression of the shear stress $\tau$ as a general power law function of the shear rate $\dot{\gamma}$ is as follows:

$$\tau = m\dot{\gamma}^n$$

where $\dot{\gamma}$ is the shear rate, and $m$ and $n$ are consistency and non-Newtonian indices respectively; $m$ and $n$ are constant for a given hematocrit and chemical composition. To allow for the presence of a yield stress, the power law expression can easily be extended by adding the yield stress $\tau_y$:

$$\tau = m\dot{\gamma}^n + \tau_y$$

Bingham Model

The Bingham fluid's shear stress expression is a linear relation, the line not passing through the origin.

$$\tau = \tau_y + \eta\dot{\gamma} \qquad |\tau| \geq \tau_y$$

$$\dot{\gamma} = 0 \qquad |\tau| < \tau_y$$

where $\eta$ is a constant.

Casson Model

This model attempts to describe both the yield stress property of Bingham plastic fluid and the pseudoplastic behaviour, as shown in Fig.C-1. The Casson fluid's shear stress expression (Casson, 1959) is given as follows:

$$|\tau|^{1/2} = \tau_y^{1/2} + \eta_c\dot{\gamma}^{1/2} \qquad |\tau| \geq \tau_y$$

$$\dot{\gamma} = 0 \qquad |\tau| < \tau_y$$

where $\eta_c$ is the Casson viscosity.

Biviscosity Model

This is a modified Bingham model developed to simulate the pulsatile flow behaviour in slurries (Nakamura and Sawada, 1987). The difference between this model and the Bingham model is that when the velocity gradient tends to zero, the apparent viscosity

coefficient tends to infinity in a Bingham model, while having a finite value in a biviscosity model. The constitutive equation is written as follows:

$$\tau_{ij} = 2(\mu_B + \tau_y(2\pi)^{1/2})e_{ij} \quad \pi \geq \pi_c$$

$$\tau_{ij} = 2(\mu_B + \tau_y(2\pi_c)^{1/2})e_{ij} \quad \pi < \pi_c$$

where $\tau_{ij}$ is the (i,j) component of the deviatoric stress tensor, $e_{ij}$ is the (i,j) component of the deformation rate tensor, $\mu_B$ is the plastic viscosity, and $\pi_c$ is a constant satisfying the relation $\mu_B(2\pi_c)^{1/2} \ll 1.0$

Walburn and Schneck model

This is a general power law model modified to account for the various factors that influence whole blood behaviour such as the shear rate, the hematocrit, and the total protein minus albumin (TPMA) (Walburn and Schneck, 1976). The resulting expression of the shear stress is:

$$\tau = C_1 e^{C_2 H}[e^{C_4(TPMA/H^2)}]\dot{\gamma}^{1-C_3 H}$$

where $C_1, C_2, C_3, C_4$ are constants, and $H$ is the hematocrit.

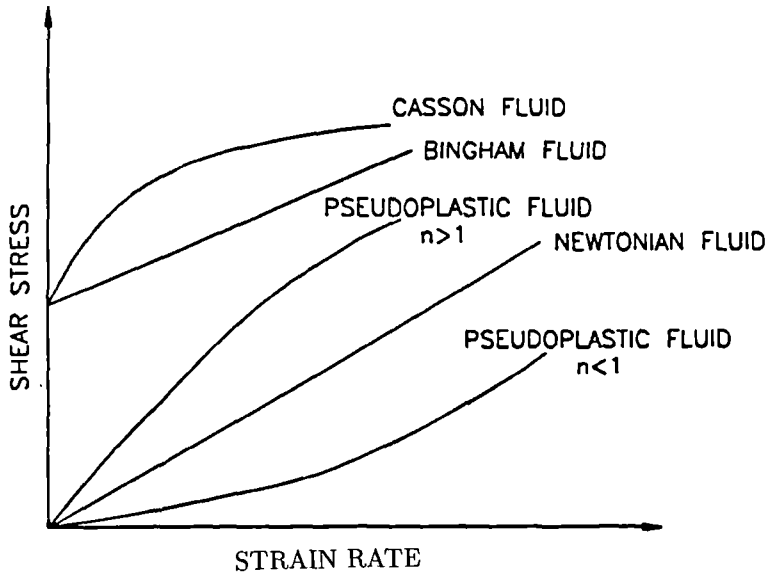


Figure C-1 Rheogram for different types of flow behaviour assuming constant pressure and temperature.

# APPENDIX D

## Stress Distribution in a Thick-Walled Ellipsoidal Ventricle Model

Wong and Rautaharju (1968) calculated the stress distribution within the left ventricular wall approximated as a thick ellipsoidal shell. They assumed that:

1. the left ventricle was a thick ellipsoidal shell, with two equal minor semi-axes;
2. the myocardium was an elastic, isotropic, and homogeneous material. Thus, the strain tensor $l_{ij}$ can be expressed as:

$$l_{ij} = \frac{1+\mu}{E}\sigma_{ij} - \frac{\mu}{E}\delta_{ij}\sigma_{ii} \qquad (D-1)$$

   where $\mu$ is Poisson's ratio, E is Young's modulus, $\sigma_{ij}$ is the stress tensor.
3. the myocardial distorsion was a purely radial displacement, and the intraventricular pressure acting normal to the surface is the only load on the heart;
4. bending moments and shears were neglected because of the symmetrical geometry;
5. inertia effects were neglected;
6. the ventricle wall is in equilibrium and the following stresses act: (i) the radial stress $\sigma_{RR}$ which acts normal to the surface, and is balanced by (ii) the radial components of the longitudinal stress $\sigma_{\phi\phi}$ and the latitudinal stress $\sigma_{\theta\theta}$ acting within the wall.

The contour at any point P on the endocardial surface of the ventricle is given by the principal radii of curvature $r$ and $R$ (Fig. D-1), related by the following expression:

$$r = (1 + \lambda sin^2\phi)R$$

where $\phi$ is the angle between the semimajor axis OA and $R$ or $r$. $\lambda$ is a parameter $< 1$. A shell element is shown in Fig. D-2(a). When subjected to the radial, latitudinal, and longitudinal stresses, the shell will be distorted by a displacement $u$, which is a function of $R$ only, like the stresses. From eq.(D-1) stresses and strains are related by the equations:

$$l_{RR} = \frac{du}{dR} = \frac{1}{E}(\sigma_{RR} - \mu(\sigma_{\theta\theta} + \sigma_{\phi\phi}))$$

$$l_{\theta\theta} = \frac{u}{r} = \frac{1}{E}(\sigma_{\theta\theta} - \mu(\sigma_{\phi\phi} + \sigma_{RR}))$$

$$l_{\phi\phi} = \frac{u}{R} = \frac{1}{E}(\sigma_{\phi\phi} - \mu(\sigma_{RR} + \sigma_{\theta\theta}))$$

The equilibrium condition for the volume element shown in Fig. D-2(b) is:

$$\frac{d}{dR}(\sigma_{RR}rR) - R\sigma_{\theta\theta} - r\sigma_{\phi\phi} = 0 \qquad (D-2)$$

Combining eq.(D-2) with eq.(D-1), $\sigma_{RR}$, $\sigma_{\phi\phi}$, and $\sigma_{\theta\theta}$ are obtained:

$$\sigma_{RR} = \frac{PR_0^{\frac{n+3}{2}}}{(R_0+T)^n - R_0^n} R^{\frac{n-3}{2}} \left(1 - \frac{(R_0+T)^n}{R^n}\right)$$

$$\sigma_{\theta\theta} = \frac{1}{C_0 + \frac{1}{k}} \frac{P R_0^{\frac{n+3}{2}}}{(R_0+T)^n - R_0^n} R^{\frac{n-3}{2}} \left( \left( \frac{n+1}{2} - C_1 \right) + \frac{\left( C_1 - \frac{1-n}{2} \right) (R_0+T)^n}{R^n} \right)$$

$$\sigma_{\phi\phi} = \frac{1}{C_0 + \frac{1}{k}} \frac{P R_0^{\frac{n+3}{2}}}{(R_0+T)^n - R_0^n} R^{\frac{n-3}{2}} \left( \left( C_0 \frac{n+1}{2} + \frac{C_1}{k} \right) - \left( C_0 \frac{1-n}{2} + \frac{C_1}{k} \right) \frac{(R_0+T)^n}{R^n} \right)$$

where

$$n = \frac{4k\mu(1-k) + (1-\mu)(4+5k^2)}{k^2(1-\mu)}, \qquad k = 1 + \lambda sin^2\phi,$$

$$C_0 = \frac{k+\mu}{1+k}, \qquad C_1 = \frac{\mu(1-k)}{1+k\mu}.$$

$P$ is the internal pressure, $R_0$ the endocardial radius of curvature of the meridian for a certain constant value $\phi$, and T the thickness. For a spherical shell $\lambda = 0$, $n = 3$, and $k = 1$. The longitudinal, and the latitudinal stresses are:

$$\sigma_{RR} = \frac{P R_0^3}{(R_0+T)^3 - R_0^3} \left( 1 - \left( \frac{R_0+T}{R} \right)^3 \right)$$

$$\sigma_{\theta\theta} = \sigma_{\phi\phi} = \frac{P R_0^3}{(R_0+T)^3 - R_0^3} \left( 1 + \frac{1}{2} \left( \frac{R_0+T}{R} \right)^3 \right)$$

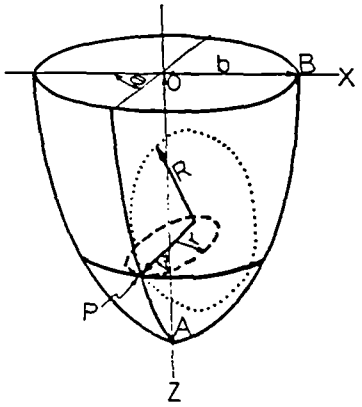


Figure D-1 Schematic represantion of the coordinate system.

(a)

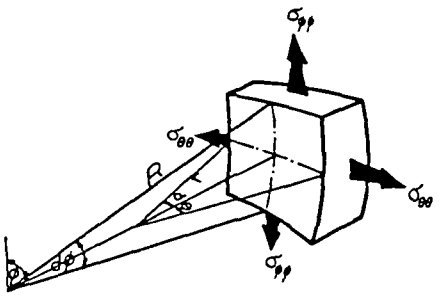


(b)

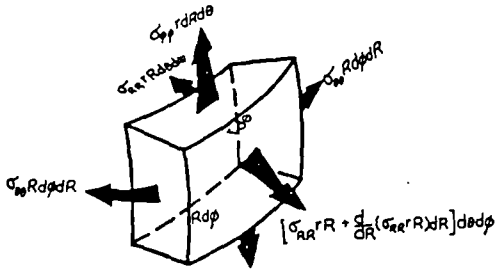


Figure D-2 (a) Shell element. (b) Volume element.

# APPENDIX E

## Finite Element Continuum Mechanics Approach for Left Ventricle Modelling

Finite Element Methods for Continuum Analysis of the Left Ventricle

Hunter et al. (1988) derived the Galerkin finite element equations for three-dimensional finite elasticity in prolate spheroidal coordinates. These equations generally represent the equations for the formulation of virtual work. Neglecting body forces and inertia, the virtual work principle is expressed as:

$$\int_V P^{IJ} F^{\alpha}_{J} \delta u_{\alpha} \mid_I \, dV = \int_{A_2} s \cdot \delta u dA \qquad (E-1)$$

where

$$F^{\alpha}_{J} = \frac{\partial \theta^{\alpha}}{\partial \nu^J} \qquad \text{and} \qquad \delta u_{\alpha} \mid_I = \frac{\partial \delta u_{\alpha}}{\partial \nu^I} - \Gamma^{\beta}_{\alpha I} \delta u_{\beta}$$

where

$$\Gamma^{\beta}_{\alpha I} = g^{(\theta)}_{\alpha,I} \cdot g^{(\theta)\beta} = \frac{\partial}{\partial \nu^I} \left[ \frac{\partial x^r}{\partial \theta^{\alpha}} \right] \frac{\partial \theta^{\beta}}{\partial x^r}$$

On the left hand side, $P^{IJ}$ are contravariant components of the second Piola-Kirchhoff stress tensor referred to fibre $\nu^I$ - coordinates in the undeformed body, whereas $\delta u_{\alpha}$ are covariant components of the virtual displacement vector referred to prolate spheroidal geometric $\theta^{\alpha}$ - coordinates in the deformed state. $F^{IJ}$ are components of the deformation gradient tensor that maps an undeformed vector referred to fibre coordinates into a deformed vector referred to geometric coordinates. Because the covariant derivatives are with respect to fibre coordinates, the Christoffel symbols $\Gamma$ are not symmetric with respect to the lower two indices. $g^{(\theta)}_{\alpha}$ and $g^{(\theta)\beta}$ are covariant and contravariant base vectors of the geometric coordinates. $x^r$ are rectangular cartesian coordinates in the deformed state. In keeping with the Bubnov-Galerkin finite element method, both the geometric coordinates and the virtual displacements in eq.(E-1) were approximated by finite element interpolations

$$\theta_{\alpha}(\xi) = \Psi_{n(e)}(\xi) \cdot \theta^{n(e)}_{\alpha} \qquad \text{and} \qquad \delta u_{\alpha}(\xi) = \Psi_{n(e)}(\xi) \cdot \delta u^{n(e)}_{\alpha} \qquad (E-2)$$

where $\theta^{n(e)}_{\alpha}$ and $\delta u^{n(e)}_{\alpha}$ are prolate spheroidal coordinates and virtual displacements at a local node $n$ in element $(e)$, and $\Psi_{n(e)}$ are trilinear Lagrangian basis functions of element $\xi$ - coordinates. When assuming eqs(E-2) substituted in eq.(E-1), the volume integral becomes the sum of element volume integrals and the right hand sides are integrated over the element boundaries $A_2$ on which components of the surface traction vector $s$ act.

Diastolic Constitutive Law

For passive loading of the ventricular wall, a strain energy potential $W$ was chosen that was an exponential function of Lagrangian-Green's strain tensor components $E_{IJ}$

referred to fibre coordinates:

$$W = \frac{C}{2}(e^Q - 1)$$

and

$$E_{IJ} = \frac{1}{2}\left(\frac{\partial x^r}{\partial \nu^I}\frac{\partial x^r}{\partial \nu^J} - \delta_{IJ}\right)$$

where $Q$ is given below and $\delta_{IJ}$ is the Kronecker delta. The stress components $P^{IJ}$ in the virtual work equation (E-1) are obtained from the strain energy function using the constitutive relation

$$P_{IJ} = \frac{1}{2}\left(\frac{\partial W}{\partial E_{IJ}} + \frac{\partial W}{\partial E_{JI}}\right) - pg^{(\nu)IJ} \qquad (E-4)$$

where

$$g^{(\nu)IJ} = \frac{\partial \nu^I}{\partial x^r}\frac{\partial \nu^J}{\partial x^r}$$

The hydrostatic pressure $p$ was introduced, as the Lagrangian multiplier needed, to enforce the kinematic constraint that the third principal strain invariant equals one. Following Guccione et al. (1991), the following form for exponent $Q$ was chosen to describe the special case of three-dimensional transverse isotropy with respect to fibre, $\nu^1$, cross-fibre, $\nu^2$, and transmural, $\nu^3$, coordinates:

$$Q = b_f E_{11}^2 + b_t(E_{22}^2 + E_{33}^2 + E_{23}^2 + E_{32}^2) + b_{fs}(E_{12}^2 + E_{21}^2 + E_{13}^2 + E_{31}^2)$$

Material constants $C, b_f, b_t, b_{fs}$ may be found in (Guccione et al., 1991). These allowed a cylindrical model of the left ventricle to match strains measured in an intact canine heart preparation during passive left ventricular filling.

Active Contraction Model

Systolic contraction was modelled by defining the stress tensor in eq.(E-1) as the sum of the passive component and an active fibre-directed component $T$, which was a function of external calcium concentration $Ca_0$ and sarcomere length $l$ (Guccione et al., 1993b; 1993c):

$$T = T_{max}\frac{Ca_0^h}{Ca_0^h + ECa_{50}^h}$$

where $T_{max}$ is the peak tension developed at maximum $Ca_0$ and $h$ is the Hill coefficient. The calcium sensitivity $ECa_{50}$ was treated as a length-dependent relation:

$$ECa_{50}^h = \frac{(Ca_0)_{max}^h}{e^{[B(l-l_0]} - 1}$$

where $B$ is a constant and $l_0$ is the sarcomere length at which no active tension is developed. The parameters of the active contraction model are based on experimental measurements of sarcomere length and peak active tension in isolated cat trabeculae.

# APPENDIX F
## The Immersed Boundary Method

The Immersed Boundary Method considers the problem of a viscous incompressible fluid containing an immersed system of elastic or contractile fibres. The fibres are massless force-generating elements, and form a composite material with the fluid in which they are immersed, for which the equations of motion are

$$\rho\left(\frac{\partial \mathbf{u}}{\partial t}+\mathbf{u}\cdot\nabla\mathbf{u}\right)+\nabla p=\mu\nabla^2\mathbf{u}+\mathbf{F} \qquad (F-1)$$

$$\nabla\mathbf{u}=0 \qquad (F-2)$$

$$\mathbf{F}(\mathbf{x},t)=\int \mathbf{f}(q,r,s,t)\delta^3(\mathbf{x}-\mathbf{X}(q,r,s,t))dqdrds \qquad (F-3)$$

$$\frac{\partial \mathbf{X}(q,r,s,t)}{\partial t}=\mathbf{u}(\mathbf{X}(q,r,s,t),t)=\int \mathbf{u}(\mathbf{x},t)\delta^3(\mathbf{x}-\mathbf{X}(q,r,s,t))d^3x \qquad (F-4)$$

$$\mathbf{f}=\frac{\partial(T\bar{\tau})}{\partial s} \qquad (F-5)$$

$$T=\sigma\left(\mid\frac{\partial \mathbf{X}}{\partial s}\mid;q,r,s,t\right) \qquad (F-6)$$

$$\bar{\tau}=\frac{\partial \mathbf{X}/\partial s}{\mid\partial \mathbf{X}/\partial s\mid} \qquad (F-7)$$

These equations are based on a mixed Eulerian-Lagrangian description of the motion. The Eulerian variables are the velocity $\mathbf{u}(\mathbf{x},t)$, the pressure $p(\mathbf{x},t)$, and the force $\mathbf{F}(\mathbf{x},t)d^3x$ which is applied by the fibres to the fluid in which they are immersed. $\mathbf{X}$ denotes position in space, $d^3x$ is the volume element, and $t$ is the time. The Lagrangian variables are the fibre point position $\mathbf{X}(q,r,s,t)$, the fibre tension $T(q,r,s,t)dqdr$, the unit tangent to the fibres $\bar{\tau}(q,r,s,t)$ and the resultant fibre force $\mathbf{f}(q,r,s,t)dqdrds$. $q$, $r$, and $s$ are curvilinear coordinates chosen in such a way that $(q,r)$ labels a particular fibre and $(q,r,s)$ labels a particular material point.

Eqs ((F-1) - (F-7)) may be divided into three groups. Eqs (F-1) and (F-2) are the Navier-Stokes equations in the independent variables $(\mathbf{x},t)$, where the force density $\mathbf{F}$ arises fromthe fibres immersed in the fluid. Eqs ((F-5) - (F-7)) are the fibre equations in the independent variables $(q,r,s,t)$, that may be used to determine the Lagrangian fibre force density $\mathbf{f}$ from the fibre configuration $\mathbf{X}$ at time $t$. In eq.(F-6) $\mid\partial\mathbf{X}/\partial s\mid$ determines the fibre strain, and the function $\sigma$ defines the (possibly nonlinear) stress-strain relation of the fibres. Eqs (F-3) and (F-4) are the interaction equations that connect the functions of $(\mathbf{x},t)$ and the functions of $(q,r,s,t)$. Both involve integral trasformation in which the Dirac delta function appears as a kernel. Eq. (F-4) is the familiar no-slip condition, which plays the unfamiliar role of an equation of motion for the fibres, because the fibre motion is not specified in advance.

The equations ((F-1) - (F-7)) are solved by using the immersed boundary method. In this method, the Eulerian (fluid) variables are defined on the fixed cubic computational

lattice, the structure of which is not altered or interrupted in any way by the presence of the fibres. Lagrangian variables are defined on discrete computational fibres, each of which is a list of discrete fibre points that are thought of as being connected by (possibly nonlinear) springs, the elastic parameters of which may be time-dependent. The fibres move freely through the computational lattice of the fluid: there is no requirement that the fibre points and the lattice points should coincide.

At the beginning of each time step, the fluid velocity **u** is given. These quantities are updated as follows:

1. Use the fibre configuration **X** to determine the Lagrangian density **f** of the fibre force, applying eqs ((F-5) - (F-7)) in the finite difference form. Only the fibre data are involved.

2. Determine the Eulerian force density **F** from **f**, by discretizing eq. (F-3).

3. Update the fluid velocity **u** under the influence of **F**, by numerically integrating of eqs (F-1) and (F-2), using the projection method (Chorin, 1967).

4. Interpolate the fluid velocity at the fibre points and update the fibre configuration **X**, by discretizing equation (F-4).

# APPENDIX G

## Calculation of Vortex Core Position from the Velocity Vector Field

The position of the vortex core was determined using a computer program which estimates the position of the minimum velocity in a limited, predefined, area.

The velocities in all cells are dumped to a file at the end of the numerical calculations. The dump file is then read and the velocity field displayed on the workstation screen at each time step, using a Gino program. This allows visual determination of the approximate position of the vortex core, at that particular time. A surrounding box is then placed around the vortex core. The physical coordinates of the grid node with the minimum velocity within this area is then determined. This nodal location is then selected to be the origin of a local coordinate system, in computational space, spanning the eight neighbouring nodes. A biquadratic function is then fitted to the nine points and the location of the minimum of this function determined.

This biquadratic function may be written as:

$$\phi(\xi,\eta) = a_1 + a_2\xi + a_3\eta + a_4\xi\eta + a_5\xi^2 + a_6\eta^2 + a_7\xi^2\eta + a_8\xi\eta^2 + a_9\xi^2\eta^2$$

where $\xi = \xi(x,r)$ and $\eta = \eta(x,r)$ are coordinates in computational space (see Fig. G-1).

The coefficients $a_1, a_2 ... a_9$ are found from the nodal values of velocity.

The location, in computational space, of the minimum velocity is determined by differentiating the above equation by $\xi$ and by $\eta$ separately, and then setting the resulting equations to zero. i.e.,

$$\frac{\partial\phi}{\partial\xi} = a_2 + a_4\eta + a_5\xi + 2a_7\xi\eta + a_8\eta^2 + 2a_9\xi\eta^2 = 0$$

$$\frac{\partial\phi}{\partial\eta} = a_3 + a_4\xi + a_6\eta + a_7\xi^2 + 2a_8\eta\xi + 2a_9\xi^2\eta = 0$$

Rearranging gives,

$$\xi = \frac{-a_2 - a_4\eta - a_8\eta^2}{2a_5 + 2a_7\eta + 2a_9\eta^2}$$

$$\eta = \frac{-a_3 - a_4\xi - a_7\xi^2}{2a_6 + 2a_8\xi + 2a_9\xi^2}$$

Then the position in physical space relative to the grid node with minimum velocity, $\Delta x$ and $\Delta r$, is found using:

$$\Delta x = \overline{\frac{\partial x}{\partial\xi}}\xi + \overline{\frac{\partial x}{\partial\eta}}\eta$$

$$\Delta y = \overline{\frac{\partial y}{\partial\xi}}\xi + \overline{\frac{\partial y}{\partial\eta}}\eta$$

The overbar denotes an average value over $\xi$ and $\eta$.

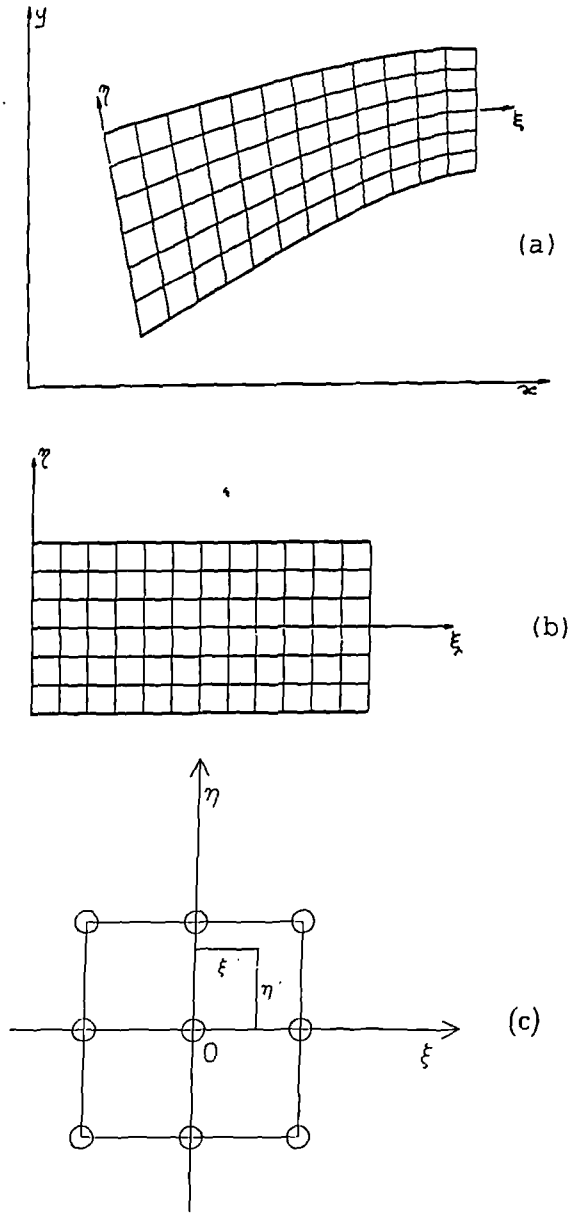


Figure G-1 (a) Computational domain in the physical space. (b)Computational domain in the computational space. (c) Location of the minimum velocity point ($\xi'$, $\eta'$) in the computational space

# APPENDIX H

## Calculation of the fluid shear stress fields in a tube and in an expanding/contracting pipe

Comparisons of numerically predicted and analytical distributions of shear stress in a rigid tube and in a semi-infinite expanding/contracting pipe are presented below. This study was performed to check the ability of CFDS-FLOW3D to predict shear stresses, particularly over grid inter-block boundaries. The computational grid used for these calculations was topologically similar to that used for the SMV predictions discussed in Chapter 7.

### Calculation of Shear Stress

The components of the shear stress are:

$$\tau_{xy} = \mu\left(\frac{\partial u}{\partial y} + \frac{\partial v}{\partial x}\right)$$

$$\tau_{yz} = \mu\left(\frac{\partial v}{\partial z} + \frac{\partial w}{\partial y}\right)$$

$$\tau_{zx} = \mu\left(\frac{\partial w}{\partial x} + \frac{\partial u}{\partial z}\right)$$

The shear stresses in the flow are not printed out by CFDS-FLOW3D, although they are computed internally as part of the solution. On the recommendation of CFDS staff, the stresses were initially calculated using the utility subroutine GRADDV, which calculates the spatial gradients of a specified velocity component at the centre of each control volume. The routine was called from USRTRN, where shear stresses were then calculated from the velocity gradients. Details on the use of GRADDV subroutine are in the user manual (Anonymous, 1994a). The velocity gradients are stored by the code in the arrays UGRAD, VGRAD, and WGRAD.

An alternative method of obtaining the shear stresses from velocity gradients is to calculate the latter in a uniformly spaced computational domain and then transform them to the physical space. If $(x, y, z)$ are the generic coordinates in the physical space and $(\xi, \eta, \zeta)$ are the generic coordinates in the computational space, a general transformation of the form

$$\xi = \xi(x, y, z)$$

$$\eta = \eta(x, y, z)$$

$$\zeta = \zeta(x, y, z)$$

can be used to transform the governing equations from the physical domain $(x, y, z)$ to the computational domain $(\xi, \eta, \zeta)$. The gradient of the generic velocity component $\phi$ may be written as

$$\frac{\partial \phi}{\partial x} = \frac{\partial \phi}{\partial \xi}\frac{\partial \xi}{\partial x} + \frac{\partial \phi}{\partial \eta}\frac{\partial \eta}{\partial x} + \frac{\partial \phi}{\partial \zeta}\frac{\partial \zeta}{\partial x}$$

$$\frac{\partial \phi}{\partial y} = \frac{\partial \phi}{\partial \xi}\frac{\partial \xi}{\partial y} + \frac{\partial \phi}{\partial \eta}\frac{\partial \eta}{\partial y} + \frac{\partial \phi}{\partial \zeta}\frac{\partial \zeta}{\partial y}$$

$$\frac{\partial \phi}{\partial z} = \frac{\partial \phi}{\partial \xi}\frac{\partial \xi}{\partial z} + \frac{\partial \phi}{\partial \eta}\frac{\partial \eta}{\partial z} + \frac{\partial \phi}{\partial \zeta}\frac{\partial \zeta}{\partial z}$$

where

$$\frac{\partial \xi}{\partial x} = \frac{1}{\bar{J}}\left(\frac{\partial y}{\partial \eta}\frac{\partial z}{\partial \zeta} - \frac{\partial y}{\partial \zeta}\frac{\partial z}{\partial \eta}\right)$$

$$\frac{\partial \xi}{\partial y} = -\frac{1}{\bar{J}}\left(\frac{\partial x}{\partial \eta}\frac{\partial z}{\partial \xi} - \frac{\partial x}{\partial \zeta}\frac{\partial z}{\partial \eta}\right)$$

$$\frac{\partial \xi}{\partial z} = \frac{1}{\bar{J}}\left(\frac{\partial x}{\partial \eta}\frac{\partial y}{\partial \zeta} - \frac{\partial x}{\partial \zeta}\frac{\partial y}{\partial \eta}\right)$$

$$\frac{\partial \eta}{\partial x} = -\frac{1}{\bar{J}}\left(\frac{\partial y}{\partial \xi}\frac{\partial z}{\partial \zeta} - \frac{\partial y}{\partial \zeta}\frac{\partial z}{\partial \xi}\right)$$

$$\frac{\partial \eta}{\partial y} = \frac{1}{\bar{J}}\left(\frac{\partial x}{\partial \xi}\frac{\partial z}{\partial \zeta} - \frac{\partial x}{\partial \zeta}\frac{\partial z}{\partial \xi}\right)$$

$$\frac{\partial \eta}{\partial z} = -\frac{1}{\bar{J}}\left(\frac{\partial x}{\partial \xi}\frac{\partial y}{\partial \zeta} - \frac{\partial x}{\partial \zeta}\frac{\partial y}{\partial \xi}\right)$$

$$\frac{\partial \zeta}{\partial x} = \frac{1}{\bar{J}}\left(\frac{\partial y}{\partial \xi}\frac{\partial z}{\partial \eta} - \frac{\partial y}{\partial \eta}\frac{\partial z}{\partial \xi}\right)$$

$$\frac{\partial \zeta}{\partial y} = -\frac{1}{\bar{J}}\left(\frac{\partial x}{\partial \xi}\frac{\partial z}{\partial \eta} - \frac{\partial x}{\partial \eta}\frac{\partial z}{\partial \xi}\right)$$

$$\frac{\partial \zeta}{\partial z} = \frac{1}{\bar{J}}\left(\frac{\partial x}{\partial \xi}\frac{\partial y}{\partial \eta} - \frac{\partial x}{\partial \eta}\frac{\partial y}{\partial \xi}\right)$$

and where $J$ is the Jacobian of the transformation

$$J = \begin{vmatrix} \frac{\partial \xi}{\partial x} & \frac{\partial \xi}{\partial y} & \frac{\partial \xi}{\partial z} \\ \frac{\partial \eta}{\partial x} & \frac{\partial \eta}{\partial y} & \frac{\partial \eta}{\partial z} \\ \frac{\partial \zeta}{\partial x} & \frac{\partial \zeta}{\partial y} & \frac{\partial \zeta}{\partial z} \end{vmatrix}$$

Velocity gradients are calculated at the centres of the volumes of the computational grid by using central difference approximations in the inner grid points and forward and backward difference approximations at the block grid boundaries. This procedure may be summarized for $\frac{\partial \phi}{\partial \xi}$ as follows:

$$\frac{\partial \phi}{\partial \xi} \approx \frac{\phi_{i+1} - \phi_{i-1}}{2} \qquad 1 < i < NI$$

$$\frac{\partial \phi}{\partial \xi} \approx \frac{3\phi_i - 4\phi_{i+1} + \phi_{i+2}}{2} \qquad i = 1$$

$$\frac{\partial \phi}{\partial \xi} \approx \frac{-3\phi_i + 4\phi_{i+1} - \phi_{i+2}}{2} \qquad i = NI\text{-}2$$

as $\Delta\xi$=1. NI is the number of cells in the I direction.

## Fully-developed Flow in a Rigid Tube

### Analytical Solution

For steady, fully-developed laminar flow in a circular tube, the velocity profile is parabolic. Hence, the shear stress distribution, being proportional to the velocity gradient, is linear, with a maximum value at the wall and zero at the tube centreline. The wall value is given by:

$$\tau_w = -\frac{1}{2}GR$$

where R is the radius of the tube and G is the pressure gradient along the pipe length. For a horizontal tube, the pressure gradient is found to be proportional to the volume flow rate $Q_v$:

$$G = \frac{8\mu}{\pi R^4} \times Q_v$$

where $\mu$ is the kinematic viscosity.

For example, a pipe of 10 mm radius, through which is flowing a fluid with viscosity $\mu = 4.0 \times 10^{-3}\ Pas$, and density $\rho = 1.0 \times 10^3\ Kg/m^3$, at a mass flow rate of $Q_v = 94.2 \times 10^{-6}\ m^3/s$ would experience a wall shear stress of $\tau = 4.8 \times 10^{-1}\ Pa$ ($\tau = 4.8\ dynes/cm^2$). The corresponding Reynolds number is $Re$=1500, which is comparable to the one calculated in the aorta under normal conditions or as the mean value in the SMV's duct, for the same pipe.

### Numerical Predictions

While it is not necessary to use a multi-block grid to solve for the flow in a tube, this type of grid was used because a similar grid was employed in the SMV calculations. The solution domain comprised a quarter of the tube in cross section similar to the grid employed in the SMV calculations, of 10 mm in radius, and 40 cm in length. The grid comprised three blocks (see Fig. H-1). This allowed a check of CFDS-FLOW3D's numerical solution at interblock interfaces. A symmetry plane boundary condition was applied on the perpendicular planes which bounded a quarter of the tube. Fully developed flow conditions were applied to both ends of the tube. The mass flow rate was set to be $Q_m = 94.2 \times 10^{-3}\ Kg/s$. The grid was constructed with the objective of having a more uniform grid spacing over the cross-sectional plane. Each block had $8 \times 8 \times 8$ grid cells; the total number of cells being 1536.

The results of the calculations for the fluid shear stresses are shown in Figs. H-2 and H-3 for the two different methods used. As can be seen, for both methods predicted shear stresses are distributed around the analytical solution over the entire radius. However, when the first method was used (use of the GRADDV subroutine) closer inspection of the predicted values for the individual blocks shows that the predictions in block 1 (the centre block) match the analytical solution in the 'inner' cells, but become a little less accurate in the interblock cells, and significant deviation is seen for the cell that is at the interface with the other two blocks. Similar trends are seen in blocks 2 and 3. It

may be concluded that although an accurate result was expected as the grid appeared uniformly spaced, the prediction appeared to be sensitive to the grid distortion presented (non-orthogonal faces).

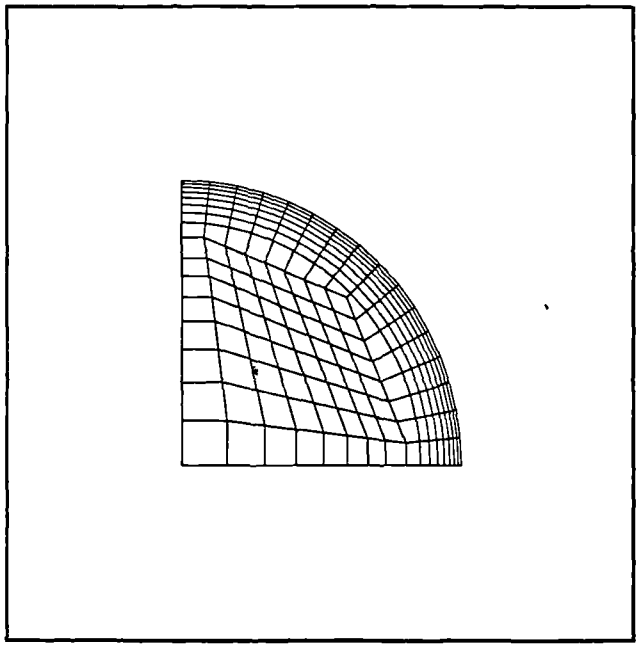

Figure H-1 Cross sectional view of the grid.

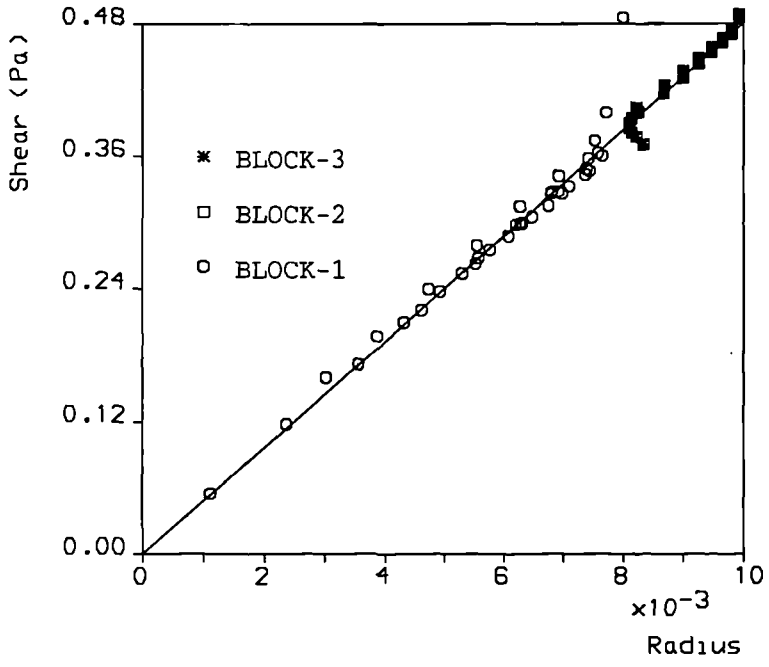


Figure H-2 Comparison of the predicted shear stresses with the analytical solution when the subroutine GRADDV was used.

Predicted shear stresses are compared with the analytical distribution in Fig. H-3 when the second method (calculation in the computational space) was used. As can be seen, this method produced an improvement in the values of predicted shear stress compared with the analytical solution. Therefore, this was used to calculate the shear

stresses for the following problem of flow with moving boundaries.

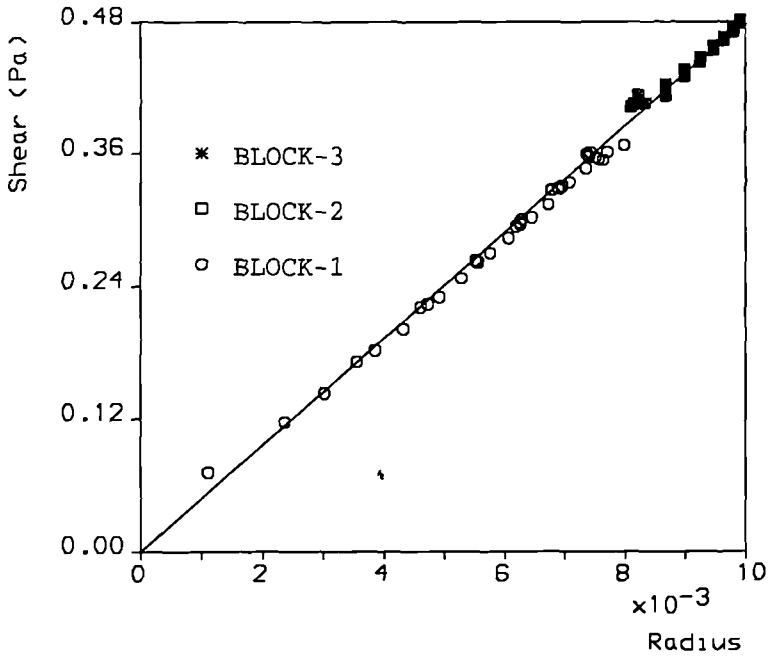


Figure H-3 Comparison of the predicted shear stresses with the analytical solution when the interpolation in the computational space was used.

## Transient Flow in an Expanding/Contracting Pipe

Analytical Solution

The analytical solution of the transient flow in an expanding/contracting pipe has been extensively discussed in Chapter 4. For such a solution, flow shear stresses may be calculated (Uchida and Aoki, 1977) from:

$$\tau = \mu\left(\frac{dv}{dx} + \frac{du}{dr}\right) = \frac{\rho\nu^2 x}{a^3}\eta\left(\frac{F_\eta}{\eta}\right)_\eta$$

Because the radial velocity profiles are similar in $x$, $\frac{dv}{dx} = 0$. Therefore only the axial velocity component is required to calculate the shear stress. This can be determined for each case considered from $u/u_m$ (calculated in Chapter 4) for given axial location and time. Considering eqs. (4.6) and (4.11), $\tau$ can be calculated as

$$\tau = \mu\frac{du}{dr} = \mu\frac{d(u/u_m)}{d\eta}\frac{1}{a}\left(\frac{-2\alpha\nu x}{a^2}\right)$$

where $a$ is given by eq. (4.8).

By differencing $u/u_m$ (calculated previously) at discrete points, and using a central difference approximation in the inner points and forward and backward difference approximations in the boundary points, the shear is calculated as a function of $\eta$ for a given time and location. Shear stress profiles are shown in Fig. H-4 as continuous lines for three cases with different expansion and contraction rates.

Numerical Predictions

Initial calculations were performed on a 'one-block' grid as used to validate the flow patterns in Chapter 4. The same simulation parameters were used. Three cases were considered at different wall Reynolds number $\alpha$: (a) $\alpha = 1.0$, (b) $\alpha = -10$, and (c) $\alpha = 1.67$. Results are shown in Fig. H-4 where they are compared with the analytical solution. Very good agreement was reached between the numerical and analytical solutions. For the 'three-block' configuration the grid is shown in Fig. H-1. Simulation parameters were identical to the 'one-block' case except the cross sectional grid. Numerical results have been compared in Chapter 7.

Particular attention was required in the choice of the axial location in order to have a good matching. The numerical model of the theoretical semi-infinite geometry is actually a finite pipe. Although velocity profiles were similar for quite a good axial extension far either from the closed end or the outlet of the numerical finite pipe, velocity gradients appeared to be very sensitive to the axial location. While a certain time of simulation is required to have a similar solution in time, it is also necessary to consider the flow patterns far from the closed end and outlet to have an axial similarity. Because the more the pipe expands or contracts the more the condition at the outlet is transported by convection toward the closed of the pipe, it is also necessary to consider an appropriate time of simulation. A compromise to overcome these two inconveniences requires the performance of simulations for different times and pipe lengths and subsequently to pick the shear distribution at various axial locations until a satisfactory matching solution is reached. Details of the time of simulation and location used for each of the cases shown in Fig. H-4 and Fig.7.61 are indicated in the figures.

The results discussed above lead to the conclusion that predicted shear stresses agree in general with the analytical solution. Small differences may be seen at the grid block interfaces due to the manner in which the flow variables are interpolated over the interfaces. However, some caution is required at grid-block interfaces especially when considering the calculation of the velocity gradient from GRADDV. The main reason for the inaccuracy at the interfaces is believed to be due to the way in which cell information is interpolated over the interfaces, and how this affects the calculation of velocity gradients.

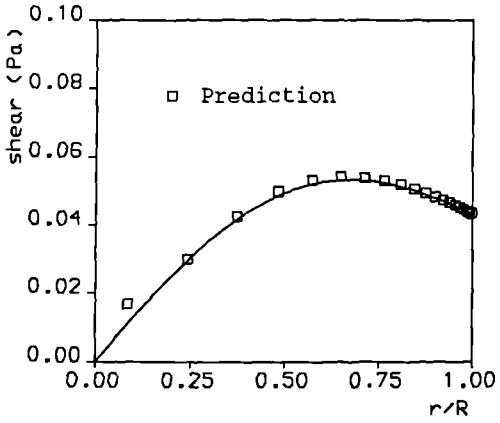


(a)

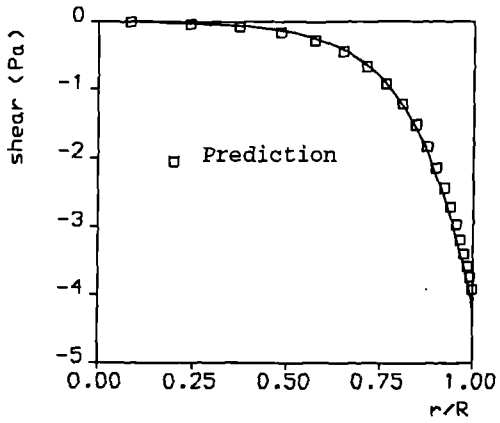


(b)

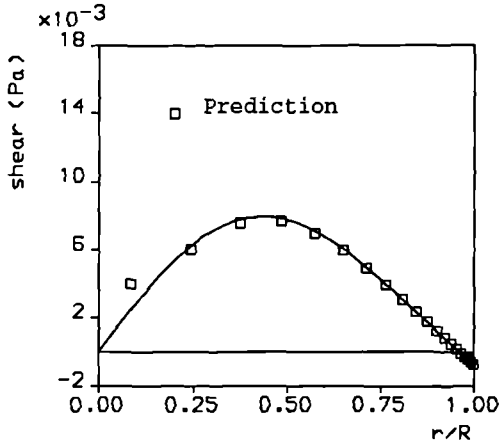


(c)

Figure H-4 Comparisons of the distributions of flow shear stress. (a) Expansion at $Re$=1.0; axial location X=0.046 m; time of simulation T=1.0 s. (b) Contraction at $Re$=10; X=0.13 m; T=1.0 s. (c) Expansion at $Re$=1.67; X=0.0154 m; T=3.0 s. One-block grid topology.

# APPENDIX I
## Published Papers

Shortland A., Iudicello F., Jarvis J.C., Henry F.S., Black R.A., Collins M.W. and Salmons S. (1993): Physical and numerical simulation of blood flow within a skeletal muscle ventricle.Proceedings of the World Symposium of Cardiomyoplasty and Biomechanical Assist, Paris (1993)

Iudicello F., Henry F.S., Collins M.W, Shortland A., Jarvis J.C., Black R.A., Salmons S. (1993): Numerical Simulation of the Flow in Model Skeletal Muscle Ventricles. Proc. Computers in Cardiology, London 1993 pp.377-380

Iudicello F., Henry F.S., Collins M.W., Shortland A.P., Jarvis J.C., Black R.A., Salmons S. (1994): Flow Structures Predicted in Model Skeletal Muscle Ventricles. BME 1994, Hong Kong pp.13-16

Henry F.S., Iudicello F., Shortland A., Black R.A., Jarvis J.C., Collins M.W., Salmons S. (1994): Modelling Wall Driven Cardiovascular Flows. Submitted to International Mechanical Engineering Congress & Exposition, Nov 6-11 1994, Chicago

Shortland A.P., Black R.A., Jarvis J.C., Henry F.S., Iudicello F., Collins M.W., Salmons S. (1995): Flow Visualization of Vortex Formation and Travel in a Model Ventricle: Application to the Design of a Skeletal Muscle Ventricle, 1994. Journal of Biomechanics. In Press

Henry F.S., Shortland A., Iudicello F., Black R.A., Jarvis J.C.,Collins M.W., Salmons S. (1995): Flow in a simple ventricle: Comparison between numerical and physical simulations. Submitted to ASME Journal of Biomechanical Engineering. Previsionally accepted.

# Numerical Simulation of the Flow in Model Skeletal Muscle Ventricles

F Iudicello[1], FS Henry[1], MW Collins[1],
A Shortland[2], JC Jarvis[3], RA Black[2], S Salmons[3]

[1]Thermo-Fluids Engineering Research Centre, City University, London, U.K.
[2]Department of Clinical Engineering, University of Liverpool, Liverpool, U.K.
[3]Department of Human Anatomy & Cell Biology, University of Liverpool, U.K.

## Abstract

*Numerical predictions of the flow created by a closed-end pipe expanding or contracting radially were compared with an analytical solution. Both single- and multi-block versions of the finite volume code FLOW3D were used. Flows of this type are of interest because they can be used as simple models of the flow in potential assist devices known as Skeletal Muscle Ventricles (SMVs). The work to be discussed is part of a comprehensive research programme on SMVs which comprises in vivo, in vitro and numerical studies. The main objective of the numerical study is to help in the design or streamline of an optimum ventricle shape and inlet/outlet configuration. Predictions of the flow fields inside simple model SMVs are presented.*

## 1. Introduction

During systole, contraction of muscle in the wall of the left ventricle reduces the vessel's internal volume and force the blood through the aortic valve. Throughout this pumping stage, the mitral valve is closed, and hence the ventricle resembles a closed-end cylinder which is contracting radially. In diastole, the muscle relaxes, the aortic valve closes, the mitral valve opens, and the ventricle refills. Again, the ventricle resembles a closed-end cylinder, but in this case the cylinder is expanding.

Similar physiological flows occur in a potential cardiac assist device known as a Skeletal Muscle Ventricle (SMV). An SMV is constructed by diverting a patient's own skeletal muscle from its normal function to perform a cardiac assist role [1,2]. Knowledge of the dynamics of the flow in such devices is of interest as high shear stresses can lead to haemolysis and platelet activation, while regions of stagnant flow can lead to thrombosis [3].

The purpose of the work to be described in this paper was to study numerically the flow in simple model SMVs, and to test whether the Computational Fluid Dynamics (CFD) code chosen to perform these calculations could predict accurately flows that are driven by the movement of the vessel wall. Calculations for the flow in a semi-infinite pipe which is either expanding or contracting are first compared with the analytical solution due to Uchida and Aoki [4]. Then calculations due to flow in somewhat more realistic models are presented and compared with *in vitro* data.

## 2. Model 1. The expanding/contracting pipe

The problem considered by Uchida and Aoki [4] was that of unsteady laminar flow in a semi-infinite contracting or expanding pipe. The closed end of the pipe was idealized as a compliant membrane which prevents axial motion of the fluid, but allows radial motion.

All calculations to be discussed were performed using Harwell-FLOW3D, which is a general purpose CFD code. The code uses body-fitted coordinates, and has a moving wall/grid facility. Since the flows considered were generated by moving boundaries, the latter feature was essential. Details of the code may be found in references [5-7]. Calculations using both the single-block version (Release 2.4), and the more versatile multi-block version (Release 3.1.2) of FLOW3D were tested against the solution of Uchida and Aoki [4]. Because of the simplicity of the solution domain, a grid comprising only a single axisymmetric block was in fact used in the multi-block calculations, which meant that the grids used in the two versions were identical. Also, polar coordinates were used in physical space in both versions.

0276-6547/93 $3.00 

In the numerical model, the pipe was defined to be fifteen diameters in length. The closed end was modelled as a symmetry plane, and the inlet/outlet plane was taken to be at athmospheric pressure. While the latter was not consistent with the analytical solution, it was found not to affect the predictions away from the boundary. Following Uchida and Aoki [4], the temporal variation of the pipe radius, $a$, was defined using the following formula.

$$a/a_0 = \sqrt{1 + 2\alpha(\nu t/a_0^2)} \qquad (1)$$

where $a_0$ is the initial pipe radius, taken as 10 $mm$,

$$\alpha = a'a/\nu = a_0'a_0/\nu$$

$\nu$ is the kinematic viscosity, taken as $4 \times 10^{-3}$ $m^2/s$ (the viscosity of the liquid used in the *in vitro* work), t is the time, and $a'$ is the time rate of change of the radius. The parameter $|\alpha|$ is a constant and can be taken to represent the Reynolds number of the flow. The sign of $\alpha$ indicates whether the pipe is contracting or expanding; e.g., $\alpha$ is negative when the tube is contracting.

In this paper only one case will be presented; an expansion with a Reynolds number equal to 1.67. This is an interesting case as a (small) reverse flow region was predicted analitically (Fig.6 in [4]). Various other rates of expansion and contraction were studied and these are discussed in Iudicello et al. [8]. Numerical and analytical results, in terms of axial and radial velocities, are given in Figs. 1 and 2 for the single-block version, and in Figs. 3 and 4 for the multi-block version. It can be seen that the predictions match well the analytical curves. However, it was found necessary to have a larger simulation time to establish the correct velocity profiles for this case, namely 3.0 s as opposed to 1.0 s used for the other cases. This was found to be true for both single- and multi-block grids.

The current numerical predictions are entirely consistent with Uchida and Aoki's solution [4], the chief feature of which is similarity in both in both $x$, the axial direction, and time. While the solution is restricted to a type of wall motion that does not represent well that of an SMV; i.e., it is not periodic, but is either expanding or contracting, and the Reynolds number (based on the wall speed) is rather low, it does offer some useful features. For instance, it is not restricted to small wall movements, in contrast to the solution of a flow in a channel with pulsating walls given by Secomb [9]. Also, being a solution of the full Navier-Stokes equations, it represents the viscous nature of blood flow as opposed to the model of Jones [10] for the unsteady flow of an inviscid fluid in pulsating bulbs.

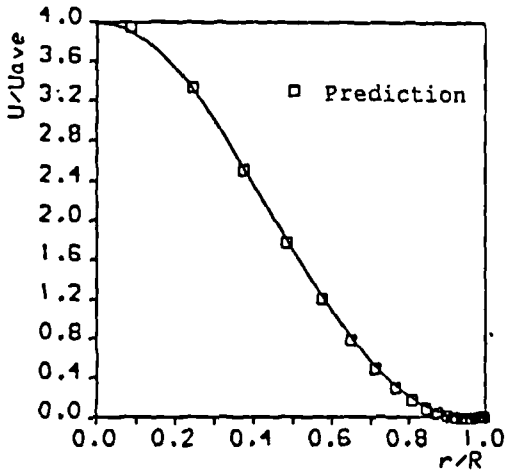


Figure 1. Axial velocities. Single-block version.

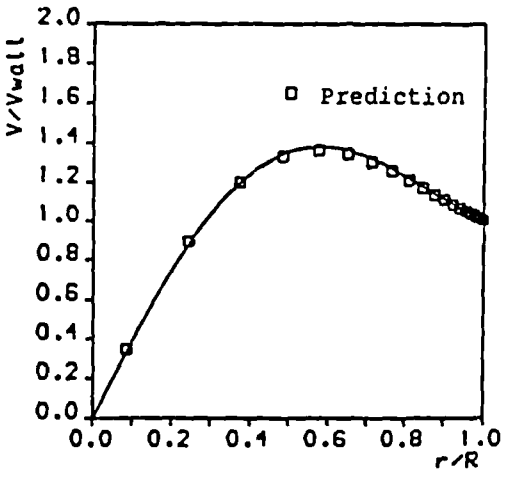


Figure 2. Radial velocities. Single-block version.

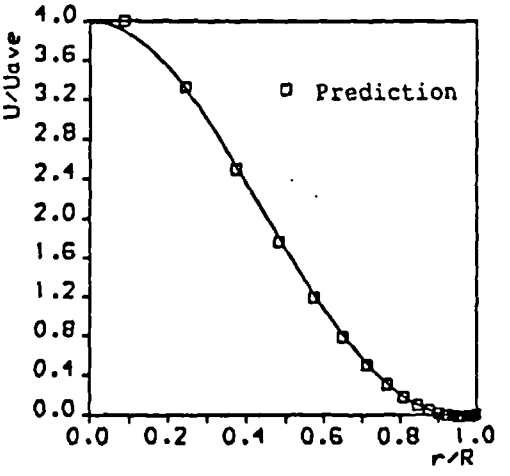


Figure 3. Axial velocities. Multi-block version.

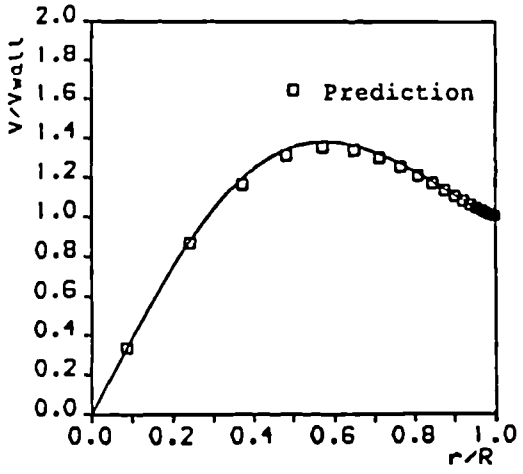


Figure 4. Radial velocities. Multi-block version.

## 3. Model 2. The rigid/compliant pipe

The obvious limitation of the model considered in the previous section is that an SMV has a finite length, and hence a similarity solution in $x$ cannot be developed. Also, the pulsatile motion of the SMV wall means that a similarity solution in time is not possible. Further, it is likely that the SMV will be fed by a rigid tube. While an analytical solution encompassing the preceding features is almost certainly unattainable, the authors have performed *in vitro* studies with which numerical predictions can be compared. The preceding model was modified to include a rigid inlet/outlet tube, and the wall motion was made sinusoidal. This will be referred to as the rigid/compliant pipe model.

In the *in vitro* studies, the flow fields inside elastomer models were visualized throughout the cycle using a plane of laser light illuminating suspended particles in the fluid, and photographs were taken in diametral planes [11]. A typical *in vitro* model SMV is shown in Fig.5. All the model SMVs studied to date have rigid inlet tubes, and hence, over part of the cycle at least, the flow geometry resembles that of a sudden pipe expansion. As would be expected, this produces flow separation and recirculation. The primary recirculation is usually accompanied by a second and possibly a third recirculating region. This complex pattern occurs when the ventricle's volume is approaching its maximum value.

The essential features of the flow in an SMV can be compared with a channel with a symmetrical indentation. Numerical and experimental works have been presented on the flow in channels with indentation. Tutty [12] studied pulsatile flows through a plane channel with an indentation and his predicted results are supported by the experimental finding of Sobey [13]. The flow fields show trains of counter-rotating vortices which show different features for different frequencies and Reynolds numbers of the upstream flows. Furthermore, Pedley [14] has described experimental and theoretical two-dimensional unsteady flows in a channel with a time-dependent indentation which moves sinusoidally.

Predictions using the single-block version of the code are given in Figs 6 and 7 of the flow in the rigid/compliant pipe models for a time of maximum ventricular volume; the model in Fig.7 represents a ventricle of twice the length of the model in Fig.6. Note only part of the ventricle is shown in Fig.7 in order to better show the recirculation regions. The moving boundary in the compliant section undergoes a sinusoidal variation of the radius of $\Delta r = 40\%$, and of the length of $\Delta x = 20\%$. It is noted that the characteristic two-vortex structure can be seen in both figures.

Work is underway to describe more accurately the geometry of the *in vitro* model SMVs. Wall movement data taken from photographs of the *in vitro* models are being used to drive the numerical simulations.

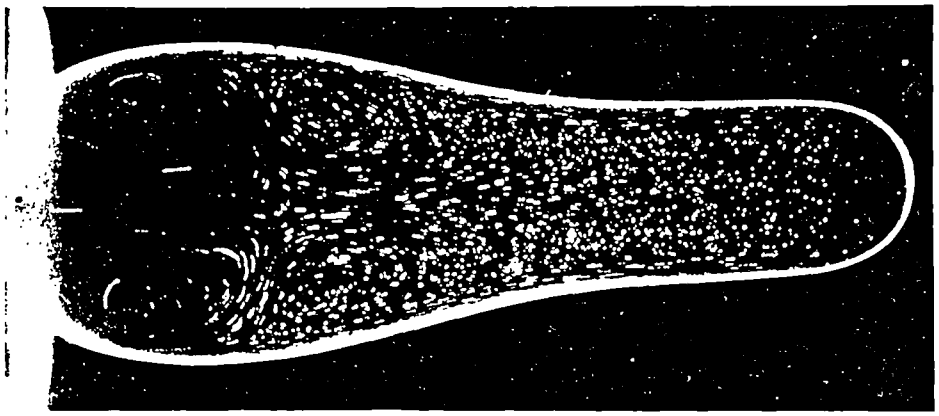

Figure 5. *In vitro* model SMV.

Both single- and multi-block models are being constructed. To date, while these more realistic models predict most of the features seen in the experimental data, they do not predicted the second vortex at maximum ventricular volume. The reason, or reasons, for this disparity is currently being investigated.

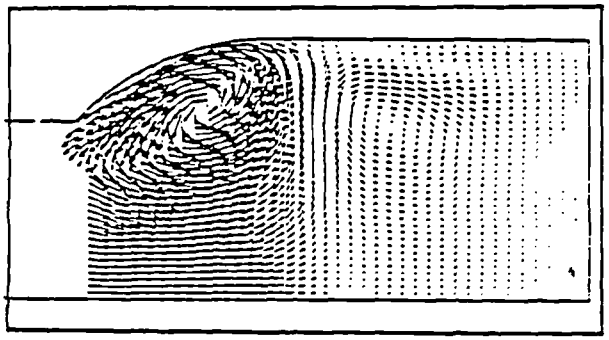

Figure 6. Rigid/compliant model SMV ($L_{ventricle} = 3 \times R_{inlet}$).

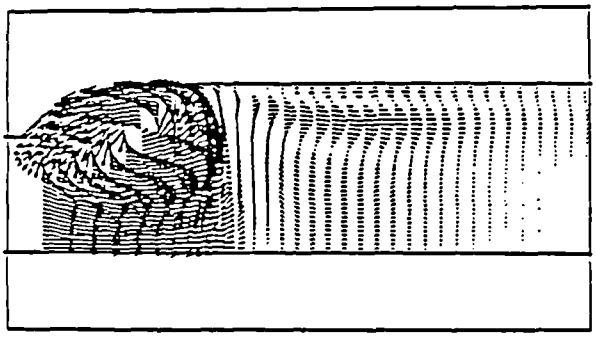

Figure 7. Rigid/compliant model SMV ($L_{ventricle} = 6 \times R_{inlet}$).

## 4. Conclusion

Predictions of the flow generated by a semi - infinite expanding pipe have been performed and have been shown to agree with an analytical solution due to Uchida and Aoki [4]. Also, predictions of the flow within model SMVs using sinusoidally prescribed motion of the wall are presented. The predicted flow fields show good agreement over the period with the experimental flow field seen in the *in vitro* study for a similar model. This work is being extended by simulating the flow in the same model SMV analyzed above using the *in vitro* data for the wall position throughout the cycle.

## Acknowledgements

This work has been supported by grants from the British Heart Foundation.

# References

[1] Acker MA, Hammond RL, Mannion JD, Salmons S, Stephenson LW. Skeletal muscle as the potential power source for a cardiovascular pump: assessment in vivo. Science 1987; 236;324-327

[2] Salmons S, Jarvis JC. Cardiac assistance from skeletal muscle: a critical appraisal of the various approaches. Br Heart J 1992;68:333-338.

[3] Stein PD, Sabbah HN. Measured turbulence and its effect on thrombus formation. Circ Res 1974; 35:608-614.

[4] Uchida S, Aoki H. Unsteady flows in a semi-infinite contracting or expanding pipe. J Fluid Mech 1977; 82:371-387

[5] Hawkins IR, Wilkes NS. Moving Grids in Harwell FLOW3D. AEA Industrial Technology, Harwell Laboratory, Oxfordshire, U.K 1991.

[6] Anonymous. FLOW3D Release 2.4: User Manual. AEA Industrial Technology, Harwell Laboratory, Oxfordshire, U.K 1991.

[7] Anonymous. FLOW3D Release 3.1.2: User Manual. AEA Industrial Technology, Harwell Laboratory, Oxfordshire U.K. 1991.

[8] Secomb TW. Flow in a channel with pulsating walls. J Fluid Mech 1977; 88: 273-288

[9] Jones RT. Motions of a liquid in a pulsating bulb with application to problems of blood flow. Med & Biol Eng 1970, 8:45-51

[10] Iudicello F, Henry FS, Collins MW. A Comparison between numerical and analytical solutions of unsteady flows in a contracting or expanding pipe. Internal Report, City University, London, U.K 1993.

[11] Shortland AP, Iudicello F, Jarvis JC, Henry FS, Black RA, Collins MW, Salmons S. Physical and numerical simulation of blood flow within a skeletal muscle ventricle. Paris: Proc World Symp Cardiomyoplasty and Biomechanical Assist 1993.

[12] Tutty OR. Pulsatile flow in a constricted channel. ASME J Biomech Eng 1992; 114:50-54

[13] Sobey IJ. Observation of waves during oscillatory flow. J. Fluid Mech 1985; 151: 395-426

[14] Pedley TJ. Flow along a channel with a time-dependent indentation in one wall: the generation of vorticity waves. J Fluid Mech 1985; 160: 337-367

Adress for correspondence.

Francesca Iudicello
Thermo-Fluids Engineering Research Centre,
City University, Northampton Square,
London EC1V 0HB, U.K..

# FLOW STRUCTURES PREDICTED IN MODEL SKELETAL MUSCLE VENTRICLES

F. Iudicello[1], F.S. Henry[1], M.W. Collins[1],
A. Shortland[2], J.C. Jarvis[3], R.A. Black[2], S. Salmons[3]
[1]Thermo-Fluids Engineering Research Centre, City University, London, U.K.
[2]Department of Clinical Engineering, University of Liverpool, Liverpool, U.K.
[3]Department of Human Anatomy & Cell Biology, University of Liverpool, U.K.

## INTRODUCTION

Computational Fluid Dynamics (CFD) represents a new method of research into blood flow in the cardiovascular system [1]. Modern CFD codes solve the equations governing unsteady, three-dimensional flows in complex, moving geometries. Numerical simulations of flows in cardiac assist devices can be used to study the effect on the flow of the shape and size of the device, and of the orientation of inlet and outlet ducts. The objective is to optimize performance , while at the same time minimizing the risk of haemolysis and thrombogenesis. Among such devices the Skeletal Muscle Ventricle (SMV) shows much promise. An SMV is obtained by diverting a patient's own skeletal muscle from its normal function and configuring it as an auxiliary pump [2,3].

The essential features of the flow in an SMV are (i) flow separation and (ii) regions of recirculation. Similar features have been shown to exist, both experimentally [4] and numerically [5], in pulsatile flows in channels with rigid constrictions. These flow fields show trains of counter-rotating vortices whose features are related to the frequency and Reynolds number of the upstream flow. Further, Pedley [6] has shown similar flow patterns in an experimental and theoretical study of two-dimensional unsteady flow in a channel with a time-dependent indentation that moves sinusoidally.

Flow in an SMV is driven by the movement of the ventricle wall, and it is therefore essential to use a CFD code with a moving wall/grid facility. The general purpose code CFDS-FLOW3D provides this in both the single-block version (Release 2.4) and multi-block versions (Release 3.2.1). A multi-block grid allows problems with complex geometries to be gridded more efficiently. Details of the code can be found in references [6,7]. Validation of the moving-grid capability of the single- and multi-block versions of CFDS-FLOW3D was performed by the authors [9,10] for the flows in a semi-infinite expanding/contracting pipe. Good agreement was found between predictions and analytical solution.

In this paper, flow patterns in two numerical model SMVs are presented: a simple rigid/compliant model and a spherical-end rigid/compliant model. Calculations were performed using both single- and multi-block versions of CFDS-FLOW3D.

## SIMPLE RIGID/COMPLIANT MODEL

The simple model comprises a compliant closed-end cylinder attached to a rigid inlet tube. An example of the predicted flow field in this model is shown in Fig.1. The walls of the compliant section were prescribed to expand radially in a simple sinusoidal

fashion. The radius changed from a minimum of 11.5 mm, to a maximum of 16.1 mm, while the length was fixed at 30 mm . The ejected volume was approximately 28% of the minimum ventricular volume . More details of this model may be found in reference [10].

The flow field shown in Fig.1 was predicted using the multi-block version of CFDS-FLOW3D, and represents the flow at maximum ventricular volume, that is, at the time when the ventricle is passing from the filling to the pumping phase. The cycle frequency is 1.33 $Hz$. A clear two vortex structure is visible, while a third weaker vortex ring is shown close to the wall of the straight compliant tube. This configuration was not significantly affected by a change in frequency between 1.0 and 2.0 $Hz$. The same results were predicted by the single-block version of the code with the same grid and simulation parameters.

## SPHERICAL-END COMPLIANT/RIGID MODEL

This model was defined by reference to data from the first series of *in vitro* SMV studies [3]. The model is similar to the above simple model, but it has a spherical rather than a square end. The model undergoes a significant change in shape, from a cylinder with a spherical end at minimum ventricular volume to an almost totally spherical shape, at maximum ventricular volume (Fig.2). The wall expands radially in the same fashion as in the simple model. The cycle frequency was changed within the range of 0.3-3$Hz$. The same grid was used for both single- and multi-block versions of the code.

As in the previous case, the chief feature of the predicted flows in the spherical-end model is the formation of recirculation regions, or vortex rings, at the time of maximum ventricular volume. In this case, however, different flow structures are predicted as the frequency of the wall motion varies. At low frequencies, only the primary recirculation, close to the inlet wall, is predicted to occur. This is shown in the flow field given in Fig.3, which represents the flow structure at the time of maximum ventricular volume with the ventricle driven at a frequency of 0.3 $Hz$. Above this frequency, a second recirculation forms. Two vortex rings can be seen in the flow field given in Fig.4, which represents the flow in the ventricle at a frequency of 1.25 $Hz$. At a frequency between 1.25 and 1.33 $Hz$, a third vortex is formed. The three-vortex flow structure can be seen in Fig. 5, for a frequency of 1.33 $Hz$. The frequency was increased to 3.0 $Hz$ without further vortices appearing. The result for a frequency of 3.0 $Hz$ is shown in Fig.6.

The flow fields presented in Figs. 3 to 6 were predicted using the multi-block version of the code. Predictions using the single-block version were performed for the same frequency range. While the predicted flow fields agreed in general, the frequency at which three vortices were formed was found to be somewhat lower than in the multi-block version. Table 1 summarizes the predicted results for the flow structures over the frequency range 0.3-3.0 $Hz$ for both versions of the code. The reason for the differences is as yet unexplained.

## CONCLUSIONS

Numerical simulations of the flow in model SMVs were performed. The flows are driven by prescribed sinusoidal motion of the wall in both radial and axial directions. The predicted flow structures show that the number of vortex rings formed at the time

of maximum ventricular volume is a function of the frequency of the wall motion. The number of vortices increased with the frequency.

A similar connection between vortex structure and frequency has been seen in the *in vitro* model SMVs [11]. These results indicate that modern CFD codes, such as CFDS-FLOW3D, are probably capable of simulating physiological flows in actual SMVs.

ACKNOWLEDGEMENT

We are grateful to the British Heart Foundation for their financial sponsorship.

Table 1
Vortex structures over the frequency range

| Number of vortices | 1 | 2 | 3 |
|---|---|---|---|
| Single-block version | below 0.3 $Hz$ | 0.3-1.38 $Hz$ | 1.38-3.0 $Hz$ |
| Multi-block version | below 0.3 $Hz$ | 0.3-1.25 $Hz$ | 1.25-3.0 $Hz$ |

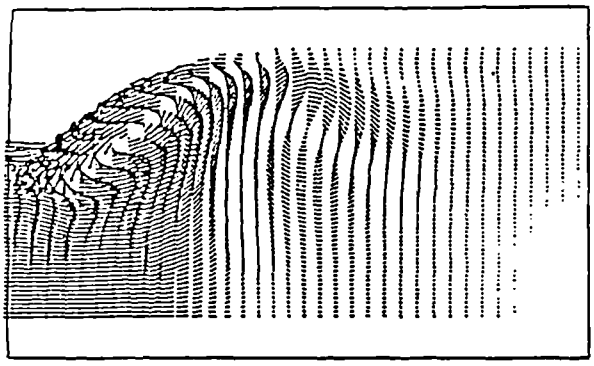

Figure 1. Simple rigid/compliant model using the multi-block version of FLOW3D

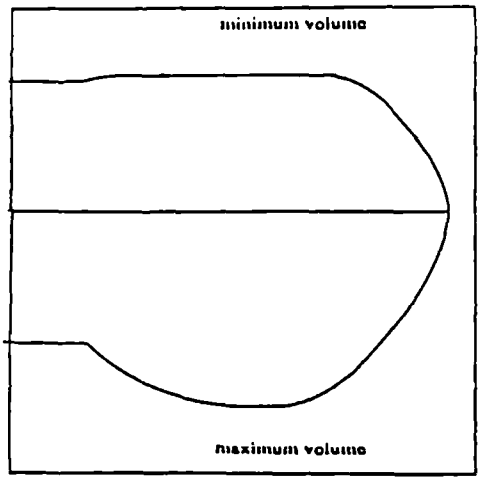


Figure 2. Spherical-end model at minimum and maximum volume

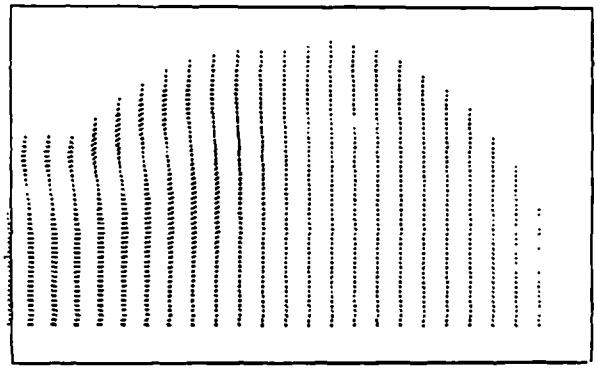

Figure 3. Spherical-end model: $f = 0.3\ Hz$

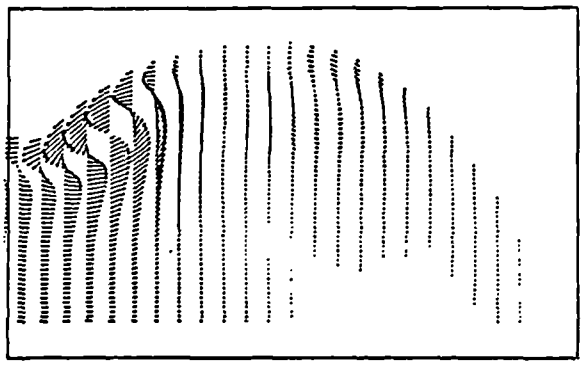

Figure 4. Spherical-end model: $f = 1.25\ Hz$

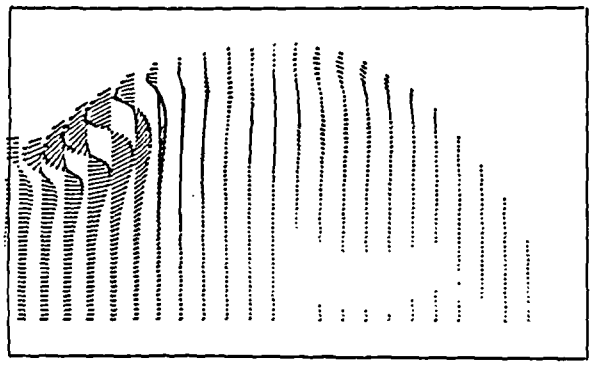

Figure 5. Spherical-end model: $f = 1.33\ Hz$

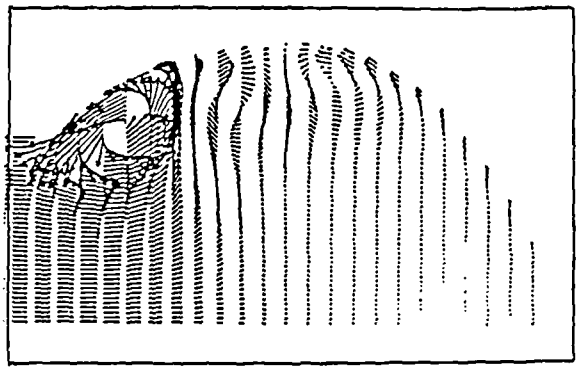

Figure 6. Spherical-end model: $f = 3.0\ Hz$

REFERENCES


[1] Henry F.S., Collins M.W. In: Advances in Haemodynamics and Haemorheology, ed., T.V. How, JAI Press, London 1993.

[2] Acker M.A., Hammond R.L., Mannion J.D., Salmons S., Stephenson L.W. Science 236: 324-327, 1987.

[3] Salmons S., Jarvis J.C. British Heart J 68: 333-338, 1992.

[4] Sobey I.J. J. Fluid Mechanics 151: 395-426, 1985.

[5] Tutty O.R. ASME J Biomechanical Engineering 114: 50-54, 1992.

[6] Pedley T.J. J. Fluid Mechanics 160: 337-367, 1985.

[7] Anonymous. FLOW3D Release 2.4: User Manual. AEA Industrial Technology, Harwell Laboratory, Oxfordshire, U.K 1991.

[8] Anonymous. FLOW3D Release 3.1.2: User Manual. AEA Industrial Technology, Harwell Laboratory, Oxfordshire U.K. 1991.

[9] Iudicello F., Henry F.S., Collins M.W. Internal Report, City University, London, U.K 1993.

[10] Iudicello F., Henry F.S., Collins M.W, Shortland A., Jarvis J.C., Black R.A., Salmons S. Proc. Computers in Cardiology, London 1993.

[11] Shortland A.P., Iudicello F., Jarvis J.C., Henry F.S., Black R.A., Collins M.W., Salmons S. Paris: Proc. World Symp. Cardiomyoplasty and Biomechanical Assist 1993.

BED-Vol. 28, 1994 Advances in Bioengineering
ASME 1994

# MODELLING WALL-DRIVEN CARDIOVASCULAR FLOWS

**Frank S. Henry, Francesca Iudicello, and Michael W. Collins**
Dept. of Mechanical Eng. and Aeronautics
City University
London, United Kingdom

**Adam Shortland and Richard A. Black**
Dept. of Clinical Engineering
University of Liverpool
Liverpool, United Kingdom

**Jonathan C. Jarvis and Stanley Salmons**
Department of Human Anatomy and Cell Biology
University of Liverpool
Liverpool, United Kingdom

## ABSTRACT

Wall-driven flows are common in biofluid mechanics, but detailed analysis of this class of flow has been hampered by the general lack of closed-form solutions for viscous flows with moving boundaries. Modern computational methods promise a solution to these difficulties, and the results of a series of calculations for a particular wall-driven flow are discussed in this paper. It is concluded that while it is possible to calculate the general features of such flows, great care should be exercised in applying these methods to situations for which experimental data does not exist.

## INTRODUCTION

Wall-driven flows occur naturally in the heart, lungs, and bladder. Flows in many artificial hearts and cardiac assist devices are also generated by the setting of all or part of their walls in motion. While this type of flow is evidently prevalent in biofluid mechanics, analyses of such flows are few. Mathematical analysis of wall-driven viscous flow is impossible for all but the simplest of geometries. However, recent advances in computational methods means that numerical analysis of such flow is possible, at least in principle. In practice, the scope of an investigation may be restricted by the available computing power, and a lack of data of sufficient quality with which to validate the numerical predictions. There are several Computational Fluid Dynamics (CFD) codes available today that offer a moving grid/wall facility. The purpose of this paper is to examine the ability of one such code to predict the flow in a model cardiac assist device. Whole-field measurements of the flow in the model device were available for comparison.

## THE PHYSICAL MODEL

The device considered is known as a Skeletal Muscle Ventricle (SMV), see Salmons and Jarvis (1992). The *in–vitro* model SMV comprises a thin-walled, translucent elastomer ventricle which is submerged in a sealed, fluid-filled, chamber. The general shape of the ventricle is that of a closed-end cylinder. The ventricle was attached to a rigid inlet/outlet tube, which was in turn attached to a constant head tank. The working fluid was a 40% aqueous-glycerol solution. The fluid was seeded with a small amount of 150-200 micron diameter Rilsan Blue particles (Atochem, Puteaux, France) to allow flow visualization. The tank was filled with the same aqueous-glycerol solution. Wall movement was generated by the action of a computer-driven, positive-displacement, pump attached to the fluid-filled chamber. Video and still photographs of the flow in the SMV were taken in diametral planes which were illuminated by a sheet of laser light. Measurements in different diametral planes, revealed the flows to be axisymmetric. Various ventricle shapes and wall-movement profiles have been studied.

## THE NUMERICAL MODEL

The Navier-Stokes equations were solved on a moving grid using CFDS-FLOW3D (AEA Technology, Harwell, UK). The code is based on the finite volume method, and uses fully-implicit time marching when the moving grid option is invoked. A variety of pressure correction schemes, and several advection models are available. As well as flow details, the experimental set up allowed the wall position to be measured at 40 *ms* intervals. At each time interval, the radial and axial positions of 40 equi-spaced points along the vessel wall were recorded. These data were used to drive the numerical solution. The entrance to the inlet/outlet tube was assumed to be a plane of constant pressure. The flow was assumed to be axisymmetric, and to remain laminar at all times.

## RESULTS AND DISCUSSION

A common feature of the flow in the model SMV is the appearance of a strong vortex ring downstream of the ventricle entrance. The vortex forms in the filling phase, and is a consequence of the main flow separating from the wall at the ventricle entrance. In the case of oscillatory wall motion, a second

vortex ring usually forms, downstream of the first. However, if the ventricle wall motion is arrested at maximum volume, the second vortex ring does not form, and the first vortex is seen to travel down the ventricle towards the apical end, where it eventually dissipates.

Given in Fig. 1 is a velocity vector plot of the predicted flow field in a typical model SMV. The time history of a point on the ventricle wall is given in Fig 2, and it can been seen that this is a case where the wall motion is arrested at maximum volume. Specifically, the wall follows a sigmoidal path and then remains at the maximum value. The flow field of Fig. 1 is for a time of 480 *ms* which can be seen from Fig. 2 to be towards the end of filling phase. Clearly, the vortex is well established at this point.

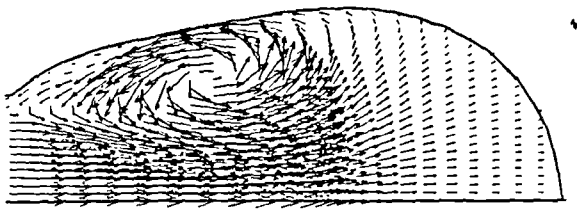

Figure 1. Flow at T = 480 *ms*

Given in Fig. 3 are the predicted and measured positions of the vortex core as it moves towards the apical end. The curves represent the distance travelled by the vortex core in one second, starting from inception. The vortex appeared in the *in-vitro* model at 280 *ms*, whereas it was discernible at 240 *ms* in the prediction. Inspection of Fig. 3 reveals that the measured vortex core moves closer to the ventricle centreline as the filling phase comes to an end. The radial movement is well predicted for about a quarter of the overall time, when it diverges to an overestimate of about 20% However, no further divergence occurs. Also, the predicted overall axial distance travelled is quite close to that measured.

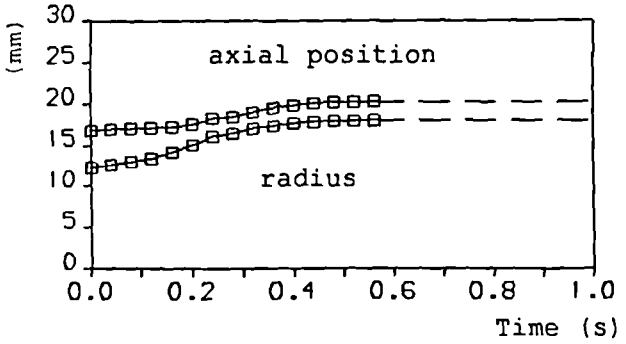


Figure 2. Time history of typical wall point

Similar differences between experiment and prediction have been found in the other ventricle shapes and wall-movement profiles studied. Being able to predict accurately the dynamics of the vorticies is important clinically, as this will affect the prediction of residence times, and shear stresses at the wall and within the flow. It is not possible to discuss fully here the details of the other predictions, but some general points can be made. On the positive side, the code appears able to predict the general features of wall-driven flow. It has been found to be robust, and mass conservative. However, the dynamics of the vortex rings have not been well predicted, in general. The particular advection model and pressure correction scheme used has been found to have only marginal effects on the resulting predictions. The grid and time-step dependency studies that have been carried out suggest that the errors are not due to these types of inaccuracy. However, due to computer CPU time and memory limitations, completely grid and time-step independent solutions have not yet been achieved in the oscillatory cases.

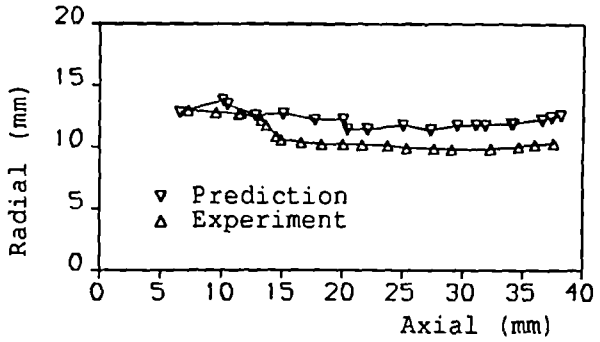


Figure. Vortex core path 3

## CONCLUSIONS

A general purpose CFD code with a moving grid capability has been applied to the prediction of the flow in a model cardiac assist device. It has been shown that while the code can predict the qualitative features of the flow, quantitative differences of about 20% were found between the predictions and corresponding experimental data. It is noted that the flows considered, being axisymmetric, are somewhat simpler than would be found either in nature, or in the *in-vivo* SMV. Modelling the whole flow field, as opposed to a diametral slice, would greatly increase the size of the grid, and hence, increase the cost of the computation. This would further limit the amount of grid and time step refinement possible. These considerations underline the need for a cautions approach to the application of CFD to complex flow situations for which data of sufficient accuracy is not available for validation purposes.

## ACKNOWLEDGMENT

This work is funded by a grant from the British Heart Foundation.

## REFERENCES

Salmons, S. and Jarvis, J.C., 'Cardiac Assistance from Skeletal Muscle: A Critical Appraisal of the Various Approaches,' British Heart Journal, 68, pp. 333-338, 1992.